

**A Crack Growth Based Approach to the
Fatigue Assessment of Cast Iron Components**

Volume 1

by

P.M. Hughes BSc(Hons) CEng MIMechE

**Submitted in partial fulfillment of the requirements for
the award of the degree of
DOCTOR OF PHILOSOPHY
in the Department of Engineering,
University of Leicester
December 1998**

UMI Number: U536074

All rights reserved

INFORMATION TO ALL USERS

The quality of this reproduction is dependent upon the quality of the copy submitted.

In the unlikely event that the author did not send a complete manuscript and there are missing pages, these will be noted. Also, if material had to be removed, a note will indicate the deletion.



UMI U536074

Published by ProQuest LLC 2013. Copyright in the Dissertation held by the Author.
Microform Edition © ProQuest LLC.

All rights reserved. This work is protected against
unauthorized copying under Title 17, United States Code.



ProQuest LLC
789 East Eisenhower Parkway
P.O. Box 1346
Ann Arbor, MI 48106-1346

DECLARATION

I hereby declare that I am the sole author of this thesis and that all work presented is my own, with the exception of references made to the work of other authors. I also declare that this work has not been submitted as an exercise for a degree to any other universities or colleges.

I authorise the University of Leicester to lend or copy this thesis on request.


P.M. Hughes

December 1998

ACKNOWLEDGEMENTS

I wish to express my thanks to Dr Bill Manners for his guidance, support and patience during the long period over which this work has spanned.

I would like to thank the team involved in BRITE/EURAM Project ENDDURE, particularly Dr Derek Allen of what is now ALSTOM Energy Technology Centre, Whetstone. Without BRITE, and the support for this research provided by Derek, many of the resources to carry out this work would not have been available.

I would like to thank Dr Pam Murrell of Cast Metals Development Ltd. The experimental data generated through links with this organisation has been extremely valuable to this work, and should provide much useful data to researchers for years to come.

I should also like to thank Don Sinha of Ruston Diesels Ltd. It was Don who originally posed the problem to me of assessing the fatigue strength of cast iron components when finite element analysis results are available. Almost ten years on, and a lot of interesting work has been done. I hope that the work described here goes some way towards providing a solution.

A Crack Growth Based Approach to the Fatigue Assessment of Cast Iron Components

P.M. Hughes

ABSTRACT

This work focusses on the problem of predicting the fatigue strength of engineering components where the geometry and stress distribution differ from conventional notched fatigue test specimens. The traditional approach based on the use of a net section nominal stress is therefore difficult to apply. The use of estimated local surface stresses and strains can lead to misleading and often highly erroneous predictions of the fatigue strength at high ($\approx 10^7$) cycles, particularly for components manufactured in cast iron, since this type of material exhibits a relatively high notch insensitivity in fatigue tests.

The work is of a theoretical nature, but makes use of the availability of a significant quantity of recent experimental data on cast iron test specimens of various grades, geometries and loading conditions. An approach based on the calculation of the condition for crack arrest has been investigated as a means of predicting fatigue strength. The finite element method has been used to help calculate the range of stress intensity factor (ΔK) values for cracks in notched fatigue specimens of various geometries. The ΔK value at a number of different crack sizes is compared with the apparent short crack threshold value. If the ΔK value for a growing crack becomes less than the threshold value (ΔK_{th}) then the crack is assumed to arrest.

Comparisons between the predicted strengths and the estimated values from the test data show that a crack growth assessment procedure based on a continuous surface crack geometry at the notch root gives a reasonable approximation to the data and can account for the effects of geometry, stress distribution and mean stress. The inclusion of a short crack model makes the procedure particularly relevant to assessments of cast iron components, however, limited comparisons with notched data for other materials were also favourable.

CONTENTS

DECLARATION	i
ACKNOWLEDGEMENTS	ii
ABSTRACT	III
CONTENTS	iv
NOTATION	viii
1. INTRODUCTION	1
2. HIGH CYCLE FATIGUE DESIGN METHODS FOR STRESS CONCENTRATIONS: A REVIEW	5
2.1 An Overview of Published Notched Fatigue Data	5
2.2 Nominal Stress Based Approaches	7
2.3 Local Strain Based Approaches	10
2.3.1 Local Surface Stresses and Strains	10
2.3.2 Sub-surface Behaviour (Critical Depth Approaches)	18
2.4 Fracture Mechanics Based Approaches for Notches	21
2.4.1 Geometrically Small Stress Concentration Features and Short Cracks	25
2.4.2 Short Fatigue Cracks at Notches	33
2.5 Discussion	39
3. CAST IRON NOTCHED TEST DATA AND ANALYSES	41
3.1 Grade 17 Grey Iron Tests (BRITE Project Specimens)	41
3.1.1 Experimental Procedure	41
3.1.2 Experimental Results	49
3.1.3 Description of Analysis Models of Test Specimens	56

3.1.4 Description of Analysis Results	58
3.1.5 Comparison of Calculated and Measured Notched Specimen Response	60
3.1.6 Discussion	64
3.2 Grade 250/350 Grey Iron, Grade 400/500 SG iron (BCIRA Project)	66
3.2.1 Experimental Procedure	66
3.2.2 Experimental Results	70
3.2.3 FE Analyses of Notched Specimens	71
3.3 Grade 300 Grey Iron	72
3.4 Diesel Engine Bedplate Example	75
3.5 Discussion	76
4. A REVIEW OF THE LITERATURE ON FATIGUE FAILURE MECHANISMS IN CAST IRON	79
4.1 Fatigue Failure Mechanisms Generally Observed in Metals	79
4.2 Fatigue Failure Mechanisms Observed in Grey Cast Iron	82
4.3 Fatigue Failure Mechanisms Observed in Spheroidal Graphite Cast Iron	89
4.4 Fatigue Mechanisms Observed at Notches in Various Materials	90
4.5 Discussion	95
5. A CRACK GROWTH BASED APPROACH FOR CAST IRON	97
5.1 Overall Description of the Approach	97
5.2 Linear Elastic Analyses of Cracks at Notch Roots by Finite Element Analysis	100
5.2.1 The Use of F.E. for Crack Analyses	100
5.2.2 Two-Dimensional/Axisymmetric Analyses of Notched Specimens	104
5.2.3 Three-Dimensional Crack Analyses: Straight and Curved Crack Fronts	108
5.2.4 Simulation of Crack Growth in Linear Elastic Stress Fields at Notches	112
5.2.5 Three-Dimensional Crack Analyses of Grey Iron Notched Specimens	122
5.3 Simulation of the Effects of Residual Stresses on Notch Root Cracks	125
5.3.1 Description of the Method of Analysis	125
5.3.2 Description of the Analyses and Results	126
5.4 Approximation Procedures for Stress Intensity Factor Estimation	136

5.4.1 Method of Albrecht and Yamada (1977)	137
5.4.2 Method of Newman and Raju: Semi-elliptical Defect in a Plate (1979)	139
5.4.3 Method of Kopsov (Ref. 1992)	141
5.4.4 K Estimate based on Local Stress Value	142
5.4.5 K Estimate Based on Two-dimensional K Solution	142
5.4.6 Comparison of Estimates with 3-D FE K Solutions	143
5.4.7 Estimation of the Effects of Local Notch Root Plasticity	143
5.5 Analytical Representation of Crack Growth Threshold	146
5.6 Discussion	146
6. COMPARISON OF PREDICTED NOTCHED SPECIMEN FATIGUE STRENGTHS WITH TEST RESULTS	149
6.1 Introduction	149
6.2 Grade 17 Grey Cast Iron	149
6.2.1 BRITE Notch 1 ($K_t=2.2$)	150
6.2.2 BRITE Notch 2 ($K_t=5.6$)	152
6.2.3 BRITE Simulated Component ($K_t=3.8$)	153
6.2.4 BRITE Three-Point Bend Specimen ($K_t=2.4$)	154
6.2.5 BRITE Three-Point Bend Specimen ($K_t=6.3$)	154
6.2.6 Engine Bedplate with 12 thou Fillet	154
6.2.7 Engine Bedplate with 1/8th in. Fillet	155
6.3 Grade 250 Grey Cast Iron	156
6.3.1 Description of the Analysis Method	158
6.3.2 Description of the Results	159
6.4 Grade 350 Grey Cast Iron	161
6.4.1 Description of the Analysis Method	161
6.4.2 Description of the Results	162
6.5 Grade 400 Spheroidal Graphite Cast Iron	163
6.5.1 Description of the Analysis Method	164
6.5.2 Description of the Results	164
6.6 Grade 500 Spheroidal Graphite Cast Iron	165
6.6.1 Description of the Analysis Method	166
6.6.2 Description of the Results	166
6.7 Discussion	166

7. CONCLUSIONS	175
8. REFERENCES	180

Figures

NOTATION

Symbol	Description	Section Nos.
A	Constant in eqn. for K_f (Isibasi, 1952)	4.4
A_0	Coefficient in stress equation	5.4.2
A_1	Coefficient in stress equation	5.4.2
A_n	Coefficient in stress polynomial	5.4.3
B	Constant in eqn. for K_f (Isibasi, 1952)	4.4
C	Coefficient in the equation $\sigma^n l = C$	2.4.1
	Constant in fatigue eqn (Bullough, 1995)	3.2, 6.3.2
	Coefficient in Paris law for crack growth	4.2
C_1	Material constant in fatigue strength eqn.	2.4.1
C_{1n}	Equation constants (Kopsov, 1992)	5.4.3
C_{2n}	Equation constants (Kopsov, 1992)	5.4.3
C_{Neuber}	Constant in Neuber's rule ($\sigma \cdot \epsilon$)	3.1
D	Notch depth	2.4
	Defect size	2.4.1
E	Elastic modulus	2
E^*	=E or $E/(1-\nu^2)$ for plane stress or strain	5.2.1
F	Geometry correction factor	2.4
	K correction factor (Newman & Raju's eqn)	5.4.2
F_E	Factor to account for elliptical crack fronts	5.4.1
F_G	Factor to account for non-uniform crack opening stresses	5.4.1
F_S	Factor to account for the crack intersecting a free surface	5.4.1
F_{Stress}	Factor to account for notch root plasticity of local stresses and K solution	5.4.7
F_W	Factor to account for finite width bodies	5.4.1
G	Constant in surface strain conc. factor eqn.	2.4.1

$G(x)$	Green's function	5.4.1
G_1	Function of (a/c)	5.4.2
G_2	Function of (a/c)	5.4.2
H	K correction factor (Newman & Raju's eqn)	5.4.2
H_1	Function of (a/t) and (a/c)	5.4.2
H_2	Function of (a/t) and G_1 and G_2	5.4.2
H_B	Brinell hardness	3.1
$H_{(n)}$	Function of $H_{(1n)}$, $H_{(2n)}$ and p	5.4.3
$H_{(1n)}$	Function of (a) , C_{1n} and (a/c)	5.4.3
$H_{(2n)}$	Function of (a) , C_{2n} , (a/t) and (a/c)	5.4.3
H_v	Vickers hardness	2.4.1
I_1	Input to a system	5.4.1
I_2	Input to a system	5.4.1
$I(x)$	General input to a system	5.4.1
J	J-contour integral	5.2.1
\bar{J}	Energy release rate per unit area of virtual crack advance	5.2.1
$J(s)$	Point value of J on crack front s	5.2.1
K_f	Fatigue notch factor	2, 3, 4, 5, 6
K_t	Stress concentration factor	2, 3, 4, 5, 6
K	Stress intensity factor	2, 5
K_{2-D}	K solution from a 2-D crack analysis	5.4.5
K_I	Stress intensity factor (mode I)	5.2
K_{II}	Stress intensity factor (mode II)	5.2
K_{III}	Stress intensity factor (mode III)	5.2
K_{max}	Max stress intensity factor	2.4.1, 5.3
$K_{max,th}$	Max stress intensity factor at threshold	2.4.1
$K_{max,th\infty}$	Max stress intensity factor at long crack threshold	2.4.1
K_{op}	Value of K at crack opening	2.4.1, 5.3
$K_{op,th}$	Value of K_{op} at threshold condition	2.4.1

$K_{op,th\infty}$	Value of K_{op} at long crack threshold	2.4.1
$K_{elastic}$	Value of K under purely linear elastic stress	5.3.2
$K_{plastic}$	Value of K after initial plasticity (i.e. under superimposed elastic + residual stresses)	5.3.2
K_{ratio}	Ratio ($K_{plastic}$)/ $K_{Elastic}$	5.3.2
K_{ϵ}	Strain concentration factor	2.3
K_{σ}	Stress concentration factor	2.3
L	Crack depth in an unnotched specimen	2.4
L_p	Surface reversed plastic zone size	2.4.1
M_1	Polynomial coefficient	5.4.2
M_2	Polynomial coefficient	5.4.2
M_3	Polynomial coefficient	5.4.2
P	Point load applied to body	5.4.1
P_g	Probability of crack growth	4.2
P_{max}	Maximum applied load in a cycle	4.2
P_{min}	Minimum applied load in a cycle	4.2
P_{SWT}	Smith-Watson-Topper parameter	2.3
Q	Crack shape correction factor	5.4.2
Q_{ϵ}	Surface strain concentration factor	2.4.1
R	R-ratio ($\sigma_{min}/\sigma_{max}$)	2, 3, 4, 5, 6
R_1	Response of a system to an input I_1	5.4.1
R_2	Response of a system to an input I_2	5.4.1
$R(y)$	General response of a system to inputs $I(x)$	5.4.1
R_{II}	K ratio = K_{II}/K_I	5.2.1
R_{III}	K ratio = K_{III}/K_I	5.2.1
R.F.	Reserve factor (Experimental/Predicted)	6.7
S	Nominal stress	2
S_{op}	Crack opening stress level	2.4.1
$S_{op,max}$	Steady state value of S_{op} (for long cracks)	2.4.1
S_{alt}	Alternating stress $\Delta S/2$	3.1
S_b	Bending component of stress	5.4.2
S_{max}	Maximum stress in cycle	

S_{mean}	Mean stress $(S_{\text{max}}+S_{\text{min}})/2$	3.1
S_{min}	Minimum stress in cycle	
S_t	Tensile component of stress	5.4.2
UTS	Ultimate tensile strength	2
W	Strain energy density	5.2.1
Y	Geometry correction factor	2.4.1
a	Material constant in K_f expression	2.2
	Crack depth	2, 5
	Ratio of principal stresses	2.3
	Constant in fatigue eqn (Bullough, 1995)	3.2
a_0	Material constant representing the Intersection point on Kitagawa diagram defined by plain fatigue limit line and long crack threshold condition $a_0 = \left(\frac{\Delta K_{th}}{Y\Delta\sigma_0} \right)^2 \frac{1}{\pi}$	2.4
a'_0	Value of a_0 based on $\Delta K_{\text{eff,th}\infty}$	2.4.1
a_1	Material constant representing point at which defects begin to affect threshold stress	2.4.1
a_2	Material constant representing point of deviation from long crack threshold line on Kitagawa diagram	2.4.1
a_c	Crack depth at notch root (Taylor, 1996)	2.4
a_e	Equivalent 2-D crack in an infinite plate	2.4.1
a_{e21}, a_{e31}	Ratio of elastic principal stresses	2.3
a_{eff}	Effective crack depth $a_{\text{eff}} = a - L_p / 2$	2.4.1
a_n	Crack depth equivalent to a notch of the same depth (Taylor, 1996)	2.4
a_{np}	Nonpropagating crack length	2.4.1
area _s	Projected area of a defect (Murakami, 1989)	2.4.1
b	Ratio of principal stresses	2.3
	Constant in fatigue eqn (Bullough, 1995)	3.2, 6.3.2

c	Half surface length of surface crack	5.3
c ₁	Crack size above which K _{op,th} increases	2.4.1
c ₂	Crack size at which K _{op,th} = K _{op,th∞}	2.4.1
c _{np}	Nonpropagating crack size	2.4.1
d	Grain size	2.4.1
	Constant in fatigue eqn (Bullough, 1995)	3.2, 6.3.2
dC	Infinitesimal element of line contour	5.2.1
e	L - I (Smith and Miller, 1977)	2.4
e ₁ , e ₂ , e ₃	Elastic principal strains	2.3
f _i	Component of body force in direction i	5.2.1
f _w	Constant in correction factor eqn.	5.4.2
f _φ	Constant in correction factor eqn.	5.4.2
g	Crack geometry correction factor	5.4.2
l	Crack depth at the root of a notch	2.4
m	Constant in fatigue eqn (Bullough, 1995)	3.2, 6.3.2
	Exponent in Paris law for crack growth	4.2
n	Exponent in the equation $\sigma^n l = C$	2.4.1
n ₁	Surface normal	5.2.1
p	Function of (a/t) and (a/c)	5.4.2, 5.4.3
q	Notch sensitivity parameter	2
	Weight function for J domain integral	5.2.1
r	Notch root radius	2
	Distance from crack tip	5.2.1
Γ _{pc}	Cyclic crack tip plastic zone size	2.4.1
Γ _{pc,w}	Cyclic crack tip plastic zone size at Δσ _w	2.4.1
s ₁ , s ₂ , s ₃	Elastic local principal stresses	2.3
s _d	Stress at a depth equal to a graphite flake	4.4
s _{max}	Maximum elastic stress at the root of a notch	4.4
t	Plate thickness	5.4.2
u	Crack face displacement (x-direction)	5.2.1
u _{j,1}	Derivative of displacement with respect to x	5.2.1
u _{max}	Crack mouth opening displacement (Max.)	5.4.7

u_{min}	Crack mouth opening displacement (Min.)	5.4.7
v	Crack face displacement (y-direction)	5.2.1
w	Crack face displacement (z-direction)	5.2
x_0	Distance of point load P from central axis	5.4.1
x_i	Distance from origin to start of ith element	5.4.1
x_{i+1}	Distance from origin to start of i+1th element	5.4.1
α	Semi-axis of an ellipse	2.4
	Coefficient of thermal expansion	5.2.1
β	Semi-axis of an ellipse	2.4
β_R	Empirical factor applied to K_I to account for free surface effects on crack growth rate	5.2.4
χ	$\chi = 3 - 4\nu$ or $\chi = \frac{3 - \nu}{1 + \nu}$ Plane strain/stress	5.2.1
δ_{kj}	Kronecker's delta	5.2.1
ϵ	Strain	2.3
$\epsilon_1, \epsilon_2, \epsilon_3$	Principal strains	2.3
ϵ_{eq}^p	Equivalent plastic strain	2.3
$\epsilon_1^p, \epsilon_2^p, \epsilon_3^p$	Principal plastic strains	2.3
ϕ	Angle defining the position around the crack front	5.4.2
ϕ_{total}	Total shear deformation parameter	4.4
δ	Overstressed depth (Noguchi, 1989)	2.3.2
θ	Temperature	5.2.1
ρ	Empirical constant in equation for K_r	2.2
	Notch root radius or hole radius	2.4, 4.4
ν	Poisson's ratio	2, 5
ν'	Effective Poisson's ratio	
σ	Stress	2
σ_0	Plain specimen fatigue limit	2.4
$\sigma_1, \sigma_2, \sigma_3$	Principal stresses	2.3
$\sigma_{1,elastic}$	Elastic principal stress	5.4.7
$\sigma_{1,Neuber}$	Neuber corrected principal stress	5.4.7

σ_{elastic}	Value of σ under purely linear elastic stress	5.3.2
σ_{n}	Alternating stress at fatigue limit	5.5
σ_{Local}	Uncracked body stress at a depth corresponding to the crack depth	5.4.3
σ_{plastic}	Value of σ after initial plasticity (i.e. under superimposed elastic + residual stresses)	5.3.2
σ_{ij}	Stress tensor	5.2.1
σ'_i	deviatoric stresses	2.3
σ_{m}	Mean stress in load cycle	6.2
σ_{max}	Maximum stress in a cycle	2.3
$\sigma_{\text{max,w}}$	Maximum stress at the fatigue limit	2.4.1
σ_{net}	Applied normal stress	2.4.1
σ_{NFL}^*	Experimental normalised fatigue limit	3.2, 6.3.2
σ_{eq}	Equivalent stress	2.3
σ_{w}	Stress at the fatigue limit of a cracked body	2.4.1
σ_{xi}	Stress over element i	5.4.1
σ_{yc}	Cyclic yield stress	2.4.1
$\sigma(x)$	Distributed pressure load on a body	5.4.1
Δa	Virtual crack advance	5.2.1
Δarea	Increase in crack area due to virtual crack advance Δa	5.2.1
Δe	Elastic strain range	2
ΔJ	Cyclic component of J (J-contour integral)	4.3
ΔK	Range of stress intensity factor	2
ΔK_0	Long crack threshold value of ΔK	2, 5.5
ΔK_{eff}	Effective $\Delta K = K_{\text{max}} - K_{\text{op}}$	2.4.1, 5.3
$\Delta K_{\text{eff,th}}$	Effective threshold ΔK	2.4.1
$\Delta K_{\text{eff,th}\infty}$	Effective long crack threshold ΔK	2.4.1
ΔK_{th}	Threshold value of ΔK for negligible growth	2, 5
ΔK_{ϵ}	Range of strain intensity factor	4.4
ΔS	Nominal range of stress	2

ΔS_o	Nominal range of stress at the fatigue limit	2
ΔS_{ith}	Intrinsic threshold stress range	2.4.1
ΔS_{nom}	Nominal stress range	6.2.1, 6.3.1
Δe	Strain range	2.4.1
$\Delta \varepsilon$	Strain range	2
$\Delta \sigma$	Stress range	2
$\Delta \sigma_0$	Fatigue limit stress range at $\sigma_m = 0$	6.2
$\Delta \sigma_n$	Fatigue limit stress range ($=2 \cdot \sigma_n$)	5.5
$\Delta \sigma_w$	Stress range	2.4.1
Γ	Line contour around crack tip	5.2.1

1. INTRODUCTION

Cast irons have been used in engineering components since the industrial revolution. Their use continues in the present day even though many higher strength metals and alloys have been developed over the years. Cast irons may still have an advantage where cost, castability and machinability are important.

Over recent years, the introduction of relatively low cost computers and easy to use codes for numerical methods of analysis such as the finite element method have had a significant impact on the design of engineering components. This is certainly the case in highly stressed engine components. Engine designs are becoming more competitive, such that even the larger diesel engines are becoming reliant on accurate stress and temperature predictions, and consequently, component strength predictions.

These developments have highlighted a particular problem area. Detailed predictions of stress fields in a component can be obtained under different running conditions, particularly for regions of stress concentration, since these are the areas which are susceptible to fatigue cracking. However, the design analyst can be faced with a dilemma. This can be illustrated by a simple example.

Having obtained detailed predictions of the stress field in two engine designs, one of which has been used successfully for years, and the other, a newer, more highly stressed design which develops cracks; the design analyst discovers that the peak stresses in *both* are above the alternating stress which will cause fatigue failure in 10^7 cycles or less, as determined by plain specimen fatigue tests. Will a simple change to the geometry of the new design such that the peak stress is just lower than that in the older successful design alleviate the problem? Alternatively, should all future designs avoid any peak stresses which are above this limit? To test the actual component to failure would be costly, as would a test programme for notched fatigue specimens for each design detail. For typical notched specimen geometries there is often no obvious relationship between the stresses in the component and those in a test specimen, therefore the traditional fatigue assessment route based on fatigue notch factors and nominal stresses is difficult

to follow. Given the choice therefore, the first design option appears the most attractive, i.e. increase the fillet radius and reduce the peak stress. Experience has shown however, that this can lead to costly failures.

The objective of this work has been to identify methods for predicting the fatigue strength of a component which makes direct use of the stress field which is predicted for the component, using for example, the finite element method. The strategy was to base a method on current knowledge of the mechanisms of fatigue damage development in the materials of interest, and try to reproduce the observed dependence of fatigue strength on the geometry and stress field of a body. In this work, the term 'fatigue strength' will be used to describe the typical alternating stress below which fatigue failure does not occur after 10^7 cycles. Where the term is being used to refer to shorter lives, then the life will be stated. The term 'fatigue limit' is sometimes used, and in this work has the same definition, but its use is restricted to 10^7 cycles. The work is restricted to cases involving constant amplitude loading.

Much of the work centres around modelling how a fatigue crack would develop, and whether it will continue to grow or not. In other words, the aim is to try to predict whether a crack will cease to propagate after a short distance. The assumption is made that if a crack has not grown to failure after 10^7 cycles, then it would not grow to failure at all, i.e. the crack has stopped.

The first section sets out to define the problem by means of a review of existing fatigue design methods for notches (stress concentrations). In view of the enormous quantity of fatigue literature, only the more widely known and more recent methods are covered. First of all, nominal stress based approaches are described, but this is kept relatively brief because the main emphasis of this work is to avoid the use of a nominal stress as conventionally defined. Local strain based approaches are then described, and how these have been applied to both large and small stress concentrations.

Over the last twenty five years, a number of fracture mechanics based approaches to notch fatigue assessments have been proposed, particularly, the

concept of representing the notch as a crack of similar depth. The treatment of small stress concentrations (inherent defects, machined notches etc.) using fracture mechanics methods has also been addressed by many workers, including Frost, Kitagawa, El Haddad and Murakami. The growth of short cracks through stress fields associated with stress concentrations has received particular attention over the years, much of the work relating to the apparent high early growth rates of cracks. However, of interest to the problem described here is the threshold condition for growth. A number of papers in the recent literature have described the use of crack closure models to describe the behaviour of notch fatigue cracks.

Much of the analytical work which will be described in this thesis relates to a significant set of test data on cast iron which has been generated over the period from 1990 to 1995 at ALSTOM Energy Technology Centre, Whetstone. These data cover a range of grades of cast iron tested under many different conditions and using a range of notch geometries. Overall these data provide a good test for candidate theoretical models. Section three therefore gives a description of the materials, the specimen geometries and the experimental procedures used. Details of finite element stress analyses are described, with particular reference to predictions of local notch root stresses and strains. Also included in this section is a description of a diesel engine bedplate detail. This is given as an example of a typical application for which some details of service experience are available. This example in fact provided much of the original motivation for this research work.

Following this in section four, a review of fatigue failure mechanisms observed in test specimens is presented. By way of introduction, the mechanisms observed in typical structural metals are briefly described. However, the main area of interest in this work, the failure of cast irons, is described in the main body of the section. This is followed by observations on notched specimens. Investigation of the likely fatigue failure mechanisms which were to be expected in the cast iron specimens and components was considered to be important to the formulation of any theoretical model. However, greater reliance than was preferred had to be placed on information from the literature because the facilities were not available to study the development of damage in the specimens described in section three.

Having provided the background to the current work in sections two to four, the development of a crack growth based approach for cast iron is described in section five. The work is based on the use of linear elastic fracture mechanics to characterise the crack tip stress field. The main subjects of interest are the estimation of the crack tip stress intensity parameter for the specimen geometry and loading conditions, and the prediction of the threshold condition. The complex behaviour of grey cast iron with respect to both deformation and damage development suggested the need for two- and three-dimensional crack analyses, with allowance for the effects of nonlinear material behaviour which predominantly occurs during initial loading. This section therefore gives particular attention to these aspects and methods for the estimation of the important parameters.

In section six, the results of crack growth predictions are presented for the test conditions described in section three. Since the current work attempted to address all the experimental testing conditions, the results are given in the form of a relatively large number of figures. The effects of sensitivity to material properties and model details have been assessed and included as additional results. These results are discussed, and finally, conclusions arising from this work are presented in section seven.

2. HIGH CYCLE FATIGUE DESIGN METHODS FOR STRESS CONCENTRATIONS: A REVIEW

2.1 An Overview of Published Notched Fatigue Data

The stress acting in a notched test specimen is traditionally described by the net section average stress, or 'nominal' stress (S). In fatigue test specimens, this quantity is relatively straightforward to calculate with a high level of accuracy, and avoids the need for detailed work to estimate the point values of stress (σ) in the region of the notch root. Under constant amplitude loading, the fatigue strength of a notched specimen can therefore be described in terms of the amplitude of the nominal stress ($\Delta S_\sigma/2$). The fatigue limit of a plain (uniformly stressed) fatigue specimen will be denoted by $\Delta\sigma_\sigma/2$. The ratio of the plain specimen fatigue limit ($\Delta\sigma_\sigma/2$) to the fatigue limit of the notched specimen ($\Delta S_\sigma/2$) provides a measure of how detrimental particular geometric features are to the fatigue strength. This ratio is generally called the Fatigue Notch Factor (K_f):

$$K_f = \frac{\text{Fatigue limit of plain specimen}}{\text{Fatigue limit of notched specimen}} \quad (2.1)$$

and is often used in the literature alongside the theoretical elastic stress concentration factor K_t to describe high cycle fatigue test results for notched specimens. The definition of K_t is conventionally given as:

$$K_t = \frac{\text{Theoretical maximum elastic stress}}{\text{A nominal stress}} \quad (2.2)$$

The publication by Frost, Pook and Marsh (1974) provides a review of a selection of experimental data on notched fatigue specimens, much of this dates from the 1940s and 1950s. The majority of test results are from rotating bending type specimens for wrought ductile metals and alloys in the as-machined condition. Surfaces may therefore be in a work hardened condition and may contain residual stresses.

Most of the data shows some notch sensitivity effects with $1.0 \leq K_f \leq K_t$, the value of K_f is strongly dependent on K_t and root radius. At high K_t , K_f is generally much less than K_t (notch insensitive), whereas for low K_t , K_f can equal K_t (notch sensitive), but is generally slightly less than it.

Several data sets covering mild steel, nickel-chromium alloy steel, several aluminium alloys and copper show a tendency for K_f to decrease and become less than K_t when the notch root radius (and depth) is less than 0.5mm. i.e. as the notch becomes smaller, the specimen becomes less sensitive to it.

Results for SAE 1035 steel show that stress relieving of as-machined specimens can reduce the notched fatigue strength (K_f approaches K_t), probably by the removal of compressive residual stresses.

The material grain size has been shown to influence the notch sensitivity of some materials. Data for 0.4% C steel showed no significant effect in axial specimen tests, but 70/30 brass, mechanically and thermally treated to produce various grain sizes did show an effect when tested in rotating bending.

- Smallest grain size (0.047mm) - $K_f \approx K_t$
- Largest grain size (7.75mm) - $K_f \approx 1.0$

Intermediate values were obtained for intermediate grain sizes. The plain specimen fatigue limit was also noted to change significantly with grain size:

- Smallest grain size (0.047mm) - $\Delta\sigma/2 = \pm 276$ MPa
- Largest grain size (7.75mm) - $\Delta\sigma/2 = \pm 62$ MPa

Cast materials exhibit a slightly different response compared with wrought ductile materials when tested with notches. Again Frost, Pook and Marsh (1974, p.173) summarize the results of several investigators. The principal observations are:

- Cast materials give a lower K_f than similar wrought materials.
- If the plain specimen fatigue limit of a cast material is associated with flaws then:
 - The fatigue notch factor $K_f \ll K_t$.
 - For small shallow notches, $K_f \rightarrow 1.0$, particularly if the notch size is comparable with the inherent flaw size.
- The deeper the notch and larger the root radius (at a constant K_t), the more $K_f \rightarrow K_t$.

Frost (1974) also reproduces results from tests carried out by other workers:

Cast iron	Plain fatigue limit (MPa)	Notched fatigue limit (MPa)	K_f
Ferritic flake	±85	±70	1.2
Pearlitic flake	±155	±110	1.4
Ferritic nodular	±210	±155	1.35
Pearlitic nodular	±300	±195	1.55

**Table 2.1 Notched rotating bend specimen test results
- 18mm O.D., $K_t = 3.5$, Circumferential V-groove
(3.8mm deep, 2.5mm root radius)**

All four cast irons exhibit significant notch insensitivity. What the controlling parameters are cannot be determined from this limited data set.

2.2 Nominal Stress Based Approaches

The results described above indicate that notch fatigue strength can be influenced by a number of factors. To help avoid the need for many tests, much work has been done to try to predict the effects. The sensitivity of the fatigue strength of a specimen to the presence of a notch can be expressed by the Notch Sensitivity Parameter q (Peterson, 1959):

$$q = \frac{K_f - 1}{K_t - 1} \quad (2.3)$$

where q varies from 0 (no notch effect on fatigue strength), to 1 (notch fatigue factor $K_f =$ stress concentration factor K_t). Rearranged this can be used to estimate K_f (Peterson):

$$K_f = q(K_t - 1) + 1 \quad (2.4)$$

The parameter q must be obtained from test results. In the absence of test data, Peterson provides a chart of q versus notch root radius r , which is an average of all notch fatigue data which was available to him. It is applicable to notches having a depth of less than four times the notch root radius in the following types of materials:

- Quenched and tempered steels
- Annealed or normalised steels
- Aluminium alloy

Peterson points out that this design chart is approximate, and scatter can be considerable.

Various formulae have been proposed to provide approximate values for q and K_f . Peterson has referred to the Kuhn-Hardrath formula which is based on Neuber's work:

$$K_f = 1 + \frac{K_t - 1}{1 + \sqrt{\rho' / r}} \quad (2.5)$$

where r is the notch root radius and ρ' is a material constant representing a dimension characteristic of the material microstructure, and is determined by test data. This formula is applicable to parallel sided groove geometries. Peterson

presents a graph which is based on an analysis of several hundred test results by Kuhn and Hardrath, relating the value of $\sqrt{\rho'}$ to tensile strength in steels.

Peterson has also referred to a formula by Heywood which is based on the concept that all materials contain inherent flaws, each having a characteristic length a :

$$K_f = \frac{K_t}{[1 + 2\sqrt{a/r}]} \quad (2.6)$$

so that when r is large relative to a , the value of K_f will approach K_t . When r is a similar size to that of the inherent flaws, the notch will make little difference to the fatigue strength. The value of a must be determined experimentally. This formula is based on the concept of an inherent population of flaws in the material. When the notch (or root radius) becomes equal to that of the inherent flaw sizes, then it is assumed to have no effect on the overall fatigue strength. The formula is only applicable when $r \geq a$ (i.e. K_t is always ≥ 1.0). The Kuhn-Hardrath formula (2.5) is based on the Elementary Block concept of Neuber in which fatigue failure is governed by the average stress over an elementary block of material (Forrest, 1955). With the latter formula, a notch is predicted to have some effect on the fatigue strength no matter how small it is.

Peterson has proposed a design relation which is based on a linear stress distribution, and the q versus a curve is shifted to start at $r=0$, $q=0$:

$$K_f = 1 + \left[\frac{K_t - 1}{1 + a/r} \right] \quad (2.7)$$

Typical values for the material constant a , are 0.0625mm for quenched and tempered steels, 0.25mm for annealed or normalised steels, and 0.5mm for aluminium alloy sheets and bars. The value can be expressed as a function of tensile strength to provide an estimate for most ferrous metals (Frost, Pook and Marsh, 1974):

$$a = 0.0254 \left[\frac{2079}{UTS} \right]^{1.8} \quad (2.8)$$

where a is in millimetres, and UTS is the Ultimate Tensile Strength in MPa.

2.3 Local Strain Based Approaches

Over the last thirty years, a period which has witnessed significant developments in the fields of both numerical methods of stress analysis such as the finite element method (Zienkiewicz, 1977), and digital computing power, much emphasis has been placed on the estimation of the stress and strain behaviour in regions local to stress concentrations in components. These techniques have consequently also been applied to the analysis of test specimens. Within the region at the heart of a typical stress concentration such as a notch root, the stresses may be of a sufficient level to exceed yield and may consequently differ significantly from values calculated based on the assumption of linear elasticity. The approach usually entails detailed predictions of local stress-strain behaviour using a model for material deformation behaviour, and also the assessment of results with an appropriate fatigue criterion.

Approaches to notch fatigue assessment which make use of local stresses and strains can be classified into two categories, depending on the location at which the quantities are calculated:

- 1) Surface stresses and strains
- 2) Sub-surface (critical depth approaches)

2.3.1 Local Surface Stresses and Strains

The stress-strain behaviour at the surface local to the stress concentration may be estimated in several ways:

- a) Strain measurements (electrical resistance gauges, etc.) followed by stress calculation
- b) Nonlinear finite element analysis
- c) Approximate methods based on an elastic solution (Neuber etc.)

The resulting local alternating and mean stresses and strains are then compared with uniaxial plain specimen fatigue test data to determine life, on the assumption that the latter is representative of the local behaviour (Dowling, 1977).

Neuber (1961) proposed that the geometrical mean value of the stress and strain concentration factors K_σ , K_ϵ (based on the local inelastic stress and strains for any stress-strain law) is equal to the Hookian stress concentration factor (K_t):

$$\sqrt{K_\sigma K_\epsilon} = K_t \quad (2.9)$$

This was derived for two-dimensional shear in his paper, but has been extended to more general states of stress.

The solution for σ and ϵ at the notch root is found from the Neuber relation (which forms a hyperbola), in combination with the material stress-strain law. The point at which this hyperbola crosses the stress-strain curve is assumed to provide an approximation of the local notch root stress and strain. Procedures have been developed to apply this method to complex load histories (Landgraf et al, 1975).

2.3.1.1 Extension to Multiaxial Stress States

This basic procedure is applicable to cases involving uniaxial stresses only. A method is described in the ASME Boiler and Pressure Vessel Code (Code Case N-47) for applying the Neuber procedure to multiaxial stress conditions. This approach only involves equivalent stress and strain ranges, and does not break these down into local inelastic stress and strain components. It does however provide a formalised procedure for dealing with cases where the stress components vary in a nonproportional manner.

For proportional multiaxial loading, Hoffman and Seeger (1985) have proposed a generalised method for estimating the cyclic stress and strain components from the elastic stresses at the root of a notch. The method is based on three simplifications:

- An approximation formula for equivalent stresses and strains (e.g. Neuber)
- An assumption concerning one of the stresses or strains
- Use of Henky's rule instead of the exact Prandtl-Reuss flow rule.

The procedure they describe delivers the complete information about the multiaxial elastic-plastic stress-strain state at the notch, and thereby allows mean, minimum and maximum stresses to be evaluated. It is applicable only to proportional loading due to the use of Henky's rule, and involves the extension of approximation formulae such as Neuber's rule from uniaxial to multiaxial equivalent quantities. Alternative approximation formulae to Neuber's rule have been proposed (e.g. Glinka, Hoffman & Seeger) which it is claimed are more accurate than Neuber's rule.

2.3.1.2 Estimation of Local stress and Strain Components

In the procedure described by Hoffman and Seeger, the principal elastic-plastic stresses and strains ($\sigma_1, \sigma_2, \sigma_3$ and $\varepsilon_1, \varepsilon_2, \varepsilon_3$) are estimated from the equivalent stresses and strains with Henky's rule and an assumption concerning one of the stress or strain components.

The flow rule of Prandtl-Reuss relates the plastic strain increments $d\varepsilon_i^p$ to the deviatoric stresses σ_i' .

$$d\varepsilon_i^p = \frac{3d\varepsilon_{eq}^p}{2\sigma_{eq}} \cdot \sigma_i' \quad i = 1, 2, 3 \quad (2.10)$$

where σ_{eq} and $d\varepsilon_{eq}$ are the von Mises equivalent stress and increment of equivalent strain respectively. If the ratio between the deviatoric stress components remains constant during loading then it reduces to Henky's rule in which the plastic strains are assumed to be a function of the deviatoric stresses:

$$\varepsilon_i^p = \frac{3\varepsilon_{eq}^p}{2\sigma_{eq}} \cdot \sigma_i' \quad i = 1, 2, 3 \quad (2.11)$$

The procedure and its application are described in detail in Hoffman and Seeger's paper (1985), in summary, for a traction free surface:

I. Input

- Material law
- Elastic solution (principal stresses & directions)
- Plastic limit load (if close to gross section yielding)

II. Approximation procedure

- Neuber's rule
- or Seeger's formula (applicable to low hardening materials and if highly accurate notch stresses and strains are required)

III. Flow criterion

- e.g. von Mises flow criterion

IV. Flow rule

- Henky's flow rule

V. Boundary conditions

- Fixed principal stress direction
- Assumption about fixed strain ratios & values of surface normal stress

With a suitable choice of boundary conditions, the procedure can be made applicable for use with linear elastic finite element analysis results for stress concentrations.

2.3.1.3 Application to Axisymmetric FE Results

A local coordinate system can be defined as shown in figure 2.1 with axes 1 and 2 in the plane of the model, and axis 3 in the hoop direction. Axis 2 is defined normal to the surface. In the following, e_1 , e_2 and e_3 are the elastically calculated principal strain components, and s_1 , s_2 and s_3 are the elastically calculated principal stress components, corresponding to the three axes. The estimated inelastic strains, which are made up of an elastic part and a plastic part are denoted by the greek characters ε_1 , ε_2 and ε_3 . The local inelastic stresses are denoted by: σ_1 , σ_2 and σ_3 .

An initial assumption is made that the local inelastic strain ratio is approximately equal to the elastic strain ratio:

$$\frac{\varepsilon_3}{\varepsilon_1} \approx \frac{e_3}{e_1} \quad (2.12)$$

Defining the following notation for the elastic stress ratios:

$$a_{e_{21}} = \frac{s_2}{s_1} \quad a_{e_{31}} = \frac{s_3}{s_1} \quad (2.13)$$

The local inelastic strain ratio can be described by:

$$\frac{\varepsilon_2}{\varepsilon_1} = \frac{[a_{e_{21}} - \nu'(a_{e_{31}} + 1)]}{[1 - \nu'(a_{e_{21}} + a_{e_{31}})]} \quad (2.14)$$

where the effective Poisson's ratio ν' is given by:

$$\nu' = \frac{1}{2} - \left(\frac{1}{2} - \nu\right) \frac{\sigma_{eq}}{E\varepsilon_{eq}} \quad (2.15)$$

where σ_{eq} and ε_{eq} are the von Mises equivalent stress and equivalent strain respectively determined from the application of the approximation formula (e.g. Neuber's rule) with the elastic von Mises equivalent stress (s_{eq}) defined as:

$$s_{eq} = \frac{1}{\sqrt{2}} \sqrt{((s_1 - s_2)^2 + (s_2 - s_3)^2 + (s_3 - s_1)^2)} \quad (2.15a)$$

A further assumption can be made about the in-plane stress ratio σ_2/σ_1 , the inelastic and elastic stress ratios can be assumed to be similar. For a surface position:

$$a = \frac{\sigma_2}{\sigma_1} = \frac{s_2}{s_1} = 0 \quad (2.16)$$

otherwise, for a sub-surface position:

$$a = \frac{\sigma_2}{\sigma_1} = a_{e_{21}} = \frac{s_2}{s_1} \quad (2.17)$$

The out-of-plane stress ratio is then given by:

$$b = \frac{\sigma_3}{\sigma_1} = \frac{a \cdot \nu'(1 - \varepsilon_3 / \varepsilon_1) + \nu' + \varepsilon_3 / \varepsilon_1}{(1 + \nu' \cdot \varepsilon_3 / \varepsilon_1)} \quad (2.18)$$

The maximum principal inelastic stress is:

$$\sigma_1 = \frac{\sigma_{eq}}{[1 + a^2 + b^2 - b - a(1 + b)]^{1/2}} \quad (2.19)$$

and the maximum principal inelastic strain is:

$$\varepsilon_1 = \frac{[1 - \nu'(a+b)] \cdot \varepsilon_{eq}}{[1 + a^2 + b^2 - b - a(1+b)]^{1/2}} \quad (2.20)$$

The assumptions made in the above would be expected to be more accurate at the surface than at subsurface positions. This was tested in a comparison of the results from the above procedure with the results of an inelastic FE analysis.

2.3.1.4 Comparison with Inelastic FE Results

An axisymmetric model was constructed to represent a circumferentially notched cast iron test specimen (see figure 2.2). The notch geometry is semi-circular in section. The stress concentration factor for this specimen is 2.2. Two FE analyses were carried out:

- a) Linear elastic
- b) Elastic-plastic

The elastic-plastic analysis was carried out for a monotonically increasing load up to a maximum value equal to 59.304kN, equivalent to 135 MPa net section stress. The stress-strain curve for the material, which represented a grade 17 grey cast iron, was modelled by a piecewise linear curve (figure 2.3). Isotropic hardening was assumed to allow the use of this material description, unloading was not carried out in the analysis, a kinematic hardening model was therefore unnecessary.

The results from the two analyses are compared in figures 2.4 to 2.7 together with the results of the multiaxial Neuber procedure which made use of the elastic FE results, as defined in the previous section in equations 2.12 to 2.20. In this case very good agreement is obtained close to the surface. The subsurface values retain a reasonable degree of accuracy over the region where the stress concentration effect still dominates, but further outside this region (deeper into the body of the specimen) the accuracy falls off. The main requirement for obtaining the subsurface values is for fracture mechanics type assessments for which the stress and strain distributions close to the surface are most critical.

2.3.1.5 Local Strain Based Approach for Small Defects

The thesis by Mitchell (1976) outlines a procedure for predicting the fatigue strength of ferrous based materials containing inherent defects. This procedure is based upon the use of estimated K_t and K_f factors, together with stress-strain and strain-life data which is representative of the matrix material. The predictions obtained using this procedure were compared with experimental fatigue data for several materials including grey cast iron, spheroidal graphite cast iron, cast steel and wrought steel.

Firstly, an estimate of the theoretical elastic stress concentration factor K_t is made based on a consideration of the geometry and behaviour of the likely inherent defects. A fatigue notch factor K_f is then estimated using Petersons formula:

$$K_f = 1 + \frac{K_t - 1}{1 + a/r} \quad (2.21)$$

where r is the notch root radius, and the material constant a is estimated from either:

$$a = 10^{-3} \left(\frac{300}{UTS} \right)^{1.8} \quad (2.22)$$

or

$$a = 10^{-3} \left(\frac{600}{BHN} \right)^{1.8} \quad (2.23)$$

where a is in units of inches, UTS is the ultimate tensile strength in ksi, and BHN is the Brinell hardness.

Neuber's rule, written in the form:

$$K_f \Delta S = (\Delta \sigma \cdot \Delta \epsilon)^{1/2} \quad (2.24)$$

is then used to obtain the local inelastic strain range, where $\Delta\sigma$ and $\Delta\varepsilon$ are the local stress range and strain range respectively. ΔS is the nominal stress range. Note that the parameter K_f is used rather than K_t . Knowing the local strain range, the fatigue life is calculated from the strain-life curve relevant to the matrix material surrounding the defect. In the case of grey iron, this was assumed by Mitchell to be equivalent to a high silicon wrought steel.

The procedure was shown to give reasonably successful predictions of the plain specimen fatigue strength of the materials considered. In the case of discrepancies, these were explained with reference to some of the assumptions about defect size and shape. For example, for SG iron, the initial predictions using the graphite nodule geometry for the K_f estimate lay above the actual fatigue strengths. With revised estimates based on the larger microshrinkage cavities close to the surface, the agreement was shown to be much improved.

More recently, Heuler et al (1992) have analysed the behaviour of defects in 2¼CrMo steel castings. Two methods were considered:

- a) The Local Strain Approach
- b) Fracture mechanics approach

It was concluded that the Local Strain Approach more accurately describes the initiation potential of the defects found than fracture mechanics based methods. The latter were found to produce very conservative estimates in many cases. The main elements of the Local Strain analysis involved:

1. Determination of a stress concentration factor, K_t
2. Derivation of a fatigue notch factor, K_f
3. Analysis of local stress-strain response
4. Comparison with fatigue-life curves

The fatigue notch factor equation proposed by Peterson was used (equation 2.1), and the constant a being given by:

$$a = 0.0254 \left(\frac{2070}{UTS} \right)^{1.8} \quad (2.25)$$

where UTS is the ultimate tensile strength (MPa) and a is in mm. The local stresses and strains were predicted using Neuber's rule, but with the fatigue notch factor K_f in place of K_t :

$$\Delta\sigma\Delta\varepsilon = K_f^2 \cdot \Delta S\Delta e \quad (2.26)$$

to allow for stress gradient and size effects. The fatigue-life curve was derived from strain controlled fatigue tests on sound material, and to account for mean stress effects, was expressed in the form of the Smith-Watson-Topper (Smith, et al, 1970) parameter (P_{SWT}) versus life, where:

$$P_{SWT} = (\sigma_{\max} \cdot \Delta\varepsilon / 2 \cdot E)^{1/2} \quad (2.27)$$

The Local Strain Approach was found to describe the crack initiation from defects having notch root radii $>0.02\text{mm}$ very well. Overall, the local strain based predictions were found to describe the crack initiation potential of these defects more accurately than fracture mechanics based approaches.

2.3.2 Sub-surface Behaviour (Critical Depth Approaches)

Work by Noguchi on notch sensitivity of cast iron (Noguchi, 1989) has made use of finite element stress analysis techniques (linear and nonlinear) to determine sub-surface notch root stress distributions. Two notch geometries were investigated analytically and experimentally:

Kt	Notch root radius (mm)	Notch depth (mm)
1.6	2.0	2.0
2.8	0.7	2.0

Table 2.2 Notch geometry details (Noguchi, 1989)

Tensile and High Cycle Fatigue (HCF) fatigue tests were performed on three cast irons:

- Pearlitic flake graphite cast iron
- Ferritic flake graphite cast iron
- Spheroidal graphite cast iron (50% ferrite)

The fatigue tests were carried out at a loading rate of 2-10Hz, and continued up to failure or 5×10^6 cycles.

Noguchi identified a region where the cyclic stress exceeds the fatigue strength for smooth specimens. This 'overstressed depth' δ was dependent on the stress level, material ductility and notch radius. The minimum δ was inferred to be an initiation condition for macrocracks with one eutectic cell diameter, and the larger values of δ are propagation conditions. The eutectic cell diameter in grey cast iron is the final size of the roughly spherical lump of austenite and graphite formed during solidification after casting. The graphite within this cell is made up of a continuous branched skeleton of graphite (Rollason, 1973). Microscopic observations of fatigue specimens showed that in HCF, macrocracks of size 0.5 to 1.0mm form towards the end of life by the linking of microcracks. This is a similar length to δ . It was suggested that some small stressed area is required for macrocrack formation in fatigue.

Under conditions corresponding to the fatigue endurance limit, the value of δ is smallest and could be estimated from elastic stress distributions alone. In the ferritic flake iron studied, $\delta \approx 0.8\text{mm}$. In the pearlitic flake iron $\delta \approx 0.6\text{mm}$, and in the spheroidal iron, $\delta \approx 0.4\text{mm}$. The mean graphite eutectic cell diameter for the ferritic and pearlitic flake irons used is around 0.6mm.

An assessment procedure based on this method would therefore only require the elastic stress distribution in the component, and the fatigue strength at the relevant R-ratios.

A critical depth fatigue criterion has also been proposed by Flavenot and Skalli (Flavenot, 1989). Test results for several different steels and notch geometries were analysed under loading conditions of $R = -1$ and $R = 0.1$ (where R is the ratio of minimum to maximum load). A multiaxial fatigue failure parameter was calculated at various depths below the surface for each test geometry under loading conditions corresponding to the actual notched specimen fatigue limit. The value of depth which gave the best correlation of the fatigue failure parameters was calculated. Values obtained ranged from $40\mu\text{m}$ to $180\mu\text{m}$ depending on the material and heat treatment. For steel 35CD4, the values were shown to vary with tensile strength:

UTS (MPa)	Critical depth (μm)
915	50
1000	50
1500	40

Table 2.3 Calculated critical depth values for steel 35CD4
(Flavenot, 1989)

These values were based on test results for three different notch geometries:

K_t	Notch radius (mm)
1.035	55.0
1.7	2.0
3.3	0.35

Table 2.4 Notched specimen geometries for steel 35CD4
(Ref. Flavenot, 1989)

The best correlation was achieved for the test results where no local notch root plasticity takes place. The use of inelastic FE analysis improved the correlation of the other points, but did not fully correlate all the test data.

Their recommended procedure involved the use of average stresses over a volume corresponding to twice the critical depth. This was justified on the basis that microstructural features exhibit a length scale (e.g. grain diameter), and it is the average stress over a grain which controls the initiation of microcracks by shearing of crystallographic planes.

2.4 Fracture Mechanics Based Approaches for Notches

In recognition of the fact that conventional approaches to notch fatigue strength assessments do not explicitly account for the presence of a crack, Smith and Miller (1977) turned to fracture mechanics to help explain the fatigue behaviour of notched specimens, and provide simple design rules. The concept of equivalent cracks was defined. Cracks in unnotched and notched specimens will be equivalent when their rates of growth are the same, and the notch effect can be defined as:

$$e = L - l \quad (2.28)$$

where L is the depth of a crack in an unnotched specimen and l is the depth of a notch root crack. An expression for the range of stress intensity factor, ΔK , can be written by making use of published K solutions for notch root cracks:

$$\Delta K = F\Delta\sigma\sqrt{\pi(\alpha + l)} \quad (2.29)$$

where α is the semi-axis of an ellipse normal to the applied stress, and F is the geometry correction factor. For the simple case of a uniformly loaded sheet with a central crack of length $2l$, the following equation applies:

$$\Delta K = \Delta\sigma\sqrt{\pi L} \quad (2.30)$$

Comparing these two, the following terms are equivalent:

$$F\sqrt{(\alpha + l)} = \sqrt{L} \quad (2.31)$$

The non-dimensional notch contribution can be given as:

$$\frac{e}{\alpha} = F^2 \left(1 + \frac{l}{\alpha} \right) - \frac{l}{\alpha} \quad (2.32)$$

(for an edge notch replace F by $\bar{F}/1.12$). For application to general notch shapes, accounting for both notch shape and size, the l/α parameter is multiplied by an ellipse shape parameter α/β , where these are the two semi-axes. This gives:

$$\frac{l}{\alpha} \cdot \frac{\alpha}{\beta} = \frac{l}{\beta} \quad (2.33)$$

If the notch depth is defined as D , and the root radius ρ is set equal to β^2/α , then this becomes:

$$\frac{l}{D} \sqrt{\frac{D}{\rho}} = \frac{l}{\beta} \quad (2.34)$$

Which gives a term D/ρ to characterise shape, and $1/D$ to characterise size. From these, simplified expressions were proposed as approximations to the notch contributions:

For a fatigue crack within the notch field:

$$\frac{e}{D} = 7.69 \frac{l}{\sqrt{D\rho}} \quad \left(0 < \frac{l}{\sqrt{D\rho}} < 0.13 \right) \quad (2.35)$$

and for a crack outside the notch field:

$$\frac{e}{D} = 1 \quad \left(\frac{l}{\sqrt{D\rho}} > 0.13 \right) \quad (2.36)$$

Considering the conditions for a crack to stop propagating, these would be expected after the initial increase in K within the notch stress field. The effective crack length becomes $D+l$, but for sharp notches, l will often be much less than D , and the condition under which the crack will just begin to grow is:

$$1.12\sigma\sqrt{\pi D} = \Delta K_{th} \quad (2.37)$$

The approximate minimum nominal stress to cause failure is then (Smith and Miller, 1978):

$$\sigma = \frac{0.5\Delta K_{th}}{\sqrt{D}} \quad (2.38)$$

This expression was derived for fully reversed loading. For other conditions, account must be taken of the R-ratio dependence on ΔK_{th} . Furthermore, for very small notches, Smith and Miller (1978) suggest the use of the 'apparent' crack growth threshold which can be derived from the Kitigawa-Takahashi diagram.

For relatively blunt notches, Smith and Miller (1978) proposed the equation:

$$\sigma = \sigma_0 / \left[1 + 7.69\sqrt{D/\rho}\right]^{0.5} \quad (2.39)$$

where σ_0 is the plain specimen fatigue limit.

The use of the above equations were demonstrated in connection with published notch fatigue data for steels, and was shown to provide a reasonable description of the behaviour (Smith and Miller, 1977 & 1978).

The notched fatigue behaviour of cast irons has been addressed by Taylor (1996a) using a fracture mechanics approach. Three grades of cast iron were considered: Grade 17 grey iron, a ferritic SG iron, and a pearlitic SG iron. For all three of these, notched fatigue data were available. In this work Taylor extended the approach proposed by Smith and Miller (1978) in which the notch depth is

considered to be a crack of the same depth (a_n), by augmenting the notch depth with a crack length a_c . The stress intensity factor is therefore given by:

$$K = F\sigma\sqrt{\pi(a_n + a_c)} \quad (2.40)$$

where F is the geometric constant for the assumed crack geometry. The fatigue strength of a sharply notched specimen is assumed to correspond to the condition when K as calculated using equation 2.40 equals the value of the long crack ΔK_{th} . Values of a_c were arrived at by reversing this process: knowing the notched fatigue strength σ_0 , the ΔK_{th} and the notch depth a_n , the value of a_c which gave the lowest error was determined. These were then shown to possess similar values to the parameter a_0 in the El Haddad short crack model (El Haddad, 1979) which is estimated by the equation:

$$a_0 = \left(\frac{\Delta K_{th}}{\Delta \sigma_0} \right)^2 \frac{1}{\pi} \quad (2.41)$$

The values obtained are shown in table 2.5.

Material	a_c (mm)	a_0 (mm)
Grade 17 grey iron	3.0	3.15
Pearlitic SG iron	0.9	0.93
Ferritic SG iron	0.55	0.48

Table 2.5 Comparison of crack sizes (from Taylor, 1996a)

The value of a_c is assumed to represent the length of a nonpropagation crack at the notch root. The parameter a_0 was considered by Taylor to provide a good estimate of the value for a_c . Therefore, for cast iron, it is necessary to allow for the presence of a notch root crack, whereas for many other materials for which a_0 is typically small, this term is not so important. The effects of section size are accounted for simply through the effect that the crack length a_c has on the net

section size, and therefore the K value. Material properties were assumed to be independent of section size in Taylor's calculations.

Taylor (1996b) has also considered the problem of assessing the fatigue strength of arbitrarily shaped components containing stress concentrations. Orientated towards the direct use of finite element stress analysis results, the approach which is proposed involves comparing the uncracked body stress field close to the stress concentration with the known stress solution for a centre cracked infinite plate. If the stress concentration is sufficiently high, then a good match can be obtained between the two stress distributions, and an effective ΔK estimated. This is then compared with the threshold value, ΔK_{th} . Good agreement has been found with test results for cast iron (Taylor, 1997).

2.4.1 Geometrically Small Stress Concentration Features and Short Cracks

In this work, small stress concentration features can include inherent defects as typically occur in castings and forgings, surface roughness, scratches and also intentional geometric features such as artificial cracks. In an earlier section, the use of the Local Strain approach was described for predicting the fatigue strength of cast irons, cast steels and wrought steels. Many workers have proposed the use of fracture mechanics to describe the effects of these features. In his review of models for predicting the effects of defects, inclusions and inhomogeneities on the fatigue strength of metals, Murakami (1994) loosely classified the available models into three groups:

1. Frost's model and other similar models
2. Approaches based on fatigue notch factor
3. Fracture mechanics based approaches

The first of these can be considered to be based on the expression:

$$\sigma^n l = C \tag{2.42}$$

where σ is the fatigue limit, l is a dimension representing the size of the defect, n and C are constants. When $n = 3$, the equation describes Frost's model (Frost, Pook and Marsh, 1974), described in the next section. Another model was

proposed with $n = 4$, and a model proposed by Murakami and described later in this section is obtained with $n = 6$:

$$\sigma^6 \sqrt{area} = C \quad (2.43)$$

where area is the projected area of the defect. Murakami has pointed out that the difference in exponent n is due to differences in defect sizes considered. The higher exponent values ($n \rightarrow 6$) being more relevant to the smallest defects.

The second of these approaches has been described earlier under the heading *Local Strain Based Approach for Small Defects*, and relates particularly to the work of Mitchell (1976) and Heuler et al (1992).

The third approach is based on the use of the range of stress intensity factor ΔK for an equivalent crack, and an expression for the threshold for growth ΔK_{th} .

Scarlin, Berger and Mayer (1986) used Linear Elastic Fracture Mechanics (LEFM) methods to describe the behaviour of defects in steel forgings. Several forgings of low alloy steels which had been rejected on account of ultrasonic test findings were cut up, and fatigue specimens were machined and tested. In all cases where crack growth occurred, the ΔK value estimated from the actual initiating defect lay above the threshold value for growth ΔK_{th} . The crack growth rates however exhibited significant deviations. At low ΔK values (small crack sizes), the growth rates were generally higher than the LEFM predictions, while at moderate ΔK values, the growth was generally lower than predicted. These effects were attributed to the short crack effect and relative stiffness effects between inclusions and the surrounding matrix affecting the local stress levels.

Linear Elastic Fracture Mechanics has also been proposed as a method for assessing initial material quality for aircraft airframe materials. Magnusen et al (1990) has described how Al-Zn-Cu-Mg 7050 alloy thick plate contains populations of microflaws such as microvoids and inclusions.

One approach to quantifying the defect population is to carry out fractographic examinations of failed fatigue specimens. A less labour intensive alternative which is proposed is to back calculate the crack growth from some final crack size to an Equivalent Initial Flaw Size (EIFS) using LEFM procedures. To enable this to be done, the Paris law (Paris, 1963) is extrapolated to low ΔK values. For the particular material examined by Magnusen, the EIFS was in general agreement with the actual flaw sizes. They were however found to be statistically different to some extent. It was proposed that durability assessments of components can be carried out using the EIFS data and simple LEFM prediction methods, so avoiding complications arising from the short crack effect. For defects outside the range of sizes considered, the predictions may not be valid.

Yu, DuQuesnay and Topper (1990) investigated the relationship between the defect size distribution and the fatigue strength distribution for cast iron, cast steel and wrought steel. It was found that both the defect size distributions (in terms of the parameter $1/\sqrt{D}$) and the fatigue strength for the cast materials could be represented by bi-modal distributions. Predictions of the fatigue strength distribution for the cast iron were made based upon the defect size distribution and using the equation:

$$\sigma = \frac{\sigma_0}{1 + C_1 \sqrt{D}} \quad (2.44)$$

where σ_0 is the fatigue strength for the defect free material, C_1 is a material constant ($0.384\text{mm}^{1/2}$) and D is the defect size. Reasonable agreement was obtained with the experimental data.

The work done by Heuler (1992) covered both the use of the Local Strain approach for describing the fatigue behaviour of steel castings (described earlier), and the use of fracture mechanics. For the latter, the defects were idealised as two-dimensional elliptical cracks oriented perpendicular to the direction of loading. The evaluation involved:

- The determination of the geometry factor Y for the K solution
- Consideration of mean stress effects by allowing for crack closure
- Allowance for elastic-plastic effects using a strain-based intensity factor

- Comparison with fatigue threshold ΔK
- Crack propagation calculations using the Paris growth law.

In some cases, no crack initiation and propagation was found even though some ΔK values were well above the threshold value. This was attributed to a long incubation period for these defects. In other cases, crack growth occurred even at ΔK values below the threshold. It was pointed out that the latter generally involved the smallest crack sizes, and that the size of these cracks was less than the crack size a_0 which defines the intersection point between the plain fatigue limit and long crack fatigue threshold behaviour on a Kitagawa diagram (see below). The apparent threshold may therefore be expected to be less than the long crack threshold for these defects. The best agreement between the fracture mechanics based predictions and the experimental data was for those defects for which the crack growth was at least 1mm.

In 1976, Kitagawa and Takahashi (1976) published the results of work involving the study of the fatigue crack growth of small surface cracks in high strength steel plates. One aspect of their work involved the measurement of the threshold stress levels for crack growth for various crack sizes. For crack sizes above 0.5mm, conventional fracture mechanics relations can be applied, and the threshold stress level was given by:

$$\Delta\sigma = \frac{\Delta K_{th}}{Y\sqrt{\pi a}} \quad (2.45)$$

where Y is the geometry correction factor for the crack, ΔK_{th} is a material constant equal to 15.5 MPa \sqrt{m} . For crack sizes below 0.5mm, the threshold stress level tends towards the uncracked smooth specimen fatigue limit. These results were presented on a plot of threshold stress range versus crack length, on a log-log scale, as shown schematically in figure 2.8. This type of diagram has since become known as the Kitagawa-Takahashi diagram.

The reasons given for this behaviour included (a) the shape of the crack surface is not constant as it grows, (b) the constant ΔK_{th} relation based on linear elastic fracture mechanics can not be applied. The latter implies that the magnitude of the crack tip stress field which controls the rate of growth is no longer characterised uniquely by the parameter K, due possibly to the influence of microstructural features such as grain boundaries, preferential slip planes etc.

Smith and Miller (1978) proposed that an estimate of the threshold stress intensity factor ΔK_{th} could be obtained based on the assumption of a constant plain fatigue limit for crack sizes less than a_0 . At larger sizes than this the threshold condition is given by the long crack ΔK_{th} value.

A model to describe the behaviour of short cracks such as these was proposed by El Haddad (1979). A strain based intensity factor was defined as:

$$\Delta K = E\Delta e\sqrt{(\pi(a + a_0))} \quad (2.46)$$

where a is the crack length, Δe is the applied strain range, and a_0 is a constant for a given material and material condition. For elastic conditions, $E\Delta e = \Delta S$. Knowing the fatigue limit for the material ($\Delta\sigma_0$) and the long crack threshold ΔK value (ΔK_{th}), the value of a_0 may be obtained from:

$$a_0 = \left(\frac{\Delta K_{th}}{\Delta\sigma_0} \right)^2 \frac{1}{\pi} \quad (2.47)$$

This model was shown to describe the threshold behaviour of smooth fatigue specimens of CSA G40.11 steel containing different size cracks. The model was also applied to the problem of non-propagating cracks at notch roots, which will be addressed in the next section.

El Haddad et al (1981) went on to apply this model to the prediction of the fatigue life of both smooth and notched specimens of AISI 4340 steel, G40.11 steel and 1015 steel.

The El Haddad model may be written in a form to describe the apparent dependence of crack growth threshold on crack length for short cracks:

$$\Delta K_{th} = \Delta K_0 \left[\frac{a}{a + a_0} \right]^{1/2} \quad (2.48)$$

where

$$a_0 = \left(\frac{\Delta K_0}{Y \cdot \Delta \sigma_0} \right)^2 \frac{1}{\pi} \quad (2.49)$$

and Y is the crack geometry correction factor for K , and ΔK_0 is the long crack growth threshold.

The El Haddad model has been shown to be a special case of the Blocked Slip Band (BSB) model developed by Tanaka et al (1981). The model is based on the assumption that a process zone of a certain length is required ahead of the crack for it to grow. The slip band extending from the crack tip is blocked by a grain boundary. This must be able to propagate into the next grain for crack growth to take place. Whereas El Haddad considered that the a_0 term was required to account for the effect of the boundary on the crack tip stresses, and also the reduced flow resistance in surface grains, Tanaka provided evidence that the build up of crack closure with crack length is a major factor. This conclusion is supported by other work described by Suresh and Ritchie (1984). A deviation from the theoretical relation was observed for hard metals. this was explained by the effects of inherent defects, and a modification was proposed in the form:

$$\Delta K_{th} = \Delta K_0 \left[\frac{a}{a + a_0 - a_1} \right]^{1/2} \quad (2.50)$$

where a_1 is the size of the inherent flaws in the material. This relation applies when a is greater than a_1 . When a is less than a_1 , then the stress intensity factor

expression is meaningless for fatigue fracture. A similar expression is obtained from the expressions for fatigue threshold stress level proposed by Lukás at al (1989).

Taylor and Knott (1981) examined the concept of a critical length below which some fatigue cracks tend to grow anomalously fast. They defined two other crack lengths in addition to a_0 ; these are a_1 and a_2 . a_0 and a_1 are defined in the same way as above. a_2 is the point of deviation from the constant ΔK_{th} line on the Ktiagawa diagram (figure 2.8). In their paper, it is concluded that the point a_1 might correspond to the grain size, and a_2 represents the crack length beyond which microstructural interactions no longer produce non-uniform effects on the crack growth rate, and in mild steel corresponds to about 10 grain diameters, or approximately 4 times a_0 . Work by Ravichandran (1997) appears to provide a possible explanation for these values. Computer simulations were performed to model the effect that individual grains could have on the aspect ratio of short cracks. At about 10 grain diameters, the variations in crack aspect ratio arising from the grains becomes very small, whereas initially, the variations are large.

An alternative approach to describing this type of behaviour is provided by Usami and Shida (1979). A fatigue limit criterion is proposed, based on the cyclic plastic zone size at the crack tip (r_{pc}) being constant at the fatigue limit. The value of r_{pc} is related to the value of K for a defect, and the cyclic yield stress (σ_{yc}). Then using the Dugdale strip-yield model, the fatigue limit criterion of a specimen containing a crack is given by:

$$r_{pc(w)} = a_e \left[\sec \left(\frac{\pi \cdot \Delta \sigma_w}{4 \sigma_{yc}} \right) - 1 \right] \quad (2.51)$$

when $R \geq 0$, and

$$r_{pc(w)} = a_e \left[\sec \left(\frac{\pi}{2(2\sigma_{yc} / \sigma_{\max,w} + R)} \right) - 1 \right] \quad (2.52)$$

for $R \leq 0$, where $\Delta\sigma_w$ is the stress range and $\sigma_{max,w}$ is the maximum stress at the fatigue limit. a_e is half the length of an equivalent two-dimensional crack assumed in an infinite plate:

$$a_e = \frac{(K / \sigma_{net})^2}{\pi} \quad (2.53)$$

and σ_{net} is the applied normal stress. With this model, the effects of both stress ratio and yield strength on short crack behaviour are claimed to be accounted for. The equations do reproduce the characteristic shape of the threshold stress versus crack size curve which is typical of Kitagawa diagrams. Suresh and Ritchie (1984) argued that this is a special case of a blocked slip band model.

Predictions made using this model were compared with fatigue limit data for four different metals containing defects of various sizes: Mild steel, 13Cr cast steel, Maraging steel, cast iron. The defect types included surface roughness, micro-shrinkage cavities and inclusions. Close agreement was reported. No experimental evidence was however available that $r_{pc(w)}$ is constant for both long and short cracks.

Murakami (1989) has proposed the following relation to describe the observed crack size dependence of the threshold stress intensity factor range ΔK_{th} for small cracks:

$$\Delta K_{th} = 3.3 \times 10^{-3} (Hv + 120) (\sqrt{area_s})^{1/3} \quad (2.54)$$

where Hv is the Vickers hardness, $area_s$ is the area of the defect in μm^2 , and ΔK_{th} is in $\text{MPa m}^{1/2}$. Making an approximation for the maximum stress intensity factor K_{max} for a surface breaking defect:

$$K_{max} = 0.65 \sigma_{max} (\pi \sqrt{area_s})^{1/2} \quad (2.55)$$

where σ_{max} is the maximum tensile stress, then an expression for the fatigue limit was proposed given by:

$$\sigma_w = \frac{1.43(Hv + 120)}{(\sqrt{area_s})^{1/6}} \quad (2.56)$$

These equations assume that as far as the fatigue limit is concerned, a three-dimensional defect is equivalent to a crack. Similar expressions are presented for sub-surface defects. The application of this \sqrt{area} model to a number of different problems has been described by Murakami (1994). These include:

- Fatigue of small holes
- Small cracks
- Surface scratches
- Surface roughness
- Non-metallic inclusions
- Corrosion pits
- Carbides in tool steels
- Second phase in Al-Si eutectic alloys
- Spheroidal graphite in cast irons

The upper limit of the validity of the \sqrt{area} model is considered to be approximately 1mm (Murakami, 1994).

2.4.2 Short Fatigue Cracks at Notches

Analysis of notch specimen test data by Frost, Pook and Marsh (1974) indicated that even if the applied stress was sufficient to form a crack at the root of a notch, there still existed a definite fatigue limit. An empirical relationship was proposed between crack length and the maximum value of alternating stress that would just not cause a crack to grow:

$$\sigma^3 a = C \quad (2.57)$$

where σ is the alternating stress and a is the crack depth. If $\sigma^3 a > C$ then the crack will grow. This model was based on tests where notch fatigue cracks were formed, and then the specimens were reprofiled to remove the notch, but leaving the crack. The relation therefore applies to edge cracks in a uniformly stressed body. If a crack is assumed to be small with respect to the depth of a notch in a specimen, then the fatigue notch factor can be defined as:

$$K_f = \frac{\Delta\sigma_0 / 2}{(C/D)^{1/3}} \quad (2.58)$$

where $\Delta\sigma_0/2$ is the plain specimen fatigue limit. This therefore predicts that the 'notch sensitivity' will be dependent on specimen size (notch depth, D).

Further analysis of test results indicated that the critical value of stress intensity factor above which a crack will grow was different between longer cracks and short cracks, the value being lower for short cracks. On the basis of this, it was proposed that a macrocrack will only grow to failure if the range of stress intensity factor ΔK remains greater than the threshold value ΔK_{th} for both short and long crack lengths. For plain specimens this will always be the case, but for notch root cracks, ΔK can sometimes increase more slowly with crack length than the threshold value ΔK_{th} , leading to crack arrest.

The possible link between the growth behaviour of short cracks at notches and the development of crack closure was illustrated by Tanaka and Nakai (1983). After demonstrating that growth rates could be correlated through the use of an effective stress intensity factor ($\Delta K_{eff} = K_{max} - K_{op}$), a method was proposed for estimating the effective threshold stress intensity factor $\Delta K_{eff,th}$ for short cracks. Their approach is based on an adaption of the El Haddad model in which effective stress intensity factors are used. The ratio of effective short crack threshold to effective long crack threshold is shown to be given by:

$$\frac{\Delta K_{eff,th}}{\Delta K_{eff,th\infty}} = \left[\frac{a_{np}}{a_{np} + a_0} \right]^{1/2} \frac{F(a_{np})}{F(a_{np} + a_0)} \quad (2.59)$$

where a_{np} is a non-propagating crack length, $F()$ is crack geometry correction factor (a function of crack length). The terms a_0 and a_0' are given by:

$$a_0 = \left(\frac{\Delta K_{th,\infty}}{\Delta \sigma_0} \right)^2 \cdot \frac{1}{\pi} \quad (2.60)$$

$$a_0' = \left(\frac{\Delta K_{eff th,\infty}}{\Delta \sigma_0} \right)^2 \cdot \frac{1}{\pi} \quad (2.61)$$

A 'Resistance-curve' method was proposed by Akiniwa et al (Akiniwa, Tanaka, Taniguchi, 1990) for predicting the growth threshold of short fatigue cracks growing from a notch root. Their resistance-curve is based on the theory that crack opening and closing stress levels increase with increasing short crack size. The model describes an increasing growth threshold value with increasing crack size for crack sizes below a certain R-ratio dependent value. Above this value, the growth threshold is equal to the conventional 'long-crack' threshold value. The threshold for crack propagation is expressed as the sum of two terms:

1. the crack opening SIF, $K_{op th}$
2. and the effective range of SIF at threshold $\Delta K_{eff th}$

The latter term is assumed to be constant, and therefore the same for both short and long cracks. The threshold SIF is therefore given by:

$$K_{max,th} = K_{op,th} + \Delta K_{eff,th} \quad (2.62)$$

where $K_{max,th}$ is the maximum SIF in the cycle when the growth rate tends towards zero. Two crack lengths are defined, c_1 and c_2 . Below c_1 the crack is assumed to be a stage I crack, and can only grow beyond c_1 if the stress is sufficient to give a K value which exceeds $\Delta K_{eff th}$. For crack sizes greater than c_1 the level of K to open/close the crack ($K_{op th}$) increases from zero up to the value for 'long-cracks' $K_{op,th\infty}$ at a crack size of c_2 . An expression for the crack opening K value at threshold $K_{op th}$ was proposed by Akiniwa et al as:

$$K_{op,th} = K_{op,th\infty} \left[\frac{c_{np} - c_1}{c_2 - c_1} \right]^{1/2} \quad c_1 \leq c_{np} \leq c_2 \quad (2.63)$$

$$K_{op,th} = K_{op,th\infty} \quad c_2 \leq c_{np}$$

where c_{np} is the nonpropagating crack length. For a 'long-crack':

$$K_{max,th\infty} = K_{op,th\infty} + \Delta K_{eff,th\infty} \quad (2.64)$$

The parameters $K_{max,th\infty}$, $\Delta K_{eff,th\infty}$, c_1 and c_2 must be determined experimentally.

This description of a short crack length dependent growth threshold is similar to the simple empirical relation of El Haddad (1979) when cast in the form to give ΔK_{th} . The expressions are compared graphically in figure 2.9, where for the Akiniwa model:

$$K_{max,th} = 7 \left[\frac{c_{np} - 0.00046}{0.01 - 0.00046} \right]^{1/2} + 6 \quad (2.65)$$

and for the El Haddad model:

$$\Delta K_{th} = 13 \left[\frac{a}{a - 0.00046 + a_0} \right]^{1/2} \quad (2.66)$$

$$a_0 = \frac{1}{\pi} \left[\frac{13}{1.12 * 70 * 2} \right]^2$$

Both models imply that below a certain crack size, there will be no effect, and with suitable choice of parameters, the curve shapes can be broadly similar.

In the work by Akiniwa et al, results obtained using the model were compared with experimental results from fatigue tests of single edge notched plates of low carbon

steel at various stress ratios. Good agreement was obtained in terms of fatigue strength values and nonpropagating crack sizes. SIF values for short notch root cracks were estimated using the weight function technique, and account was taken of notch root plasticity effects using nonlinear FE analysis. The model appeared to successfully predict which load levels would cause non-propagating part-through cracks to form, which would cause non-propagating through-thickness cracks to form, and also which would generate cracks which would grow to failure.

A crack closure model was used by Abdel-Raouf (1992) to predict the fatigue limits of notched fatigue specimens and the lengths of non-propagating cracks. A particular characteristic of this work was the use of a surface strain concentration factor which is related to the microstructure. The theory assumes that surface strain concentration will come about due to a combination of favourably oriented grains and reduced support for the surface grain from surrounding grains, relative to grains in the interior of the material. For a crack in an elastic stress field around a notch root, the range of stress intensity factor ΔK is given by:

$$\Delta K = F \cdot K_t \cdot Q_\epsilon \cdot \Delta S \cdot \sqrt{\pi a} \quad (2.67)$$

where:

- F = Shape factor
- K_t = Geometric stress concentration factor for notch
- Q_ϵ = Inherent surface strain concentration factor
- a = Crack depth

The inherent strain concentration factor is presented in the form:

$$Q_\epsilon = \frac{\Delta \epsilon}{\Delta e} = 1 + G \exp(-a / d) \quad (2.68)$$

G is a constant and d is the grain size. A value of $Q_\epsilon = 6.3$ was given for the grain most favourably oriented for slip. the value of q was therefore taken as 5.3. The

development of crack closure with increasing crack length was described using an equation of the following form:

$$S_{op} = S_{op,max} [1 - \exp(-ka_e)] \quad (2.69)$$

where k is a material constant, S_{op} is the crack opening stress, $S_{op,max}$ is the steady state opening stress for a long crack, and a_{eff} is the effective crack length, given by:

$$a_{eff} = a - L_p / 2 \quad (2.70)$$

L_p is the surface reversed plastic zone. Closure is assumed to start when the crack reaches the centre of L_p . It was proposed that for a crack to propagate, the applied stress range must exceed the sum of the crack opening (closure) stress S_{op} and the intrinsic threshold stress range ΔS_{ith} :

$$\Delta S > S_{op} + \Delta S_{ith} \quad (2.71)$$

The intrinsic threshold stress range ΔS_{ith} is the minimum stress range above the opening stress required to grow a crack, and must be determined from smooth specimen fatigue tests at high R-ratio, or crack growth threshold tests at high R-ratio.

The predicted notched fatigue strengths obtained using this approach compared well with notched fatigue data generated using 2024-T351 aluminium alloy. No details were available to check the predictions of nonpropagating crack length for this material. Predictions of non-propagating crack lengths were however compared with the data generated by Frost (1955a & b) using BS L65 aluminium alloy. Reasonable agreement appeared to be obtained, although the data was presented on a log-log scale.

A model has been proposed by Ahmad and Yates (1994) to represent the growth rates of cracks growing through a notch root plastic zone. For short cracks, an

elastic-plastic crack growth model based on the Hobson equation was proposed. For long cracks at notches, a crack growth law which includes a constant term to represent the threshold was proposed. The models are shown to describe the measured growth behaviour of cracks growth at a 1mm deep circumferential notch, $K_t=2.3$, particularly the decreasing growth rates down to a minimum, after which growth accelerates again. The tests did not however include the generation of non-propagating cracks, nor were measurements of crack opening/closure included.

2.5 Discussion

Traditional approaches to fatigue design and fatigue data analysis have made much use of the 'nominal stress' approach described in section 2.2. One obvious reason for this is that for test specimens, and relatively simple idealised structures, a nominal stress can easily be defined. Current methods of designing engineering components make frequent use of the finite element method for stress analysis, and the trend is towards more detailed finite element models which give more and more precise predictions of the stress fields in a component during operation. A consequence of this is that the nominal stress used by the material scientists to characterise the notched fatigue behaviour of test specimens, can often not be easily related to the stress field in a component. The methods described by Peterson for example, are therefore not particularly relevant for use with finite element based stress analysis.

The 'Local Strain' approach described in section 2.3 is very well suited to use with the finite element method of stress analysis, because by its very nature, it makes direct use of stresses and strains calculated at the point of interest. The recent extensions to multiaxial stress states (at least, for simple load cycling) further enhance its usefulness. The drawback with the Local Strain approach on its own is the problem of predicting the fatigue strength of components with relatively high stress concentrations where crack growth may be experienced, and also in cases where defects (inherent or otherwise) are present. Some workers have demonstrated success with this approach for dealing with inherent defects (Mitchell, 1976; Heuler, 1992), but this is dependent on the type of defects considered, and their shape. Critical depth based approaches attempt to address

the problem of dealing with high stress gradients, and some success appears to have been achieved. However, a number of fatigue tests on notched specimens may be required to determine the value of the critical depth.

For small defects, particularly those with a planar crack-like form, models based on empirical descriptions of crack growth characteristics, and presented in the form of the Kitagawa plot have gained much support (e.g. the El Haddad short crack model, El Haddad, 1979). Mechanistic models based on blocked slip bands at grain boundaries, and crack closure behaviour appear to support these. These mechanistic models rely on the use of experimentally determined crack opening stress levels or the identification of microstructural barriers. The advantage and usefulness of models such as the El Haddad model is its simplicity, and the fact that it is mainly dependent on commonly measured material parameters.

At stress concentrations, models based on crack closure development have been used to help explain instances of crack arrest (Akiniwa, 1990; Abdel-Raouf, 1992), and fatigue notch insensitivity. However, the general concept of making use of the apparent crack growth threshold for short cracks at notches was suggested much earlier (Smith and Miller, 1978; Frost, Pook and Marsh, 1974).

For many materials, the short crack effect does not extend very far, and for sharp notches in simple geometries, the approximation of effective crack depth to notch depth is acceptable for engineering assessments (i.e. the presence of a notch root crack can be neglected). Taylor (1996a) modified this for application to cast irons where the short crack effect can extend a relatively large distance, by augmenting the effective crack depth by a_0 (as defined in figure 2.8). Overall however, the analysis of notched fatigue behaviour of cast iron specimens and components in terms of the growth of short notch root cracks does not appear to have been addressed in the literature to anywhere near the same extent as steels, aluminium alloys etc.

3. CAST IRON NOTCHED TEST DATA AND ANALYSES

Recent work carried out at ALSTOM Energy Technology Centre has involved the generation of a large quantity of test data on cast iron. In this section, the details of this comprehensive experimental work are described. The data is important because it covers a range of grades of cast iron, tested mainly under conditions of uniaxial loading, thus removing many of the uncertainties of bending tests, and also, a variety of notched specimen geometries have been used. Overall, six grades of cast iron have been used in test programmes involving tensile, high cycle fatigue and crack growth threshold tests. The effects of several important parameters were investigated, including notch geometry, cast section size, R-ratio and surface condition.

The materials used in the tests were:

- Grade 17 (260 MPa) Flaked Graphite (F.G. or grey) cast iron
- Grade 250 grey iron
- Grade 300 grey iron
- Grade 350 grey iron
- Grade 400/18 Spheroidal Graphite (S.G.) iron
- Grade 500/7 S.G. iron

The tests and the results are described for each grade of material in the following sections.

3.1 Grade 17 Grey Iron Tests (BRITE Project Specimens)

3.1.1 Experimental Procedure

These tests were carried out as part of a BRITE/EURAM project: ENDDURE (Devlukia, 1991). The material for the specimens was obtained from 25, 32 and 50mm diameter cast test bars (plain specimens), and also from a diesel engine crankcase cut up specifically for these tests (fig. 3.1 and 3.2). The graphite flake structure was Type A in a pearlitic matrix. The material characterisation data for the cast test bars is summarised in tables 3.1 to 3.6 and figures 3.3 to 3.5. The crankcase material was not subjected to a material analysis.

Material:	Grade 17 grey cast iron							
Source:	Richards Foundary							
Form:	1" dia. cast test bars							
Sample ID:	MT573-575							
Condition:	As-cast							
Chemical analysis:								
Element	C	S	P	Mn	Si	Cr	Ni	Cu
% WT	3.34	0.08	0.03	0.52	2.20	0.08	0.07	0.19
Tensile Properties:								
Sample ID	UTS (MPa)	0.1% P.S. (MPa)	0.2% P.S. (MPa)	E (GPa)	R in A (%)	Elong. (%)		
MT573	250	194	227	129	<1	<1		
MT574	285	191	225	115	<1	<1		
MT575	298	201	237	119	<1	<1		
Hardness:								
3000Kg, 10mm ball				Impact:				
H _B				Energy (J)				
a	207			a	2			
b	207			b	2			
c	223	c	2					
		d	2					
		e	2					

**Table 3.1 Mechanical property summary: 1" (25mm) dia. cast test bars
for BRITE/EURAM project**

Material:	Grade 17 grey cast iron							
Source:	Richards Foundary							
Form:	1.25" dia. cast test bars							
Sample ID:	MT563-565							
Condition:	As-cast							
Chemical analysis:								
Element	C	S	P	Mn	Si	Cr	Ni	Cu
% WT	3.32	0.09	0.03	0.49	2.10	0.08	0.07	0.19
Tensile Properties:								
Sample ID	UTS (MPa)	0.1% P.S. (MPa)	0.2% P.S. (MPa)	E (GPa)	R in A (%)	Elong. (%)		
MT563	293	201	235	126	<1	<1		
MT564	238	197	227	120	<1	<1		
MT565	280	197	228	126	<1	<1		
Hardness:								
3000Kg, 10mm ball		H _B		Impact:				
						Energy (J)		
a		207		a		2		
b		207		b		2		
c		207		c		2		
				d		2		
				e		3		

Table 3.2 Mechanical property summary: 1.25" (32mm) dia. cast test bars for BRITE/EURAM project

Material:	Grade 17 grey cast iron							
Source:	Richards Foundary							
Form:	1.25" dia. cast test bars							
Sample ID:	MT566-568							
Condition:	As-cast							
Chemical analysis:								
Element	C	S	P	Mn	Si	Cr	Ni	Cu
% WT	3.32	0.09	0.03	0.49	2.10	0.08	0.07	0.19
Tensile Properties:								
Sample ID	UTS (MPa)	0.1% P.S. (MPa)	0.2% P.S. (MPa)	E (GPa)	R in A (%)	Elong. (%)		
MT566	289	193	229	145	<1	<1		
MT567	260	193	228	146	<1	<1		
MT568	288	196	228	136	<1	<1		
Hardness:								
3000Kg, 10mm ball		H _B		Impact:				
				Energy (J)				
a	207			a	2			
b	207			b	2			
c	204			c	2			
				d	2			
				e	3			

Table 3.3 Mechanical property summary: 1.25" (32mm) dia. cast test bars for BRITE/EURAM project

Material:	Grade 17 grey cast iron							
Source:	Richards Foundary							
Form:	1.25" dia. cast test bars							
Sample ID:	MT569-571							
Condition:	As-cast							
Chemical analysis:								
Element	C	S	P	Mn	Si	Cr	Ni	Cu
% WT	3.32	0.09	0.03	0.49	2.10	0.08	0.07	0.19
Tensile Properties:								
Sample ID	UTS (MPa)	0.1% P.S. (MPa)	0.2% P.S. (MPa)	E (GPa)	R in A (%)	Elong. (%)		
MT569	238	195	228	130	<1	<1		
MT570	285	200	231	118	<1	<1		
MT571	278	203	235	121	<1	<1		
Hardness:								
3000Kg, 10mm ball		H _B		Impact:		Energy (J)		
a	207			a				
b	204			b				
c	212			c				
				d				
				e				

**Table 3.4 Mechanical property summary: 1.25" (32mm) dia. cast test bars
for BRITE/EURAM project**

Material:	Grade 17 grey cast iron							
Source:	Richards Foundary							
Form:	1.25" dia. cast test bars							
Sample ID:	MT572							
Condition:	As-cast							
Chemical analysis:								
Element	C	S	P	Mn	Si	Cr	Ni	Cu
% WT	3.32	0.09	0.03	0.49	2.10	0.08	0.07	0.19
Tensile Properties:								
Sample ID	UTS (MPa)	0.1% P.S. (MPa)	0.2% P.S. (MPa)	E (GPa)	R in A (%)	Elong. (%)		
MT572	267	194	227	129	<1	<1		
Hardness:			Impact:					
3000Kg, 10mm ball	H _B				Energy (J)			
a	207				a	2		
b					b			
c					c			
					d			
					e			

Table 3.5 Mechanical property summary: 1.25" (32mm) dia. cast test bars for BRITE/EURAM project

Material:	Grade 17 grey cast iron							
Source:	Richards Foundary							
Form:	2" dia. cast test bars							
Sample ID:	MT576-578							
Condition:	As-cast							
Chemical analysis:								
Element	C	S	P	Mn	Si	Cr	Ni	Cu
% WT	3.29	0.09	0.03	0.50	1.8	0.05	0.07	0.20
Tensile Properties:								
Sample ID	UTS (MPa)	0.1% P.S. (MPa)	0.2% P.S. (MPa)	E (GPa)	R in A (%)	Elong. (%)		
MT576	246	186	212	105	<1	<1		
MT577	259	177	208	128	<1	<1		
MT578	241	157	187	133	<1	<1		
Hardness:								
3000Kg, 10mm ball					Impact:			
H _B					Energy (J)			
a	190				a	2		
b	187				b	3		
c	187				c	4		
					d	3.5		
					e	2.5		

Table 3.6 Mechanical property summary: 2" (50mm) dia. cast test bars for BRITE/EURAM project

Four types of test were carried out:

1. High cycle axial fatigue tests

High cycle fatigue tests were carried out at ambient temperature on both plain and notched specimen geometries, using an Amsler Vibrophore resonance machine at a frequency of 100 Hz and various mean stress levels.

The plain specimen geometry is shown in figure 3.6. Three notched axial test specimen geometries were considered as shown in figures 3.7, 3.8 and 3.9. In addition, three notched bend specimen geometries were tested. The axial specimens were:

1. Circumferential 'U' notch: $K_t = 2.2$
2. Circumferential 'V' notch: $K_t = 5.6$
3. Shoulder fillet: $K_t = 3.8$

The design of the first two were based on fillet radii existing in a diesel engine crackcase. The last of these ($K_t=3.8$) was designed by the author to provide a better simulation of the type of notch geometries observed in engine components, while at the same time providing a third K_t value, and also retaining the simplicity of a compact axial test piece. Whereas the first two notched specimens have notches of a well defined depth, this third specimen geometry does not, thus making it difficult to use approaches based on the concept of a notch behaving as a crack of similar depth. As in an actual component, attention must be focussed on the local notch root behaviour.

In total 82 tests were performed on these geometries, made up of:

- 29 plain specimens
- 18 notched $K_t=2.2$
- 12 notched $K_t=5.6$
- 23 notched (simulated component) $K_t=3.8$

2. High cycle bending fatigue tests

The bend tests were carried out with a three-point bend configuration. The test bars had overall dimensions of 45x45x250mm. Three notch geometries were tested as shown in figure 3.10, all with a notch depth of 3.175mm and notch root radii and K_t values of:

$R = 11.71\text{mm}$	$K_t = 1.5$
$R = 3.175\text{mm (1/8th in.)}$	$K_t = 2.394$
$R = 0.305\text{mm (12 thou.)}$	$K_t = 6.3$

Testing was continued on each component until complete fracture or an endurance of approximately 3×10^7 cycles, whichever was sooner.

3. Fatigue crack growth threshold tests

Fatigue crack growth threshold tests were also carried out using compact tension specimens (Figure 3.10a) at several R-ratios. The method used was to test at a constant R ratio (min. to max. load ratio) using a load shedding technique.

Threshold was defined as the highest value of stress intensity factor range at which growth does not exceed 10^{-10} m/cycle over a period of not less than 5×10^6 cycles.

4. Tensile tests

In addition to fatigue tests, 26 tensile tests were carried out using specimens manufactured from both cast test bars and engine crankcases.

3.1.2 Experimental Results

The test results for the plain and notched axial specimens are shown in tables 3.7 to 3.10. Figures 3.11 to 3.14 show the data plotted on Goodman diagrams with the data points marked only as failures or run-outs. In both the plain specimen results and the notched specimen results the mean net section stress appears to

have a non-linear influence on the fatigue limit, with a concave shape to the boundary between failures and run-outs. This is unusual for plain specimen results. It is interesting however, to compare this data with some results presented by Usami and Shida (1979). Figure 2 of this reference illustrates fatigue test results for mild steel at various mean stress levels, and with specimens containing cracks of different lengths. The test results from specimens containing significant crack lengths exhibit a similar concave shape to the present results for grey iron.

The estimated fatigue strengths at $R = -1$ for the different axial specimen geometries (based on the average stress from the highest run-out and the lowest failure) are as follows in table 3.11:

Spec.	Cycles	Smean (MPa)	Salt (±MPa)	R-ratio	Result
MT1383	1.90E+05	162.5	22.5	0.76	Fail
MT1384	1.57E+07	160	20	0.78	Run-out
MT1385	7.75E+06	160	25	0.73	Fail
MT1387	1.30E+07	160	15	0.83	Run-out
MT1388	1.57E+06	160	20	0.78	Fail
MT1389	6.33E+05	120	30	0.6	Fail
MT1390	9.81E+05	120	25	0.66	Fail
MT1675	1.05E+06	0	87	-1	Fail
MT1676	1.44E+06	0	81	-1	Fail
MT1677	2.02E+06	0	72.5	-1	Fail
MT1678	1.24E+07	0	58	-1	Run-out
MT1679	1.25E+07	0	81	-1	Run-out
MT1680	4.99E+07	0	73	-1	Run-out
MT1681	1.61E+07	0	71	-1	Run-out
MT1683	4.39E+05	0	84	-1	Fail
MT1687	1.35E+07	0	75	-1	Run-out
MT1689	1.50E+07	140	28	0.66	Run-out
MT1692	1.46E+05	84	48	0.273	Fail
MT1693	1.13E+05	84	48	0.273	Fail
MT1695	6.10E+04	120	20	0.714	Fail
MT1699	6.15E+04	120	45	0.45	Fail
MT1700	1.53E+06	120	30	0.6	Fail
MT1703	1.28E+07	165.6	24.3	0.74	Run-out
MT1704	4.00E+05	0	88.3	-1	Fail
MT1705	1.00E+06	165.6	27.6	0.71	Fail
MT1706	1.39E+07	120	30	0.6	Run-out
MT1707	9.62E+05	0	85.5	-1	Fail
MT1708	1.19E+07	0	75	-1	Run-out
MT1709	9.10E+05	102	32	0.52	Fail

Table 3.7 Plain specimen fatigue test results for grade 17 grey iron

Spec.	Cycles	Smean (MPa)	Salt (\pm MPa)	R-ratio	Result
MT1003	6.06E+04	120	40	0.5	Fail
MT1014	2.02E+05	120	30	0.6	Fail
MT1204	3.30E+06	120	20	0.71	Fail
MT1206	7.44E+07	77	25	0.51	Run-out
MT1208	4.60E+07	120	15	0.78	Run-out
MT1254	2.56E+07	77	25	0.51	Run-out
MT1255	1.10E+06	97	25	0.59	Fail
MT1256	4.69E+06	77	25	0.51	Fail
MT1258	6.90E+05	44	39	0.06	Fail
MT1259	1.86E+07	68	23	0.49	Run-out
MT1668	1.92E+06	0	55	-1	Fail
MT1669	1.38E+07	0	45	-1	Run-out
MT1671	3.26E+05	40	40	0	Fail
MT1673	1.61E+07	170	10	0.89	Run-out
MT1684	1.50E+07	40	30	0.143	Run-out
MT1685	6.80E+05	170	20	0.79	Fail
MT1686	1.46E+07	0	50	-1	Run-out
MT1688	1.29E+07	170	15	0.84	Run-out

Table 3.8 Fatigue test results for grade 17 grey iron notched specimens ($K_t=2.2$)

Spec.	Cycles	Smean (MPa)	Salt (\pm MPa)	R-ratio	Result
MT1002	2.45E+04	120	40	0.5	Fail
MT1013	9.29E+04	120	30	0.6	Fail
MT1203	1.20E+06	120	20	0.71	Fail
MT1207	4.37E+07	120	15	0.78	Run-out
MT1249	1.25E+07	170	12.5	0.86	Run-out
MT1251	1.64E+06	120	20	0.71	Fail
MT1252	1.63E+05	55	47	0.078	Fail
MT1696	1.13E+06	170	15	0.83	Fail
MT1697	1.61E+07	0	50	-1	Run-out
MT1698	1.21E+06	0	55	-1	Fail
MT1701	3.52E+06	40	30	0.143	Fail
MT1702	3.95E+06	70	20	0.56	Fail

Table 3.9 Fatigue test results for grade 17 grey iron notched specimens (K_t = 5.6)

Spec.	Cycles	Pmean (kN)	Palt (\pm kN)	Dia.(mm)	R	Result
MT3577	1.16E+08	0	7.5	11.98	-1	Run-out
MT3579	2.02E+07	0	7	11.92	-1	Run-out
MT3580	4.54E+07	0	6.5	12	-1	Run-out
MT3572	1.96E+07	0	6	11.96	-1	Run-out
-----	2.78E+05	0	6.5	12	-1	Fail
MT3573	2.00E+07	0	5.5	12	-1	Run-out
MT1691	3.10E+05	0	8	12	-1	Fail
MT3270	4.74E+05	6.22	5.09	12	0.1	Fail
MT3273	2.78E+07	5.87	4.81	12.01	0.1	Run-out
MT3271	2.36E+07	5.53	4.52	12	0.1	Run-out
MT3575	1.12E+05	6.11	5	11.95	0.1	Fail
MT3574	1.23E+06	10.11	3.37	11.96	0.5	Fail
MT3269	9.06E+05	9.5	3.2	12.01	0.5	Fail
MT3275	4.11E+07	9.33	3.11	12	0.5	Run-out
MT3267	2.66E+07	8.48	2.83	12	0.5	Run-out
MT3274	9.26E+05	10.18	3.39	12	0.5	Fail
MT3268	5.10E+04	13.57	4.52	12	0.5	Fail
MT3576	2.02E+05	16	2.8	11.95	0.7	Fail
MT3581	2.03E+07	13	2.3	12	0.7	Fail
MT3578	3.42E+06	14	2.5	11.99	0.7	Fail
MT3272	2.40E+07	14	2.5	12	0.7	Run-out
MT3265	1.02E+06	17	3	12.01	0.7	Fail
MT3266	2.88E+07	16	2.8	12.01	0.7	Run-out

**Table 3.10 Fatigue test results for grade 17 grey iron notched specimens
(Simulated component, $K_t = 3.8$)**

K_t	Nominal fatigue strength (\pm MPa)
1	76.8
2.2	50.0
3.8	61.9
5.6	52.5

**Table 3.11 Effect of K_t on estimated nominal fatigue strength
- Grade 17 grey iron**

This data is illustrated in figure 3.15. The value for $K_t = 3.8$ must be treated with caution because the geometry is different, and consequently the nominal stress may not be directly comparable with the nominal stress of the other specimens. However, the data does indicate a distinct 'insensitivity' to the K_t values beyond $K_t = 2$.

In total, 13 notched three-point bend specimens were tested. The results are shown in table 3.12. The fatigue life at a given nominal stress level is significantly longer in the bend specimens than in the axial specimens. The nominal stress is defined in terms of the net section dimensions:

$$\sigma_{nom} = \frac{3 Pl}{2 bh^2} \quad (3.1)$$

where P is the applied load, l is the span between supports (180mm), b is the thickness (45mm) and h is the height at net section ($45 - 3.175 = 41.825$ mm).

Spec. No.	Block no.	K_t	Load (kN)	Stress (MPa)	Cycles
1007	B1	1.5	34.98±11.66	120±40	1.77x10 ⁶
1010	C1	1.5	34.98±8.75	120±30	2.39x10 ⁷ (Unfailed)
1018	C2	2.394	34.98±11.66	120±40	6.28x10 ⁵
979	D3	2.394	34.98±11.66	120±40	7x10 ⁵
1005	A3	2.394	34.98±8.75	120±30	4.56x10 ⁶
1011	C3	2.394	26.24±11.66	90±40	1.34x10 ⁶
1017	A2	6.3	52.48±2.92	180±10	1.05x10 ⁷ (Unfailed)
			34.98±11.66	120±40	3.2x10 ⁵
1004	A1	6.3	34.98±11.66	120±40	4.1x10 ⁵
1006	A4	6.3	6.1±2.5	30±12.4	1.6x10 ⁶
			6.74±3.06	33±15	
			34.98±8.75	120±30	1.98x10 ⁶
1012	C4	6.3	26.24±11.66	90±40	1.79x10 ⁶
980	D4	6.3	34.98±11.66	120±40	4.79x10 ⁵
1009	B4	6.3	34.98±5.83	120±20	1.27x10 ⁷ (Unfailed)

Table 3.12 Three-point bend notched specimen results

The measured tensile strength values were found to exhibit a high degree of scatter as shown in figure 3.16. The values range from 196 MPa to 290 MPa, with a mean value of 235 MPa. The stress-strain curves are shown in figure 3.17, and illustrate that the scatter in the tensile results is not simply due to the UTS value, it is also due to the variability in the overall curve, and the fracture strain. To isolate the scatter it is not sufficient to simply normalise the curves with respect to UTS value. Figure 3.18 shows that the general shape of the stress-strain curve can be obtained by normalisation with respect to the stress at a given strain, after fitting a Ramberg-Osgood curve to each test result and making the interpolation from this curve. Each of the curves shown in the figure is therefore plotted as the ratio of stress from the actual curve to the stress from the fitted curve for that specimen.

The fatigue crack growth threshold tests gave the results shown in figure 3.19. The measured ΔK_{th} values are clearly dependent on the R-ratio. A straight line least squares fit was made to this data giving the following expression:

$$\Delta K_{th} = 12.3168 \cdot (1 - 0.78R) \quad (3.2)$$

3.1.3 Description of Analysis Models of Test Specimens

The finite element method was used to calculate the stress distributions within the specimens, particularly in the region close to the notch root. This is the same procedure which would be followed in any analysis of an engine component design detail. Axisymmetry was assumed for the analyses of axial specimens, with additional assumptions of symmetry about the mid-diametral plane. This allowed the use of efficient two-dimensional representations of the geometry, as illustrated in figures 3.20, 3.21 and 3.22. The element type used was an eight noded isoparametric element, giving a quadratic displacement distribution and a linear stress distribution. The three-point bend specimens with $K_t = 2.4$ and 6.3 were analysed using two-dimensional 8-noded plane strain finite elements with a thickness of 45mm. These are shown in figures 3.23 and 3.24.

The load on the axial specimen models was applied as a series of equal concentrated loads at element corner nodes along the face representing the threaded portion of the specimen. Any nonuniformity in the loading distribution at the specimen threads was not included. The region of application of the load is quite well removed from the region of interest close to the notch. St. Venant's Principle was assumed to apply, which means that the change in distribution of the load from that which would be expected in practice will have only a local effect of the stresses in the specimen, and not influence the notch region. The loading on the bend specimens was applied as a single point load on the opposite face to the notch.

For all the analyses, typical material properties for cast iron have been assumed:

Modulus of elasticity: 120000 MPa
 Poisson's ratio: 0.26

These values are based on published BCIRA data for grey cast iron (Gilbert, 1977). The modulus of elasticity is defined in this reference as the slope of the tangent through the origin to the stress-strain curve rather than the secant modulus at some small percentage of the tensile strength based on the assumption that the curve is initially straight. The modulus for a typical cast iron varies with the tensile strength in the following way:

Modulus (GPa)	Strength (MPa)
100	150
120	220
135	300
145	400

Table 3.13 Effect of tensile strength on elastic modulus in cast iron

Information on the tensile strengths of the specimens indicated that the tensile strength was in the region of 220 MPa. For nonlinear analyses, the material stress-strain curve has been discretized to give a piecewise-linear fit as shown in figure 3.25. This curve is based on a monotonic tensile test carried out at ALSTOM. The tensile strength was in this case 235 MPa.

3.1.4 Description of Analysis Results

Elastic stress analyses for the circumferentially notched specimens gave the following values for net section stress concentration factor: $K_t = 2.156$ for 1/8th in. notch radius (BRITE Notch 1), and $K_t = 5.606$ for 0.012in. notch radius (BRITE Notch 2). These values were compared with estimates based on the formulae given by Katô (1992). From these formulae, the respective K_t values are: 2.156 and 5.605. This provides additional confidence in the validity of the stress analysis results.

The elastic stress distributions from the notch root into the body of the specimens are shown in figure 3.26. It is observed that the peak stress field for the sharp notch is highly localised and exhibits a high stress gradient. Figure 3.27 shows the stress distributions obtained for the bend specimens.

In all the specimen tests, the loads were of sufficient magnitude for yielding to take place on initial loading up, assuming that during HCF loading, the small volume close to the notch root behaves in a similar manner to the bulk material properties which are measured in a tensile test. For both of the circumferentially notched specimens (Notch 1, $K_t = 2.2$, and Notch 2, $K_t = 5.6$), plasticity analyses were carried out using the material curve described earlier and incremental plasticity theory with isotropic hardening. The analyses were carried out using the finite element program ABAQUS 4.8 (Hibbit Karlsson and Sorensen Inc.). A single load step was considered, consisting of initial loading from zero to maximum load in order to obtain a relationship between the applied load and the local stress and strain components. This information could then be used to relate the peak load in each test to the expected local stresses and strains.

Figure 3.28 shows the relationship between the nominal stress and the local notch strain component in the specimen axial direction (axial test specimens). Figure 3.29 gives the corresponding results for the local stress. The maximum nominal stress applied in the axial specimen tests was 190 MPa. So for the 0.012in. notch root radius specimen (Notch 2, $K_t = 5.6$), the tensile strength of the bulk material is exceeded at the notch root. For the purpose of the analyses, the material stress-strain curve was assumed to continue with zero slope beyond the strain corresponding to the tensile strength. The curve for notch 2 ($K_t = 5.6$) therefore contains an abrupt change when the tensile strength is reached according to the von Mises criterion.

From these graphs the local stresses and strains at maximum load in a given test could be obtained. For many of the specimen tests for the 1/8th in. notch radius (Notch 1, $K_t = 2.2$), the cyclic behaviour is predicted to be predominantly elastic. This prediction is based upon the local range of stress and twice the estimated value of the yield stress (for grey iron, the point at which nonlinear behaviour starts to become significant). For the sharper notch (Notch 2, $K_t = 5.6$), the cyclic behaviour at the root is predicted to be inelastic in the majority of cases. For the purpose of predicting the cyclic stresses and strains in these cases, approximate method of analysis has been used, based upon Neuber's rule:

$$\Delta\sigma \cdot \Delta\varepsilon = C_{Neuber} \quad (3.3)$$

The local alternating and mean stresses for Notches 1 and 2 are shown in figure 3.30. Here the stresses are normalised with respect to the tensile strength, for which a typical value of 235 MPa has been taken.

As would be expected from a knowledge of the nominal stresses, the results for the 0.012in. root radius specimen (Notch 2) indicate an apparent strengthening of the material locally around the root in comparison to the blunt notch (Notch 1). Many of these points lie on a straight line because the local stress is limited by the

tensile strength on the stress-strain curve. The results for Notch 1 are also high with respect to the plain specimen results.

In work on plain (unnotched) specimens of grey iron Weinacht and Socie (1987) demonstrated that under multiaxial loading conditions, the Smith-Watson-Topper parameter $\sigma_{max}\Delta\varepsilon$ (Smith et al, 1970) could be adapted to provide a reasonable correlation of uniaxial and torsional test data, thus extending its earlier use in correlating the fatigue data under different mean stresses (Fash and Socie, 1982). Fash and Socie suggested that the maximum stress at the half life should be used in the SWT model. The range of validity was for lives up to 10^6 cycles. The present test results are presented in terms of this parameter (written in the form $\sqrt{\sigma_{max}\Delta\varepsilon E}$) in figure 3.31.

These figures indicate that the notched specimen test results are not correlated by this parameter. These results therefore demonstrate that assessments based on the surface stresses and strains can be quite significantly in error.

3.1.5 Comparison of Calculated and Measured Notched Specimen Response

In addition to fatigue tests, strain gauge measurements are also available. The results of these measurements have been used to make comparisons with the theoretical predictions of local strain response at the root of the notch using finite element analysis. The objective of this investigation is to help to verify that the assumptions made in the theoretical analysis about material behaviour are correct.

An axial fatigue test specimen containing a 1/8th in. root radius (Notch 1) was used for these strain measurements. Four gauges with a 0.015in. gauge length were positioned at 90° to each other as close to the notch root as possible. Loads were then applied to produce the following strains in the notch:

	Min. strain ($\mu\epsilon$)	Min. nominal stress (MPa)	Max. strain ($\mu\epsilon$)	Max. nominal stress (MPa)
Case (a)	1084	49.28	2036	98.66
Case (b)	1466	65.54	2418	115.69

Table 3.14 Measured strains and nominal stresses from two different tests using the Notch 1 specimen ($K_t = 2.2$)

In each case, the specimen was loaded up to the maximum strain value, then partially unloaded to the minimum strain. Load cycling between the minimum and maximum was repeated a total of five times as illustrated schematically in figure 3.32 (a) and (b). The loading rate in each case was 2kN/min, with the load application being interrupted to take strain readings. The measured strains are summarised in tables 3.15 and 3.16.

Point (figure 24a)	Load (kN)	Net section stress (MPa)	Local strain ($\mu\epsilon$)
A	24.37	55.47	1084
B	33.94	77.26	1560
C ₁	43.34	98.66	2036
C ₂	43.21	98.36	2036
C ₃	43.06	98.02	2036
C ₄	43.0	97.88	2036
C ₅	42.97	97.82	2036
D ₁	32.05	72.96	1560
D ₂	31.99	72.82	1560
D ₃	31.84	72.48	1560
D ₄	31.81	72.41	1560
D ₅	31.76	72.30	1560
E ₁	21.65	49.28	1084
E ₂	21.52	48.99	1084
E ₃	21.35	48.60	1084
E ₄	21.28	48.44	1084
E ₅	21.25	48.37	1084

Table 3.15 Measured load versus strain data for cycling between strain limits of 1084 and 2036 microstrain (Case a)

Point (figure 24a)	Load (kN)	Net section stress (MPa)	Local strain ($\mu\epsilon$)
A	32.96	75.03	1466
B	42.87	97.59	1942
C ₁	50.82	115.68	2418
C ₂	50.37	114.66	2418
C ₃	50.27	114.34	2418
C ₄	50.16	114.18	2418
C ₅	50.16	114.18	2418
D ₁	39.34	89.55	1942
D ₂	39.17	89.17	1942
D ₃	39.11	89.02	1942
D ₄	39.05	88.89	1942
D ₅	39.04	88.87	1942
E ₁	28.79	65.53	1466
E ₂	28.55	64.99	1466
E ₃	28.42	64.69	1466
E ₄	28.37	64.58	1466
E ₅	28.33	64.49	1466

Table 3.16 Measured load versus strain data for cycling between strain limits of 1466 and 2418 microstrain (Case b)

The notched specimen behaviour was simulated using a combination of elastic-plastic and purely elastic analyses. The principal assumption in these loading cases was that the initial loading from zero to maximum strain causes some initial plasticity in the notch root, then subsequent cycling is of sufficiently small amplitude that the material behaviour at the root is linear elastic.

The finite element model used has been described earlier. For the initial loading in each of case (a) and (b), nonlinear material behaviour was assumed. Two material stress-strain curves have been considered. The tensile behaviour of cast iron shows significant variability, and the two monotonic stress-strain curves used correspond to two quite different tensile strengths, 235 MPa and 275 MPa. These are typical of the range of measured values for this batch of cast iron. The two

curves are shown in figure 3.33 together with the piecewise linear approximation for each which was used in the analysis.

The stresses and strains in the notch root up to maximum load were obtained from the nonlinear analysis results. For the subsequent cycling, linear elastic behaviour was assumed. Two different values of unloading modulus were considered: 107000 MPa and 120000 MPa. The measured values of initial loading modulus for cast iron exhibit a certain amount of variability, significantly more than in most other metals. Furthermore, the unloading modulus in cast iron can decrease with increasing load. The two values chosen are typical of the range of values which have been measured in this batch of material.

The finite element analysis results are shown in figures 3.34, 3.35 and 3.36, alongside the strain gauge results. Figure 3.34 applies to case (a) with the lower strain limits of 1084 and 2036 $\mu\epsilon$. The finite element analysis results for the 235 MPa UTS material are given, and the predicted effects of two different unloading moduli are shown.

Figure 3.35 shows similar results for case (b) with the higher strain limits. In figure 3.36, the strain gauge and finite element results are presented for case (b) again, but this time showing the effect of assuming different stress-strain curves.

3.1.6 Discussion

In both cases, the loads applied to the specimen produce local plastic deformation, which shows up in the strain gauge results as a residual strain on final unloading. The cycling between the maximum and minimum strain in the cycle is observed to approximately follow a linear elastic line. Over the five repeated cycles some slight decrease in mean load occurs (1.1 - 1.4%).

The strain range for each case is the same. For case (a), the measured load range was approximately 49.5kN, and for case (b) it was approximately 50kN (slight variations taking place over the cycles). The load range derived from finite element results was 50kN for $E = 107000$ MPa, and 56kN for $E = 120000$ MPa.

Therefore if the unloading modulus is about 107000 MPa, then the experimental results agree with the FE results.

The maximum load required to achieved a strain level of $2036\mu\epsilon$ in case (a) was 98.7-97.8 kN. This compares with 93.2 and 107 kN obtained using the two different stress-strain curves. For case (b) the actual loads were 115.7-114.2 kN, compared with 105 and 122 kN from the finite element results. The FE results bound the test results in both cases.

Therefore within the bounds of uncertainty of the material properties, the test results and FE results are in good agreement. If there is a hysteresis loop in the local cyclic stress-strain response, then the measurements indicate that it must be sufficiently small so as not to affect the overall specimen response, which appears to undergo cycling in a linear elastic manner, and this behaviour can be predicted analytically.

3.2 Grade 250/350 Grey Iron, Grade 400/500 SG iron (BCIRA Project)

3.2.1 Experimental Procedure

A programme of experimental work was carried out at GEC ALSTHOM Mechanical Engineering Centre, supported by Cast Metals Development Ltd (A BCIRA Group Company). The main task in this work involved a large testing programme on four grades of cast iron:

- I. Grade 250 grey iron
- II. Grade 350 grey iron
- III. Grade 400/18 SG iron
- IV. Grade 500/7 SG iron

The material for the test programme was obtained in two forms:

- a) Cast cylindrical bars for high cycle fatigue and tensile tests
- b) Keel blocks for fatigue crack growth and threshold tests.

These materials were analysed by CMDL. The composition is given in tables 3.17 and 3.18.

Grade	Melt number	Element (%)								
		C	Si	Mn	S	P	Cu	Mo	Al	Ti
250	G041	3.10	1.76	0.54	0.07	0.01	-	-	0.005	0.014
	G061	3.22	1.89	0.55	0.09	0.02	-	-	0.005	0.014
	G070	3.14	1.87	0.77	0.10	0.02	-	-	0.007	0.014
	G079						-	-		
	G080						-	-		
	G081						-	-		
	G082						-	-		
	G106	3.23	1.88	0.80	0.08	0.03	-	-	0.007	0.017
	G223	3.19	1.78	0.55	0.06	0.02	-	-	0.007	0.010
	G323	3.21	1.81	0.66	0.09	0.03	-	-	0.005	0.019
350	G197	3.12	1.55	0.54	<0.01	0.02	0.93	0.22	0.006	0.010
	G322	3.15	1.51	0.60	0.06	0.03	0.97	0.23	0.005	0.010

Table 3.17 Chemical compositions of grey iron melts (Murrell, 1997)

Grade	Melt number	Element (%)								
		C	Si	Mn	S	P	Mg	Cu	Al	
400/18	G290	3.61	2.03	0.25	0.02	0.02	0.050	0.03	0.030	
	G297	3.64	2.09	0.22	<0.01	0.02	0.058	0.04	0.030	
	G320	3.50	2.12	0.15	<0.01	0.03	0.039	0.03	0.027	
	G321	3.62	2.15	0.20	<0.01	0.03	0.042	0.02	0.024	
	G324	3.63	2.19	0.21	<0.01	0.03	0.042	<0.02	0.026	
	G328	3.62	2.21	0.25	<0.01	0.03	0.034	<0.02	0.026	
	G331	3.63	2.22	0.22	<0.01	0.03	0.044	<0.02	0.029	
	G433	3.50	2.08	0.17	<0.01	0.02	0.052	<0.02	0.033	
500/7	G298	3.59	2.17	0.32	<0.01	0.02	0.044	0.20	0.026	

Table 3.18 Chemical compositions of ductile iron melts (Murrell, 1997)

Materials I. and III. were evaluated using a relatively comprehensive test matrix, whereas a much reduced matrix was used for each of materials II. and IV. The overall test matrix covered the effects of the following parameters on the high cycle fatigue strength properties of these materials:

- Stress concentration (K_t)
- Mean stress
- Cast section size (10mm, 30mm and 50mm)

All tests were carried at ambient temperature. Fatigue tests were conducted under load control on Amsler Vibrophore resonance fatigue machines. Ten specimens were assigned for the generation of each fatigue S-N curve. Testing was continued until 2×10^7 cycles, or failure, whichever was achieved first.

In addition to plain (unnotched) specimens, notched test specimens were designed by the author for this programme. Three notch geometries were employed for each cast section size, with K_t values of 1.5, 2.5 and 5. The notch was positioned in the centre of the gauge length and took the form of a circumferential groove. The notched specimen geometries used are illustrated in figures 3.37, 3.38 and 3.39.

Fatigue crack growth threshold tests were carried using a constant R, load shedding technique with compact tension specimens (Figure 3.39a). Threshold was defined as the highest value of stress intensity factor range at which the rate of growth does not exceed 10^{-10} m/cycle over a period of not less than 5×10^6 cycles. These tests were carried out at R-ratios of 0.1 and 0.5 on grade 250 and 350 grey iron, and grade 500/7 SG iron. In all cases the material was from 10mm cast section size, except for one test which was from 50mm cast section.

A total of 207 tensile tests were performed, 87 of these included the generation of full stress-strain curves.

The fatigue test matrix is illustrated in table 3.19 to 3.22.

Cast section size (Dia. mm)	R-ratio	Stress concentration factor (K_t)			
		1	1.5	2.5	5
10	-1	10	10	10	10
	0.1	10	10	10	10
	0.5	10	10	10	10
30	-1	40	10	10	10
	0.1	10	10	10	10
	0.5	10	10	10	10
	0.7	10	-	-	-
50	-1	10	10	10	10
	0.1	10	10	10	10
	0.5	10	10	10	10

**Table 3.19 Grade 250 grey iron axial fatigue test matrix
- 400 specimens (BCIRA programme)**

Cast section size (Dia. mm)	R-ratio	Stress concentration factor (K_t)			
		1	1.5	2.5	5
30	-1	10	-	-	-
	0.1	10	10	-	10
	0.5	10	10	-	10

**Table 3.20 Grade 350 grey iron axial fatigue test matrix
- 70 specimens (BCIRA programme)**

Cast section size (Dia. mm)	R-ratio	Stress concentration factor (K_t)			
		1	1.5	2.5	5
10	-1	10	10	10	10
	0.1	10	10	10	10
	0.5	10	10	10	10
30	-1	40	10	10	10
	0.1	10	10	10	10
	0.5	10	10	10	10
	0.7	10	-	-	-
50	-1	10	10	10	10
	0.1	10	10	10	10
	0.5	10	10	10	10

**Table 3.21 Grade 400/12 SG iron axial fatigue test matrix
- 400 specimens (BCIRA programme)**

Cast section size (Dia. mm)	R-ratio	Stress concentration factor (K_t)			
		1	1.5	2.5	5
30	-1	10	-	-	-
	0.1	10	10	-	10
	0.5	10	10	-	10

**Table 3.22 Grade 500/7 SG iron axial fatigue test matrix
- 70 specimens (BCIRA programme)**

3.2.2 Experimental Results

A brief summary of the results will be presented here. A full analysis of the data was carried out by Bullough (1995).

The tensile strength values are reproduced in table 3.23.

Material	Parameter	Section size (mm)		
		10	30	50
250 grey	Range (Max.)	419	295	248
	Mean	380	268	232
	Range (Min.)	305	237	216
350 grey	Range (Max.)	-	411	-
	Mean	-	377	-
	Range (Min.)	-	348	-
400/18 SG	Range (Max.)	451	429	446
	Mean	414	406	423
	Range (Min.)	399	390	408
500/7 SG	Range (Max.)		584	
	Mean		523	
	Range (Min.)		491	

Table 3.23 Tensile strength values from BCIRA programme on cast iron

The grey iron tensile values indicate that they are dependent of cast section size; decreasing with increasing size. The SG iron values do not seem to show a trend. Bullough points out that UTS values obtained from fatigue run-out specimens tend to be lower than those from new material. The normalised stress-strain curves for the grey iron and SG iron are shown in figure 3.40 (reproduced from the data presented by Bullough). The data for the two grades of grey iron have been pooled, similarly for the SG iron. The elongation to failure of the SG iron is noted to be more than an order of magnitude greater than the grey iron.

The normalised plain specimen fatigue data from Bullough is shown in figure 3.41 for the pooled grey iron and the pooled SG iron. The normalisation is based on the UTS values reproduced in table 3.23. The curves for grey iron are more concave

than the SG iron. This trend was also observed in the data for grade 17 grey iron described earlier. The effects of K_t on the normalised fatigue strengths of grey and SG iron are shown in figures 3.42 and 3.43 respectively. The following empirical model was fitted by Bullough to the data:

$$\sigma_{NFL}^* = C(1 - R)^m K_t (K_t - a)^b + d \quad (3.4)$$

where σ_{NFL}^* is the experimental normalised fatigue limit (mean of highest run-out and lowest failure), and C , m , a , b and d are the fitted coefficients.

The fatigue crack growth threshold test results were fitted to a model which describes the effect of R-ratio. The model chosen was the Walker model with an exponent of 0.5. For grey cast iron:

$$\Delta K_{th} = 11.0(1 - R)^{0.5} \quad (3.5)$$

and for SG iron:

$$\Delta K_{th} = 8.5(1 - R)^{0.5} \quad (3.6)$$

3.2.3 FE Analyses of Notched Specimens

Each of the notched specimen geometries were analysed using elastic axisymmetric finite elements. The objective was to firstly confirm the estimated K_t values, and secondly to obtain the elastic stress distribution close to the notch root in each specimen. The models were then used subsequently for FE based crack analyses. These however, will be described later. The stress distributions are illustrated in figures 3.44, 3.45 and 3.46, for the cast section sizes 50mm, 30mm and 10mm respectively. The graphs show that although similar K_t values are obtained across different section sizes, the stress gradients close to the notch root are higher in the smaller section specimens.

3.3 Grade 300 Grey Iron

This material was cast in the form of dumb-bell shaped specimens to investigate the effects of as-cast surface finish on the fatigue properties of grey iron. Of particular interest in these tests was the effects of casting defects. The material was sourced from two different foundries (British and French), and the specimens were prepared with two different surface finishes:

- As-cast
- Ground

High cycle fatigue tests were carried out at ambient temperature using an Amsler Vibrophore resonance machine at a frequency of 100 Hz. All failed specimens were examined, and initiation sites identified. Initiating defects were measured. The fatigue results are listed in tables 3.23 and 3.24, and illustrated in the form of stress versus life plots in figures 3.47 and 3.48. Many of the specimens contained intentional casting defects (generally porosity at the surface). The measured defect sizes in the failure specimens are given in the tables. The run-out specimens were also examined visually for defects. The specimen surfaces were not smooth, but only one was found to contain a measurable pore. The results were then plotted on Kitagawa-Takahashi diagrams in an attempt to show the influence of defects on the fatigue strength, figures 3.49 and 3.50. Unfortunately, many of the data points relate to failures at higher stress levels, with very few run-out specimens data points. This does not allow the shape of the limiting curve to be defined in any detail. However, the results for the British specimens suggest that the Smith model may describe the dependence of strength on defect size better than the El-Haddad model.

Stress (±MPa)	Cycles to failure	Defect size (mm)		Comment
		Depth	Width	
100	1.34 x 10 ⁴	0.94	1.19	Sub-surface
100	1.70 x 10 ⁴	0	0	
90	2.73 x 10 ⁴	0	0	
90	6.73 x 10 ⁴	0.89	0.74	Sub-surface
86.6	6.00 x 10 ⁴	0	0	
85	4.80 x 10 ⁴	0.76	2.54	Surface
80	5.01 x 10 ⁴	1.02	2.16	Surface
80	9.82 x 10 ⁴	0.38	0.96	Surface
80	1.62 x 10 ⁵	0	0	
80	1.81 x 10 ⁵	0	0	
75	1.32 x 10 ⁵	0.84	3.66	Surface
75	1.67 x 10 ⁵	0	0	
75	3.10 x 10 ⁵	0	0	
75	3.85 x 10 ⁵	0.94	1.27	Sub-surface
70	1.42 x 10 ⁵	1.80	5.0	Surface
70	2.61 x 10 ⁵	0	0	
70	1.13 x 10 ⁵	0.64	1.90	Surface
70	2.04 x 10 ⁵	1.55	2.99	Surface
65	1.69 x 10 ⁵	0	0	
65	2.86 x 10 ⁵	1.60	2.84	Surface
65	1.68 x 10 ⁷ **	-	-	
65	4.17 x 10 ⁷ **	-	-	
65	8.42 x 10 ⁷ **	-	-	
GROUND SPECIMENS				
90	2.49 x 10 ⁴	0	0	
85	3.17 x 10 ⁴	0	0	
80	6.16 x 10 ⁴	0	0	
75	2.97 x 10 ⁴	0	0	
70	4.41 x 10 ⁵	0	0	
65	6.48 x 10 ⁷ **	0	0	

Table 3.24 High cycle fatigue test results for Grade 300 grey cast iron (British foundry) As-cast and ground surface condition (Run-out)**

Stress (±MPa)	Cycles to failure	Defect size (mm)		Comment
		Depth	Width	
80	3.70×10^4	1.32	3.28	Sub-surface (0.53)
80	6.10×10^4	2.0	2.5	Surface
80	2.56×10^4	1.88	1.7	Surface
75	1.69×10^4	2.29	2.97	Sub-surface (0.30)
70	1.47×10^5	2.57	4.29	Surface
70	3.98×10^4	4.57	8.5	Surface
70	2.60×10^4	2.36	5.41	Surface
65	4.94×10^4	2.46	4.04	Sub-surface (0.46)
60	1.73×10^7	1.65	2.51	Surface
60	7.20×10^5	2.0	2.36	Surface
60	8.20×10^4	3.15	2.51	Surface
55	3.04×10^5	1.12	2.34	Sub-surface (0.94)
55	3.54×10^5	2.28	2.11	Surface
55	1.04×10^5	3.63	3.81	Surface
50	4.39×10^5	4.19	2.44	Surface
50	4.86×10^7 **	-	-	
50	4.05×10^7 **	-	-	
GROUND SPECIMENS				
80	2.84×10^4	0.86	1.44	Surface
75	5.70×10^4	1.80	1.90	Surface
70	3.89×10^7	0	0	
70	3.05×10^5	0.68	2.39	Surface
65	6.02×10^6	0	0	
60	1.45×10^5	1.35	2.49	Surface
60	7.20×10^7	0	0	
55	3.52×10^6	0.94	2.84	Surface
55	1.78×10^8 **	-	-	
50	6.79×10^7 **	-	-	

Table 3.25 High cycle fatigue test results for Grade 300 grey cast iron (French foundry) As-cast and ground surface condition (Run-out)**

3.4 Diesel Engine Bedplate Example

This case study concerns the service experience with three design variants on a bedplate cast in grade 17 grey cast iron. The bedplate is a large casting, and contains a number of bolt holes which are located close to the side wall of the bedplate. The bolts at these locations transmit the reaction forces due to the firing pressure loads which pass through the crankcase and down into the bedplate to the main bearings. In addition to these cyclic loads, there is a clamping load which is passed into the surrounding material of the bedplate. The top of the bolt hole is machined flat to support the bolt head. At the edge of the flat area, there is a small 90° fillet radius where the flat meets the side wall (figure 3.51). This fillet radius was found to be a critical region and was the subject of design modifications.

Design (a): Seacat 12 thou fillet

This design contains a sharp fillet radius of 12 thou. (0.305mm), and is subjected to a high firing pressure load. Out of 20 components in service, 10 developed cracks in the sharp-fillet radius and are classed as failures (Al-Sened, 1997).

Design (b): RKC 12 thou fillet

This is geometrically the same as design (a), but the firing pressure load is low (69 to 77% that of design (a)). No cracking has been found.

Design (c): Seacat 1/8th in. fillet

The fillet radius is larger in this design, at 1/8th in. (3.175mm). The firing pressure load is the same as design (a). Out of the 20 components with this design detail, 13 developed cracks (Al-Sened, 1997).

In all three designs, the bolt clamping load is the same.

These designs were analysed using the finite element method in both three-dimensions (Squire-Taylor, 1994), and also by the author in two-dimensions. Firstly a global three-dimensional analysis of the bedplate was carried out. This was followed by local three-dimensional analyses of the fillet region in which one model contained the 1/8th in. fillet and another contained a sharp corner

representing the 12 thou. fillet design. The loads applied to these local models were prescribed displacements at the boundary, obtained by interpolation from the global model.

In order to obtain a detailed description of the stress field surrounding the fillets, the author constructed two-dimensional plane strain F.E. models of each geometry, with boundary constraints interpolated from the local three-dimensional analysis results which were supplied by Squire-Taylor. The three- and two-dimensional models are shown in figures 3.52, 3.53, 3.54 and 3.55. Figures 3.56, 3.57 and 3.58 show the resulting stress distributions for the three designs described above. The peak stresses are summarised below:

Design	Bolt load only (MPa)	Bolt + firing load (MPa)
Seacat (12 thou.)	715	1279
RKC (12 thou.)	715	1105/1149
Seacat (1/8th in.)	213	384

Table 3.26 Peak stresses in the fillet predicted from two-dimensional F.E. analysis

The surface stresses predicted for design (c) - Seacat 1/8th in. are observed to be the lowest. However, as described above, service experience with these engines has shown that both the Seacat designs suffered cracking from the fillet region, while the RKC engine has not experienced any failures.

3.5 Discussion

A large database of information on notched specimens of cast iron has been assembled. This will be valuable to test the application of different theories. Conditions experienced in service components are varied, and any candidate design assessment procedure should be able to account for all these conditions (mean stress, size, geometry, material grade etc.).

The test data generated exhibits the characteristic notch insensitivity of cast iron. The diesel engine bedplate example highlights this characteristic and the problems it can create in an actual component. The stress analyses show a significant difference in the calculated local elastic stress field, but little difference in strength. Furthermore, the nature of the stress field in the bedplate means that the traditional approach of employing a nominal stress and K_t or K_f factor is difficult to apply. This also raises the question of what is actually controlling whether the notch root material fails in fatigue. The nonlinear deformation behaviour of grey iron may have an influence on the notch fatigue behaviour, but whether a model based on the macroscopic material behaviour is applicable at a notch root is difficult to assess.

When predictions of local stress-strain response are calculated using conventional analysis procedures (inelastic finite element analysis or approximation procedures based on Neuber's rule), the result is an apparent strengthening of the notch root material. These local stress-strain calculations are open to some criticism with respect to the assumed material stress-strain curves used. These are based on the typical stress-strain response of a tensile test piece, whereas the notch root material is stressed over a significantly smaller volume. According to the predictions, the local stresses in many of the sharp notch specimens will exceed tensile strength of the material. To investigate the nonlinear behaviour of very small volumes of material would require special testing techniques which are beyond the scope of the current work.

Conventional strain gauging techniques were used in an attempt to provide some validation of the FE predictions. For practical reasons these were restricted to use on the 1/8th in. notched specimens only. The results indicate that the predicted response is probably within the bounds of the scatter in material stress-strain behaviour. In the sharp notched specimens, these techniques cannot easily be applied. Therefore, there is some doubt about the actual stress-strain conditions at these locations.

At this point it is useful to review the observed behaviour of cast iron, in particular, the behaviour leading up to failure or local cracking. This will be covered in the next section.

4. A REVIEW OF THE LITERATURE ON FATIGUE FAILURE MECHANISMS IN CAST IRON

4.1 Fatigue Failure Mechanisms Generally Observed in Metals

Fatigue can be described as a progressive fracturing of a material by the growth of cracks under cyclically varying load. In metals it has been observed to consist of the following basic stages (Keith and Gilman, 1959, Forsyth, 1959, Hempel, 1959, Mughrabi et al, 1983, Suresh and Ritchie, 1984):

1. The formation of slip bands in material close to the surface by cyclic plasticity accompanied by cyclic softening or hardening
2. The initiation and propagation of microcracks in a shearing mode
3. Coalescence of microcracks
4. The development of these into macrocracks aligned normal to the maximum principal stress direction

Close examination of the crack initiation phase may often reveal microcrack growth over substantial portions of the total life, and blurs the distinction between the initiation and propagation phases. Modern fatigue limit criterion such as that due to Dang Van and co-workers (1987) are based on the concept that a critical cyclic stress level exists on a microstructural level. Below this level, a state of elastic shakedown will exist and no fatigue failure will occur. Above this level, cyclic plastic strains will be generated within a grain which will lead to the formation of fatigue cracks. The work by Hempel (1959) on aluminium indicates that slip lines can be observed in a few grains at stresses corresponding to approximately half the fatigue limit. Tests on single crystals of alpha iron showed that the fatigue limit corresponded quite closely with the static yield strength value.

Work by Mughrabi (1983) has shown that extrusions are formed relatively quickly in persistent slip bands. In high-cycle, low strain conditions, the local deformation is restricted to one slip system. This is followed by relatively slow growth, and a gradual roughening of the surface, attributed to random irreversible slip. The formation of extrusions was found to be more pronounced in single crystals than in

polycrystals. Notch-like valleys subsequently appear which are sites for crack formation. Cracks were also observed to form at grain boundaries.

Tanaka et al (1983a) also observed crack initiation at grain boundaries as well as in slip bands. Observations of the growth of these cracks showed that the growth rate is affected by the mode of crack growth (or path) which was found to vary from grain to grain. Tokaji and Ogawa (1992) used replica techniques to study the growth of microstructurally short cracks in a variety of materials (low and medium carbon steels, high tensile steel, low alloy steel, dual phase stainless steel, aluminium alloy and titanium) and found that crack growth rates often temporarily decrease at grain boundaries, triple points and boundaries between two phases. The longer fatigue life observed in the fine grained material compared to coarse grain was attributed to the blocking effect of grain boundaries reducing the mean crack growth rates. They concluded that it is the stage I (crystallographic) phase of crack growth which is most affected by microstructural effects, and the transition from microstructurally short crack growth to a mechanically small crack growing in stage II is at a size of approximately eight microstructural units (grain size, distance between phases etc.).

Evidence has been presented in the literature based on studies of some materials that the fatigue limit is instead a crack growth threshold condition (Tanaka, 1983a). Microcracks have been observed to have formed at stress levels below the fatigue limit, but cease to propagate once they reach a significant microstructural barrier such as a grain boundary.

Likely mechanisms by which grain boundaries may affect growth include (Suresh and Ritchie, 1984) blocking of slip bands or containment of the plastic zone within the grain, reorientation and reinitiation of the crack as it tranverses the boundary, influence of harder second phases and crack deflection.

The development of crack closure has been studied in short fatigue cracks. James and Morris (1983) and Tanaka (1983b) have found evidence that crack closure is a function of crack size. Consideration of results from a variety of sources has lead Suresh and Ritchie (1984) to conclude that the development of crack closure

is the principal factor contributing to the anomalous growth behaviour of short fatigue cracks.

In some materials, for example high strength steels and alloys, high strength nickel alloys, and cast irons the fatigue behaviour can in fact be governed by the presence of inherent defects such as shrinkage pores, inclusions, and graphite precipitates. These act as small stress concentrators or notches which can accelerate the crack initiation and early growth phase.

Cast steels may contain discontinuities in the form of gas bubbles generated during deoxidization, as well as nonmetallic inclusions of sulphides, oxides and silicates (Mitchell, 1976). These invariably act as crack initiators in fatigue. The most common types of initiator being microshrinkage cavities and gas porosity. Heuler et al (1992) investigated fatigue crack initiation and growth in 2¼CrMo cast steel. Analysis of the fracture surface revealed that the largest defects were hot tears having a mean area of 11mm², followed by inclusions (sand and slag), blowholes and intergranular cracks. Defects were found both at the surface and sub-surface, but were larger on the surface. The most effective surface crack initiators were found to be pinholes, slag inclusions, small surface defects in welded areas and arc strikes.

Another example is given by Verpoest et al (1985) in which drawn pearlitic steel wires were fatigue tested. Cracks were found to initiate from pits (from pickling), scratches, longitudinal grooves, local decarburisation spots, broken martensitic layers and inclusions and holes. The latter sites were shown to be most significant for polished specimens.

Due to the hot working received during the processing of wrought steels, many of the microshrinkage cavities and gas pores are eliminated (Mitchell, 1976). Fatigue cracking will generally initiate in these materials from nonmetallic inclusions such as sulphides, silicates and oxides (Mitchell, 1976; Scarlin, Berger and Mayer, 1986). The deformable sulphide inclusions may elongate during hot working, whereas oxides and silicates, being harder, maintain a more spherical shape.

Murakami (1989) has investigated the effects of inclusions on the fatigue strength of high strength steels. In his review of the literature, evidence is presented that the ultimate tensile strength must be greater than a critical value for the effects of inclusions to become significant. Furthermore, the size and shape of inclusions, the bond between the inclusion and the matrix and the elastic constants can all have an effect. A common feature of fatigue fracture origins in these materials is the presence of a 'fish-eye' pattern with an inclusion located at the centre. As a result of studies on a number of different materials, Murakami demonstrated that the fatigue strength of high strength steels could be related to both the material hardness and the projected area of the inclusion. For super clean steels, the fatigue strength followed the same linear relationship with hardness as the low-to-medium strength steels.

Analysis of failed fatigue specimens of forged IN718 nickel alloy revealed that initiation generally occurred at carbide particles (Heuler and Bergmann, 1997). The sizes of the carbides (NbC) varied between 10 x 10 μm and 20 x 40 μm . In these LCF tests there was a clear tendency to multiple crack initiation and secondary cracking at higher strain ranges. After initiation at these carbides, the crack growth was initially stage I with a transcrystalline, crystallographic mode of growth (Wanhill and Boogers, 1997). Transition to stage II growth took place along grain boundaries at a crack depth of typically 50 to 90 μm . Crack growth rates estimated from striations spacing measurements indicate that growth rates during the stage I growth phase were higher than measured growth rates from corner cracked specimens with crack sizes greater than 300 μm .

4.2 Fatigue Failure Mechanisms Observed in Grey Cast Iron

Formally specified as flaked graphite cast iron, but often referred to as Grey Iron due to the grey colour of its fracture faces, it is very widely used and possesses good machinability, vibration damping and tribological properties. Mechanical properties are highly dependent on the microstructure, principally the graphite flakes. Structural applications are limited by its poor tensile strength which is much

lower than the compressive strength. Mitchell (1976) has described the solidification process:

- Separation of austenite in the form of primary dendrites
- Progressive enrichment of carbon in the remaining liquid.
- Separation of graphite and austenite between 1130 and 1160°C as a eutectic from a number of nuclei following a roughly spherical front
- Growth of these eutectic cells continues until no liquid is left
- Solid state transformation of the austenite matrix

What is left is a three-dimensional array of graphite flakes. The graphite colony is continuous to the edge of the eutectic cell. The graphite flakes themselves have the form of a layered hexagonal structure with a tensile strength of approximately 20 MPa.

Under fluctuating loads, fatigue cracks have been observed to form quickly at the tips of graphite flakes oriented perpendicular to the maximum principal stress on the surface of the specimen. Models to represent the fatigue behaviour of grey cast iron must therefore reflect the dominant role of the graphite flakes distributed throughout the material.

Observations of Deformation Behaviour and Damage Accumulation

Grey iron has a nonlinear stress-strain response over practically the entire load range (BCIRA Broadsheet 157-1, 1977). Furthermore, the behaviour is different in tension from that in compression. The deformation behaviour of grey cast iron under cyclic load and the observed fatigue damage accumulation has been reviewed by Weinacht and Socie (1987).

Under tensile load, plastic deformation of the matrix material takes place readily due to the notch effect of the graphite flakes. A volume increase in the graphite and, at the surface, cracking or debonding of the graphite flakes oriented perpendicular to the load also contributes to the nonlinear behaviour. In compression, the graphite becomes effectively an incompressible layer which can transfer compressive stress to the matrix.

Tests on grey iron under multiaxial conditions by Wang and Brown (1994) have shown that while the deformation response under cyclic axial strain controlled loading at $R = -1$ produced an asymmetric stress-strain response, under cyclic torsional loading, the loops were symmetric. The test results presented also demonstrate the influence of the magnitude of tensile stress on the elastic modulus (both peak tensile stress and mean tensile stress). It was concluded that in the initial stages, the effective load carrying area in the material (and therefore the amount of graphite which can be opened) is dependent on the applied stress level, rather than irreversible fatigue damage. Subsequent crack growth would however be expected to reduce the load carrying ability in time.

Fatigue cracks initiate quite early in life, and particularly under high strains, multiple crack systems develop over the surface. Isibasi (1952) cites work dating from 1936 in which fatigue cracks have been observed to form from tips of graphite flakes and minute serrations in the walls of flakes. Fash, Socie and Russell (1981), used surface replication techniques to show that the development of these crack systems relate closely with the observation of tensile load drop-off in strain controlled tests. Damage rate in the form of development of cracks increases with increasing strain amplitude.

Fash, Socie and Russell describe how spherical colonies of flake graphite form within the steel matrix during solidification. The graphite structure is continuous throughout a small region called a Eutectic cell. Many Eutectic cells form as the steel solidifies initially as austenite when the edge of each cell represents the boundary between solid and liquid (Rollason, 1973). Under loading, cracks form in the graphite, creating a discontinuity or defect across the diameter of the eutectic cell. The eutectic cell size has been used by Mitchell (1976) as the size of a surface discontinuity or notch for fatigue life predictions to crack initiation based on the use of macroscopic strain-life concepts. Reasonable correlation was obtained for lives greater than 10^3 cycles.

Fash, Socie and Russell (1981) also make reference to work by others that for grey iron, decreasing the graphite flake size improved the material's fatigue

properties, and matrix hardness was found to have a greater effect than changing the microstructure.

During fatigue cycling, Fash, Socie and Russell (1981) observed that deformation of the matrix material occurs on initial tensile loading, and critically oriented graphite flakes crack or debond from the matrix causing crack-like voids. The cracks grow by a process of propagation through the matrix material and incremental extensions through crack coalescence. Crack arrest was also observed when a crack links with graphite flake structures which are oriented parallel to the loading direction.

Damage accumulation at large strain amplitudes ($\Delta\epsilon/2 = 0.003$) occurred by a process of crack formation throughout the material, within the first 4% of life, followed by linking of the largest of these (up to two millimetres in length) close to failure. At smaller strain amplitudes ($\Delta\epsilon/2 = 0.001$), cracks were found to initiate within the first 10% of life. Fewer crack systems developed, and very few grew to two millimetres in length. The growth rates of small cracks were found to increase with increasing strain range, larger matrix deformation was also observed.

A gradual increase in specimen compliance accompanied by a decrease in peak tensile stress was observed in the strain controlled tests. This was consistent with crack growth trends, and was therefore attributed to crack formation rather than cyclic softening. The observed load drop rate was lower at lower strain amplitudes.

Gilbert and Kemp (1980) reported the results of strain controlled tests which showed that for a flaked graphite cast iron (UTS=280 MPa) tested under load control, the inelastic strain increased on each load cycle. For load cycles giving peak stresses in excess of 54% of the UTS, the inelastic strain increments increased throughout the life. When the peak stress was less than 54% of UTS, the strain increment settled to an almost constant value.

Later work by Gilbert (1985) involving strain controlled tests showed that tensile stress relaxation occurs throughout life accompanied by a smaller change in the

maximum compressive stress. The tensile stress relaxation was attributed to the increasing volume occupied by the graphite during cycling, and the increase in magnitude of the compressive stress was associated with strain hardening of the steel-like matrix structure.

Castillo and Baker (1984) have studied grey cast iron in fatigue using plain specimens. They concluded from their work that the fatigue limit is dominated by the graphite eutectic cell size and is insensitive to the microstructure of the matrix. They proposed that a fracture mechanics model can be used to predict the fatigue limit based on an initiating defect which is determined by the eutectic cell size, and the threshold stress intensity for propagation.

Their work consisted of both plain specimen tests and fatigue crack growth tests on pre-cracked specimens, using several types of grey iron, varying in matrix microstructure and flake size. The fatigue crack growth data was found to obey the Paris' law at high ΔK values, but with an unusually high exponent of 7. It was suggested that the growth involved a substantial contribution from brittle fracture mechanisms. This theory was supported by the observation of a strong R-ratio dependence.

High ΔK_{th} values were observed, and these were attributed to enhanced crack closure effects due to surface roughness, associated with the monotonic fracture processes. ΔK_{th} was lower for the material with a small graphite flake size, and was accompanied by a smoother fracture surface. The heat treated irons showed similar behaviour, compared with the as-cast iron.

Their test results and fractographic observations lead them to conclude that the flakes act as pre-existing defects. A model was proposed for the threshold stress intensity factor for a graphite nucleated short crack:

$$\Delta K_{th} = 0.7 \sigma_{max} (1 - R) \sqrt{\pi a} \quad (4.1)$$

where:

- σ_{max} = Max. stress at the fatigue limit (at a given R-ratio)
- a = Size of a single semi-circular shaped edge crack

(representing a surface breaking graphite cell)

Using mean measured cell diameters, short crack ΔK_{th} values of 3.6 - 4.4 MPa \sqrt{m} were calculated. These are shown in table 4.1 together with their other results. The difference between the long and short crack values was attributed to the existence of significant crack closure behaviour for long cracks. For short cracks there is no preceding fracture surface and hence nothing to prevent complete closure of the faces.

Matrix micro-structure	Eutectic cell size (mm)	Tensile strength (MPa)	Fatigue load ratio (P_{min}/P_{max})	Fatigue limit σ_{max} (MPa)	Crack growth parameters (Paris law)			Predicted ΔK_{th} from the fatigue limit (MPa \sqrt{m})
					C ($\times 10^{-12}$)	m	ΔK_{th} (Long cracks) (MPa \sqrt{m})	
Pearlite	0.49	294	0.1	112	4.1	6.6	9.2	3.6
Pearlite	1.51	253	0.1	78	0.7	7.0	10.9	4.4
Tempered Martensite	1.51	404	0.1	72	6.7	6.4	7.4	4.1
Ferrite	1.51	160	0.1	60	4.9	6.6	7.0	3.4
Pearlite	1.51	253	0.3	-	2.6	7.4	6.9	-

Table 4.1 Fatigue results for grey cast iron produced by Castillo and Baker (1984)

Hornbogen's work on fatigue crack growth mechanisms (1985) showed that for all loading conditions, cracks pass through the graphite phase. At low amplitudes, interlamellar crack growth through the pearlite matrix takes place, whereas at high amplitudes, expansion of the surrounding graphite flakes leads to the formation of parallel cracks and crack branches. The process is illustrated in figure 4.1 by a schematic drawing which has been based on a similar illustration by Hornbogen.

Mitchell (1976) also presents evidence that cracks initiate on the first tensile reversal at the tips of the flakes and then propagate through the matrix by progressive cleavage and linking with cracks initiated from other flakes.

The initiation and development of fatigue cracks in grey iron was studied by Jianchun (1993) using the technique of surface replication. In this study, grade 17 grey iron was tested in four-point bending at a load ratio of $R = 0.1$. The material is the same as that described in the previous chapter. The cast iron was found to generate a large number of cracks per unit area (hundreds in each replica), and consequently an area mapping and crack numbering technique was used which involved measuring and counting both cracks and graphite flakes, since the two were found to be indistinguishable. Replicas were taken every 5000 to 10000 cycles.

No specific crack initiation sites were found in the grey iron apart from the graphite flakes. The crack distribution over the surface for specimens tested under lower stress levels ($\Delta\sigma \approx 140$ MPa) was found to be non-uniform with a number of clusters of cracks. At higher stress levels ($\Delta\sigma \approx 170$ MPa), twice as many cracks were generated, and these were distributed more uniformly over the surface. The average size of graphite flakes and cracked graphite flakes was approximately $120\mu\text{m}$.

Coalescence was a major feature of crack growth. In some cases this would be between pairs of parallel cracks, while in others it would involve several cracks linking together like a spiral nebula. The total number of very short crack/flakes ($a < 100\mu\text{m}$) was found to decrease during the test, from which it was inferred that there was a high probability of growth in this range. There was no change in the number of cracks in the range $100 - 200\mu\text{m}$ (growth is difficult). The total number of cracks/flakes reduced during the test, implying a significant amount of crack coalescence.

The statistical data generated in Jianchun's work was used to generate crack growth probability curves ('P-a curves'). The probability of growth is defined as:

$$P_g = \frac{\text{No. of growing cracks}}{\text{Total number of cracks}} \quad (4.2)$$

This quantity is calculated over a range of crack size intervals.

4.3 Fatigue Failure Mechanisms Observed in Spheroidal Graphite Cast Iron

Spheroidal graphite cast iron is being used in an increasing number of applications due to its relatively low cost, high castability, good machining properties and higher strength than grey iron. But the material has a lower fatigue strength than cast steels and lower strength wrought alloys. Studies of the mechanisms of fatigue damage and fracture mechanics based predictive models have been done by Starkey and Irving (1982a, and 1982b).

Fatigue cracks are initiated from several types of sites. For a machined surface, cracks have been found to initiate at micropores exposed by machining. An inverse relationship was found to exist between fatigue life and initiating pore size. Cracks were observed to form within the first 15% of life. Cracks also formed at graphite nodules, but not until much later in life. The surface of the graphite nodules have been observed to debond forming spherical cavities, compared to the more irregularly shaped micropores. Mitchell (1976) also presented evidence that crack initiation tended to occur from surface imperfections such as microshrinkage cavities rather than from the debonded interface at the graphite nodules.

Specimens of SG iron with as-cast surfaces exhibit different behaviour to those with machined surfaces. SG iron is prone to form a grey iron surface layer containing flakes of graphite. Fatigue cracks have been found to form at dross defects and surface irregularities, the former causing the greatest reduction in strength. Casting quality naturally has an effect, both in terms of surface texture (dependent on sand texture or the surface dressing) and impurities. Impurities can produce flake or chunky graphite and dross.

Life is dominated by microcrack growth, and the endurance can be related to the initial defect size by using a Paris' type growth law for less than 10^5 cycles (the extent of the test data available to Starkey and Irving). The ΔJ parameter was found to correlate the growth data better than ΔK (material behaviour was elastic-plastic). Reasonable agreement was achieved. However, it was concluded that the crack growth threshold is crack size dependent.

Starkey and Irving have also shown that for smooth specimens under low strain conditions, the variation in observed lives can be related to the variation in pore size within the iron. At high strains, multiple crack initiation and coalescence occurs, and the scatterband is much narrower. The reduction in scatter may be the result of a reduced dependence on the extremes of defect size.

4.4 Fatigue Mechanisms Observed at Notches in Various Materials

Frost, Pook and Marsh (1974) describe some of the typical crack growth behaviour observed in notched specimens.

For sharply notched specimens under low loads, cracks may form at the notch root, but not propagate across the specimen cross-section. A definition of the notched fatigue limit was given in terms of the following two criteria:

- I. Max. cyclic stress which will just not initiate a crack at the notch root.
- II. Max. cyclic stress which will just not cause a crack to grow to cause complete failure.

Growing cracks develop in a way which is dependent on the load level and notch geometry. For circumferentially notched specimens:

- Sharp V-notch, low nominal stress
 - Crack forms all the way round the periphery of the notch root.
 - Uniform radial growth inwards.
 - Final fracture area is more central the higher the nominal stress.
- Blunt notch root, low nominal stress
 - Crack forms and develops from a single point, particularly if the nominal stress is close to the fatigue limit.
 - Final fracture is on the opposite side.
- Blunt notch root, high nominal stress
 - Cracks form all the way round the periphery.
 - Final fracture is towards the centre.

The existence of non-propagating cracks in notches has been known for many years. Frost, Pook and Marsh (1974) makes reference to work dating back as far as 1949 in which non-propagating cracks have been found in materials such as:

- Mild steel and other steels
- Aluminium alloys
- Copper and copper alloys
- Nickel alloys

It was found that they only occur when the cyclic stress level is below a certain value, and the stress concentration factor K_t exceeds a critical value. Test results are described for circumferentially V-notched (5mm deep, 0.05mm root radius) mild steel specimens. When cyclically loaded at levels down to half the notched specimen fatigue limit, small cracks of 0.025 to 0.05mm depth were found after 10^8 cycles. These cracks formed before 50000 cycles.

Frost, Pook and Marsh describe tests on aluminium alloy specimens in which replicas of the surface were produced at intervals. These revealed that cracks formed at an early stage, and to do this, required a nominal alternating stress S_{alt} of:

$$S_{alt} \geq \frac{\text{Nominal fatigue limit}}{K_t} \quad (4.3)$$

Crack depths measured by sectioning non-failed specimens in both mild steel and aluminium alloys have been shown (Frost, 1955a, 1955b) to be related to the level of the applied nominal stress on the specimen. Furthermore, using Neuber's solution for the stress field around a hyperbolic notch, and the estimated plain specimen fatigue limit, Frost showed that the measured nonpropagating crack depths lie close to the distance over which the elastic stress distribution is greater than or equal to the plain specimen fatigue limit (for loading at zero mean stress).

Frost (1955c) has illustrated the notched fatigue behaviour of aluminium alloy specimens and mild steel specimens in terms of plots of fatigue notch factor K_f

versus stress concentration factor K_t . Below the critical K_t value for the formation of nonpropagating cracks, the value of K_f can be approximated to K_t . Although, as the critical K_t is approached, the values deviate more and more, particularly for notched rotating bend specimens. Above the critical K_t value, K_f was shown to decrease to a certain extent with increasing K_t .

Frost also speculated about the reasons why small notches or stress raisers do not realise their full theoretical K_t values, even below the critical K_t value (Frost, 1955b). If there is a minimum depth over which the local stress level must exceed the fatigue limit, then for small notches the stress gradients set up will not be sufficiently deep to permit the initiation of cracks, unless the nominal stress level is raised to a higher level than expected for the given K_t value for the specimen.

The effects of notch size on the fatigue strength of grey cast iron have been investigated by Isibasi (1952). The motivation for this work was the observation described in the literature of the particular notch insensitivity of grey iron, and how the fatigue notch factor varies with notch and specimen size. Tests were therefore carried out on tubular specimens of grey iron under rotating bend type loading. Two tube outer diameters were considered: 23mm O.D. and 12mm O.D. Several hole sizes were used. The material used in the work had a mean tensile strength of 225 MPa (from five tensile tests). The mean length of graphite flakes was given as 0.1-0.2 mm. The stress concentrations were created by the use of transversely drilled holes through the walls of the specimens.

The specimens with the smallest holes were found to give fatigue notch factors of approximately unity (i.e. no effect of the notch). This effect was strongest for the smaller size test specimens. The test results were compared with a theoretical prediction of the fatigue notch factor based on a function containing the ratio s_d/s_{max} , where s_d is the stress at a depth equal to the length of a graphite flake from the notch root, and s_{max} is the maximum elastic stress at the root of the notch:

$$K_f = K_t A \frac{s_d}{s_{max}} \left(1 - \frac{B}{\rho} \right) \quad (4.4)$$

A and B are constants (assumed to be 1.3 and 0.5 respectively), and ρ is the hole radius. Good agreement was found between the predictions and test results, although no justification was given for the values of these constants. Furthermore, the flake length used to estimate s_d was increased significantly to account for roughness of the hole surface. However, the work illustrates an early attempt to make use of the graphite flakes and their possible effect on stress concentrations.

The growth behaviour of short cracks at a notch in a structural low-carbon steel is described by Tanaka and Nakai (1983b). The specimen was a centre-notched plate with a notch root radius of 0.16mm, and $K_t=8.48$. Load cycling was carried out at 35Hz for R-ratios of -1, 0.0 and 0.4. Crack growth rates were determined over a range of crack sizes for several load levels.

At low stress levels, growth rates were observed to decrease until the crack stopped growing at a size less than 0.1mm. For a slightly higher stress, growth rate decreased to a minimum at just over 0.1mm, and then increased with increasing crack size. When the stress was higher still, no initial decrease in growth rate was observed.

The point of crack opening was determined based on measurements of crack opening displacement as the cracks progressed. The calculated value of K at the point of crack opening (K_{op}) was found to increase over the range of crack sizes for which the growth rate was decreasing. When the crack growth data was then plotted against the effective range of stress intensity factor ΔK_{eff} ($\Delta K_{eff} = K_{max} - K_{op}$), all the points were shown to be clustered around a single curve. Furthermore, from their measurements of non-propagating crack length (c_{np}), they deduced that it was not a unique function of maximum nominal stress, and that therefore there is no single relation between c_{np} and monotonic plastic zone size due to the notch stress field.

The closure of cracks growing from the root of notches in AISI 316 stainless steel was measured by Shin and Smith (1985). The work was carried out on 2.6mm

thick plate with double edge notched geometries. The elliptical notches were spark eroded to a depth of 35mm with three minor radii of 3.75, 5.0 and 7.0 mm, giving K_t values of 22.5, 17.0 and 12.4 respectively. Closure of the continuous surface cracks at the notch roots were measured by three methods:

- Crack tip strain gauge
- Crack tip clip gauge
- Notch mouth clip gauge

These measurements were also compared with a limited number of plastic replica measurements. The gauges located at the crack tip were found to give the more representative results. Significant crack closure was measured under low R-ratio loading conditions ($R = 0.05$), whereas at high R-ratios, little closure was observed; the cracks remained open throughout the load cycle. The crack lengths at which minimum crack growth was observed corresponded well with the crack length at which the closure was a maximum. Allowance for crack closure effects could not explain the growth rates of the smallest crack sizes using the crack tip parameters considered in the work (ΔK , ΔK_{eff} , ΔK_c and ϕ_{total} which is a total shear deformation parameter).

Jianchun (1993) studied the initiation and growth of cracks from notch roots in Ly12 cz aluminium alloy (similar to 2024-T3). A total of twenty-two centre notched and double edge notched specimens were tested under constant amplitude loading up to final fatigue fracture. Endurance cycles lay in the range 170000 to 575000 cycles. Cracks were measured by two methods: Replicas at intervals of 5000-10000 cycles, and optically using a travelling microscope.

Multiple short cracks (2-6) were found to initiate from inclusions, growing mainly as corner cracks though a few semi-elliptical surface cracks were observed. Most of the cracks grew to about 150 μ m before arresting. Only one crack continued to grow to failure. Often, this crack would initiate later and grow at a slower rate than the others. This was explained by the fact that initiation was influenced by the presence of defects, but the location of the crack which causes final failure is dictated to a great extent by the magnitude of the local stress field.

Examination of crack growth rates indicated the presence of relatively large scatter in growth rate for the shorter cracks. Many of the cracks also exhibited a minimum growth rate at crack lengths generally between 200 μm and 300 μm . The crack length for minimum growth rate appeared to be unaffected by the magnitude of the applied load level. Comparisons between the measured crack growth rates and predicted growth rates based on crack closure models indicated crack closure due to microstructural effects such as crack face roughness are at least as important as plasticity induced crack closure effects for the modelling of short crack growth.

4.5 Discussion

The first part of this section dealt with fatigue failure mechanisms in metals in general. Crack initiation and early growth is influenced very much by the material microstructure. It is apparent from the literature that in typical engineering materials, fatigue cracks will often form at inherent defects. The distribution, size and shape of these defects will affect the overall fatigue behaviour of a material. Cast irons have their own characteristic set of microstructural features and defects. In the case of grey iron, the obvious features are the graphite flakes, whereas in spheroidal graphite (SG) iron, the common crack initiators are pores, dross defects and in some cases the graphite nodules.

Grey iron appears to be the special case when compared against many other materials. The high density of graphite flakes can lead to the initiation of large numbers of fatigue cracks, particularly at high peak stresses. The presence of the flakes and evolving crack population also influence the overall deformation behaviour of the material, and give grey iron its characteristic nonlinear response to load. The higher the load, the greater the departure from linearity, and the more the elastic modulus changes. Load cycling can lead to the growth by coalescence of many cracks, and this damage development can also make its presence felt by a gradual reduction in load carrying capacity.

Furthermore, when the size of typical graphite flakes are compared with local design details such as notch fillet radii, it tends to suggest that the stresses calculated on the basis of a homogenous isotropic material may not be very representative of actual conditions, rather it is the conditions necessary to grow a crack from a graphite flake (or flakes) that is more relevant. The last section on fatigue mechanisms at notches highlights the importance of crack growth in explaining the behaviour of sharper notches. In the case of grey iron, although very little direct observation of notch root crack development has been carried out, it would be expected that the high stresses which are typically present at a notch root would rapidly lead to the formation of many notch root cracks, and it is therefore the development of these which is of importance for fatigue assessments of components. The difficulty with grey iron compared with, for example, SG iron, is the relative size of the cracks and the significant nonlinear response which would be obtained close to the notch root.

In the next section, theoretical models to describe the conditions for growth of notch root cracks are considered, focussing on the particular difficulties of grey iron.

5. A CRACK GROWTH BASED APPROACH FOR CAST IRON

5.1 Overall Description of the Approach

In the previous section, evidence was presented which indicated that micro cracks can form and grow in cast iron from a quite early point in the life of a specimen. In grey iron, it is the graphite flakes which act as the initiation sites, and the number of cracks which form appears to be affected by the load level. The size of these newly initiated cracks will be of the same order of magnitude as the surrounding microstructural features of the material (the graphite flakes). The growth characteristics of cracks of this size may therefore differ from those of cracks commonly used in conventional fracture mechanics test specimens (compact tension etc.). Studies of short cracks in various materials show that the reasons for this may include crack depth dependent closure effects and interaction with microstructural features.

The work by Kitagawa and Takahashi, El Haddad et al, and others, which is described earlier, attempts to provide an empirical method to account for the effects of crack size on fatigue strength, and the observation that, below a certain crack size, there will be little or no affect on fatigue strength. When these models are presented in the form of a Kitagawa-Takahashi diagram, they provide a very useful design assessment tool for predicting the fatigue strength of relatively uniformly stressed bodies containing specific defect types.

However, for cracks which exist in highly non-uniform stress fields, such as notches, a single stress value alone is no longer appropriate for assessing the strength, and the stress field in the region of the stress concentration should be taken into account. In linear elastic fracture mechanics, the crack tip parameter, K , can be calculated for a crack in a non-uniform stress field. If a criterion can be defined in terms of K for predicting the conditions under which a short crack will just continue to grow, then this may provide a route towards defining a design procedure for notches in cast iron which makes use of local quantities, rather than requiring a nominal stress with its associated problems which have been described earlier. Of interest in the present work, is the prediction of the conditions

for crack growth given in terms of the crack tip parameter K , together with an empirical crack growth threshold model for short cracks which is appropriate for cast iron.

In order to do this, assumptions must be made about the crack geometry at the point of initiation, and during subsequent growth. Analytical methods can then be used to estimate the crack tip K values corresponding to the applied loading cycle. As the crack grows, the range of K values (ΔK) due to the cyclic load are compared with the threshold value for growth (ΔK_{th}). The Kitagawa-Takahashi plot implies that for a given crack geometry, the threshold for growth (ΔK_{th}) becomes crack size dependent below a particular crack size. Therefore, by assuming a crack geometry, and reformulating the models which describe the dependence of fatigue strength on crack size, an apparent short crack growth threshold value can be defined which increases with crack size, up until the conventional 'long crack' threshold value is reached.

If the loading level is very low, a crack may not initiate, or may initiate but not grow. At a higher load level, a crack may form and start to grow, but after a certain amount of growth, if the rate of increase of ΔK with crack size is not as high as the rate of increase of ΔK_{th} , then the crack may cease to grow. If the load level is sufficiently high, ΔK may remain greater than ΔK_{th} and the crack will continue to grow to failure. This is illustrated in figure 5.1.

A major assumption in this type of approach is the shape of the initial crack geometry, and how that shape will develop as a crack grows. In the case of grey iron, the graphite flakes would suggest that a semi-circular surface crack geometry would approximate the initial form of a crack, based on the observation that the graphite flakes open up under loading and cracks grow from the flake tips. Therefore the initial approach that is taken in this work is to assume a semi-circular surface crack, with a depth equal to the typical graphite flake size. At a notch root, many of these cracks are likely to form at the surface on account of the high surface stress values predicted by the F.E. analyses described earlier, and

the observations that the number of cracks formed increases with load level (see section 4).

After a short amount of crack growth, these discontinuous cracks would be expected to coalesce to form a continuous surface crack. No measurements of crack development have been made in this work to quantify the crack sizes and shapes, and the point at which coalescence occurs to form a continuous surface crack. However, bearing in mind the high density of graphite flakes, it is assumed that cracks can grow to no more than twice their size before they coalesce with surrounding cracks/flakes. After coalescence, the crack shape will be assumed to be continuous along the surface with a constant depth. Observations by Jianchun (1993) of crack development in grade 17 grey cast iron plain fatigue specimens showed that the combined number of cracks and flakes at shorter lengths decreased during the test, while there was almost no change in the range 100-200 μm . The total number of cracks and flakes reduced during the test. It was concluded that a significant amount of crack coalescence was taking place.

For most sharp notches, stress analyses based on the assumption of homogeneous, isotropic material behaviour indicate that a certain amount of plasticity will be experienced close to the surface of a notch root. Since this may influence the behaviour of a crack, the effects of this have been investigated analytically, and included in the predictions of crack behaviour where appropriate.

The remainder of this section is concerned with the analysis of the crack geometries which are of interest, particularly the evaluation of ΔK values. Since the finite element method is one of the most important tools for this type of work, emphasis is placed on its application to notch root cracks. The section finishes with a description of the analytical model used to describe the apparent crack growth threshold.

5.2 Linear Elastic Analyses of Cracks at Notch Roots by Finite Element Analysis

5.2.1 The Use of F.E. for Crack Analyses

5.2.1.1 Introduction

The calculation of crack tip characterising parameters is one of the main tasks in crack assessments, since the value of these has been shown to have an important influence on the growth behaviour of cracks, for example in fatigue crack growth (Paris, 1963). When the extent of crack tip plasticity is small, i.e. when conditions are predominantly linear elastic, the Stress Intensity Factor K is usually used to characterise the mechanical environment in the region of the crack tip. The analyses due to Westergaard (1939) expressed the magnitude of the characteristic spatial distribution of stresses around the crack tip under linear elastic conditions in terms of the parameter K . Similar expressions can be given in terms of strains and displacements. Later, Irwin (1957) showed that K could be related to the strain energy release rate G . This opened up the possibility of calculating K in a number of alternative ways, and the introduction of the finite element method for stress analysis provided an important tool for calculating the stress and strain fields around crack geometries of practical interest in engineering components (Zienkiewicz, 1977), many of which are three-dimensional. For example, semi-elliptical surface cracks and corner cracks.

A number of different methods are available for evaluating the stress intensity factors for two- and three-dimensional crack geometries using the finite element method (Pickard, 1986, Shields et al, 1992, Gallagher, 1978). These include:

- a) Stress substitution method: Uses the crack tip stress field and the Westergaard equations (Westergaard, 1939)
- b) Displacement substitution method: Uses the crack tip displacement field and the Westergaard equations
- c) Explicit calculation of the change in strain energy between two analyses with differing crack lengths to obtain the energy release rate and hence K .
- d) Virtual crack extension method

- e) J-Contour integral calculation to obtain J and hence K. This involves a contour integration over a line or surface surrounding the crack tip (Rice, 1968)
- f) J-Domain integral calculation to obtain J and hence K (Shih et al, 1986). The energy release rate for a virtual crack extension is obtained by a numerical integration procedure over a surface or volume surrounding the crack tip.

For three-dimensional crack geometries where point values of J and K are required, the last of these methods has been found to provide an accurate and straightforward procedure (Hughes, 1992). The use of the Westergard equations together with the crack face displacements is also straightforward, but less accurate. The other methods in the list are either less accurate (a), difficult to extend to three-dimensional (e), cumbersome to use (c) or require changes to the FE source code (d).

5.2.1.2 Displacement Substitution Method

The stress intensity factors are calculated by substituting the displacements obtained at nodes close to the crack tip into the Westergard equations for K in terms of the displacement field around the crack tip (as the distance from the crack tip r tends to zero). Since the material around the crack tip can deform in three distinct modes (see figure 5.2), three different displacement fields can be described, leading to the concept of three components of K. These are commonly denoted as: K_I , K_{II} and K_{III} , and expressed in terms of the crack face displacements by:

$$\begin{aligned}
 K_I &= \frac{E}{(1+\nu)} \left[\frac{2\pi}{r} \right]^{1/2} \frac{v}{(\chi+1)} \\
 K_{II} &= \frac{E}{(1+\nu)} \left[\frac{2\pi}{r} \right]^{1/2} \frac{u}{(\chi+1)} \\
 K_{III} &= \frac{E}{4(1+\nu)} \left[\frac{2\pi}{r} \right]^{1/2} w
 \end{aligned} \tag{5.1}$$

where for plane strain:

$$\chi = 3 - 4\nu$$

and for plane stress:

$$\chi = \frac{3 - \nu}{1 + \nu}$$

u , v and w are the displacements in the x , y and z directions respectively for points lying on the crack face (assumed to be in the plane of the crack), with a local coordinate system defined with the x -direction normal to the crack front and in the same plane as the crack, the y -direction normal to the plane, and the z -direction tangential to the crack front (see figure 5.3).

The values of K are calculated for a number of points on a radius from the crack tip. The K values at radius=0 are then obtained by extrapolating a straight line least squares curve fit through these points.

5.2.1.3 J-Domain Integral Method

In two-dimensions, and in the absence of body forces, thermal strains and crack face tractions, the J contour integral is normally shown as a path independent line integral (Rice, 1968):

$$J = \int_{\Gamma} (W \delta_{,i} - \sigma_{ij} u_{j,i}) n_i dC \quad (5.2)$$

In three-dimensions, the J contour integral consists of an integration over a surface around a particular point on the crack front (Li, 1985). This surface is in general difficult to define and the integration itself is difficult to perform in a three-dimensional FE model compared with a volume integration. In the presence of body forces and thermal strains an additional area integration is required in two-dimensional configurations, and an additional volume integration for three-dimensions.

An alternative derivation of the J -integral by Shih et al (1986) has been implemented in a computer program MELFRAM (Hughes, 1992) and also in the ABAQUS FE program (HKS, 1996) in which the integration has been recast in the form of a domain integral:

$$\bar{J} = \int_V \left[(\sigma_{ij} \frac{\partial u_j}{\partial x_k} - W \delta_{ki}) \frac{\partial q_k}{\partial x_i} + (\alpha \sigma_{ii} \frac{\partial \theta}{\partial x_k} - f_i \frac{\partial u_i}{\partial x_k}) q_k \right] dV \quad (5.3)$$

where:

- W = Strain energy density
- σ_{ij} = Stress tensor

$\partial u_j / \partial x_k$	= Displacement derivatives
δ_{ki}	= Kroneckers delta
α	= Coefficient of thermal expansion
$\partial \theta / \partial x_k$	= Derivative of temperature
f_i	= Body force
q	= Weight function (Varies smoothly from 0 on the outer contour to 1 at the crack tip)
$\partial q / \partial x_k$	= Derivative of weight function
\bar{J}	= Energy release rate per unit area of virtual crack advance

In twodimensional crack geometries, this consists of an integration over the area enclosed within a contour surrounding the crack tip. In three-dimensional crack geometries, it is an integration over the volume enclosed within a surface contour surrounding the crack tip. To a first approximation, pointwise values of J can be obtained from:

$$J(s) = \frac{\bar{J} \cdot \Delta a}{(\Delta area)} \quad (5.4)$$

where $\Delta area$ is the increase in crack area due to virtual crack advance Δa , as shown in figure 5.4.

The derivation corresponds to the virtual crack extension method (Shih, 1986), and includes terms to account for thermal strains and body forces. The method has been shown to be accurate (DeLorenzi, 1985, & Hughes, 1992), and being based on area integrals in two-dimensions and volume integrals in three-dimensions, is well suited to implementation using standard FE routines. Furthermore it is readily extended to three-dimensional configurations for the accurate determination of pointwise values of energy release rate around a crack front.

Knowing J at a point, the stress intensity factor K can be obtained when linear elastic conditions exist, from:

$$K = \sqrt{E^* J} \quad (5.5)$$

where E^* is the Young's Modulus E in plane stress, and $E^*=E/(1 - \nu^2)$ in plane strain conditions. For sub-surface crack front positions, conditions tend towards plane strain, and therefore the second of these terms is usually used in three-dimensional crack analyses.

Under mixed mode loading conditions, J on its own does not allow the different mixed mode K values to be determined (K_I , K_{II} and K_{III}). One approach is to extend the method in (Shih, 1986) directly by considering the separate components of the vector J -integral. J is actually the first component of the vector J -integral. The additional components can be evaluated in the same way as the first component J_1 . Under linear elastic conditions, the components of J can be related to the three K values. However, J_2 has been found to be significantly less accurate than the corresponding values of J_1 (Hughes, 1990).

A simpler method has been developed based on a combination of the J -integral method and the previously described displacement substitution method. The following procedure (Hughes & Wood, 1994) gives accurate values for K_I , K_{II} and K_{III} :

1. Evaluate K_I , K_{II} and K_{III} first using the displacement substitution method.
2. Store the ratios: $R_{II} = K_{II}/K_I$, and $R_{III} = K_{III}/K_I$.
3. Evaluate J using the J -domain integral method.
4. Calculate K_I , K_{II} and K_{III} from:

$$K_I = \frac{\sqrt{J}}{\left[\frac{1}{E^*} + \frac{R_{II}^2}{E^*} + \frac{R_{III}^2}{2\mu} \right]^{1/2}} \quad (5.6)$$

$$K_{II} = K_I R_{II}$$

$$K_{III} = K_I R_{III}$$

5.2.2 Two-Dimensional/Axisymmetric Analyses of Notched Specimens

The FE method is particularly useful for the analysis of cracks in non-standard geometries, complex stress fields etc. The circumferentially notched cast iron fatigue specimens are an example of this. Any cracks present close to the notch

root of any of these will be subjected to a highly non-uniform stress field. Furthermore, the material close to the root of the notch will probably deform in a nonlinear manner under loading, and this can complicate the local stress field even more.

If the magnitude of the loading is sufficiently high, then as load cycling continues, microcracks will form at the notch root and gradually grow into the body of the specimen. In earlier sections it was described how in some materials, long continuous surface cracks may form at a notch root, and subsequently cease to propagate. It was considered relevant to investigate how any continuous surface cracks would behave if they were present. The results could then be compared with subsequent analyses of non-continuous (e.g. semi-circular) surface cracks.

A continuous surface crack can generally be analysed using a two-dimensional FE representation. In the case of the notched specimens, the model assumes conditions of axisymmetry. An additional plane of symmetry exists in the plane of the notch root, separating the two faces of the crack. The FE model therefore only requires displacement constraints along the plane of symmetry as far as the crack tip, and by removing more of these constraints, different crack lengths could be modelled.

In the case of the BRITE specimen Notch 1 ($K_t=2.2$), 13 crack depths were considered, ranging from 0.0976mm to 0.4744mm. For Notch 2 ($K_t=5.6$), 26 crack depths were considered, from 0.046mm to 4.07mm.

A larger number of crack analyses were also carried out for the BCIRA notched specimens with K_t values of 1.5, 2.5 and 5.0. All three cast section sizes were considered, making a total of nine notched specimen geometries. Crack sizes ranged from 0.012mm to 1.3mm.

The FE meshes used were a simple rectangular style rather than 'focussed' to allow different crack lengths to be considered easily. For the same reason, crack tip midside nodes were left at the mid-point and not moved to the quarter-point. Previous work by the author indicated that the penalty on accuracy of the resulting

K values would be small, typically 1-2%, which for this application is not critical. Typical FE meshes for the two specimen geometries are shown in figure 5.5. K values were derived by the J-integral method described earlier. The analyses described in this section are purely linear elastic with the elastic modulus $E=120000\text{MPa}$ and Poisson's ratio $\nu=0.26$. As described earlier, these values are typical for grade 250 grey iron.

Loading on the models was applied as a series of point loads to nodes in the region of the threaded portion of the specimens. Loading was assumed to be applied equally to all nodes along the thread region. On the basis of St. Venant's principle, the should have a negligible effect on the results.

The K solution results for both BRITE notched specimen geometries are plotted in terms of K versus crack depth in figure 5.6. These results are compared in this figure with the handbook solution from Rooke and Cartwright (1976) for a circumferential crack in a solid cylinder. For this latter solution, the crack depth used to calculate K was taken as the sum of the actual crack depth (a) and the notch depth, i.e. at $a=0$, the crack depth was taken as 3.175mm.

These results illustrate the behaviour described in the literature in which at very small crack sizes the K value is appropriate to a surface crack of length a in a stress field given by the local notch root field. But at larger crack sizes, the K value approaches that for a crack equal to the sum of the notch depth and the crack depth a. For Notch 2 ($K_t = 5.6$), this occurs at a crack depth of approximately 0.2 to 0.3mm, whereas for Notch 1 ($K_t = 2.2$) it is greater than 0.5mm.

The FE results for Notch 2 show a consistent difference of a few percent from the handbook solution, over all the crack lengths. This effect has been observed in many FE crack analyses with different mesh types for a double edge cracked plate geometry (Hughes, 1992). Since this difference is observed with both J-integral and displacement substitution methods, it is concluded that it is more likely to be due to limitations in the handbook solution.

The series of points in figure 5.6 which make up the Notch 2 results come from FE models of two different mesh densities. At a distance of 1mm, the mesh density changes again. These changes affect the J-integral solution. It is observed that K tends to be higher with the higher mesh densities.

The K solutions for the BCIRA notched specimens are shown in figures 5.7, 5.8 and 5.9. Figure 5.7 applies to the 10mm cast section size, figure 5.8 applies to 30mm, and figure 5.9 to 50mm. Each figure gives results for specimens with three different K_t values.

The results for the 10mm cast section, $K_t=5$ (figure 5.7) are made up of two sets of data. At the smallest crack sizes (0.018mm to 0.15mm), a submodelling technique was used. A small region of the specimen was modelled, close to the notch root. Displacement boundary conditions were applied around the 'cut' to simulate the effects of the surrounding material. These displacements were extracted from the results of a global FE analysis of the specimen with a coarser mesh. Because the loading consists of fixed displacements, the validity of the model breaks down at larger crack lengths when the presence of the crack should be affecting a region of the specimen larger than the extent of the submodel. The results do however show where the K solutions for the global model should follow on from the K solutions for the submodel.

The general trend in the BCIRA specimen crack analysis results is similar to that for the BRITE specimens. In the sharper notches with the higher K_t values, the K solutions exhibit a rapid increase at small crack sizes, but then merge towards the K solutions results for the smaller K_t geometries at larger crack sizes. An additional trend which is observed is that these results also appear to lie above the Rooke and Cartwright handbook solution at larger crack lengths.

5.2.3 Three-Dimensional Crack Analyses: Straight and Curved Crack Fronts

5.2.3.1 Straight Crack Fronts

Crack analyses for semi-elliptical surface cracks are three-dimensional problems. The method adopted in this work involved the use of three-dimensional FE analysis in combination with the three-dimensional formulation of the J-domain integral method described earlier.

Of interest to the current work is the effect on the J solution of how the crack is discretised by the three-dimensional finite element model. Therefore several tests were carried out, firstly to study the effects of mesh design radially outwards from the crack tip, and secondly to study the effects of discretisation along a curved crack front.

For the first of these, a double edge cracked plate model was used. The mesh types considered can be categorised into either *rectangular* or *focussed*, as shown in figure 5.10.

The HKS (1995) recommend the use of a focused mesh with 'quarter point' nodes. The element types considered included:

- 8-noded brick elements with extra-nodeless shape functions
- 20-noded brick elements
- 15-noded wedge elements at the crack tip
- Degenerate 20-noded brick elements at the crack tip
- Degenerate 20-noded crack tip elements with mid-side nodes at the quarter point.

The analyses and the results are summarised in table 5.1. These results are compared with the value obtained from Rooke and Cartwright (1976):

$$K = 4.36 \text{ MPa } \sqrt{\text{m}}$$

Job I.D.	Mesh type	Crack tip elements			K solution MPa \sqrt{m} (% difference from handbook)	
		Type	Mid-side node position	Element size/ Crack length	Displ. subst. method	J-integral method
CR3D	Rectangular (2½ elements over half plate width)	8-noded brick + extra nodeless shape function	N/A	0.25	4.03 (-7.6)	4.48 (+2.8)
CR3D20	"	20-noded brick	Mid point	0.25	4.40 (+0.9)	4.63 (+6.3)
AB3D1	Focussed (5 elements over half plate width)	15-noded wedge	Mid-point	0.1	4.59 (+5.2)	4.68 (+7.4)
AB3D2	"	Degenerate 20-noded brick	Mid-point	0.1	Unavailable	4.72 (+8.3)
AB3D3	"	Degenerate 20-noded brick	Quarter-point	0.1	Unavailable	4.74 (+8.8)
AB3D4	Rectangular (8 elements over half plate width)	20-noded brick	Mid-point	0.1	Unavailable	4.71 (+8.0)

**Table 5.1 Comparison of K solutions from 3-D FE model of double edge cracked plate with handbook solution
- Effect of different crack tip meshes**

The first point to note is that the FE results tend towards a solution which lies above the handbook K solution. The FE K solutions apply to a point on the crack front mid-way through the plate width. Both methods of calculating K show a similar trend. The conclusion from this is that the actual K solution for this geometry may lie above the handbook solution. Of greater interest to the present work however is the relative difference between the FE K solutions. In particular, the use of 8-noded brick elements, even with extra nodeless shape functions to create a quadratic displacement function, leads to a low K value.

An advantage of the use of 8-noded bricks in 3-D analyses is that the model size in terms of number of nodes is significantly lower than for a 20-noded brick model with the same number of elements. But for 3-D crack analyses, these results show that the resulting K values may not be as accurate as for 20-noded bricks. Furthermore, the best results may be obtained with the use of a focussed mesh and quarter point nodes in a degenerate 20-noded brick, as recommended by HKS (1995).

5.2.3.2 Curved Crack Fronts

Many cracks of practical interest have a curved crack front (e.g. semi-circular surface cracks). A brief investigation was carried out to study the accuracy of FE analyses of these types of cracks, because of the direct relevance it has on some of the analyses carried out in this research work. This investigation was prompted by the appearance of large fluctuations in K and J values around a curved crack front when 3-D elements with mid-side nodes were used in crack analyses carried out by the author on one of the notched specimen geometries described in section 3. These analyses will be described in detail in section 5.2.5.

To investigate the problem further, a 3-D crack geometry was chosen for which a K solution was also available from other sources. The geometry selected was a semi-circular surface crack in a large uniformly stressed solid. A mesh was constructed representing a cubic body of material. A quarter circular crack geometry was incorporated into one corner of the mesh as shown in figure 5.11. The ratio of crack depth to cube width was 0.15.

A uniform tensile stress was applied over the top face. Symmetry conditions were applied on two planes such that only one quarter of the crack needed to be modelled. Elastic properties assumed for this analysis were $E=200$ GPa and $\nu=0.3$. 20-noded brick elements were used to construct the model. At the crack tip, these were collapsed to form a focussed mesh. Mid-side nodes adjacent to the crack front were moved to the quarter point position to provide an improved approximation to the $1/\sqrt{r}$ singularity at the crack tip.

Two FE models were then created:

- a) With a faceted crack front (mid-side nodes on the crack front lie exactly at the mid-point)
- b) With a smoothed crack front (mid-side nodes moved to a position on a smooth crack front curve).

The pointwise K values around the crack front were calculated from the J-integral values obtained from the ABAQUS FE program. Four contours were requested. The K values were calculated from the mean J value from these, excluding the first contour. The results from the two analyses are shown in figure 5.12. These are compared with handbook solutions. The solution for this geometry given in Rooke and Cartwright (1976) is:

$$K = 0.65 \cdot \sigma \sqrt{\pi a} \quad (5.7)$$

and the solution given by Pickard (1986) is:

$$K = 0.672 \cdot \sigma \sqrt{\pi a} \quad (5.8)$$

This latter result is based on the results of FE analyses.

At the deepest point on the crack front, geometry correction factors can be calculated from the FE results given the K value, crack depth and nominal applied stress. The respective values for case a) and b) are 0.602 and 0.650. The results from the model with the faceted crack front show a significant variation from corner nodes to mid-side nodes, and the deepest point corner node value is over 7% lower than the handbook solution of Rooke and Cartwright. The results from the smoothed crack front model on the other hand are in much better agreement with the handbook solution, and the variation from corner node to mid-side node is less than 2%. A variation between corner node and mid-side node values for J-integral has been pointed out in HKS documentation on the use of ABAQUS for fracture mechanics analyses (HKS, 1995), and was also observed by Judge and Marsden (1995).

Based on these results it can be concluded that a smoothed crack front is desirable for accurate analyses of curved crack fronts. It also indicates that the accuracy of K solutions which are based on the results from 8-noded brick models (even with extra nodeless shape functions) may be questionable.

A further result of interest is illustrated in figure 5.13. This shows the distribution of K values around the crack front in the notched specimen referred to above, with two different mesh densities in the crack front direction. One mesh has 18 elements around 90° of arc, and the other has only 6 elements. Approximately the same mesh density is used in the direction radially outwards from the crack front.

The K values for the coarse mesh generally lie within the range of values describing the fine mesh results, and seem to show a smaller variation from corner nodes to mid-side nodes. The corner node K values are slightly greater in the coarse mesh model than the fine mesh. The reasons for this behaviour are not clear.

5.2.4 Simulation of Crack Growth in Linear Elastic Stress Fields at Notches

5.2.4.1 Introduction

One aspect of the analysis of cracks by numerical methods such as finite elements is the calculation of K values around the crack front. The methods available, and some of the problems have been described above. The next major area of concern is the prediction of how a crack will grow. i.e. from a knowledge of the range variation of the Stress Intensity Factors (SIF) under cyclic loading, the growth behaviour of the crack is required to be estimated. The results presented above illustrate the general problem, which is that the K values, in general, vary around the crack front. This implies that different points on the crack front will grow at different rates, and change the shape of the crack, which in turn will change the distribution of K values (analogous to a feedback loop).

If the growth of a crack through a component is being predicted, then clearly, the finite element mesh needs to be updated regularly to reflect this growth. The key tasks are therefore:

- Create crack model
- Evaluate K (or ΔK) values along the crack front
- Calculate growth
- Update crack model

In order to investigate how cracks will behave in the region of a notch root, particularly, how the predicted shape would develop when growth is calculated at each point around the crack front, a series of analyses were performed for a crack in a notch root for which measured growth data was available. The specimen geometry, and the material to which it relates, are only relevant to the series of analyses described in this section concerning crack shape development. A description of the tests are therefore given below, and not included in earlier sections of this thesis. The analyses were carried out using a program called ZENCRACK, a proprietary software product of ZENTECH International Ltd

5.2.4.2 Summary of Features

ZENCRACK works in conjunction with ABAQUS or MARC finite element analysis programs and provides the ability to:

- Generate 3-D FE meshes of cracked components (possibly with multiple cracks)
- Evaluate the energy release rates along the crack front (gives the SIF for linear elastic conditions)
- Calculate fatigue crack growth at each position on the crack front
- Update the crack geometry based on the calculated growth

The overall procedure is illustrated in figure 5.14. Input requirements to ZENCRACK are:

- a) ABAQUS input file
 - Uncracked component
 - Created according to specific rules (re: Definition of elements, boundary conditions etc.)
- b) ZENCRACK input file

- Element no(s). to be replaced by crack block(s)
- Crack block type identifier
- Crack size and aspect ratio
- Material crack growth properties
- Crack growth control parameters

The crack orientation is defined using two node numbers on the element(s) to be replaced, and the size and shape are defined by means of ratios (figure 5.14). The element type used in the uncracked model must be a 20-noded brick. The crack tip elements created by ZENCRACK may have either mid-side nodes or quarter-point nodes to generate the stress singularity, depending upon the option specified in the ZENCRACK input file.

There are five quarter circular/elliptical and five through-crack crack blocks. The differences lie in the number of nodes around the crack front.

5.2.4.3 Description of Test Cases

Subject of ZENCRACK Test Case and Initial Growth Predictions

The test case selected is a notched fatigue test specimen for which experimental crack growth measurements are available. The design is illustrated in figure 5.15. It has a rectangular section, and contains two edge notches. The stress concentration factor for this geometry is 2.23. Crack growth calculations were initially carried out assuming a fixed crack aspect ratio, basing the crack growth rate on the ΔK value at the deepest point on the crack front.

Initial Crack Analyses and Growth Predictions (constant aspect ratio)

Crack initiation in this specimen generally occurred away from the corners, and closer to the centre of the notch. The crack analyses therefore assumed a central crack. The crack sizes considered and the SIF (K) value at the deepest point as calculated for a fixed crack aspect ratio are shown in figure 5.16. The stress analyses and K values were obtained using ABAQUS 5.4 with the J-integral option. Crack tip elements were collapsed 20-noded bricks with quarter point nodes. A constant semi-circular crack shape was maintained for all crack sizes. K

values are those for the deepest point on the crack front. A typical FE mesh is shown in figure 5.17.

These K solutions were subsequently used for crack growth predictions. The crack growth law used for this material was the Paris law with constants representing maximum, mean and minimum fits to corner crack specimen test data. The crack growth predictions assumed linear elastic fracture mechanics conditions apply. The effects of residual stresses due to plasticity on initial loading are taken into account using an approximation procedure based on Neuber's rule. Crack growth predictions for two specimens are shown in figure 5.18.

Measured Crack Growth

Low cycle fatigue tests were carried out at MTU on the notched specimen shown in figure 5.15. The material is IN718 at 600°C. The development of crack size and shape during the test was deduced from post-test inspection of the fracture surface to identify markings due to regularly applied marker loads during the test. The results of these measurements are presented by Affeldt (1994). Figure 5.18 shows two sets of measurements alongside the crack growth predictions. The measurements made from these tests indicate that the crack generally maintains a constant aspect ratio which is close to a semi-circle under pure fatigue loading, although there are variations on this from test to test.

5.2.4.4 ZENCRACK Analyses

Three ZENCRACK analyses were carried out:

ZENEX1

Involving the generation of a crack model with crack depth $a = 0.5\text{mm}$ and a semi-circular shape from an uncracked FE model. Output from ZENCRACK was the distribution of K values around the crack front.

ZENEX2

Similar to ZENEX1, but with a smaller crack size ($a = 0.3\text{mm}$).

ZENEX3

In this example, a full crack growth assessment is carried out within the limits set by the original uncracked FE mesh. The initial crack size was taken as 0.3mm. Material crack growth data for IN718 at 600°C was supplied. This consisted of the Paris law constants, the same values as used in the previous work. The load cycle considered was that corresponding to the TA31 specimen DTF150, nominal stress = 80/800 MPa (R = 0.1). This load cycle was defined within the ZENCRACK input file using load factors on the F.E. results of 0.0889 and 0.8889.

The F.E. model used as input to the ZENCRACK analysis is illustrated in figure 5.19(a). As for the earlier model used (figure 5.17) there are three planes of symmetry.

Limits on the ZENCRACK calculations can be applied by defining:

- The material fracture toughness
- Maximum number of fatigue crack growth cycles
- Maximum number of finite element analyses

The growth is also limited by the size of the original element being replaced by the crack block. In practice, if the crack length exceeds approximately 70 - 80% of the original element size, then the program will stop and the original model must be remeshed with a larger element size, if the growth calculations are to be continued. In the present case, only one original mesh was used.

5.2.4.5 Presentation of Results

Figure 5.19(b) illustrates a typical cracked mesh resulting from ZENCRACK. The K values obtained at the deepest points on the crack in cases ZENEX1 and ZENEX2 are illustrated in table 5.2, together with values obtained in the initial crack analyses with a constant aspect ratio.

Crack depth (mm)	K (MPa√mm) (ZENCRACK)	K (MPa√mm) (Initial crack analyses)
0.3	12.22	12.13
0.5	13.86	13.76

Table 5.2 Comparison of K values from ZENCRACK and from initial calculations based on a constant crack aspect ratio and deepest point K solution (10 MPa net section nominal stress on model)

The ZENCRACK results for the deepest point on the crack front agree with the previously obtained results to within 0.8%.

The results from example ZENEX3 are illustrated in figure 5.20. In this example, the crack is allowed to grow. The growth rate is highest at the point where the crack intersects the free surface at the root of the notch. The growth rate at this point also increases with cycle number, whereas the growth rate at the deepest point remains approximately constant. At the 130th cycle, or 5th F.E. analyses, the crack growth calculations were terminated by ZENCRACK because the next increment of crack growth would have exceeded the crack block size. The initial and final F.E. meshes around the crack are illustrated in figure 5.21 for comparison.

5.2.4.6 Discussion of Results

K Solutions and Cracked Mesh Generation

One of the initial reservations about the ZENCRACK procedure for creating cracked F.E. meshes was the fact that only one element in the original mesh is replaced with a crack block. It is widely recognised that in a conventional F.E. analysis, a high mesh density is required close to a stress concentration in order to predict accurate local stresses. In a ZENCRACK analysis, the crack which is constructed can only extend over a fraction of an element length (where 'element length' refers to the uncracked mesh). The displacement distribution acting over the edge of the crack block can therefore be no more nonlinear than a quadratic,

and no more than linear for stresses. The mesh used in the initial work incorporated three elements along the length of a crack block. This allows for more highly nonlinear stress distributions at the expense of reduced ease-of-use.

The results from the ZENCRACK analyses in table 5.2 show that for this notch geometry and local stress distribution, the results obtained from the two approaches are very similar. The ZENCRACK results at the deepest point are slightly higher as would be expected based on the above arguments.

The experiments with generating cracked meshes indicated that for a given crack block size, cracks could be successfully generated at sizes down to 30% of the crack block length, but not at 10% of the crack block length. For very small cracks, the original mesh size should be reduced.

ZENCRACK does not automatically create any surface normal definitions within the ABAQUS input file for the cracked F.E. mesh. Surface normals are required in an analysis when the direction of virtual crack extension at a surface breaking node on the crack front is not parallel to the free surface. The surface normal defines the plane of the surface, and consequently the direction of virtual crack extension can be adjusted by the program to ensure that it does remain parallel, and does not move outside the body. Not including the surface normals may not affect the result in the majority of cases, but under some circumstances, the use of surface normals is recommended (HKS, 1996). In the present analysis, the initial crack front intersected the surface at close to 90°, but in subsequent iterations the angle became quite acute. It is possible therefore that the surface K values may have been affected by the lack of surface normals.

Crack Growth Predictions

The results of the ZENCRACK crack growth calculations do not agree with either the test results or the previous predictions. The growth rate predicted by ZENCRACK is highly excessive. As noted above, the highest growth rate is experienced where the crack intersects the free surface. The predictions in the initial analyses were based on the deepest point K values to avoid problems associated with crack behaviour close to the surface, e.g.:

- Accuracy of K solutions at the intersection with the free surface
- Nonlinear material behaviour close to the notch root

In the paper by Pook (1994), the problems associated with predicting K values at an intersection with a free surface are described. This is because of the changing nature of the crack tip singularity in this region. Basically, a mode I K value will only be finite for a certain angle of intersection between the crack front and the surface (100.4° for a surface crack in a uniformly stressed body, $\nu=0.3$). At other intersection angles it may be zero or infinite. Therefore, from a theoretical point of view under linear elastic conditions, the surface K value and local crack shape should differ from that predicted in the current FE analyses using ZENCRACK. It is also possible that errors in the surface K solution in the ZENCRACK analyses were compounded by the lack of surface normals as described above.

In the actual specimen, the material does not behave in a linear elastic manner. The effects of nonlinear material behaviour are significant in this geometry and material. Yielding occurs on initial loading, in effect, setting up a residual stress field which may lead to premature crack closure at points on the crack faces close to the surface, and consequently, the growth rate at points on the crack front in this region may be limited. Cyclic plasticity is also experienced over a smaller region close to the notch surface which may violate the conditions under which the stress intensity factor K is valid. Newman (1984) and Smith (1989) have investigated the growth of surface cracks, and highlight anomalous growth behaviour at the intersection of the the crack front with the free surface. This is attributed to lack of constraint leading to higher crack tip plasticity at this point, and higher crack closure levels. Newman proposed an empirical correction factor to apply to the local surface ΔK value to give a lower ΔK_{eff} which then gives a lower crack growth rate.

In the paper by Smith (1989) there was some discussion of the validity of K values calculated at the intersection of the crack front with the surface, and in several cases, surface K values were obtained by extrapolating from points inside the body, adjacent to the intersection.

Newman and Raju (1984) carried out crack growth predictions for surface and corner cracks based on K solutions obtained originally from FE crack analyses. Crack shapes were assumed to be semi-elliptical or quarter elliptical. Crack growth therefore only needed to be calculated at the points on the crack front which intersect the major and minor axes. The Elber crack growth model (Elber, 1971) was used to calculate the growth rates.

In earlier work, Newman and Raju (1979) observed that even though surface K values were about 10% higher than the deepest point values, the crack grew in a self-similar manner, and a factor $\beta_R = 0.9$ was applied to the local ΔK_{eff} value to account for this. Newman and Raju related this factor to differences in crack closure around the crack front. No actual closure/opening measurements are supplied to prove this, but reference is made to other workers and analytical work carried out by Newman on crack closure. An R-ratio dependent expression for β_R was proposed:

$$\beta_R = 0.9 + 0.2R^2 - 0.1R^4 \quad (5.9)$$

for $R \geq 0.0$, and

$$\beta_R = 0.9 \quad (5.10)$$

for $R < 0.0$.

More recently, Van Stone (1988) used a modified version of this model to predict the growth of surface cracks. The anomalous surface growth was attributed to a loss of constraint at the surface, leading to more plasticity and the formation of shear lips. In their model it is assumed that the reduction in K at the surface is proportional to the crack tip plastic zone size. However, the equations arrived at rely on an empirical fit to measured surface crack growth data.

For a notch root crack such as the one in this example, the growth rate at a particular point on the crack front will be dependent on both local R-ratio effects, and elastic-plastic behaviour in the region of the crack tip. At the notch surface, there may also be some time dependent stress relaxation due to creep. The inclusion of a residual stress field by means of the INITIAL CONDITIONS, STRESS option in ABAQUS provides a means of accounting for the effects initial plasticity on crack behaviour, and has been tested in previous work. Because of time constraints however, it was not possible to test whether this would work in a ZENCRACK crack growth analysis. The ZENCRACK manual does not mention this option, but there appears to be no reason why it could not be included. The calculation of local crack growth rates in ZENCRACK would require careful consideration for this type of analysis, particularly for applied loading R-ratios greater than zero.

Until these problems are resolved, the approach adopted in the previous work, where the deepest point K value is used in crack growth calculations in regions of stress concentration together with an assumed aspect ratio, appears to be the most practical solution.

5.2.4.7 Conclusions

1. ZENCRACK can successfully generate F.E. meshes for a range of crack sizes (within limits) from a given original uncracked F.E. mesh.
2. For the notched specimen geometry considered ($K_t = 2.23$), ZENCRACK was able to calculate reasonably accurate deepest point K values for a semi-circular crack at the root of the notch.
3. Problems relating to the calculation of K values at surface interacting points under linear elastic conditions still need to be resolved. This will influence predictions of crack shape development.
4. The application of ZENCRACK to crack growth problems at notch roots where local non-linear material behaviour is experienced is not recommended at present, except to generate F.E. meshes for specified crack geometries. Techniques for including the effects of residual stresses, and their effects on

predicted growth rate still need to be developed for use within a ZENCRACK analysis.

5.2.5 Three-Dimensional Crack Analyses of Grey Iron Notched Specimens

In section 3 it was described how cracks have been observed to initiate and grow in grey iron from the graphite flakes. At the beginning of section 5 the assumed sequence of events which take place at the root of a notch in a specimen or component of grey iron was described. In section 5.2.2, crack analyses were described in which the notch root cracks were continuous along the surface in a circumferential direction. The simulation of linear elastic crack behaviour in that case could then be based on models with an assumption of axisymmetry. i.e. the FE models could be two-dimensional.

This section describes FE analyses which were carried out in order to determine K values for semi-circular cracks located at the root of notches in a grey cast iron fatigue test specimens. These analyses involved the generation of three-dimensional models of the crack and a portion of the test specimen using 8-noded or 20-noded brick elements.

Initial analyses were carried out using the 8-noded elements to minimise the computer data storage requirements. Later analyses used the 20-noded bricks. Symmetry conditions were employed to reduce model sizes. Material elastic properties assumed were typical values for grade 17 grey iron. The elastic modulus E was assumed to be 120 GPa, and the Poisson's ratio $\nu = 0.26$.

Two different grey iron notched specimen geometries were considered:

1. Circumferentially 'U' notched specimen, Notch depth = 3.175mm, Notch root radius = 3.175mm, $K_t = 2.2$.
2. Circumferentially 'V' notched specimen, Notch depth = 3.175mm, Notch root radius = 0.3mm, $K_t = 5.6$.

The geometry of each of these specimens has been described in section 3. Typical examples of the FE models used for the crack analyses are shown in

figures 5.22 and 5.23, together with a description of the applied loads and boundary conditions. All of the models represented a 10° segment of the specimen, except for one (specimen $K_t=5.6$, $a=0.6\text{mm}$) which was 15°.

Circumferentially 'U' notched specimen $K_t = 2.2$

The analyses which were carried out on this specimen are listed below. The resulting K solutions are shown in figures 5.24 to 5.25.

Crack depth (mm)	Element type
0.30	8-noded brick*
0.60	"
0.1	20-noded brick
0.15	"
0.30	"
0.45	"
0.60	"

* with extra nodeless shape function

Table 5.3 Semi-circular surface crack analyses carried out on circumferentially 'U' notched specimen ($K_t=2.2$)

Circumferentially 'V' notched specimen $K_t = 5.6$

The following analyses were carried out on this specimen:

Crack depth (mm)	Element type
0.30	8-noded brick*
0.60	"
0.10	20-noded brick
0.15	"
0.30	"
0.60	"

* with extra nodeless shape function

Table 5.4 Semi-circular surface crack analyses carried out on circumferentially 'V' notched specimen ($K_t=5.6$)

The K solution results for this specimen are shown in figures 5.26 and 5.27.

The crack front K distributions in figures 5.24 and 5.26 have been smoothed by firstly considering only the corner node K values, and secondly by discarding the K values at each end of the distributions (the notch surface position, and the deepest point position), and instead linearly extrapolating out to these positions from the K values at the next two nodes in from each end.

Figures 5.25 and 5.27 compare the deepest point K values with the two-dimensional K solutions described earlier, for a range of crack sizes. These show that the three-dimensional K solutions increase at a similar rate to the two-dimensional K values over the range of crack sizes considered. Figure 5.28 illustrates this more clearly, where the ratio of K values (K_{3d}/K_{2d}) is plotted for both notches. Overall, a small decrease in the K ratio is observed with increasing crack depth, from 0.62 to 0.56 in the range of crack depths from 0.1mm to 0.6mm. Another point to note is that both notches appear to have roughly similar K ratios.

A further analysis was performed to investigate the effects of changes in the elastic material properties on the calculated K values. For this, the BRITE Notch 2 specimen ($K_t=5.6$) was used, with a crack depth of 0.1mm. The results for two analyses were compared, with the following properties assumed:

- a) $E = 120000 \text{ Mpa}$, $\nu = 0.26$
- b) $E = 200000 \text{ Mpa}$, $\nu = 0.3$

Figure 5.29 illustrates the results in terms of the percentage difference in K value around the crack front. For most points the difference is less than about 0.3%. At the point where the crack front intersects the notch surface, the difference climbs rapidly to approximately 1.8%. It is concluded therefore that the K values are insensitive to variations in the elastic constants between the different grades of cast iron being studied.

5.3 Simulation of the Effects of Residual Stresses on Notch Root Cracks

The crack analyses described in the last few sections relate to bodies which exhibit purely linear elastic behaviour. K solutions have been generated for both continuous surface cracks and semi-circular surface cracks at the root of notches where no plasticity has assumed to take place. However, the stress analyses carried out on the notched specimens, and described in section 2 indicates that local yielding at the notch root should take place for all the specimens tested.

Any yielding of the material will affect the magnitude of the stresses which hold a notch root crack open, and consequently the magnitude of the crack tip stress field and the K value (assuming K to be a valid measure). Also, the residual stress field which would be expected to be created as a result of the plasticity occurring during the first loading cycle will force the faces of the crack together at an earlier point in the cycle compared with what an elastic analysis would suggest. This premature crack closure would therefore result in a lower range of stress intensity factor ($\Delta K_{\text{eff}} = K_{\text{max}} - K_{\text{op}} < \Delta K$).

It is therefore important to make an estimate of this effect if the goal is to simulate the behaviour of small cracks growing from the notch roots of these specimens. Again, the FE method provides a means of carrying out analyses involving these effects, although the complexity increases significantly from the basic linear elastic crack analyses described earlier. Because of the extra complexity, the analyses were carried out for only a few loading conditions and crack geometries. The objective was to determine the magnitude of the effects and provide data on which to base simplified methods which could be applied more generally.

5.3.1 Description of the Method of Analysis

The effect being simulated was the influence of residual stresses on the K values for cracks at notch roots. The residual stresses of interest are those generated by the material yielding during the initial load cycle.

The first stage in the process involved carrying out an elastic-plastic analysis of the uncracked body to generate a residual stress field. The load cycle considered was:

- a) Load up to the maximum applied load
- b) Unload back to zero load

The residual stress field remaining at the end of the unloading phase were saved for input into the next stage.

Using the same FE mesh in the second step, constraints were removed which would allow the crack faces to become free. The residual stresses were supplied to a new linear elastic analysis as initial stresses. Two load steps were run:

- a) Zero load to allow the residual stresses to re-equilibrate.
- b) Loading up to the maximum applied load, and calculation of J and K values for the crack tip.

Crack face displacements were also saved in these two load steps to provide estimates of the point in the load cycle at which the crack faces close or open.

5.3.2 Description of the Analyses and Results

A number of analyses were carried out using this procedure involving different specimen geometries and stress fields, different crack geometries, different crack sizes and applied load levels. The specimen geometries considered were:

- Model turbine disc (IN718 nickel alloy): Semi-circular surface crack at the bore of the disc
- BRITE Notch 1, $K_t=2.2$ (Grade 17 grey iron): Continuous surface cracks and semi-circular surface cracks at notch root
- BRITE Notch 2, $K_t=5.6$ (Grade 17 grey iron): Continuous surface cracks and semi-circular surface cracks at notch root

The model turbine disc provides an example where the local component geometry and the local stresses are relatively uniform. Yielding takes place over a significant

volume of material. The stress fields present in the notched geometries on the other hand are highly non-uniform, particularly for Notch 2.

5.3.2.1 Model Turbine Disc Analysis

This test specimen is designed to be spin tested with a load cycle from 0 to 23000rpm. The critical region is the bore of the disc. It was required to simulated the growth of a postulated semi-elliptical surface crack. The material is the nickel alloy IN718, operating at a temperature of 400°C. Stress-strain data and crack growth data is available for this material at 400°C. Preliminary crack growth predictions based on purely linear elastic analyses indicated that the crack growth life would be short in comparison with the initiation period. What was required was an estimate of the influence of initial yielding on the crack growth.

Three-dimensional FE models were constructed of the disc using 20-noded isoparametric brick elements. Each had a semi-elliptical crack at the surface of the bore. Three different crack sizes were considered: 0.1, 0.5 and 1.0mm, with an aspect ratio (a/c) of 0.8. An example is shown in figure 5.30.

Following the procedure outlined previously, elastic-plastic analyses were carried out first, with the crack faces constrained to simulate the uncracked body. For these analyses, a piecewise linear stress-strain curve was used to represent the material behaviour:

Elastic modulus = 185900 MPa	Poisson's ratio = 0.3
Stress (MPa)	Plastic strain
850	0.0
945	0.0005
988	0.001
1028	0.002
1083	0.005

Table 5.5 Material stress-strain properties assumed for disc analysis

In this particular geometry and loading, reverse yielding on unloading from 23000rpm would not take place, and so isotropic hardening could be assumed. Table 5.6 shows a comparison of the elastic and elastic-plastic stress distributions close to the bore surface at 23000rpm (the actual stresses illustrated were obtained from an axisymmetric FE model of the disc). The stress gradient is very small, particularly over the first millimetre.

Distance below surface (mm)	Elastic stress (MPa)	Plastic stress (MPa)	Stress ratio (Plastic:elastic)
0.0	1204	1015	0.8430
0.9	1192	1015	0.8515
1.8	1181	1016	0.8602
2.7	1169	1016	0.8691
3.6	1158	1017	0.8782
4.5	1147	1017	0.8867
5.4	1136	1017	0.8952

Table 5.6 Comparison of elastic and elastic-plastic stress distributions at the model disc bore

The residual stresses remaining on unloading the three-dimensional models were saved. Elastic crack analyses were then carried out for the three crack sizes, both with and without the residual stresses. The K values around the crack front were calculated using the J-domain integral approach described earlier. The results are shown in figures 5.31, 5.32, 5.33 and 5.34.

The crack front K distributions of figures 5.31, 5.32 and 5.33 show that the K value has been reduced by a similar proportion at all angular positions, and at different crack depths, even though the K value increases significantly with crack depth (figure 5.34). This indicates that the K value depends directly on the magnitude of the local stress field. Figure 5.35 illustrates this. In this figure, the ratio of K values, which is given by:

$$K_{ratio} = \frac{K \text{ value (applied load + residual stresses)}}{K \text{ value (applied load only)}} \quad (5.11)$$

is plotted for different crack depths. The K value is the deepest point value. Also plotted in this figure is the ratio given by:

$$Stress_{ratio} = \frac{Hoop \text{ stress (Elastic-plastic analysis)}}{Hoop \text{ stress (Elastic)}} \quad (5.12)$$

The two ratios coincide almost exactly. In cases such as this therefore, the K value for the condition of applied loading + residual stresses could be estimated from the elastic K value solution and an estimate of the ratio of elastic-plastic to elastic stresses. The presence of the residual stress field would therefore be expected to influence the crack growth rate (assuming that crack closure takes place at stresses less than or equal to zero. i.e. $K_{min} \geq 0$).

5.3.2.2 BRITE Notch 1 Analysis ($K_t=2.2$)

The BRITE Notch 1 specimen has a more localised high stress region than the disc. Significant plasticity during initial loading will be restricted in most cases to a region within approximately 1mm of the surface of the notch. The effects of residual stresses due to initial yielding have been studied for two types of notch root cracks:

- a) Continuous circumferential surface cracks
- b) Semi-circular surface cracks

(a) Continuous circumferential surface cracks

Axisymmetric FE models were used to model the behaviour of cracks of the following sizes (depth in mm):

- 0.098
- 0.130
- 0.162
- 0.194
- 0.226
- 0.257

0.289

0.320

0.474

Two different maximum loads were used, giving nominal stresses of 80MPa and 100MPa. A piecewise linear stress-strain curve was used to model typical stress-strain behaviour of grade 17 grey cast iron. The curve used was the following:

Stress (MPa)	Plastic strain
50.0	0.0
100.0	0.00030
140.0	0.00065
180.0	0.00153
200.0	0.00230
215.0	0.00320
225.0	0.00410
235.0	0.00550

Table 5.7 Typical grade 17 grey cast iron stress-strain curve

Young's Modulus and Poisson's ratio were given by $E = 120000\text{MPa}$, $\nu = 0.26$. Isotropic hardening was assumed which allows the use of this type of stress-strain curve.

Figure 5.36 shows the distribution of residual stresses at the notch root in the unloaded condition after the application of a load equivalent to 80MPa net section nominal stress. The compressive stress region extends to a depth of approximately 1mm, and to between 2 and 3mm around the notch radius each side of the centreline. Figure 5.37 shows the calculated stress-strain history at the root of the notch for loading to maximum load and unloading, indicating that the behaviour is significantly nonlinear.

This residual stress field was supplied to a subsequent elastic crack analysis. The deformed shape of the largest crack size (0.474mm) at maximum load (80MPa) and after unloading are shown in figure 5.38 and 5.39 respectively. The presence of the crack is simulated in this analysis by the release of constraints on the plane of symmetry. Consequently, in the absence of contact elements along this face, the crack face is pushed down beyond the line of symmetry on unloading.

The calculated K values at maximum load with and without the residual stresses are shown in figure 5.40. The K value is affected at all crack sizes considered, and for both maximum stress conditions. At the larger crack sizes, a similar percentage reduction in K value is obtained due to the residual stresses, at both maximum load levels. The percentage reduction in K value is however affected by the maximum load level for smaller crack sizes, for example, a < 0.2mm. This effect is illustrated in figure 5.41 in which the ratio of K values ($K_{\text{plastic}}/K_{\text{elastic}}$) is plotted against crack depth.

Of interest later on, when these effects need to be estimated, is how these K ratios correlate with the ratio of stresses from the uncracked body analysis at each depth. The ratio of stresses ($\sigma_{\text{plastic}}/\sigma_{\text{elastic}}$) at the depth corresponding to the crack depth is therefore also plotted in figure 5.41. At the smallest crack size (a=0.1mm), the two ratios agree almost exactly, but at larger crack sizes, the stress ratios become higher. On the basis of the disc bore crack analyses in which the crack was embedded well within the plastic zone, it is likely that similar good agreement would be expected between the stress ratios and K ratios at crack sizes less than 0.1mm in this notched specimen.

Figures 5.42 and 5.43 supplement figures 5.38 and 5.39. They illustrate the crack face displacements for all the crack sizes considered. The magnitude of the opening displacements at maximum load are significantly greater than the magnitude of the crack face displacements in the unloaded condition, and this becomes more pronounced at larger crack sizes. The ratio of crack mouth displacements allows these effects to be quantified as shown in figure 5.44. Clearly, because the smaller cracks lie further within the plastic zone, a larger residual stress will be attempting to close the crack up in the unloaded condition.

In the limit, the ratios tend towards the ratio of the local inelastic surface stresses. These are also shown in the figure.

The good correlation between the stress ratios and displacement ratios at the smaller crack sizes highlights a possible means of estimating crack closure levels, which may be of importance in effective ΔK calculations.

(b) Semi-circular surface cracks

For these analyses, a three-dimensional FE model of a 0.3mm deep, semi-circular surface crack, as described in an earlier section, was employed. The objective of the work was to determine the effect of residual stresses on a semi-circular surface crack, which being more localised than a continuous surface crack, may be more influenced by a residual stress field.

The model consisted of 20-noded quadratic brick elements. Crack analyses were carried out with crack tip mid-side nodes positioned at the mid-point to minimise the possibility of abnormal local stresses during the initial uncracked elastic-plastic analyses.

Eight different maximum load conditions were used, which in terms of net section nominal stress values were:

- 80MPa
- 100MPa
- 135MPa
- 140MPa
- 145MPa
- 150MPa
- 155MPa
- 160MPa

Figure 5.45 shows an example of a residual stress field generated from loading to a maximum load condition and unloading. The residual stresses from each of these cases were imported into subsequent crack analyses as initial stresses, and

the K values calculated using the J-integral method. Figure 5.46 shows the distribution of K values around the crack front at different maximum loads. Also shown is the elastic K distribution for $S_{max}=160\text{MPa}$. These K distributions have been smoothed using the procedure described earlier. With the residual stresses present, the K distributions are flatter than the purely linear elastic case. Typically, the variation around the crack front is less than half that for the elastic case.

Figures 5.47 and 5.48 show how the K values at maximum load vary with the load magnitude, for the deepest point and surface point positions respectively. Also shown in these figures are the linear elastic K values, and estimated K values obtained by multiplying the linear elastic K value by the ratio of uncracked body stresses ($\sigma_{plastic}/\sigma_{elastic}$) at these locations. The greatest reduction occurs at the surface breaking position. This effect is predicted well by the stress ratios, except the absolute value of the reduction is overpredicted.

Comparing these results with the corresponding results for the continuous surface cracks, it is noted that for the semi-circular crack, no reduction is obtained at the deepest point for loads less than 100MPa, whereas a reduction of at least 11% was obtained for a 0.3mm deep continuous surface crack. A possible explanation for this may be that the mesh density used in the 3-D model is lower than that used for the axisymmetric model, leading to smaller plastic strains.

5.3.2.3 BRITE Notch 2 Analysis ($K_t=5.6$)

As with Notch 1, this sharper notch was analysed with both continuous surface cracks, and semi-circular surface cracks.

(a) Continuous circumferential surface cracks

A series of axisymmetric FE analyses were carried out. These involved elastic-plastic analyses of the uncracked geometry for two different maximum load levels, 80 and 100MPa, to generate residual stress fields for the unloaded condition, and subsequent linear elastic crack analyses for the range of crack sizes (mm):

0.046
0.070
0.097
0.129
0.165
0.204
0.248
0.296
0.353

The elastic-plastic analyses each involved two steps: load up and unload. The same piecewise linear stress-strain curve as described for the Notch 1 analyses was used for this notch, again with isotropic hardening. In the case of notch 2, reverse yielding occurs much more readily at the notch surface, as shown in figure 5.49. The plasticity model used here is not likely to provide a reliable representation of the cyclic behaviour at this position. However, it is the monotonic plasticity which is of most interest.

The K solutions for this notch geometry shown in figure 5.50 clearly illustrate the significant effect of the localised plasticity towards the surface. The results for the higher load (100MPa) give a more pronounced reduction in K at small crack sizes than the 80MPa case. At larger crack sizes, the percentage reduction is similar. The ratio of K values (plastic/elastic) is shown in figure 5.51 together with the ratio of stresses. As in the case of the Notch 1 results, the stress ratios and K ratios appear to intersect at the smallest crack size. An additional point of interest is that beyond 0.2mm crack depth, the elastic-plastic stress becomes greater than the elastic stress. It is probable that this will be due to the need for the residual stress field which is set up, to equilibrate.

The ratio of K values for the cracked geometry exhibit values significantly below unity even for the largest crack size studied. In Figures 5.52 and 5.53, contour plots of von Mises equivalent stress are respectively presented for (a) elastic behaviour only, and (b) elastic plus residual stresses. These apply to crack length $a=0.353\text{mm}$ and $S_{\text{max}}=80\text{MPa}$. These show that the crack tip stress field is

reduced by the presence of the residual stresses, even at a distance of more than one crack length from the crack tip.

The crack face displacements for the different crack sizes are shown in figures 5.54 and 5.55 for 80MPa and 100MPa maximum loads respectively. As for notch 1, the crack faces are not prevented from moving beyond the line of symmetry. To prevent this would have required the use of contact elements. This would have increased the complexity of the analyses considerably. The objective of presenting the displacement data in this way is to provide an estimate of the point in the load cycle at which the crack will close.

For the smallest crack sizes the crack face displacements are almost fully reversed, particularly at the higher load. Figure 5.56 illustrates this in terms of the ratio of crack mouth displacements. As the crack becomes larger, the effect becomes smaller. The points on this figure representing the surface stress ratios indicate that the ratio of crack face displacements approach these values as the crack size tends to zero, i.e. similar to the behaviour predicted for the notch 1 geometry.

(b) Semi-circular surface cracks

Three-dimensional FE analyses were carried out on the notch 2 geometry with similar loading and crack geometry conditions as were used for the notch 1 ($K_t = 2.2$) geometry. The FE mesh used was also based on 20-noded bricks and crack tip elements in the standard FE configuration with mid-side nodes at the mid-point. Figure 5.57 illustrates the mesh and von Mises equivalent stress contours for the 80MPa loading condition in the uncracked body elastic-plastic analysis. The crack depth is 0.3mm. The very localised stress field in comparison to the crack size is readily apparent.

The distribution of K values around the crack front obtained from the crack analyses with residual stresses superimposed are illustrated in figure 5.58. Also shown is the elastic K distribution. At low loads, the distribution is relatively flat. At higher loads, the effects of reversed plasticity on the K values close to the surface can be seen.

The deepest point K values are plotted in figure 5.59 as a function of maximum nominal stress. The figure shows that these K values begin to deviate from the elastic K solution at loads above 100MPa. This is different to the axisymmetric results with a 0.3mm circumferential crack where the ratio of K values was 0.9 for both $S_{nom}=80$ and $S_{nom}=100$ MPa. This difference in behaviour could be due to differences in the FE mesh density and the different crack geometries. The ratio of uncracked body stresses (plastic/elastic) has also been used to estimate the K values, using the formula, $K = K_{elastic} * (\sigma_{plastic}/\sigma_{elastic})$. These are also shown in the figure. For the loading conditions studied, the stress ratios at a depth of 0.3mm do not change by any significant amount from the elastic values.

5.4 Approximation Procedures for Stress Intensity Factor Estimation

The previous sections have dealt with the analysis of cracks using FE analysis. Due to the large computational effort involved in FE based crack analysis, particularly when localised plasticity has also to be accounted for, a relatively simple method to estimate the crack behaviour is required for design assessment situations, where other geometries, loads and material properties exist.

This section considers methods to estimate K values for a notch root crack based on the stress field which may be available from, for example, a two-dimensional elastic FE analysis of the uncracked component. It will be assumed that the component may be of arbitrary shape, i.e. without a definite notch depth or root radius. The effects of localised plasticity have been shown in the previous section to have a possibly significant effect on local K values for a notch root crack. Therefore, a means of estimating this effect from the uncracked body stress field has also been investigated.

Several approximate methods to estimate K values have been considered. The list is not an exhaustive one, since this was not the main objective of the overall work.

5.4.1 Method of Albrecht and Yamada (1977)

The method proposed by Albrecht and Yamada (1977), is an example of an approximate method, intended for application to cracks in regions of stress concentration where stress gradients are high.

The solution for the stress intensity factor of a cracked body subjected to distributed stresses can be written in the form:

$$K = F(a)\sigma\sqrt{\pi a} \quad (5.13)$$

where

$$F(a) = F_E \cdot F_S \cdot F_W \cdot F_G \quad (5.14)$$

which is a crack size dependent correction factor that modifies K from the reference solution of a through crack in an infinite body subjected to uniform stress σ . The individual factors which combine to give $F(a)$ represent the influence of different parameters on the K value:

F_S = Factor to account for the crack intersecting a free surface

F_E = Factor to account for elliptical crack fronts

F_W = Factor to account for finite width bodies

F_G = Factor to account for non-uniform crack opening stresses

These individual factors can be based on known solutions, but their combined use for K value estimates involves some approximation. For a semi-circular surface crack, Albrecht et al propose that $F_S = 1.12$ and $F_E = 0.65$. In the present application, F_W has been taken as unity, because the crack sizes are very small in relation to the boundary on the opposite side. In the publication by Pickard (1986), the factor corresponding to F_G is obtained from curve fits to FE generated K solutions for cracks in gradient stress fields. Albrecht et al employ an approach based on the use of Green's functions to estimate F_G .

The Green's function is defined as the response of a system to a standard input. This can be the stress field in an elastic body due to a point force. For a body containing a crack, the K value which results from the application of a point force, is a special case of a Green's function. For a Green's function to be valid, the following properties must be exhibited by the system (Cartwright and Rooke, 1979):

- Causality - No input gives no response
- Invariance - Always the same response to a given input
- Linearity - If the response to input I_1 is R_1 and the response to input I_2 is R_2 then the response to input $(I_1 + I_2)$ is $(R_1 + R_2)$.

The general response to a general input can be expressed as:

$$R(y) = \int I(x).G(x)dx \quad (5.15)$$

where $G(x)$ is the Green's function. Given an expression for K for a single point force. The K value for a crack in an arbitrary stress field may be estimated by treating the problem as a collection of point forces.

For a central crack of length $2a$ in an infinite plate, symmetrically loaded by two equal pairs of splitting forces P applied to the crack faces at a distance x_0 from the centreline, the K value can be expressed as:

$$K = \sqrt{\pi a} \frac{2P}{\pi} \frac{1}{\sqrt{a^2 - x_0^2}} = \sqrt{\pi a} \frac{2P}{\pi} G(x_0) \quad (5.16)$$

The term $G(x_0)$ can be used as a Green's function to obtain the K value for cracks with distributed loads $\sigma(x)$ applied over the faces:

$$K = \sqrt{\pi a} \frac{2}{\pi} \int_0^a \sigma(x).G(x)dx = \sqrt{\pi a} \frac{2}{\pi} \int_0^a \frac{\sigma(x)}{\sqrt{a^2 - x^2}} dx \quad (5.17)$$

If the load is discretised into a number of uniformly stressed elements, then:

$$K = \sqrt{\pi a} \frac{2}{\pi} \sum_{i=1}^n \sigma_{x_i} \int_{x_i}^{x_{i+1}} \frac{1}{\sqrt{a^2 - x^2}} dx \quad (5.18)$$

which after integration gives:

$$K = \sigma \sqrt{\pi a} \frac{2}{\pi} \sum_{i=1}^n \frac{\sigma_{x_i}}{\sigma} \left(\arcsin \frac{x_{i+1}}{a} - \arcsin \frac{x_i}{a} \right) \quad (5.19)$$

The geometry correction factor F_G can therefore be expressed as (Albrecht, 1977):

$$F_G = \frac{2}{\pi} \sum_{i=1}^n \frac{\sigma_{x_i}}{\sigma} \left(\arcsin \frac{x_{i+1}}{a} - \arcsin \frac{x_i}{a} \right) \quad (5.20)$$

5.4.2 Method of Newman and Raju: Semi-elliptical Defect in a Plate (1979)

Newman and Raju developed equations to give the K values around the crack front of a semi-elliptical crack in a finite width plate (Newman and Raju, 1979). These equations are a fit to FE results for crack aspect ratios ($0.2 \leq a/c \leq 1.0$).

For combined tension and bending load for which:

$$\sigma = A_0 + A_1 x \quad (5.21)$$

then the stress intensity factor is given by:

$$K_I = (S_t + HS_b) \sqrt{\frac{\pi a}{Q}} \cdot F \quad (5.22)$$

$$Q = 1.0 + 1.464 \left(\frac{a}{c} \right)^{1.65} \quad (5.23)$$

The functions F and H are defined so that the boundary-correction factor for tension is equal to F , and the boundary correction factor for bending is equal to the product of F and H . The function F was obtained from a systematic curve-fitting procedure by using double series polynomials in terms of a/c , a/t and angular functions of ϕ , where:

a = Crack depth

c = Crack half surface length

t = Plate thickness

ϕ = The angle defining the position around the crack front

The choice of functions was based on engineering judgement.

$$F = \left[M_1 + M_2 \left(\frac{a}{t} \right)^2 + M_3 \left(\frac{a}{t} \right)^4 \right] f_\phi g f_w \quad (5.24)$$

$$M_1 = 1.13 - 0.09 \left(\frac{a}{c} \right) \quad (5.25)$$

$$M_2 = -0.54 + \frac{0.89}{(0.2 + a/c)} \quad (5.26)$$

$$M_3 = 0.5 - \frac{1.0}{(0.65 + a/c)} + 14 \left(1.0 - \frac{a}{c} \right)^{24} \quad (5.27)$$

$$g = 1 + \left[0.1 + 0.35 \left(\frac{a}{c} \right)^2 \right] (1 - \sin \phi)^2 \quad (5.28)$$

Factors f_ϕ and f_w were assumed to be unity for this application.

$$H = H_1 + (H_2 - H_1) \sin^p \phi \quad (5.29)$$

$$p = 0.2 + \left(\frac{a}{c} \right) + 0.6 \left(\frac{a}{t} \right) \quad (5.30)$$

$$H_1 = 1.0 - 0.34\left(\frac{a}{t}\right) - 0.11\left(\frac{a}{c}\right)\left(\frac{a}{t}\right) \quad (5.31)$$

$$H_2 = 1.0 + G_1\left(\frac{a}{t}\right) + G_2\left(\frac{a}{t}\right)^2 \quad (5.32)$$

$$G_1 = -1.22 - 0.12\left(\frac{a}{c}\right) \quad (5.33)$$

$$G_2 = 0.55 - 1.05\left(\frac{a}{c}\right)^{0.75} + 0.47\left(\frac{a}{c}\right)^{1.5} \quad (5.34)$$

The accuracy of the K value is quoted to be $\pm 5\%$ for all combinations and $a/t \leq 0.8$. These equations are recommended in Appendix E of BS PD6493 (BSI, 1991) for use in crack analyses of welded joints.

5.4.3 Method of Kopsov (Ref. 1992)

Kopsov proposed an empirical solution for the stress intensity factor for a semi-elliptical surface crack in a body with a stress distribution described by a power function (Kopsov, 1992). The method is a development of the Newman and Raju equations:

$$K_I = \left(A_0 + \sum_{n=1}^j H_{(n)} A_n \right) \sqrt{\frac{\pi a}{Q}} \cdot F \quad (5.35)$$

where the interpretation of the polynomial stress function is:

$$\sigma = \sum_{n=0}^j A_n a^n \quad (5.36)$$

and

$$H_{(n)} = H_{1n} + (H_{2n} - H_{1n}) \sin^p \phi \quad (5.37)$$

$$H_{1n} = a^n (C_{1n} + 0.55a / c) \quad (5.38)$$

$$H_{2n} = a^n (C_{2n} + 0.06a / c - 0.5Ga / t) \quad (5.39)$$

The values of the constants C_{1n} and C_{2n} are given in (Kopsov, 1992) and are based on results of other authors. The equations were reported to give an average error of 4%, and a maximum error of 15% when compared with FE crack analysis results.

5.4.4 K Estimate based on Local Stress Value

A simple approach to estimating K for a semi-circular crack in a non-uniform stress field was also investigated where:

$$K = Y \sigma_{Local} \sqrt{\pi a} \quad (5.40)$$

where σ_{Local} is the stress from the uncracked body stress distribution at a depth corresponding to the crack depth (a), and Y is an empirical constant which was finally chosen to have a value of 0.71.

5.4.5 K Estimate Based on Two-dimensional K Solution

Given that 2-D FE crack analysis results have been generated for a wide range of continuous surface crack depths, and results presented earlier indicate that the 2-D and 3-D results have a reasonably constant ratio over the crack depths considered. A formula for K for a semi-circular surface crack can be given as:

$$K = 0.58 * K_{2-D} \quad (5.41)$$

5.4.6 Comparison of Estimates with 3-D FE K Solutions

These different methods for estimating K for the deepest point of a semi-circular surface crack have been applied to the case of a surface crack at the root of the grey iron circumferentially notched specimens (BRITE Notches 1 and 2). Figures 5.60 and 5.61 illustrate the results.

For the lower K_t notch in figure 5.60, the different methods all give results which lie within 13% of the 3-D FE result. The method of Newman and Raju gives the best overall result. The simple formula based on the local stress ratio (eqn. 5.40) gives results which are between 3.5% and 10% over the range of crack sizes.

The results for the higher K_t notch (figure 5.61) show greater variability; errors range up to almost 20%. The method of Newman underpredicts the K values by up to 12.3%. The stress distribution in this case differs significantly from the linear distribution assumed by the Newman-Raju model. The simple stress ratio formula (eqn. 5.40) gives good agreement at smaller crack sizes, and then begins to underpredict more and more as the crack size increases beyond 50% of the root radius. At $a=0.6\text{mm}$, the K prediction is 8% below the 3-D FE result. The prediction based on the 2-D FE K solution (eqn. 5.41) gives the best overall fit over the range $0.1 < a < 0.6\text{mm}$. At the smaller crack sizes however it tends to underpredict (similar to the behaviour in the lower K_t notch).

These results show that a K estimation model based on the simple stress ratio formula (eqn. 5.40) gives a results which are almost as good as other more complex models over the crack sizes considered. This model is therefore employed in further calculations described in the following sections.

5.4.7 Estimation of the Effects of Local Notch Root Plasticity

Earlier sections dealt with numerical simulations of the effects of localised plasticity, and the generation of residual stress fields, on the K values for notch root cracks which subsequently appear in the material. The calculations indicated that the percentage reduction in maximum K value is similar to the percentage change in the uncracked body stress at a depth equal to the crack depth. This

was shown to be particularly true for the relatively uniform stress field of the disc bore.

An approach was therefore investigated based on the multiaxial Neuber calculation procedure described in earlier sections. The normal stress at a depth equal to the crack depth was estimated using the Neuber procedures. A factor equal to the ratio of this Neuber corrected normal stress to the linear elastic normal stress at this point was calculated as:

$$F_{Stress} = \frac{\sigma_{1,Neuber}}{\sigma_{1,elastic}} \quad (5.42)$$

This factor was then applied to the maximum K value in the load cycle calculated using the K estimation formula, to give an estimate of the K value when a residual stress is present.

Figures 5.62 and 5.63 show a comparison of estimated K values for continuous surface cracks, including the effects of initial plasticity. The formula for K which was used is:

$$K = F_{Stress} \frac{0.71}{0.58} \sigma_{Local} \sqrt{\pi a} \quad (5.43)$$

For the low k_t notch in figure 5.62, the K ratio is underpredicted. The largest error being 5%. The estimated effect at the higher load is greater than the FE based K solution would suggest. In the high K_t notch of figure 5.63, the estimates underpredict the K ratio at small crack sizes, but overpredict the K ratio at larger crack sizes. Both the estimates and the FE based K solutions show that the curves for the two loads converge at longer crack lengths. This would be expected, since the notch plastic zone size is not much greater than the largest crack depth considered. Overall, both sets of results show that the estimates follow a similar trend to the FE based solutions, and agree to within approximately 5% over most of the range (10% error at the smallest crack size, $K_t=5.6$).

The corresponding estimates for semi-circular surface cracks are shown in figures 5.64 and 5.65, but in this case the results are presented for a single crack size, as a function of maximum load. Also shown in these two figures are additional K ratio estimates based on the FE elastic-plastic stress ratios. The estimates agree relatively well for the sharper notch, whereas for the low K_t notch, the estimates underpredict the K ratio (i.e. they overpredict the effect of plasticity on K). The Neuber based K ratio estimates made use of stresses from axisymmetric elastic stress analyses. The mesh density is greater close to the notch root than for the 3-D model, consequently the local elastic stresses would be higher and could affect the degree of correlation. Overall, the estimated K ratio follows a similar trend to the FE based solutions. The largest error occurs in the lower K_t results, which are underpredicted by up to 18%.

Taking into account relative mesh density effects, these results indicate that K estimates based on stress ratios can provide a reasonable prediction of the K value when residual stresses are present.

An additional effect which should be accounted for is how the residual stresses and strains will influence the crack faces, and whether the faces will contact as the load is reduced. The 3-D crack analyses were carried out without the help of contact elements at the crack faces. Inspection of the crack mouth displacement ratio should therefore give some indication of the point at which the crack mouths would first contact.

Figures 5.66 and 5.67 show graphs of the ratio of crack mouth displacements (u_{min}/u_{max}) for various crack lengths. Also shown are estimated values based on the Neuber corrected stresses at the position corresponding to the crack depth. The agreement between the curves is good for the low K_t notch of figure 5.66, but differs more significantly over the range of crack depths of the high K_t notch.

5.5 Analytical Representation of Crack Growth Threshold

The El-Haddad model is often used to represent short crack behaviour. This model can be used to describe the short crack threshold. In this work, an extra term, a_1 (equation 2.50, section 2.4.1) is introduced for grey iron where a_1 represents the typical flake size.

$$\Delta K_{th} = \Delta K_0 (1 - A.R) \left[\frac{a}{a - a_1 + a_0} \right]^{1/2} \quad (5.44)$$

ΔK_0 denotes the threshold ΔK value for no growth at an R-ratio (K_{min}/K_{max}) of zero, and A is a constant which is determined from threshold test results at different R-ratios.

$$a_0 = \frac{1}{\pi} \left[\frac{\Delta K_0 (1 - A.R)}{Y \cdot \Delta \sigma_f} \right]^2 \quad (5.45)$$

$$\Delta \sigma_f = 2 * \sigma_f \quad (5.46)$$

These relationships will be illustrated graphically in the next section for each material. A linear variation of long crack threshold with R-ratio is assumed. The plain specimen fatigue limit σ_f is dependent on mean stress, this is not a linear relationship. It is represented in a piecewise linear fashion in this model, based on the test data presented earlier.

Smith's threshold model (Smith 1978) is also used in the next section.

Comparison of both the Smith and El-Haddad models with experimental data indicates that they generally bound the short crack threshold behaviour. Smith's model is defined below. For $a < a_0$, where a_0 is given by equation 5.45:

$$\Delta K_{th} = Y \cdot \Delta \sigma_f \sqrt{\pi a} \quad (5.47)$$

and for $a \geq a_0$, the long crack threshold value is used:

$$\Delta K_{th} = \Delta K_0 (1 - A.R) \quad (5.48)$$

5.6 Discussion

The crack growth based procedure outlined at the beginning of this section relies on the availability of stress intensity factor solutions for small cracks in regions of stress concentration. Techniques based on the the use of the finite element

method for the calculation of crack tip K values have been presented. The virtual crack extension method provides relatively accurate pointwise K values around a three-dimensional crack front. This still requires a finite element mesh of a certain quality. Relatively little work has been presented in the literature on the effects of mesh quality on three-dimensional crack K solutions, particularly with curved crack fronts. Therefore the early parts of this section have dealt with the question of solution accuracy.

Three-dimensional crack problems at notches also introduce problems associated with the intersection of the crack front with the notch root free surface. Even in uniformly stressed bodies, these effects have an influence on crack growth predictions, as noted by several authors. At notch roots, the effects are compounded by the presence of localised plasticity, which, in high cycle fatigue specimens, usually occurs during initial loading; subsequent cycling is often elastic (except in highly loaded sharp notches).

The localised plasticity on initial loading has the effect of introducing a local residual stress field which modifies the K values around the front of a growing crack. The effects of typical residual stress fields have been simulated using two and three-dimensional FE analysis. Most work reported in the literature on this subject appears to make use of modifications to analytical K solutions to simulate residual stresses. The nature of the stress field and of the crack geometries of interest were such, that the full FE simulation of the effect was necessary to arrive at reasonable estimates of local K values. A similar approach for this type of problem is not known of in the literature.

The results generated by the FE based crack analyses formed a baseline against which approximate methods of calculating K could be judged. The most promising methods identified for estimating K values from the uncracked body stresses were surprisingly the simplest. For a small crack in a notch stress field, a ratio of stresses was found to provide a suitable geometry correction factor which would give reasonable results over a range of crack sizes and notch geometries. Methods to estimate the effects of residual stresses on notch root crack K values were investigated using a development of the Neuber approach for multiaxial

stress states. The accuracy of the results when compared against the full FE simulation of residual stresses in cracked geometries was variable. Further work is required to develop better approximations. However, knowing the typical errors involved, the approximate solutions developed and presented in this section were used in the analysis of the notched test specimen results. These results will be presented in the following section.

6. COMPARISON OF PREDICTED NOTCHED SPECIMEN FATIGUE STRENGTHS WITH TEST RESULTS

6.1 Introduction

In Section 2, a number of test specimen and component geometries were described which relate to cast iron. These cover five different grades of cast iron:

- Grade 17 grey iron
- Grade 250 grey iron
- Grade 350 grey iron
- Grade 400 S.G. iron
- Grade 500 S.G. iron

The crack growth based methods described in the previous section have been applied to all of these specimen geometries to predict the fatigue strength. Details of these predictions, and how they compare with the experimental results are described below under the headings for each material grade.

6.2 Grade 17 Grey Cast Iron

In total, seven different geometries relating to grade 17 grey iron have been examined:

1. BRITE Notch 1: HCF test specimen with a circumferential U-shaped notch ($K_t=2.2$)
2. BRITE Notch 2: HCF test specimen with a circumferential V-notch ($K_t=5.6$)
3. BRITE Simulated Component: Circumferential 'shoulder fillets' ($K_t=3.8$)
4. BRITE Three-point bend specimen with a U-shaped notch ($K_t=2.4$)
5. BRITE Three-point bend specimen with a V-notch ($K_t=6.3$)
6. Engine bedplate with a 12 thou fillet
7. Engine bedplate with a 1/8th in. fillet

The first two of these have been analysed using the finite element method in both the uncracked state, and with explicit modelling of 2-D and 3-D cracks at the notch roots.

This grade of iron has a graphite flake size of approximately 0.12mm (Jianchun, 1993). The UTS of the material exhibits a high degree of scatter (see figure 3.16 and 3.17). A typical value of 230MPa has been used in the calculations. The long crack threshold has been measured using compact tension specimens at various R-ratios (figure 3.19). Assuming a linear function of R-ratio, a least squares fit to the data gives the following expression:

$$\Delta K_{th} = 12.32(1 - 0.78R) \quad (6.1)$$

The plain specimen fatigue limit at zero mean stress has been assumed to be 70MPa. This corresponds to 0.32*UTS (BCIRA guide). The fatigue strength was assumed to vary linearly with mean stress according to the Goodman model:

$$\Delta \sigma_{fl} = \Delta \sigma_0 \left(1 - \frac{\sigma_m}{UTS}\right) \quad (6.2)$$

Evidence from the plain specimen fatigue test results at various mean stresses indicates that the actual dependence on mean stress may follow a nonlinear curve. However, this was not sufficiently well defined in this grade to allow this to be modelled with any confidence.

6.2.1 BRITE Notch 1 ($K_t=2.2$)

Predictions of the fatigue strength in terms of net section nominal stresses are presented in figure 6.1 on the basis of three approaches described below. In figure 6.1 and subsequent figures the notation DK and DK_{th} has been used. These are the same as ΔK and ΔK_{th} .

6.2.1.1 *Semi-circular surface crack*

A surface crack of 0.12mm depth is assumed to grow from the notch root to twice its size. The highest applied loads were determined such that the applied ΔK at the crack's deepest point does not exceed the ΔK_{th} value at this crack size. The effects of localised plasticity at the notch root on the local R-ratio at the crack tip were estimated using the multiaxial Neuber calculation described earlier. Under conditions where the local R-ratio is negative, crack closure and opening has been

assumed to occur at $K=0$. The deepest point K values have been estimated from the uncracked body elastic stresses using the procedure described in section 5.

The predicted fatigue strength exhibits a rapid decrease with increasing mean stress at low mean stress values due to the crack closure assumption. The predictions are generally conservative over the range of mean stresses, apart from when the mean stress is zero. At high mean stresses, the predictions are significantly lower than the observed fatigue strength.

6.2.1.2 Continuous surface crack

This model is intended to represent crack geometry and behaviour at what can be considered to be the opposite end of the spectrum, thereby giving some indication of the probable sensitivity to crack modelling assumptions. K values were determined from axisymmetric FE analyses of the specimen containing a range of explicitly modelled cracks. Calculations were linear elastic, and no account was taken of either residual stresses caused by initial plasticity, or crack closure at R-ratios less than zero. The fatigue strength was taken as the applied load which would just cause the ΔK due to the applied load to intersect the value of ΔK_{th} at any crack length greater than the flake size. Figure 6.2 shows an example relating to $R=0$.

Due to the limited extent of the 2-D K solutions, the K solution from Rooke and Cartwright (Ref. 1976) for a circumferential crack with a depth equal to the sum of the notch depth and the actual crack depth, was required to estimate the intersection point with the ΔK_{th} curve. The K solution given by Rooke and Cartwright is in terms of a gross section nominal stress. This was converted to the net section nominal stress by factoring it by the ratio of gross to net cross-sectional areas, where the net section area is over the minimum diameter of the uncracked notched body. All specimen test results are quoted in terms of net section stress for the uncracked geometry. For low to moderate mean stresses, the predictions lie close to the probable fatigue limit values, when these are based on the position midway between the lowest failure and highest run-out. At high mean stresses, the prediction is significantly lower.

6.2.1.3 Surface stress

For comparison, the fatigue strength was also estimated on the basis of the applied load level which will just cause the value of $K_t \Delta S_{nom}/2$ to exceed the plain fatigue limit at a mean stress equal the mean nominal stress.

At moderate to high mean stresses, the strength is predicted reasonably well. But at low mean stresses it is significantly underpredicted ($\approx 50\%$).

6.2.2 BRITE Notch 2 ($K_t=5.6$)

As with Notch 1, three different approaches were used to predict the fatigue strength in terms of net section nominal stresses. The results are compared with the test data points in figure 6.3.

6.2.2.1 Semi-circular surface crack

Calculations to model the behaviour were carried out in a similar manner to those for Notch 1. The results for this notch show a similar pattern; at high mean stresses, the strength is underpredicted, but at zero mean stress the agreement is good.

6.2.2.2 Continuous surface crack

Crack tip K values were based on axisymmetric FE crack analysis results. Relatively good agreement is obtained with the test results. However, at moderate mean stress levels, no run-outs are available in the test data which makes it difficult to estimate the actual fatigue strength. Figure 6.4 illustrates the fatigue threshold condition at $R=0$. The high surface stresses generate high ΔK values at small crack sizes. The critical crack depth is approximately 1.5mm.

6.2.2.3 Surface stress

Calculated as for Notch 1, these significantly underpredict the strength over most of the range of mean stresses.

6.2.3 BRITE Simulated Component ($K_t=3.8$)

With this geometry, all the predictions were carried out based upon the results of elastic axisymmetric F.E. stress analyses of the uncracked body. Figure 6.5 shows a comparison of the predicted fatigue strength and specimen test results. The units for each axis are kiloNewtons.

6.2.3.1 *Semi-circular surface crack*

The predicted strength is underpredicted over the range of mean stresses. At $R = -1$, the strength of 7 kN is underpredicted by 20%. At $R = 0.1$, it is underpredicted by 27%, at $R = 0.5$ it is 16% and at $R = 0.7$ it is 28%.

6.2.3.2 *Continuous surface crack*

In the absence of axisymmetric crack tip K solutions from FE, the K values for these predictions were estimated from the uncracked body stresses in a similar manner to that used for the semi-circular surface crack. The results presented in section 5 indicated that over a certain range of crack sizes, the ratio of the K solutions (semi-circular crack/continuous crack) was approximately 0.58. The 2-D K solutions were therefore estimated using this model for crack sizes up to 2.546mm. The points of intersection with the ΔK_{th} curve at various R-ratios are shown in figure 6.6. The maximum depth for nonpropagation is in the region of 2.2mm. The predicted fatigue strengths agree quite well with the test results:

R = -1	+9.7%
R = 0.1	+2.8%
R = 0.5	+11.4%
R = 0.7	- 0.5%

6.2.3.3 *Surface stress*

Strength is underpredicted over the entire range of mean loads. The largest discrepancy between these predictions and the other results is at low mean stress levels.

6.2.4 BRITE Three-Point Bend Specimen ($K_t=2.4$)

Predictions for this geometry were made on the basis of two-dimensional finite element based crack analyses for a range of crack sizes. Only the continuous surface crack geometry was considered. Figure 6.7 shows a comparison of predicted fatigue strength with test results at different mean stress levels. The load levels in this small batch of specimens were not low enough to produce any run-out tests results. All the failure points lie well above the predicted fatigue curve. Figure 6.8 indicates that the largest non-propagating cracks would be expected to have a depth of approximately 3 to 4 mm depending on the R-ratio. This is significantly longer than for the axial test geometries.

6.2.5 BRITE Three-Point Bend Specimen ($K_t=6.3$)

Similar predictions were made for the V-notched three-point bend specimen. Again, finite element crack analyses were carried out for continuous surface cracks. The results are shown in figures 6.9 and 6.10. The two run-out specimens in this small batch were obtained at high R-ratio load levels, beyond the extent of the predicted results. However, inspection of figure 6.9 indicates that they lie just above the probable position of the curve if it was extrapolated. Predicted maximum non-propagating crack lengths lie in the range of 3 to 4 mm.

6.2.6 Engine Bedplate with 12 thou Fillet

The prediction results shown in figures 6.11 and 6.12 relate to an engine bedplate with a relatively sharp corner fillet of radius 0.012 in. There are two engine types referenced in the figure, both have the same geometry and assembly loads. The Seacat engine has a higher rating than the RKC engine, however. This translates to higher firing pressures and therefore higher alternating stresses. No cracking is observed in the RKC engine, but 50% of Seacat engines have cracked.

The method used to calculate the stresses in the region of the fillet was to use a submodel locally with displacement boundary conditions taken from the global model. All the predictions were based on the uncracked body stresses from these analyses in a similar manner to the procedure used above for the BRITE

Component. The stresses given on the axes of figure 6.11 are the stresses at the surface in the fillet.

6.2.6.1 *Semi-circular surface crack*

These predictions lie significantly below the points which represent actual engine results. The greatest discrepancy is at the high mean stress end where the engine points lie.

6.2.6.2 *Continuous surface crack*

The predictions obtained by estimating the highest load which will just lead to the ΔK_{th} curve being cut lie just below the 'run-out' points for the RKC engine. Figure 6.12 illustrates the ΔK versus crack length curve for each R-ratio considered.

These highlight the fact that the predicted stress distribution across the section is continually decreasing. This has a significant influence on the predicted ΔK values at the longer crack lengths. The curves suggest that the crack analyses need to be continued to longer crack lengths. Comparison of figure 6.12 with figure 6.4 illustrates this difference for fillets of similar root radius.

6.2.6.3 *Surface stress*

The predictions given in figure 6.11 represent the condition at which the local elastic stresses at the surface exceed the fatigue limit. Consequently, for this sharp notch, a very low strength is predicted.

6.2.7 Engine Bedplate with 1/8th in. Fillet

This case represents the same operating conditions as the Seacat engine described above, except that the fillet radius is 1/8th in. This engine has experienced a failure rate of 65%. The predictions are illustrated in figure 6.13 alongside the engine operating condition.

6.2.7.1 *Semi-circular surface crack*

The predicted fatigue strength is approximately half the current operating load level.

6.2.7.2 *Continuous surface crack*

Figure 6.14 shows the curves of ΔK versus crack length, and the intersection points with the ΔK_{th} curves. The effect of the continuous stress gradient can be seen as a decrease in ΔK with increasing crack length. Comparison with the engine point in figure 6.13 indicates that failure is predicted for this engine operating condition, and the reserve factor is lower than for the 12 thou fillet design, therefore failure is predicted to be more likely for the 1/8th in. fillet.

6.2.7.3 *Surface stress*

This approach again gives the lowest predicted strength. Comparison with figure 6.1, the results for BRITE Notch 1 which has the same fillet radius, shows that there are differences in the relative positions of the curves representing the different predictions. In the case of the surface stress predictions, the results for the engine bedplate are simply the fatigue strength values at the local mean stress levels. The surface stress predictions for Notch 1 are defined as the the fatigue strength at the *nominal* mean stress, divided by the K_t factor, which in Notch 1 is straightforward to define. The relatively high prediction for the 2-D continuous surface crack is a consequence of the stress gradient across the section.

6.3 **Grade 250 Grey Cast Iron**

As described in section 2, the tests carried out with grade 250 grey cast iron covered nine different notched test specimen geometries, each with a circumferential groove. Three cast section sizes were used. The tensile test data shows that material properties for different cast section sizes can vary significantly. The geometries are listed in table 6.1.

Cast section dia. (mm)	K_t	Notch shape	Root radius (mm)	Notch depth (mm)	Net section dia. (mm)
50	1.5	Shallow circular	6.4	2	16
50	2.5	V-notch	1.42	2	16
50	5.0	V-notch.	0.265	2	16
30	1.5	Shallow circular	3.7	1.5	9
30	2.5	V-notch	0.86	1.5	9
30	5.0	V-notch	0.163	1.5	9
10	1.5	Shallow circular	2.15	0.9	5.2
10	2.5	V-notch	0.5	0.9	5.2
10	5.0	V-notch	0.1	0.9	5.2

Table 6.1 Summary of specimen geometries used in testing of grade 250 grey cast iron

Flake sizes for this grade of cast iron have been estimated (Murrell, 1995). For the 50mm cast section size it is 0.12 - 0.18mm. For the 30mm cast section it is 0.06 - 0.07mm, and for the 10mm cast section size test bars it is 0.02 - 0.03mm. For the purpose of the predictions, flake sizes of 0.15mm, 0.065mm and 0.025mm respectively were assumed. The following model was used to describe the long crack growth threshold. This is a fit to compact tension test specimen results at various R-ratios (Bullough, 1995):

$$\Delta K_{th} = 11.0(1 - R)^{0.5} \quad (6.3)$$

Tensile strength values assumed were 232.1MPa, 268.1MPa and 379.9 MPa for section sizes 50, 30 and 10mm respectively. These values are typical, based on the results of tensile tests carried out on this material (Bullough, 1995). The tensile strength values are used to calculate the fatigue strength values from the curve fits to the data which are normalised with respect to the mean tensile strength values for the cast section size of each grade. The fatigue strength, and the effect

of R-ratio is illustrated in figure 6.15, and represents a fit to the plain specimen data (Bullough, 1995).

The apparent short crack threshold is plotted in figure 6.16 for the three cast section sizes using equations 5.44 to 5.46. This is a modified form of the El-Haddad model.

6.3.1 Description of the Analysis Method

For each geometry, predictions of the fatigue strength were made using three different approaches. In the light of the results obtained from the predictions of the grade 17 grey iron specimens, only the continuous surface crack model was used for making short crack based predictions.

6.3.1.1 Continuous Surface Crack

A continuous surface crack was assumed to exist along the notch root with a size initially equal to the typical graphite flake size. The fatigue strength was taken as the applied load which would just cause the ΔK due to the applied load to intersect the value of ΔK_{th} at any crack length greater than the flake size. K values were determined from axisymmetric FE analyses of the specimen containing a range of explicitly modelled cracks. To be consistent with the predictions for grade 17 grey iron, calculations were linear elastic, and no account was taken of either residual stresses caused by initial plasticity, or crack closure at R-ratios less than zero. Section 6.2 provides a comparison of the models.

In some cases, particularly with the 10mm cast section size, the 2-D FE based K solutions had not been generated at crack sizes as small as the flake size. This caused a problem with the blunt notch geometries because the intersection point with the ΔK_{th} curve was found to be at the smallest crack sizes. For the predictions therefore, the smallest crack size for which a K solution existed was taken as the intersection point. This leads to a slight underprediction of the fatigue strength.

6.3.1.2 Surface Stress

As for the Grade 17 cast iron, the fatigue strength was also estimated as the applied load level which will just cause the value of $K_t \cdot \Delta S_{nom}/2$ to exceed the plain fatigue limit at a mean stress equal to the mean nominal stress.

6.3.1.3 Notch-as-Crack

In section 2, the fracture mechanics based approach to notch analysis was described in which the notch is considered to be a crack of the same size. The fatigue strength of the notched specimen is therefore the load which just causes the applied ΔK value to equal the crack growth threshold value. In this work, as in Smith and Miller (1977), the threshold value is taken as the conventional long crack threshold value. The fatigue strength for the three different cast section sizes is given in terms of the net section nominal strengths by the following formulae:

10mm cast section size:

$$\frac{\Delta S}{2} = \frac{11 \cdot (1 - R)^{0.5}}{1.24 \cdot \sqrt{0.9} \cdot \pi} \left(\frac{3.5}{2.6} \right)^2 \cdot 0.5 \quad (6.4)$$

30mm cast section size:

$$\frac{\Delta S}{2} = \frac{11 \cdot (1 - R)^{0.5}}{1.22 \cdot \sqrt{1.5} \cdot \pi} \left(\frac{6.0}{4.5} \right)^2 \cdot 0.5 \quad (6.5)$$

50mm cast section size:

$$\frac{\Delta S}{2} = \frac{11 \cdot (1 - R)^{0.5}}{1.175 \cdot \sqrt{2.0} \cdot \pi} \left(\frac{10.0}{8.0} \right)^2 \cdot 0.5 \quad (6.6)$$

6.3.2 Description of the Results

The results are illustrated in figures 6.17 to 6.34. For each geometry, two diagrams are presented. Firstly a Goodman diagram with axes representing alternating nominal stress and mean nominal stress, and secondly, a diagram illustrating the change of ΔK and ΔK_{th} with crack depth for a continuous surface crack.

In the Goodman diagrams, the line denoting the 'fit to test data: typical' represents a fit of the equation:

$$\sigma^*_{NFL} = C(1 - R)^m K_t (K_t - a)^b + d \quad (6.7)$$

where σ^*_{NFL} is the normalised fatigue limit (with respect to tensile strength), R is the R-ratio, K_t is the stress concentration factor, and C, m, a, b and d are fitting coefficients (Bullough 1995). For the data fitting, the data was grouped into 10mm cast section results, and 30 - 50mm cast section results.

With the 10mm cast section size (figures 6.17 to 6.22), the predictions based on the 2-D continuous surface crack model give good agreement for the two sharper notches. The blunt notch specimen ($K_t=1.5$) strength is under predicted. The mean errors between the 2-D crack prediction and the estimated fatigue limit (mean value of highest run-out and lowest failure) are given below for the three notches:

K_t	Error relative to test results (%)		
	10mm section	30mm section	50mm section
1.5	-16.6	-18.1	-11.0
2.5	-1.8	-23.4	-5.7
5.0	-0.7	-18.0	-11.1

Table 6.2 Mean error values for 2-D crack predictions relative to measured values for 10, 30 and 50mm cast section grade 250 grey iron

The 30mm cast section size results are underpredicted by the 2-D crack model. The size of the error is variable, and appears to be greatest with the intermediate K_t notch ($K_t=2.5$).

The 2-D crack prediction for the 50mm cast section size specimens are underpredicted by varying degrees. The smallest errors occurring at the highest R-ratios.

The overall mean error in the 2-D crack predictions is -11.8%. The overall error relative to the data fit curve is -14.4%.

The 'Notch-as-crack' approach and the surface stress based predictions significantly over and underestimated respectively the fatigue strength in most cases.

6.4 Grade 350 Grey Cast Iron

Tests were carried out on one cast section size (30mm) and two notch geometries:

Cast section dia. (mm)	K_t	Notch shape	Root radius (mm)	Notch depth (mm)	Net section dia. (mm)
30	1.5	Shallow circular	3.7	1.5	9
30	5.0	V-notch	0.163	1.5	9

Table 6.3 Summary of specimen geometries used in testing of grade 350 grey cast iron

The graphite flake size of this grade of iron has been estimated to be 60-70 μ m (Murrell, 1995). The mean tensile strength, based on an analysis of tensile test results (Bullough, 1995) is 377.4 MPa. The maximum and minimum values in the range are 411 and 348 MPa, i.e. approximately $\pm 9\%$.

The long crack threshold is assumed to be the same as grade 250, which itself is based on pooled data for both grades. The fatigue strength over the range of R-ratios is illustrated in figure 6.35. This curve is based on a fit to the plain specimen data (Bullough, 1995). The apparent short crack threshold is illustrated in figure 6.36 over the range of crack sizes for two R-ratios.

6.4.1 Description of the Analysis Method

The same analysis method as used for grade 250 was employed for grade 350, and have been described earlier. i.e. the three approaches are:

- Continuous surface crack
- Surface stress
- Notch-as-crack

6.4.2 Description of the Results

The results are shown in figures 6.37 to 6.40. As before, the 2-D continuous surface crack model gives the best correlation with the test results. The overall error for grade 350 iron is -11.8%. The mean error values are as follows:

K_t	Error relative to test results (%)
1.5	-19.9
2.5	-
5.0	-3.6

Table 6.4 Mean error values for 2-D crack predictions relative to measured values for 30mm cast section grade 350 grey iron

6.5 Grade 400 Spheroidal Graphite Cast Iron

Nine different notched test specimen geometries, each with a circumferential groove were tested. The dimensions used are the same as for the grey iron test specimens:

Cast section dia. (mm)	K_t	Notch shape	Root radius (mm)	Notch depth (mm)	Net section dia. (mm)
50	1.5	Shallow circular	6.4	2	16
50	2.5	V-notch	1.42	2	16
50	5.0	V-notch	0.265	2	16
30	1.5	Shallow circular	3.7	1.5	9
30	2.5	V-notch	0.86	1.5	9
30	5.0	V-notch	0.163	1.5	9
10	1.5	Shallow circular	2.15	0.9	5.2
10	2.5	V-notch	0.5	0.9	5.2
10	5.0	V-notch	0.1	0.9	5.2

Table 6.5 Summary of specimen geometries used in testing of grade 400/18 SG iron

The following model was used to describe the long crack growth threshold. This is a fit to compact tension test specimen results for grade 500/7 SG iron at various R-ratios (Bullough, 1995):

$$\Delta K_{th} = 8.5(1 - R)^{0.5} \quad (6.8)$$

Tensile strength values assumed were 422.9MPa, 406.8MPa and 414.3 MPa for section sizes 50, 30 and 10mm respectively. These values are typical, based on the results of tensile tests carried out on this material (Bullough, 1995). The fatigue strength, and the effect of R-ratio is illustrated in figure 6.41, and represents a fit to the plain specimen data (Bullough, 1995). The apparent short

crack threshold is plotted in figure 6.42 for the three cast section sizes using the modified El-Haddad model described by equations 5.44 to 5.46.

6.5.1 Description of the Analysis Method

The same analysis method as used for grade 250 and 350 grey iron was employed for grade 400/18, and have been described earlier. i.e. the three approaches are:

- Continuous surface crack
- Surface stress
- Notch-as-crack

6.5.2 Description of the Results

The results are shown in figures 6.43 to 6.60. The 2-D continuous surface crack based predictions for $K_t=1.5$ geometries generally fall slightly below the surface stress based prediction. Inspection of the ΔK v. crack depth curves (figures 6.44, 6.50, 6.56) shows that the intersection point lies at the first point on the ΔK curve (i.e. the K solution for the smallest crack size analysed). Had K solutions been generated at crack sizes of the same order as the typical microstructural features (< 0.1mm) then the predicted strength would probably have been slightly higher.

Overall, the 2-D continuous surface crack predictions lie below the estimated fatigue limits from the actual data (mean of highest runout and lowest failure), the percentage difference being -26.7. The 'Notch-as-crack' predictions on the other hand lie on average above the data (+18.7%). The latter result is however, much closer to the test data than for the grey iron geometries. The mean error values for each geometry are shown in table 6.6.

K _t	Error relative to test results (%) 2-D continuous surface crack			Error relative to test results (%) 'Notch-as-crack' predictions		
	Cast section size			Cast section size		
	10mm	30mm	50mm	10mm	30mm	50mm
1.5	-28.5	-36.9	-32.1	-0.9	-14.4	-25.6
2.5	-15.0	-40.1	-33.5	+55.9	+8.4	+1.6
5.0	-3.9	-26.3	-24.3	+81.9	+36.1	+25.7

Table 6.6 Mean error values for each specimen geometry for two different prediction methods

The greatest variability is exhibited by the 'Notch-as-crack' predictions with extremes of -25.6% to +81.9%.

6.6 Grade 500 Spheroidal Graphite Cast Iron

Test were carried out on one cast section size (30mm) and two notch geometries:

Cast section dia. (mm)	K _t	Notch shape	Root radius (mm)	Notch depth (mm)	Net section dia. (mm)
30	1.5	Shallow circular	3.7	1.5	9
30	5.0	V-notch	0.163	1.5	9

Table 6.7 Summary of specimen geometries used in testing of grade 500/7 SG cast iron

The typical tensile strength for this grade is 522.7MPa, with maximum and minimum values in the ranges of 584MPa and 491 MPa (Bullough, 1995). The fatigue strength, and the effect of R-ratio is illustrated in figure 6.61, and represents a fit to the data (Bullough, 1995). The long crack threshold is described by equation 6.8. The predicted apparent short crack threshold is illustrated for two R-ratios in figure 6.62.

6.6.1 Description of the Analysis Method

The same analysis method as used for grade 400/18 iron was employed for grade 500/7, and have been described earlier. i.e. the three approaches are:

- Continuous surface crack
- Surface stress
- Notch-as-crack

6.6.2 Description of the Results

The results are shown in figures 6.63 to 6.66. The 2-D continuous surface crack predictions again underestimate the fatigue strength. The overall error is -30.8% which is larger than for grade 400. The 'Notch-as-crack' approach gives a low overall error (-3.3%). However, as table 6.8 shows, the spread in the mean error values for each geometry is large.

K_t	Error relative to test results (%)	Error relative to test results (%)
	2-D continuous surface crack	'Notch-as-crack' predictions
1.5	-31.6	-23.6
5.0	-29.9	+17.1

Table 6.8 Mean error values for each specimen geometry for two different prediction methods

6.7 Discussion

Several different prediction methods have been considered. Of these, the 'Notch-as-crack' approach is the one which is not sensitive to the local stress distribution around the notch root. Consequently, it gives the same results for all three specimen K_t values. Table 6.6 illustrates this. The test results for all three cast section sizes exhibit a systematic decrease in strength with increasing K_t value. The 'Notch-as-crack' predictions alone do not reflect this, as shown by the change in error from negative to positive.

The 2-D continuous surface crack predictions give a less variable percentage error for the different geometries, and the overall error is negative for every geometry considered in the materials: grade 250, 350, 400 and 500. Overall, these predictions gave smaller errors for the grey iron than for the SG iron.

The 'Notch-as-crack' predictions for the grey irons (250 and 350) were widely in error; the predicted strengths generally lying well above the test data points. Similar problems were encountered by Taylor (1996) in the application of a development of the 'Notch-as-crack' approach to grey iron test specimens.

Comparisons between the prediction methods used on grade 17 grey iron specimens indicates that the 2-D continuous surface crack predictions are in the best agreement with the test data. The more complex semi-circular surface crack model can significantly underpredict the strength. This is highlighted in the case of the engine bedplate predictions where the gradient stress field through the section appears to be responsible for the high fatigue strength predicted by the 2-D continuous surface crack predictions, which agrees quite well with the service experience accumulated with the engine.

In the light of these results, it is relevant to consider what observations can be made of the test specimens, in particular, the run-out specimens (those which have not failed after 10^7 cycles). In total, fourteen run-out specimens were examined using dye penetrant and optical microscopy to try and determine whether any notch root cracks are present, and if so, what form they take. Of these specimens, only one was found to contain a crack, specimen number MT4419. The specimens examined are listed in table 6.9, together with the testing conditions. Specimen MT4419 is observed to have one of the lowest fatigue strength reserve factors, defined as:

$$R.F. = \frac{\textit{Experimentally observed fatigue limit}}{\textit{Applied stress level}} \quad (6.9)$$

The quantities given in the numerator and denominator are both measured from the origin of the Goodman diagram.

Specimen n	Grade	Type	Cast section dia. (mm)	K _t	R-ratio	$\Delta\sigma/2$ (MPa)	Reserve factor	
							Experimental	2-D crack prediction
MT2793	250	Flake	30	5	0.1	40	1.205	0.855
MT2815	250	Flake	30	5	-1	70	0.926	0.794
MT2781	250	Flake	30	2.5	-1	80	1.026	0.692
MT2746	250	Flake	30	1.5	-1	70	1	0.855
MT2757	250	Flake	30	1.5	0.1	50	1.067	0.752
MT2816	250	Flake	30	5	0.5	27.5	1.047	0.945
MT4487	400/18	SG	10	1.5	0.5	70	1.176	0.782
MT4488	400/18	SG	10	1.5	0.5	80	1.036	0.689
MT4480	400/18	SG	10	1.5	0.1	110	1.089	0.715
MT4369	400/18	SG	10	2.5	-1	110	0.979	0.867
MT4396	400/18	SG	10	2.5	0.5	55	1	0.77
MT4420	400/18	SG	10	5	0.5	45	1.056	0.922
MT4402	400/18	SG	10	5	-1	95	0.976	0.976
MT4419	400/18	SG	10	5	0.5	50	0.95	0.837

Table 6.9 BCIRA Programme: Notched fatigue specimens - Run-outs inspected using Dye penetrant

The form of the crack is illustrated in the scanning electron micrographs of figures 6.67 to 6.68. Figure 6.69 shows details of machining marks. The crack is continuous around a large part of the circumference, and is held open at around 20 to 25 μ m. The 2-D crack predictions indicate that the maximum length of a non-propagating crack will be approximately 200 to 300 μ m (see figure 6.48). The specimen was sectioned to determine the actual crack depth. Figure 6.70 shows a photograph of the crack. The depth was found to be between 2 and 3mm. This corresponds to approximately half the section diameter. Had the test been continued, then it is quite likely that failure would have occurred relatively quickly.

Other specimens examined in the scanning electron microscope were MT4420, MT2816, MT2815 and MT2793. Specimen MT2815 has the lowest strength reserve factor of this set. No continuous surface cracks were observed in these specimens. In the grey iron specimens, the locations of the graphite flakes were observed. Whether these had actually cracked could not be determined. The appearance was found to be similar to the appearance of the plain surface of the

specimen on the outside diameter, i.e. discontinuous flakes/cracks. No evidence of linking between the flakes/cracks could be found. Figures 6.71 and 6.72 illustrate the typical features observed in the grey iron, in this case, from specimen MT2816.

Another grey iron run-out specimen was also examined. Specimen MT3275, which is one of the BRITE project simulated components of grade 17 grey iron, was tested at an R-ratio of 0.5 with a load of 9.33 ± 3.11 kN. The test was stopped after 4.11×10^7 cycles. This result gave the highest run-out at this R-ratio. A visual inspection by optical microscope revealed no cracks.

The specimens examined form only a small sample, and it is possible that other run-out specimens in both grey and SG iron may have contained cracks. However, the evidence from this sample indicates that no nonpropagating cracks have been formed in test conditions at or below the notched specimen fatigue limit. The one crack which was observed occurred in a specimen which was cycled just above the estimated fatigue limit, and appeared to be propagating to failure.

It is therefore difficult to draw firm conclusions about the validity of the short crack growth based predictive models, and the absence of any visible evidence of cracks casts some doubt over this mechanism. However, the relative success of the 2-D crack predictions for the grey iron, and the fact that no continuous cracks have been observed in any of the grey iron specimens examined, highlight the possibility that rather than a discrete crack forming, a small region around the notch root may weaken by a similar mechanism to the progressive weakening observed in grey iron under high cyclic strains, as described in section 3. The overall effect may be similar to the behaviour of a short continuous surface crack at the notch root, but with no obvious visual indication of a crack, apart from the graphite flakes.

A small region close to the notch root which loses its load carrying capacity may therefore behave in a similar way to a crack of similar size. This may explain the relative success of the 2-D crack approach in grey iron. It would also explain why

the model based on the semi-circular surface crack gives such pessimistic predictions, because the damage zone may engulf the region in which the small crack surface cracks were considered to exist.

In SG iron and other higher strength materials on the other hand, microstructural features generally exist on a much smaller scale, and the value of a_0 (see the Kitagawa diagram in figure 2.8) is much smaller than for grey cast iron. The 'Notch-as-crack' approach is therefore more likely to be appropriate, particularly for the sharper notch geometries. To investigate this further, the aluminium alloy notched test specimens described by Frost (1955a, 1955b) have been analysed.

Axisymmetric finite element based crack analyses were carried out on the specimen geometry, considering a range of crack sizes from 0.0135mm to 0.778mm. This simulated the presence of a continuous surface crack along the notch root. The apparent short crack threshold was estimated in a similar way to that described earlier. The plain specimen fatigue limit was obtained from Frost's paper at $R = -1$, with a value of ± 150 MPa. A threshold value for BS L65 aluminium alloy is given in the paper by Abdel-Raouf et al (1992), $\Delta K_{th} = 4.2$ MPa \sqrt{m} . The predicted short crack threshold condition for the V-notched specimen ($K_t = 18$) is ± 39.0 MPa, with a maximum nonpropagating crack size of 0.35mm (figure 6.73 and 6.74). This compares with the estimated fatigue limit from the notched fatigue tests of ± 42.5 MPa (i.e. 8.2% difference). Note that since the loading ratio in all these tests was $R = -1$, it was assumed that the crack would only be open over half the load cycle; this will be discussed later. The 'Notch-as-Crack' approach gives a predicted fatigue strength of ± 47.4 MPa (i.e. 11.5% above the estimated fatigue limit from test).

The nonpropagating crack lengths at different alternating stress levels have also been predicted by determining the intersection point of the curve defining applied ΔK versus crack length with the curve which describes the apparent crack growth threshold. The results are plotted in two different forms in figures 6.75 and 6.76. Figure 6.75 shows that the nonpropagating crack lengths are generally underpredicted at lower stress levels. Figure 6.76 allows a direct comparison with

the predictions made by Abdel-Raouf et al (1992) which were based on a model which describes the increase in crack opening level with crack length. The latter predictions overestimate the nonpropagating crack length at all stress levels.

In table 6.10, the a_0 values for all the materials considered in this section are presented. Also given are the predicted maximum nonpropagating crack lengths obtained using the short crack threshold model.

	K_t	Material					
		Grade 17 grey	Grade 250 grey	Grade 350 grey	Grade 400 SG	Grade 500 SG	BS L65 Al alloy
a_0 (mm)		3.24	2.89	1.48	0.42	0.27	0.05
	2.2	1.7					
	5.6	1.6					
	3.8	2.2					
	2.4	≈4					
	6.3	4					
Seacat	12 thou	1.9					
Seacat	1/8th	2.1					
	1.5		≤ 0.4	≤ 0.1	≤ 0.1	≤ 0.1	
	2.5		0.6				
	5		0.6	0.5	0.45	0.4	
V-notch, R=-1	18						0.35

Table 6.10 Comparison of a_0 values and predicted maximum nonpropagating crack lengths (mm)

It is apparent from this data that all the maximum nonpropagating crack lengths for grey iron lie well below the a_0 value. For SG iron they are a similar size, and for the aluminium alloy it is well above a_0 (figure 6.77). Therefore, in the case of the aluminium, the combination of lower a_0 value and short crack length relative to the depth of the notch, means that a good approximation to the short crack prediction would be obtained from the 'Notch-as-Crack' approach in which the notch depth is taken as the equivalent crack depth for comparison with the long crack threshold. The actual crack length can then be neglected as it makes only a very small

contribution to the equivalent crack length. Including the actual crack length in the equivalent crack length reduces the differences between the different methods even further by bringing the 'Notch-as-Crack' prediction down to ± 45.12 MPa.

The specimens tested by Frost on aluminium alloy were cycled at an R-ratio of -1. The predictions described above were based on the assumption that the crack is only open when the applied stress in the cycle exceeds zero. This behaviour would be expected in a long fatigue crack, and in the light of the data in table 6.10, would appear to be a reasonable assumption in this case.

For materials and testing conditions in which the crack is close to, or less than a_0 , then behaviour characteristic of that observed for 'short cracks' would be expected. This is generally attributed to a reduction in crack closure for short cracks (see section 4). For the two-dimensional short crack based predictions of figures 6.1 to 6.66 (i.e. continuous surface cracks), any effects of crack closure were neglected, partly because the majority of tests were carried out at R-ratios greater than zero, and partly because of reduced closure observed for short cracks in other materials. The success of the 2-D predictions, even at $R=-1$ tends to support this. It is interesting to note the results for the aluminium alloy in figure 6.75 which shows that at stress levels below the notched specimen fatigue limit, the nonpropagating cracks lengths are underestimated by the short crack prediction procedure. If ΔK were effective over a larger portion of the loading cycle (i.e. minimum K value less than zero), then the predicted nonpropagating crack lengths would be larger.

Another aspect to consider with the short crack based predictions is the effect of the model used to represent the apparent short crack threshold. Section 5.5 describes the modified El Haddad model which has been used. In section 2.4.1 where the methods to describe the effects of geometrically small stress concentrations are described, the approach presented by Smith and Miller (1978) is described (see equations 5.47 and 5.48). This model would be expected to define an upper bound for small cracks in plain specimens. Figure 3.49 and 3.50 would appear to support this, however, the test data required to fully justify this is lacking from this data set.

To investigate the effect of using Smith's model (equations 5.47 and 5.48) for apparent short crack threshold on the 2-D short crack based notch fatigue strength predictions, another set of predictions were made for the BCIRA notch specimen geometries in grades 250 and 350 grey iron, and grades 400/18 and 500/7 SG iron. The results are presented in figures 6.78 to 6.125. The predicted fatigue strengths are higher than the earlier predictions made using the El Haddad model, as would be expected.

The prediction results can be compared with the test data in two ways:

- a) By comparison with a curve defined by equation 6.7 where the constants have been determined by Bullough (1995) by fitting to the test data points.
- b) By comparison with the local fatigue strength estimate at a given R-ratio, section size, notch geometry and grade. The estimate is based in the mean of the highest run-out datapoint and the lowest failure datapoint at the given conditions.

The short crack based strength predictions (with Smith's threshold model) normalised with respect to the curve fit (equation 3.3) are shown in figures 6.126 to 6.129. To give some indication of sensitivity of the short crack based predictions, figures 6.130 to 6.132 show the normalised predictions for grade 400/18 SG iron with 30mm cast section presented in the form of a band. The lower edge of the band represents the predictions made using the curve defining the minimum plain specimen fatigue limit, and minimum long crack threshold value (-3σ). The upper edge represents the corresponding maximum ($+3\sigma$). The error band lies generally in the range of 10 to 15%.

Figures 6.133 to 6.136 show the short crack based strength predictions using Smith's threshold model normalised with respect to the local fatigue limit estimate.

Figures 6.137 to 6.140 and figures 6.141 to 6.144 show the short crack based strength predictions using El Haddad's threshold model normalised with respect to the curve fit (equation 3.3) and the local fatigue limit estimate respectively. These relate to the detailed results in figures 6.17 to 6.66.

The predictions based on the El Haddad model for threshold generally under-predict the strength. This can be a significant under-prediction for SG iron (figure 6.143). Whereas for the predictions based on Smith's model for threshold generally straddle the fatigue strength determined from test results (figures 6.133 to 6.136). Compared with the predicted error bands of figures 6.130 to 6.132, the predictions are still too highly scattered. The measured strengths for the 10mm cast section in particular show the greatest deviation.

Systematic variations in the predictions are observed. The normalised prediction results for the 10mm cast section are generally higher than the others. The normalised prediction decreases with increasing R-ratio. The prediction also increases with K_t value. However, when the predictions are normalised with respect to the estimated local fatigue limit, some of these systematic variations disappear. The effect of cast section size is one effect which is still apparent in the predictions normalised with respect to local estimated fatigue limit, and should be investigated further.

7. CONCLUSIONS

1. Many methods have been proposed over the past 50 years for the fatigue assessment of bodies containing notches. The traditional approach involving the use of a Nominal Stress and Stress Concentration Factor K_t and/or Notch Factor K_f are not appropriate for use in conjunction with finite element based design assessments of complex components. A Nominal Stress that corresponds to that in a simple notch test specimen can be very difficult to define. Furthermore, the prior knowledge of the value of the Notch Factor K_f for the material under the given loading conditions is required.
2. The assessment of the fatigue strength of a notched body may alternatively be based on the predicted stress-strain behaviour at the notch root surface and an assumption that the strength in fatigue will be equivalent to that of a plain specimen under similar loading conditions. For severe stress concentrations there will be uncertainty about the appropriate material model used to describe the material stress-strain behaviour. In the present work it was shown that predictions can often give local peak stresses and strains well in excess of the tensile strength measured in standard tensile test pieces. This raises doubts about the predicted local stresses and strains at the surface, and the use of a macroscopically determined stress-strain curve.
3. The zone of high stress local to a stress concentration can extend to a similar distance as the typical microstructural length scale. This is particularly true of grey cast iron. This can cast further doubt on the validity of material stress-strain data determined from plain specimen test data.
4. Predictions of fatigue strength of notched test specimens of grade 17 grey cast iron based on estimates of local surface stresses and plain specimen fatigue data did not correlate with the observed behaviour of the notched specimens. The fatigue strength was underestimated for both $K_t = 2.1$ and $K_t = 5.6$.

5. The observed difference in fatigue lives between axial and bending specimens subjected to apparently identical nominal stresses cannot be explained on the basis of local surface stresses; the elastic stress distributions close to the notch root are almost identical.
6. A Fracture mechanics based approach to the prediction of fatigue strength of notched bodies in which the notch is assumed to be equivalent to a crack of the same depth suffers from the restriction that the geometry must be such that a notch depth can be defined. In many components this is not the case, which therefore restricts its use. An alternative approach is required to predict the fatigue strength of typical engineering components.
7. Evidence in the literature has shown that fatigue damage in cast irons develops in the form of initiation and growth of microcracks early on in the life of the test specimen. Microstructural features are generally the points of initiation for microcracks.
8. The nonlinear stress-strain behaviour of grey cast iron has been reported on in the literature. This behaviour is reported to be due to a great extent on the graphite flakes. Analysis of tensile test results as part of the current work has shown that the principal variability observed in the tensile strength values is made up of two separate components: scatter in final fracture stress and scatter in stress-strain behaviour. The stress-strain curve can be described well by the Ramberg-Osgood equation.
9. Methods for modelling the behaviour of surface cracks in highly non-uniform stress fields have been investigated. The use of the deepest point K value for a semi-elliptical crack geometry was found to provide a reasonable parameter for assessing crack growth in a notch stress field. The use of K values at many points around the crack front, including the surface breaking point, to calculate growth rate results in unrealistic growth behaviour.

10. The finite element idealisation of three-dimensional curved crack front geometries should be based on 20 noded quadratic brick elements, and follow the crack front with a smooth curve.

11. Two-dimensional and three-dimensional FE based crack analyses results for two notch geometries and a range of crack depths showed that for relatively small notch root cracks, the deepest point K values for a semi-circular surface crack was approximately a fixed percentage of the value for a continuous surface crack. Furthermore, K values could be estimated to a reasonable accuracy (in comparison with other methods) from the elastic uncracked body stresses by the use of a correction factor (F_G) based simply on the ratio of stresses:

$$F_G = \frac{\text{Stress at depth corresponding to crack depth}}{\text{Stress at surface}} \quad (7.1)$$

12. The effects of yielding in the material close to the root of a notch on the behaviour of cracks have been simulated by finite element analysis. An elastic-plastic analysis of the uncracked body results in a residual stress field, which is then applied to the cracked body as an initial stress field. The residual stresses which arise have a greater effect on crack tip K values close to the surface. The magnitude of the effect depends on both load magnitude and crack depth.

13. The effects of residual stresses on crack tip K values can be estimated from a consideration of the reduction in maximum stress at the depth of the crack compared with the corresponding linear elastic stress.

14. A three-dimensional extension of the Neuber approach can provide an approximate description of the effects of material yielding during initial loading of an uncracked body, without the computing expense of full nonlinear finite element analysis. The estimated effects of initial yielding and subsequent residual stress field on K values for cracks at notch roots were compared with K values determined by full finite element simulation (elastic-plastic analysis of

the uncracked body followed by elastic cracked analysis with the residual stress field). Agreement was found to be better for the lower K_t notch geometry.

15. The Kitagawa-Takahashi diagram of threshold stress versus defect size, and the various analytical models used to describe the observed effect of small defects on fatigue strength, are applicable to simple stress fields. For the highly nonuniform stress fields around notches, these empirical models can be transformed into relationships between the apparent threshold ΔK value and defect size, if an appropriate geometry factor can be estimated for the defects at the smaller end of the scale. This provides a route by which estimated ΔK values for a notch root crack can be compared with the apparent threshold value to assess whether growth will take place.

16. Fatigue strength predictions for cast iron specimens and components containing stress concentrations have been made. Predictions based on a semi-elliptical surface crack were found to significantly under-estimate the fatigue strength in a number of cases. These predictions will be significantly affected by the assumed shape development of a crack. Experimental measurements of crack size and shape are required to justify any improvements to this model.

17. Predictions based on the assumption of a continuous surface crack which continues to grow until either (a) a threshold condition is reached, or (b) failure occurs, gave the best overall predictions of fatigue strength for all notch geometries and grades of material. Fatigue strength was generally underpredicted using the El Haddad model to represent apparent short crack threshold. When Smith's threshold model was used, the experimental results were found to lie both above and below. The error appears to vary systematically with cast section size, K_t and R-ratio.

18. A major area of uncertainty involving the use of the short crack approach concerns the allowance for crack closure at R-ratios of less than zero. For aluminium alloy tested under $R = -1$ loading, the best correlations were obtained when the crack was assumed to be open only at stress levels greater

than zero. For this material, the threshold condition was achieved at a crack depth which can be described as being in the Long Crack regime ($a > a_0$). For SG iron and grey iron, the full ΔK was assumed to apply, irrespective of the sign of the minimum stress. For SG iron, the threshold condition is predicted to be close to the a_0 value, and for grey iron it is well below the a_0 value which places the cracks in the short crack regime.

19. Although the literature contains many references to the presence of nonpropagating cracks at notch roots, only one was found in this investigation for grey and SG iron, and this appeared to be too large for a nonpropagating crack. This raises some doubts about the validity of the short crack model, but further experimental work should be carried out to do a detailed search for notch root cracks in these materials.
20. The short crack approach does account for differing geometries and stress fields between different specimens and components. Predictions based solely on surface stresses and strains cannot do this. The short crack approach which has been described can be used in conjunction with finite element analysis results, and avoids the need for the definition of a nominal stress and K_t which relates to test specimen conditions; this is a major advantage over the traditional notch assessment methods.
21. Based on the results presented in this work, a prediction model based on the continuous surface crack geometry and Smith's threshold model (equations 5.47 and 5.48) provided the best fit to the data. The material data required for this type of assessment consists of: plain fatigue strength and crack growth threshold values at relevant R-ratios and linear elastic finite element stress analysis results for the region of interest. Methods to estimate K solutions from uncracked body stresses are described in section 5, however, ideally cracked body K solutions are required when analysing cast iron components. The procedure described will provide a prediction of the fatigue strength and the estimated length of the non-propagating notch root crack.

8. References

Abdel-Raouf, H., DuQuesnay, D.L., Topper, T.H., Plumtree, A., (1992),
Notch Size Effects in Fatigue Based on Surface Strain Redistribution and Crack
Closure,
International Journal of Fatigue, Vol. 14, No. 1, 1992, pp.57-62.

Affeldt, E.E., (1994),
LCF Test Results of Notched Specimens for Disk Rim Simulation,
MTU München, Technical Note MTUM- N94EFM-0024, 15 Nov. 1994.

Affeldt, E.E., (1996),
Handout at the 19th meeting for IEPG TA31, 10th/11th Jan. 1996.
MTU München

Akiniwa, Y., Tanaka, K, Taniguchi, N, (1990),
Prediction of Propagation and Nonpropagation of Short Fatigue Cracks at Notches
Under Mean Stresses,
JSME International Journal, Series I, Vol. 33, No. 3, pp.288-296, 1990.

Ahmad, H.Y., Yates, J.R., (1994),
An Elastic-Plastic Model for Fatigue Crack Growth at Notches,
Fatigue and Fracture of Engineering Materials and Structures, Vol. 17, No. 6,
pp.-651-660,1994.

Albrecht, P., Yamada, K., (1977),
Rapid Calculation of Stress Intensity Factors,
Journal of the Structural Division, ASCE, 1977.

Al-Sened, A., (1997),
Ruston Diesels Ltd,
Private communication, December 1997.

BCIRA (1977), Broadsheet 157-1,
Stress/Strain Behaviour of Flake Graphite Cast Irons,
BCIRA, Alvechurch, Birmingham, 1977.

BSI, (1991),
Guidance on Methods for Assessing the Acceptability of Flaws in Fusion Welded
Structures,
BSI Publication Document PD6493: 1991.

Bullough, C.K., (1995),
Optimising the Fatigue Performance of Cast Iron
Assessment of Data and Preparation of Design Values,
GEC ALSTHOM Mechanical Engineering Centre,
Working paper ERC(W)C.88.1050, 1995,

Cartwright, D.P., Rooke, D.P., (1979),
Green's Functions in Fracture Mechanics,
Proc. Symp. on Fracture Mechanics - Current Status and Future Prospects,
University of Cambridge, March 1979.

Castillo, R.N., Baker, T.J., (1984),
A Fracture Mechanics Approach to Fatigue in Flaked Graphite Cast Iron,
Advances in Fracture Research, New Dehli, India, 1984, Vol. 3-Q, pp.2057-2064.

Dang Van, K., Papadopoulos, Y.V., (1987),
Multiaxial Fatigue Failure Criterion: A New Approach,
Fatigue 87, Vol. II, pp. 997-1008, 1987.

DeLorenzi, H.G., (1985),
Energy Release Rate Calculations by the Finite Element Method,
Engineering Fracture Mechanics, Vol.21, No. 1, pp.129-143, 1985.

Devlukia, J., (1991),
Year 1 Annual Report, Project Periodic Report 2/8,
(1st March 1990 - 28th February 1991),
ENDDURE Engineering Design for Durability and Reliability,
BRITE/EURAM Project 3051, Contract 0099.

Dowling, N.E., Brose, W.R., Wilson, W.K., (1977),
Notched member fatigue life predictions by the local strain approach,
In: Fatigue under Complex Loading - Analysis and Experiments, pp.55-84,
Society of Automotive Engineers, Warrendale.

Elber, W., (1971),
The Significance of Fatigue Crack Closure,
Damage Tolerance in Aircraft Structures, ASTM STP 486,
American Society for Testing and Materials, Philadelphia, pp.230-242, 1971.

El Haddad, M.H., Topper, T.H., Smith, K.N., (1979),
Prediction of Non Propagation Cracks,
Engineering Fracture Mechanics, Vol. 11, pp. 573-584, 1979.

El Haddad, M.H., Topper, T.H., Topper, T.N., (1981),
Fatigue Life Predictions of Smooth and Notched Specimens Based on Fracture
Mechanics,
Journal of Engineering Materials and Technology, Transactions of the ASME, Vol.
103, April 1981, pp.91-96.

Fash, J.W., Socie, D.F., Russell, E.S., (1981),
Fatigue Crack Initiation and Growth in Gray Cast Iron,
Proceedings of Fatigue '81, Warwick University, SAE 1981, pp.40-51.

Fash, J.W., Socie, D.F., (1982),
Fatigue Behaviour and Mean Effects in Grey Cast Iron,
International Journal of Fatigue, July 1982, pp.137-142.

Flavenot, J.F., Skalli, N., (1989),
A Critical Depth Criterion for the Evaluation of Long-Life Fatigue Strength under
Multiaxial Loading and a Stress Gradient,
Biaxial and Multiaxial Fatigue, EGF 3, Edited by Brown, M.W., Miller, K.J.,
Mechanical Engineering Publications, London, 1989, pp. 355-365.

Forrest, G., (1955),
The Effect of Fatigue of Notches, Surface Finishes, etc.,
The Fatigue of Metals, Refresher Course 1955,
The Institution of Metalurgists, London, pp.40-81.

Forsyth, P.J.E., (1959),
Fatigue Crack Formation in Silver Chloride,
Symposium on Basic Mechanisms of Fatigue,
ASTM STP 237, American Society for Testing Materials, Philadelphia, 1959.

Frost, N.E., (1955a)
Crack Formation and Stress Concentration Effects in Direct Stress
Fatigue, No. I,
The Engineer, 1955, Vol. 200, pp. 464-467.

Frost, N.E., (1955b)
Crack Formation and Stress Concentration Effects in Direct Stress
Fatigue, No. II,
The Engineer, 1955, Vol. 200, pp. 501-503.

Frost, N.E., (1955c)

Non-Propagating Cracks in Vee-Notched Specimens Subject to Fatigue Loading,

The Aeronautical Quarterly, 1955, Vol. 8, pp. 1-20.

Frost, N.E., Pook, L.P., Marsh, K.J., (1974),

Metal Fatigue,

Clarendon Press, 1974.

Gallagher, R.H., (1978),

A review of finite element techniques in fracture mechanics,

Numerical Methods in Fracture Mechanics,

Eds. Luxmore, A.R., Owen, D.R.J.,

University of Wales, Swansea, 1978.

Gilbert, G.N.J., (1977),

Engineering Data on Grey Cast Irons - SI Units,

Report 1285, BCIRA, Alvchurch, Birmingham, 1977.

Gilbert, G.N.J., Kemp, S.D., (1980),

The Cyclic Stress/Strain Properties of a Flake Graphite Cast Iron - A progress Report,

BCIRA Report 1384, July 1980.

Gilbert, G.N.J., (1985),

The Cyclic Stress/Strain Properties and Fatigue Properties of a Flaked Graphite Cast Iron Tested Under Strain Control - A Detailed Study,

BCIRA Report 1621, March 1985.

Hempel, M.R., (1959),

Slipband Formation and Fatigue Cracks Under Alternating Stress,

Symposium on Basic Mechanisms of Fatigue,

ASTM STP 237, American Society for Testing Materials, Philadelphia, 1959.

Heuler, P., Berger, C., Motz, J., (1992),
Fatigue Behaviour of Steels Castings Containing Near-Surface Defects,
Fatigue and Fracture of Engineering Materials and Structures, Vol. 16, No. 1,
pp.115-136, 1992.

Heuler, P., Bergmann, J.W., (1997),
IEPG TA31 A Research Programme into Lifting Concepts for Military Aero-Engine
Components,
Final Report, B-TA-3602, 18 August 1997,
Industrieanlagen-Betriebsgesellschaft mbH (IABG), Ottobrunn, Germany.

HKS, (1995),
Fracture Mechanics course notes,
HKS Inc. 1995.

HKS, (1996),
ABAQUS 5.5 Theory Manual,
HKS Inc. 1996.

Hoffman, M., Seeger, T., (1985),
Generalised Method for Estimating Multiaxial Elastic-Plastic Notch Stresses and
Strains, Part 1: Theory, Part 2: Application and General Discussion,
ASME Journal of Engineering Materials and Technology, Vol. 107, Oct. 1985,
pp.250-260.

Hornbogen, E., (1985),
Fracture Toughness and Fatigue Crack Growth of Grey Cast Irons,
J. Material Science, 20, 1985, pp.3897-3905.

Hughes, P.M., (1990),
Implementation of a Finite Element Based Fracture mechanics Facility: MELFRAM
Version 1.1, Two-Dimensional Approach,
ALSTOM Energy Technology Centre,
Report ERC(W)C.12.583, Nov. 1990.

Hughes, P.M., (1992),
Implementation of a Finite Element Based Fracture mechanics Facility for 3-D
Crack Geometries: MELFRAM Version 2,
ALSTOM Energy Technology Centre,
Report ERC(W)C.15.799, Nov. 1992.

Hughes, P.M., Wood, G.A., (1994),
Life Assessment Software (LAS) Version 3.0 User Manual,
ALSTOM Energy Technology Centre,
Report ERC(W)C.25.930, 18 March 1994.

Hughes, P.M., (1997)
IEPG TA31 Programme
Lifing Concepts for Military Aero-engine Components:
Final Report on the Application of Predictive Models to
Engineering Test Specimens,
ALSTOM Energy Technology Centre,
Report MEC(W)C.84.2085, July 1997.

Irwin, G.R., (1957),
Analysis of stresses and strains near the end of a crack traversing a plate,
Journal of Applied Mechanics, 1957, Vol. 24, p.361.

Isibasi, T., (1952),
Effects of Notches on Fatigue Strength of Gray Cast Iron,
Mem. Fac. Engng. Kyushu University, 1952, Vol. 13, pp.71-86.

James, M.R., Morris, W.L., (1983),
Effect of Fracture Surface Roughness on Growth of Short Fatigue Cracks,
Metallurgical Transactions, 1983, 14A, pp.153-155.

Jianchun, L., (1993),
A Study of Short Fatigue Crack Growth,
PhD Thesis,
Department of Mechanical & Manufacturing Engineering Department,
University of Dublin, Trinity College, March 1993.

Judge, R.C.B., Marsden, B.J., (1995),
Three Dimensional Test Cases in Linear Elastic Fracture Mechanics,
NAFEMS, Ref: R0028, East Kilbride, Glasgow.

Kato, A., (1992),
Design Equations for Stress Concentration Factors of Notched Strips and
Grooved Shafts,
Journal of Strain Analysis, Vol. 27, No. 1, 1992.

Keith, R.E., Gilman, J.J., (1959),
Progress Report on Dislocation Behaviour in Lithium Fluoride Crystals During
Cyclic Loading,
Symposium on Basic Mechanisms of Fatigue,
ASTM STP 237, American Society for Testing Materials, Philadelphia, 1959.

Kitagawa, H., Takahashi, S., (1976),
Applicability of Fracture Mechanics to Very Small Cracks in the Early Stage,
Proc. 2nd Int. Conf. on Mech. Behaviour of Materials, 1976, pp. 627-631.

Kopsov, I.E., (1992),
Stress Intensity Factor Solution for a Semi-elliptical Crack in an Arbitrarily
Distributed Stress Field,
Int. J. Fatigue, 14, No. 6, 1992, pp.399-402.

Landeraf, R.W., Richards, F.D., Lapointe, N.R., (1975),
Fatigue life prediction for a notched member under complex load histories,
Paper 750040, SAE Automotive Engineering Congress & Exposition,
Detroit, MI, feb. 24-28, 1975.

Li, F.Z., Shih, C.F., (1985),
A comparison of methods for calculating energy release rates,
Engineering Fracture Mechanics, Vol.21, No.2, pp.405-421, 1985.

Lukás, P., Kunz, L., Weiss, B., Stickler, R., (1989),
Notch Size Effect in Fatigue,
Fatigue and Fracture of Engineering Materials and Structures, Vol. 12,
No. 3, pp.175-186, 1989.

Magnusen, P.E., Hinkle, A.J., Kaiser, W.T., Bucci, R.J., Rolf, R.L., (1990),
Durability Assessment Based on Initial Material Quality,
Journal of Testing and Evaluation, Vol. 18, No. 6, Nov. 1990, pp.439-445.

Mitchell, M.R., (1976),
A Unified Predictive Technique for the Fatigue Resistance of Cast-Ferrous Based
Metals and High Hardness Wrought Steels,
T&AM Report No. 412, Dept. of Theoretical and Applied Mechanics, University of
Illinois, Urbana, Illinois, 1976.

Mughrabi, H., Wang, R., Differt, K., Essmann, U., (1983),
Fatigue Crack Initiation by Cyclic Slip Irreversibilities in High Cycle Fatigue,
Fatigue Mechanisms: Advances in Quantitative Measurement of Physical
Damage, ASTM STP 811,
Langford, J., Davidson, D.L., Morris, W.L., Wei, R.P., Eds.,
American Society for Testing and Materials, 1983, pp. 5-45.

Murakami, Y., Kodama, S., Konuma, S., (1989),
Quantitative evaluation of the effects of non-metallic inclusions on fatigue strength
of high strength steels. I: Basic fatigue mechanisms and evaluation of correlation
between the fatigue stress and the size and location of non-metallic inclusions,
International Journal of Fatigue, Vol. 11, No. 5 (1989), pp. 291-298.

Murakami, Y., Endo, M., (1994),
Effects of Defects, Inclusions and Inhomogeneities on Fatigue Strength,
Fatigue, Vol. 16, April, 1994, pp.163-182.

Murrell, P.A., (1995),
The Castings Development Centre
Private communication, May 1995.

Murrell, P.A., (1997),
The Castings Development Centre
Private communication

Neuber, H., (1961),
Theory of Stress Concentration for Shear-Strained Prismatic Bodies with Arbitrary
Nonlinear Stress-Strain Law,
Transactions of the ASME, Dec. 1961.

Newman, J.C., Raju, I.S., (1979),
Analysis of Surface Cracks in Finite Plates Under Tension and Bending
Loads,
NASA TP-1578, National Aeronautics and Space Administration, Dec. 1979.

Newman, J.C., Raju, I.S., (1984),
Prediction of Fatigue Crack-Growth Patterns and Lives in Three-Dimensional
Cracked Bodies,
Proc. of 6th Int. Conf. Fracture (ICF 6), New Dehli, India, 1984.

Noguchi, T., Shimizu, K., Kegasawa, T., (1989),
Notch Sensitivity of Cast Iron,
Transactions of the American Foundrymen's Society,
Vol. 97, 1989, pp. 389-396.

Paris, P.C., Erdogan, F., (1963),
A critical analysis of crack propagation laws,
Transactions of the ASME D, Journal of Basic Engineering,
Vol. 85, p.528, 1963.

Peterson, R.E., (1959),
Notch Sensitivity,
Metal Fatigue, Eds.: Sines, G., Waisman, J.L.,
McGraw-Hill, 1959, pp.293-306.

Pickard, A.C., (1986),
The application of three-dimensional finite element methods to fracture mechanics
and fatigue life prediction,
Engineering Materials Advisory Services Ltd., 1986.

Pook, L.P., (1994),
Some Implications of Corner Point Singularities,
Engineering Fracture Mechanics, Vol. 48, No. 3, pp. 367-378, 1994.

Ravichandran, K.S., (1997),
Effects of Crack Aspect Ratio on the Behaviour of Small Surface Cracks in
Fatigue: Part I. Simulation,
Metallurgical and Material Transactions A, Vol. 28A, January 1997.

Rice, J.R., (1968),
A path independent integral and the approximate analysis of strain concentration
by notches and cracks,
Journal of Applied Mechanics, June, 1968, pp.379-386.

Rollason, E.C., (1973),
Metallurgy for Engineers, Fourth edition,
Edward Arnold, London, 1973.

Rooke, D.P., Cartwright, D.J., (1976),
Compendium of Stress Intensity Factors,
HMSO, 1976.

Scarlin, R.B., Berger, C., Mayer, K.H., (1986),
Effect of Steelmaking Defects on Fatigue Properties of Steel Forgings,
Metals and Materials, April 1986.

Shields, E.B., Srivatsan, T.S., Padovan, J., (1992),
Analytical methods for evaluation of stress intensity factors and fatigue crack
growth,
Engineering Fracture Mechanics, Vol. 42, No. 1, pp.1-26, 1992.

Shih, C.F., Moran, B., Takamura, T., (1986),
Energy Release Rate Along a Three-Dimensional Crack front in a Thermally
Stressed Body,
International Journal of Fracture, 30 (1986) pp.79-102.

Shin, C.S., Smith, R.A., (1985),
Fatigue Crack Growth from Sharp Notches,
International Journal of Fatigue, Vol. 7, No. 2, (1985), pp.87-93.

Smith, K.N., Watson, P., Topper, T.H., (1970),
A Stress-strain function for the fatigue of metals,
J. of Mater., JMLSA 5, No. 4, (December 1970), pp. 767-778.

Smith, R.A., Miller, K.J., (1977),
Fatigue Cracks at Notches,
International Journal of Mechanical Science, Vol. 19, pp. 11-22, 1977.

Smith, R.A., Miller, K.J., (1978),
Prediction of Fatigue Regimes in Notched Components,
International Journal of Mechanical Science, Vol. 20, pp. 201-206, 1978.

Smith, R.A., Cooper, J.F., (1989),
A Finite Element Model for the Shape Development of Irregular Planar Cracks,
Int. J. Pres. Ves. & Piping 36, pp.315-326, 1989.

Squire-Taylor, C., (1994),
Matrix Stress Analysis Ltd.,
Private communication, 1994.

Starkey, M.S., Irving, P.E., (1982a),
A Comparison of the Fatigue Strength of Machined and As-Cast Surfaces of SG
Iron,
International Journal of Fatigue, July 1982, pp.129-136.

Starkey, M.S., Irving, P.E., (1982b),
Predictions of the Fatigue Life of Smooth Specimens of SG Iron by Using a
Fracture Mechanics Approach,
Low Cycle Fatigue and Life Prediction, ASTM STP 770, Eds. C. Amzallag, B.N.
Leis, P. Rabbe, ASTM, 1982, pp.382-398.

Suresh, S., Ritchie, R.O., (1984),
Propagation of Short Fatigue Cracks,
International Metals Review, Vol. 29, No. 6, 1984, pp.445-476.

Tanaka, K., Nakai, Y., Yamashita, M., (1981),
Fatigue Growth Threshold of Small Cracks,
International Journal of Fracture, Vol. 17, No. 5, October 1981.

Tanaka, K., Hojo, M., Nakai, Y., (1983a),
Fatigue Crack Initiation and Early Propagation in 3% Silicon Iron,
Fatigue Mechanisms: Advances in Quantitative Measurement of Physical
Damage, ASTM STP 811,
Langford, J., Davidson, D.L., Morris, W.L., Wei, R.P., Eds.,
American Society for Testing and Materials, 1983, pp. 207-232.

Tanaka, K., Nakai, Y., (1983b),
Propagation and Non-propagation of Short Fatigue Cracks at a Sharp Notch,
Fatigue of Engineering Materials and Structures, Vol. 6, No. 4, pp.315-327, 1983.

Taylor, D., Knott, J.F., (1981),
Fatigue Crack Propagation Behaviour of Short Cracks; the Effect of
Microstructure,
Fatigue of Engineering Materials and Structures, Vol. 4,
No. 2, pp.147-155, 1981.

Taylor, D., Hughes, M., Allen, D., (1996a),
Notch Fatigue Behaviour in Cast Irons Explained Using a Fracture Mechanics
Approach,
International Journal of Fatigue, Vol. 18, No. 7, pp. 439-445, 1996.

Taylor, D., (1996b),
Crack Modelling: A Technique for the Fatigue Design of Components,
Engineering Failure Analysis, Vol. 3, No. 2, pp. 129-136, 1996.

Taylor, D., Ciepalowicz, A.J., Rogers, P., Devlukia, J., (1997),
Prediction of Fatigue Failure in a Crankshaft using the Technique of Crack
Modelling,
Fatigue and Fracture of Engineering Materials and Structures, Vol. 20, No. 1,
pp.13-21, 1997.

Tokaji, K., Ogawa, T., (1992);
The Growth Behaviour of Microstructurally Small Fatigue Cracks in Metals,
Short Fatigue Cracks,ESIS 13 (Miller, K.J., de los Rios, E.R., Eds.),
Mechanical Engineering Publications, London, 1992, pp.85-99.

Usami, S., Shida, S., (1979),
Elastic-Plastic Analysis of the Fatigue Limit for a Material with Small Flaws,
Fatigue of Engineering Materials and Structures, Vol. 1, pp.471-481, 1979.

Van Stone, R.H., Gilbert, M.S., Gooden, O.C., Laflen, J.H., (1988),
Constraint-Loss Model for the Growth of Surface Fatigue Cracks,
Fracture Mechanics: Nineteenth Symposium, ASTM STP 969,
Ed., Cruse, T.A.,
American Society for Testing and Materials, Philadelphia, 1988, pp.637-656.

Verpoest, I., Aenoudt, E., Deruyttere, A., (1985),
The Fatigue Threshold, Surface Condition and Fatigue Limit of Steel Wire,
International Journal of Fatigue, 7, No. 4, (1985), pp. 199-214.

Wang, C.H., Brown, M.W., (1994),
Modelling the Deformation Behaviour of Flake Graphite Iron under
Biaxial Cyclic Loading,
Report for BRITE/EURAM Project BR/EU 3051, contract no. 0099, 1990 to 1994.

Wanhill, R.J.H, Boogers, J.A.M., (1997),
Completing NLR Contributions to the IEPG TA31 Programme,
Part I: Low cycle fatigue testing,
Report No. NLR CR 97035 L, January 1997,
Nationaal Lucht- en Ruimtevaartlaboratorium, The Netherlands.

Weinacht, D.J., Socie, D.F.,(1987),
Fatigue Damage Accumulation in Grey Cast Iron,
International Journal of Fatigue, Vol. 9 (2), April 1987, pp.79-86.

Westergaard, H.M., (1939),
Bearing Pressures and Cracks,
Journal of Applied Mechanics, June 1939, pp.49-53.

Yu, M.T., DuQuesnay, D.L., Topper, T.H., (1990),
Distributions of Defect Size and Fatigue Resistance,
Fatigue 90.

Zentech, (1996),
ZENCRACK User Manual, Issue 4, Document i009/doc/001,
Zentech International Ltd., Feb. 1996.

Zienkiewicz, O.C., (1977),
The Finite Element Method, 3rd Edition,
McGraw-Hill, 1977.

**A Crack Growth Based Approach to the
Fatigue Assessment of Cast Iron Components**

Volume 2

by

P.M. Hughes BSc(Hons) CEng MIMechE

**Submitted in partial fulfillment of the requirements for
the award of the degree of
DOCTOR OF PHILOSOPHY
in the Department of Engineering,
University of Leicester
December 1998**

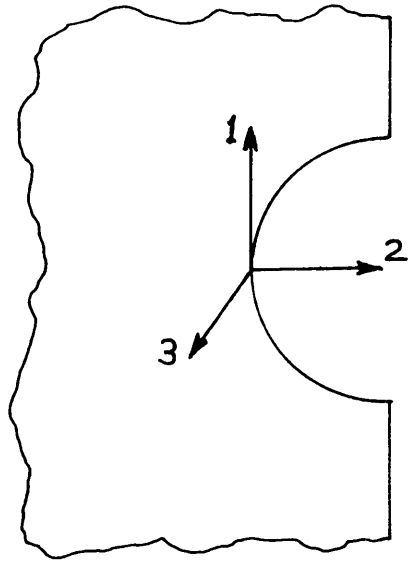


Figure 2.1 Definition of local coordinate system for local strain calculations

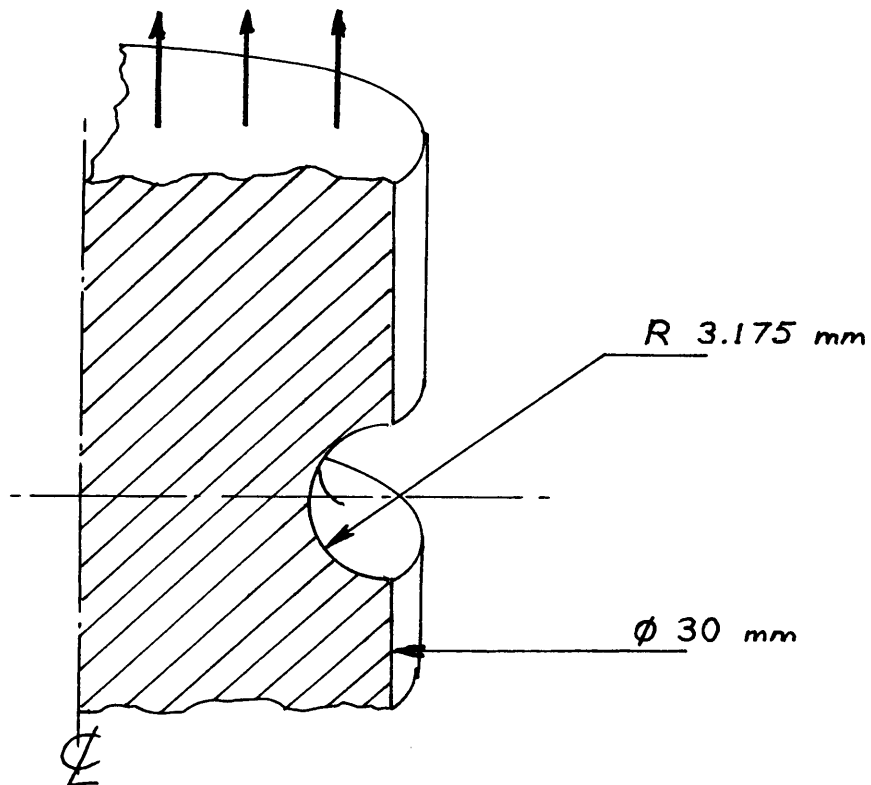


Figure 2.2 Sketch of notch geometry used to test axisymmetric local strain calculations

Figure 2.3 Ramberg-Osgood fit to Typical Stress-Strain Curve for Grade 17 Grey Iron
 $E = 100670 \text{ MPa}$, $K' = 917.4 \text{ MPa}$, $n' = 0.2455$

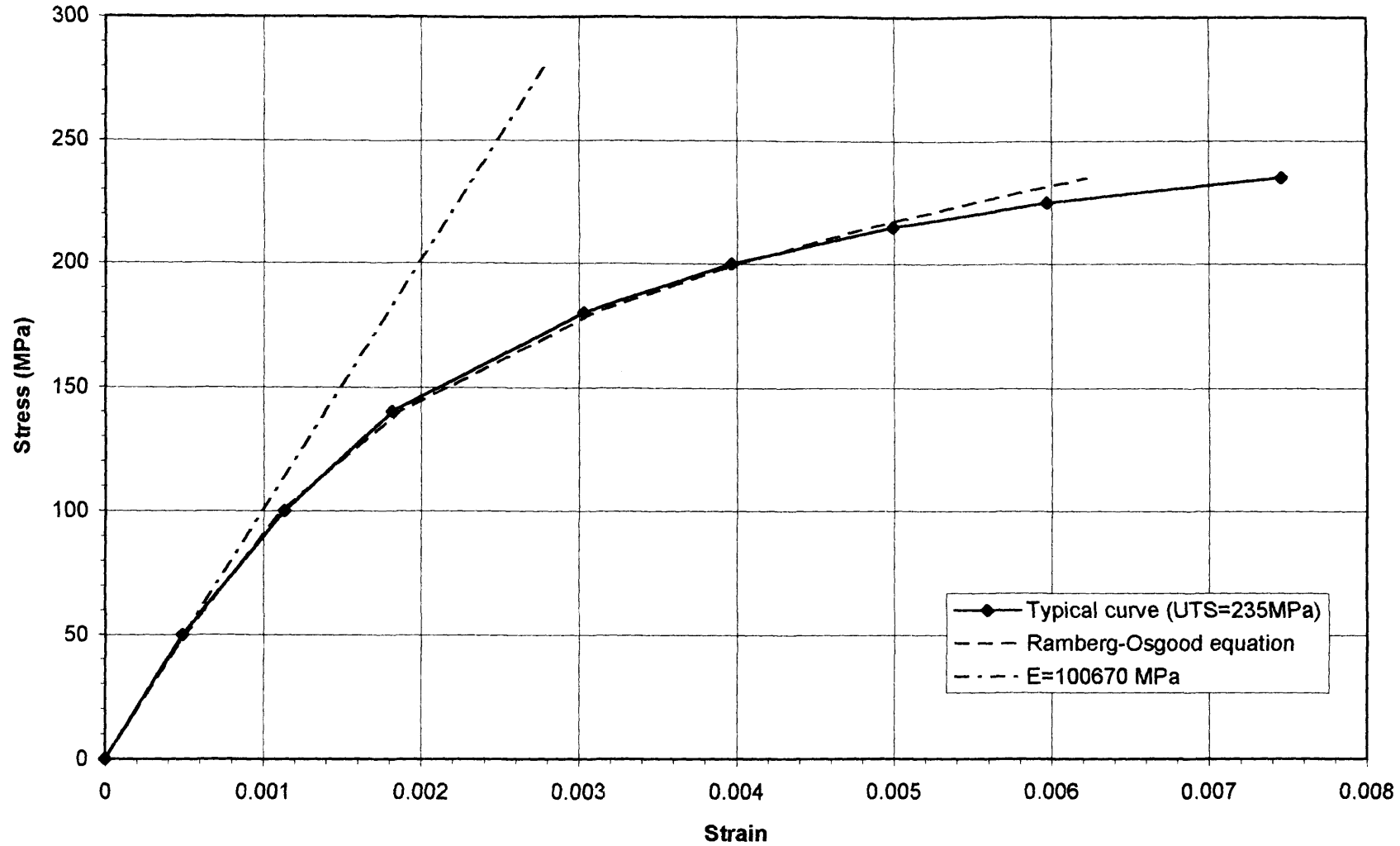


Figure 2.4 Comparison of predicted stresses at the root of a circumferentially notched specimen, $K_t = 2.2$, $S_{nom} = 135\text{MPa}$ (shown in figure 2.2)

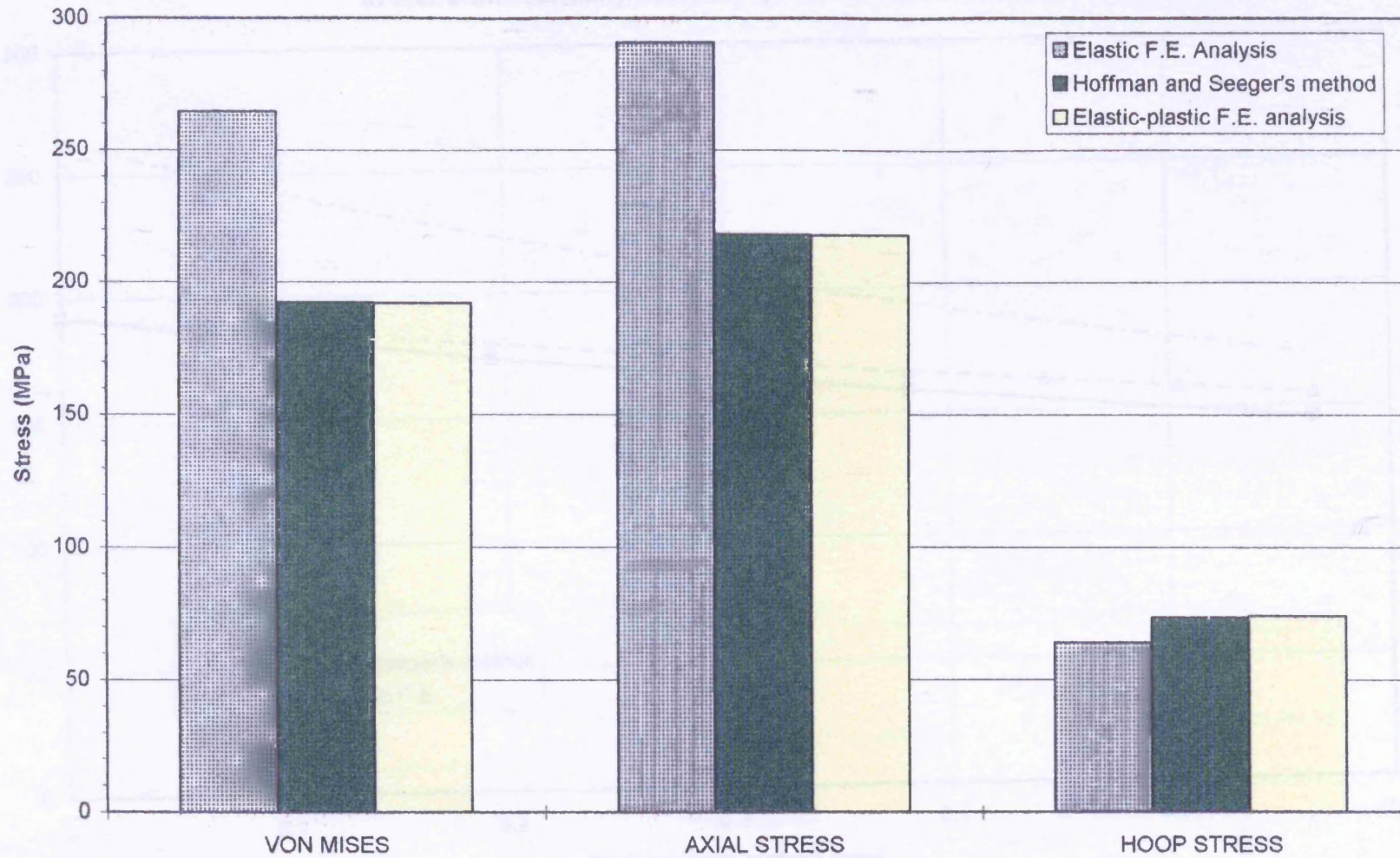


Figure 2.5 Estimated distributions of von Mises stress immediately below the surface in a circumferentially notched specimen $S_{nom} = 135 \text{ MPa}$ ($K_t = 2.2$)

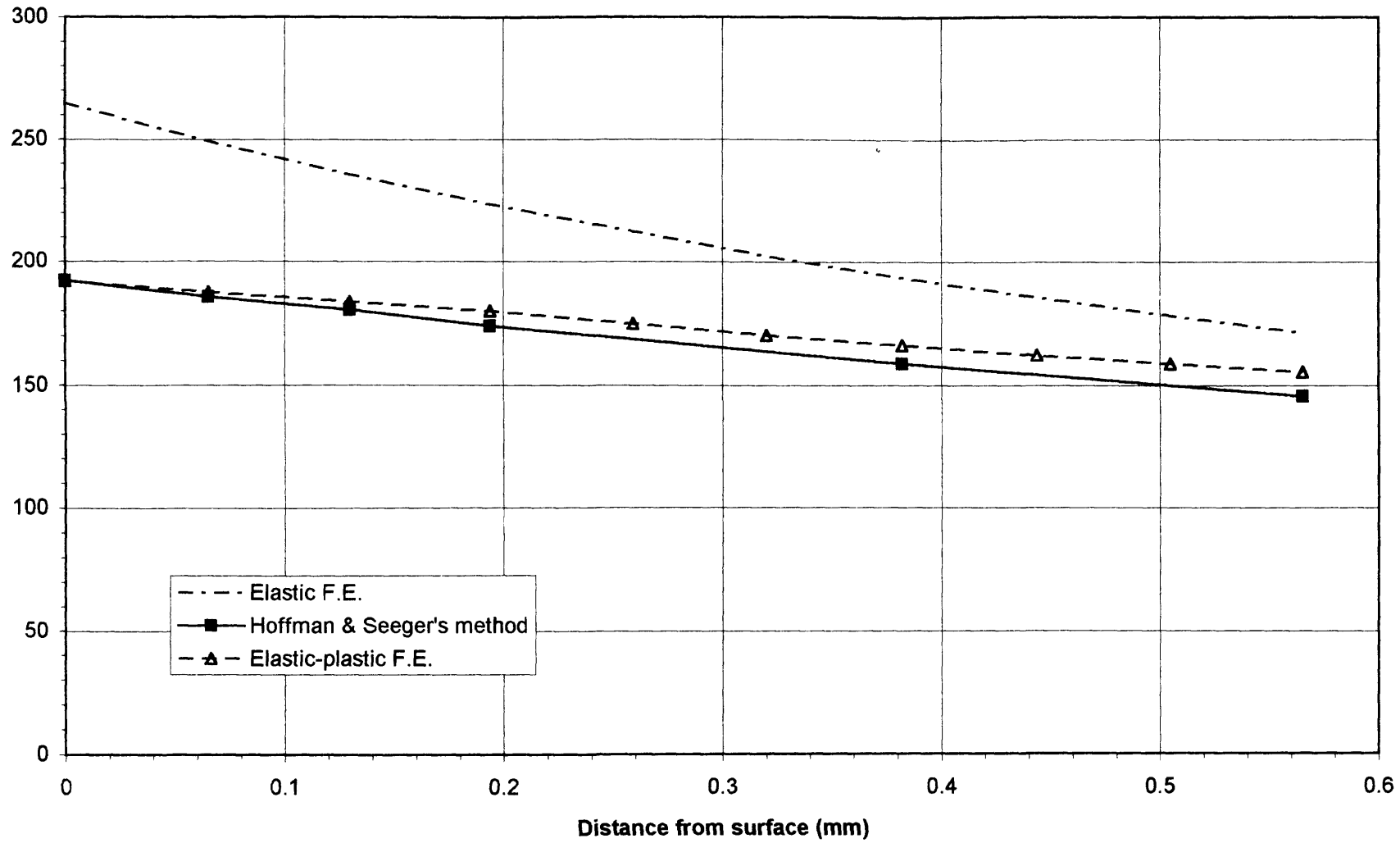


Figure 2.6 Estimated distributions of stress components immediately below the surface in a circumferentially notched specimen $S_{nom} = 135 \text{ MPa}$ ($K_t = 2.2$)

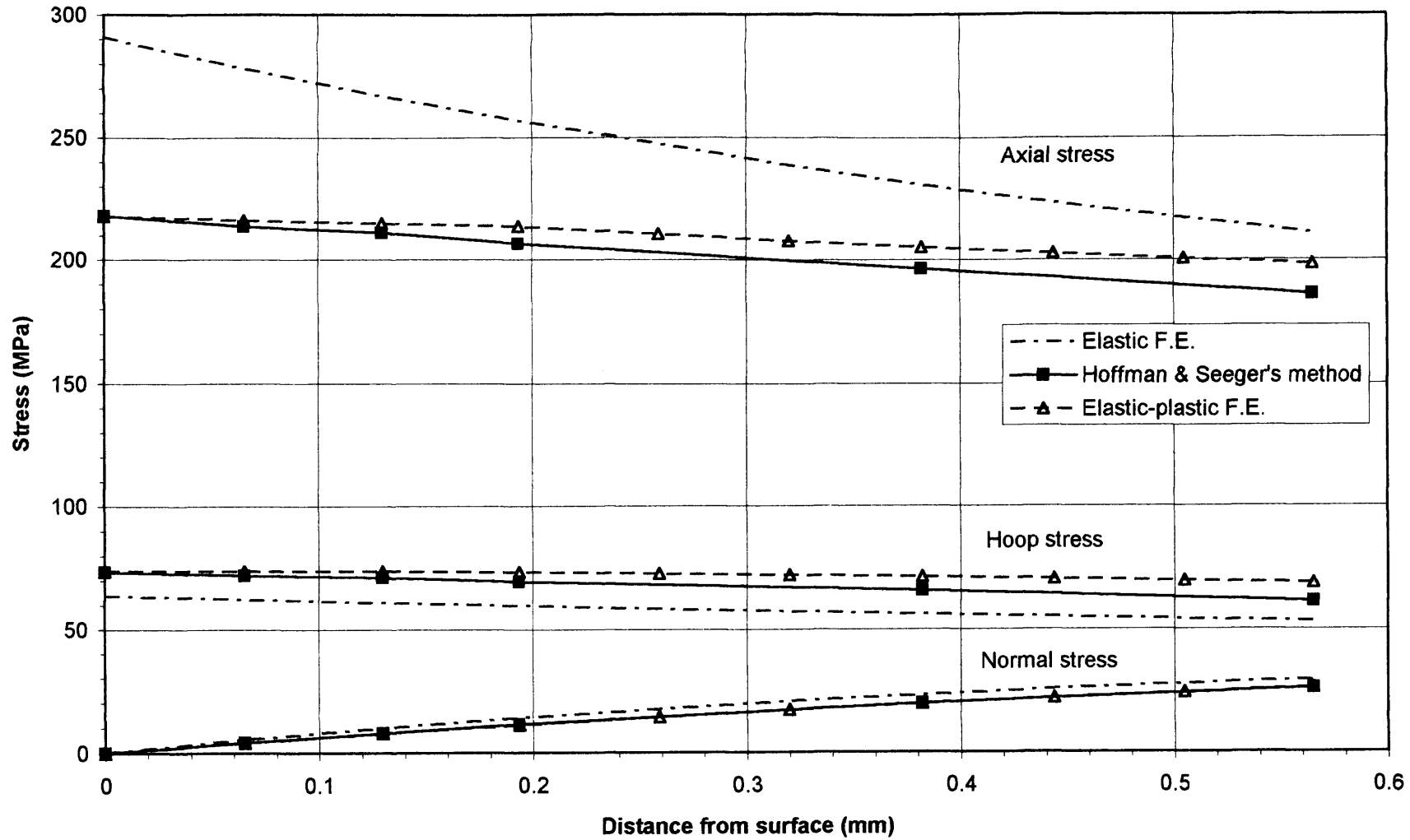


Figure 2.7 Estimated distributions of strain components immediately below the surface in a circumferentially notched specimen $S_{nom} = 135 \text{ MPa}$ ($K_t = 2.2$)

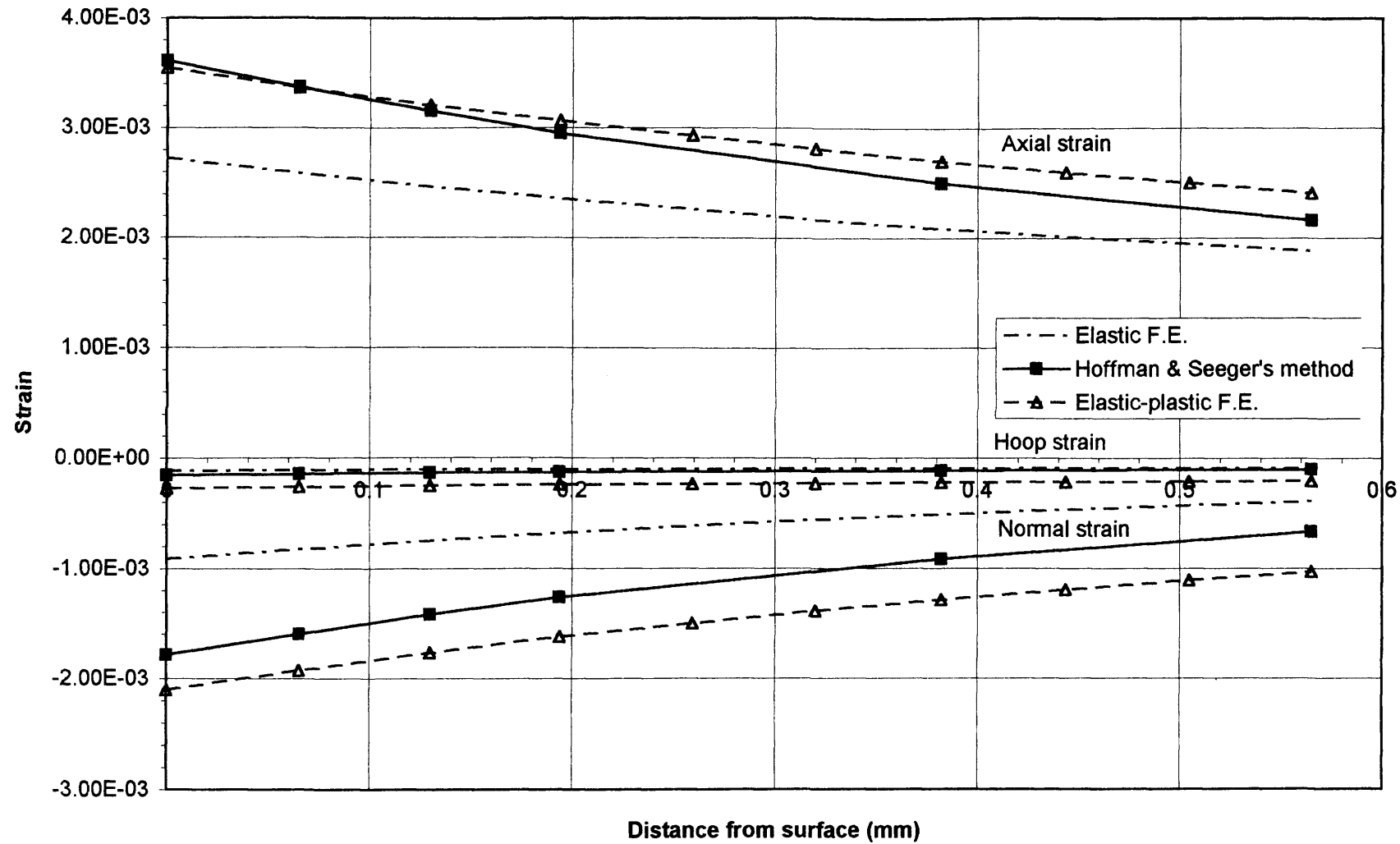
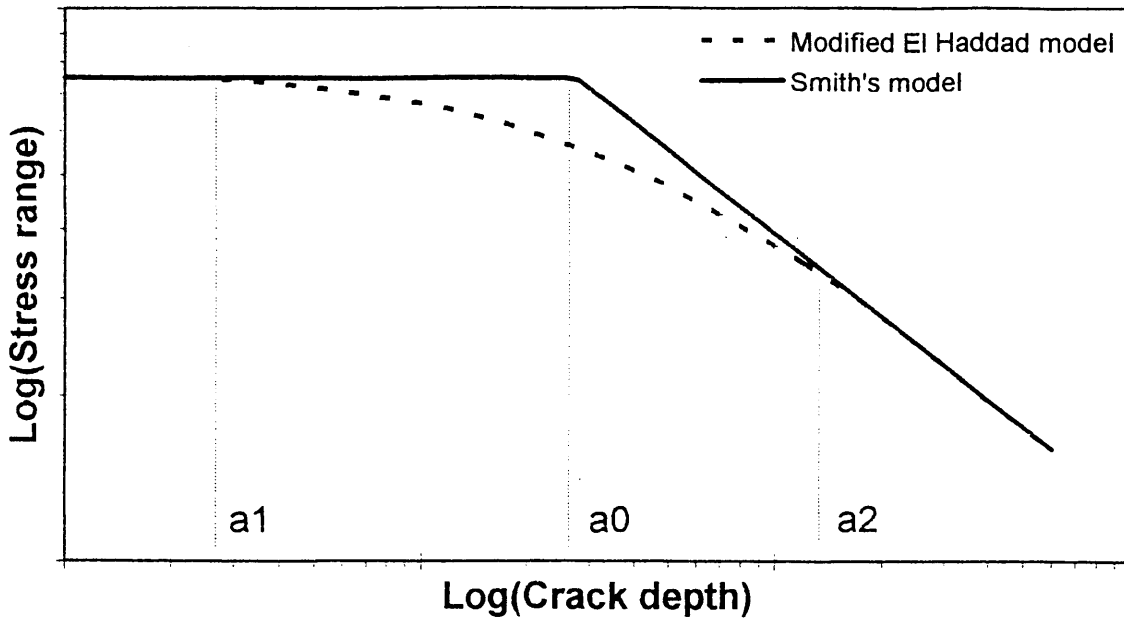
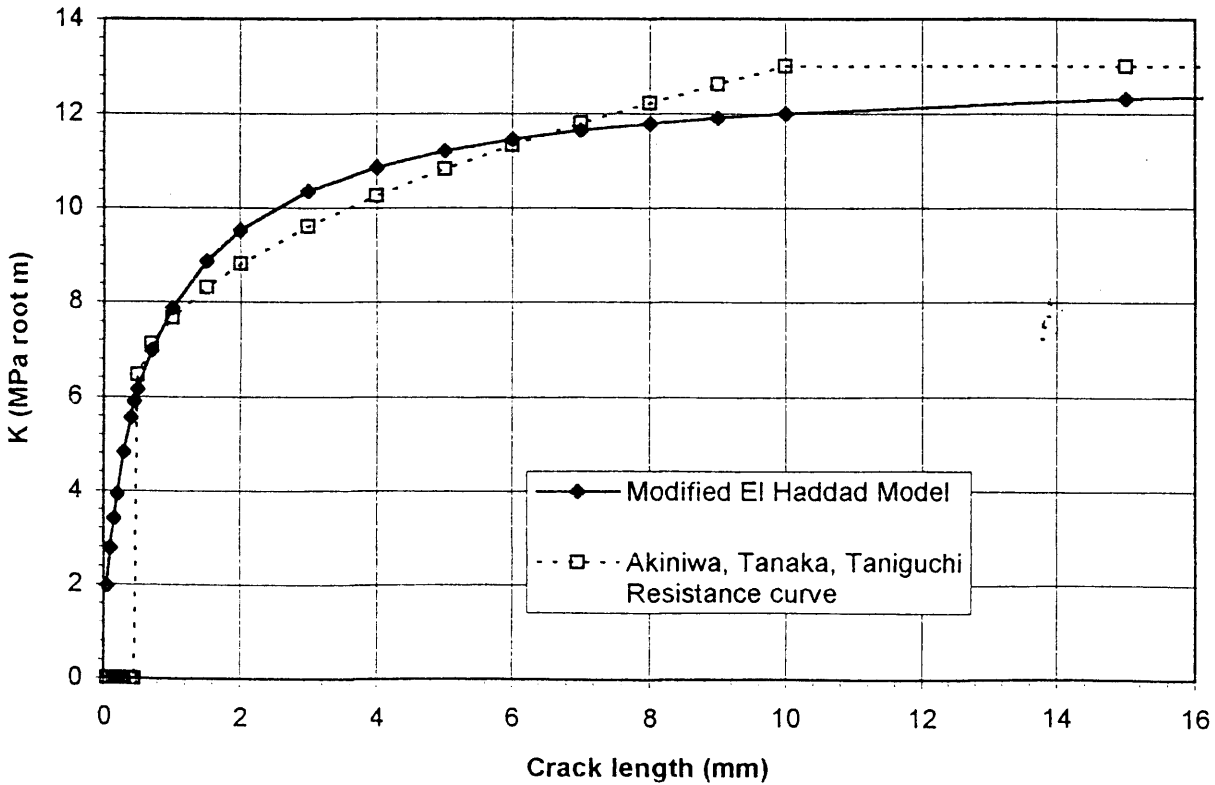


Figure 2.8 Schematic of the Kitagawa-Takahashi Diagram showing a1, a0 and a2



DEFECTS.XLS

Figure 2.9 Comparison of Models for Effective Short Crack Threshold



RCURVE.XLS

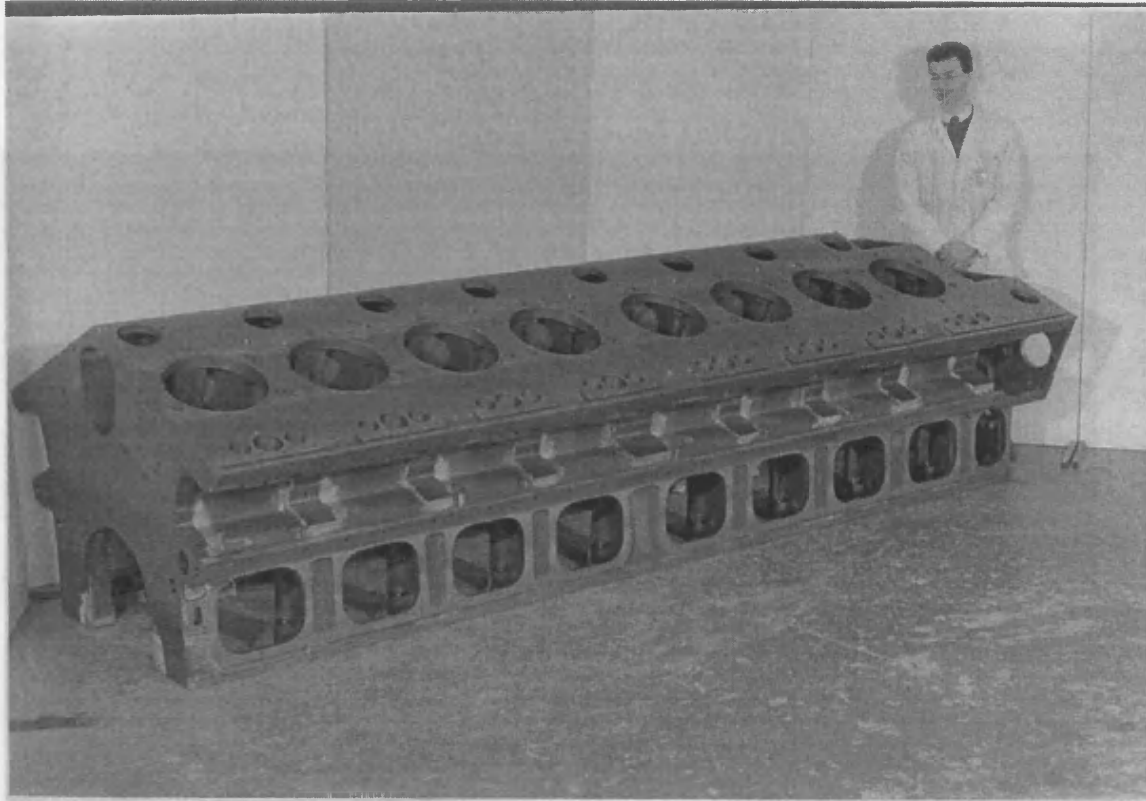


Figure 3.1 General view of diesel engine crankcase used as the source of grade 17 grey case iron for the specimen test programme



Figure 3.2 Close-up of a design detail on the diesel engine crankcase

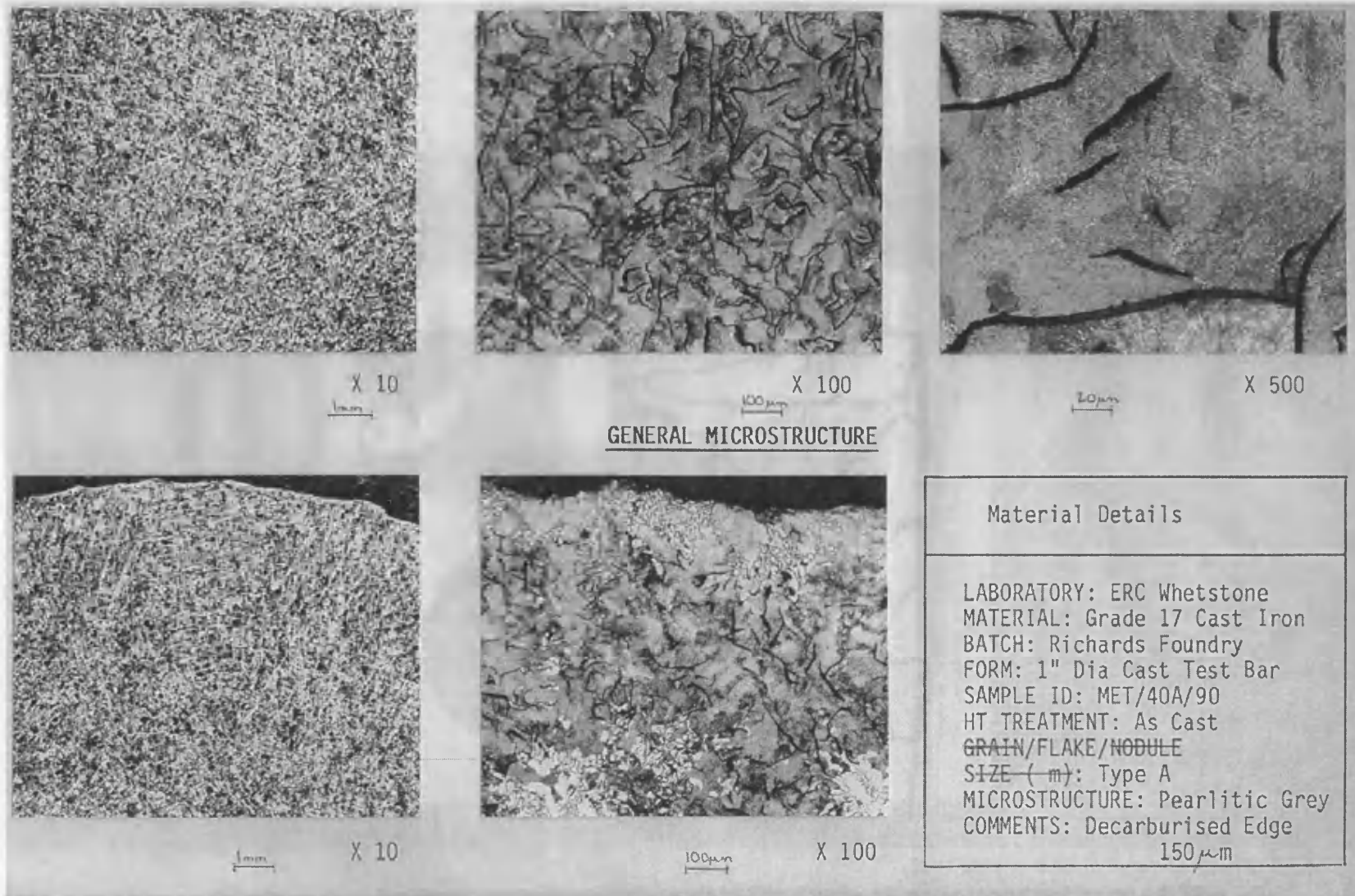


Figure 3.3 Material characterisation data for grade 17 grey iron test bars - 1.0in. dia.

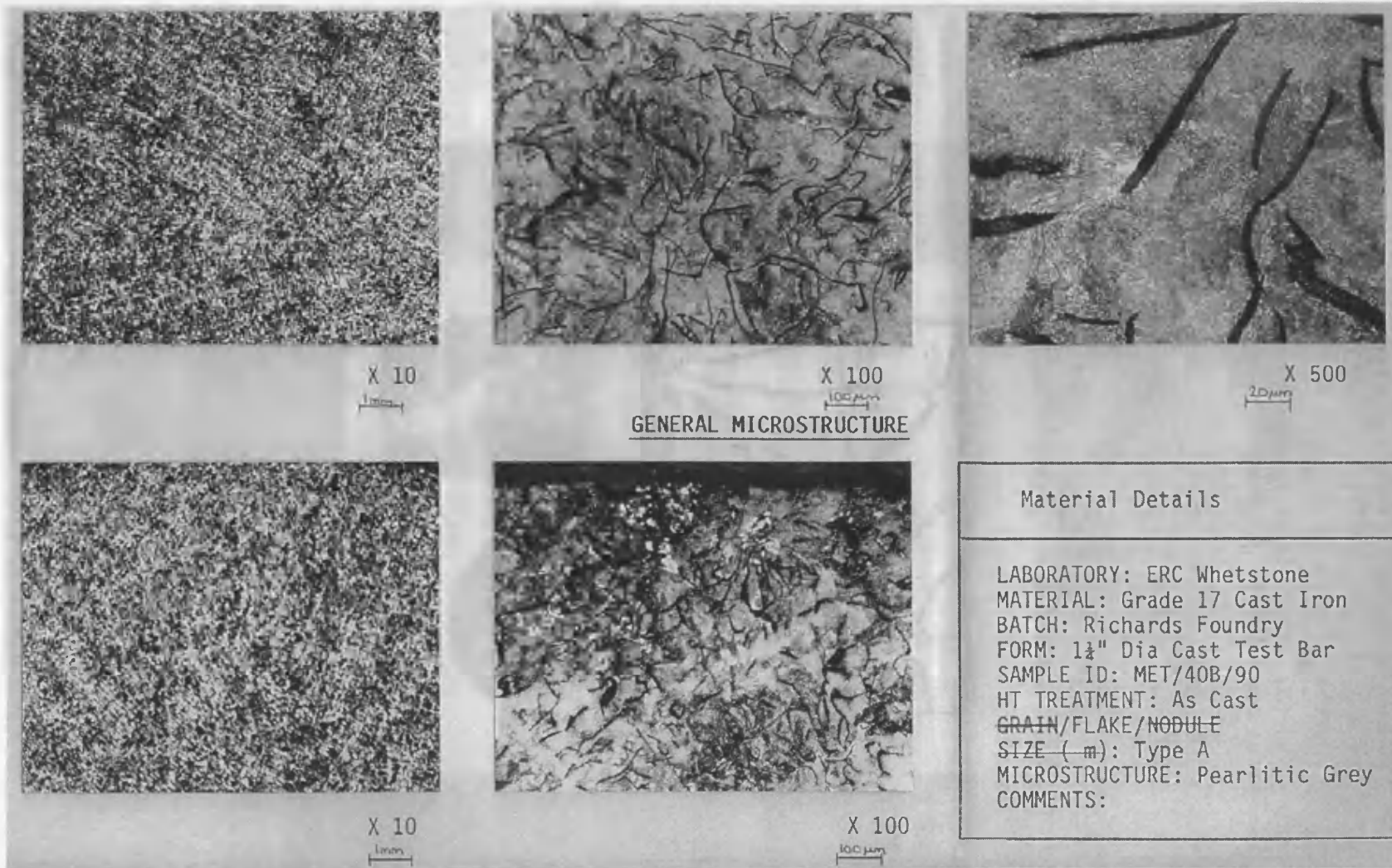


Figure 3.4 Material characterisation data for grade 17 grey iron test bars - 1.25in. dia.

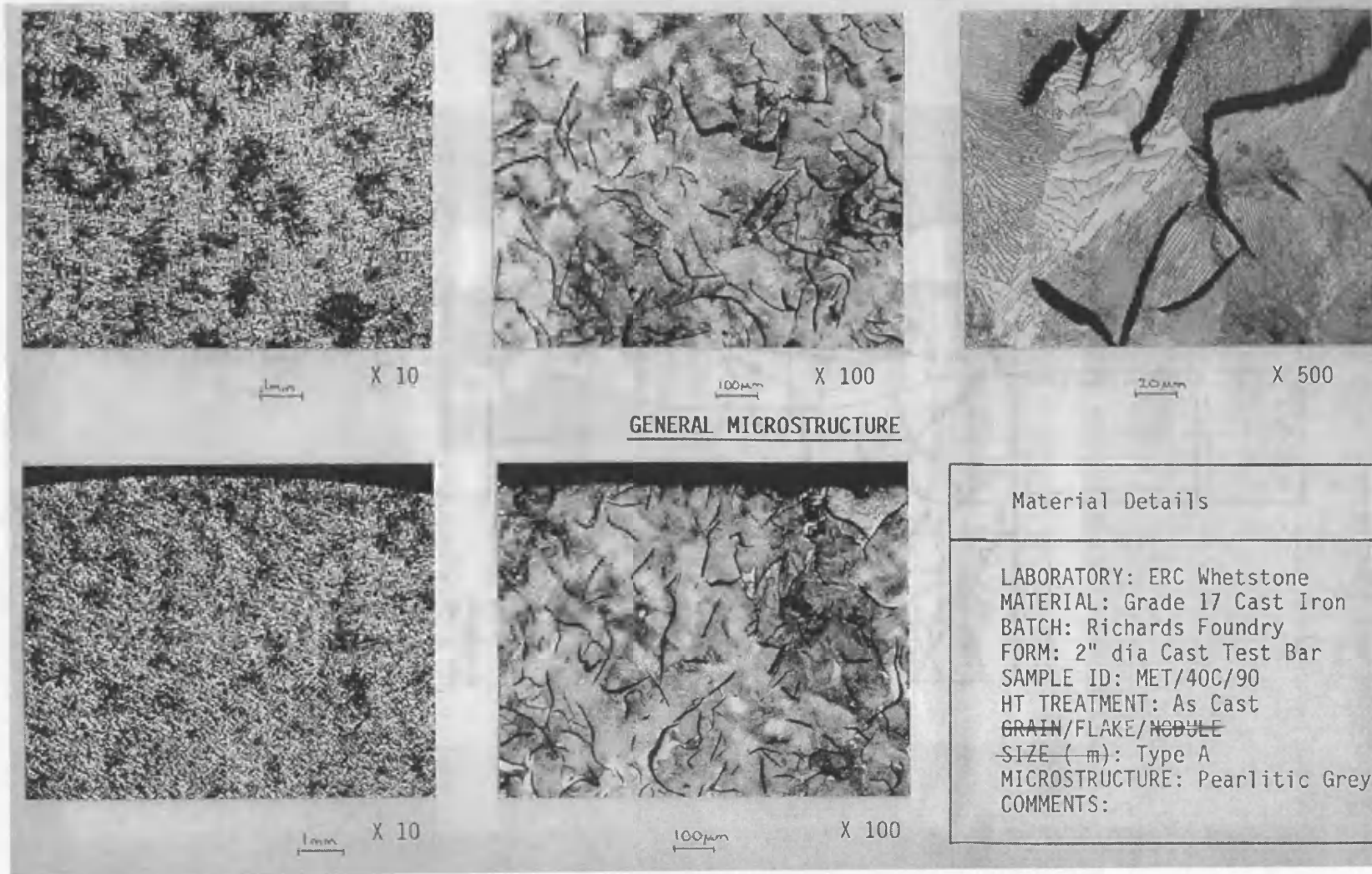


Figure 3.5 Material characterisation data for grade 17 grey iron test bars - 2.0in. dia.

Figure 3.4 2.0in. dia. grey iron plain fatigue specimen geometry

Dimensional in inch

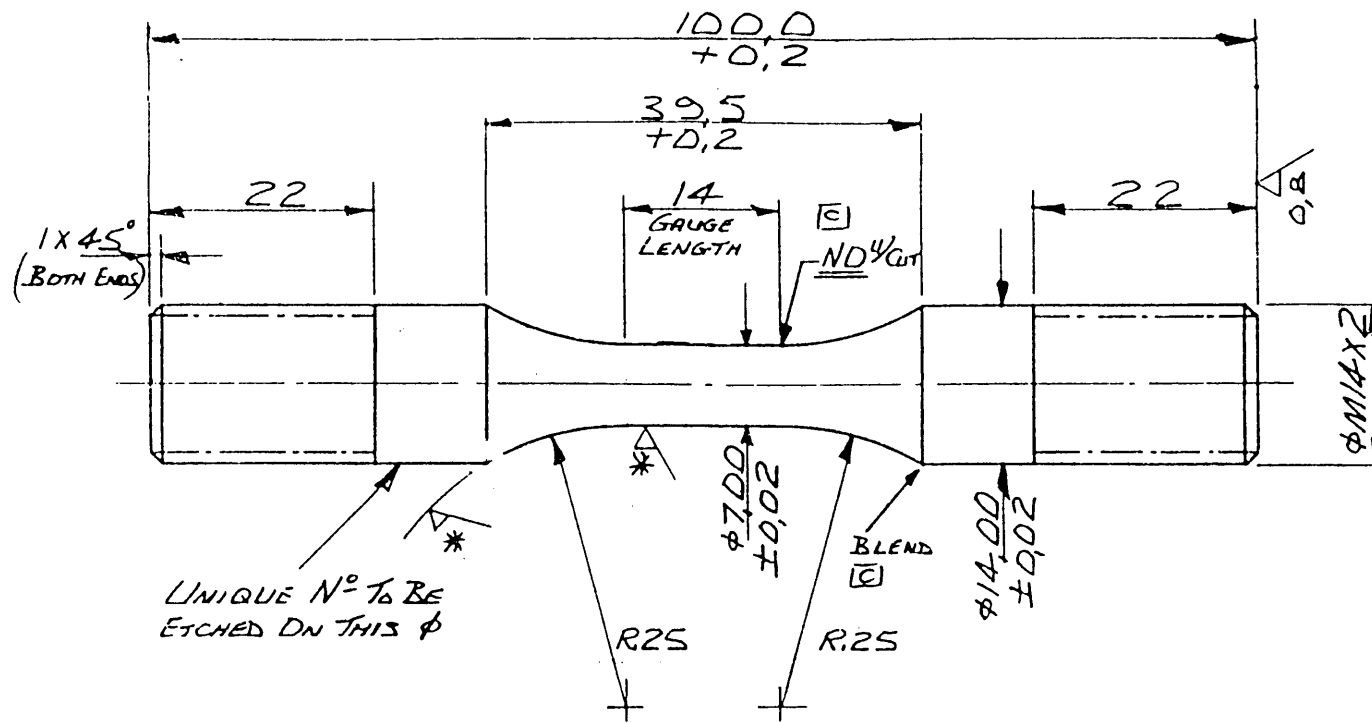


Figure 3.6 Grey iron plain fatigue specimen geometry
 Dimensions in mm

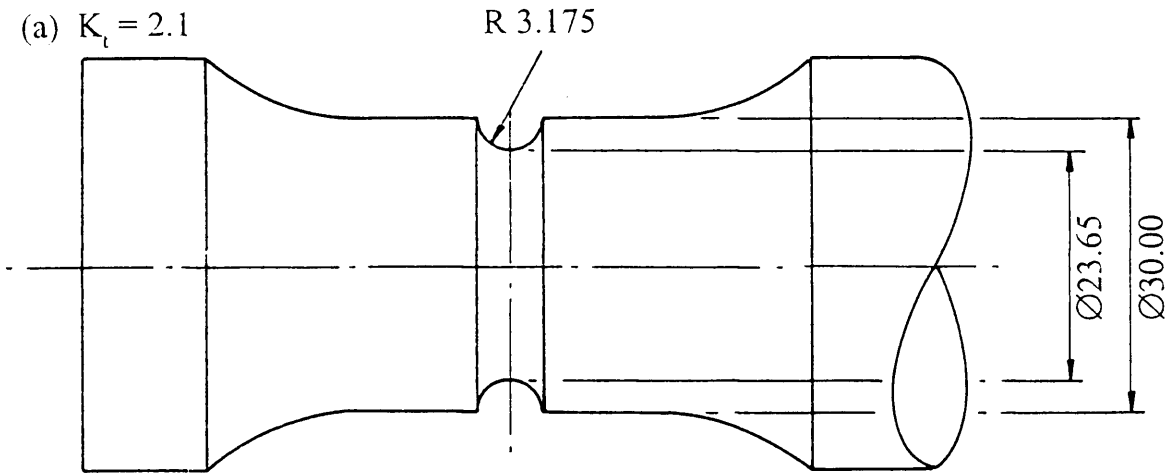


Figure 3.7 BRITE Notched axial specimen geometry ($K_t = 2.2$)

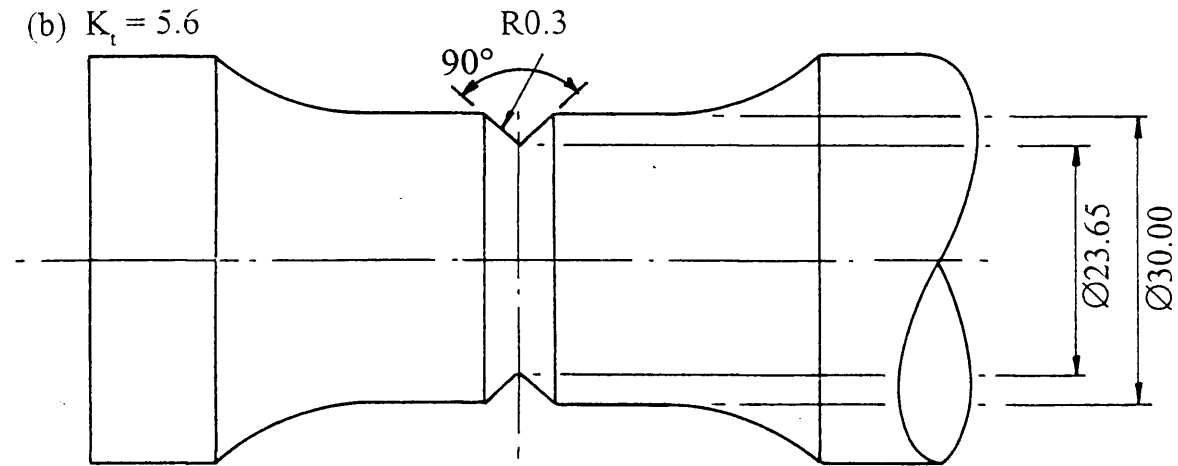
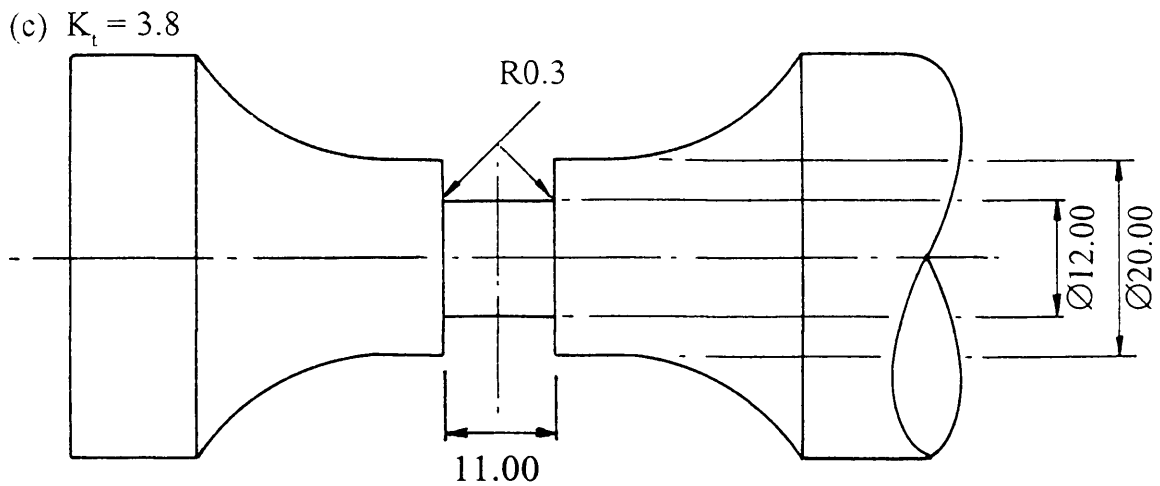


Figure 3.8 BRITE Notched axial specimen geometry ($K_t = 5.6$)



**Figure 3.9 BRITE Notched axial specimen geometry
- Simulated component ($K_t = 3.8$)**

Dimensions in mm

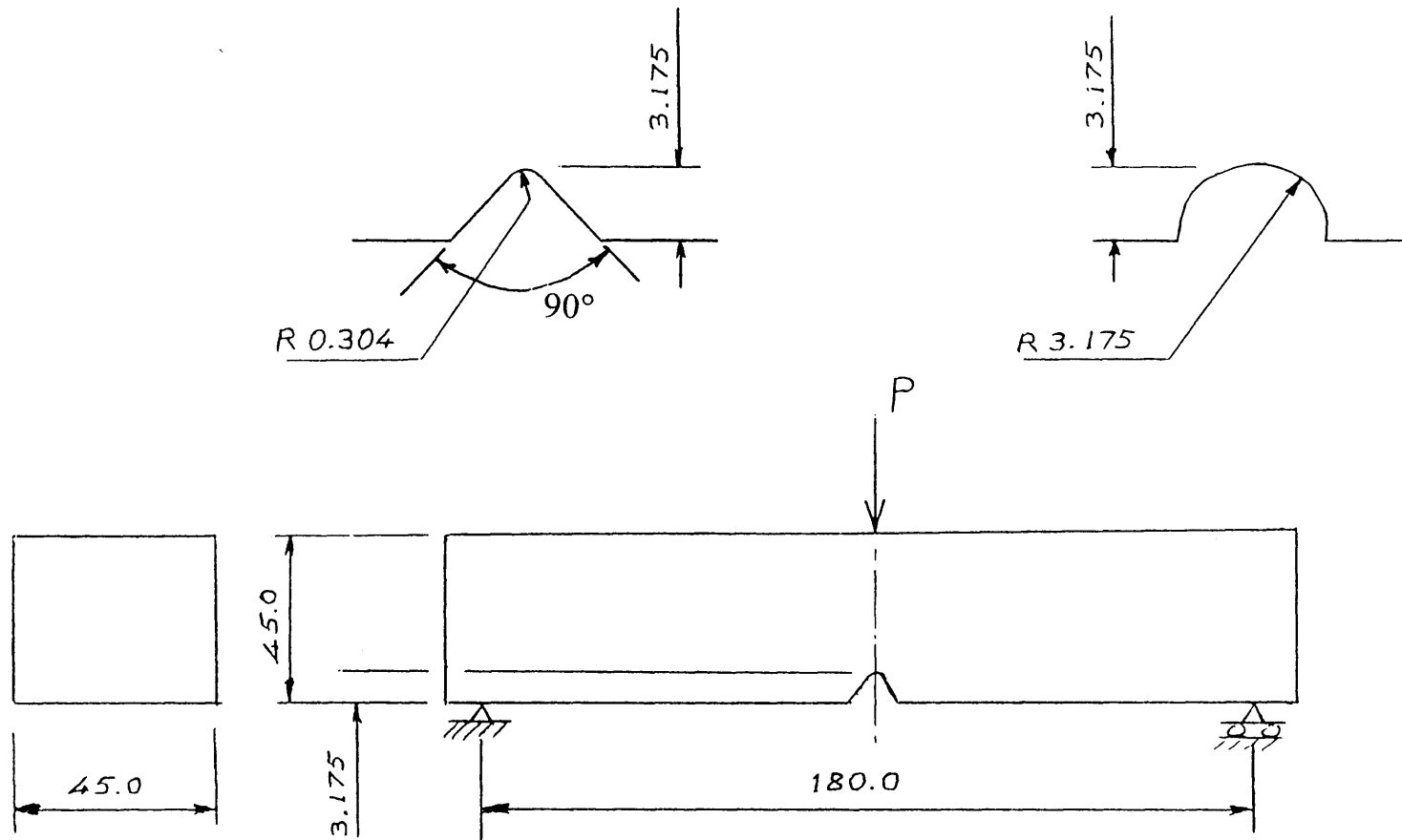


Figure 3.10 Three-point bend specimen geometries

(a) $K_t = 2.4$

(b) $K_t = 6.3$

Dimensions in mm

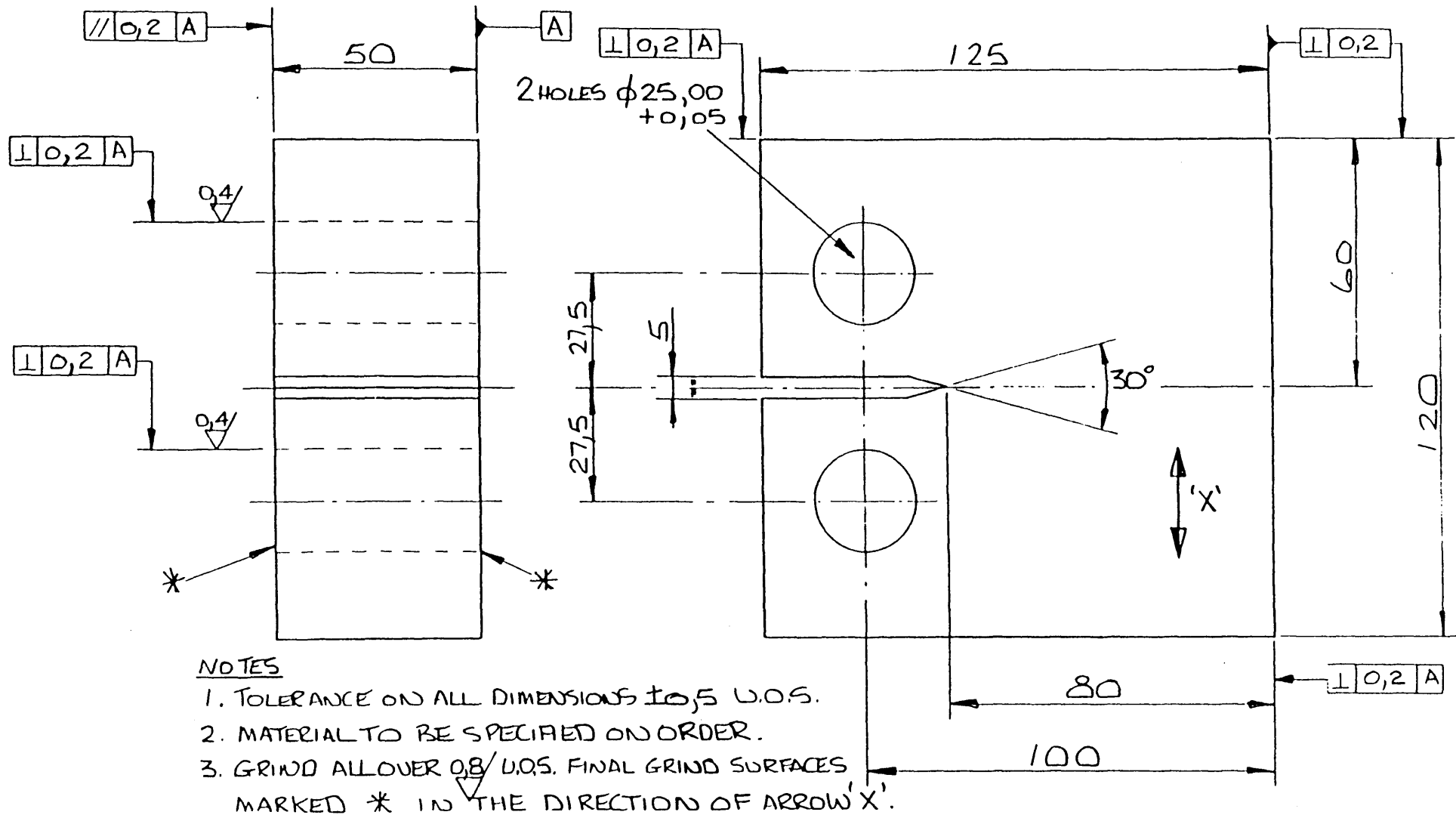
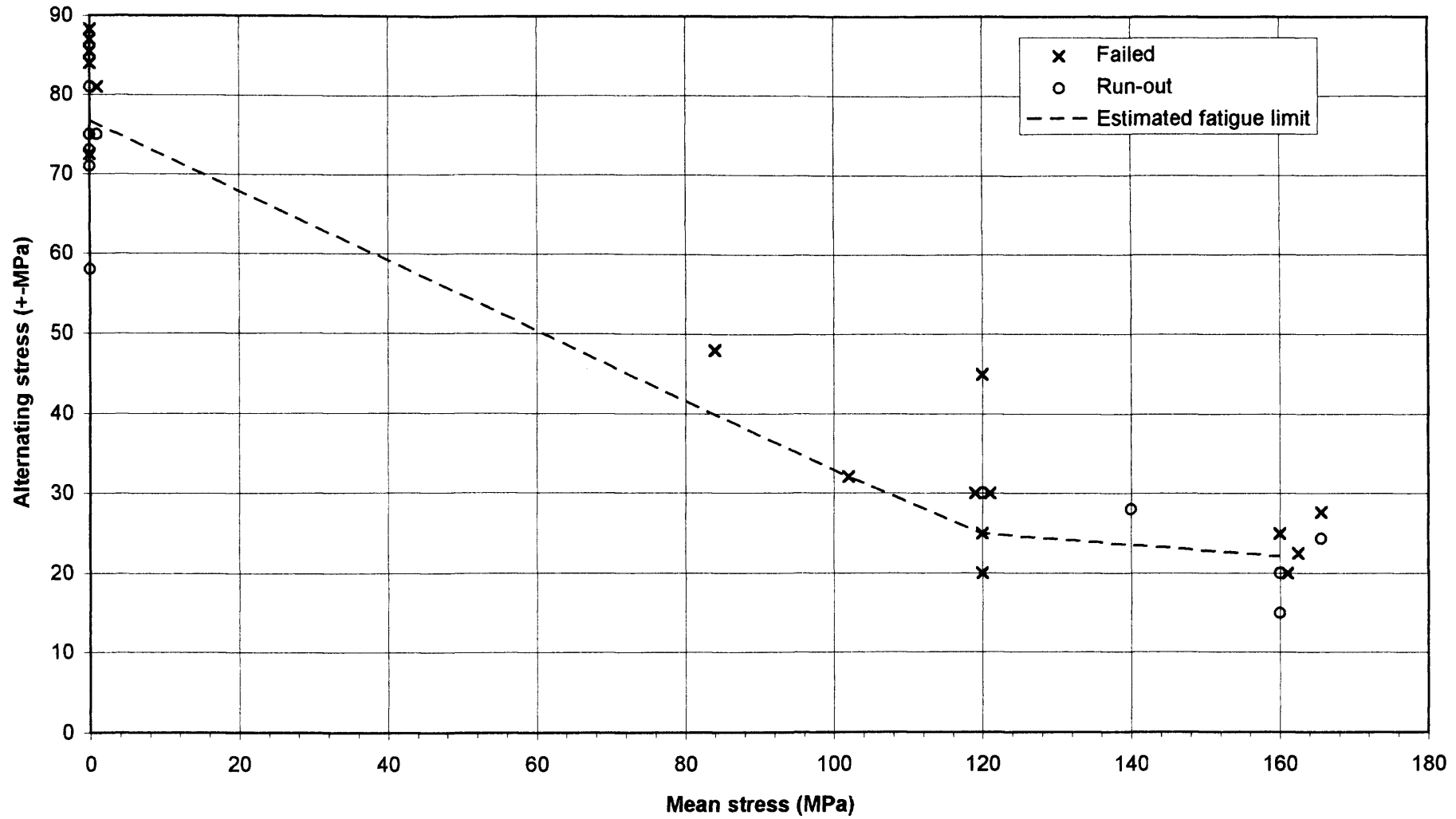


Figure 3.10a Compact tension specimen used for fatigue crack growth threshold tests on grade 17 grey cast iron and other grades cast to 50mm section size

**Figure 3.11 BRITE Project: ENDDURE
Plain Specimen Results - Effect of Mean Stress**



**Figure 3.12 BRITE Project: ENDDURE
Notched Specimen Results (Notch 1, $K_t=2.2$) - Effect of Mean Stress**

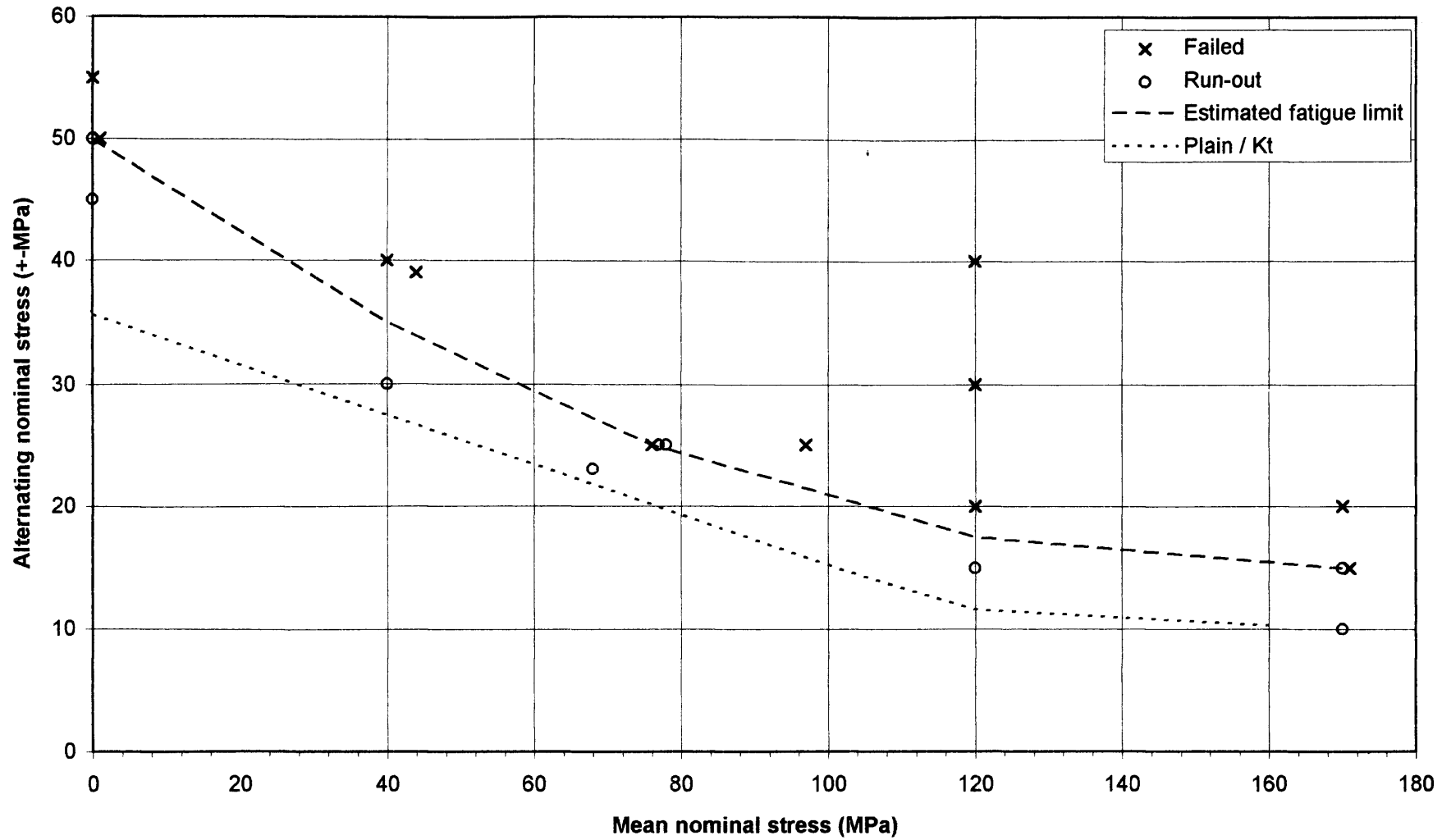


Figure 3.13 BRITE Project ENDDURE
Notched Specimen Results (Notch 2, $K_t=5.6$) - Effect of Mean Stress

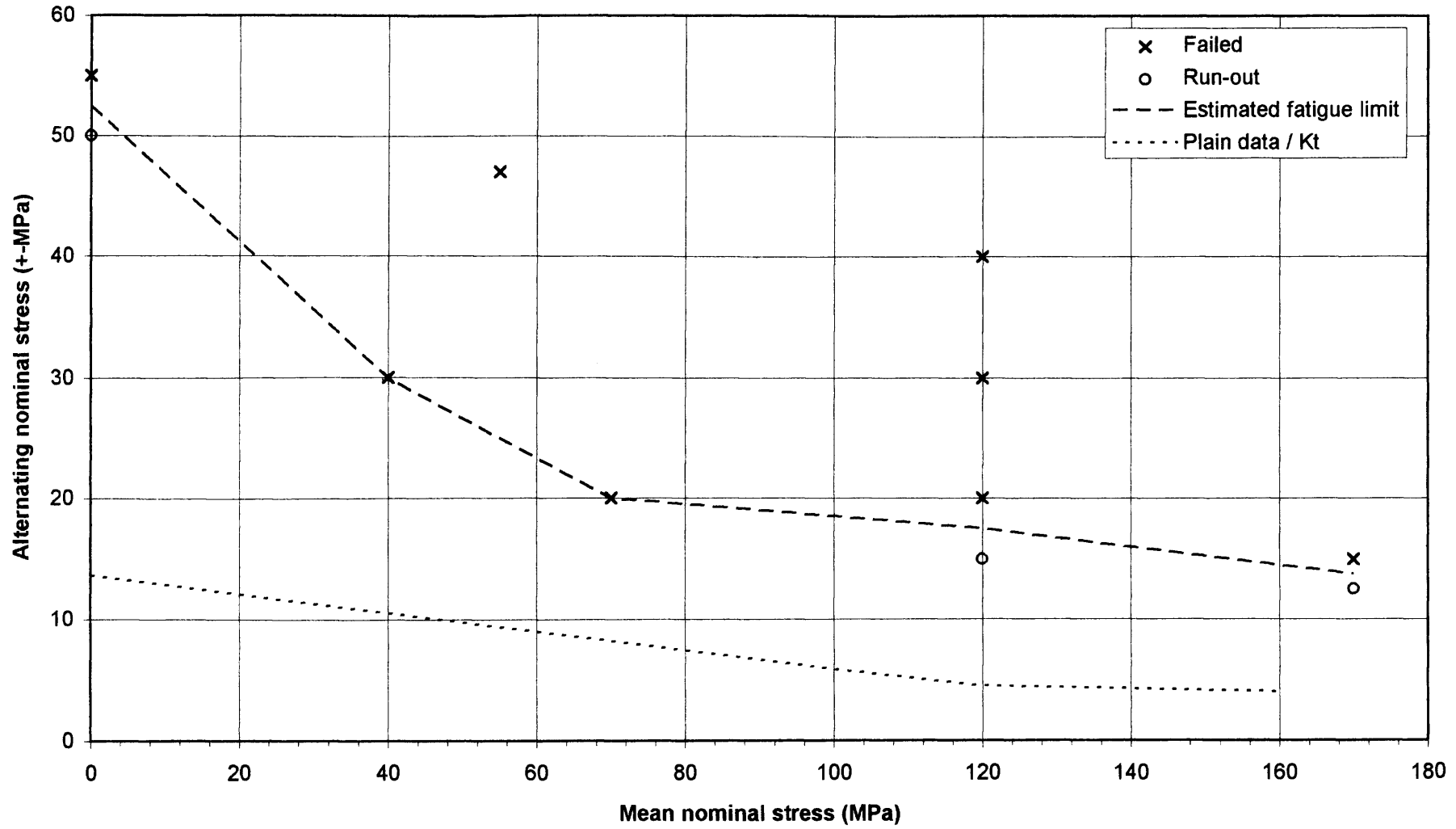


Figure 3.14 BRITE Project: ENDDURE
Simulated Component Results - Effect of Mean Load

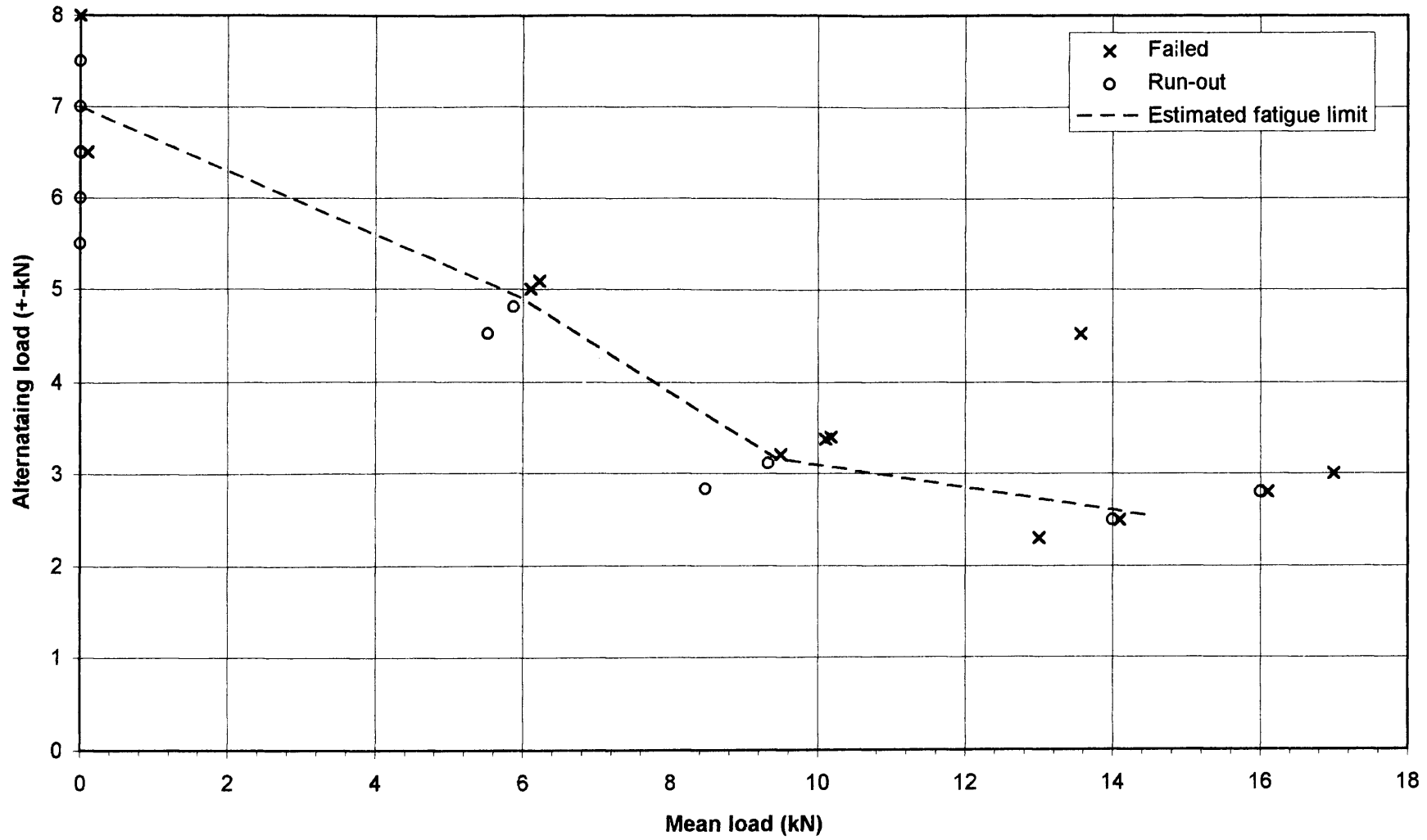


Figure 3.15 BRITE Project: ENDDURE Grey Iron Notched Specimen Results
Effect of Kt on Estimated Fatigue Strength (R=-1)

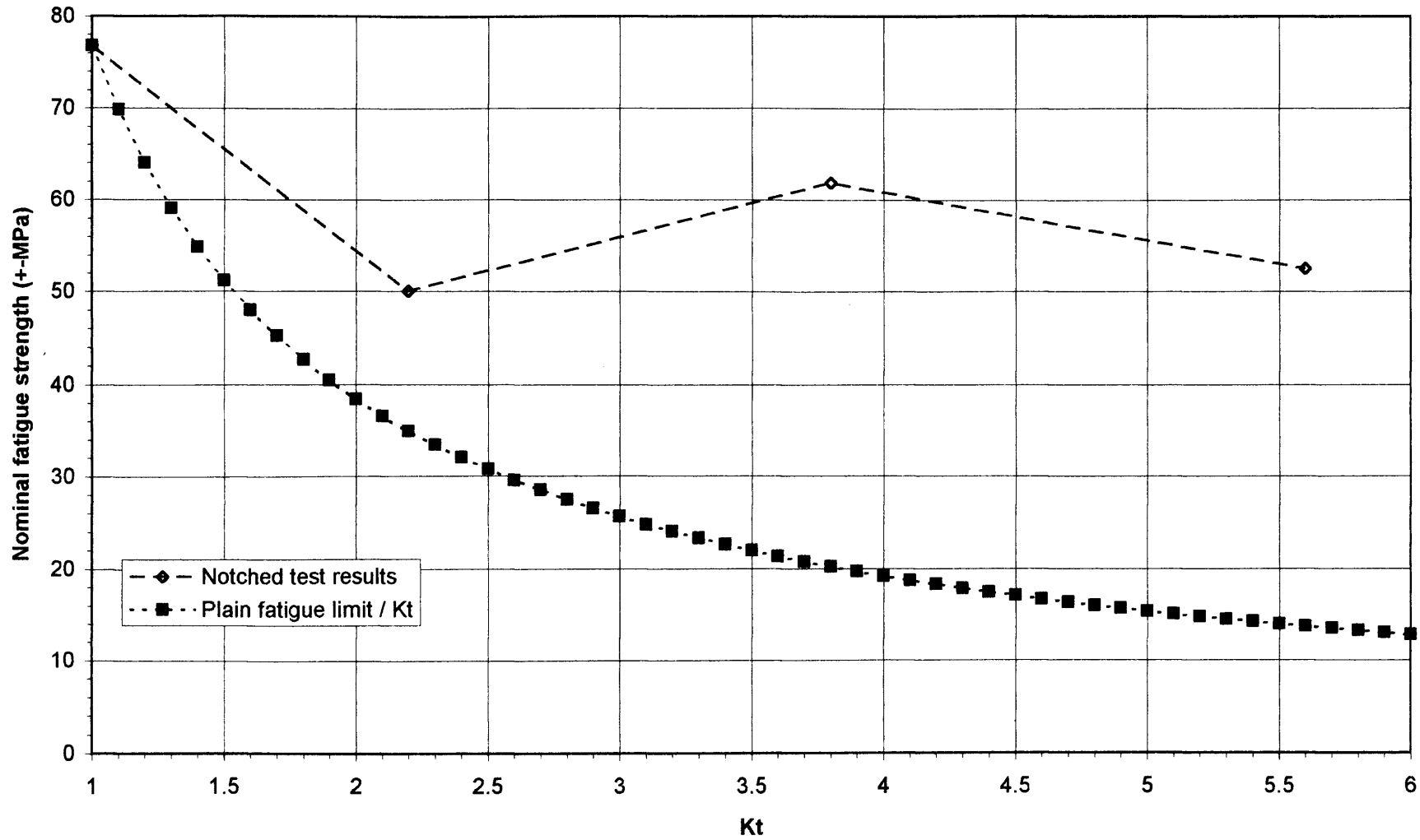


Figure 3.16 Grade 17 Grey Iron: Distribution of Tensile Strength Values

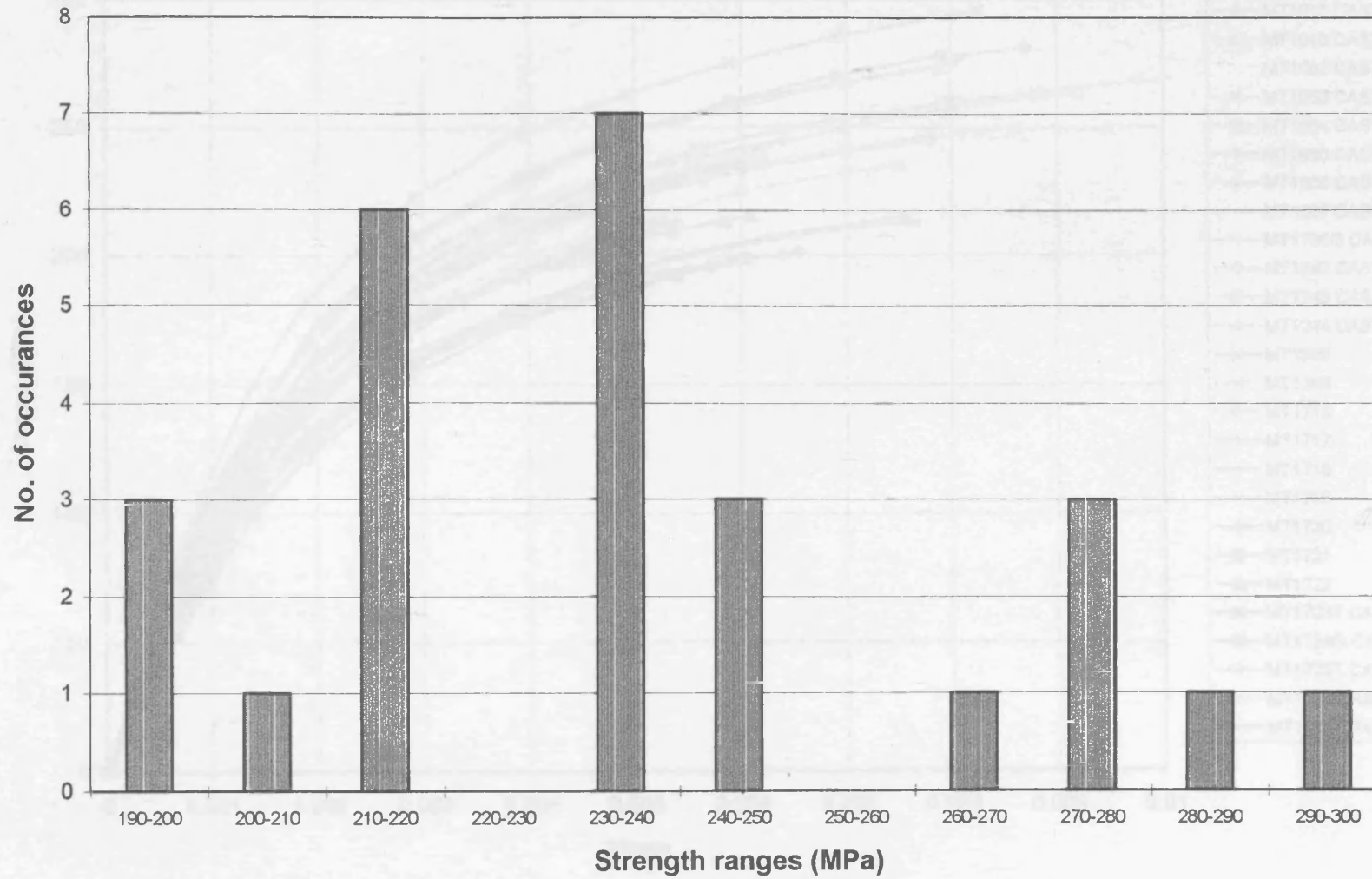


Figure 3.17 Grade 17 Grey Iron: Stress versus strain curves for monotonic loading

Stress normalized with respect to stress from Ramberg-Osgood curve fit at 0.002 strain = 0.005

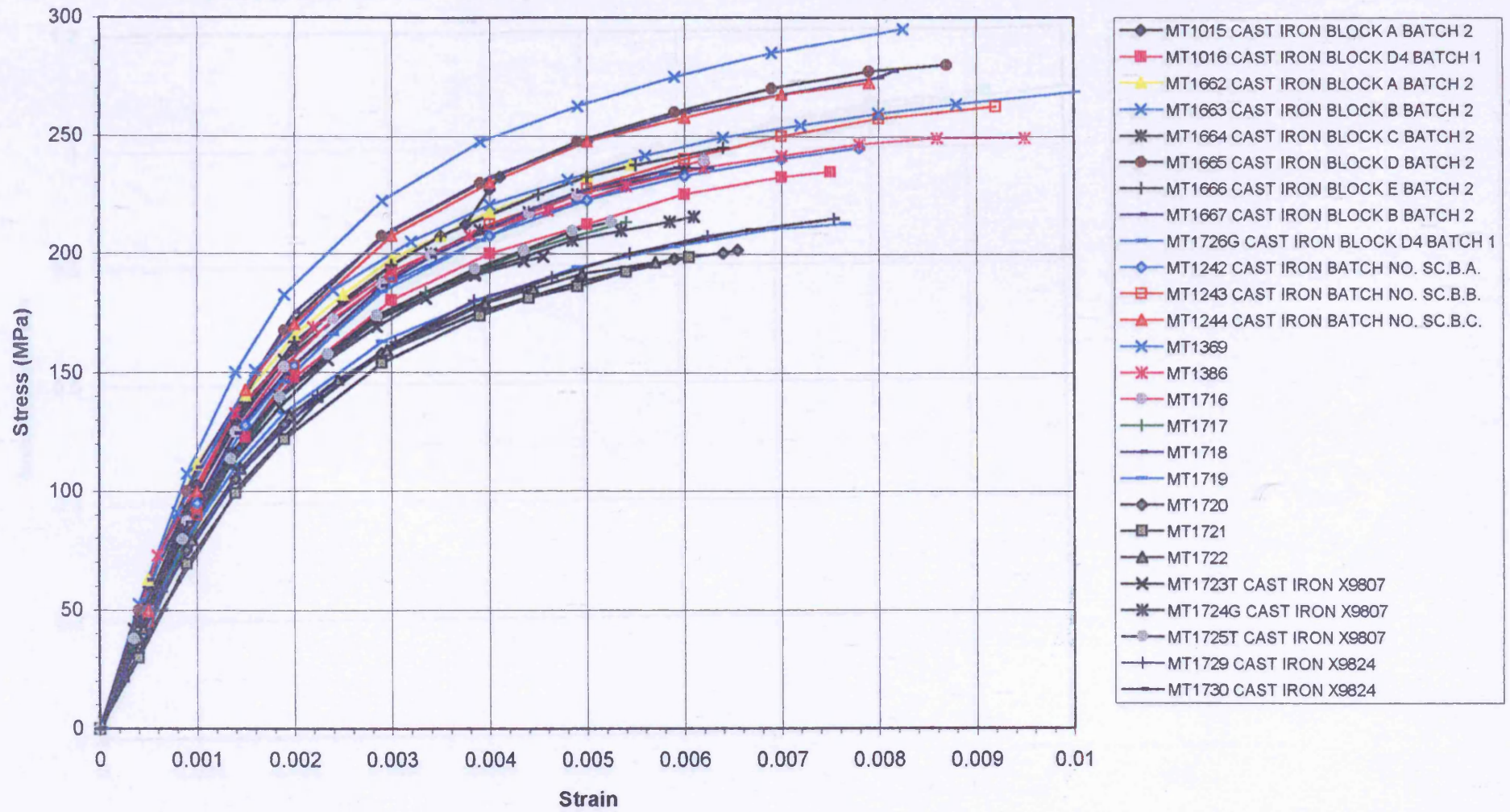


Figure 3.18 Grade 17 Grey Iron: Stress versus strain curves
 - Stress normalised with respect to stress from Ramberg-Osgood curve fit at a strain = 0.006

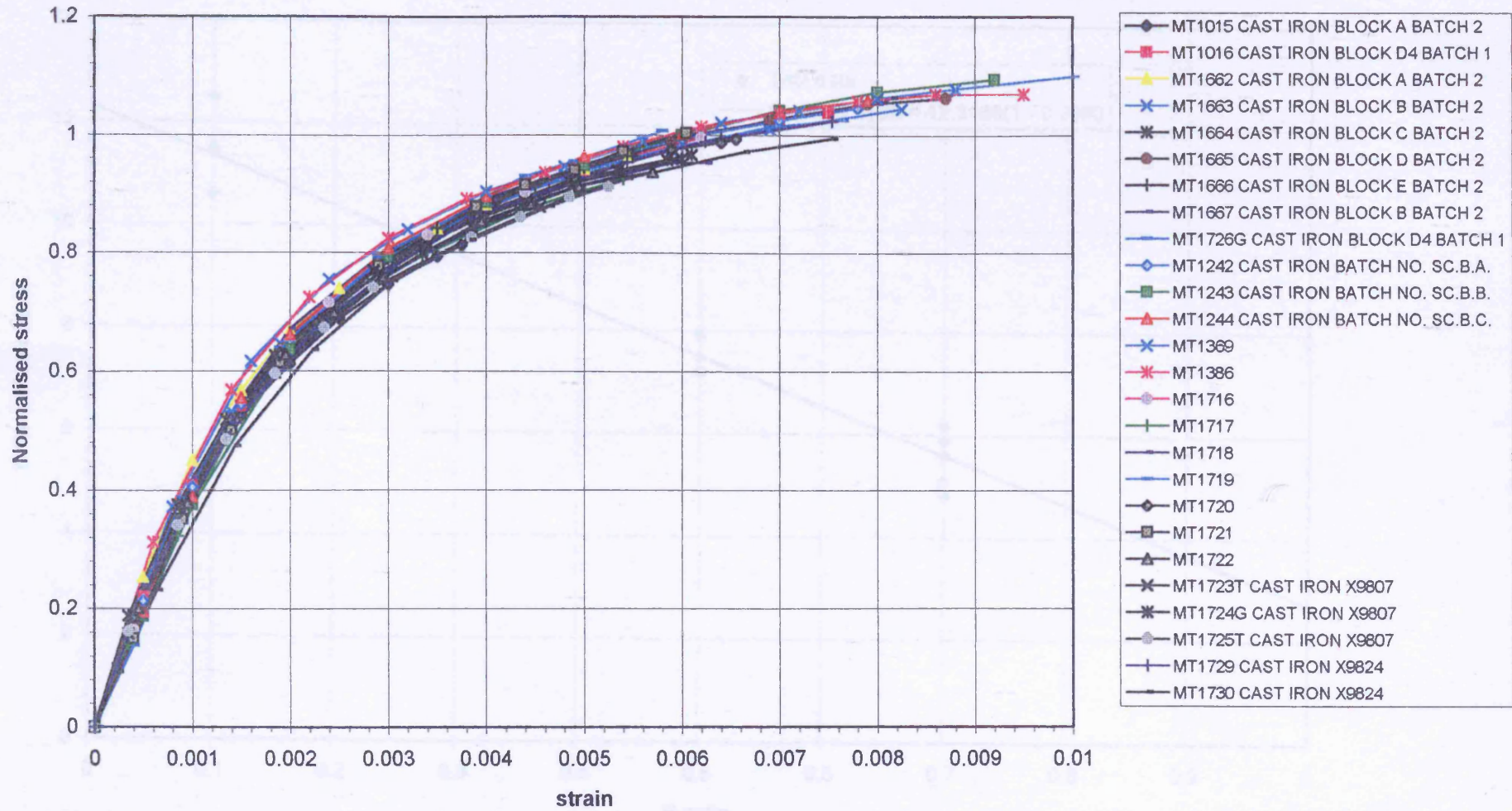
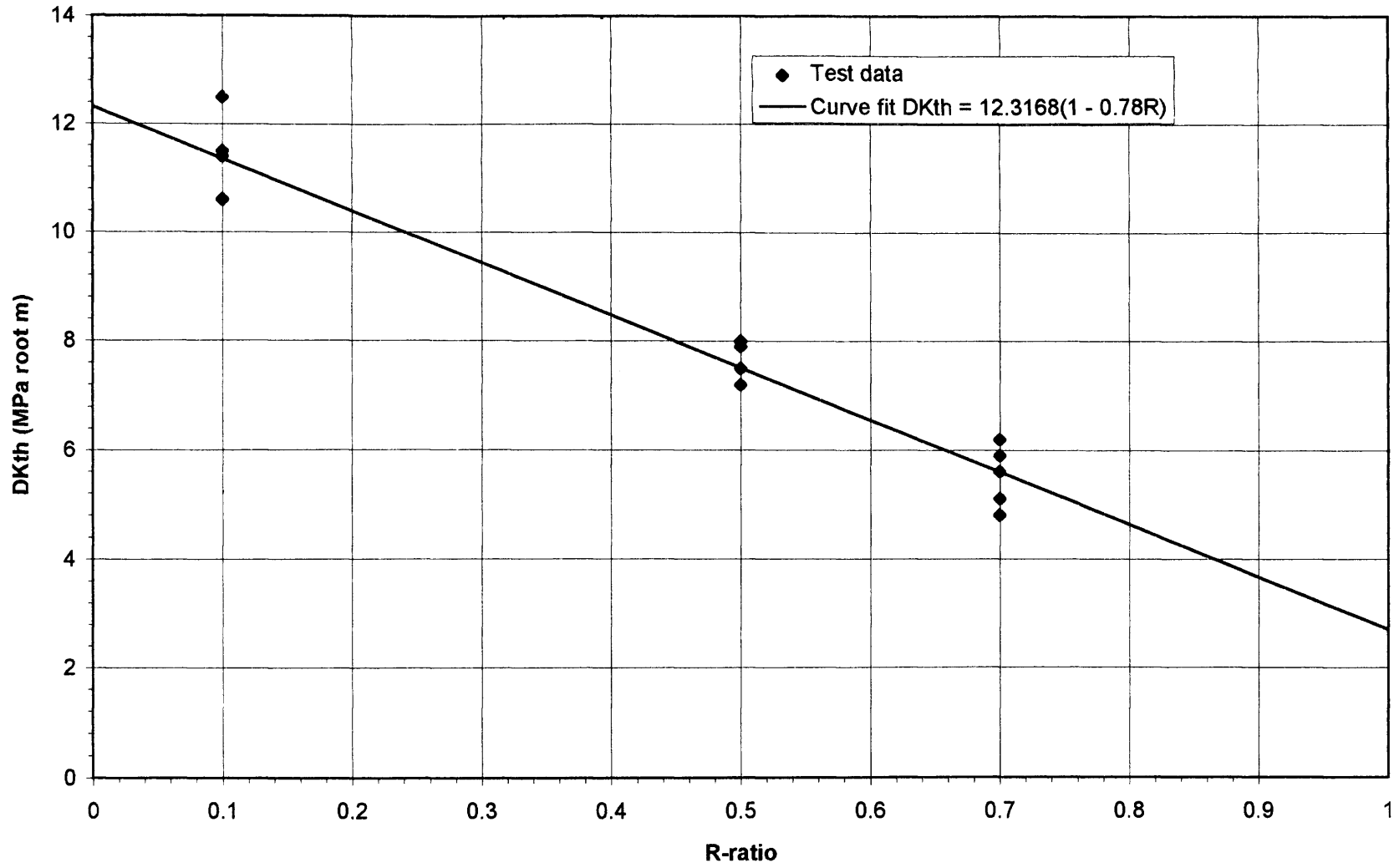


Figure 3.19 Grade 17 Grey Iron: Crack Growth Threshold Test Results and Curve Fit



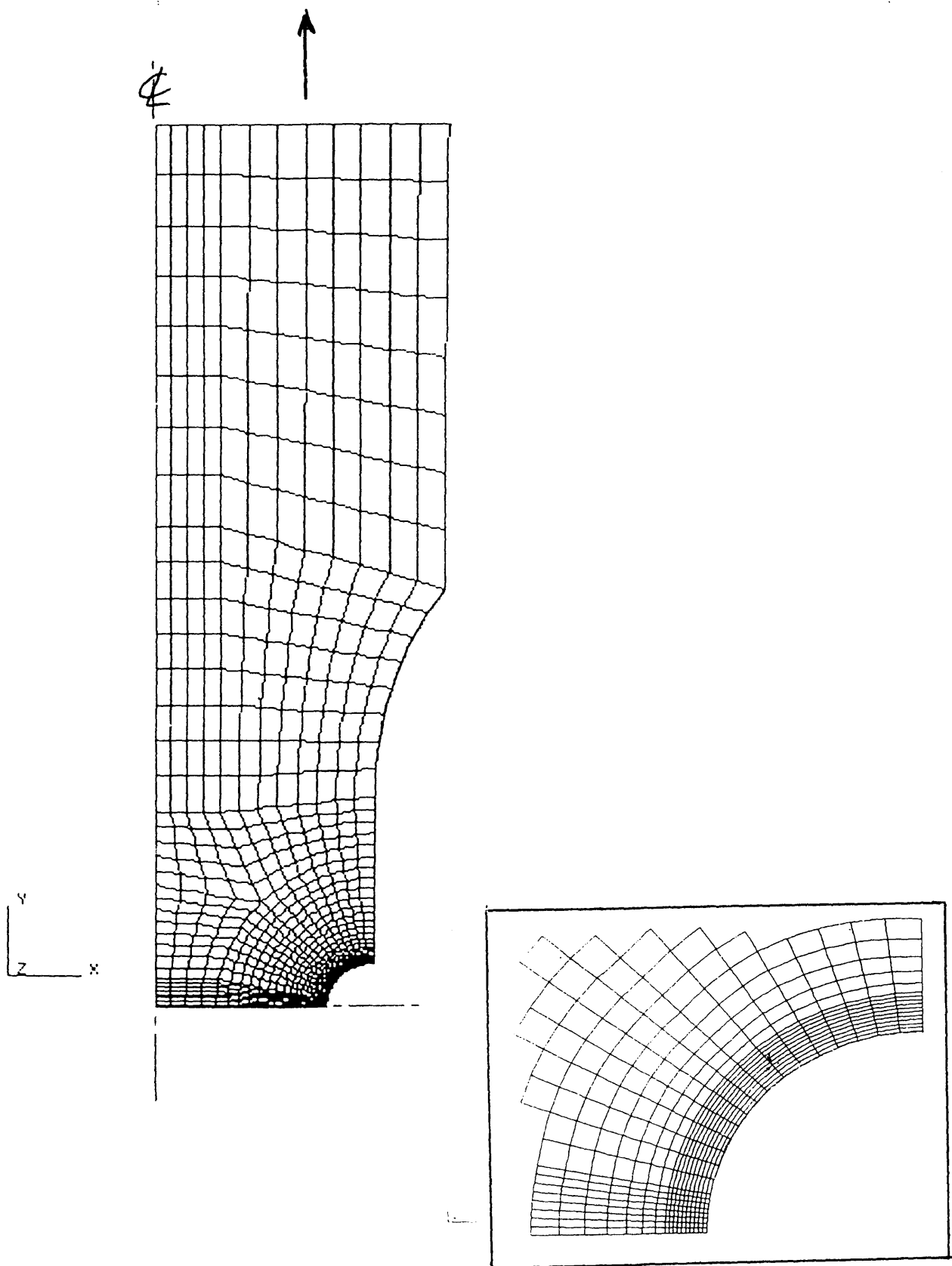


Figure 3.20 Finite element idealisation of BRITE circumferentially notched test specimen (Notch 1, $K_t = 2.2$)

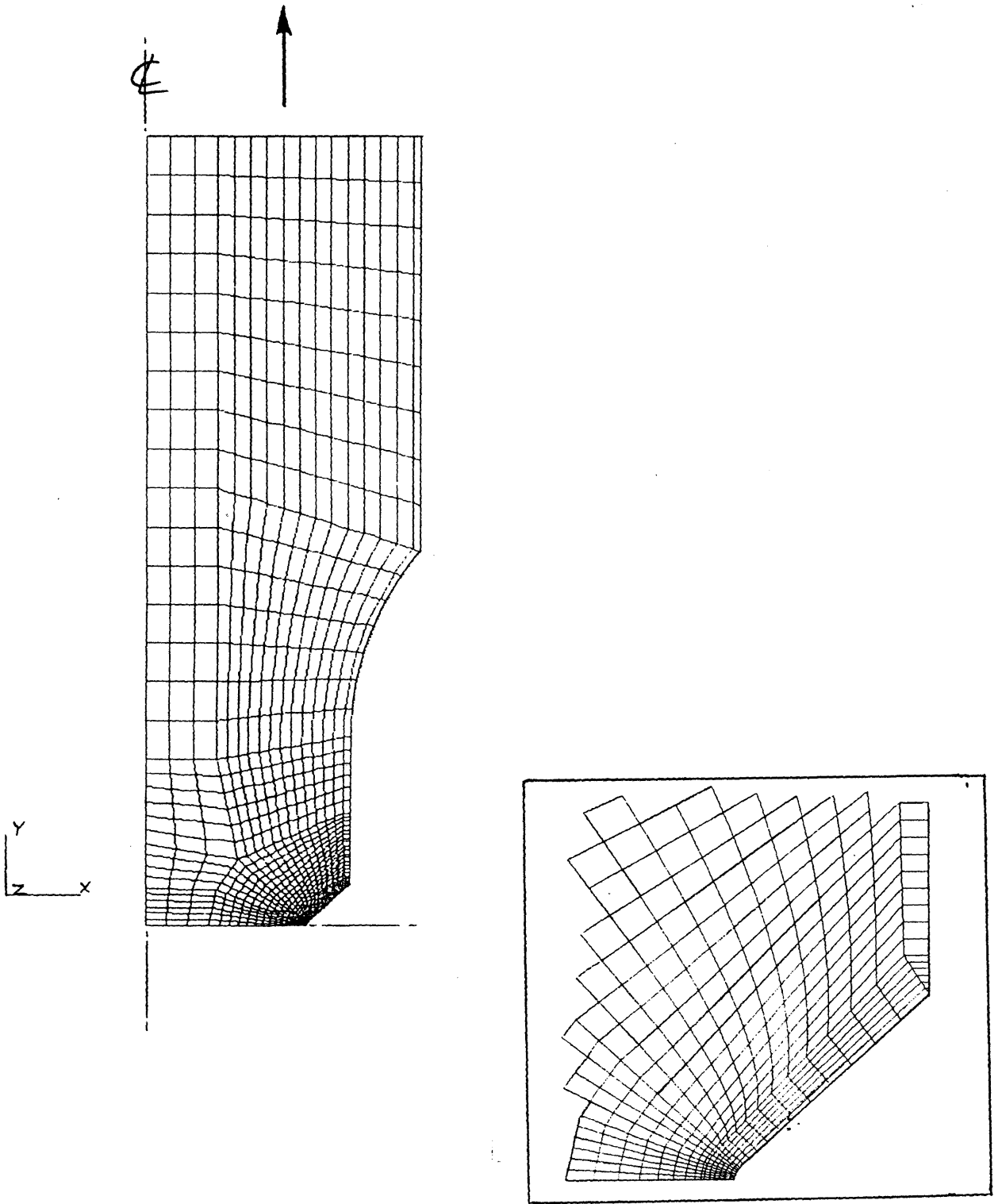


Figure 3.21 Finite element idealisation of BRITE circumferentially notched test specimen (Notch 2, $K_t = 5.6$)

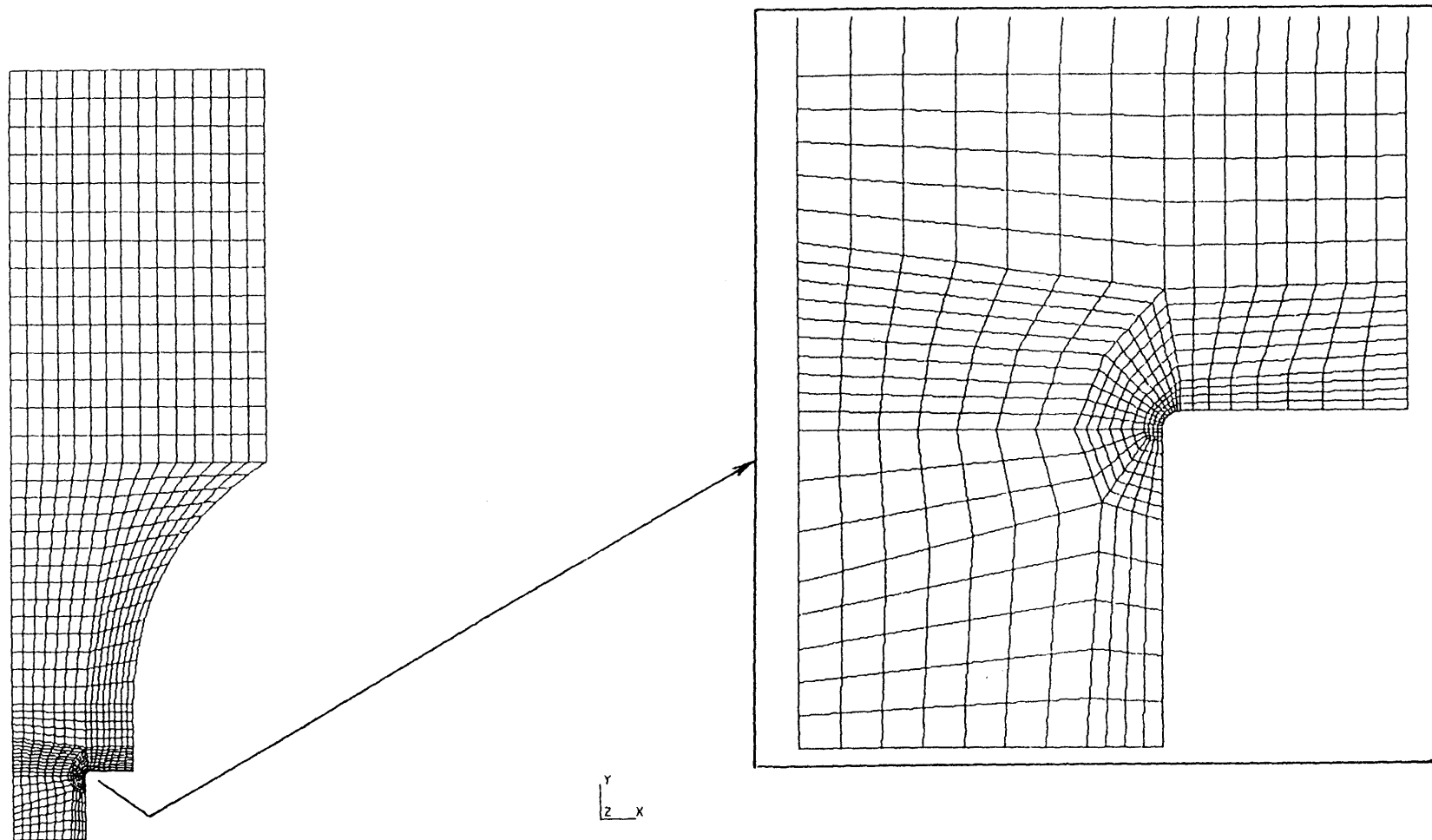


Figure 3.22 Finite element idealisation of BRITE
'Simulated Component' test specimen ($K_t = 3.8$)

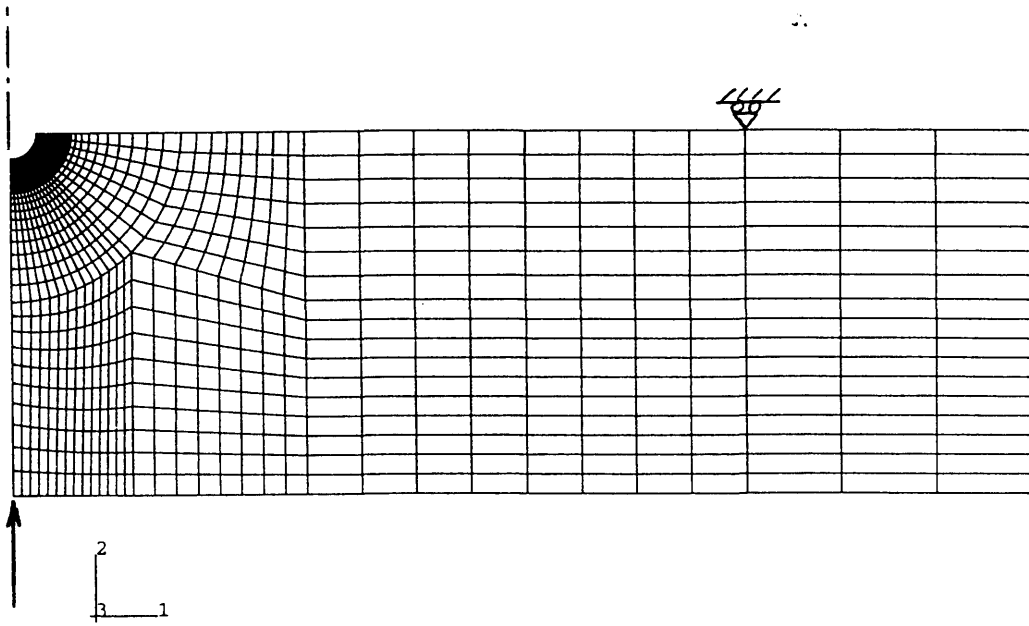


Figure 3.23 Finite element idealisation of three-point bending notched test specimen (Bend 1, $K_t = 2.4$)

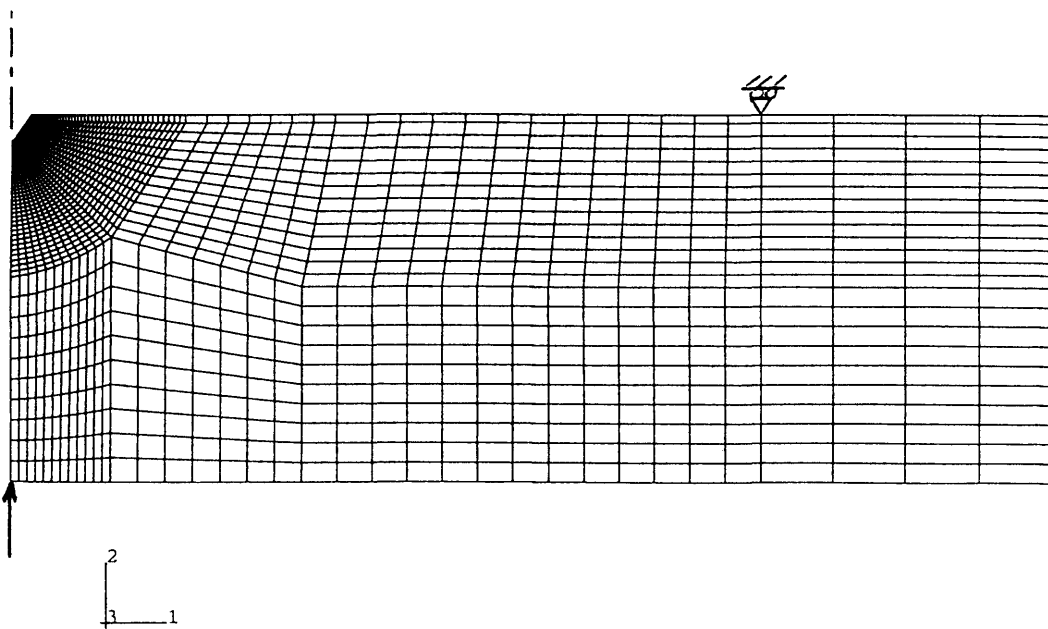


Figure 3.24 Finite element idealisation of three-point bending notched test specimen (Bend 2, $K_t = 6.3$)

**Figure 3.25 BRITE Project ENDDURE: Grade 17 Grey Cast Iron
Piecewise-Linear Fits to Typical Measured Stress-Strain Curves**

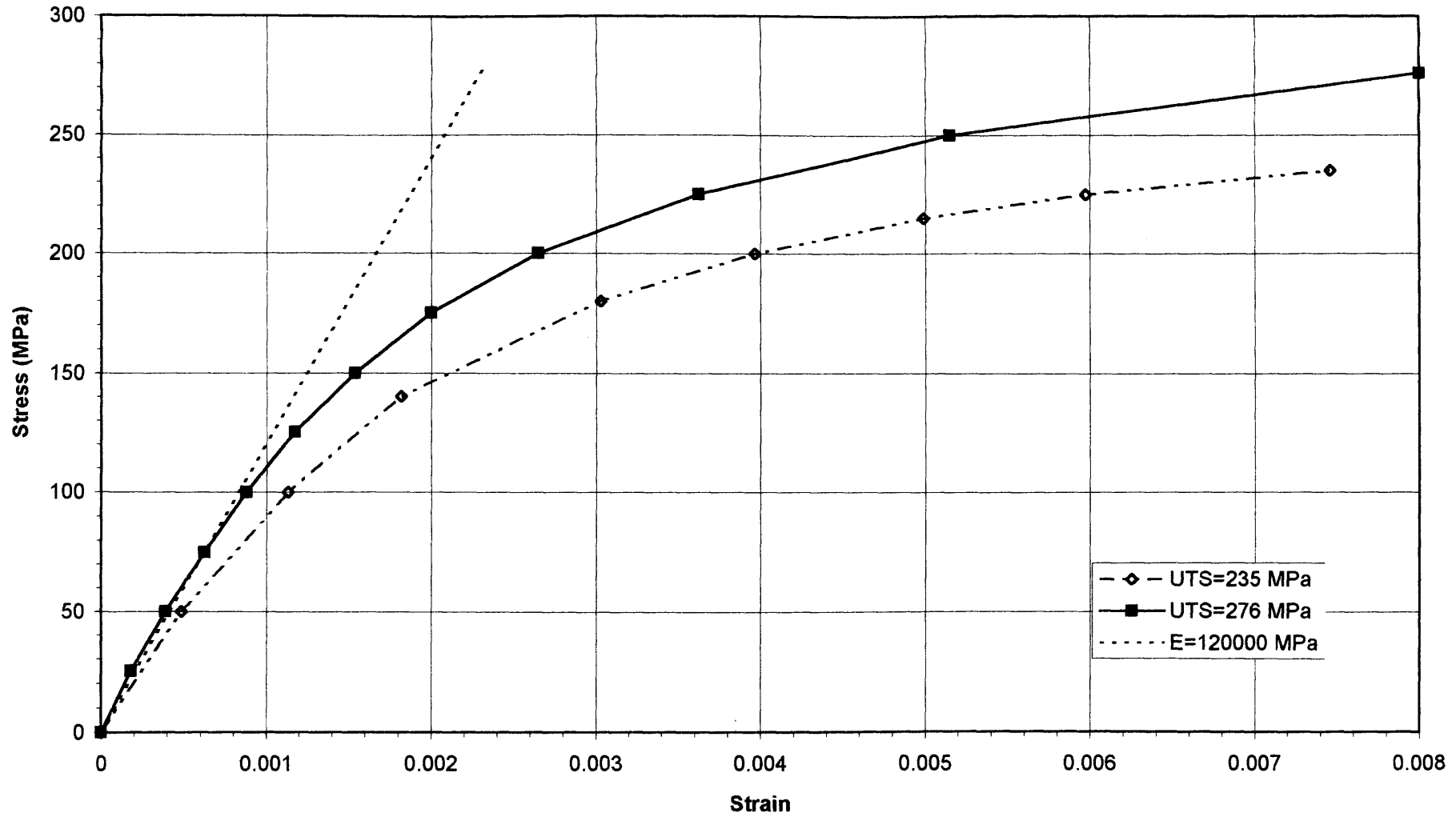


Figure 3.26 BRITE Axially Loaded Notched Specimens: Comparison of Stress Distributions
 Nominal Stress = 140 MPa Notch1: $K_t=2.2$, Notch2: $K_t = 5.6$, Component: $K_t=3.8$

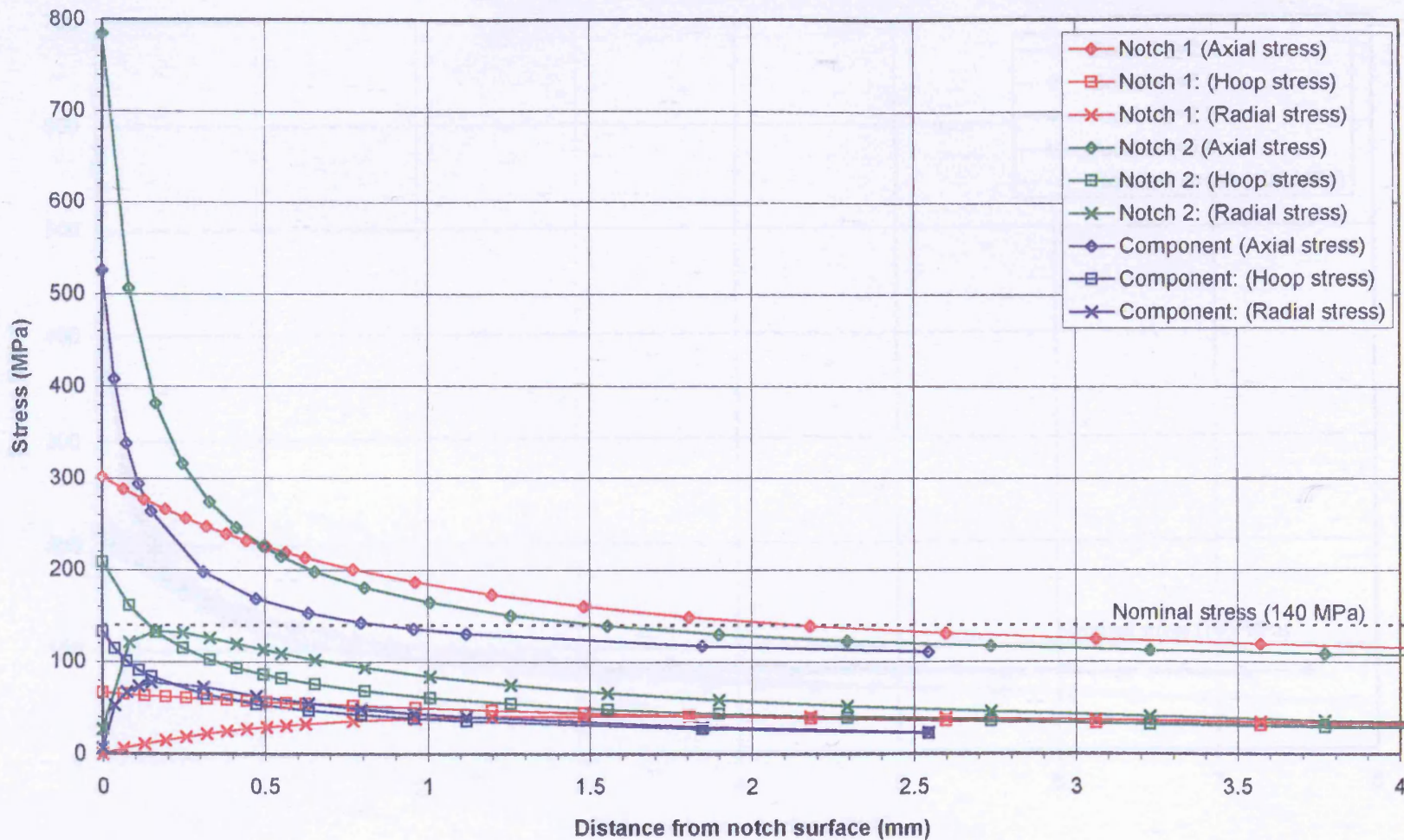
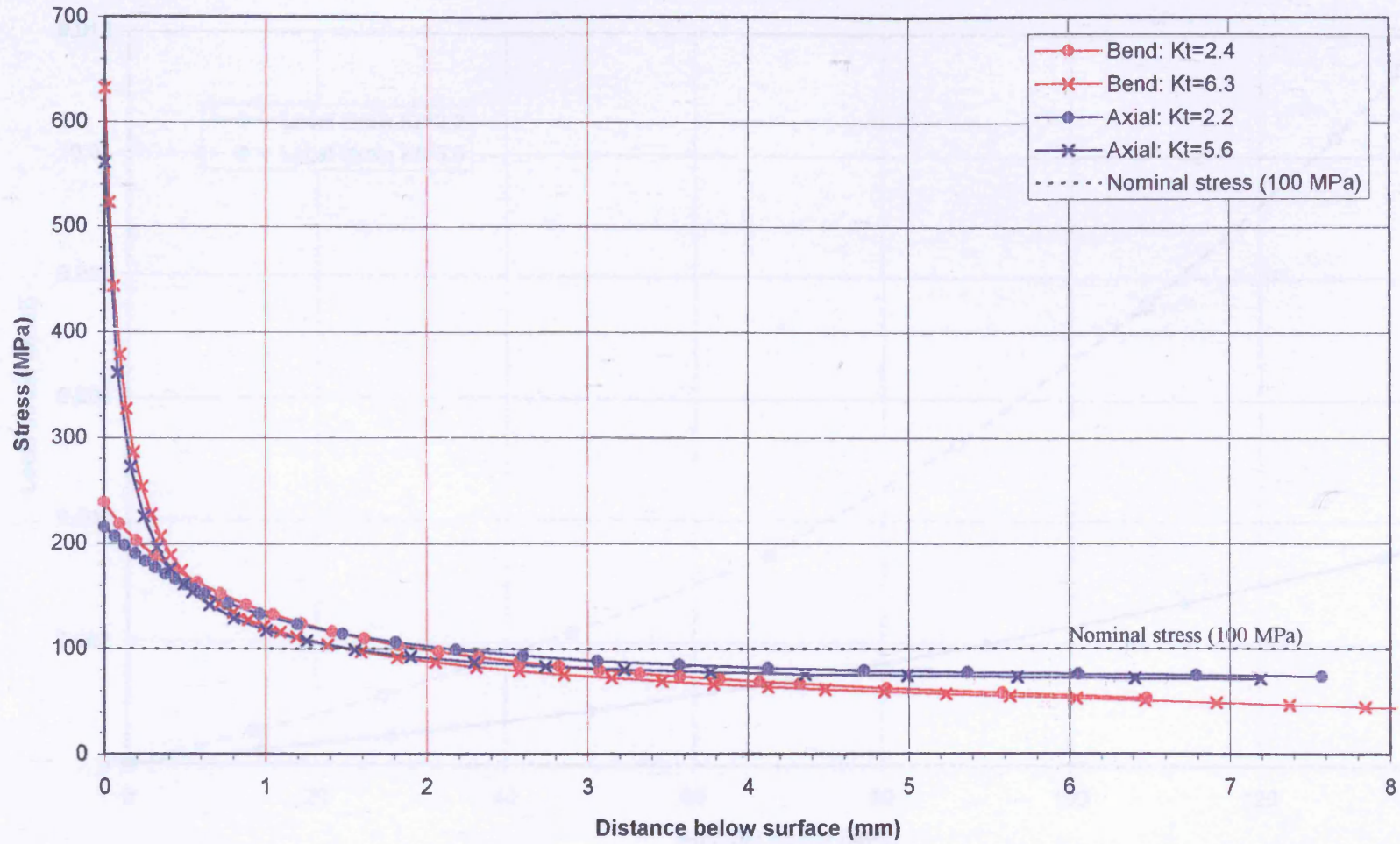
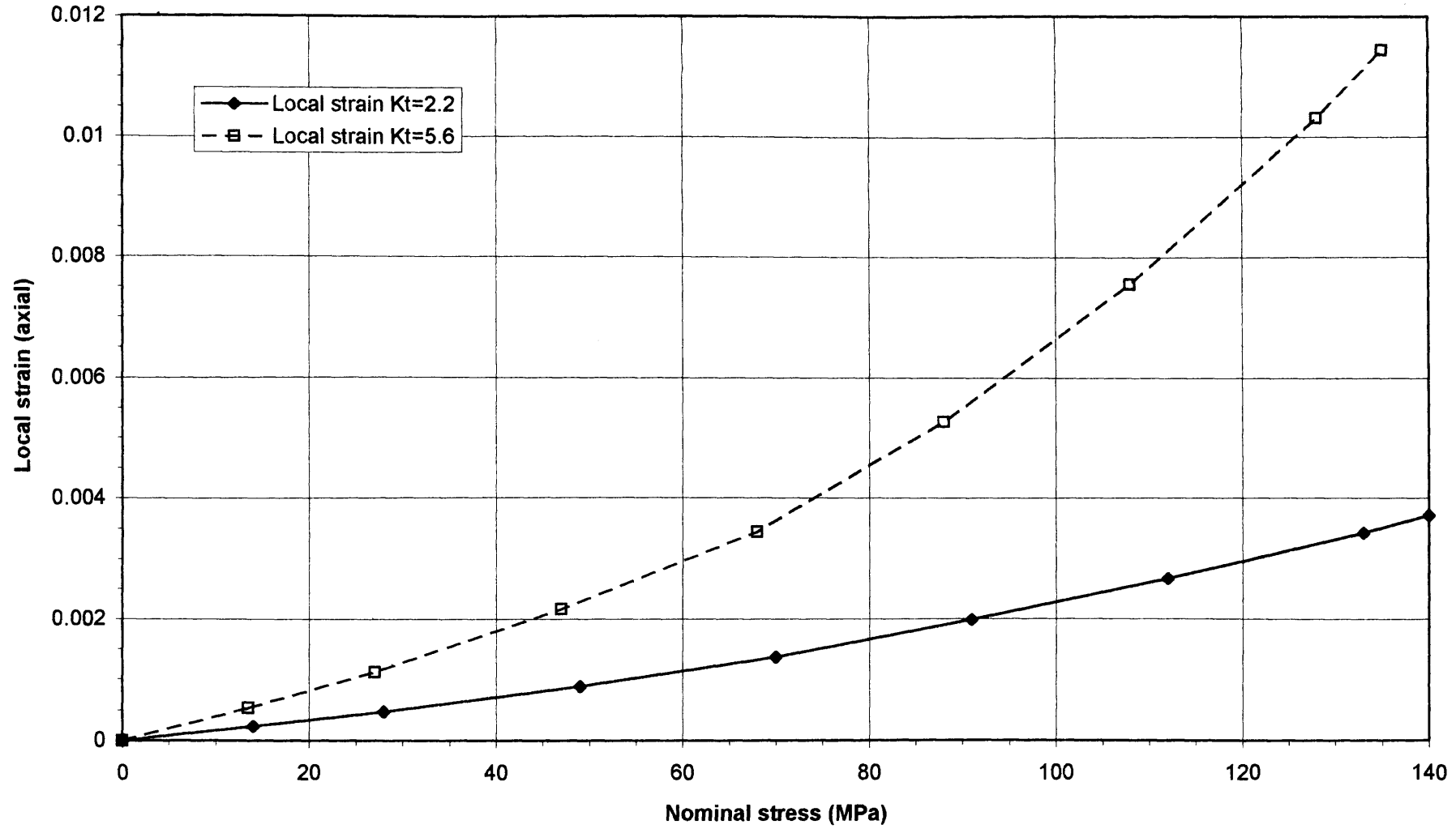


Figure 3.27 BRITE Notched Specimens: Comparison of Stress Distributions
Three-Point Bend and Axial Configurations ($S_{nom} = 100$ MPa)



**Figure 3.28 BRITE Project ENDDURE: Grade 17 Grey Cast Iron Notched Specimens
Predicted Local Strain at Notch Root Versus Nominal Stress (235 MPa UTS curve)**



**Figure 3.29 BRITE Project ENDDURE: Grade 17 Grey Cast Iron Notched Specimens
Predicted Local Stress at Notch Root Versus Nominal Stress (235 MPa UTS curve)**

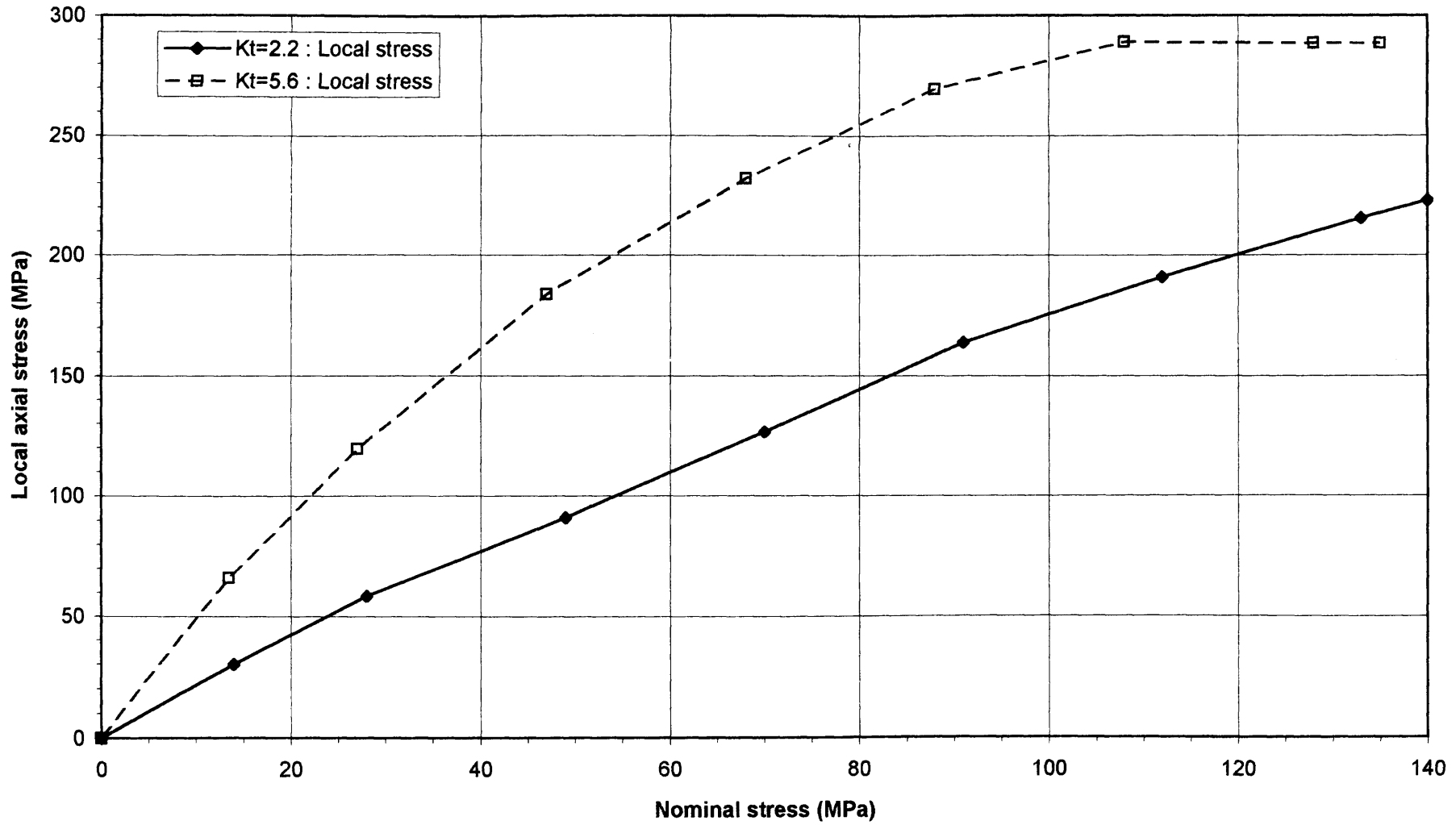
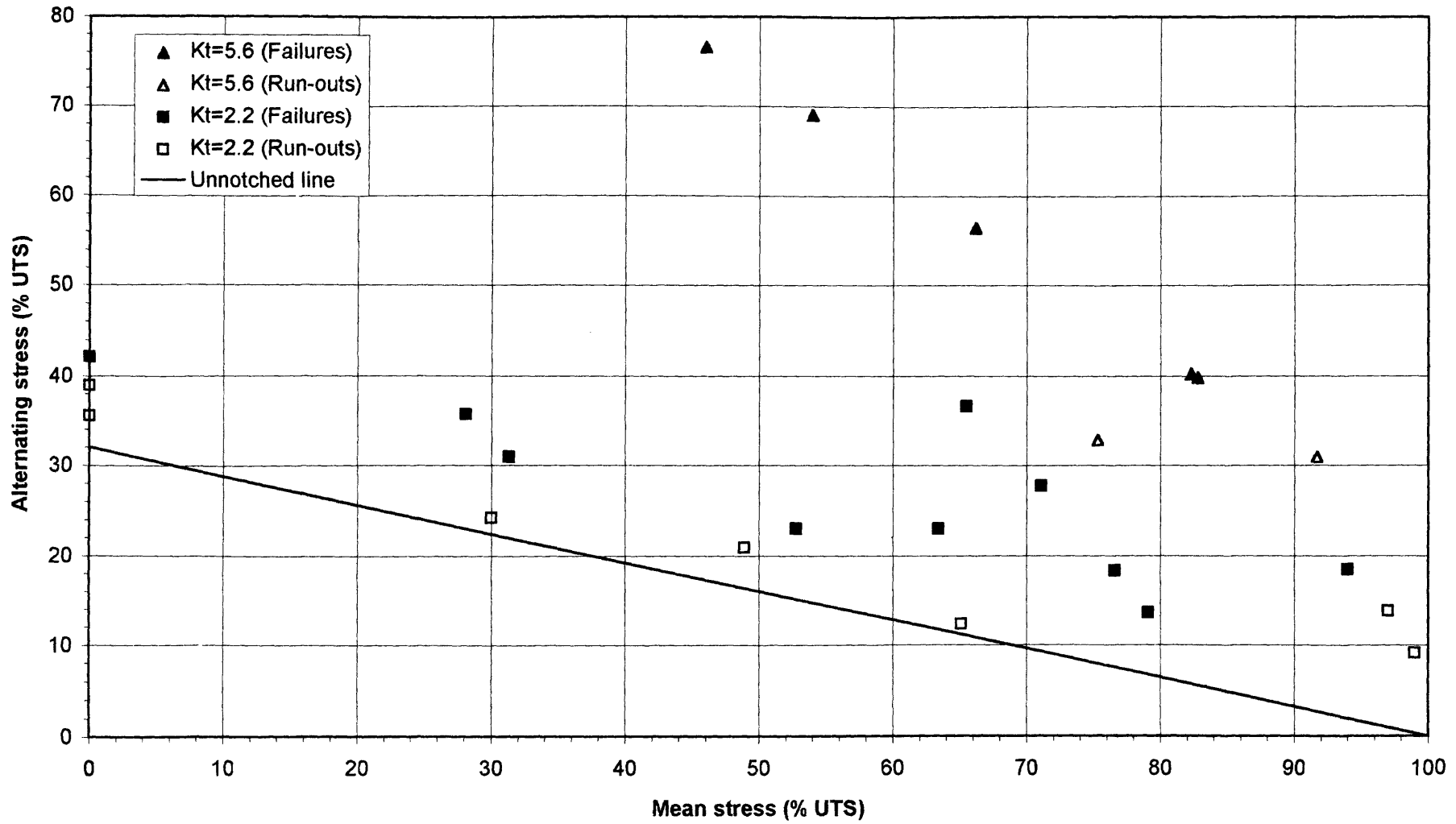
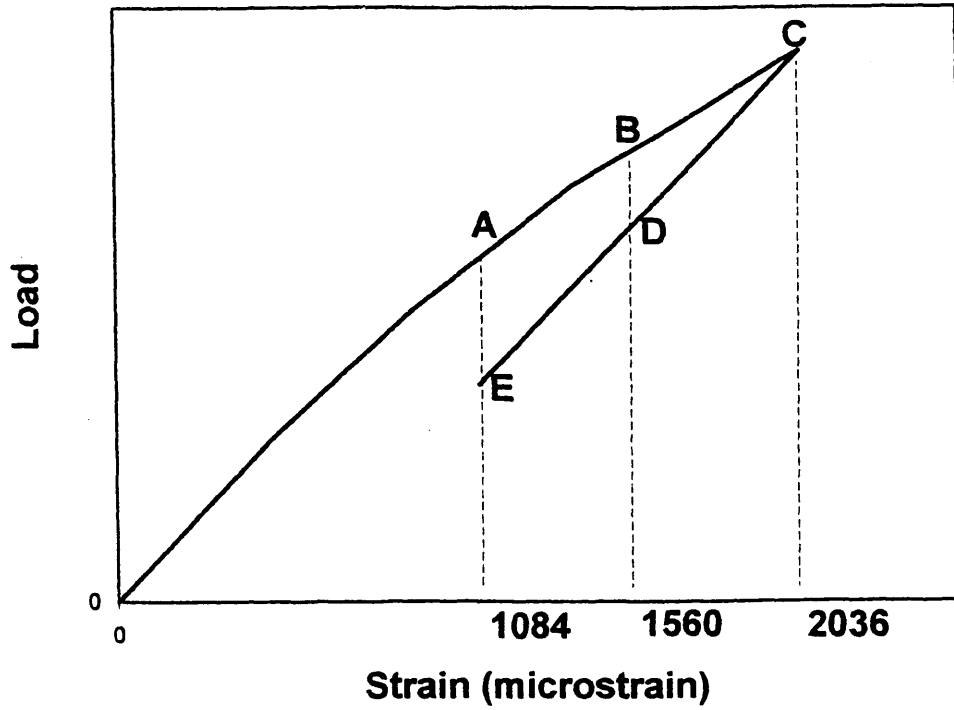


Figure 3.30 BRITE Notched Specimens (Grade 17 Grey Cast Iron)
Local Inelastic Stresses Plotted on a Goodman Diagram (Normalised by UTS)

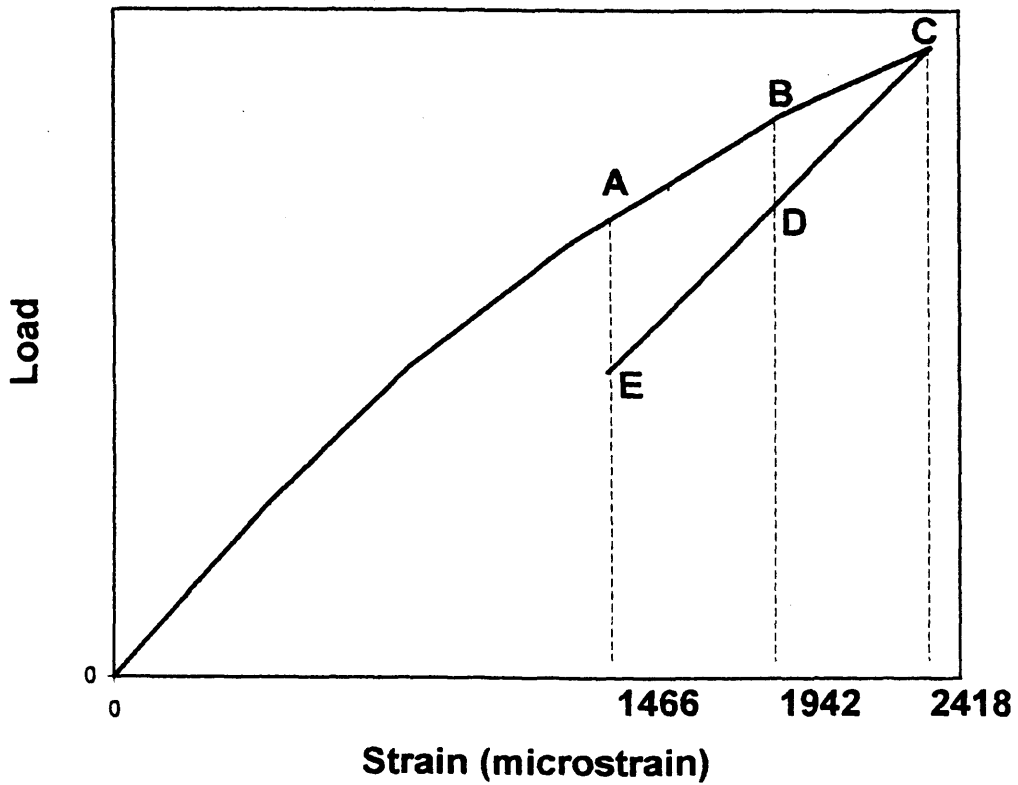


(a) Low magnitude strain test
(simulation of 17 thou bolt stretch)



STRAIN.XLS

(b) High magnitude strain test
(simulation of 23 thou bolt stretch)



STRAIN.XLS

Figure 3.32

Figure 3.33 Stress-strain curves for the 235 MPa and 275 MPa material strengths (Piecewise linear approximations for FE analysis)

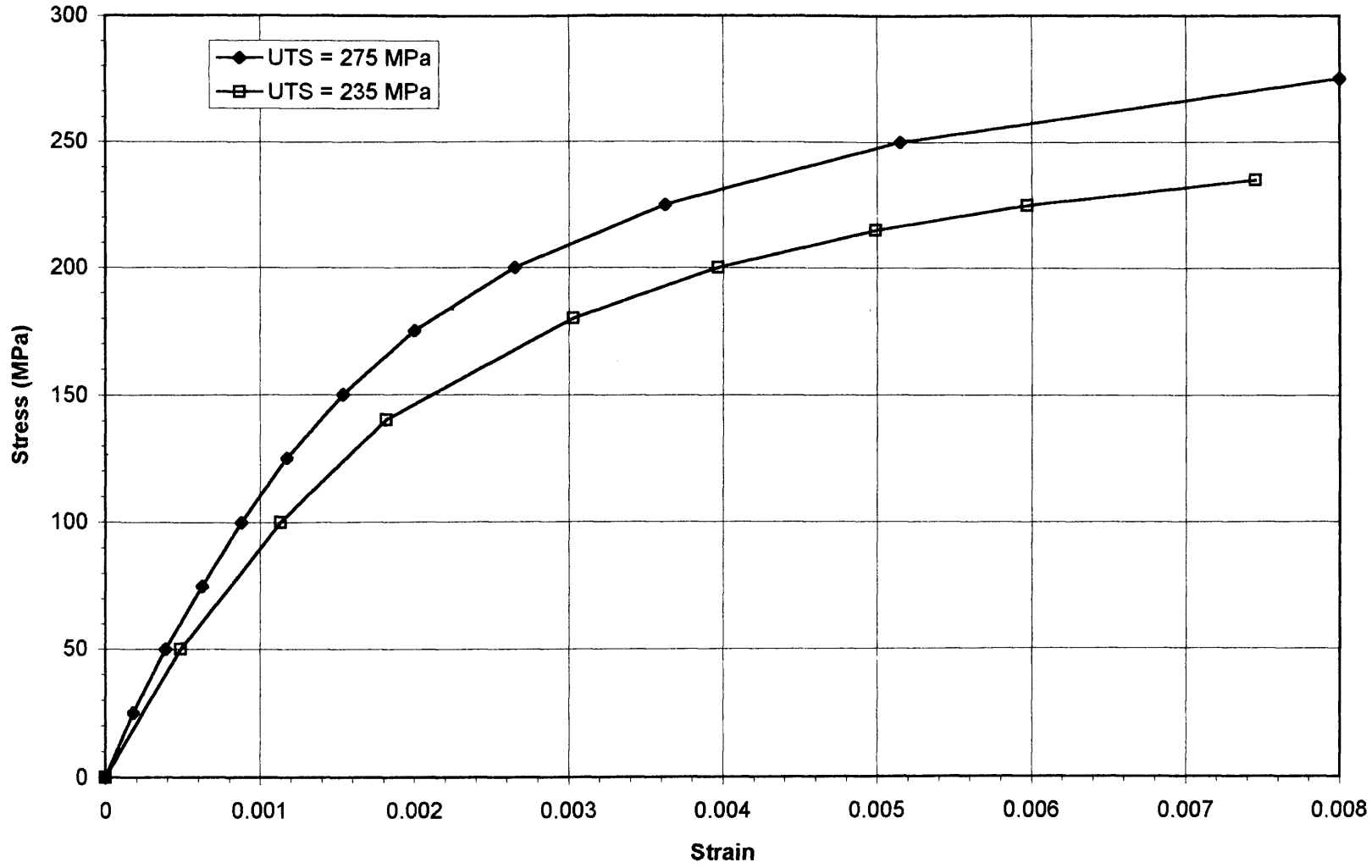


Figure 3.34 Comparison of nominal stress v. strain curves from test and FE calculation for 1/8th in. notch radius specimen cycled between fixed strain limits - Simulation of 17 thou bolt stretch in engine

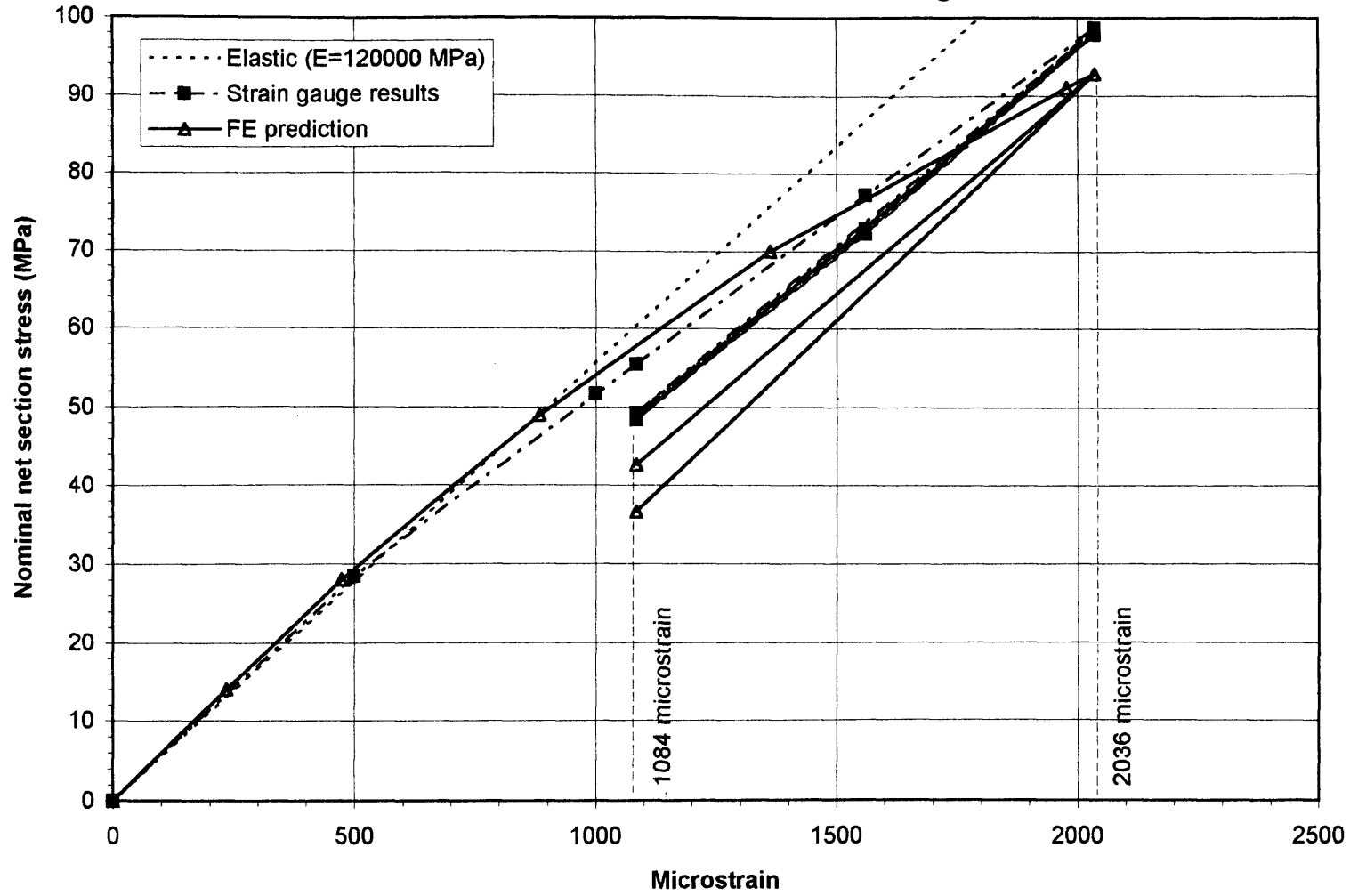


Figure 3.35 Comparison of nominal stress v. strain curves from test and FE calculation for 1/8th in. notch radius specimen cycled between fixed strain limits - Simulation of 23 thou bolt stretch in engine

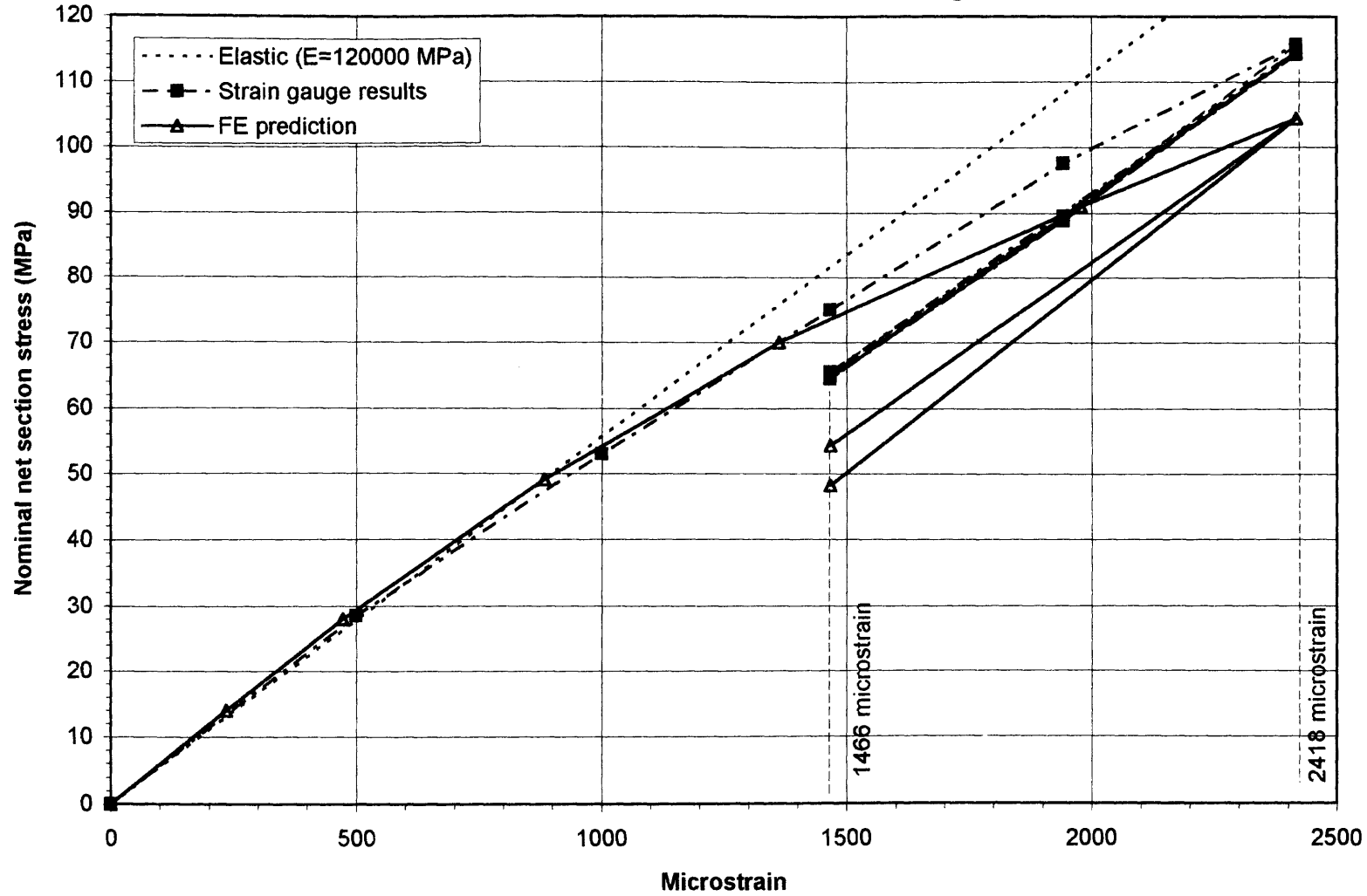
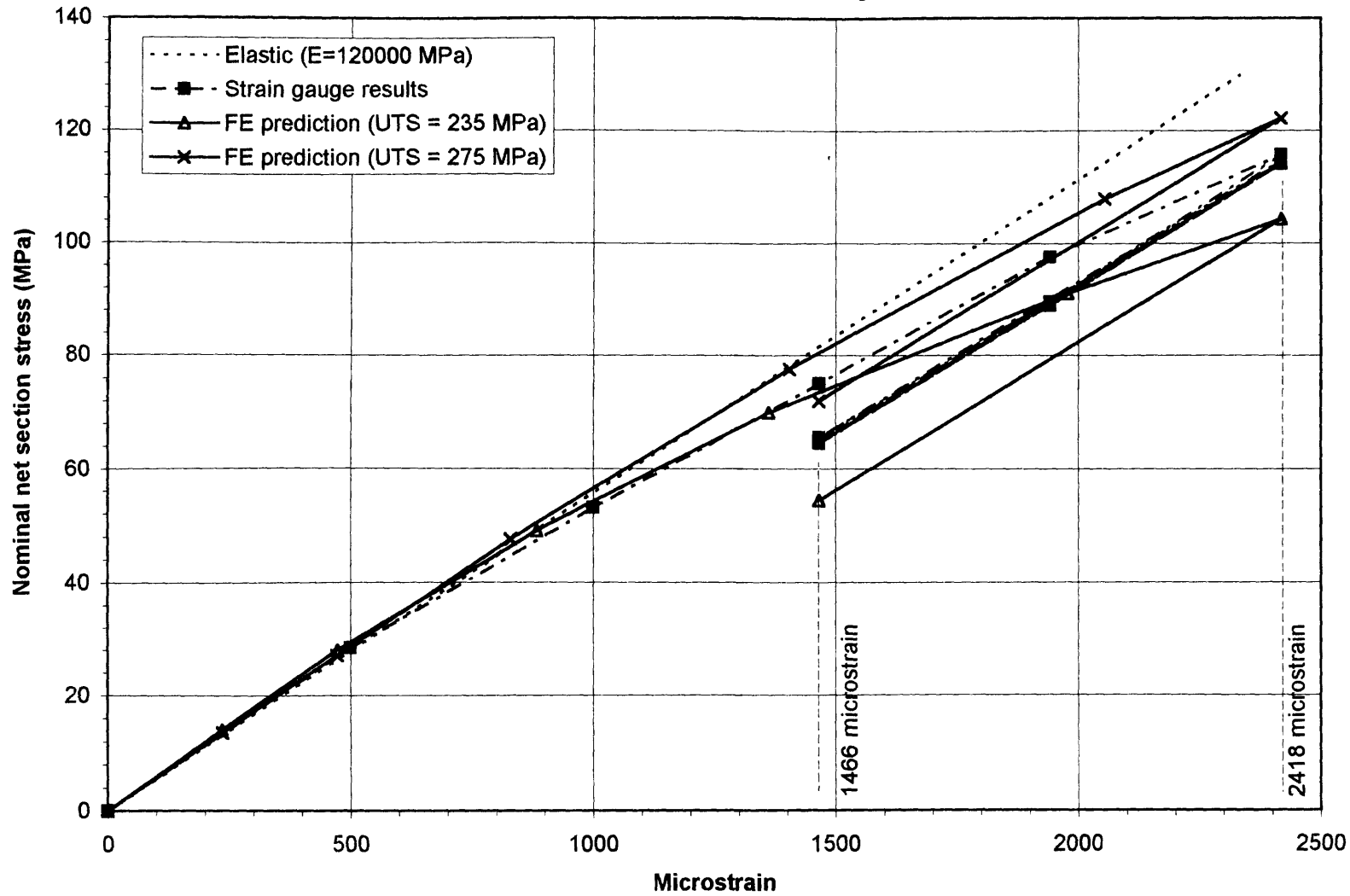
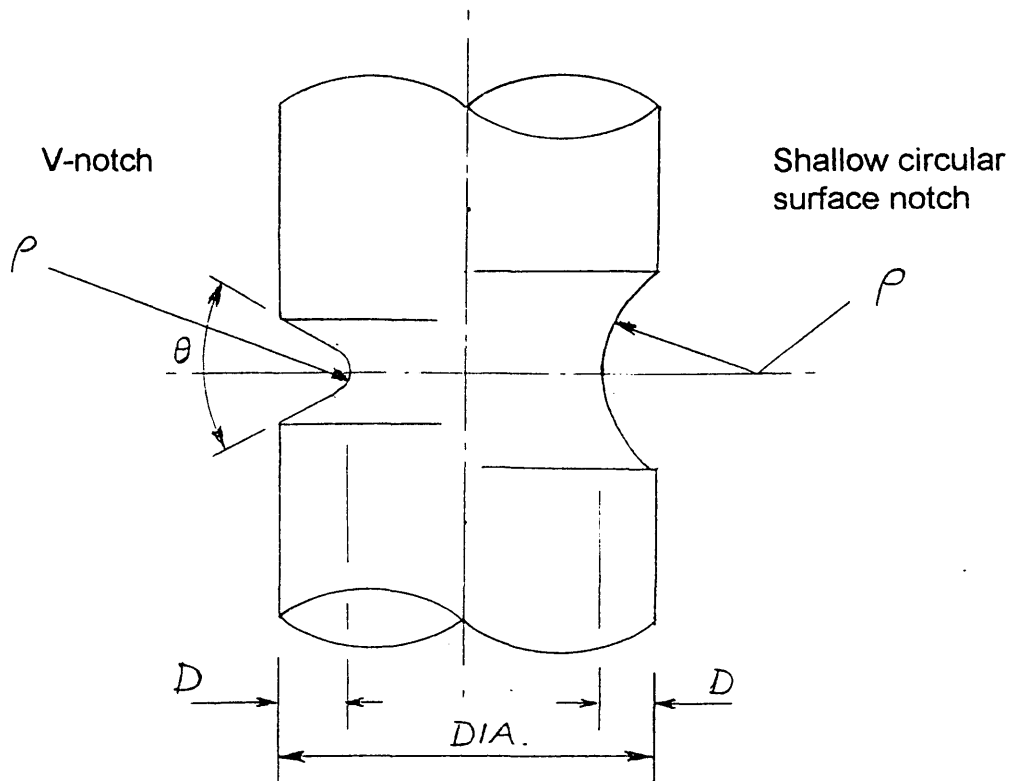


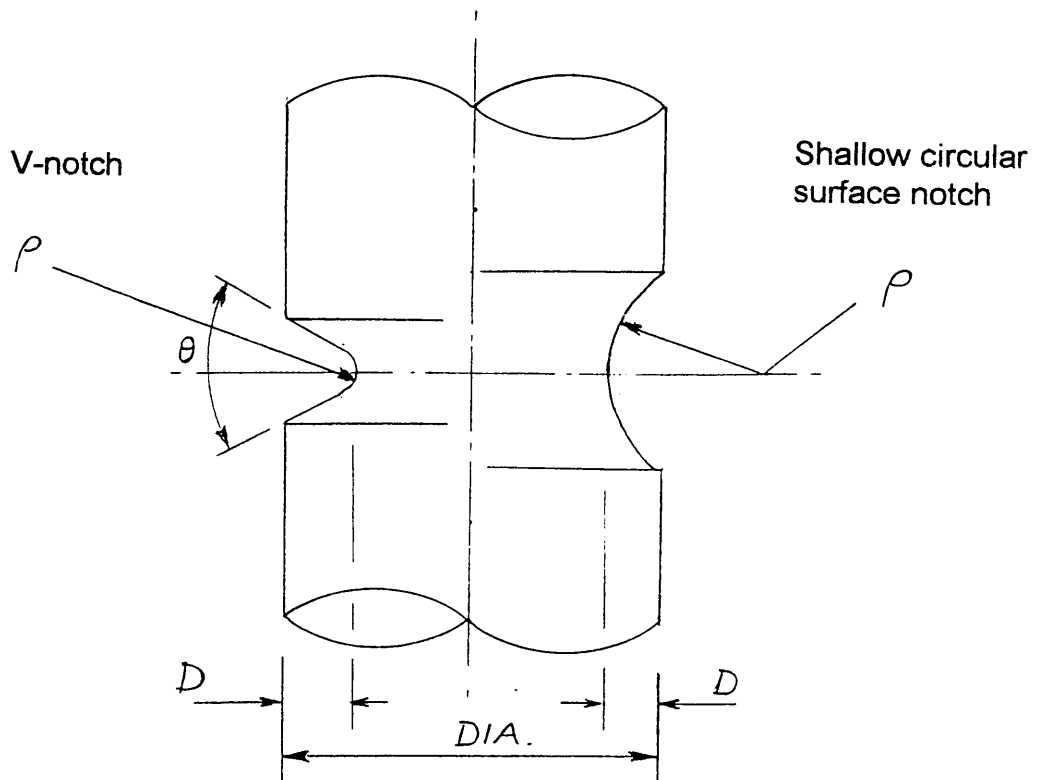
Figure 3.36 Comparison of nominal stress v. strain curves from test and FE calculation for 1/8th in. notch radius specimen cycled between fixed strain limits - Simulation of 23 thou bolt stretch in engine and effect of UTS





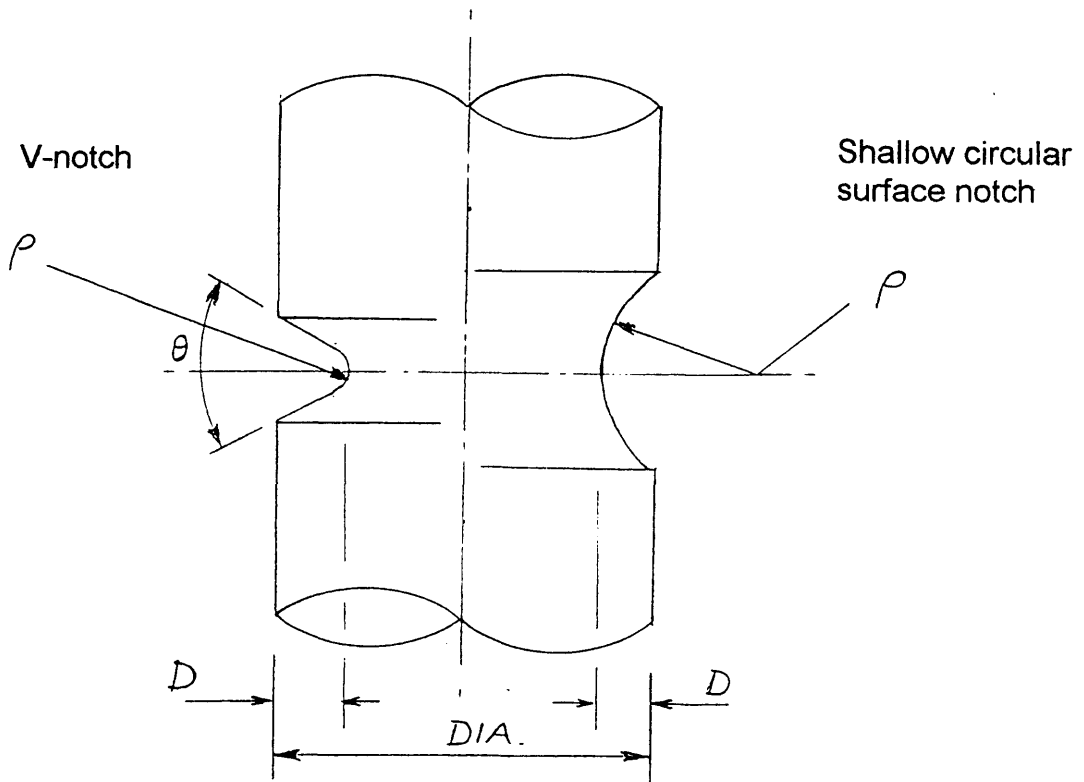
Type	Diameter (mm)	Included angle θ	Notch depth D (mm)	Root radius ρ (mm)	K_t
Shallow circular	20	90	2	6.4	1.5
V-notch	20	90	2	1.42	2.5
V-notch	20	90	2	0.265	5.0

Figure 3.37 BCIRA notch geometries for 50mm cast section size



Type	Diameter (mm)	Included angle θ	Notch depth <i>D</i> (mm)	Root radius ρ (mm)	K_t
Shallow circular	12	90	1.5	3.7	1.5
V-notch	12	90	1.5	0.86	2.5
V-notch	12	90	1.5	0.163	5.0

Figure 3.38 BCIRA notch geometries for 30mm cast section size



Type	Diameter (mm)	Included angle θ	Notch depth D (mm)	Root radius ρ (mm)	K_t
Shallow circular	7	90	0.9	2.15	1.5
V-notch	7	90	0.9	0.5	2.5
V-notch	7	75	0.9	0.1	5.0

Figure 3.39 BCIRA notch geometries for 10mm cast section size

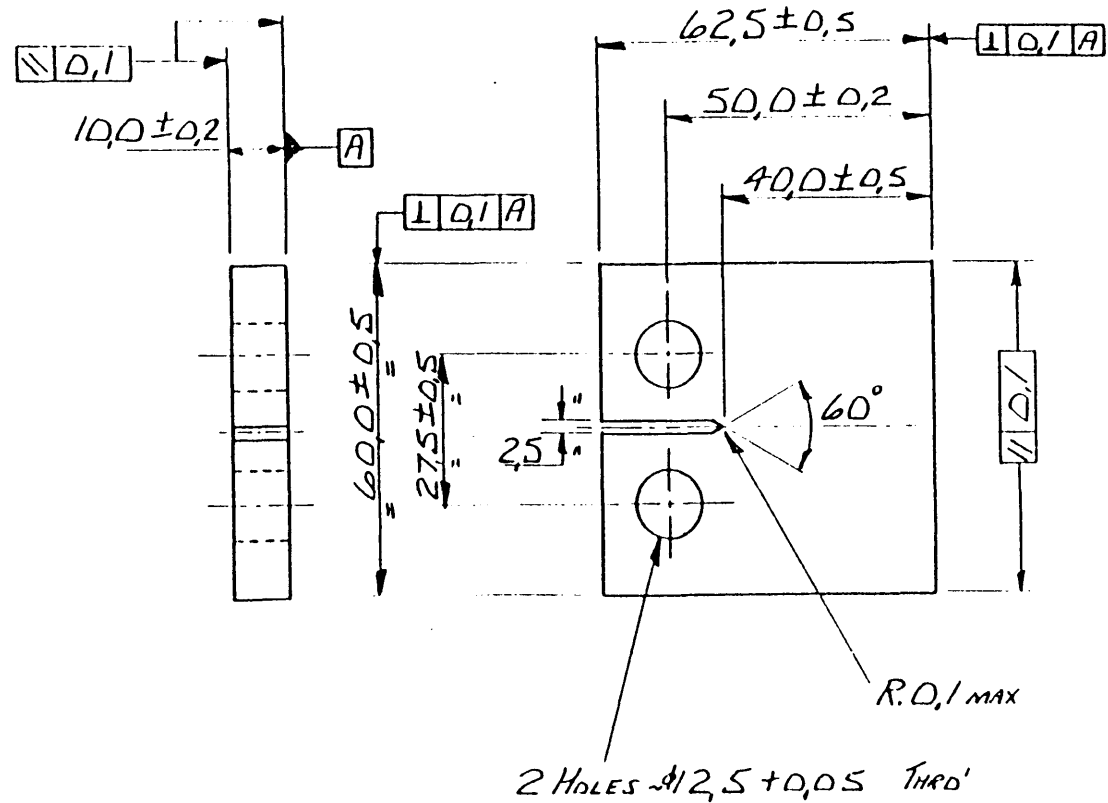


Figure 3.39a Compact tension specimen used for fatigue crack growth threshold tests on grade 250 and 350 grey iron and grade 500/7 SG iron cast to 10mm section size. (see figure 3.10a for specimen design used for 50mm cast section sizes)

Figure 3.40 Normalised Typical Stress-Strain Curves from BCIRA Programme

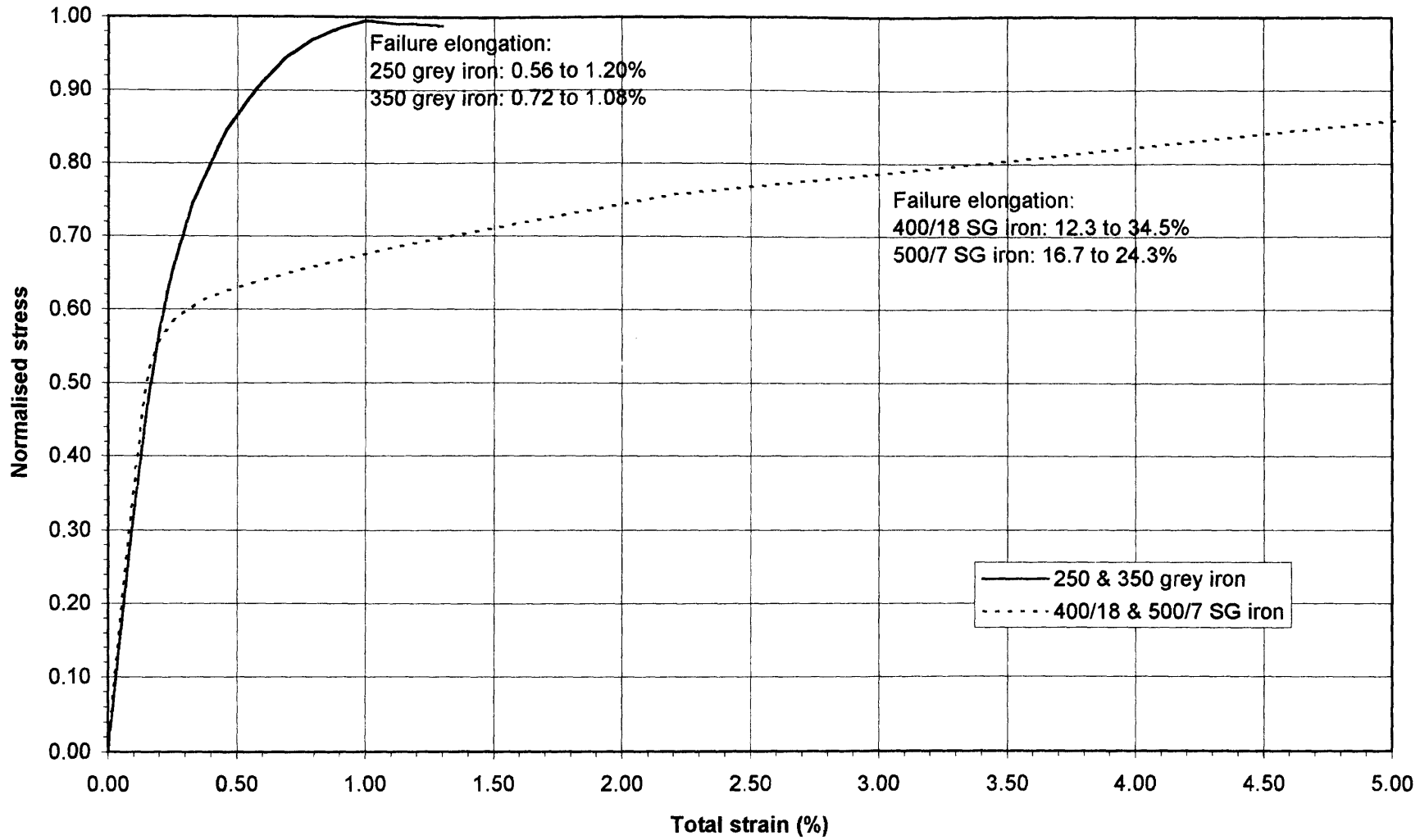


Figure 3.41 Goodman Plot of Normalised Typical Plain Specimen Fatigue Curves from BCIRA Programme

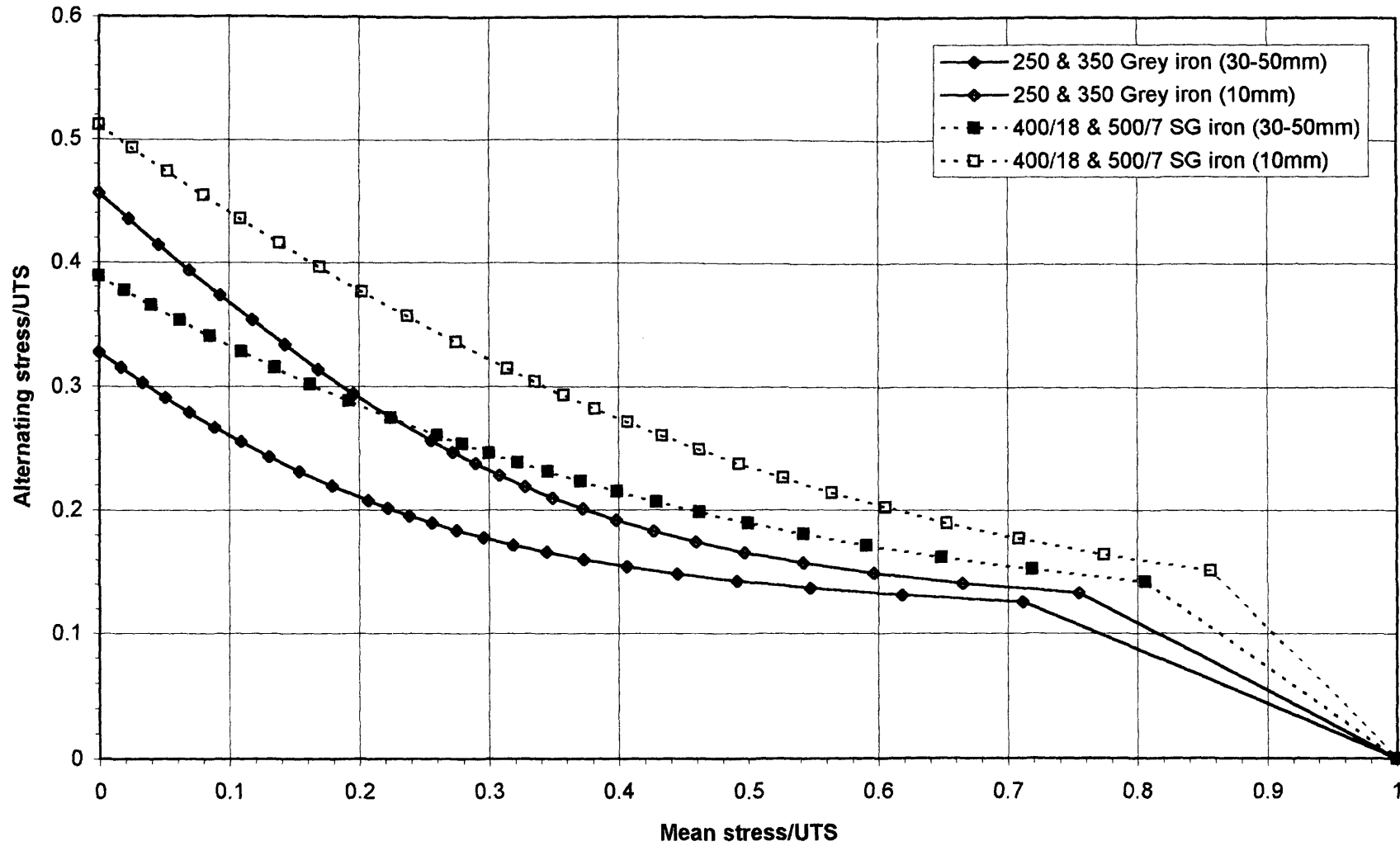


Figure 3.42 Effect of Kt on Fatigue Strength: 250 & 350 Grey Iron from BCIRA Programme

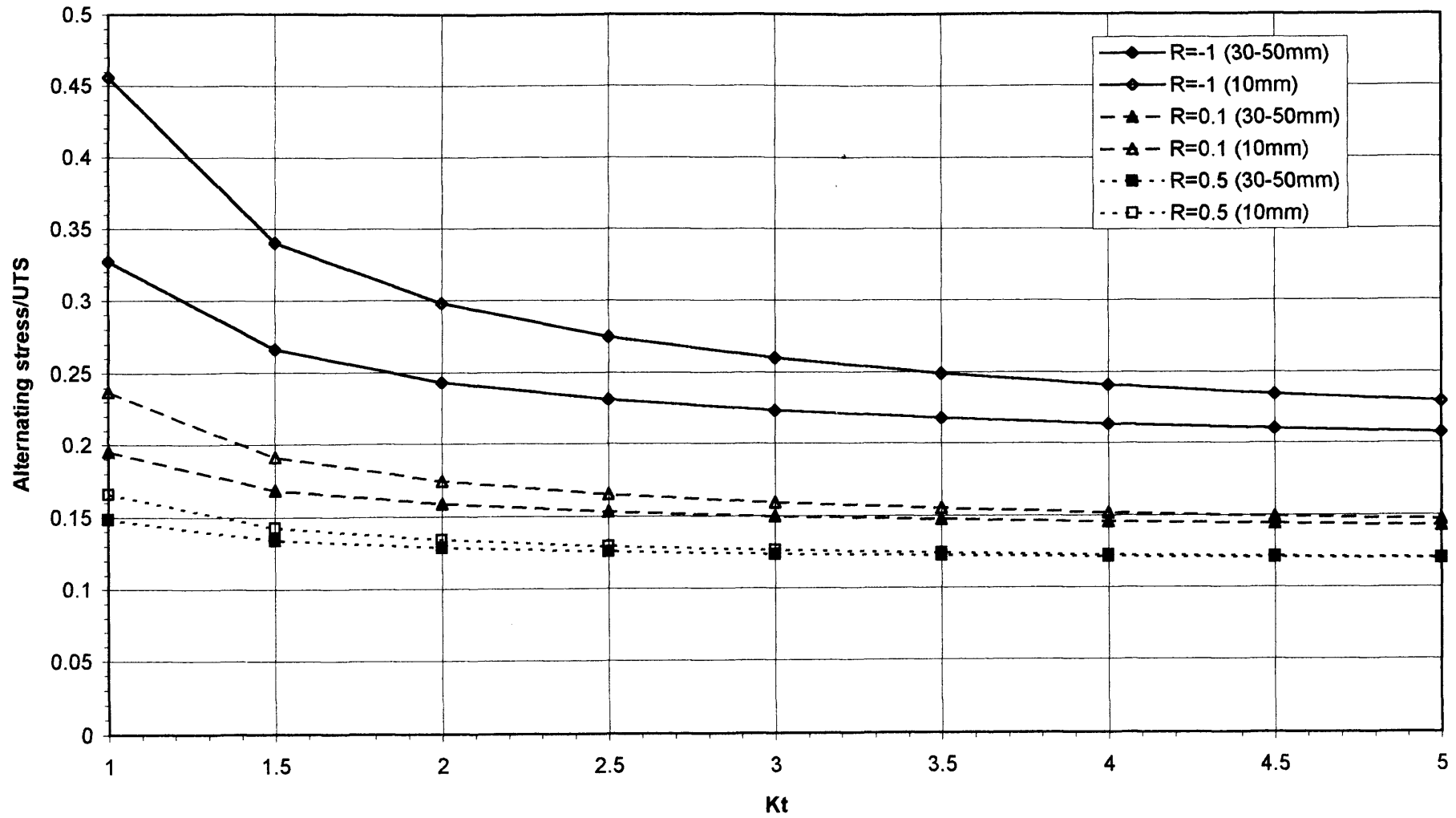
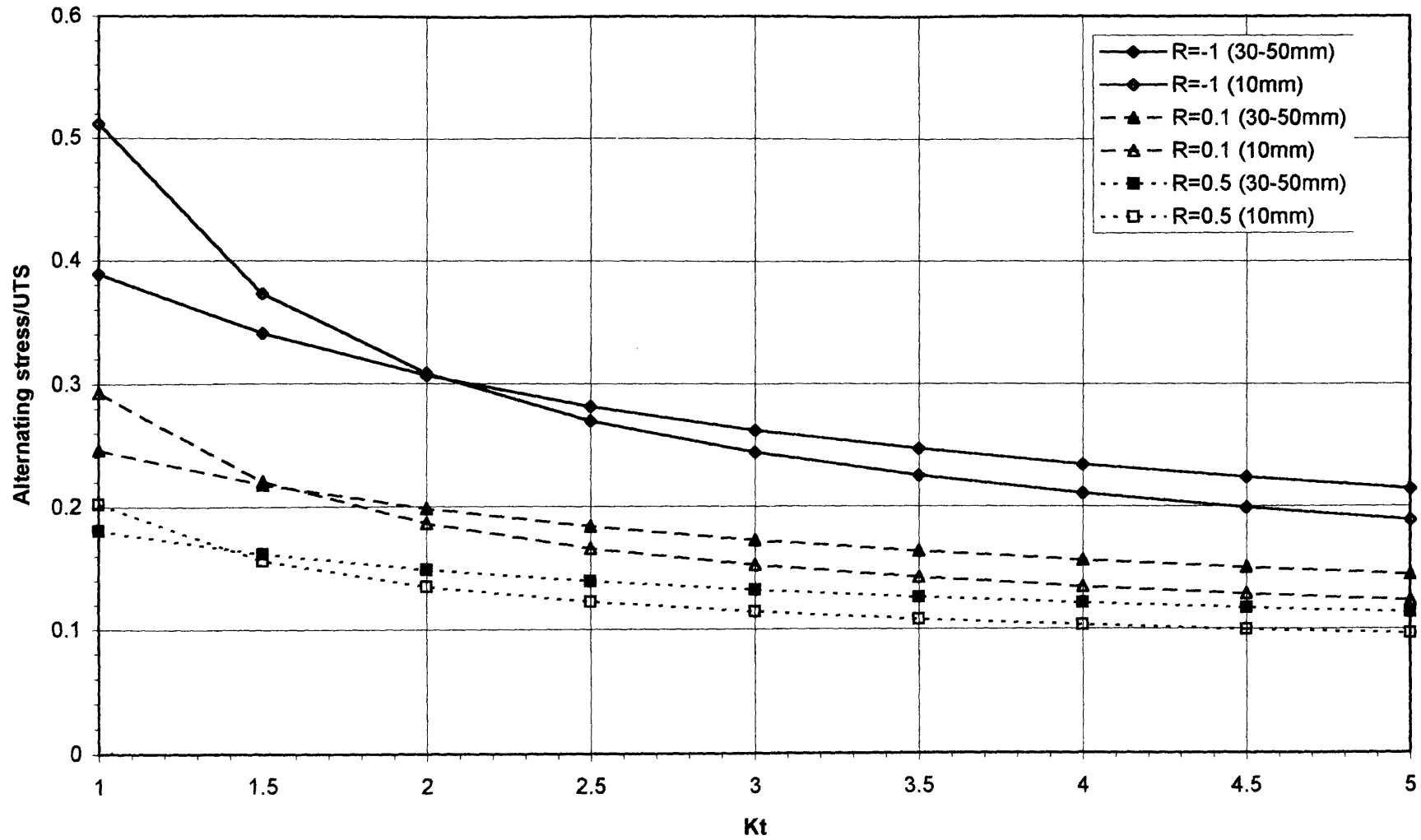
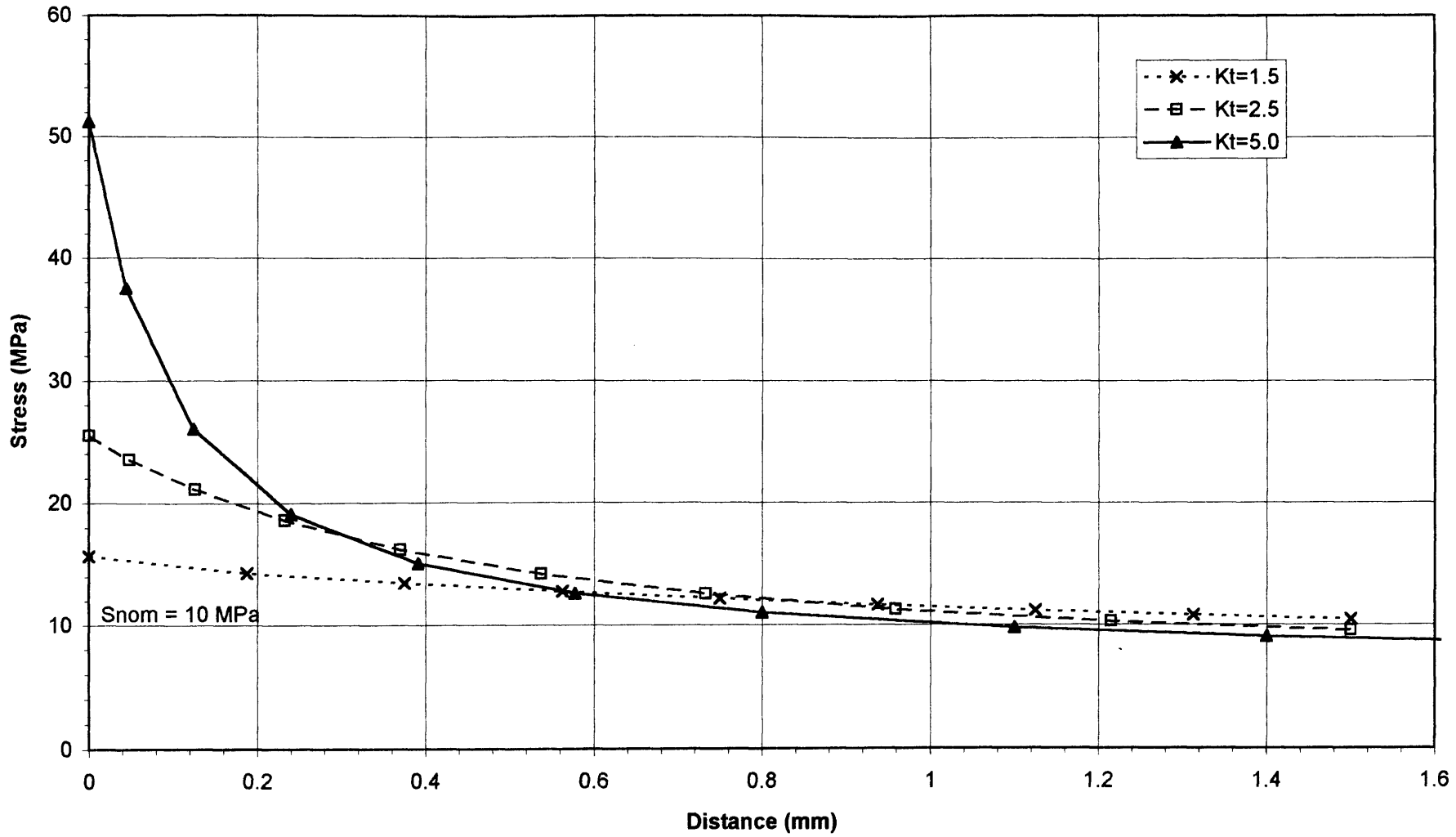


Figure 3.43 Effect of Kt on Fatigue Strength: 400/18 & 500/7 SG Iron from BCIRA Programme



**Figure 3.44 BCIRA Notched Specimens: 50mm Cast Section Size
Predicted Elastic Notch Root Stress Distributions ($S_{nom} = 10$ MPa)**



**Figure 3.45 BCIRA Notched Specimens: 30mm Cast Section Size
Predicted Elastic Notch Root Stress Distribution (S_{nom} = 10 MPa)**

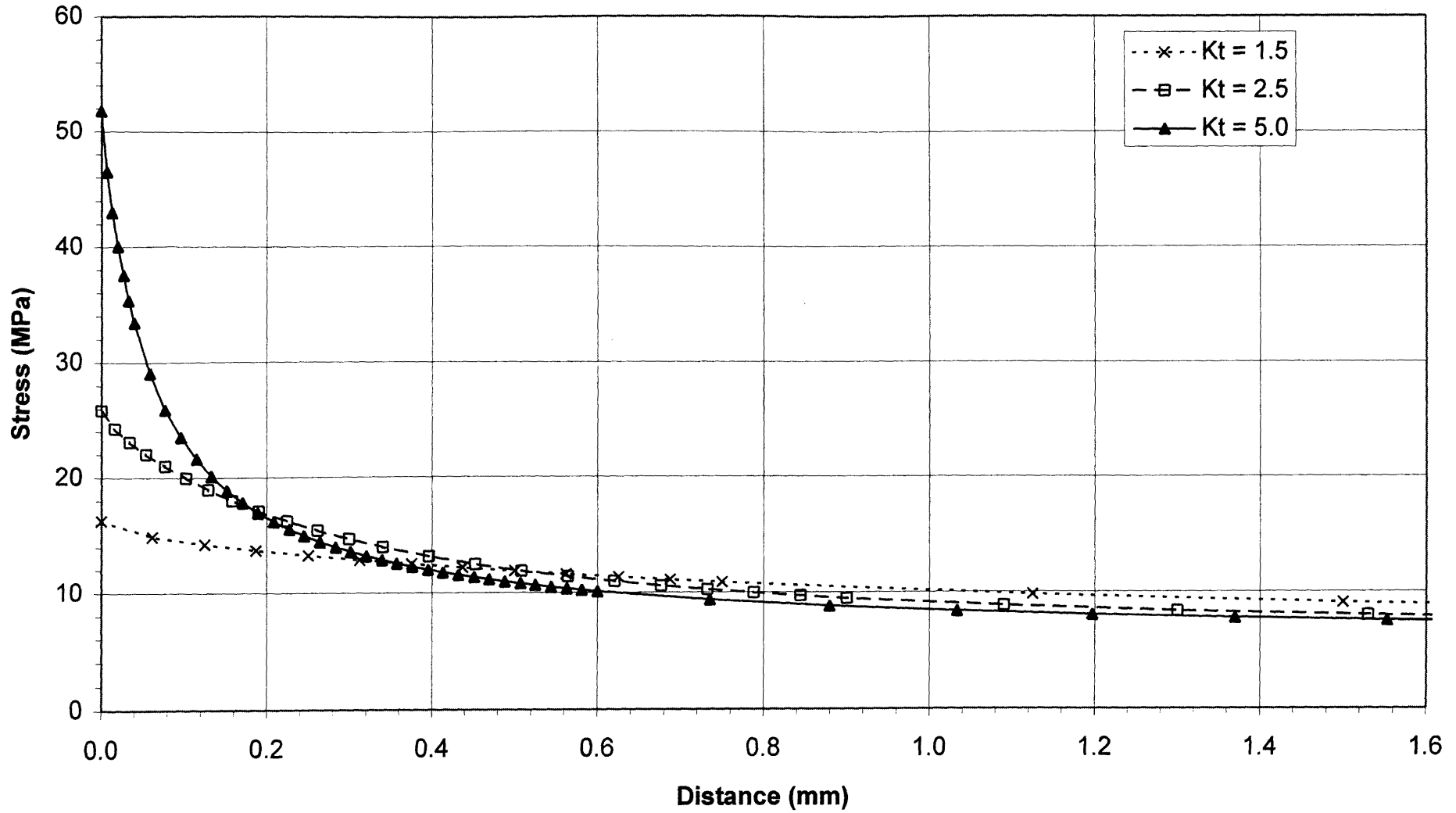


Figure 3.46 BCIRA Notched Specimens: 10mm Cast Section Size
Predicted Elastic Notch Root Stress Distributions ($S_{nom} = 10$ MPa)

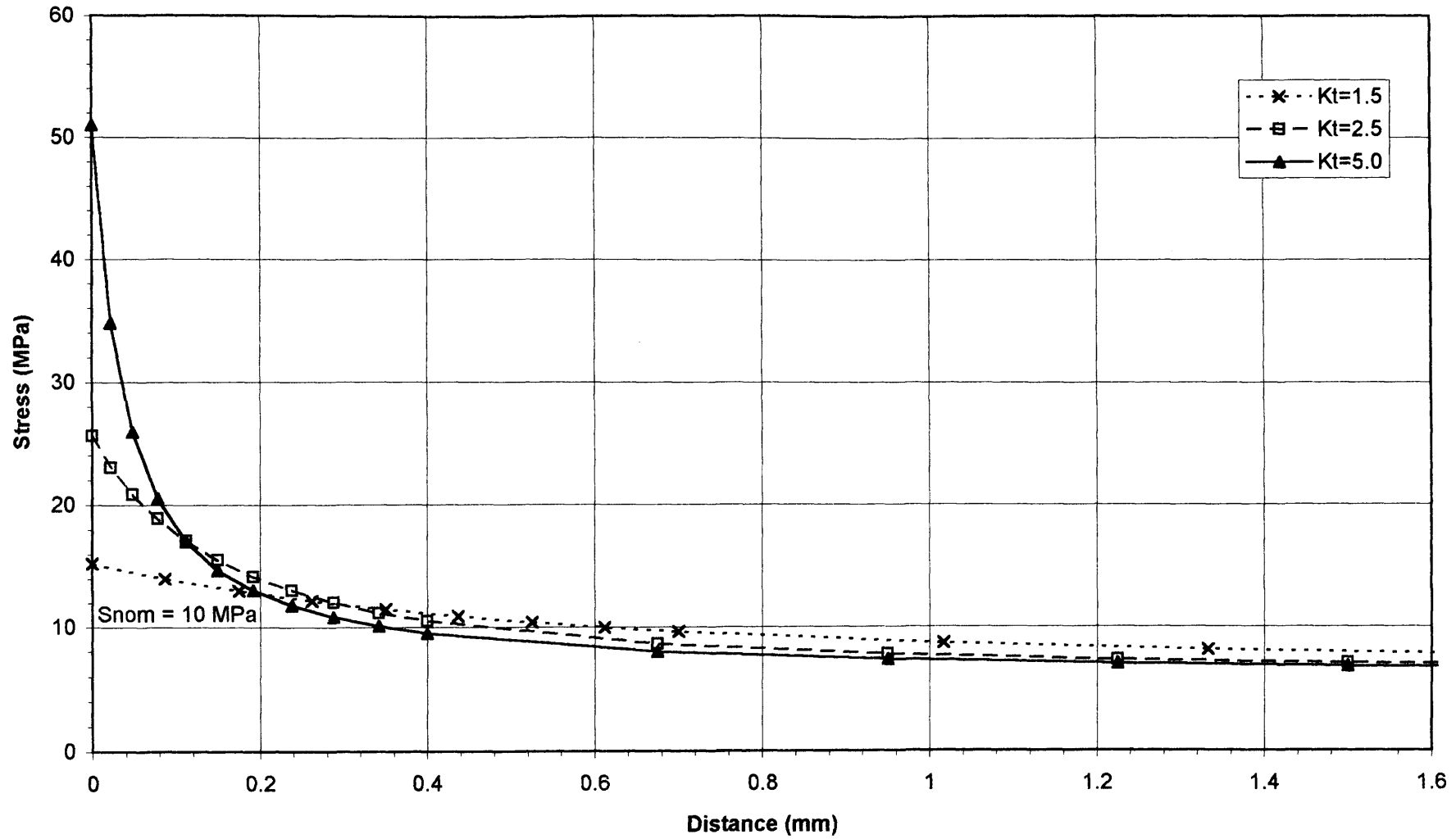


Figure 3.47 Stress-Life data for British Grade 300 Grey Cast Iron

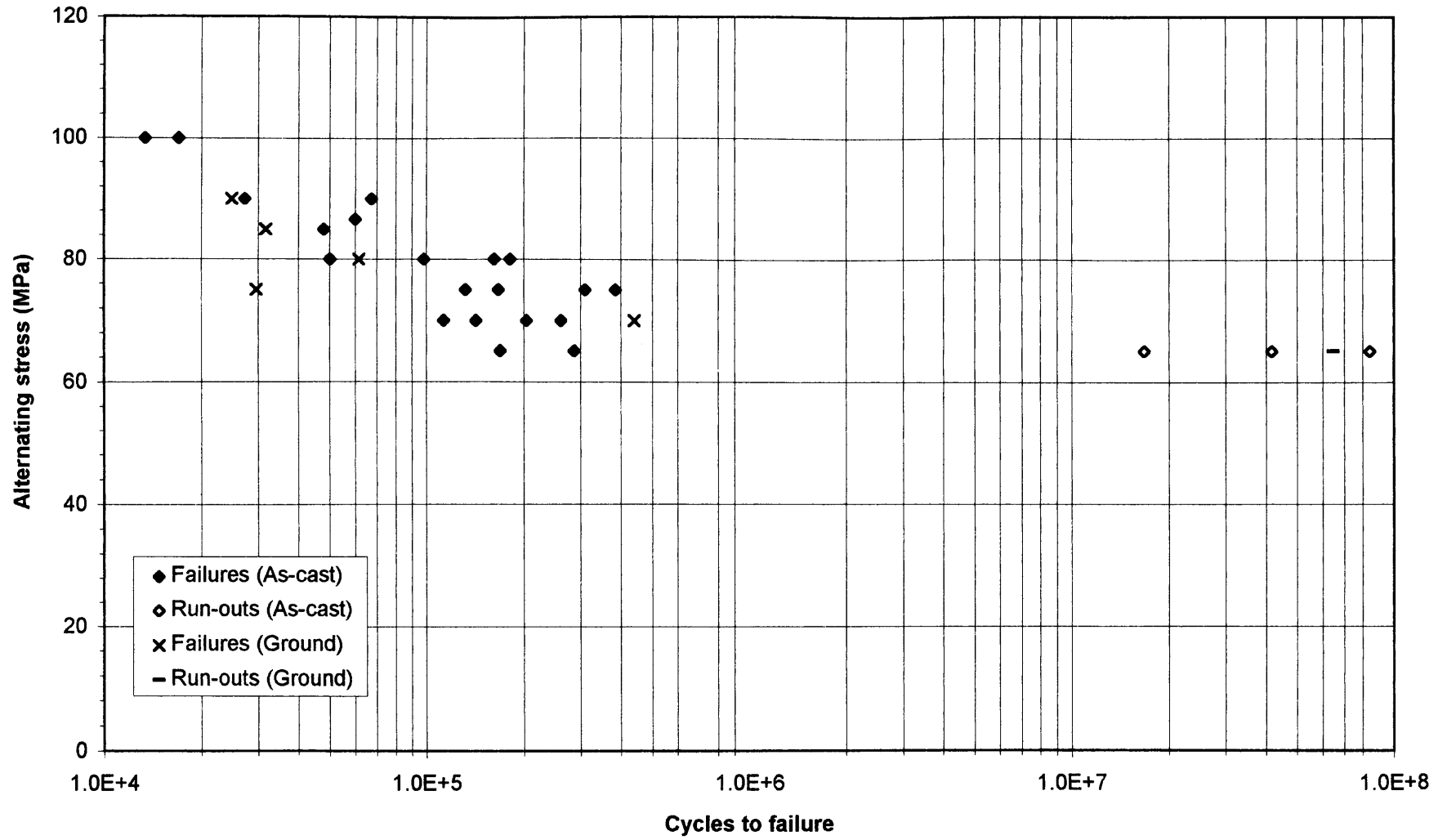


Figure 3.48 Stress-Life data for French Grade 300 Grey Cast Iron

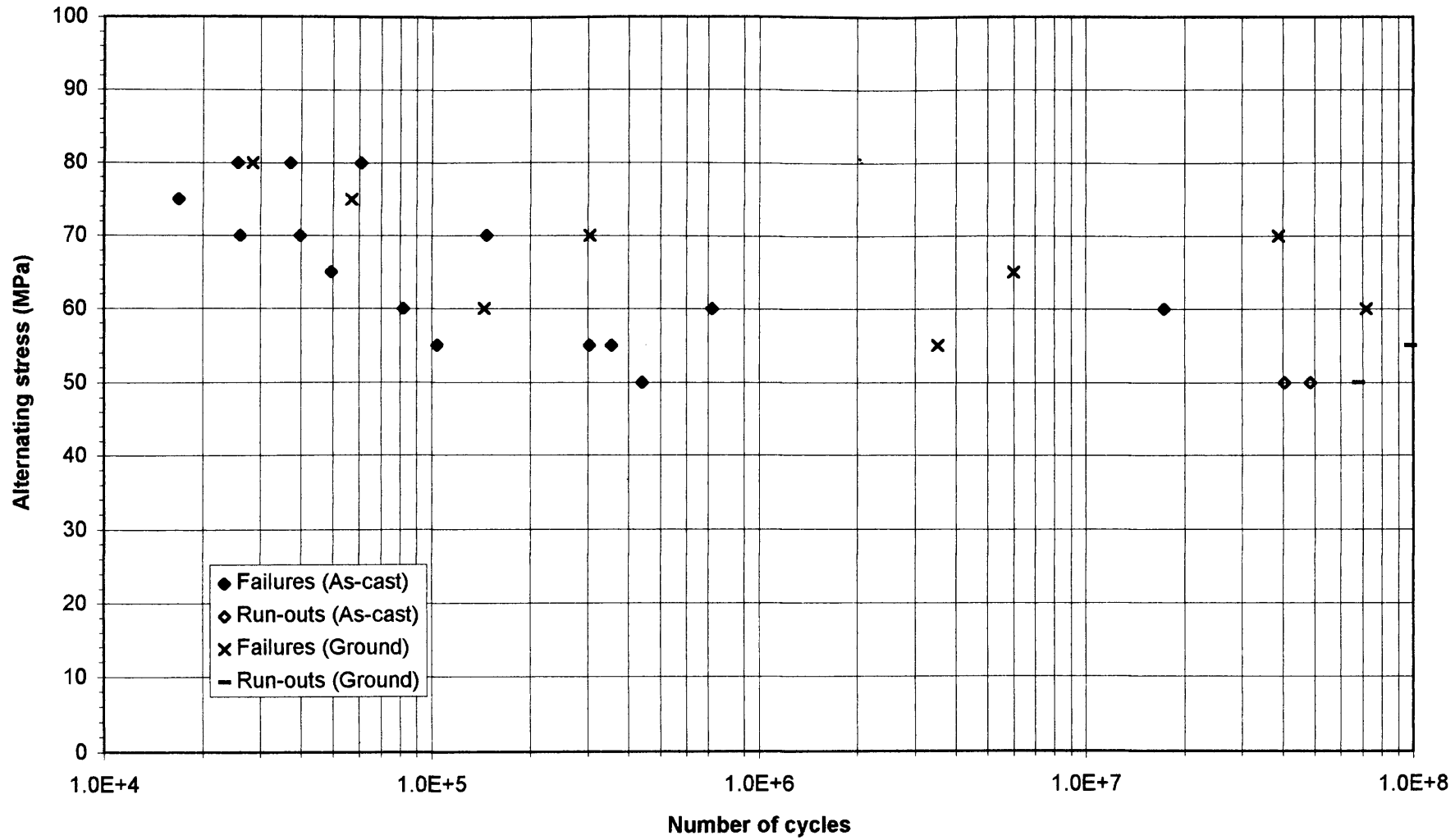


Figure 3.49 Kitagawa Diagram for British Grade 300 Grey Cast Iron Specimens
(As-cast specimens only)

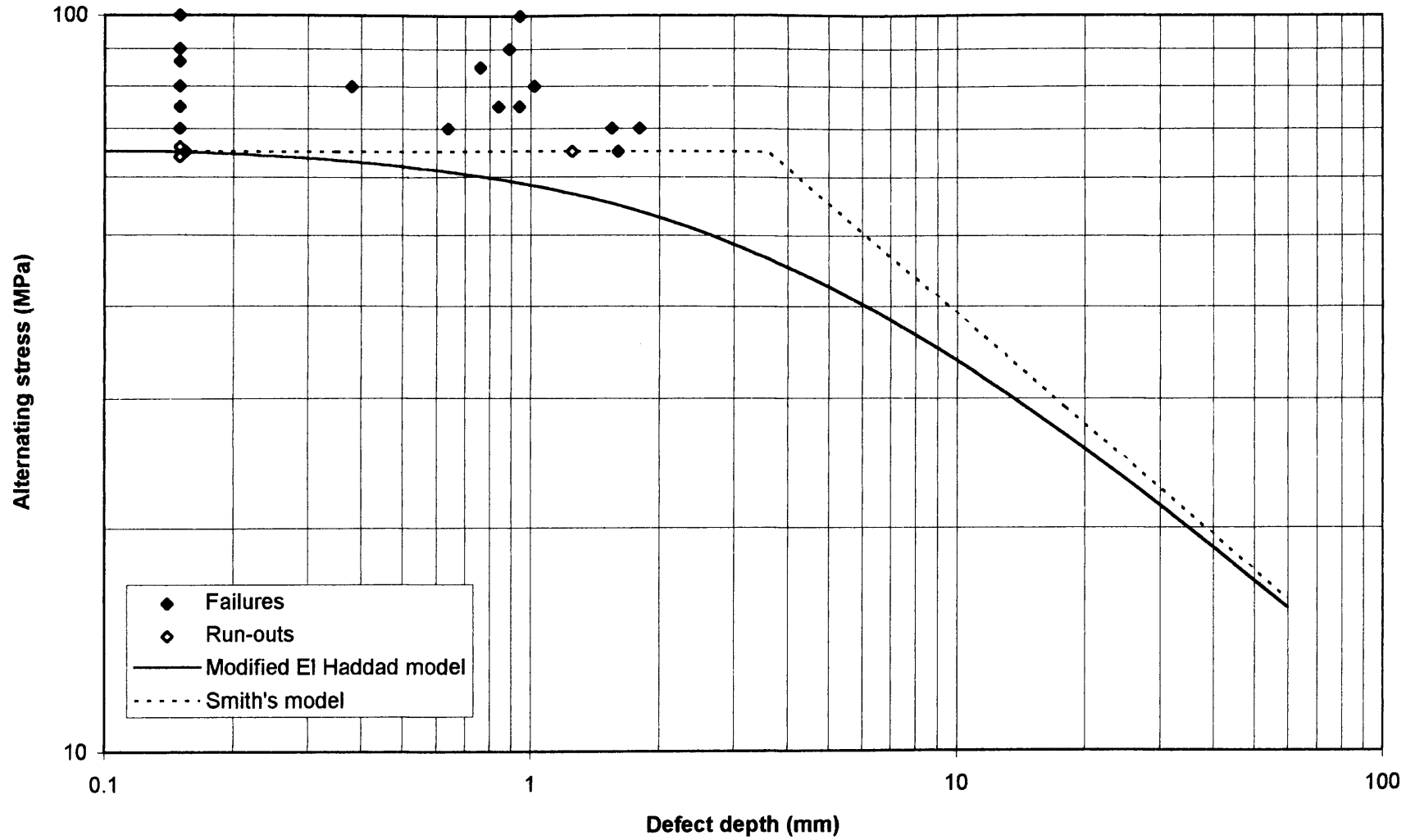
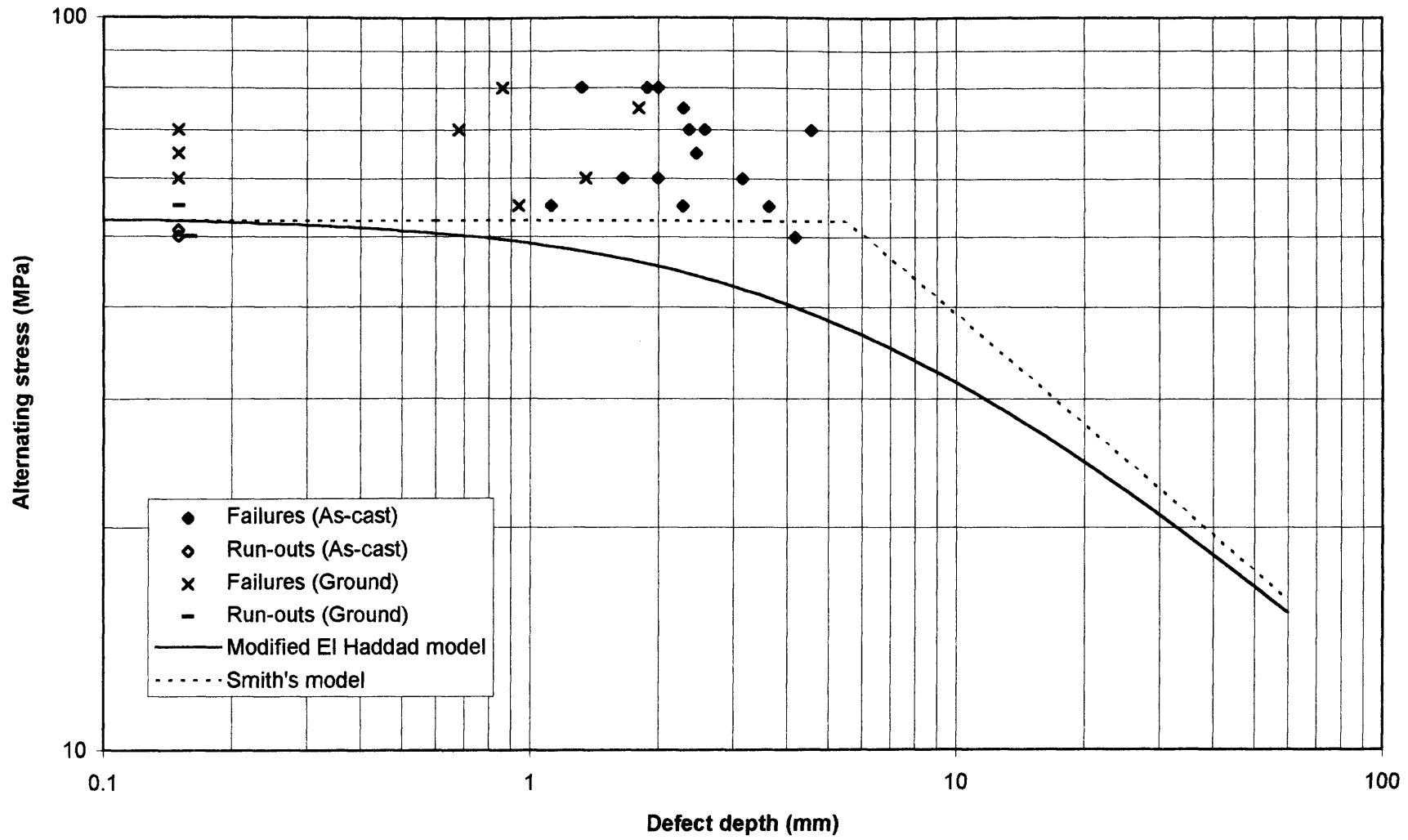


Figure 3.50 Kitagawa Diagram for French Grade 300 Grey Cast Iron Specimens



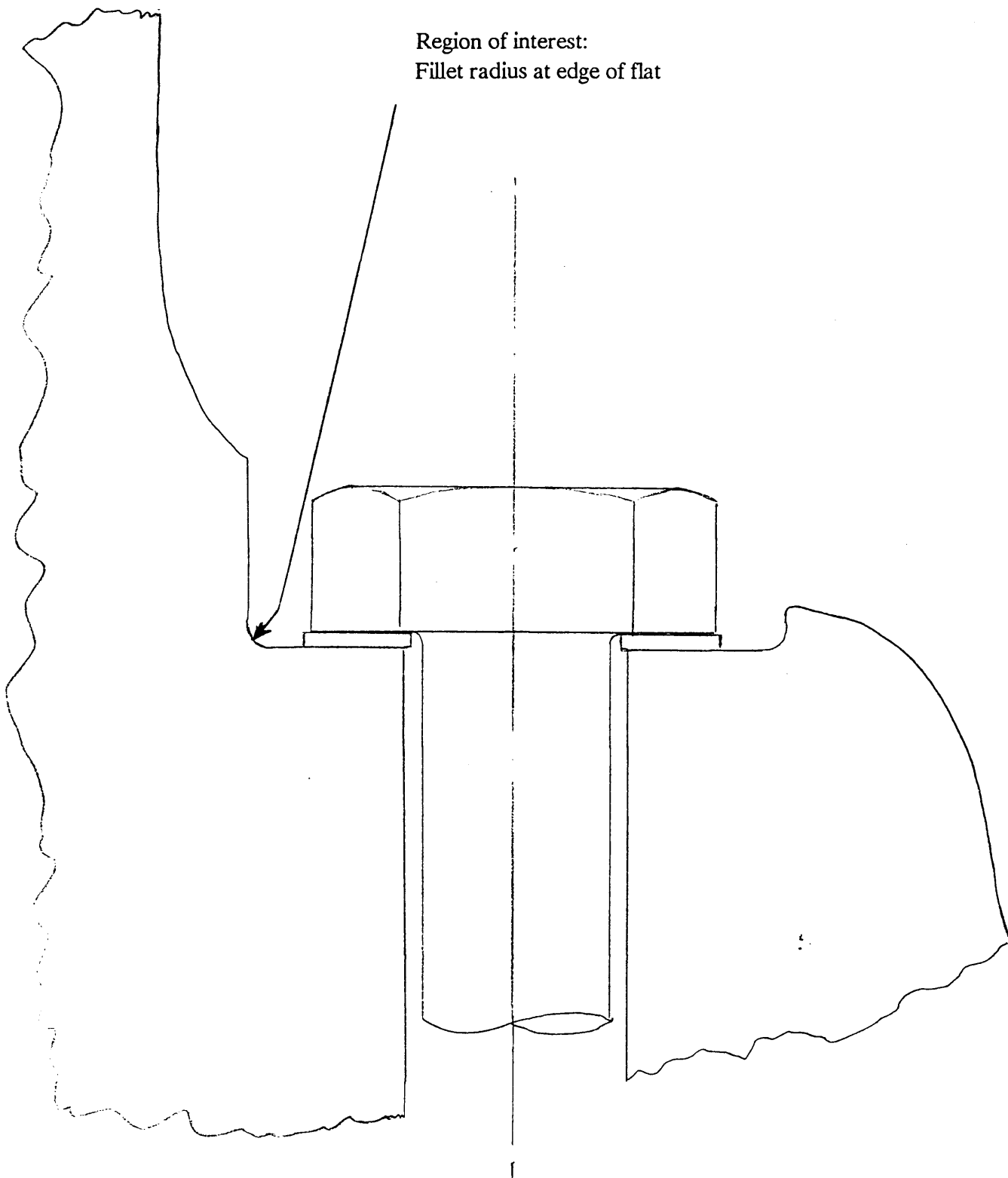


Figure 3.51 Schematic of a typical design detail of interest from a diesel engine bedplate

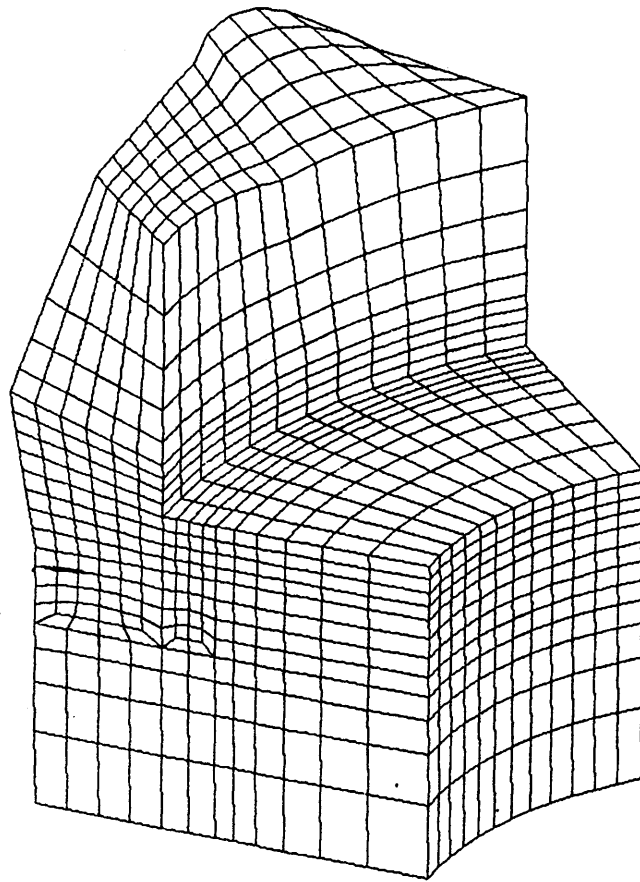


Figure 3.52 Three-dimensional local FE model of bedplate detail
- 12 thou fillet radius (modelled with sharp corner)

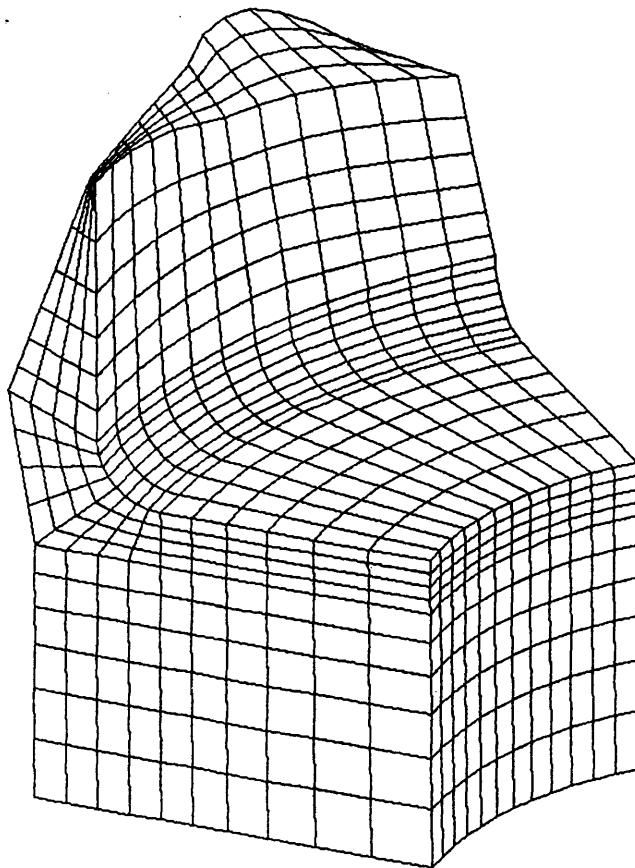


Figure 3.53 Three-dimensional local FE model of bedplate detail
- 1/8th in. fillet radius

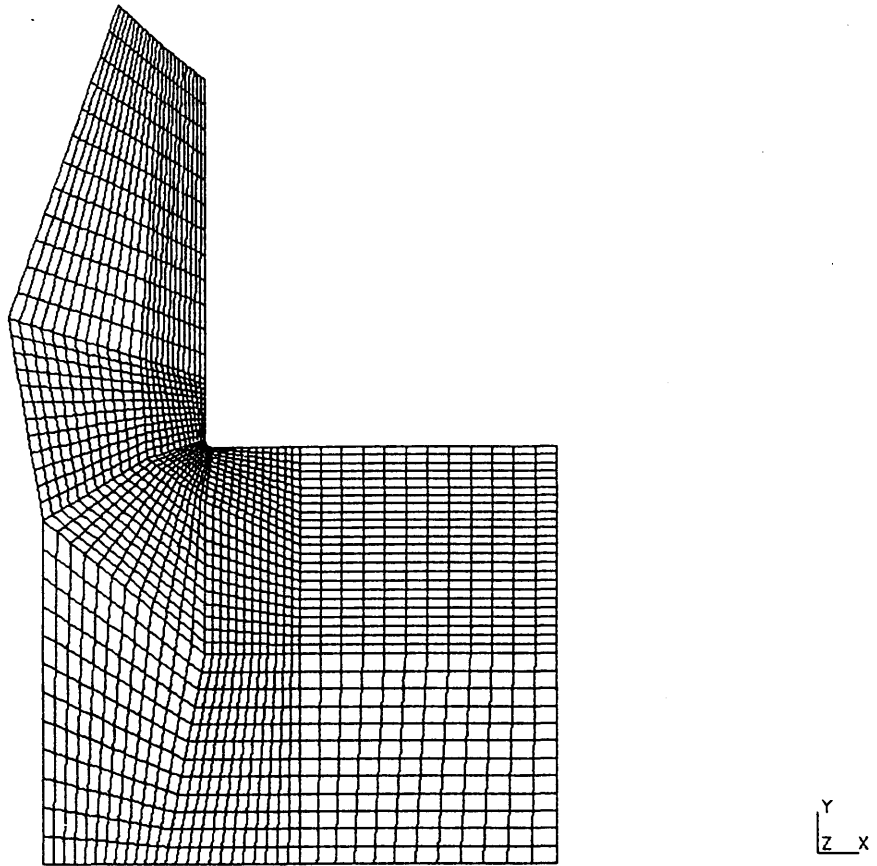


Figure 3.54 Two-dimensional local FE model of bedplate detail
- 12 thou fillet radius

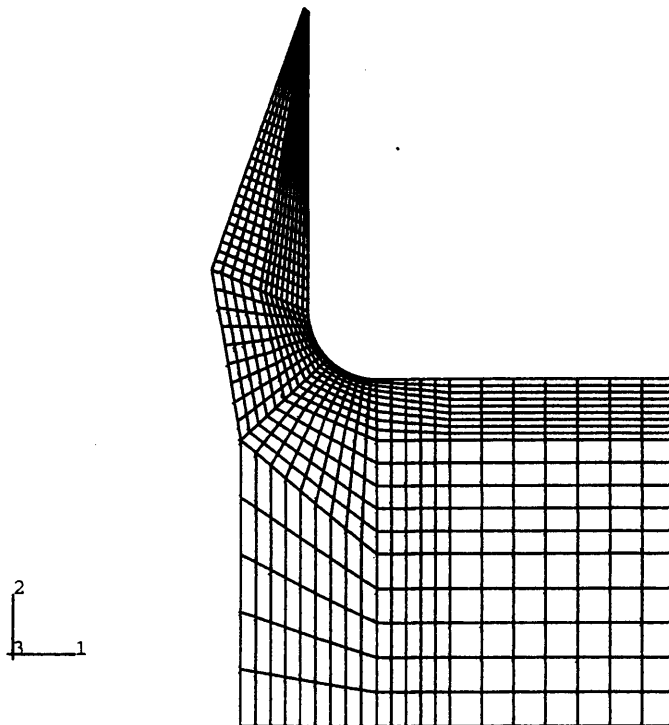
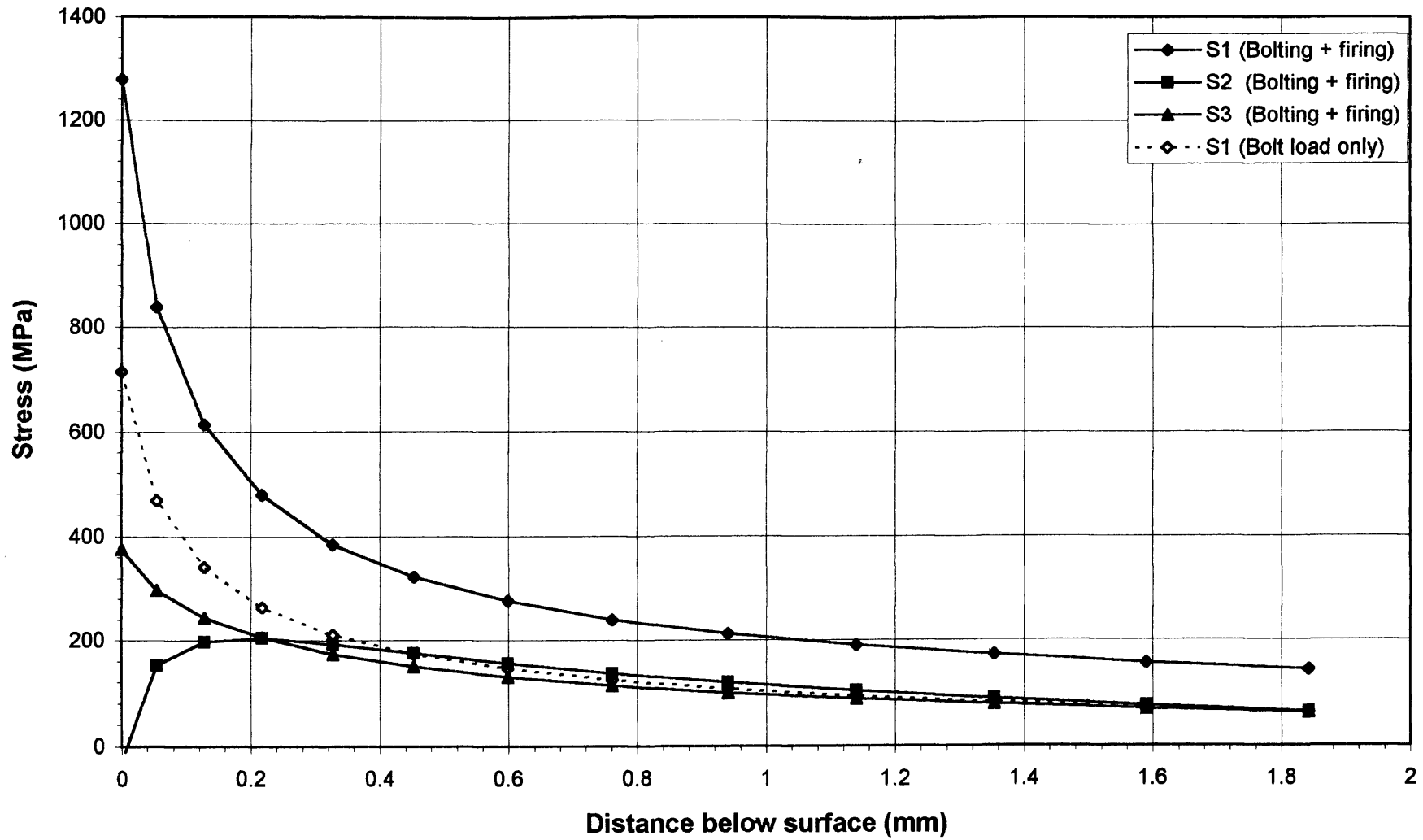
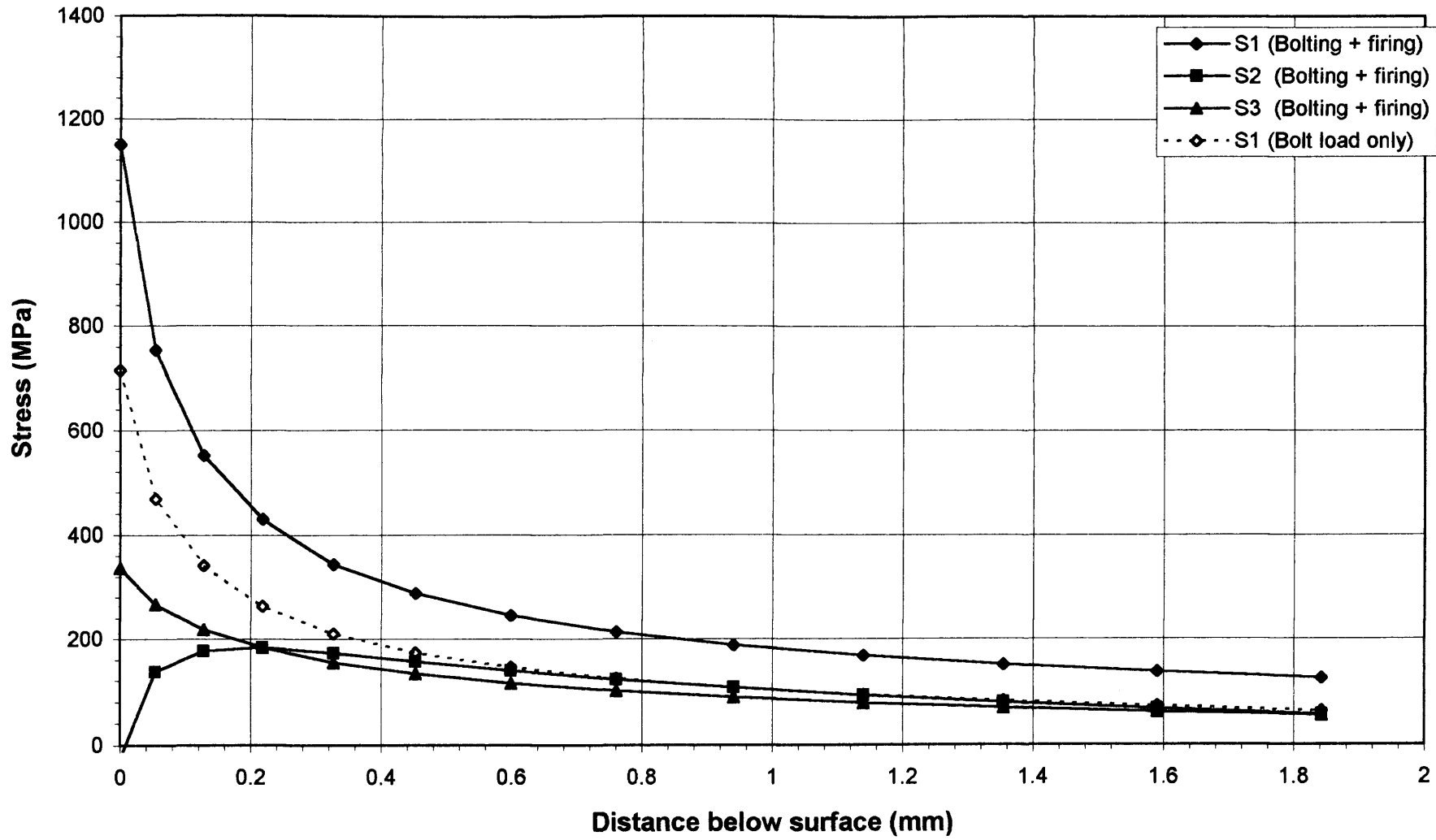


Figure 5.55 Two-dimensional local FE model of bedplate detail
- 1/8th in. fillet radius

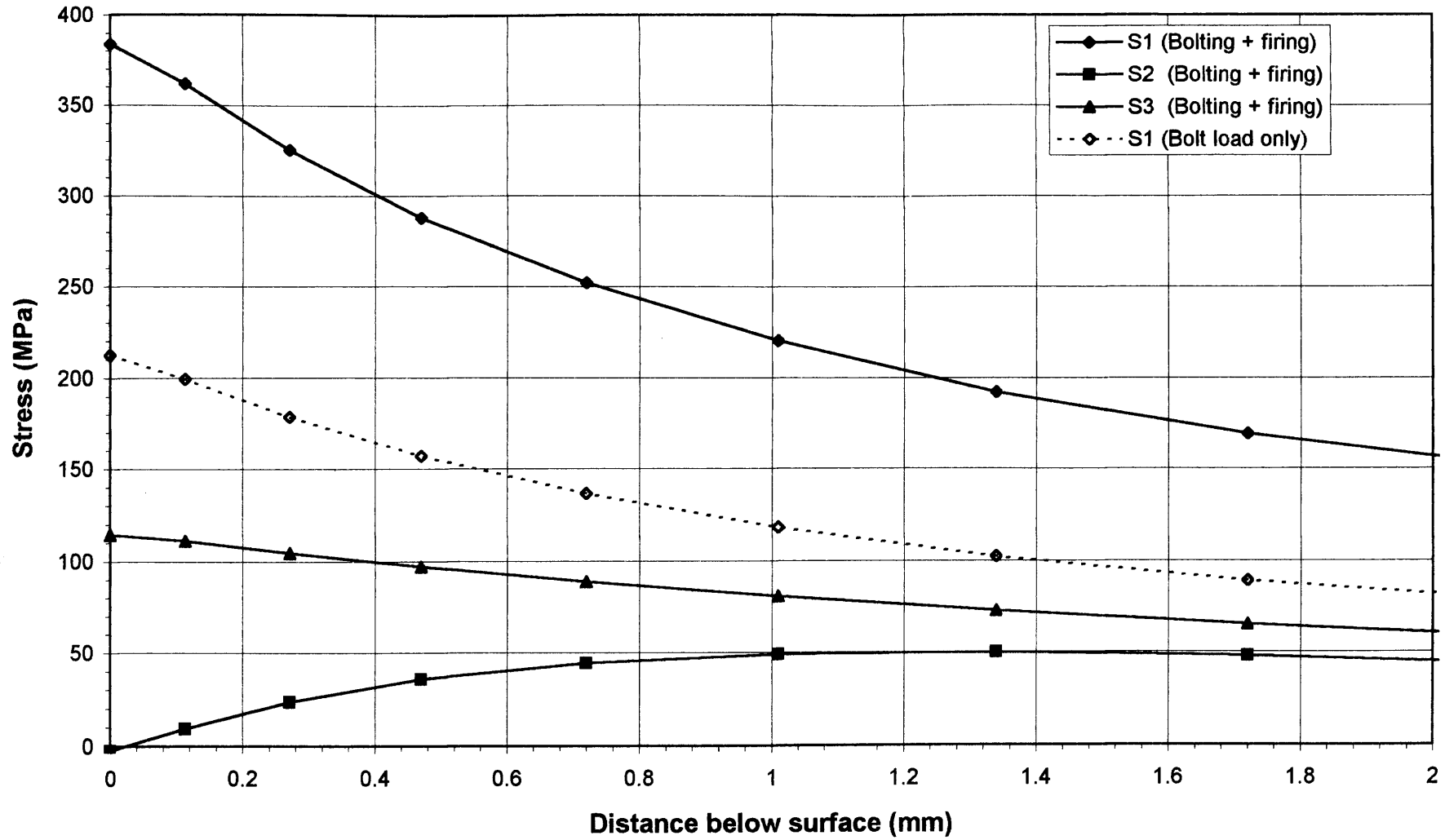
**Figure 3.56 Engine Bedplate - Seacat 12 thou Fillet
Sub-surface Stress Distributions**



**Figure 3.57 RKC Engine Bedplate - 12 thou Fillet
Sub-surface Stress Distributions**



**Figure 3.58 Seacat Engine Bedplate - 1/8th in. Fillet Radius
Sub-surface Stress Distributions**



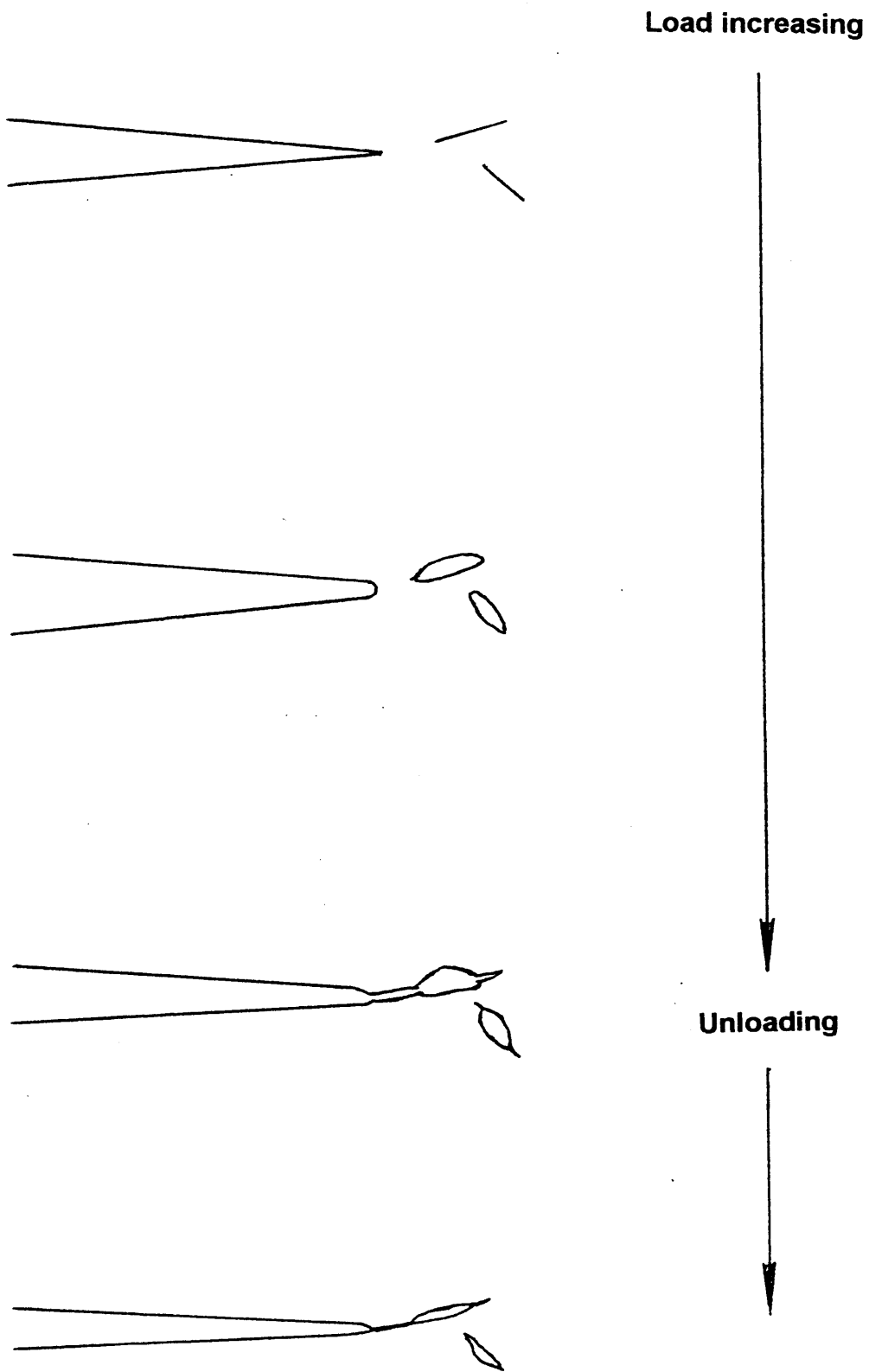


Figure 4.1 Hornbogen's interpretation of the mechanism of fatigue crack extension in cast iron

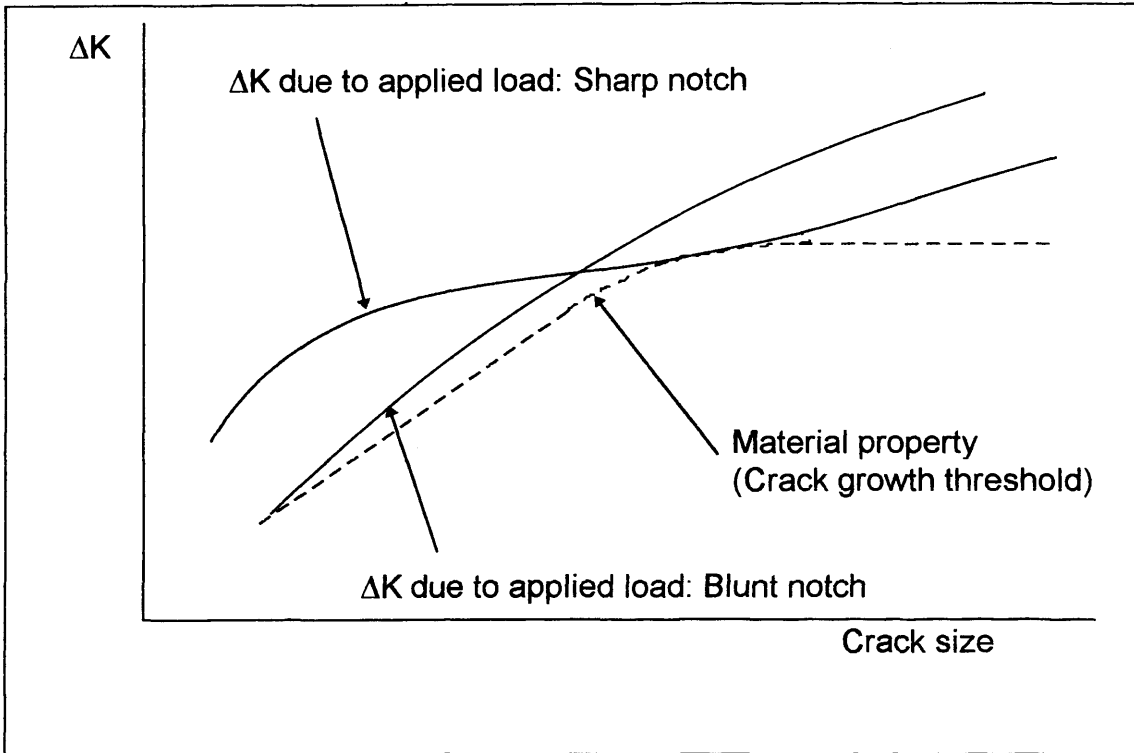


Figure 5.1 Schematic of the assumed short crack ΔK and ΔK_{th} versus crack depth relationships at notch roots

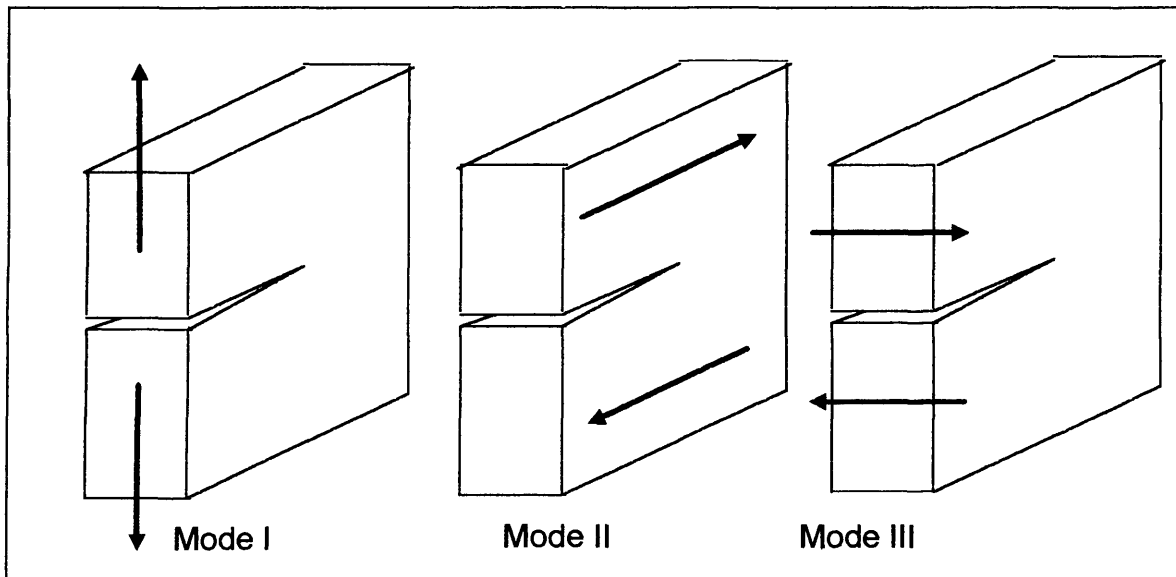


Figure 5.2 The three modes of crack deformation characterised by the three Stress Intensity Factors K_I , K_{II} and K_{III} .

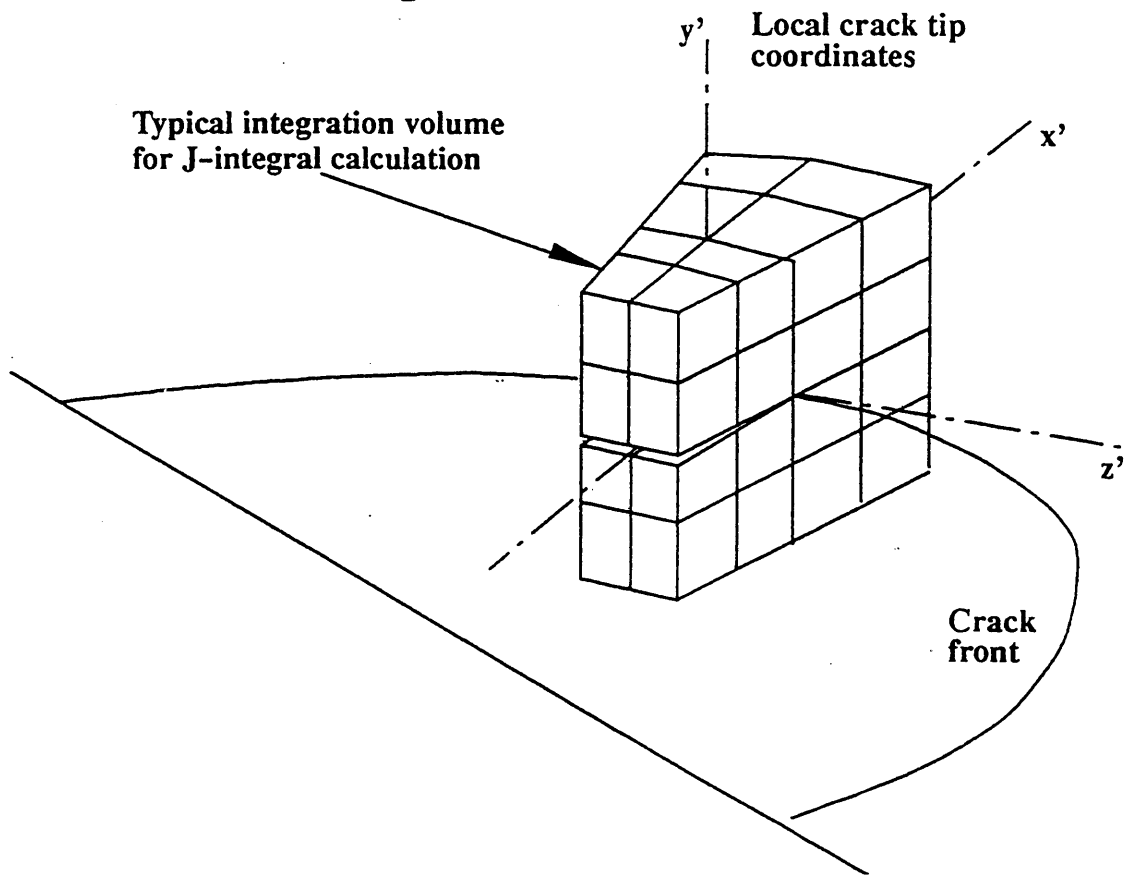


Figure 5.3 Definition of the local coordinate system used at a point on a three-dimensional crack front

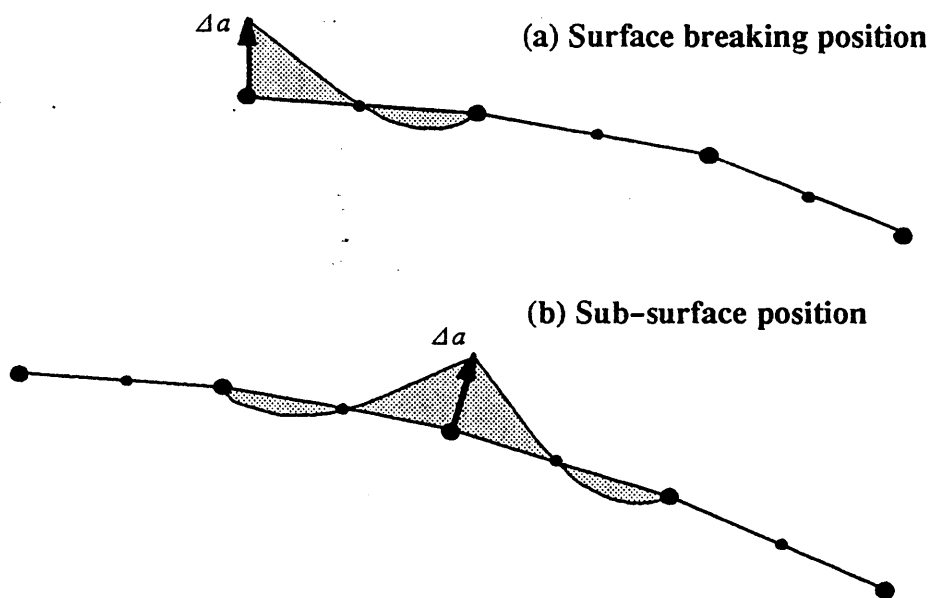


Figure 5.4 Virtual crack extension at nodes on a 3-D crack front

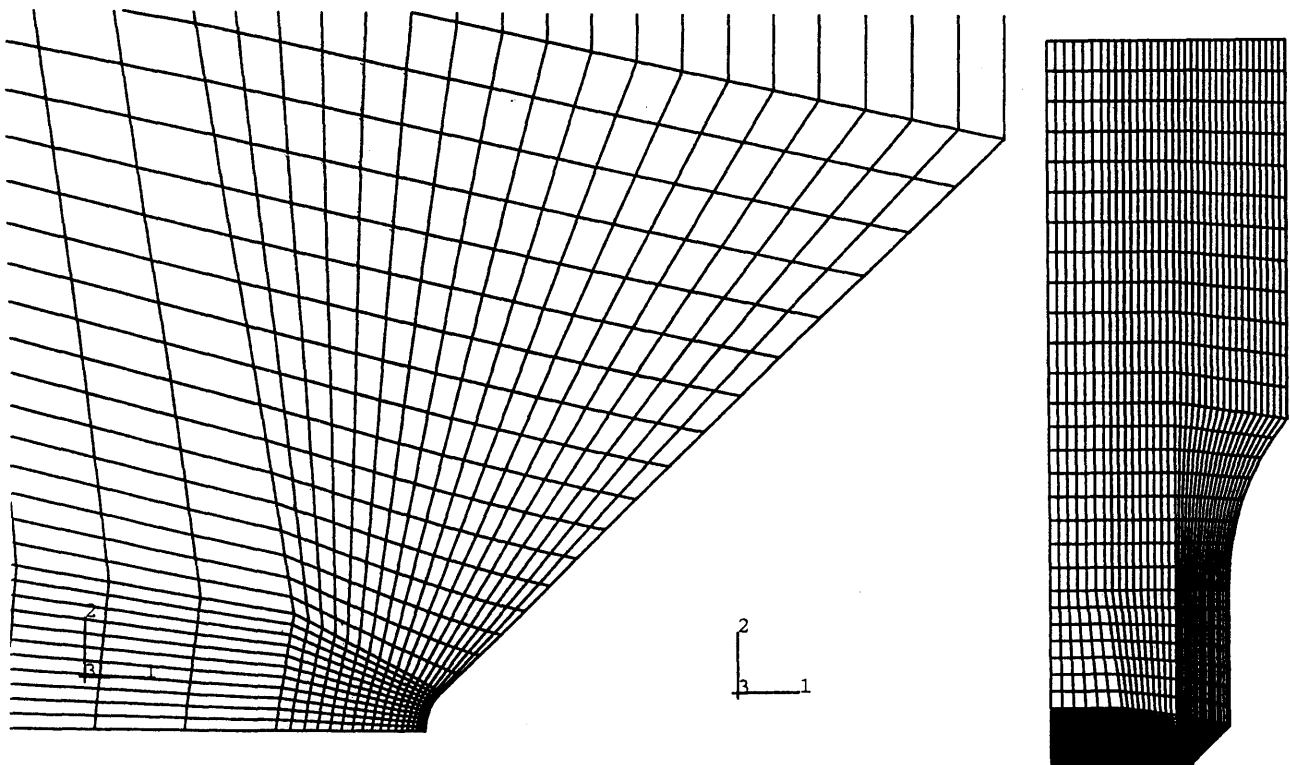
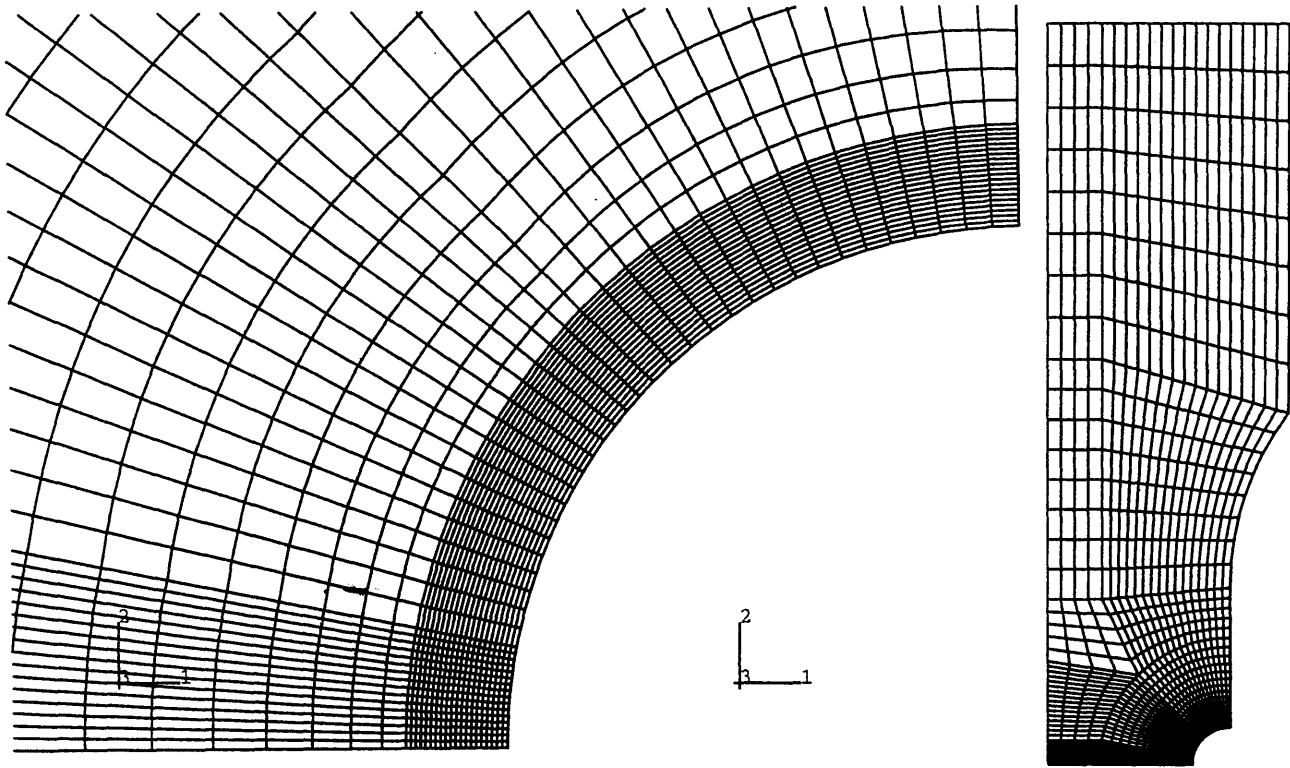


Figure 5.5 Typical axisymmetric FE models of circumferentially notched test specimens used in crack analyses

**Figure 5.6 Comparison of K solutions for Continuous Surface Cracks
Axisymmetric FE K solutions for Notched BRITE Specimens (Kt=2.2 & 5.6)
and K Solution for Circumferential Crack in a Solid Cylinder (Rooke & Cartwright, 1976)**

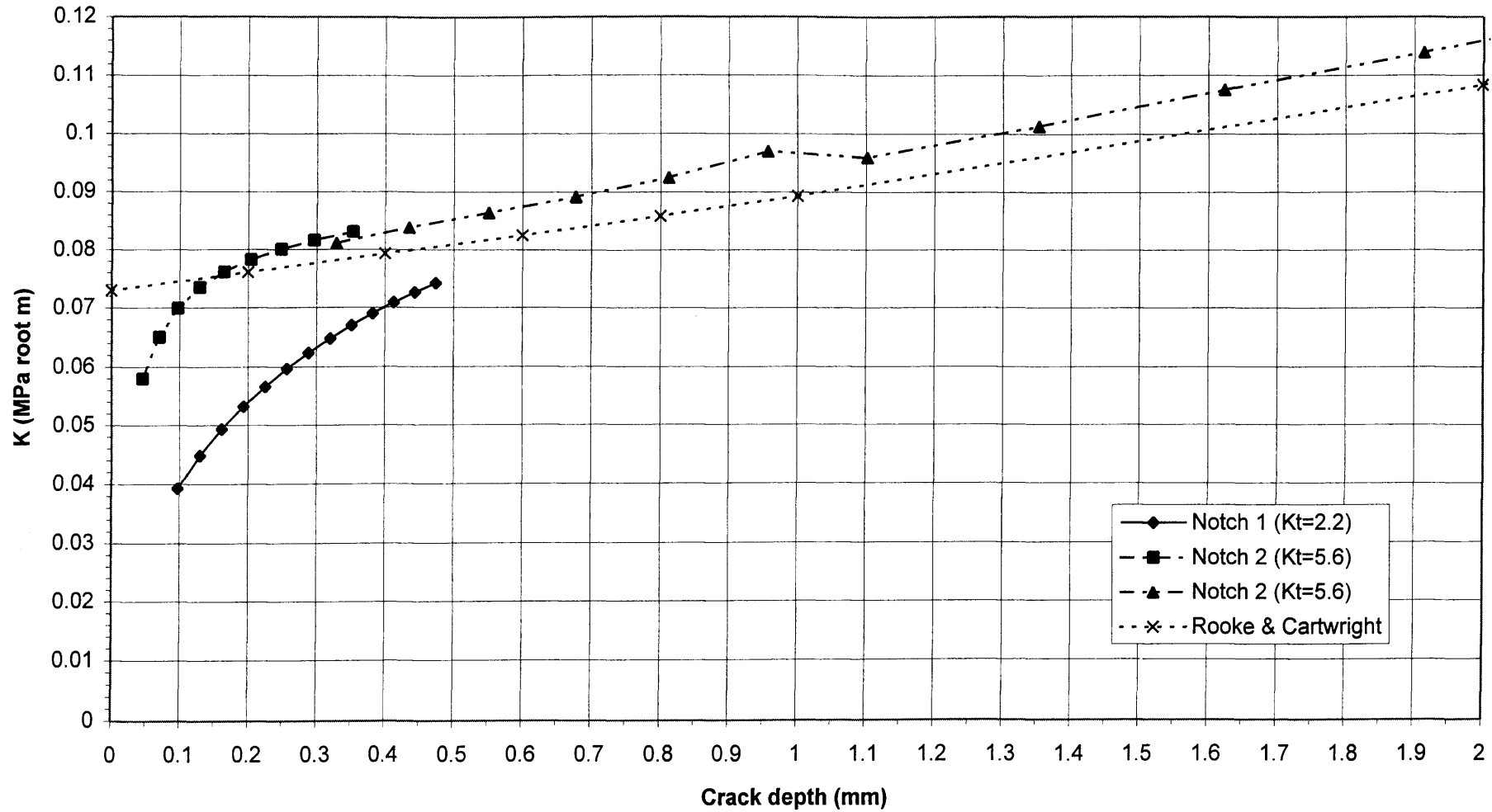
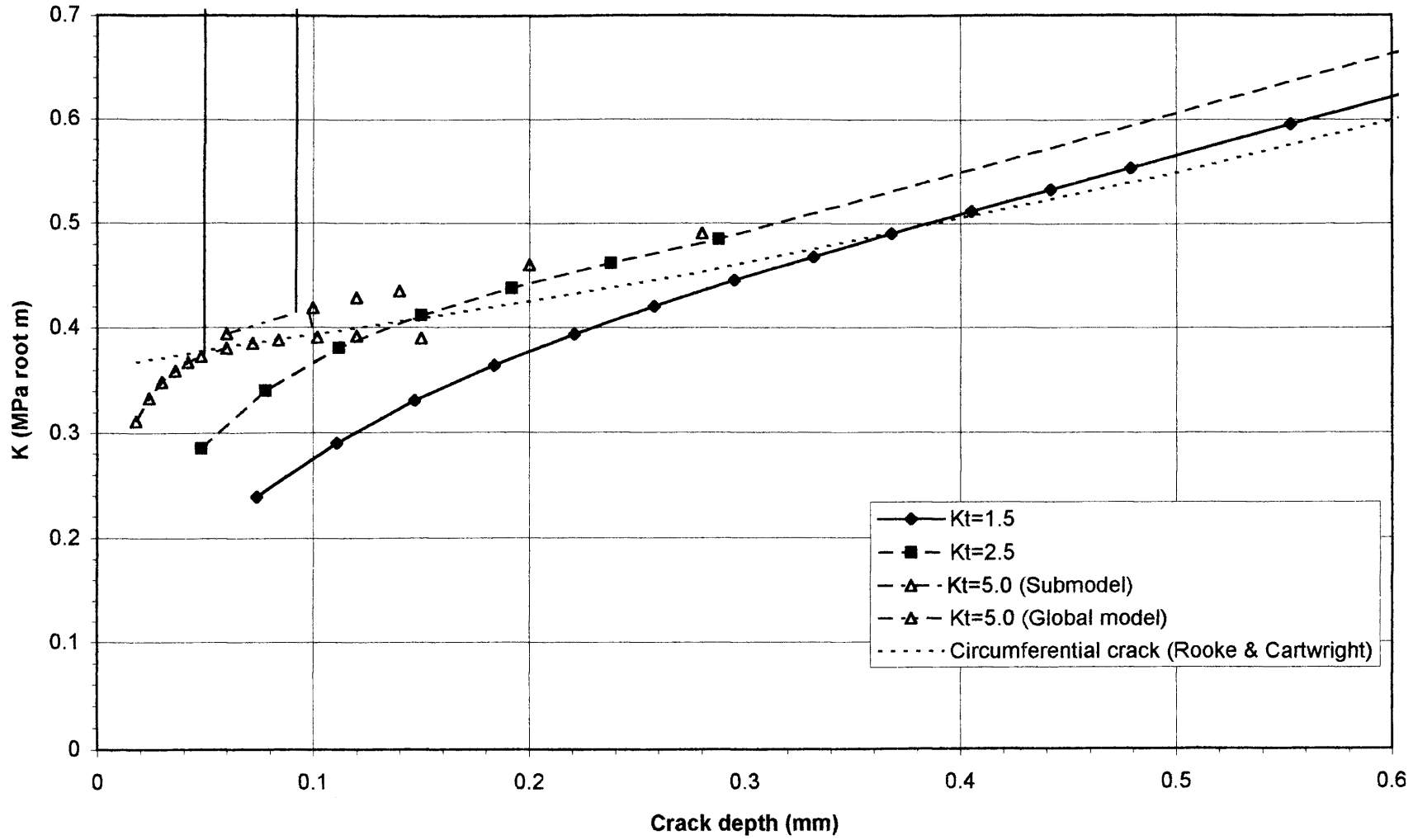


Figure 5.7 BCIRA Notched Specimen 2-D Crack Analyses
Calculated K Values for 10mm Cast Section



**Figure 5.8 BCIRA Notched Specimen 2-D Crack Analyses
Calculated K Values for 30mm Cast Section**

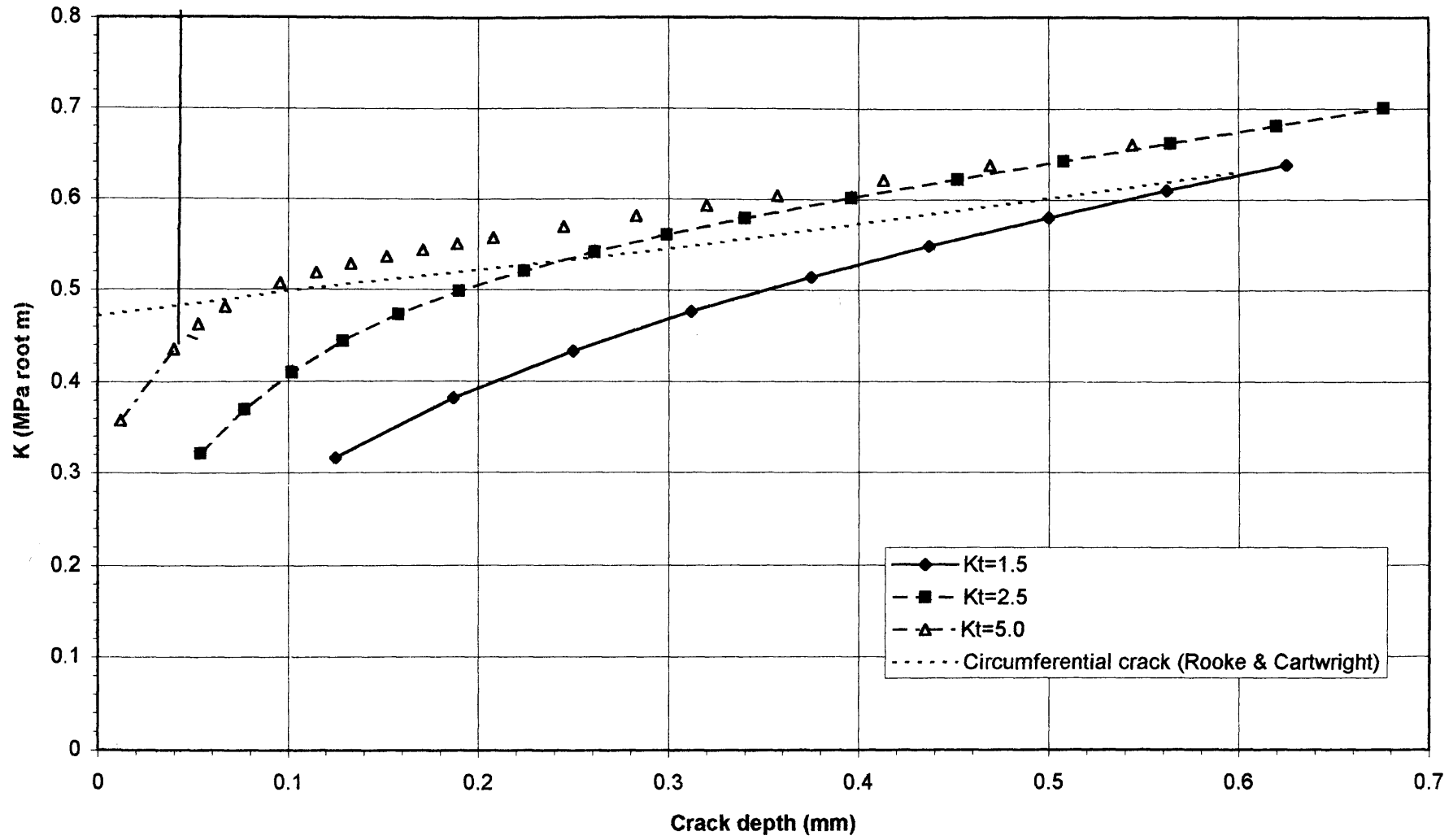
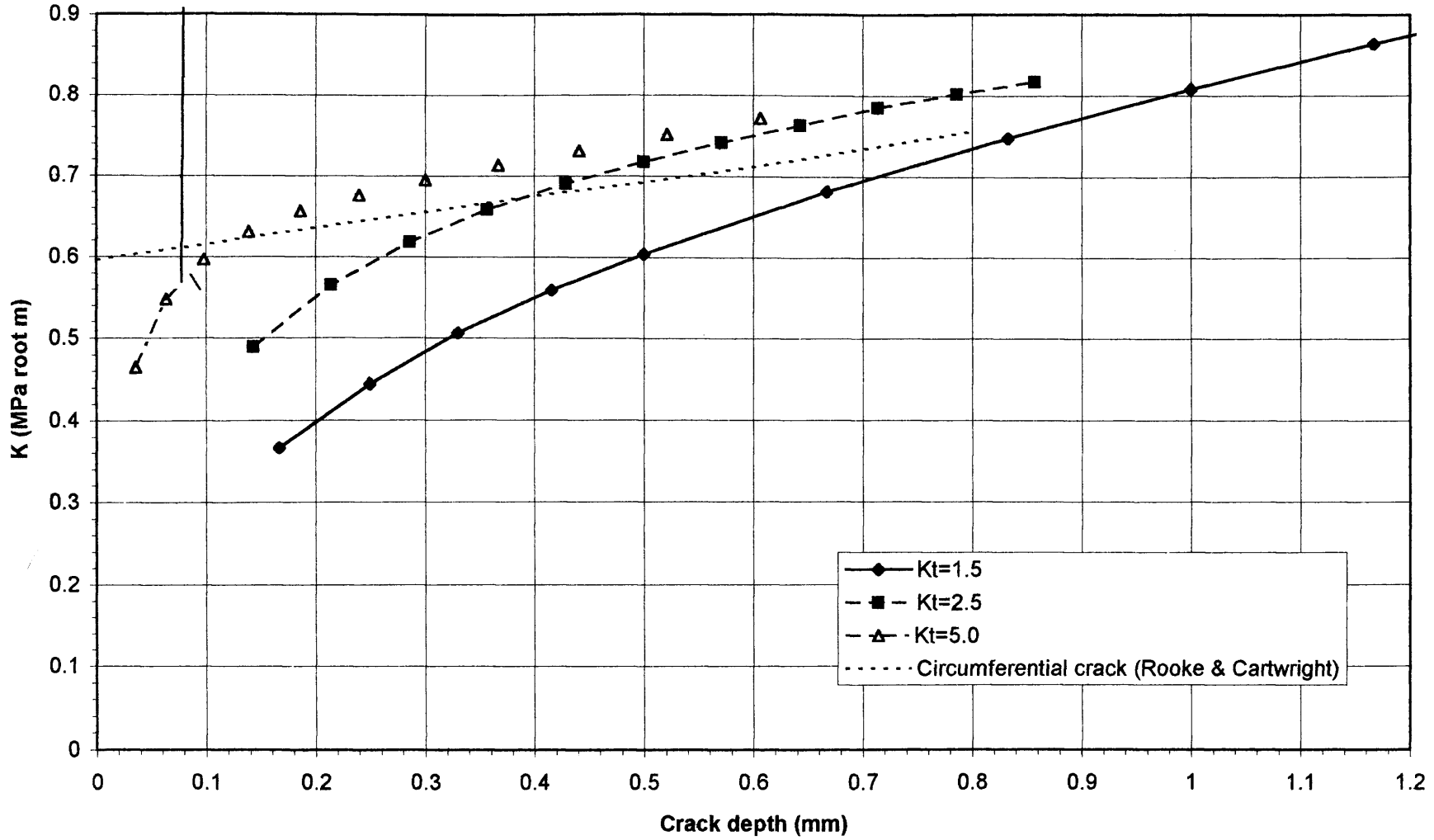


Figure 5.9 BCIRA Notched Specimen 2-D Crack Analyses
 Calculated K Values for 50mm Cast Section



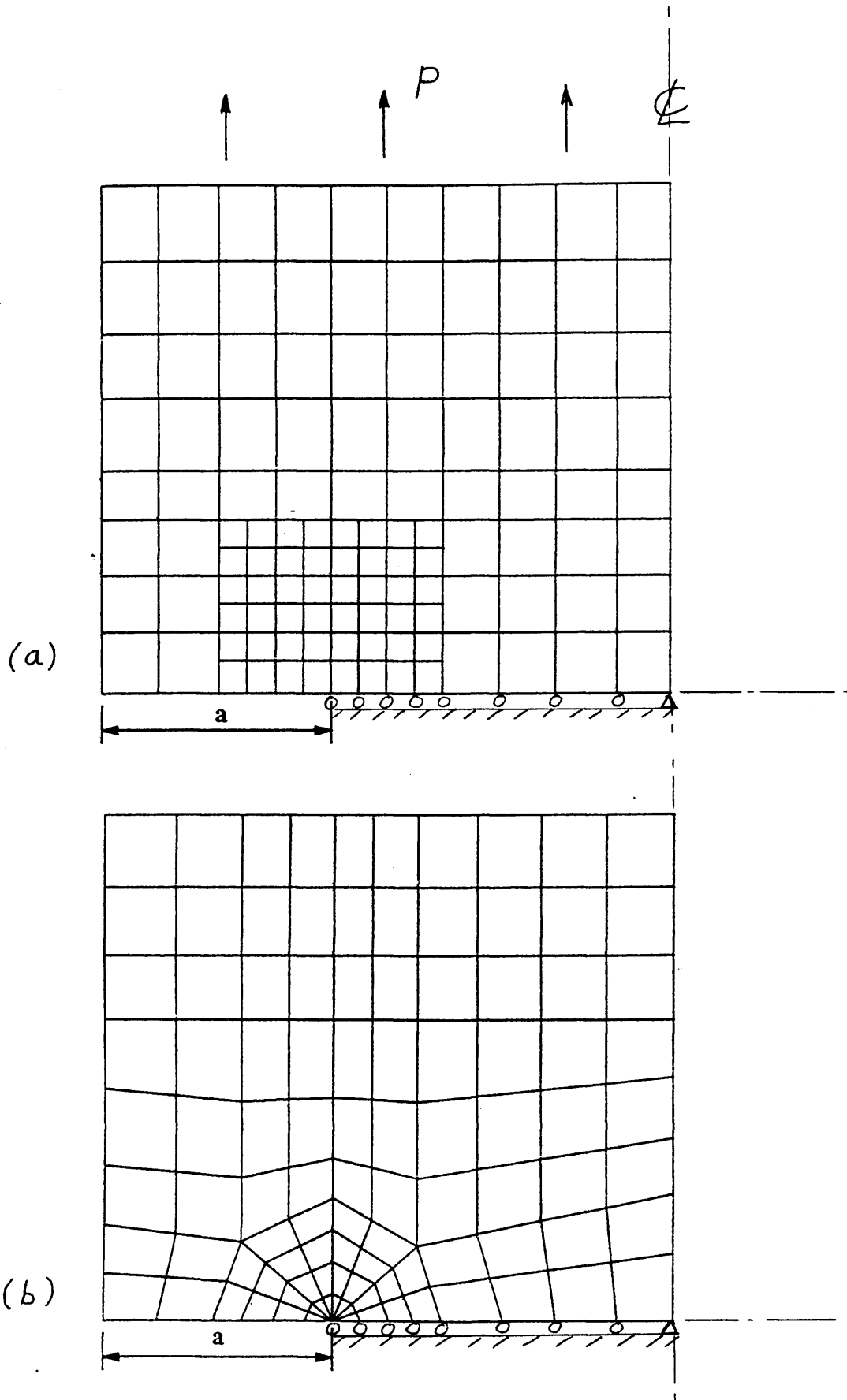


Figure 5.10 FE mesh types for double edge cracked plate model in side view - (a) Rectangular and (b) focussed

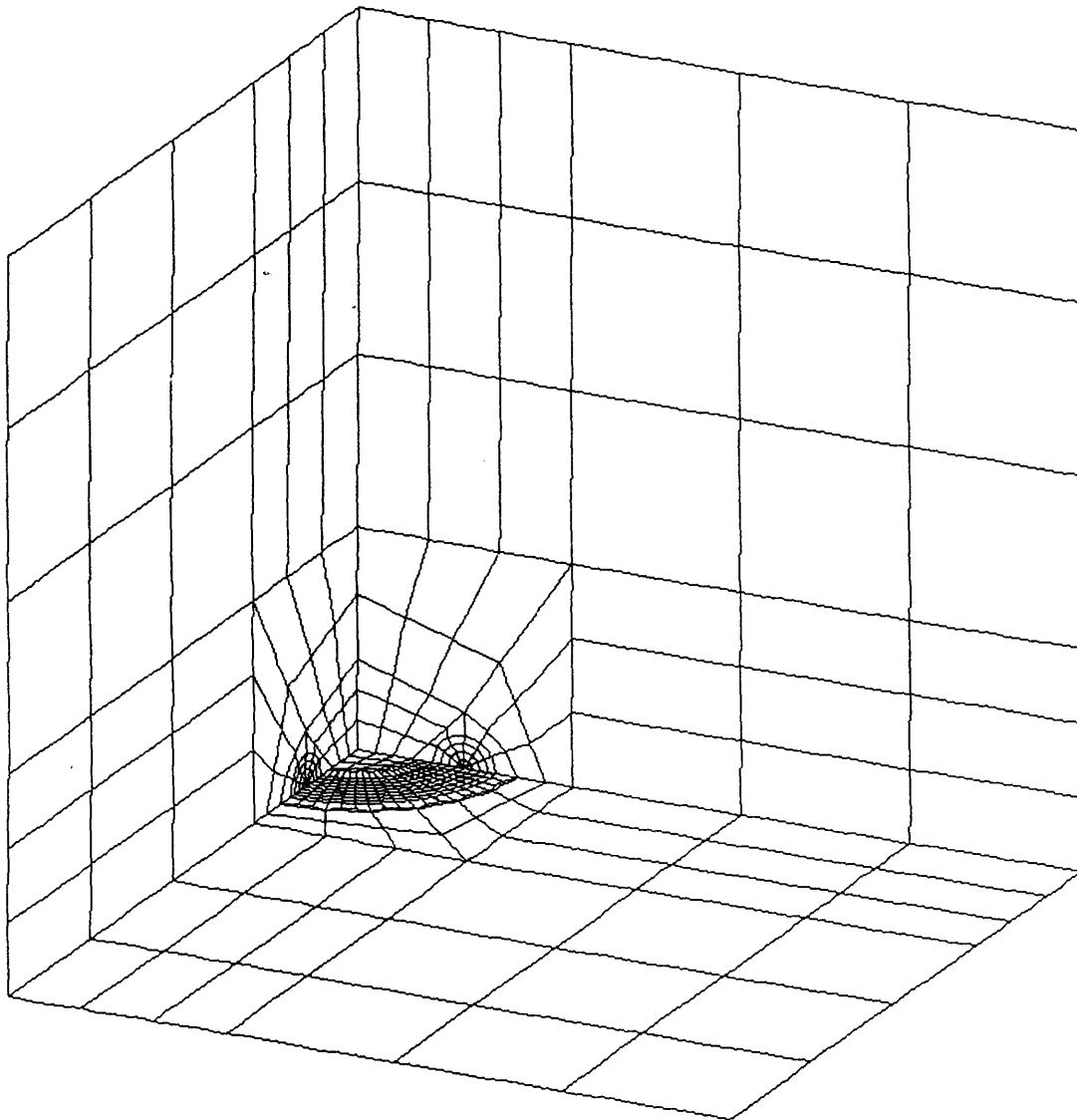
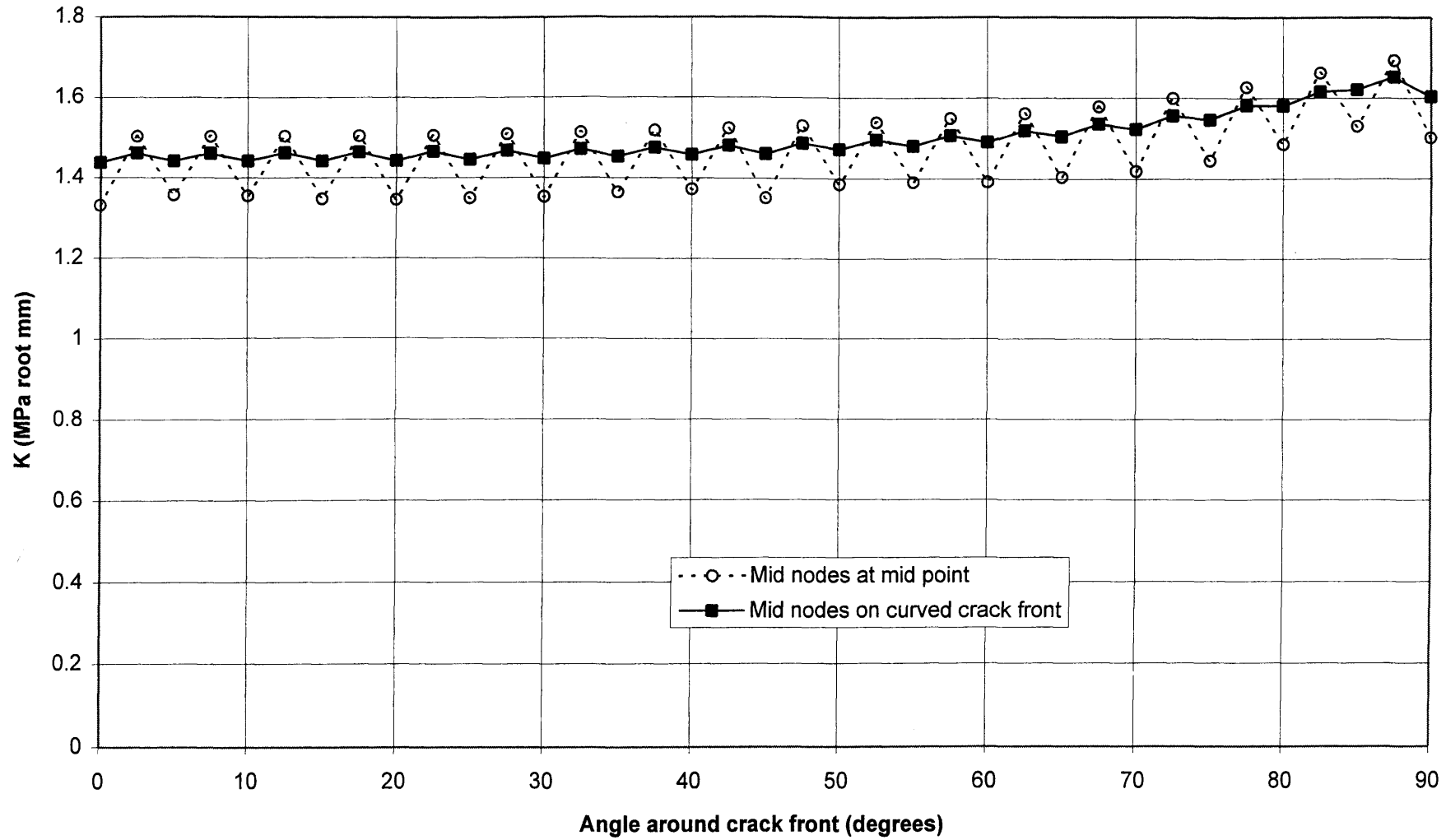
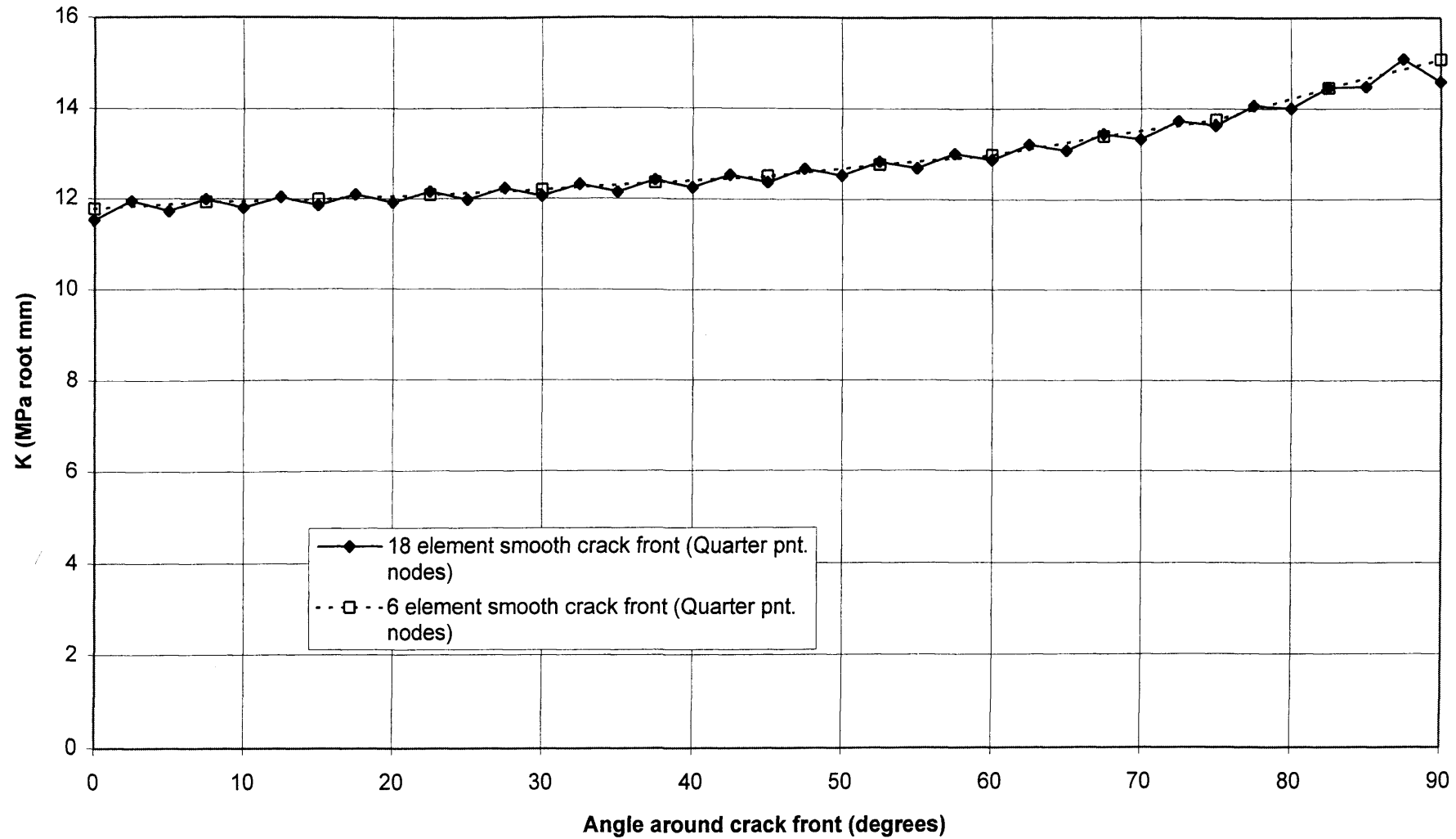


Figure 5.11 FE model used for analysis of semi-circular surface crack in a uniform body

**Figure 5.12 F.E. K Solutions for a Semi-Circular Surface Crack
- Comparison of Facetted and Smooth Crack Front Models**



**Figure 5.13 BRITE NOTCH SPECIMEN: $K_t=2.2$ SEMI-CIRCULAR SURFACE CRACK K SOLUTIONS
($a=0.3\text{mm}$) 10 MPa NOMINAL STRESS - EFFECT OF MESH DENSITY**



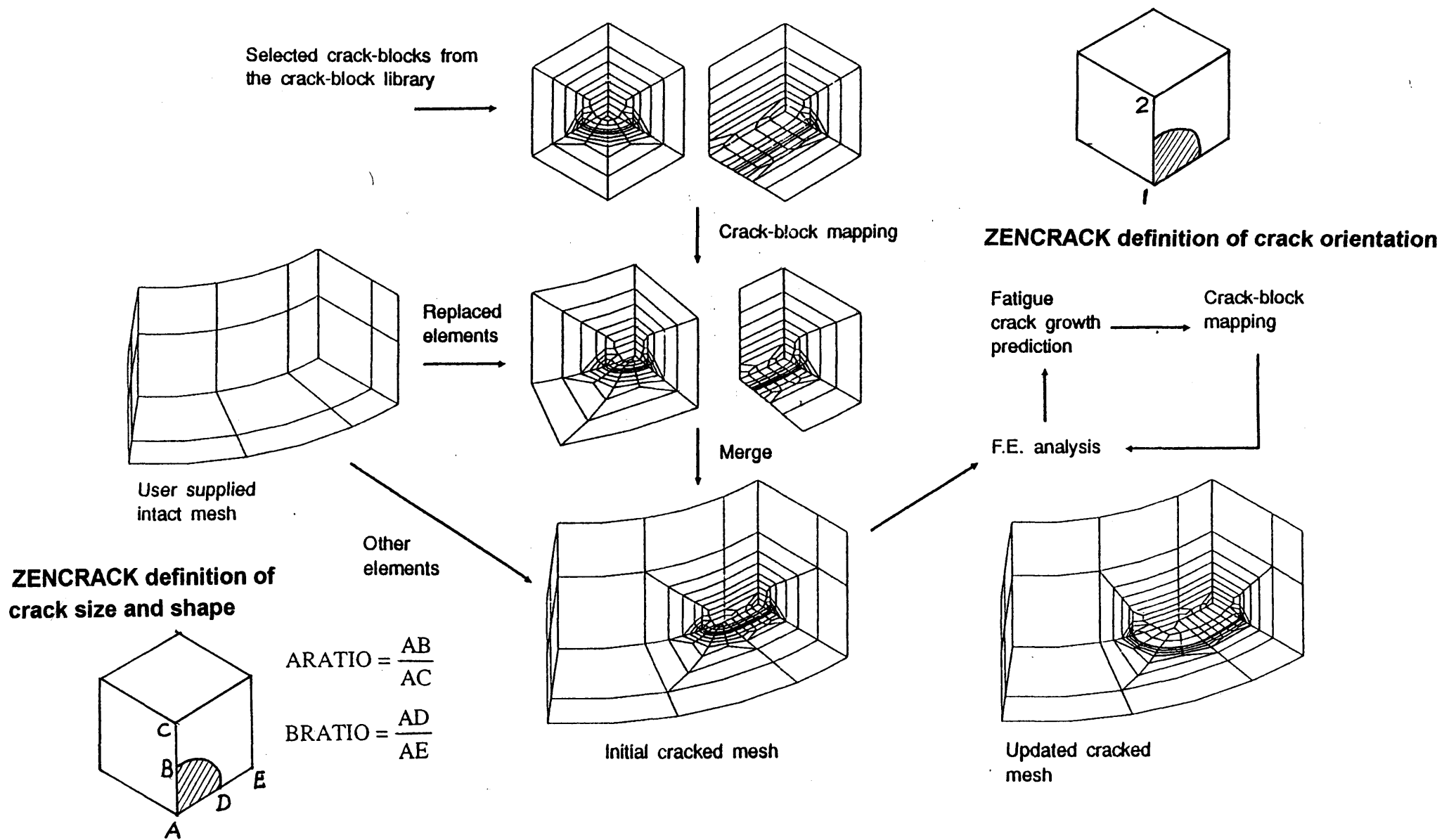


Figure 5.14 ZENCRACK Meshing and Analysis Procedure

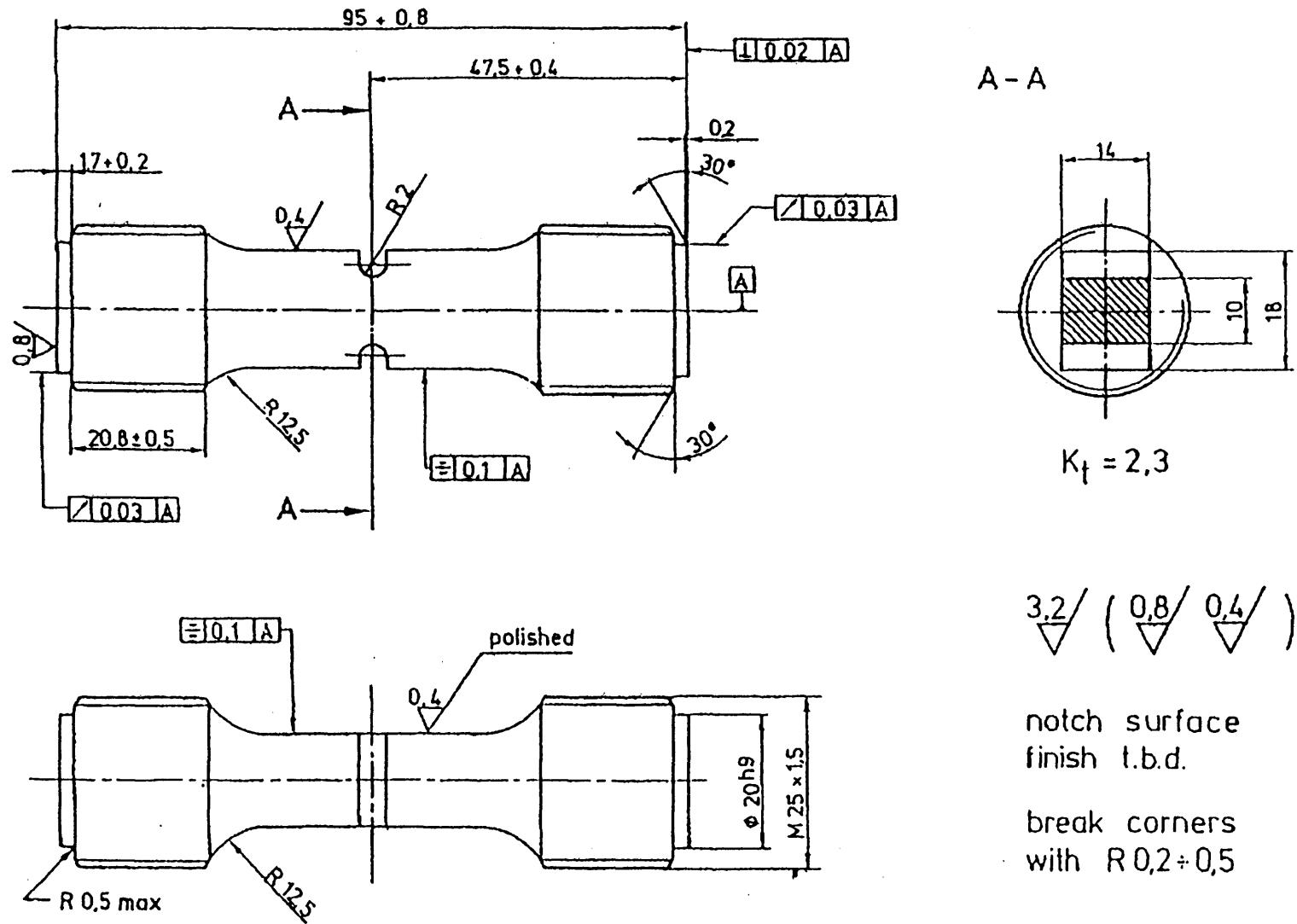


Figure 5.15 Double edge notched specimen geometry used in crack growth predictions with ZENCRACK

TA31 Engineering Rim Specimen

F.E. CRACK ANALYSES:

- Semi-circular surface crack
- Crack depths 0.05 to 1.5mm
- Net section nominal stress = 10.0 MPa
- Effective Crack Geometry Factor Calculated

$$Y = \frac{K}{S_{nom} \sqrt{\pi a}}$$

a (mm)	K (Deepest point) (MPa root m)	Y	
0.05	6.11553	1.5430	
0.10	8.17379	1.4583	
0.20	10.6338	1.3415	
0.30	12.1329	1.2498	
0.40	13.1270	1.1710	
0.60	14.3904	1.0481	
0.80	15.1626	0.9564	
1.5	16.5833	0.7639	(Symmetric cracks)
1.5	16.8219	0.7749	(Single crack)

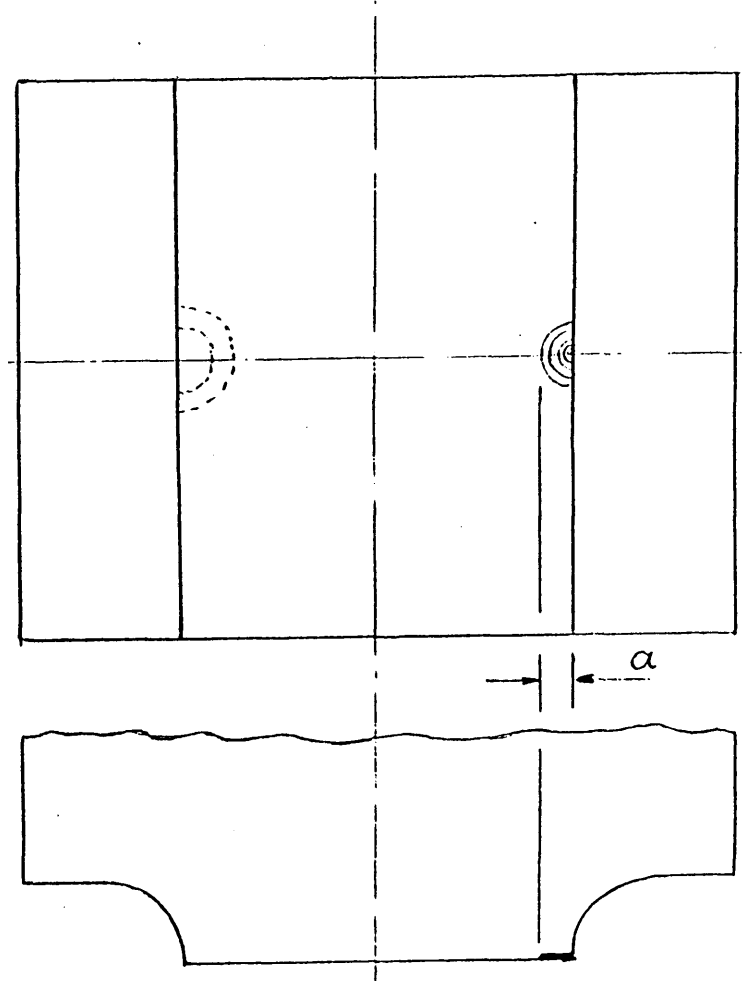


Figure 5.16 Deepest point K solution values and crack sizes for the double edge notched specimen with a fixed crack aspect ratio assumed

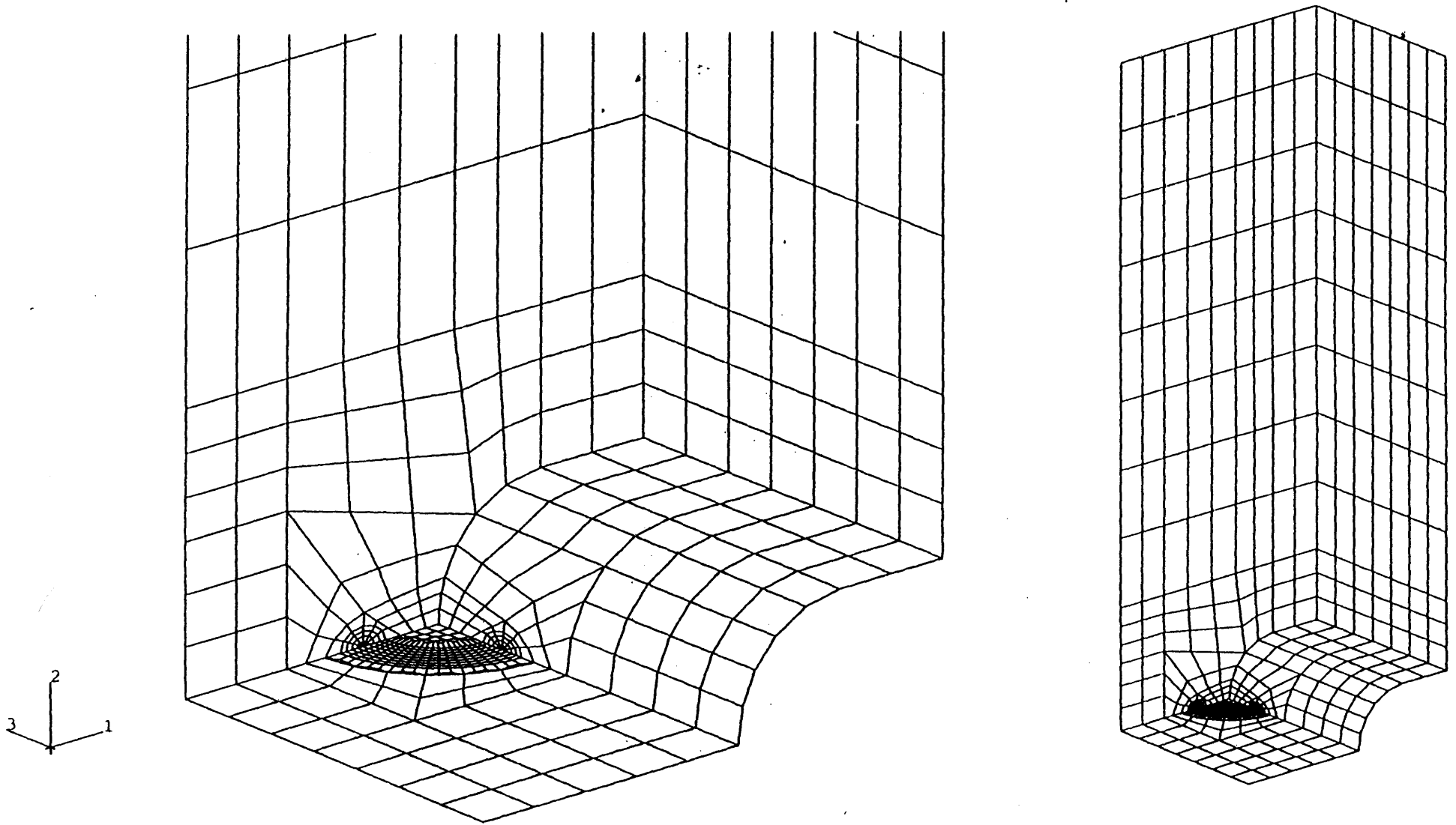
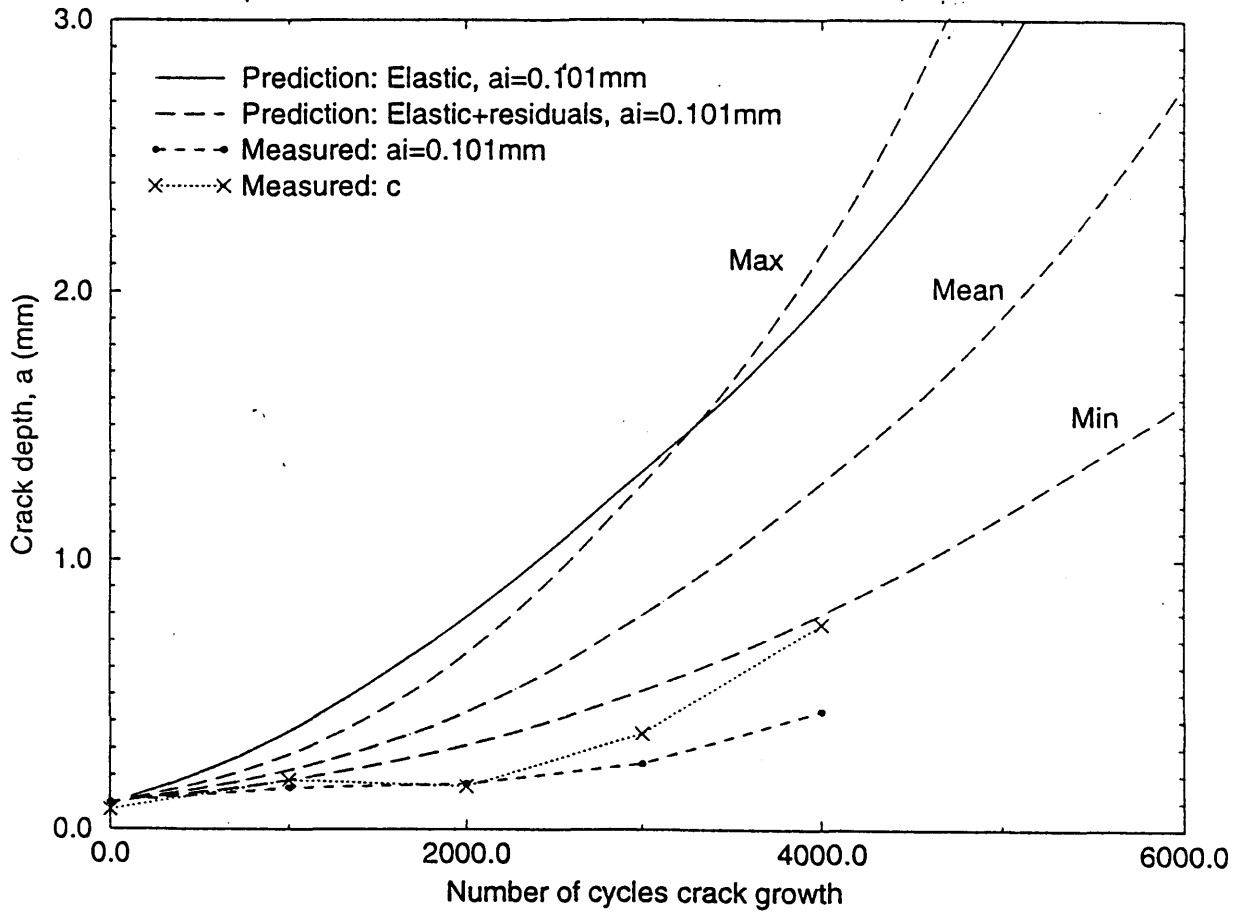


Figure 5.17 Typical FE mesh for the double edge notched specimen crack analyses

TA31 Engineering Rim Specimens Crack Growth

Specimen DTF150, Net Section Stress=80/800 MPa, Dwell=120s



Specimen DTF192, Net Section Stress=85/850 MPa, Dwell=120s

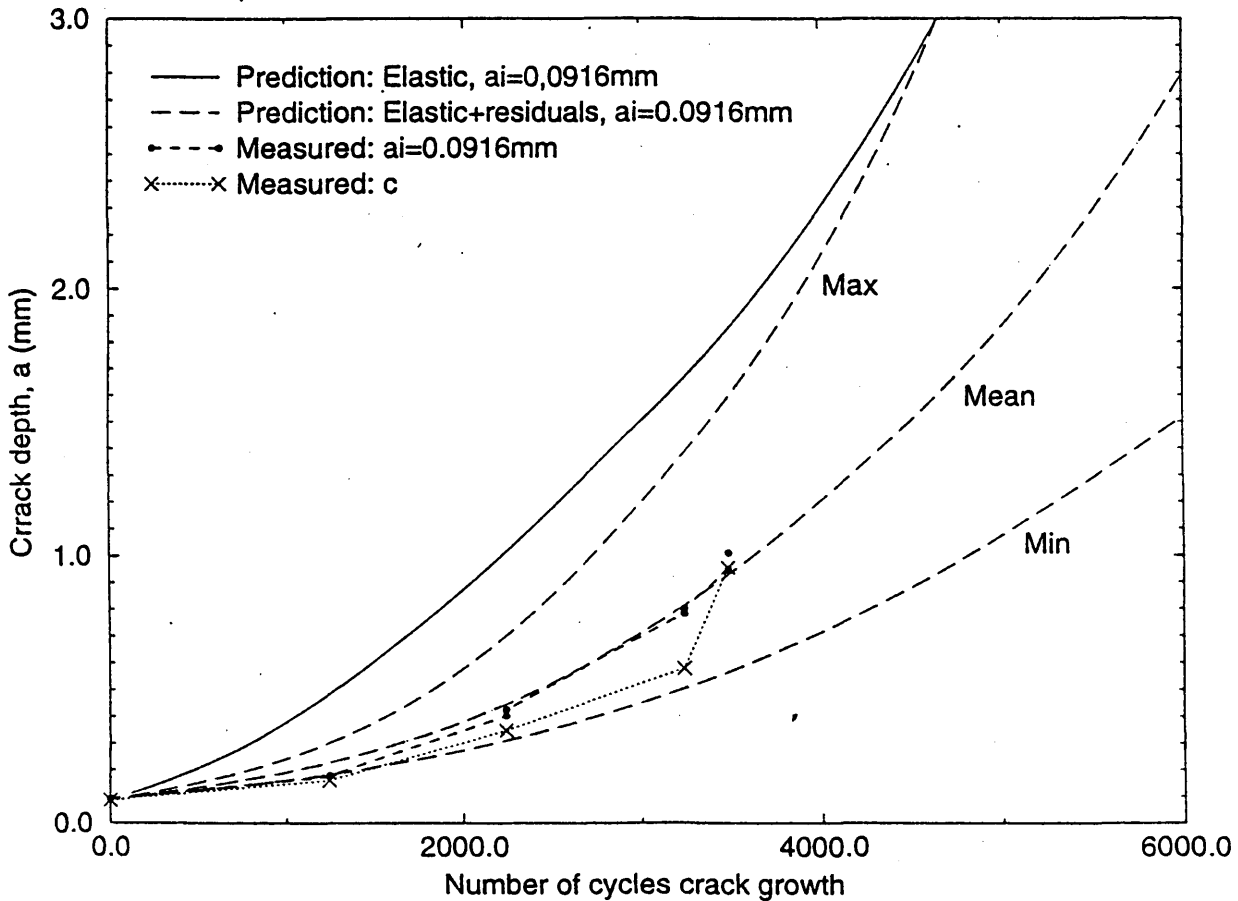
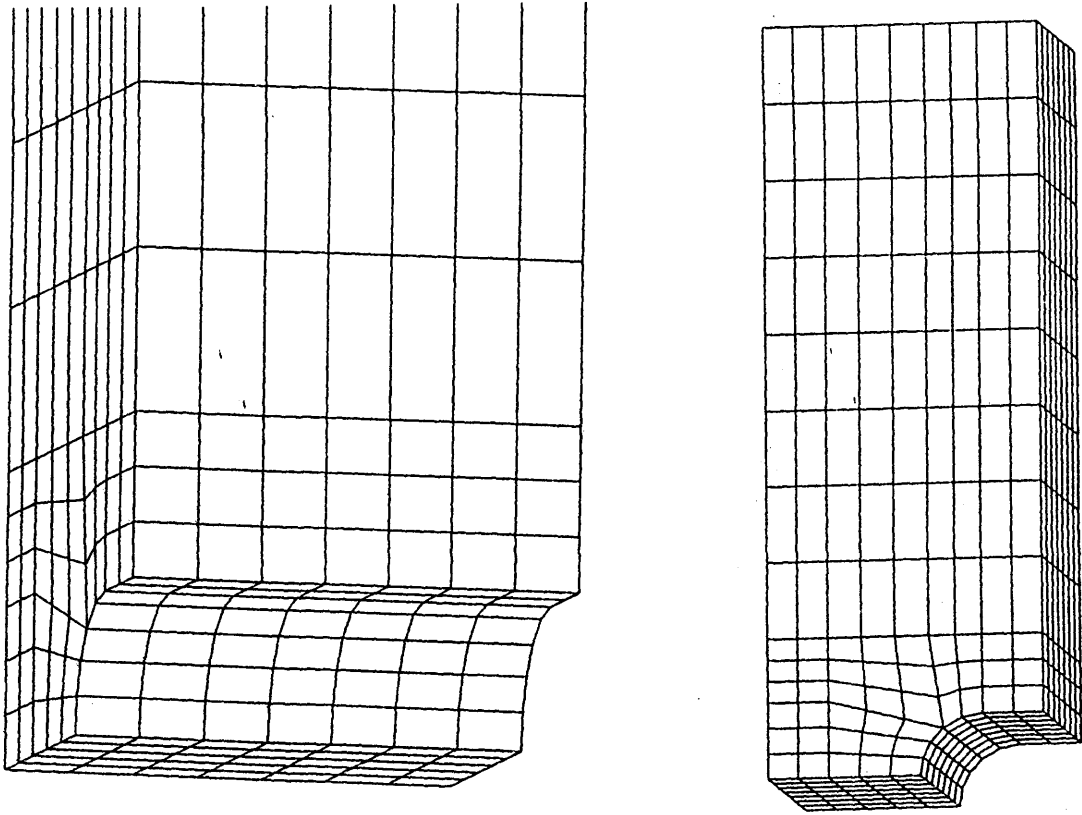
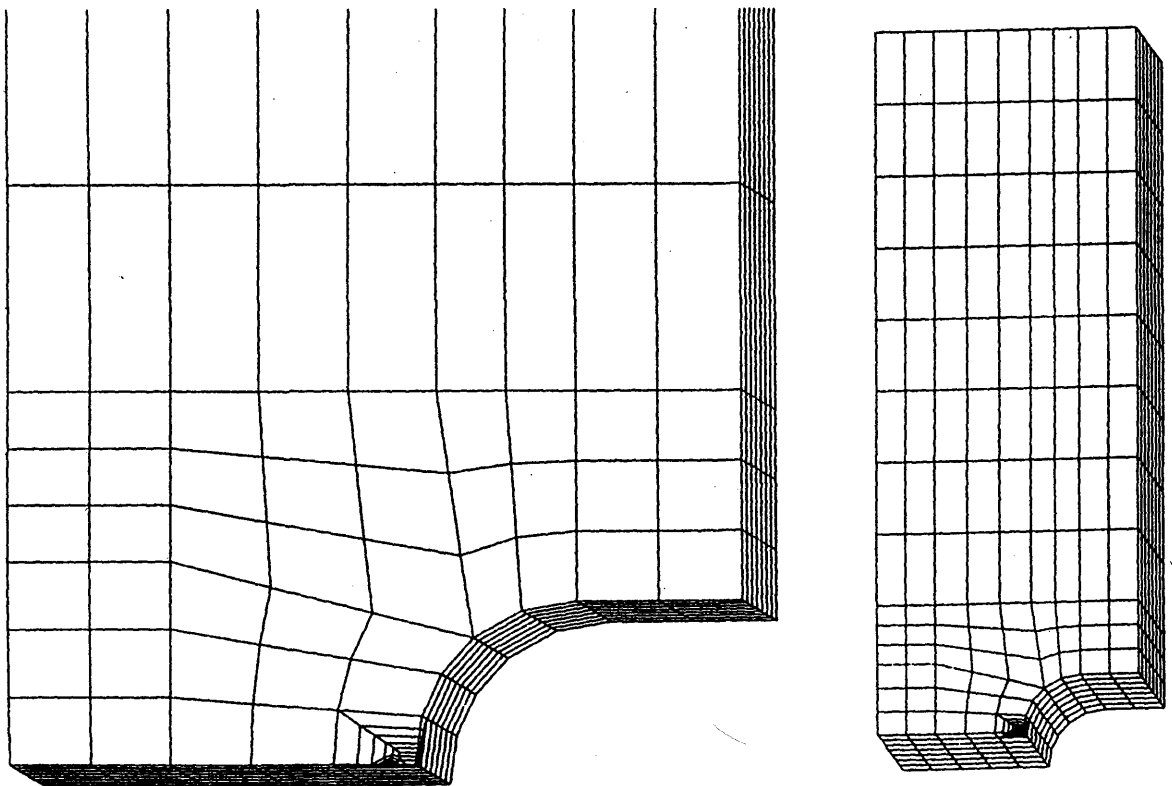


Figure 5.18 Example of crack growth predictions (constant aspect ratio and deepest point K solution) and comparisons with measured crack sizes

(a)



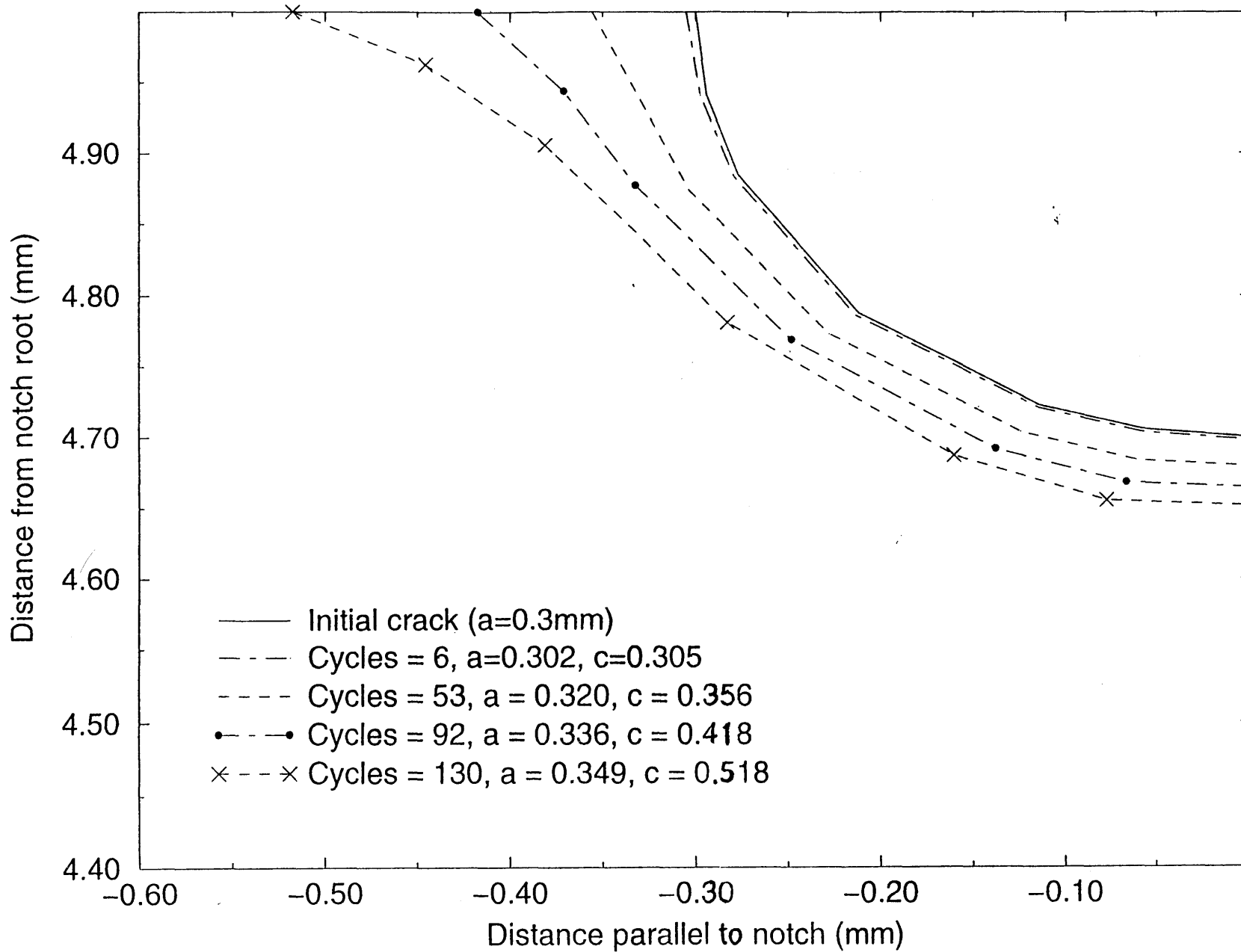
(b)



**Figure 5.19 (a) Uncracked FE model used as input to ZENCRACK
(b) Typical crack mesh generated by ZENCRACK**

Figure 5.20 Crack profiles predicted by ZENCRACK analyses

Crack Growth From 0.3mm Semi-Circular Surface Crack (TA31 Rim Specimen)



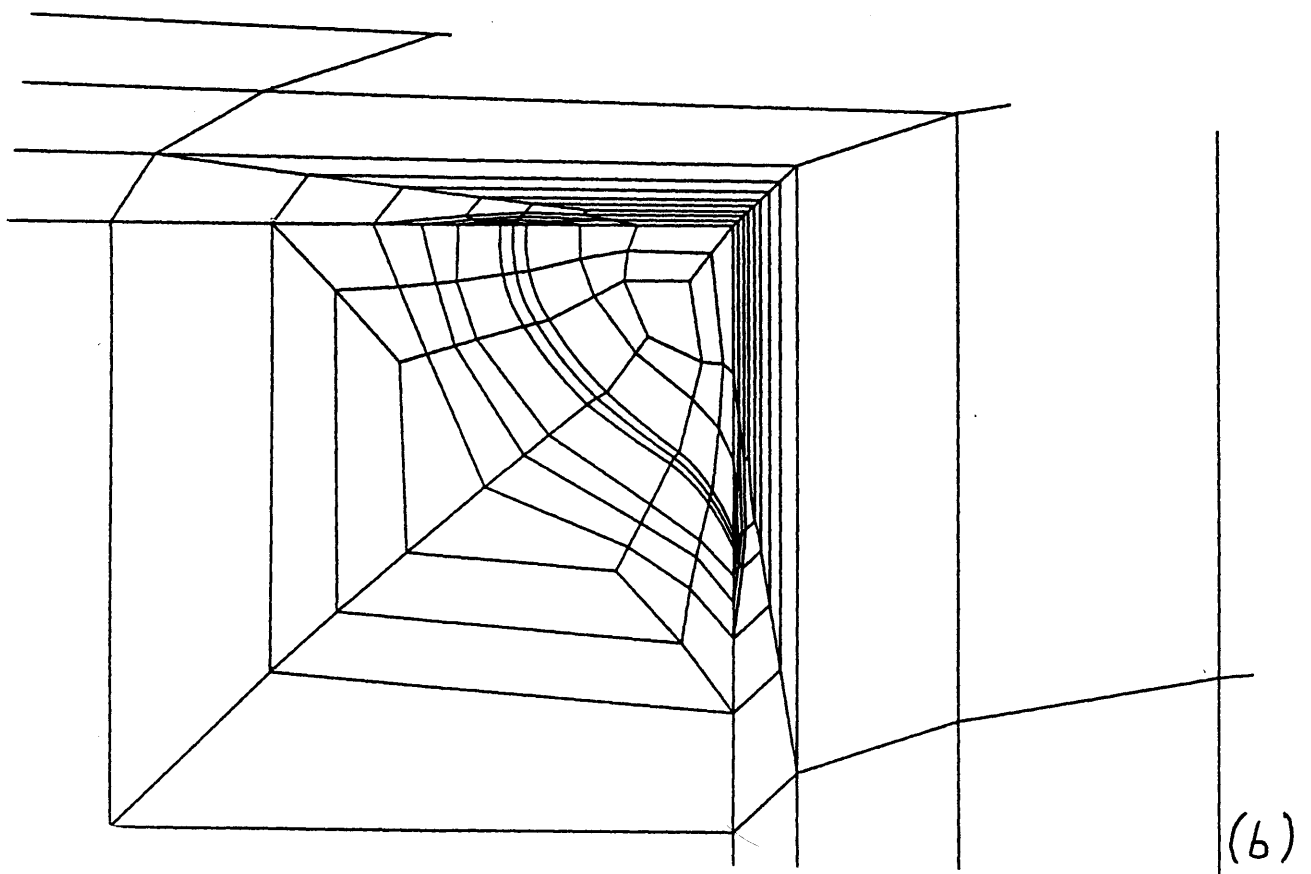
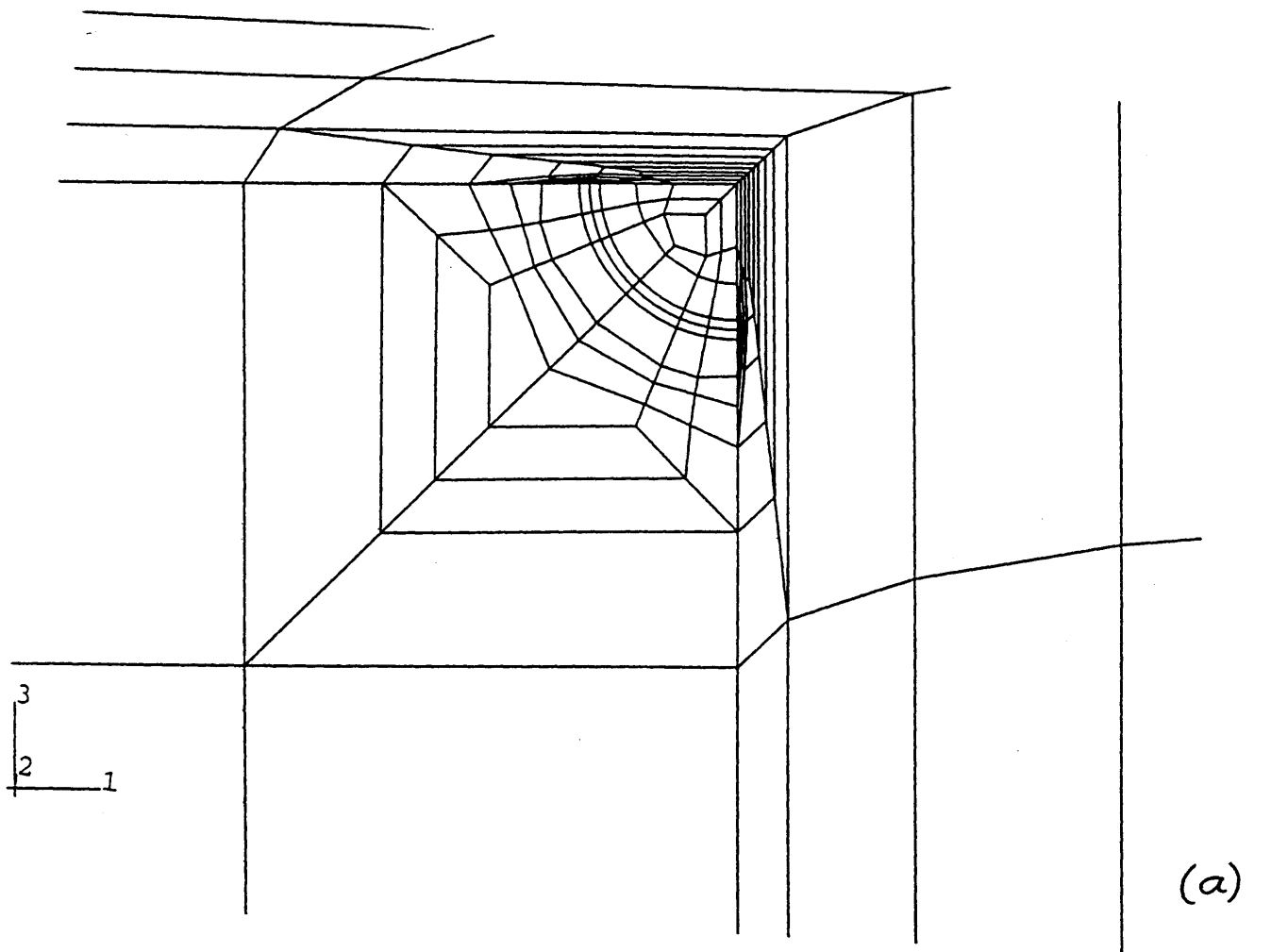


Figure 5.21 Comparison of initial and final cracked mesh geometries generated in the ZENCRACK analysis

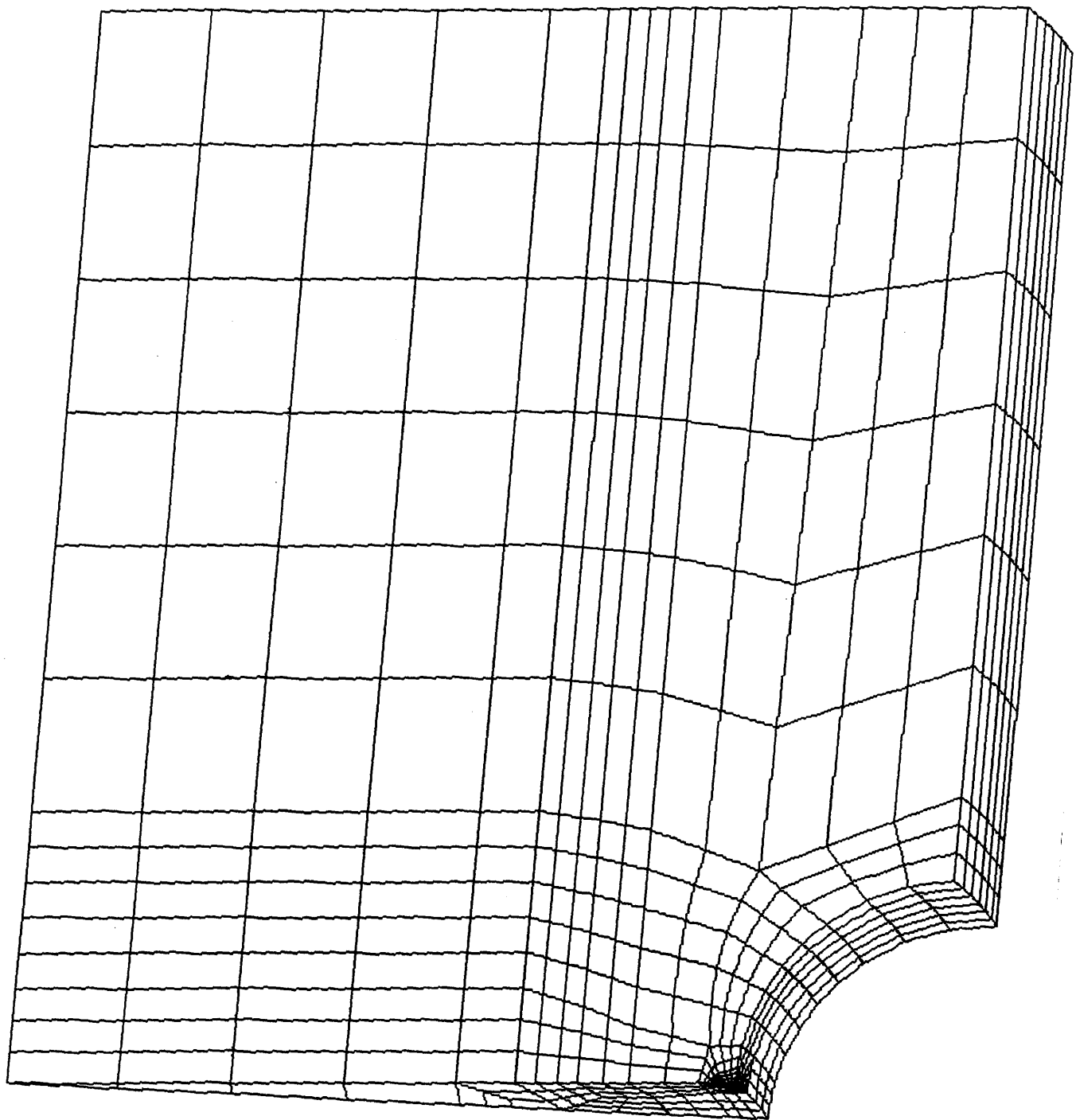


Figure 5.22 Typical FE mesh of a circumferentially 'U' notched specimen ($K_t = 2.2$) with a semi-circular surface crack

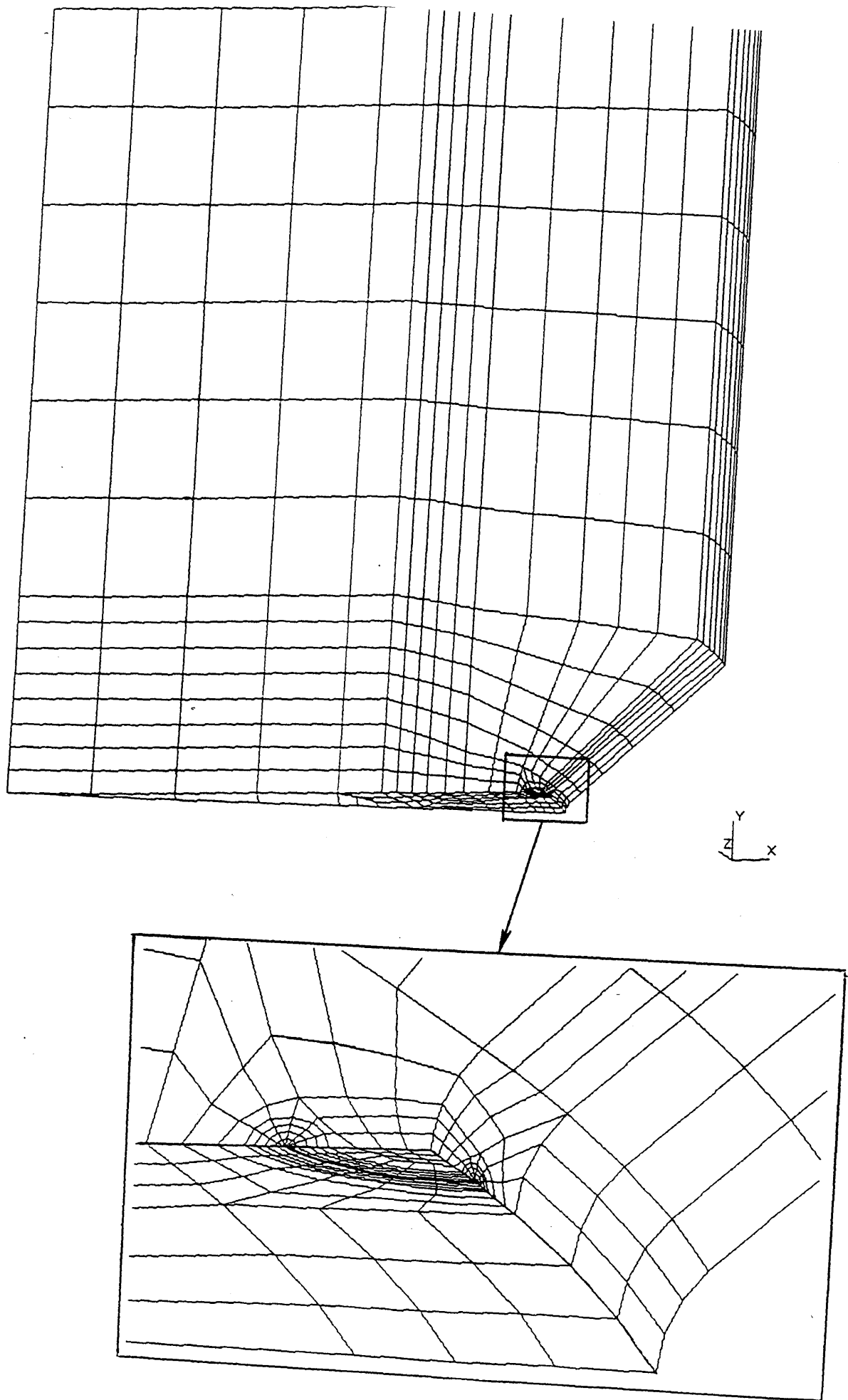


Figure 5.23 Typical FE mesh of a circumferentially 'V' notched specimen ($K_t = 5.6$) with a semi-circular surface crack

Figure 5.24 BRITE Notch Specimen $K_t = 2.2$: K Solutions for Semi-Circular Surface Cracks
Unity nominal applied stress

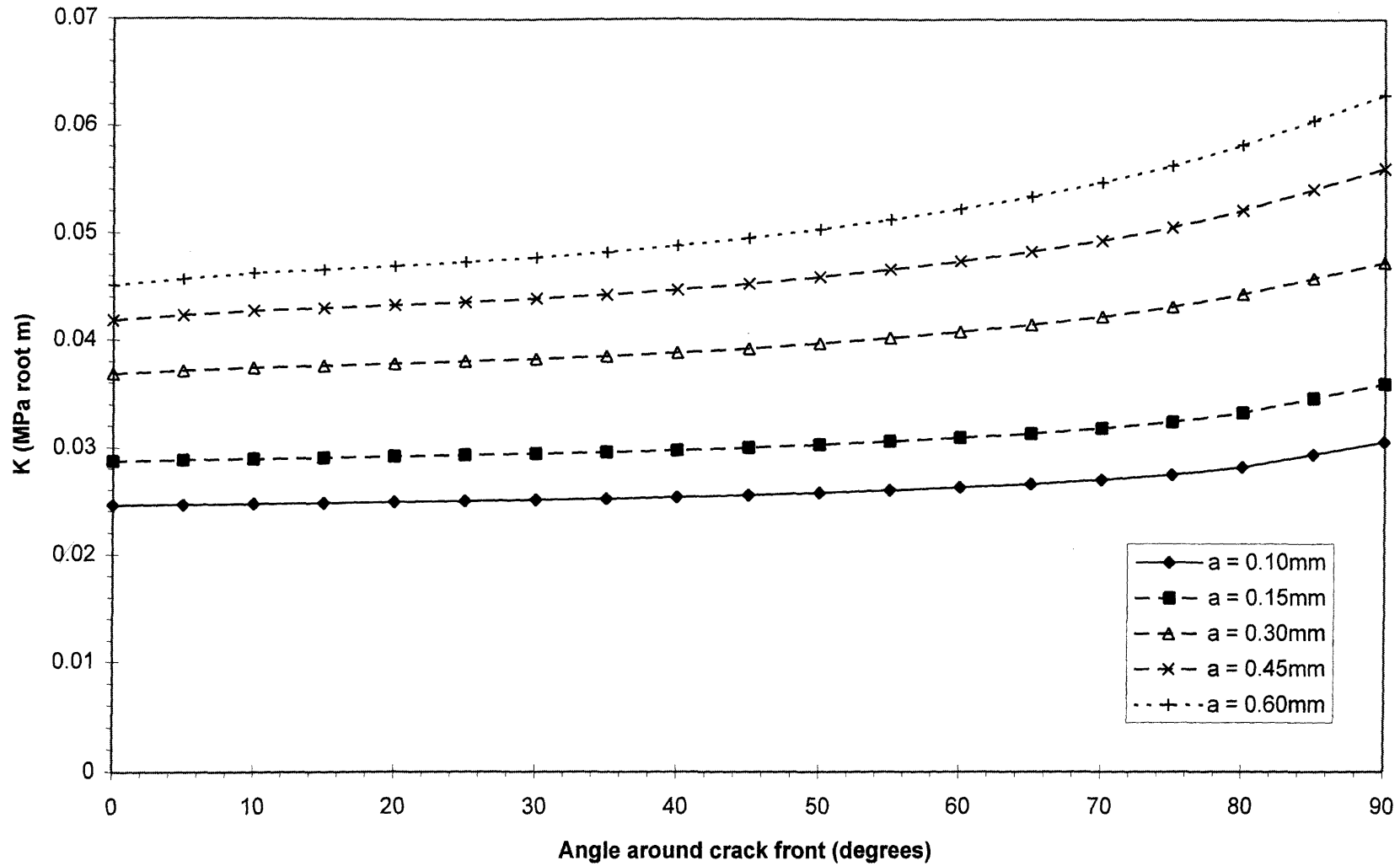


Figure 5.25 BRITE Notch Specimen $K_t = 2.2$: K Solutions for (a) Semi-Circular Surface Cracks (Deepest Point) and (b) Continuous surface cracks at the notch root. Unity nominal applied stress.

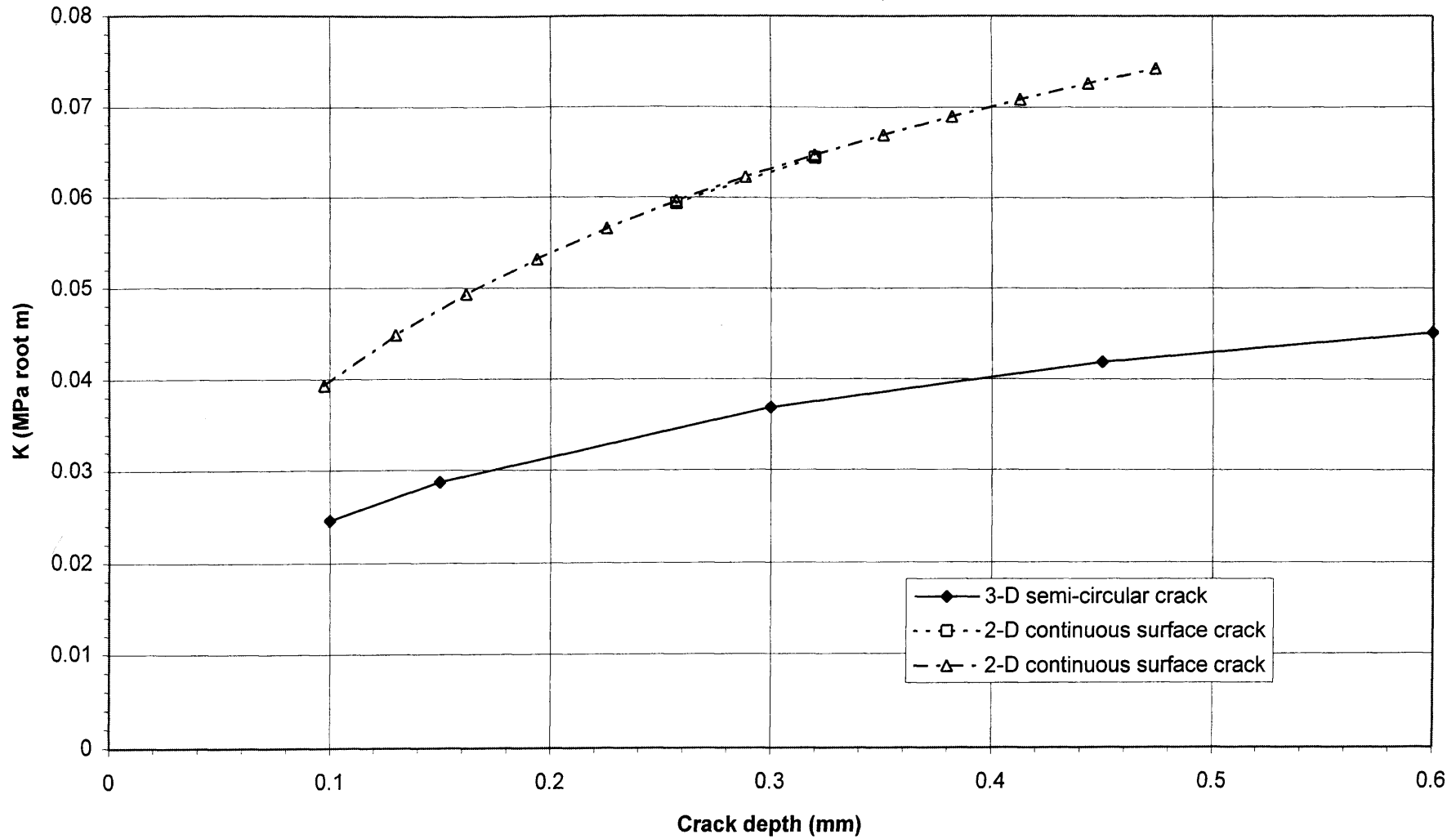


Figure 5.26 BRITE Notch Specimen $K_t = 5.6$: K Solutions for Semi-Circular Surface Cracks
Unity nominal applied stress

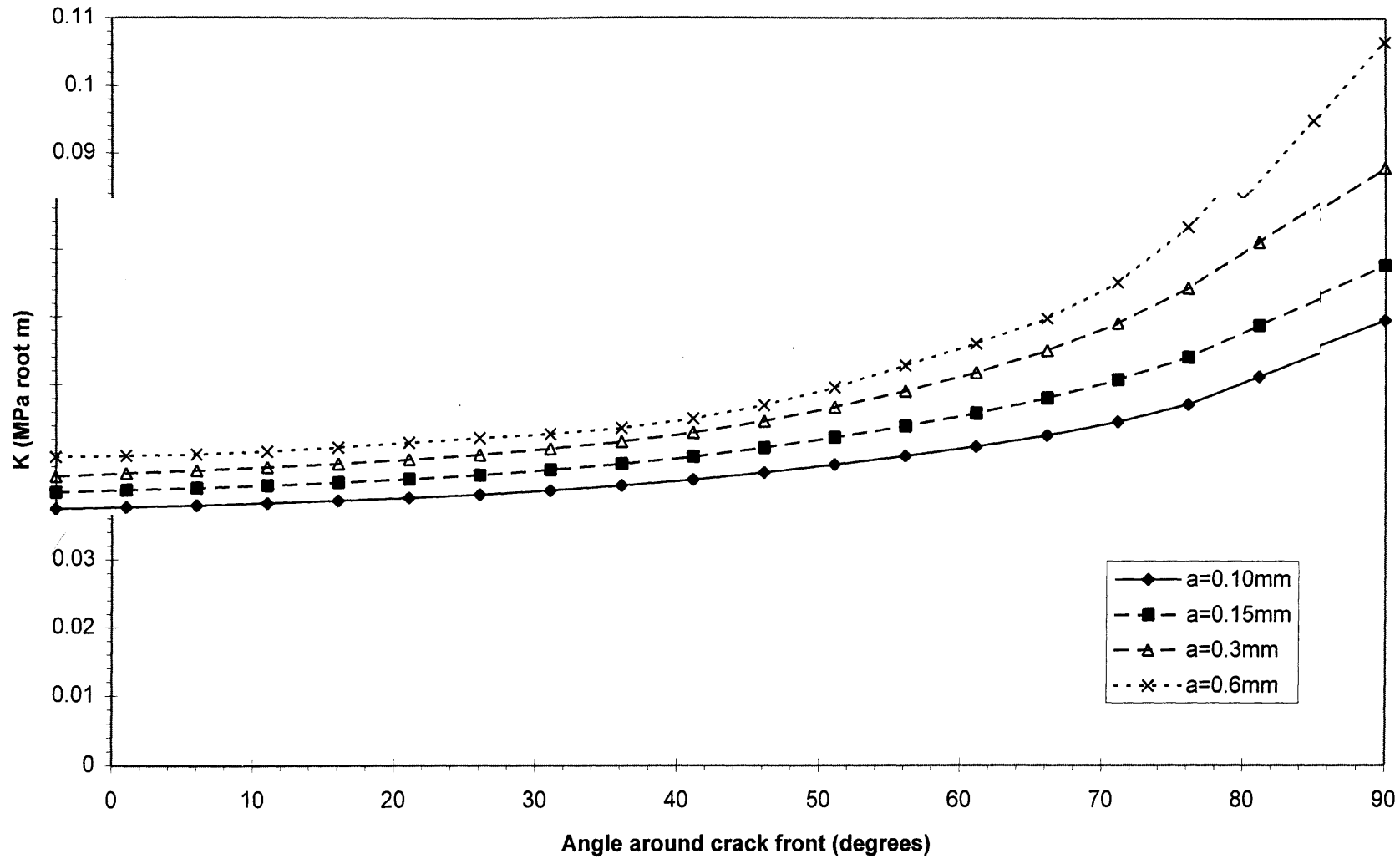
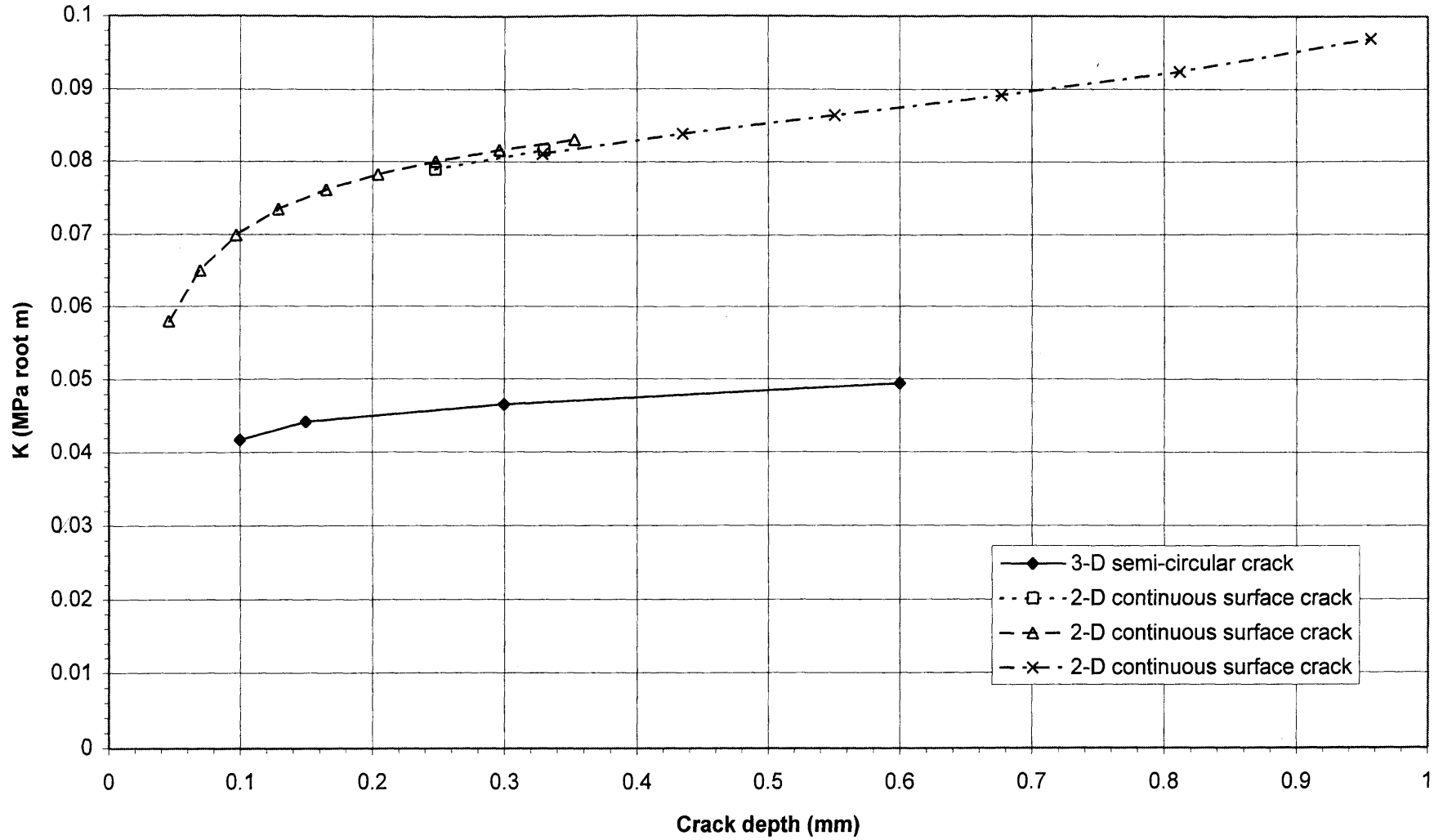
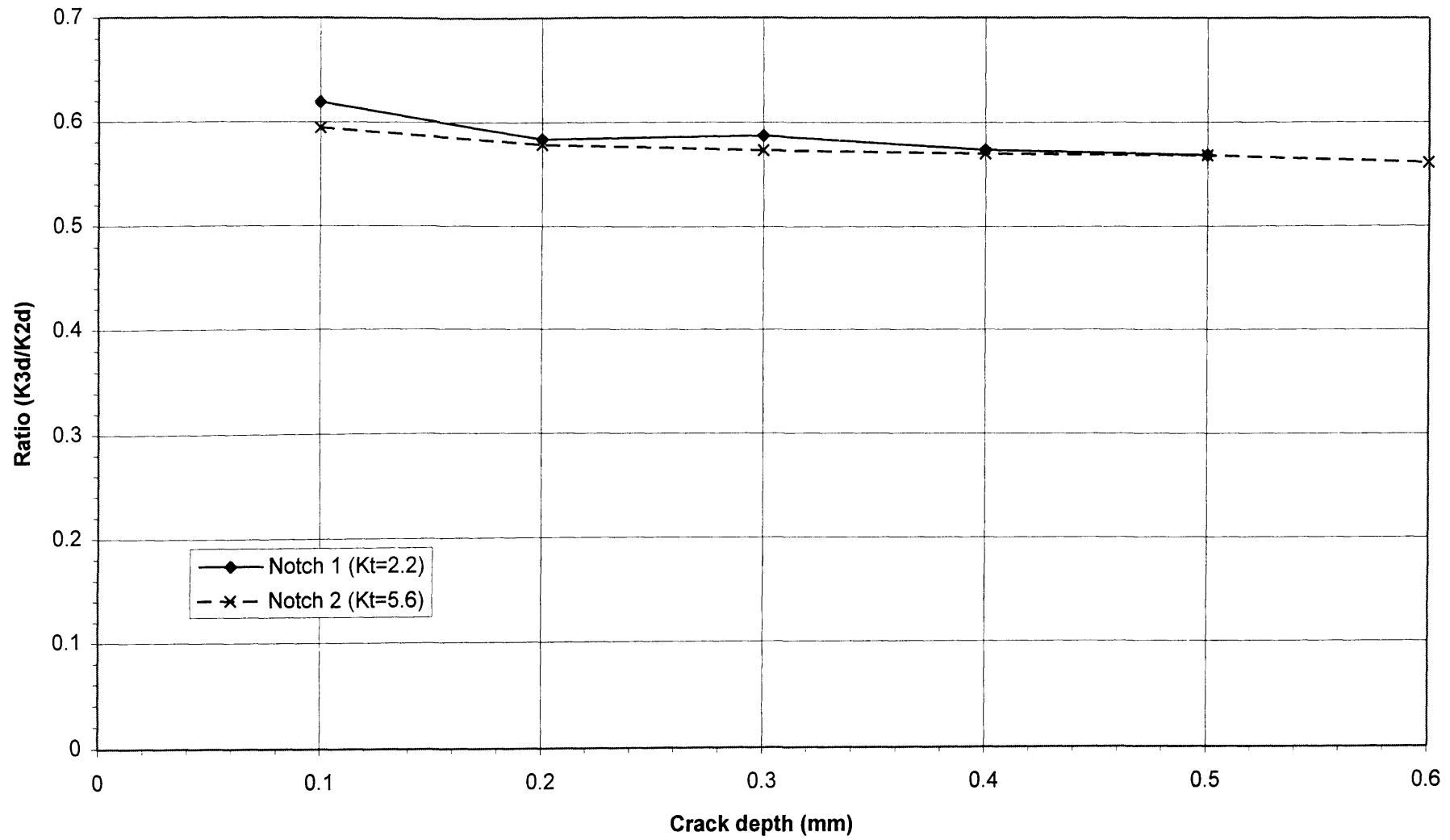


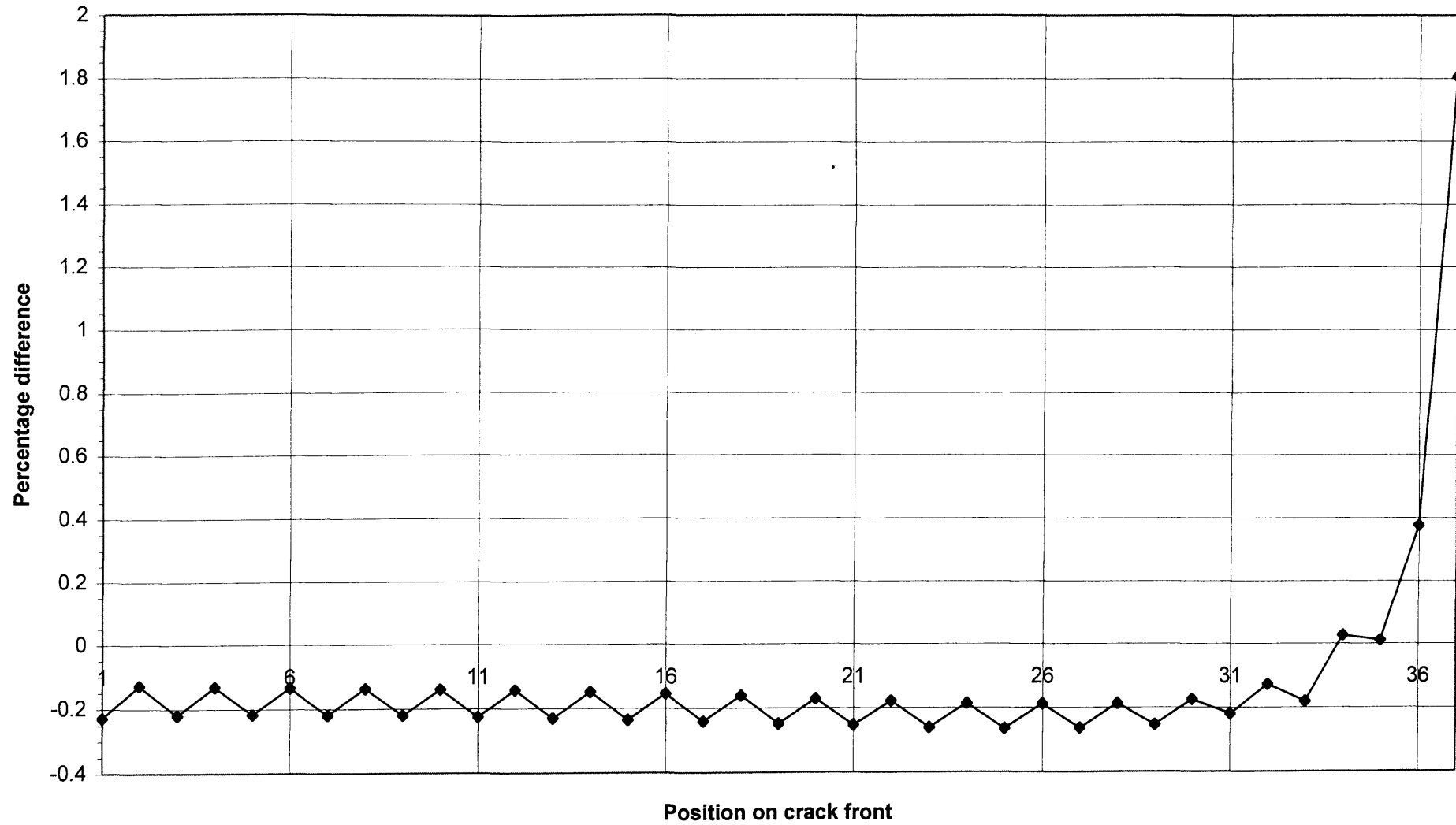
Figure 5.27 BRITE Notch Specimen $K_t = 5.6$: K Solutions for (a) Semi-Circular Surface Cracks (Deepest Point) and (b) Continuous surface cracks at the notch root. Unity nominal applied stress.



**Figure 5.28 BRITE Notched Specimen Crack Analyses
Ratio of 3-D to 2-D K Solutions for Notch 1 and Notch 2**



**Figure 5.29 Notch 2, 0.1mm Crack Depth : Effect of Elastic Properties on the Calculated K Value.
Results for E=120000 MPa, Nu=0.26 Relative to E=200000 MPa, Nu=0.3**



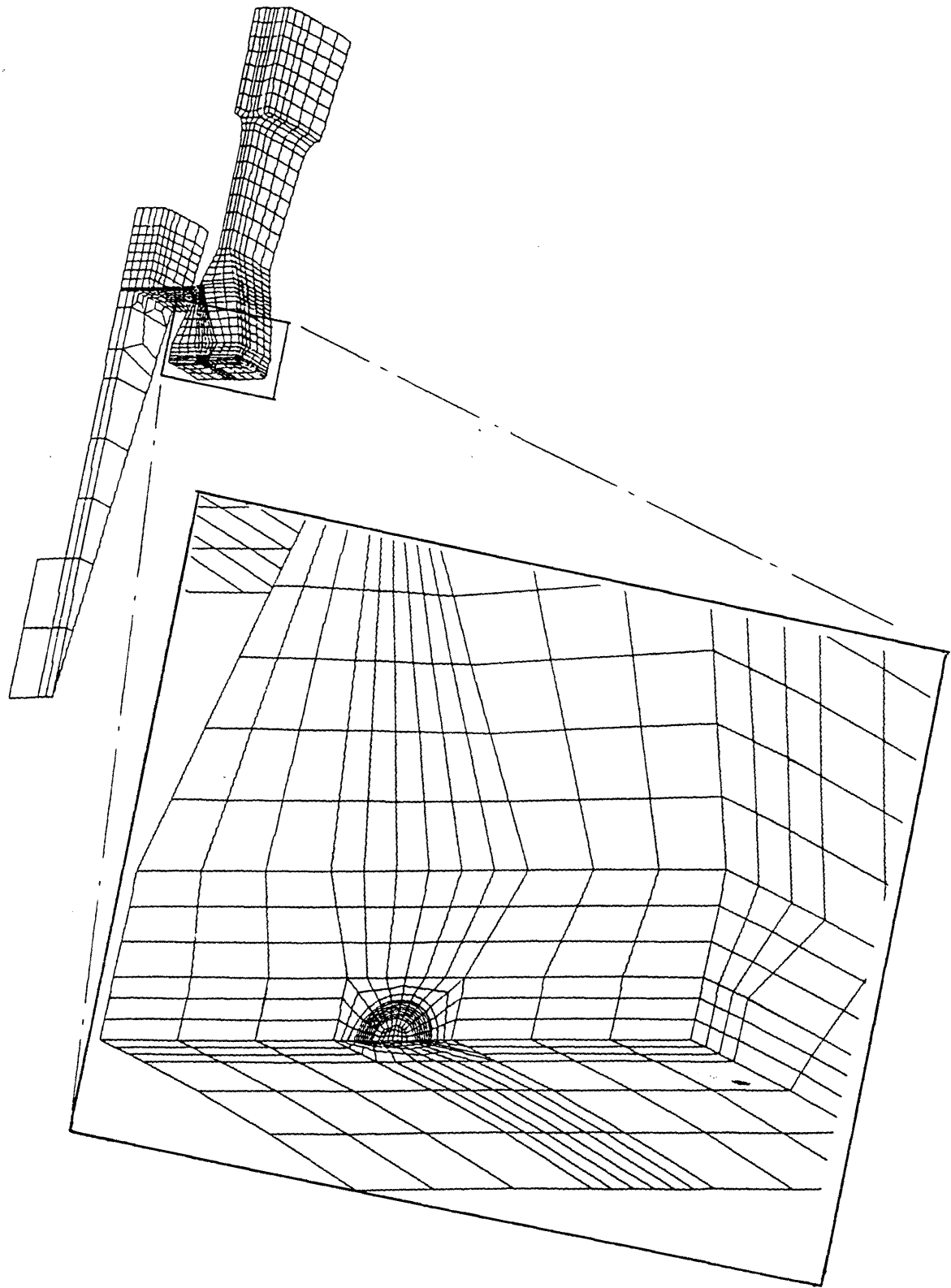
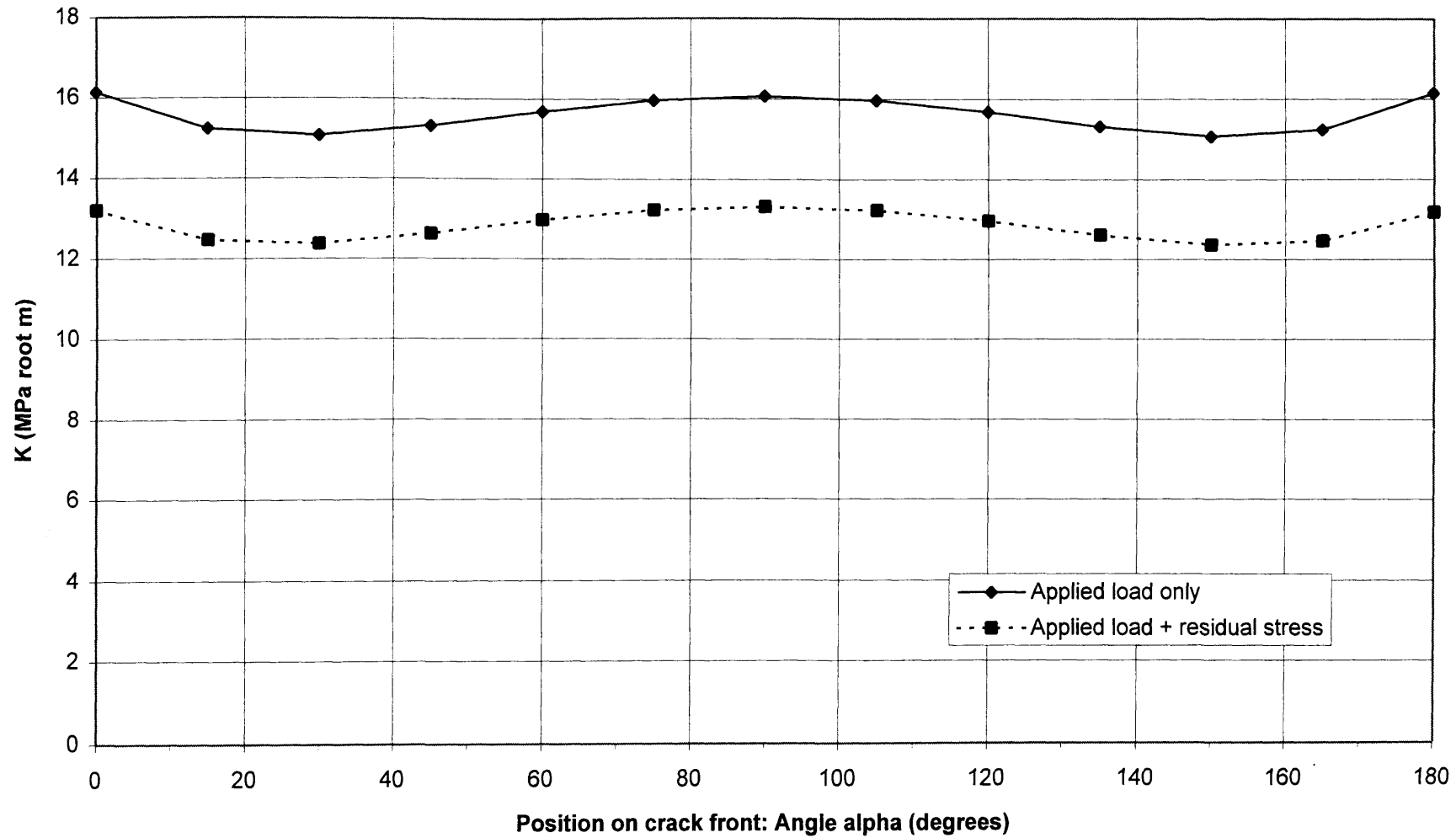
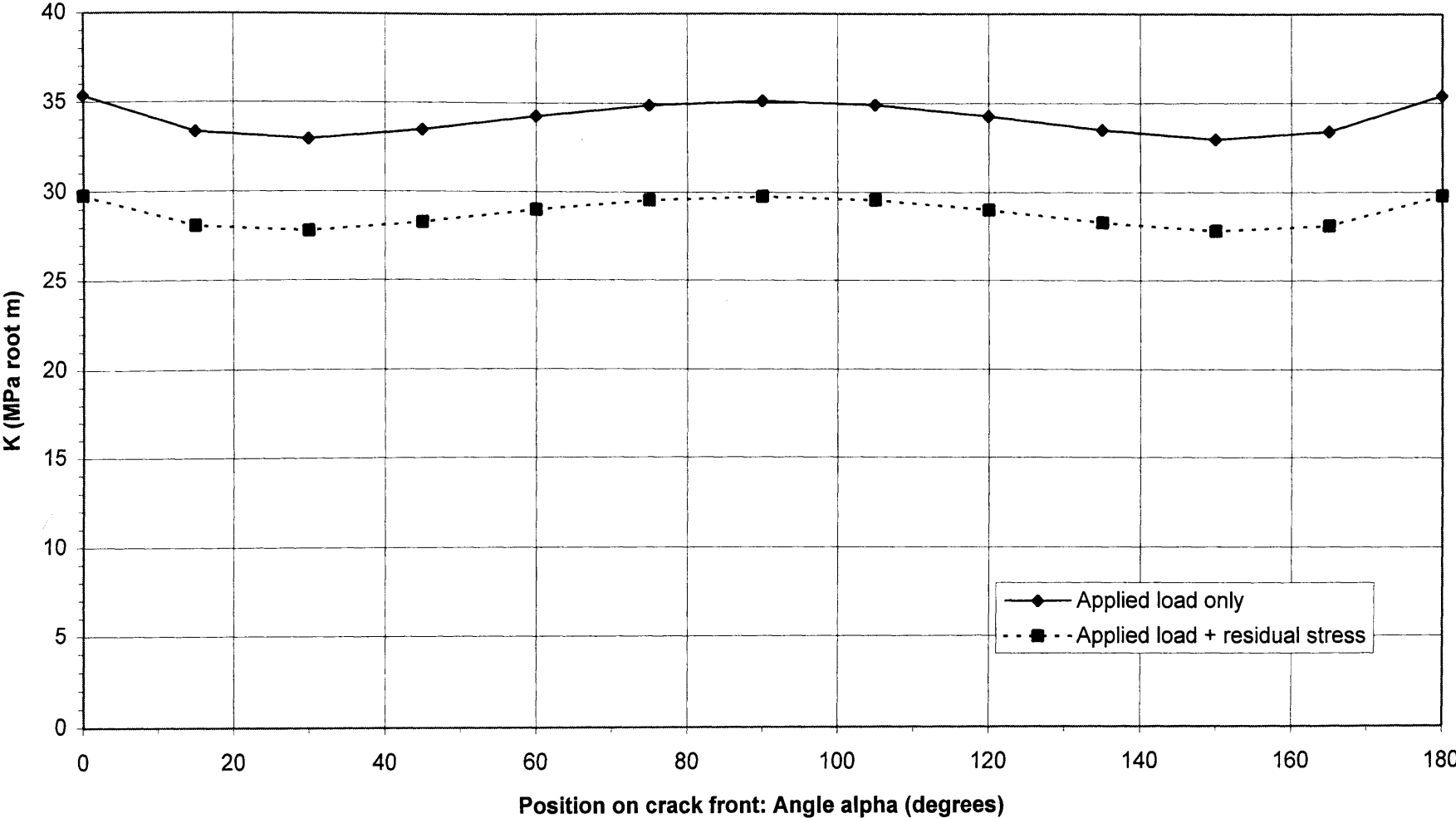


Figure 5.30 FE mesh of model disc with a surface crack:
 $a = 1.0\text{mm}$

**Figure 5.31 Model Disc Bore Crack Analysis - Effect of Residual Stresses
(SURFACE CRACK a=0.1mm 2c=0.24mm) Speed = 23000 rpm**



**Figure 5.32 Model Disc Bore Crack Analysis - Effect of Residual Stresses
(SURFACE CRACK a=0.5mm 2c=1.2mm) Speed = 23000 rpm**



**Figure 5.33 Model Disc Bore Crack Analysis - Effect of Residual Stresses
(SURFACE CRACK a=1.0mm 2c=2.4mm) Speed = 23000 rpm**

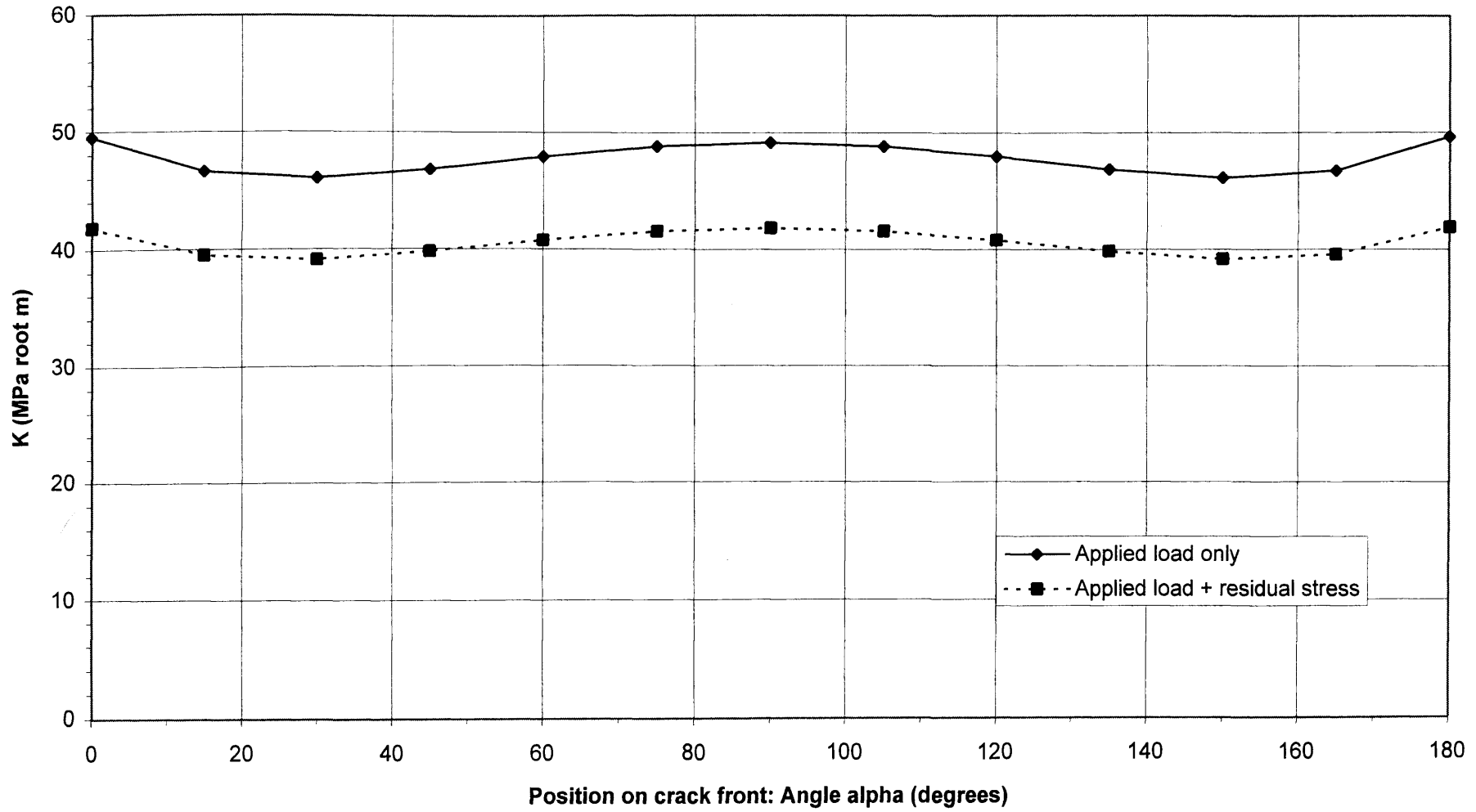
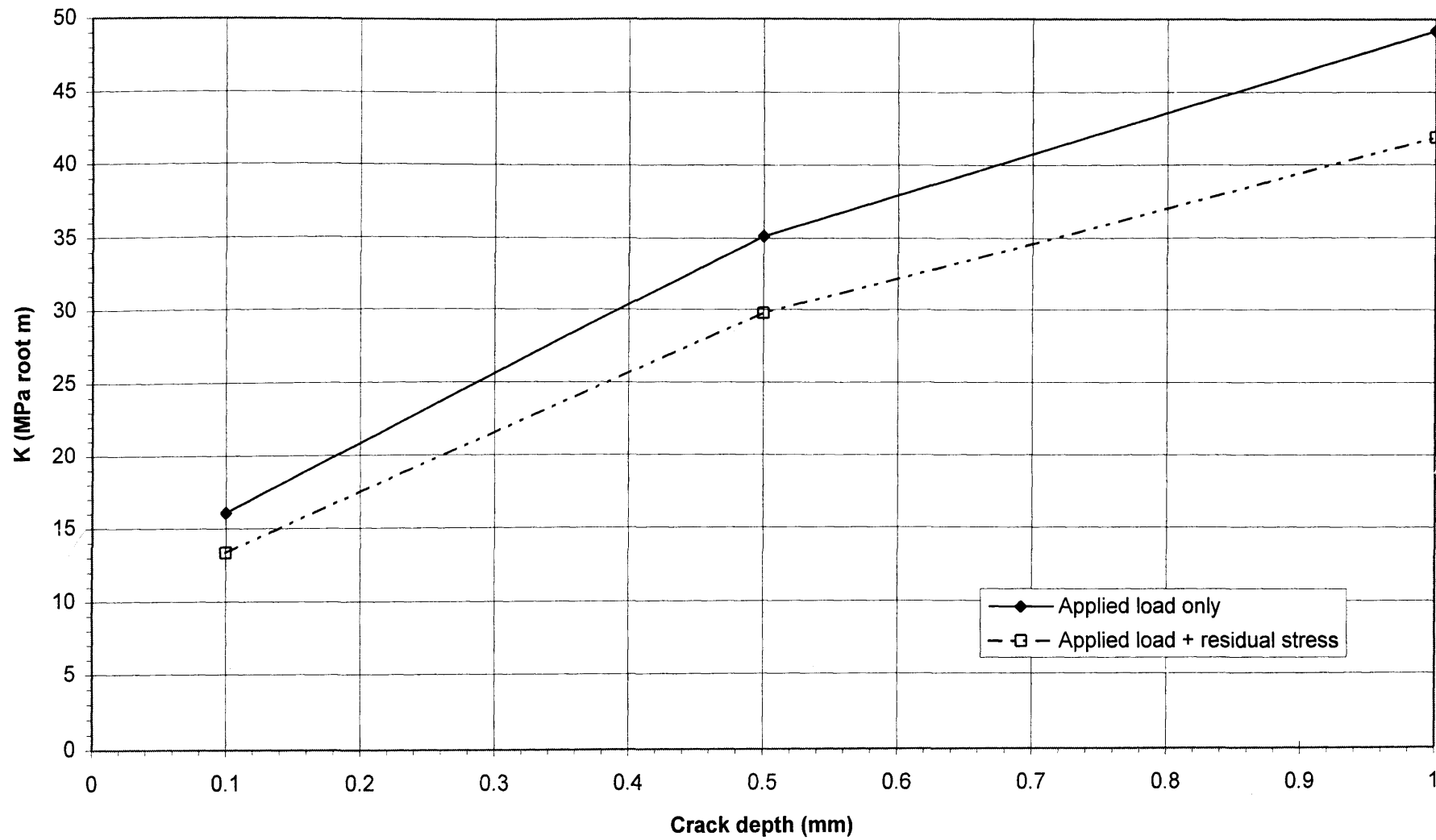
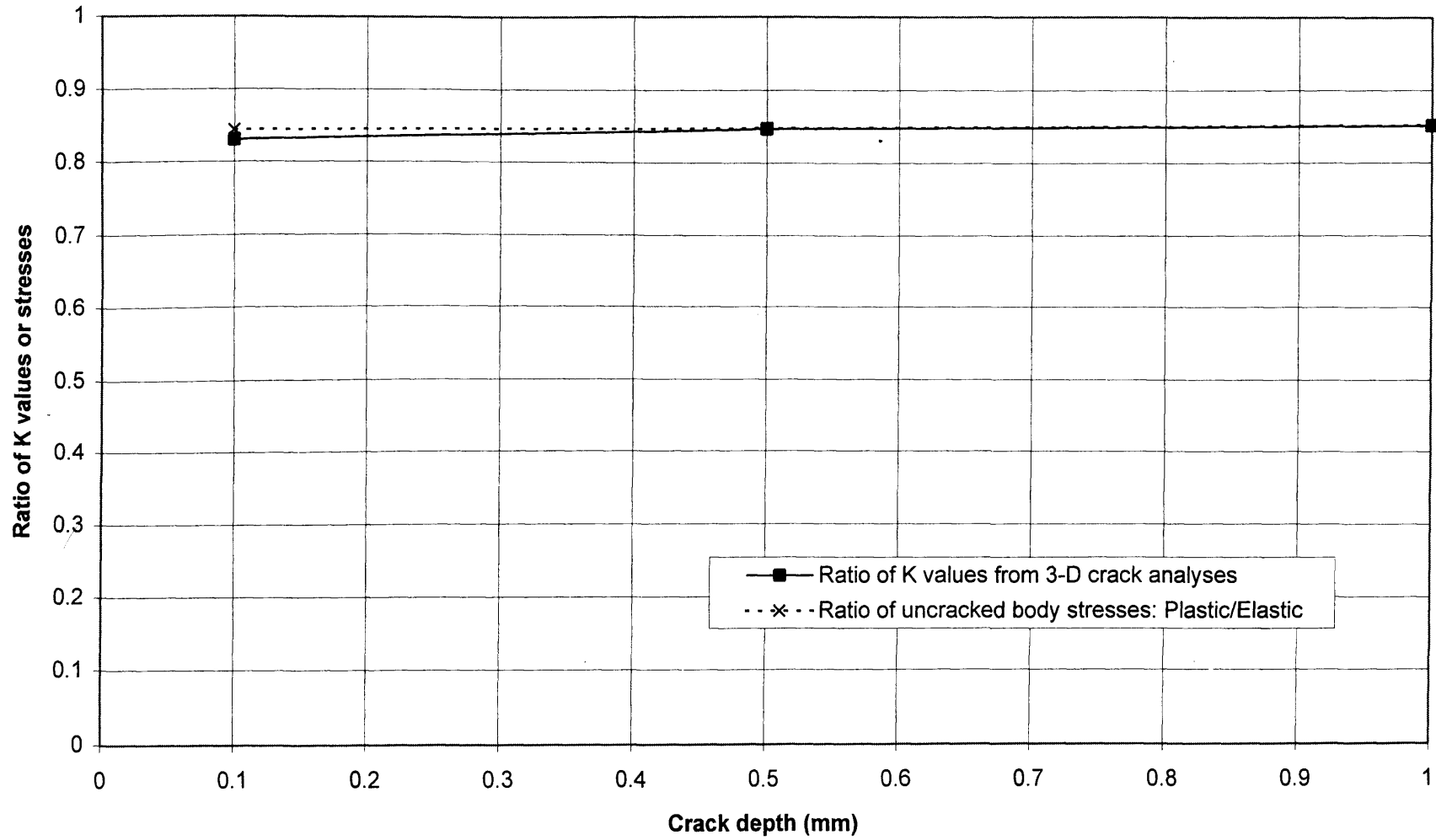
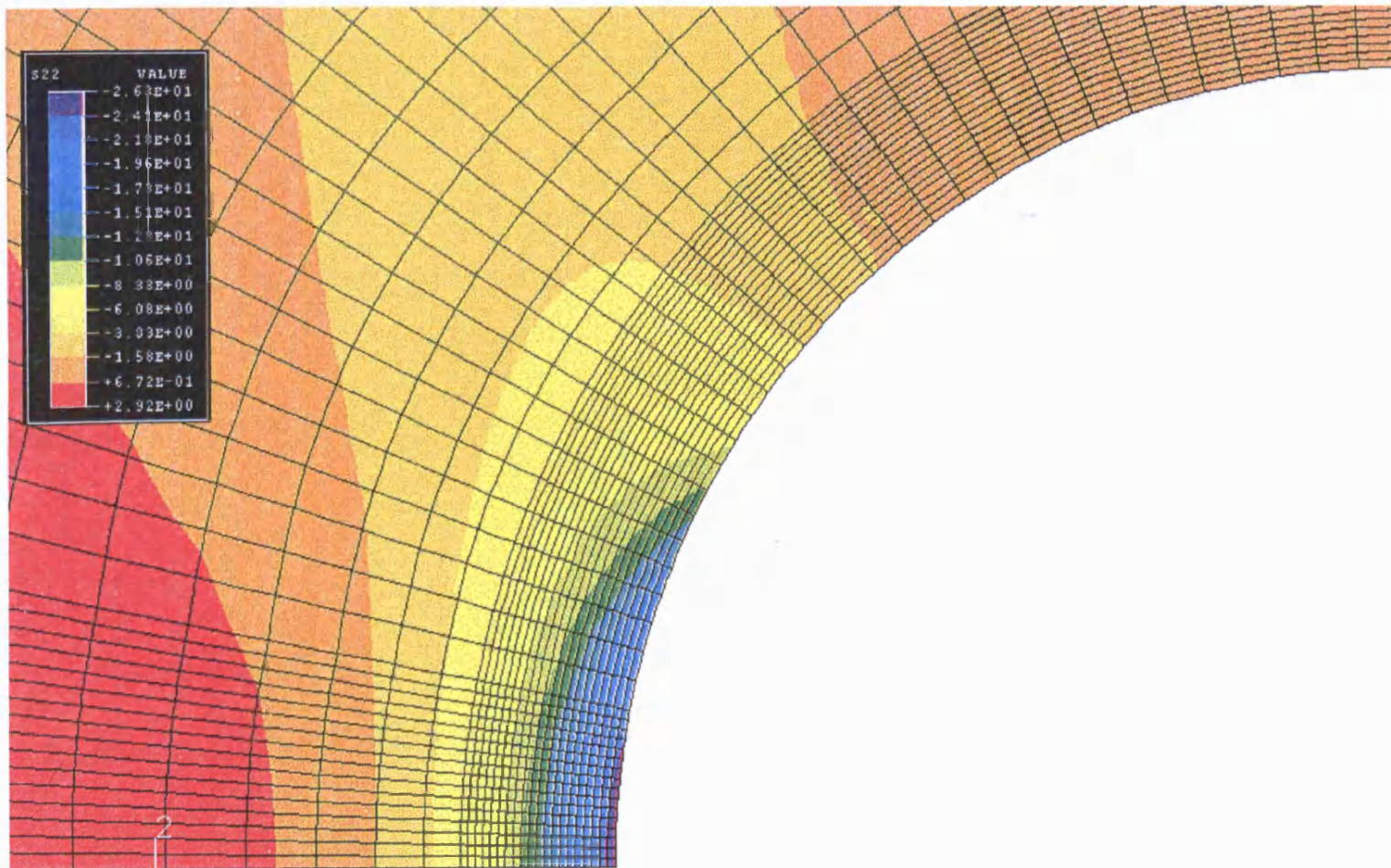


Figure 5.34 Model Disc Crack Analyses: Effect of Residual Stress Field on Deepest Point K Values



**Figure 5.35 Model Disc Bore Analysis - Effect of Residual Stresses on K Values
- Comparison of the Ratio of K Values (with/without residual stresses)
with the Ratio of Stresses (Elastic-Plastic/Elastic)**

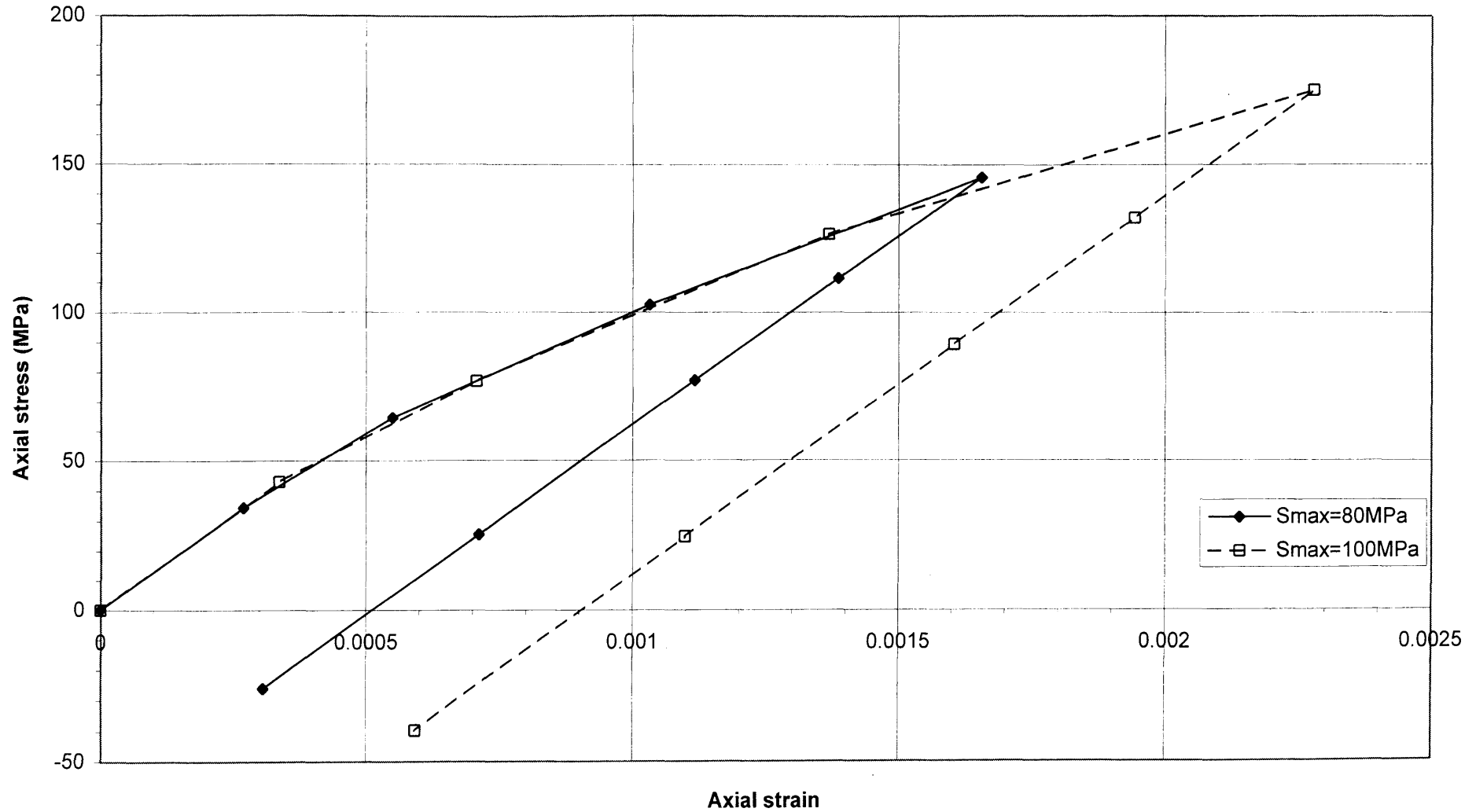


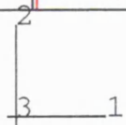
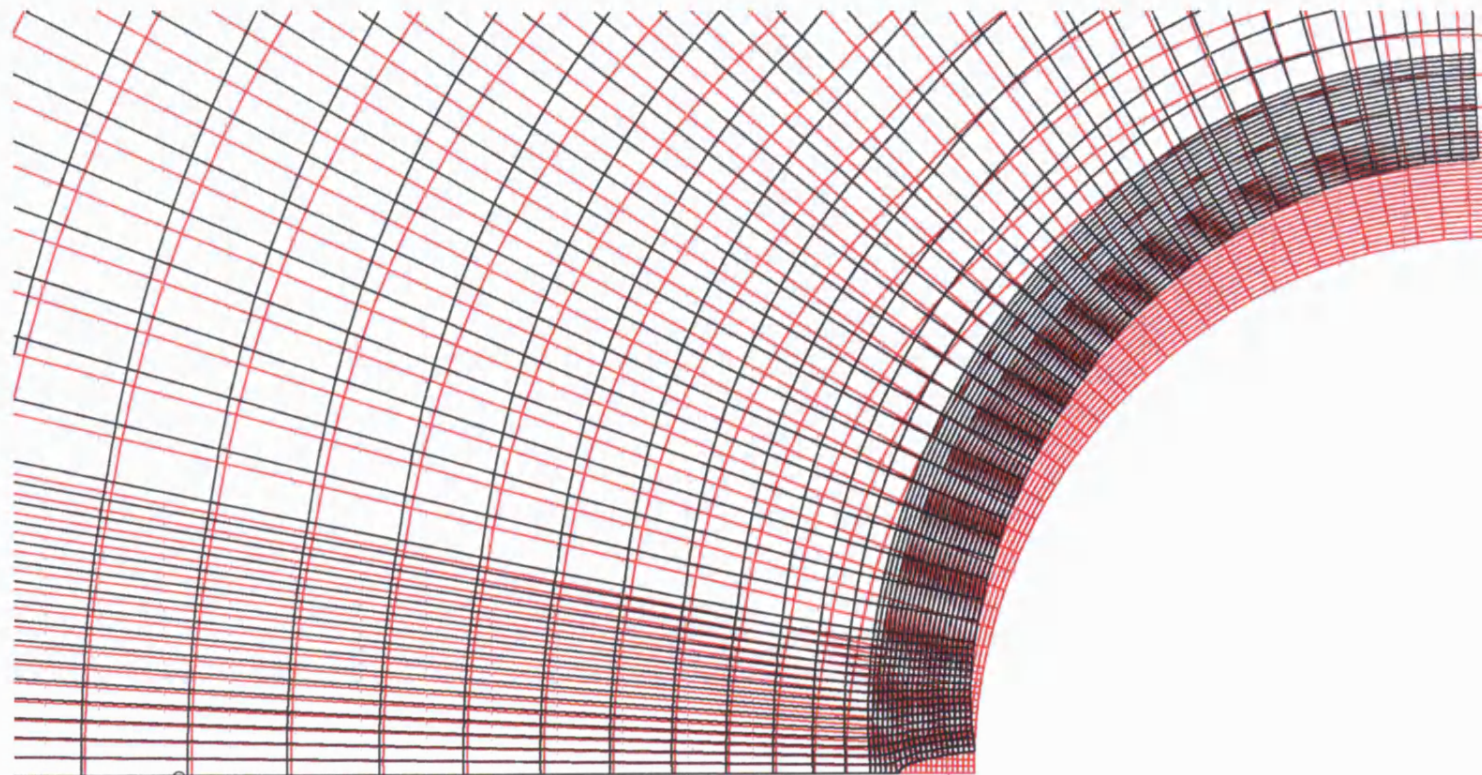


RESTART FILE = b1_epa1 STEP 2 INCREMENT 4
 TIME COMPLETED IN THIS STEP 1.00 TOTAL ACCUMULATED TIME 2.00
 ABAQUS VERSION: 5.5-1 DATE: 30-JAN-97 TIME: 10:11:12

**Figure 5.36 BRITE Notch 1 ($K_t=2.2$) axisymmetric FE analysis
 - Residual stress field created by loading to 80 MPa**

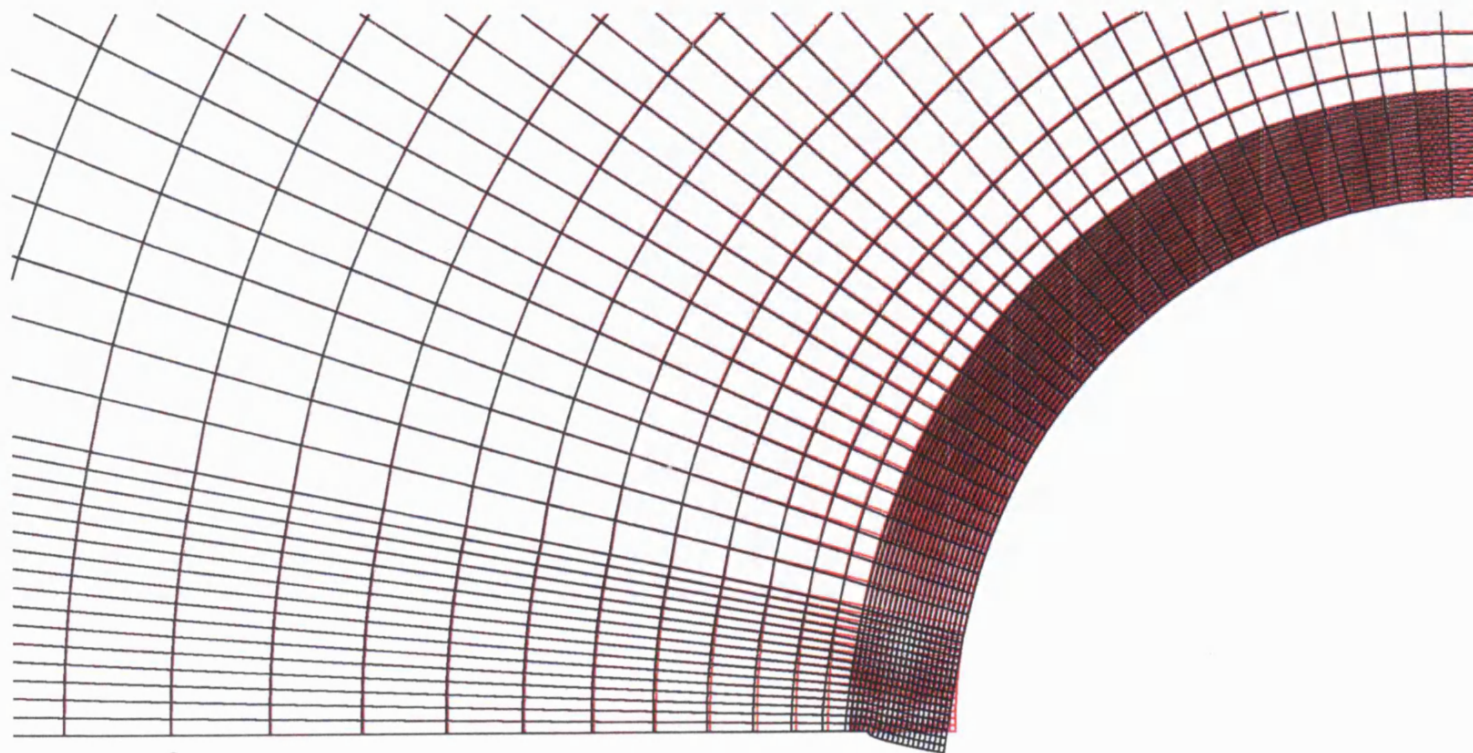
Figure 5.37 BRITE Notch 1 (Kt=2.2): Calculated Stress-Strain History at Notch Root for Two Different Maximum Stresses





DISPLACEMENT MAGNIFICATION FACTOR = 100. ORIGINAL MESH DISPLACED MESH
 TIME COMPLETED IN THIS STEP 1.00 TOTAL ACCUMULATED TIME 2.00
 ABAQUS VERSION: 5.5-1 DATE: 17-DEC-96 TIME: 09:09:33
 STEP 2 INCREMENT 1

Figure 5.38 BRITE Notch 1 ($K_t = 2.2$): Deformed shape of crack at maximum load (80 MPa) with residual stress field included (b1_ir1, 17-12-96)



2
3 1

DISPLACEMENT MAGNIFICATION FACTOR = 700.

ORIGINAL MESH

DISPLACED MESH

TIME COMPLETED IN THIS STEP 1.00 TOTAL ACCUMULATED TIME 1.00

ABAQUS VERSION: 5.5-1 DATE: 17-DEC-96 TIME: 09:09:33

STEP 1 INCREMENT 1

Figure 5.39 BRITE Notch 1 ($K_t = 2.2$): Deformed shape of crack at zero load with residual stress field included (b1_ir1, 17-12-96)

Figure 5.40 BRITE Notch 1 (Kt=2.2): Comparison of K Solutions for Continuous Surface Cracks Showing the Effect of Residual Stresses Due to Initial Yielding

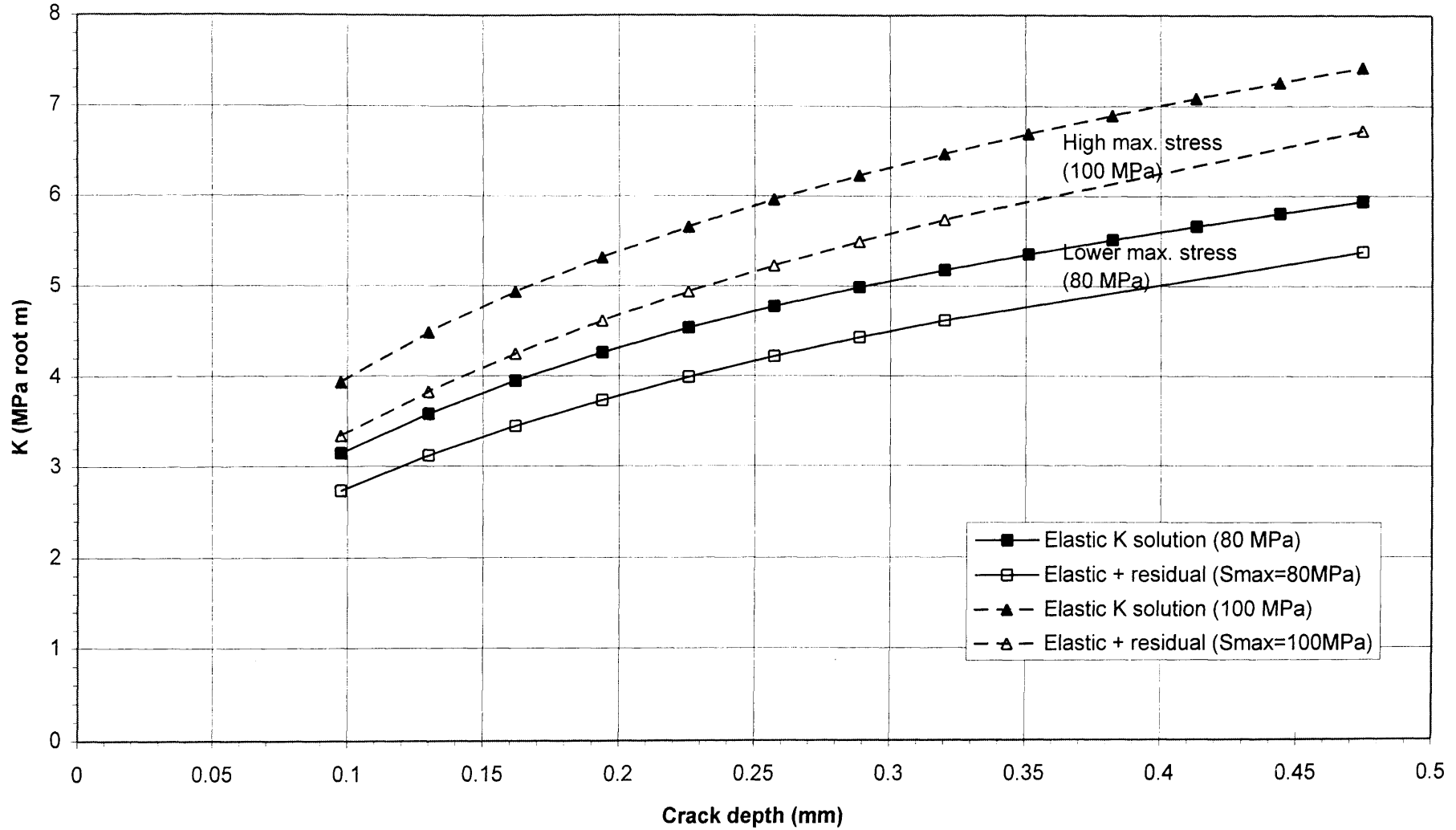


Figure 5.41 BRITE Notch1 (Kt=2.2): Effect of Residual Stresses on K Solutions for Continuous Surface Cracks of Various Depths - Plastic/Elastic Stress Ratios also Shown

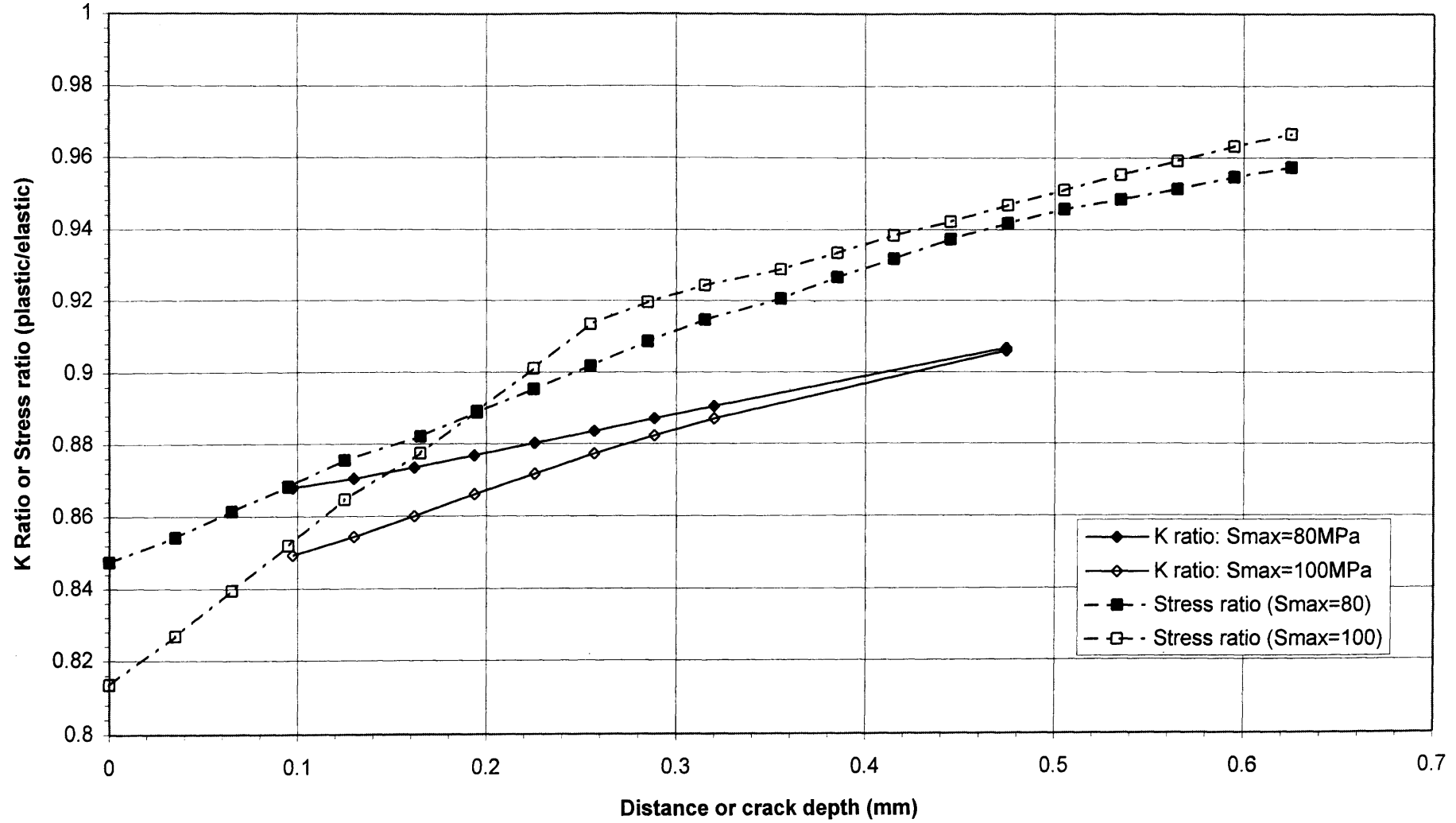


Figure 5.42 BRITE Notch 1 (Kt=2.2): Crack Face Displacements for Continuous Surface Cracks with the Effect of Residual Stress Field due to Load up to Smax=80MPa

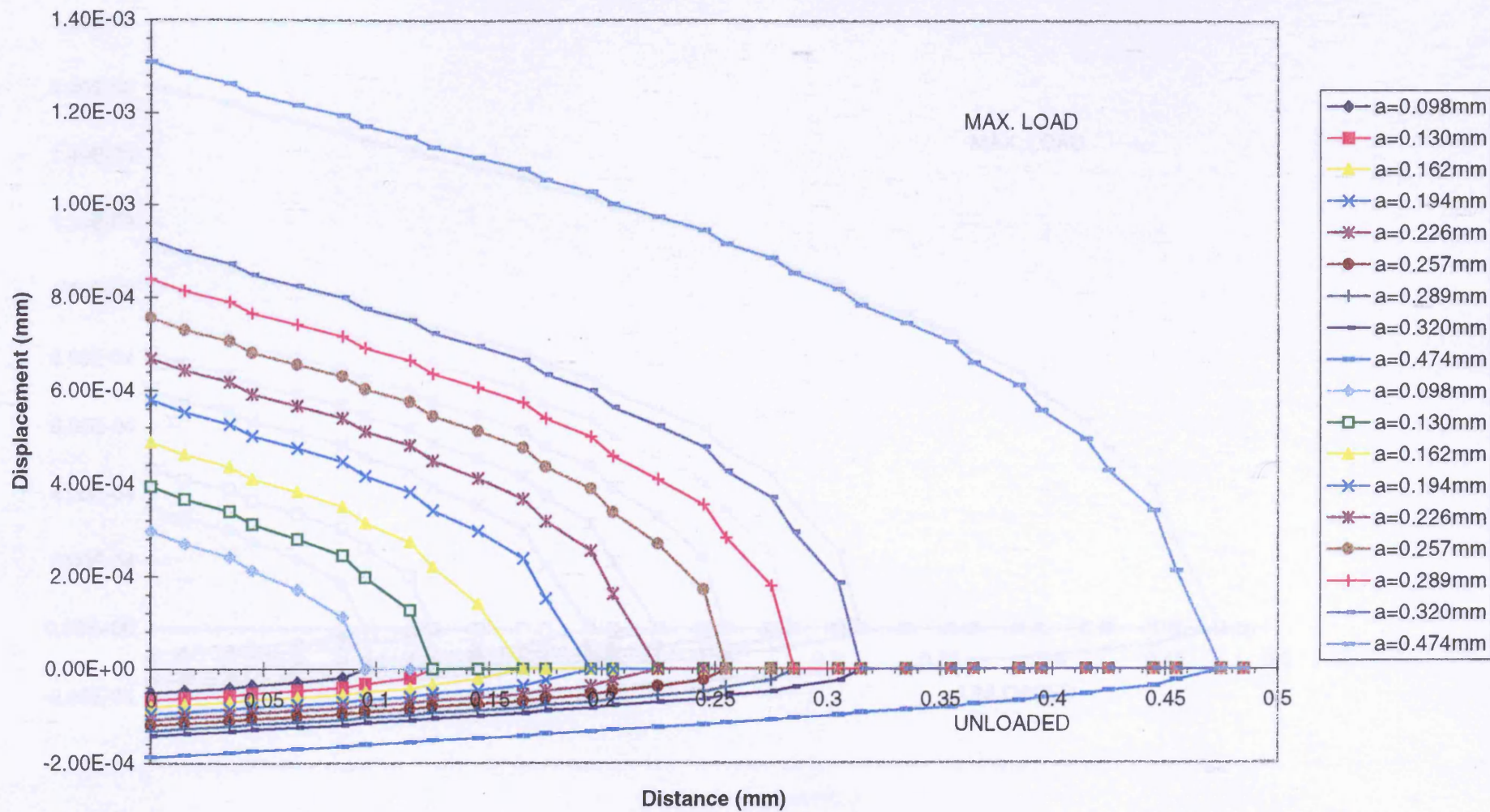


Figure 5.43 BRITE Notch 1 (Kt=2.2): Crack Face Displacements for Continuous Surface Cracks with the Effect of Residual Stress Field due to Load up to Smax=100MPa

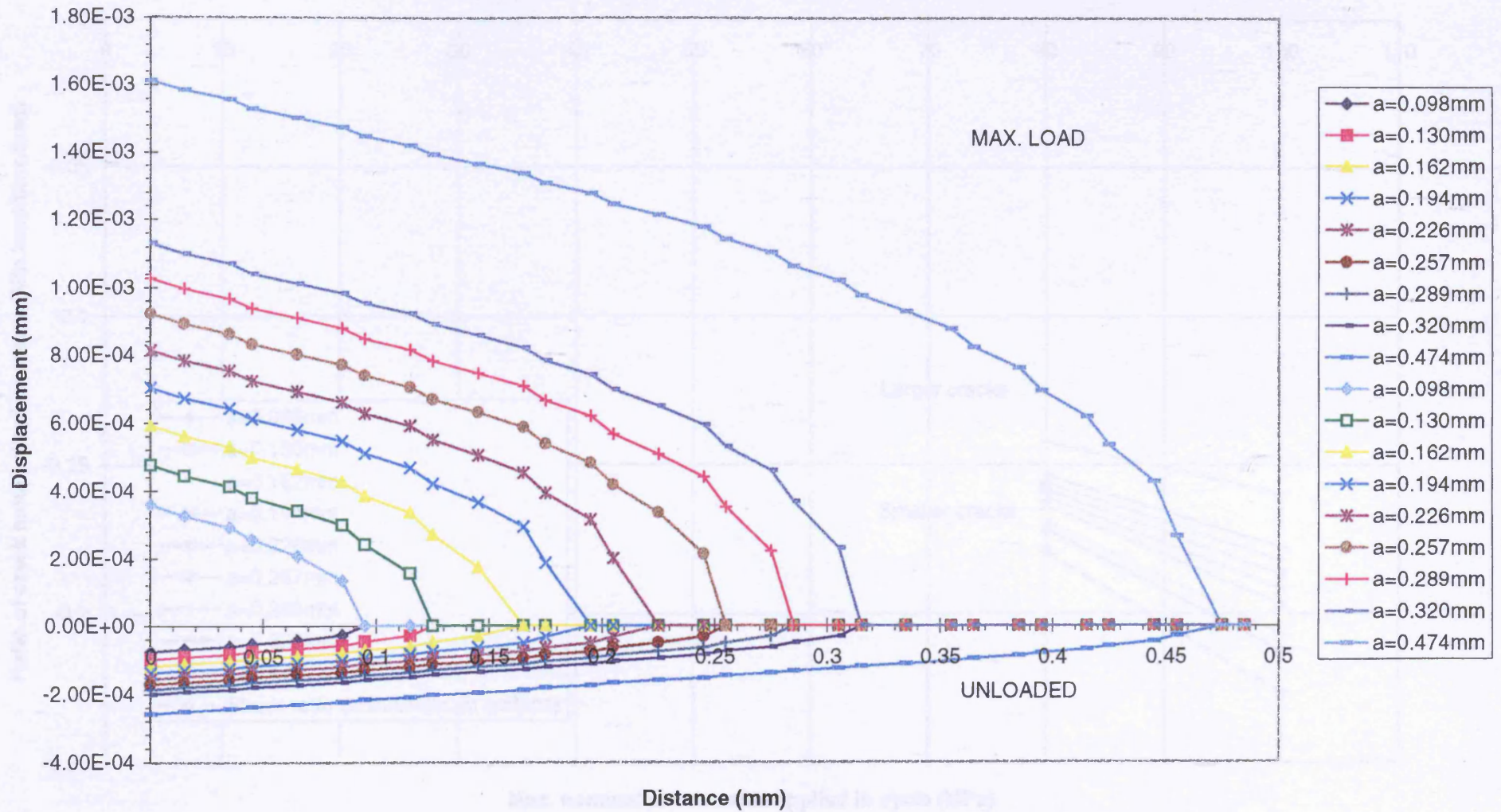


Figure 5.44 BRITE Notch 1 (Kt=2.2): Crack Mouth Displacement Ratios (Min.load/Max.load) for Various Depths of Continuous Surface Cracks - Two Different Max. Load Levels

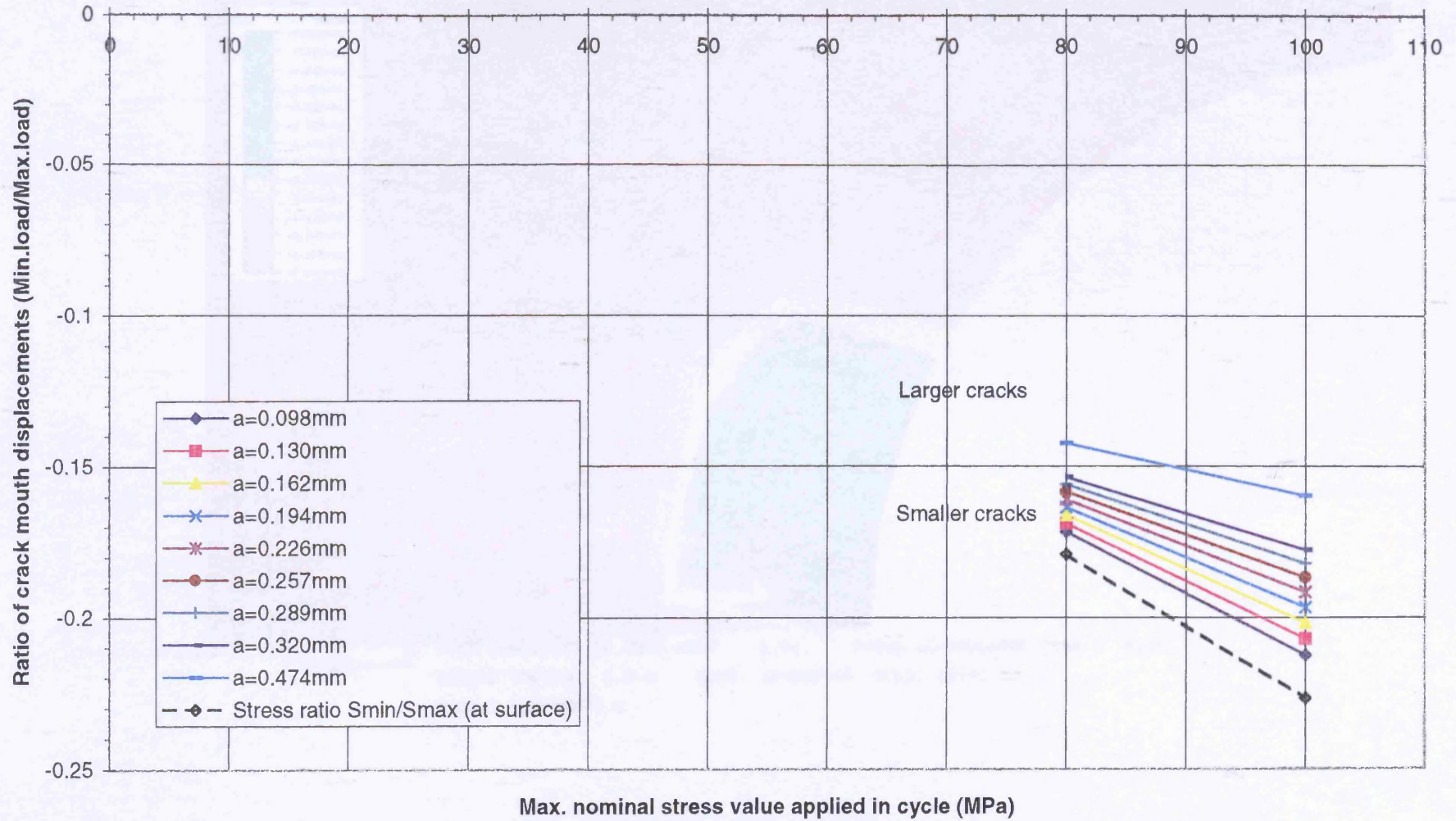


Figure 5.45 BRITE Notch 1 ($K_t = 2.2$): Effect of residual stresses on Crack Mode I Distribution

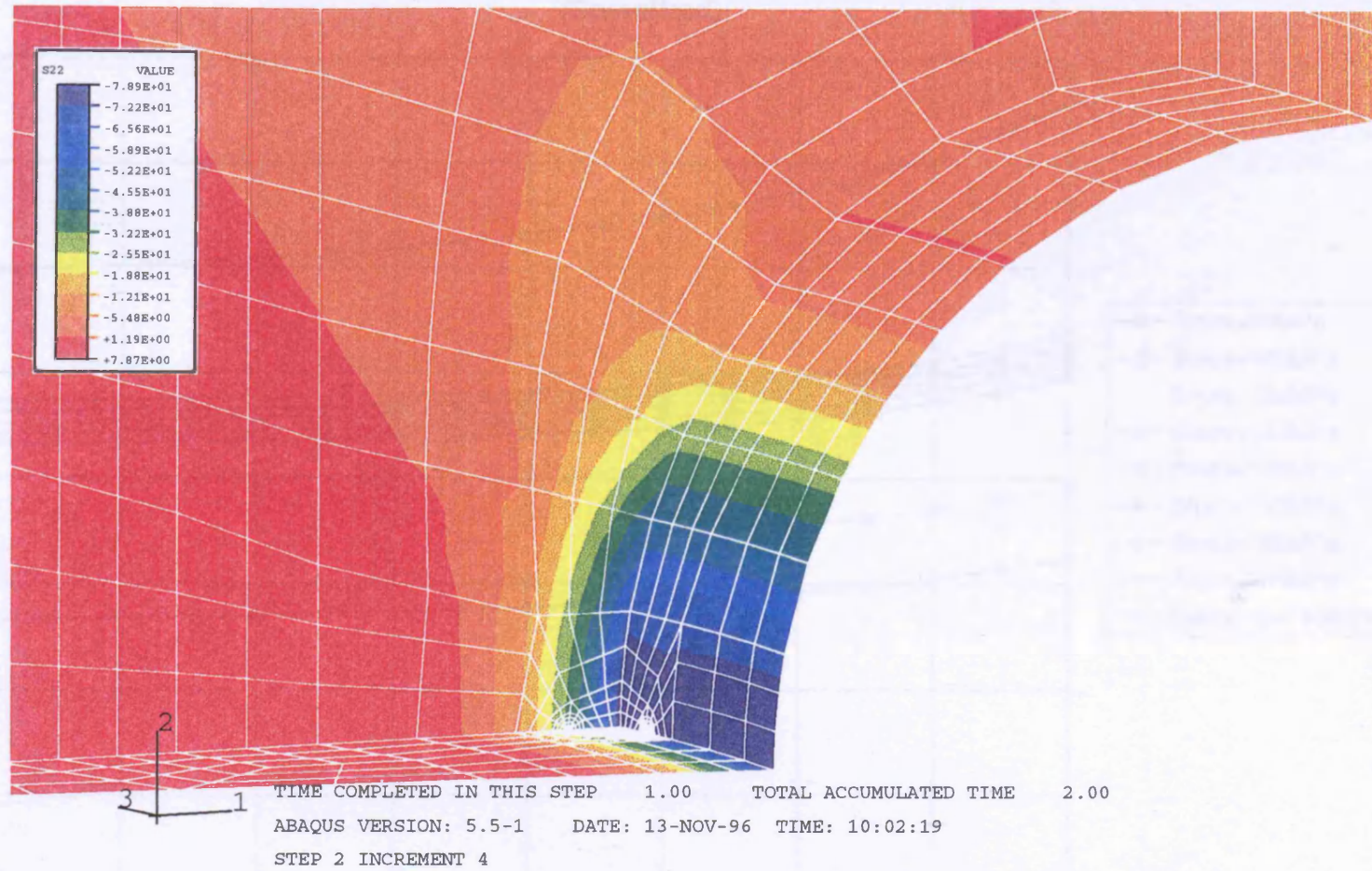


Figure 5.45 BRITE Notch 1 ($K_t = 2.2$): 3-D FE analysis
- Residual stress field created by loading uncracked body to maximum load

Figure 5.46 BRITE Notch 1 (a=0.3) Effect of residual stresses on Crack Front K Distribution (Smoothed)

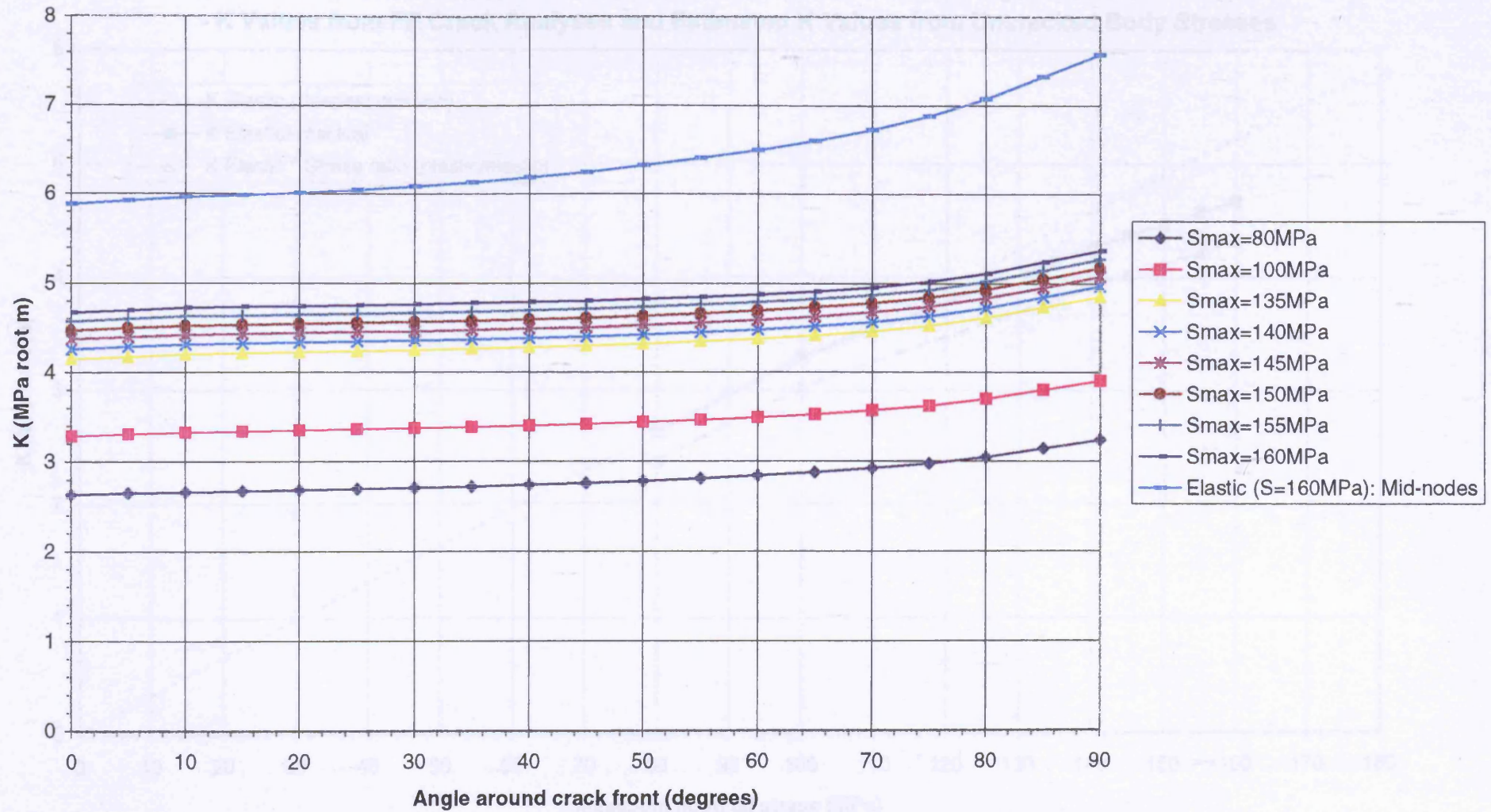


Figure 5.47 BRITE Notch 1 Calculated K values for a Semi-Circular Surface Crack (a=0.3mm)
- Effect of Residual Stresses due to Various Maximum Cyclic Loads
- K Values from FE Crack Analyses and Estimated K Values from Uncracked Body Stresses

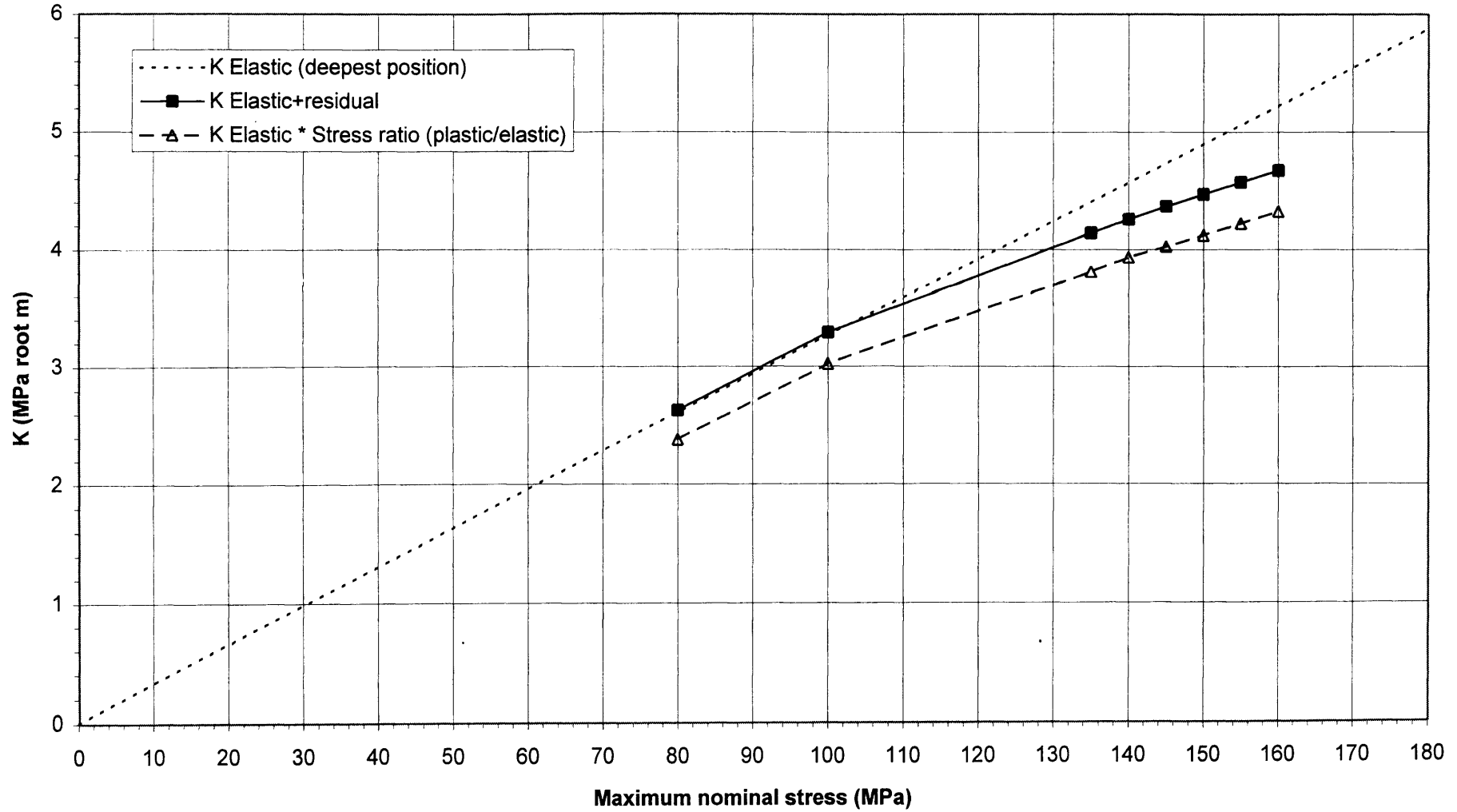


Figure 5.48 BRITE Notch 1 Calculated K values for a Semi-Circular Surface Crack (a=0.3mm)
- Effect of Residual Stresses due to Various Maximum Cyclic Loads
- K Values from FE Crack Analyses and Estimated K Values from Uncracked Body Stresses

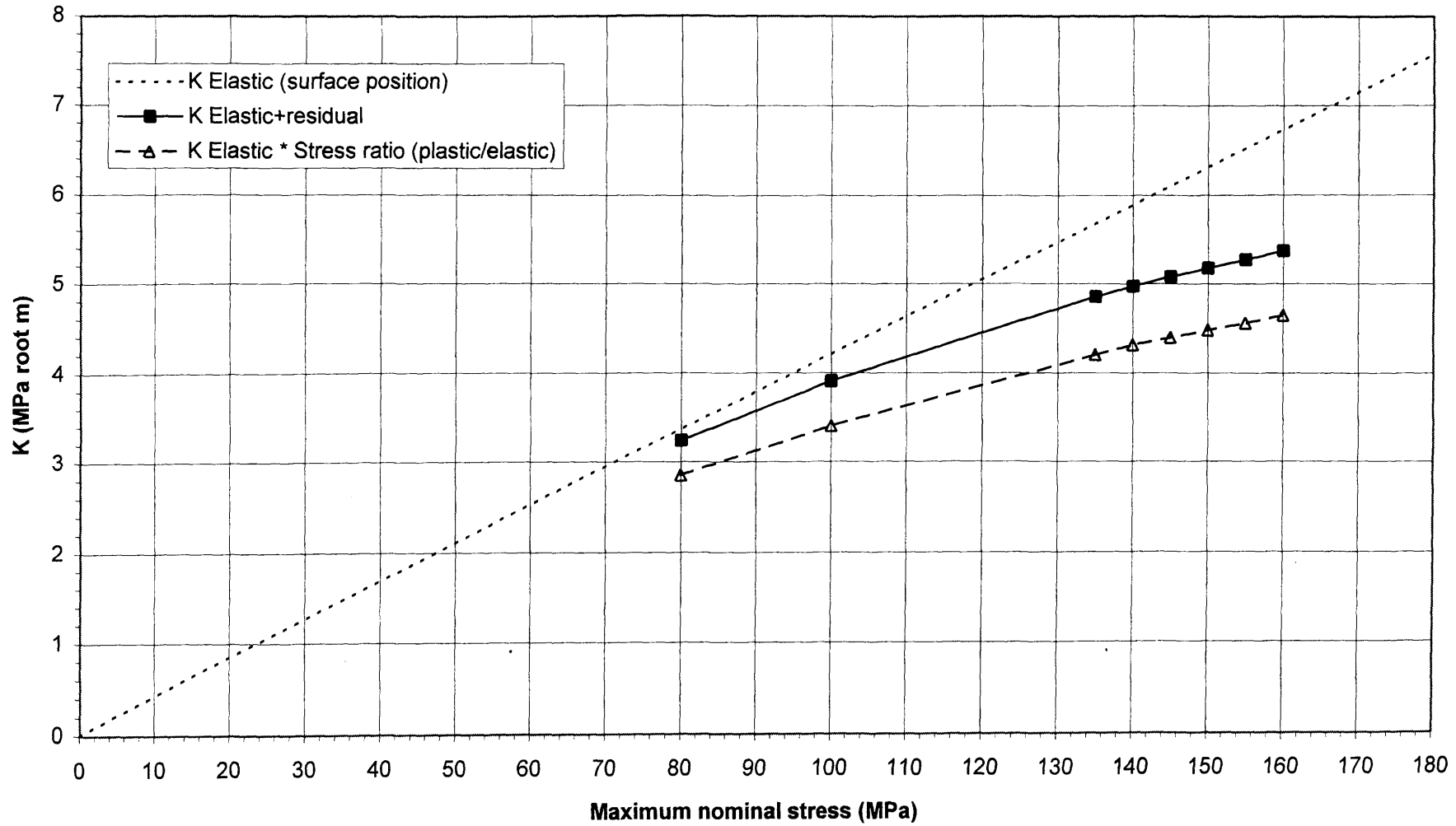


Figure 5.49 BRITE Notch 2 ($K_t=5.6$): Calculated Stress-Strain History at Notch Root for Two Different Maximum Stresses

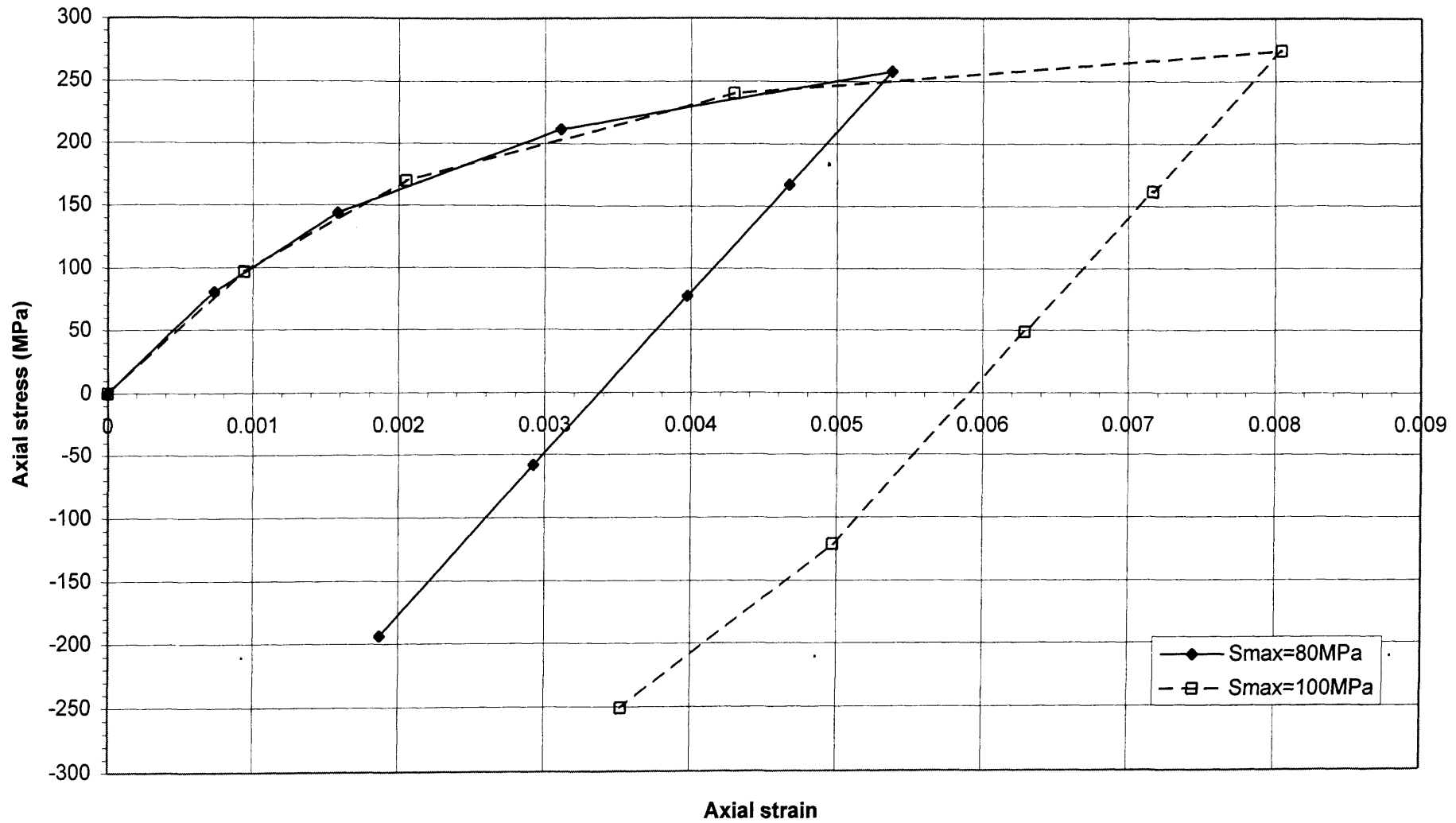


Figure 5.50 BRITE Notch 2 ($K_t=5.6$): Comparison of K Solutions for Continuous Surface Cracks Showing the Effect of Residual Stresses Due to Initial Yielding

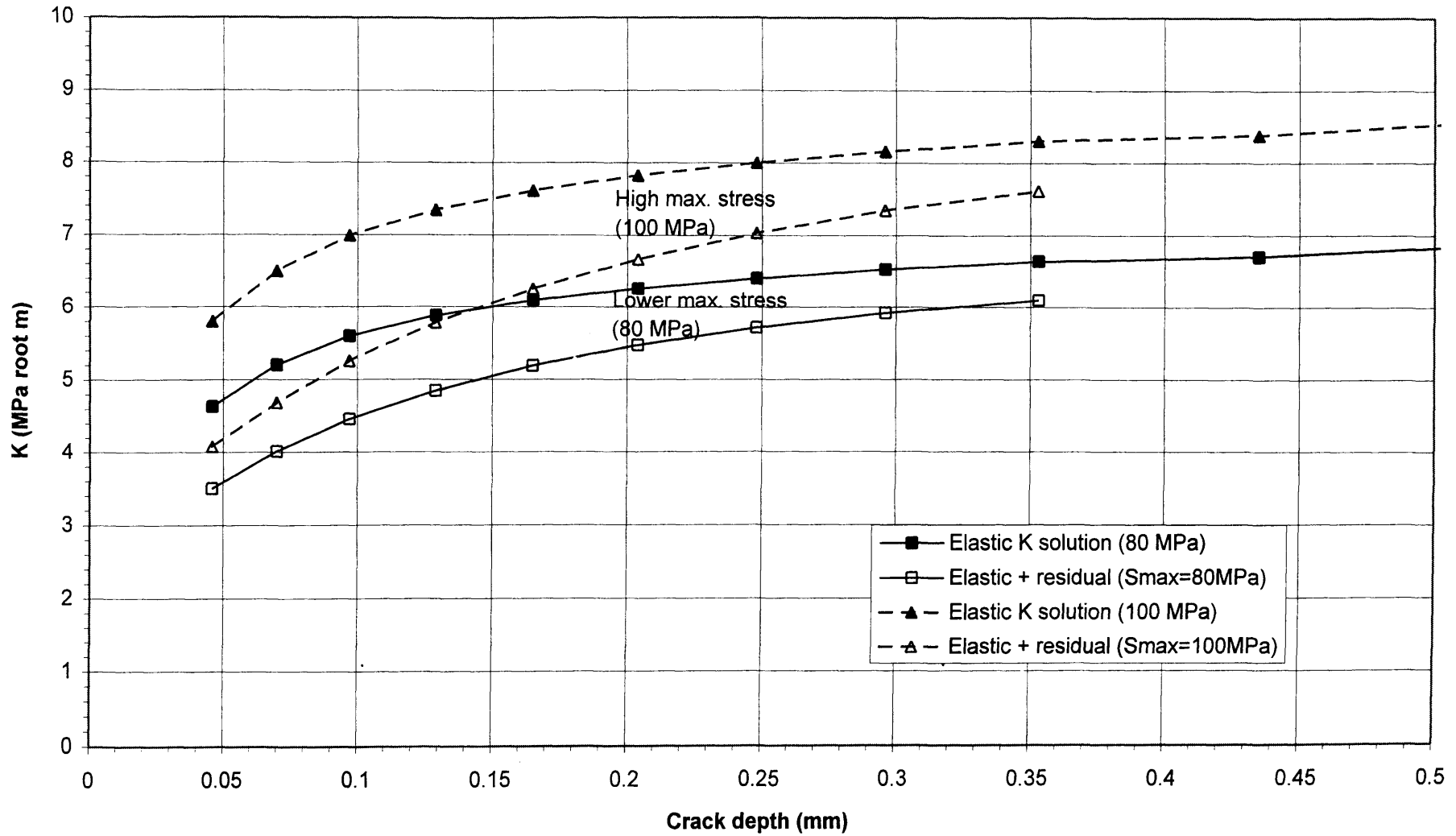
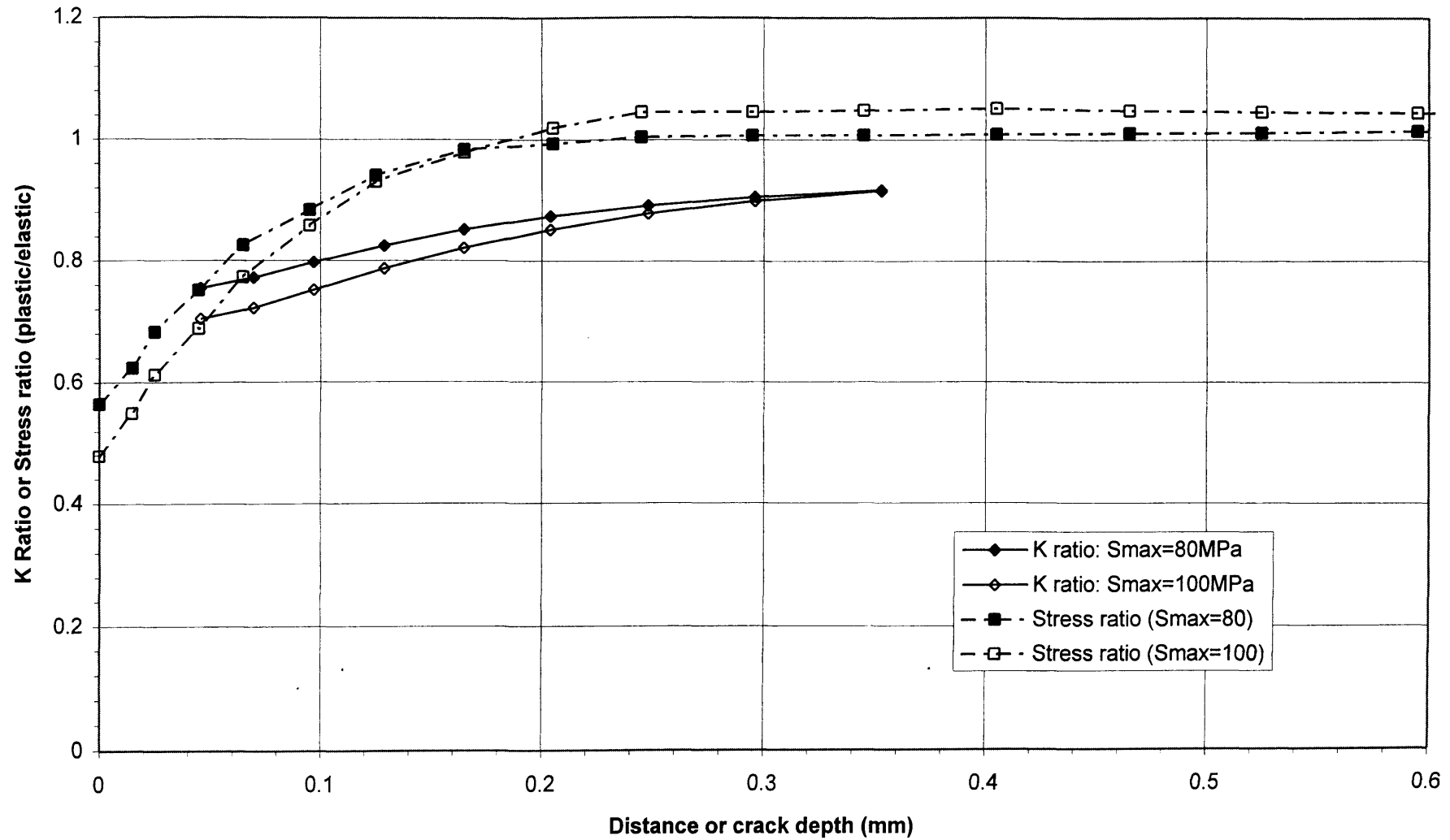


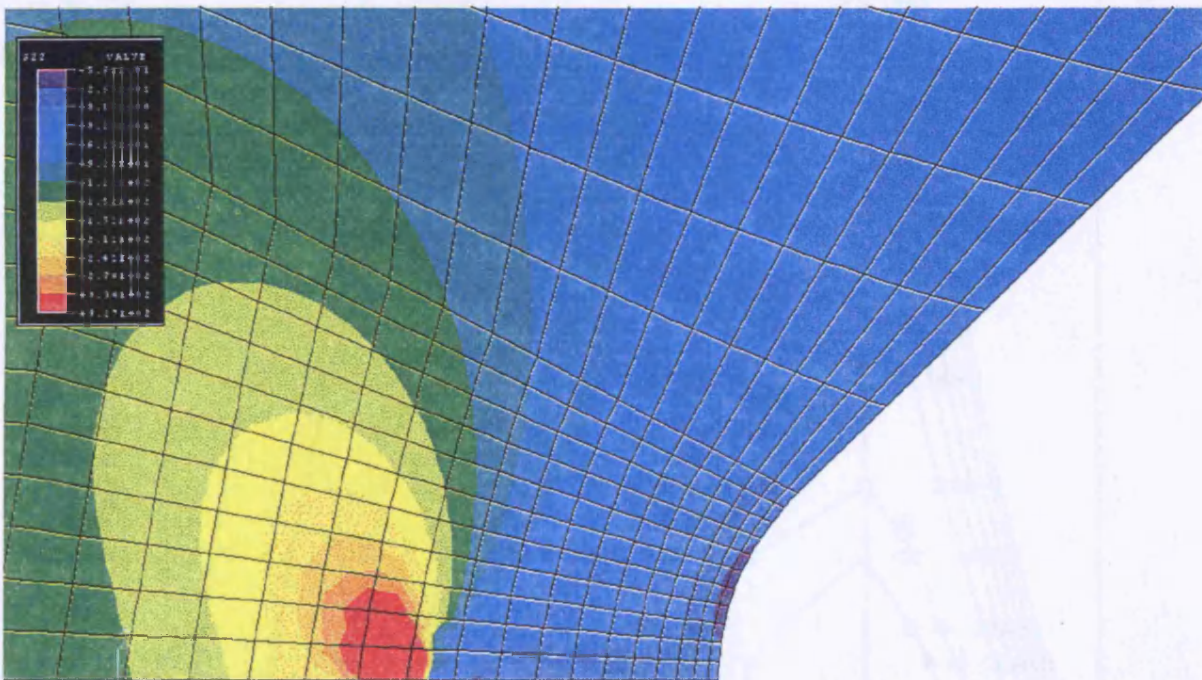
Figure 5.51 BRITE Notch 2 (Kt=5.6): Effect of Residual Stresses on K Solutions for Continuous Surface Cracks of Various Depths - Plastic/Elastic Stress Ratios also Shown





RESTART FILE = b2_1e11 STEP 1 INCREMENT 1
 TIME COMPLETED IN THIS STEP 1.00 TOTAL ACCUMULATED TIME 1.00
 ABAQUS VERSION: 5.5-1 DATE: 19-FEB-97 TIME: 10:53:37

Figure 5.52 BRITE Notch 2 ($K_t = 5.6$): Crack tip stress field (S22)
 - Elastic, $a = 0.353\text{mm}$, $S_{\text{max}} = 80\text{ MPa}$



RESTART FILE = b2_ir1 STEP 2 INCREMENT 1
 TIME COMPLETED IN THIS STEP 1.00 TOTAL ACCUMULATED TIME 2.00
 ABAQUS VERSION: 5.5-1 DATE: 02-JAN-97 TIME: 16:32:20

Figure 5.53 BRITE Notch 2 ($K_t = 5.6$): Crack tip stress field (S22)
 - Elastic + residuals, $a = 0.353\text{mm}$, $S_{\text{max}} = 80\text{ MPa}$

Figure 5.54 BRITE Notch 2 (Kt=5.6): Crack Face Displacements for Continuous Surface Cracks with the Effect of Residual Stress Field due to Load up to Smax=80MPa

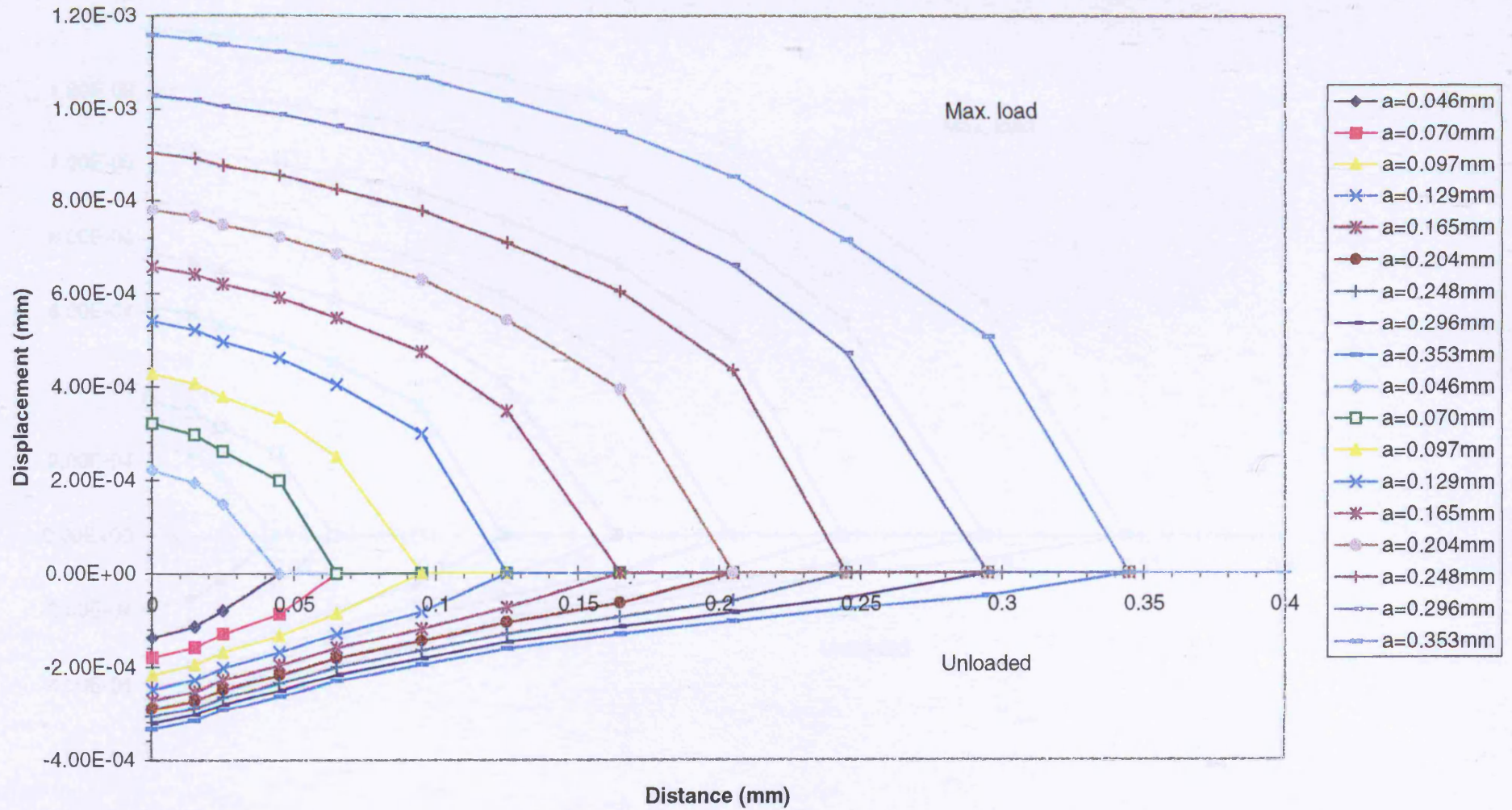


Figure 5.55 BRITE Notch 2 (Kt=5.6): Crack Face Displacements for Continuous Surface Cracks with the Effect of Residual Stress Field due to Load up to Smax=100MPa

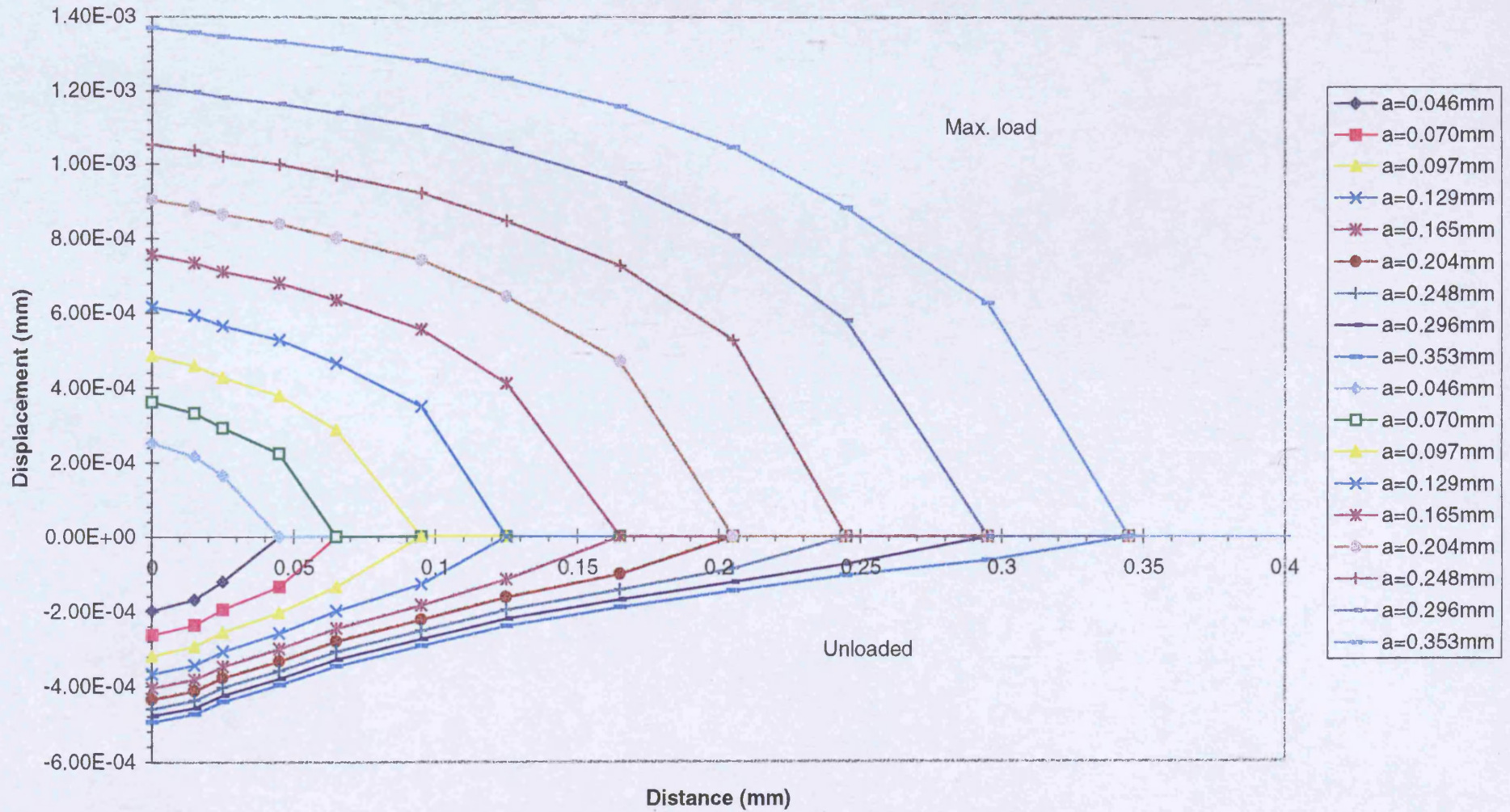
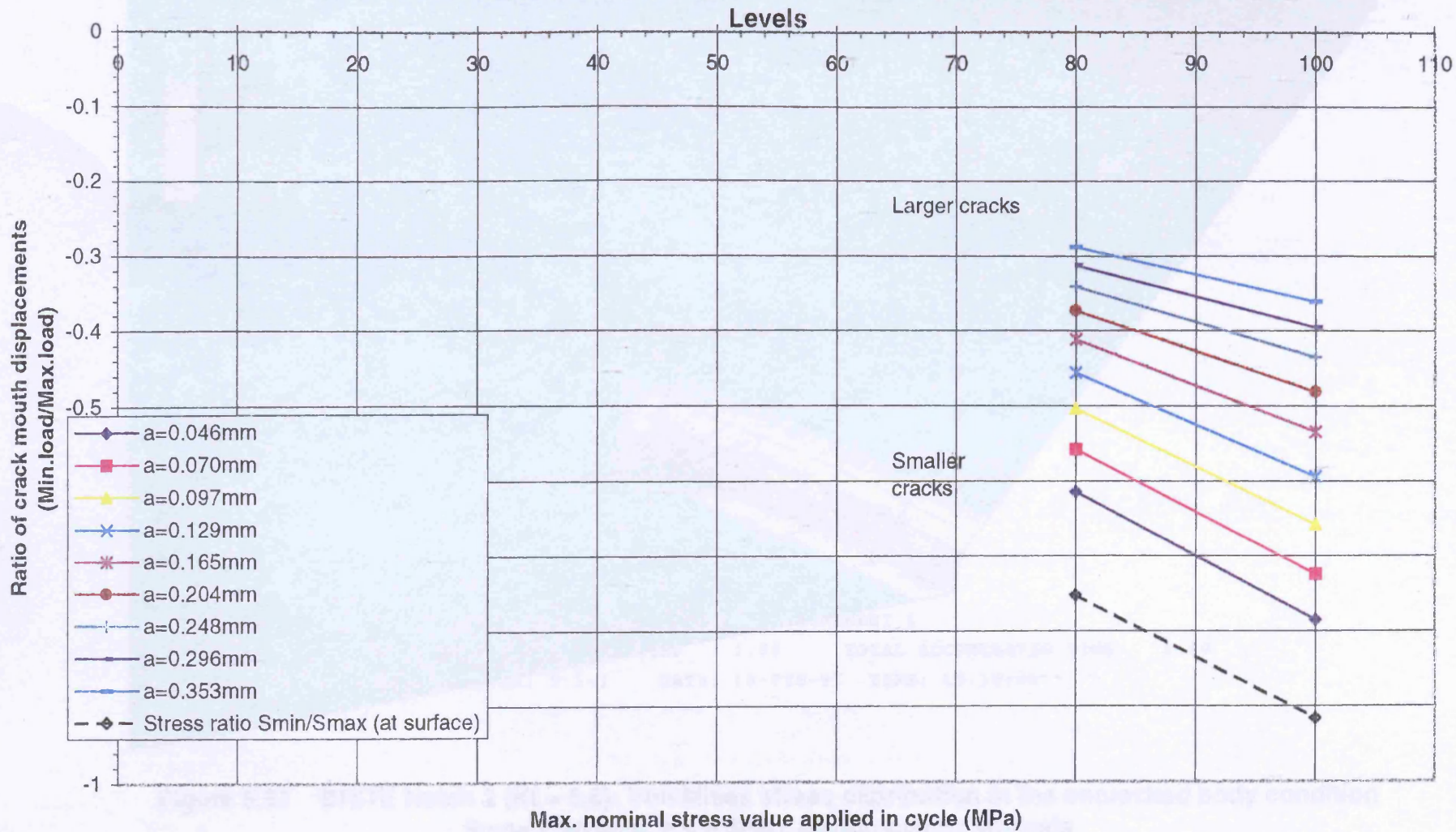


Figure 5.56 BRITE Notch 2 ($K_t=5.6$): Crack Mouth Displacement Ratios (Min.load/Max.load) for Various Depths of Continuous Surface Cracks with Residual Stresses - Two Different Max. Load Levels



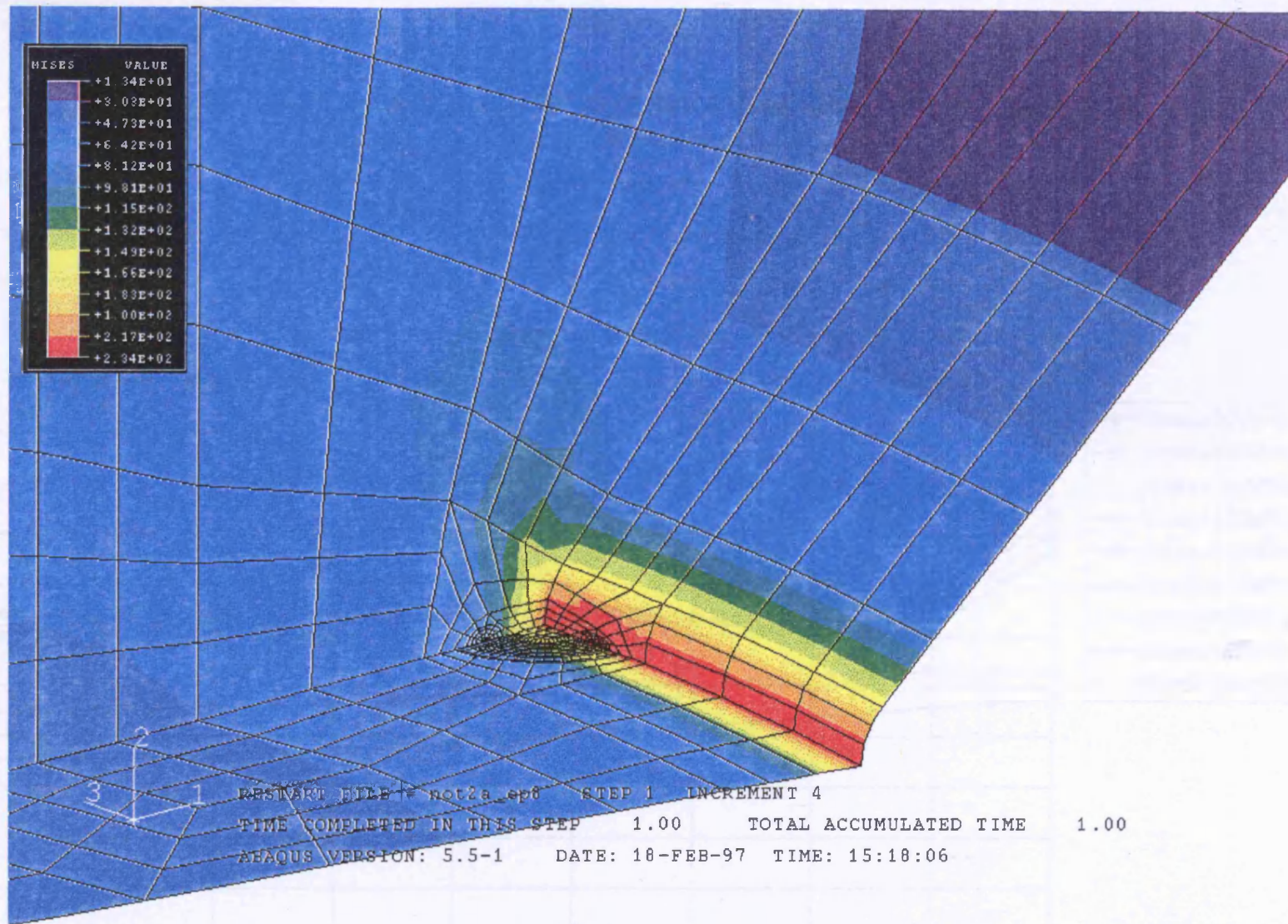


Figure 5.57 BRITE Notch 2 ($K_t = 5.6$): Von Mises stress distribution in the uncracked body condition
 $S_{max} = 80 \text{ MPa}$, $a = 0.3 \text{ mm}$, elastic-plastic analysis

Figure 5.58 BRITE Notch 2 (a=0.3) Effect of Residual Stresses on Crack Front K Distribution (Smoothed)

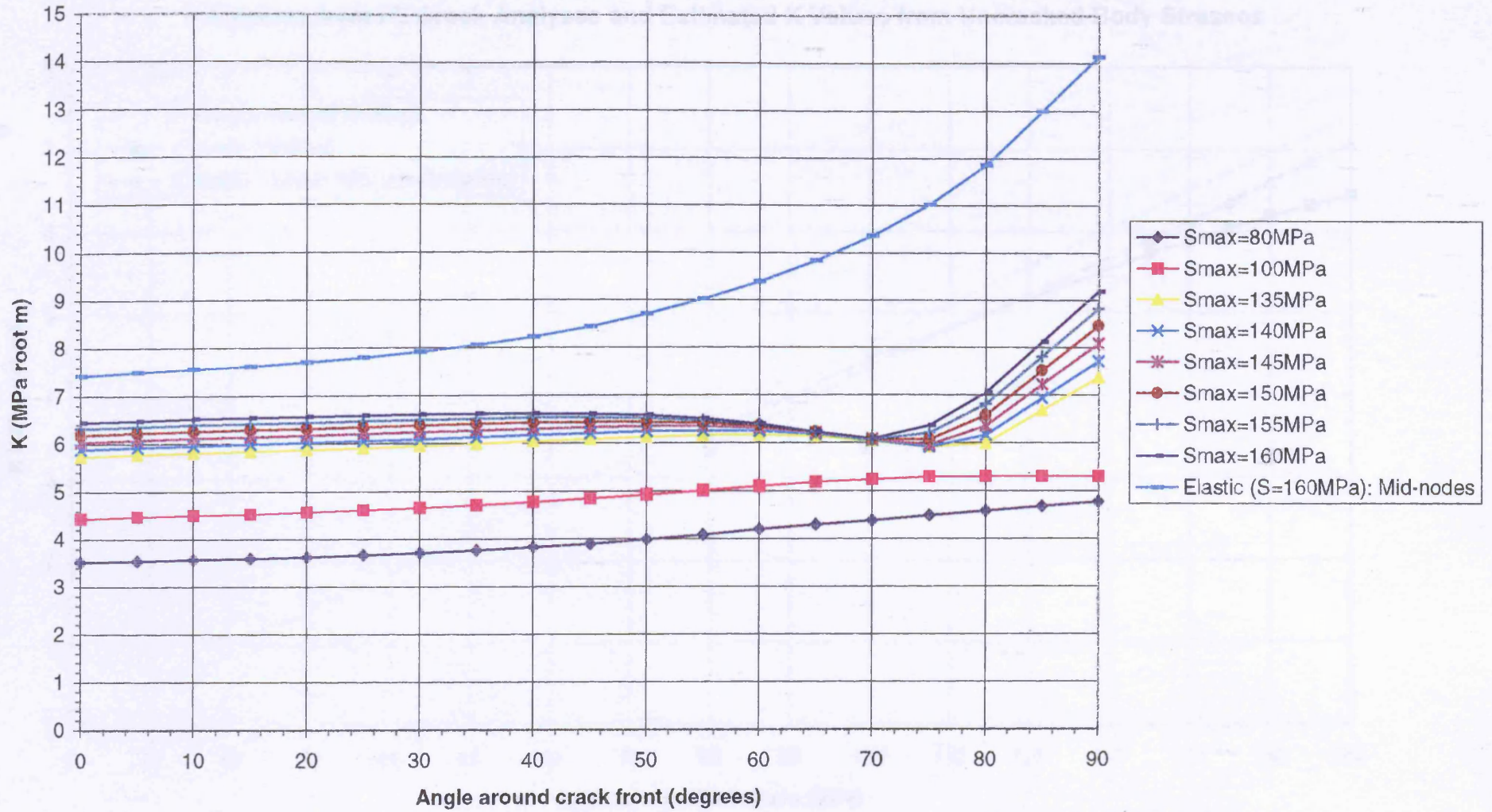


Figure 5.59 BRITE Notch 2 Calculated K values for a Semi-Circular Surface Crack (a=0.3mm)
- Effect of Residual Stresses due to Various Maximum Cyclic Loads
- K Values from FE Crack Analyses and Estimated K Values from Uncracked Body Stresses

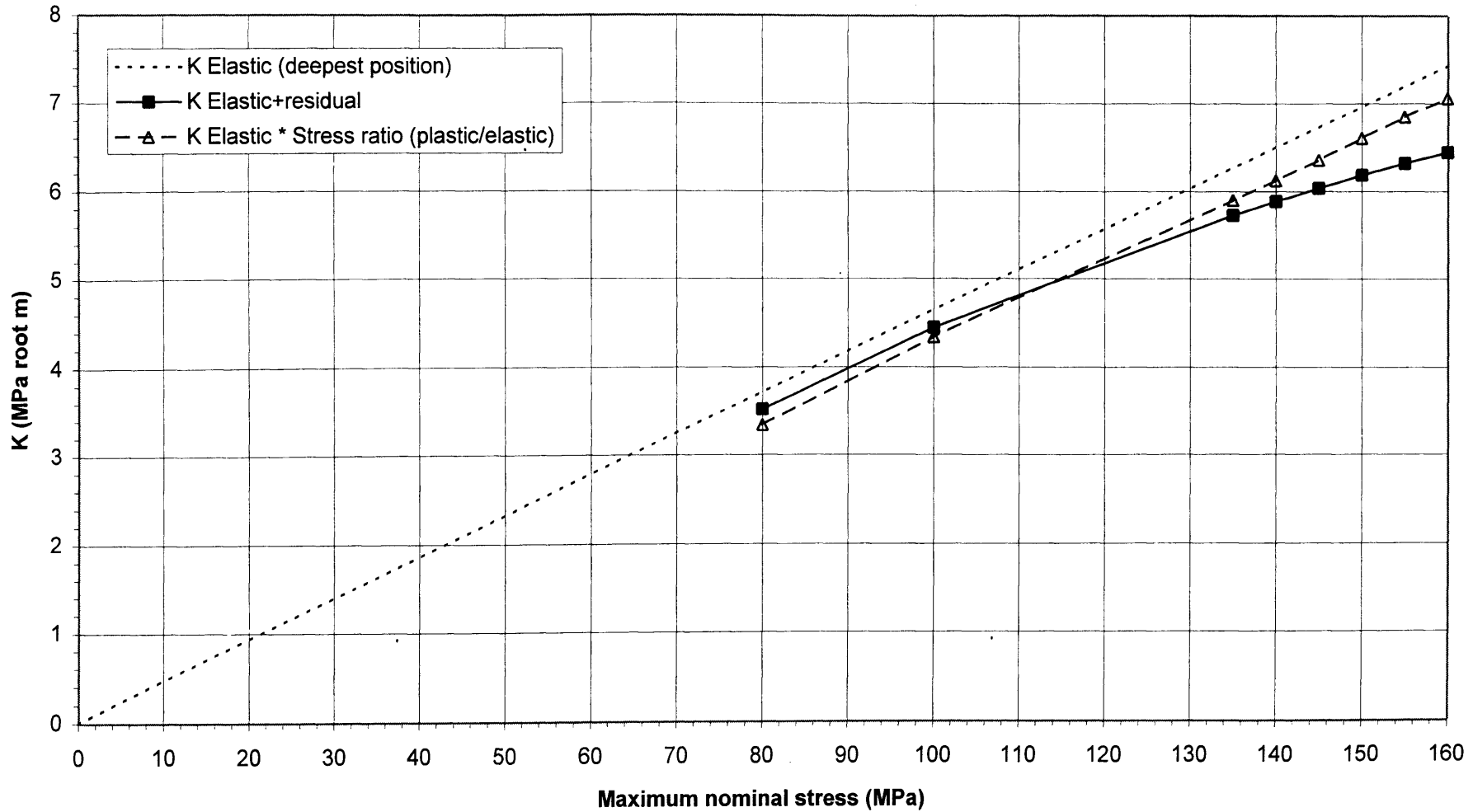


Figure 5.60 BRITE Notch 1 ($K_t=2.2$) : Comparison of K Solutions

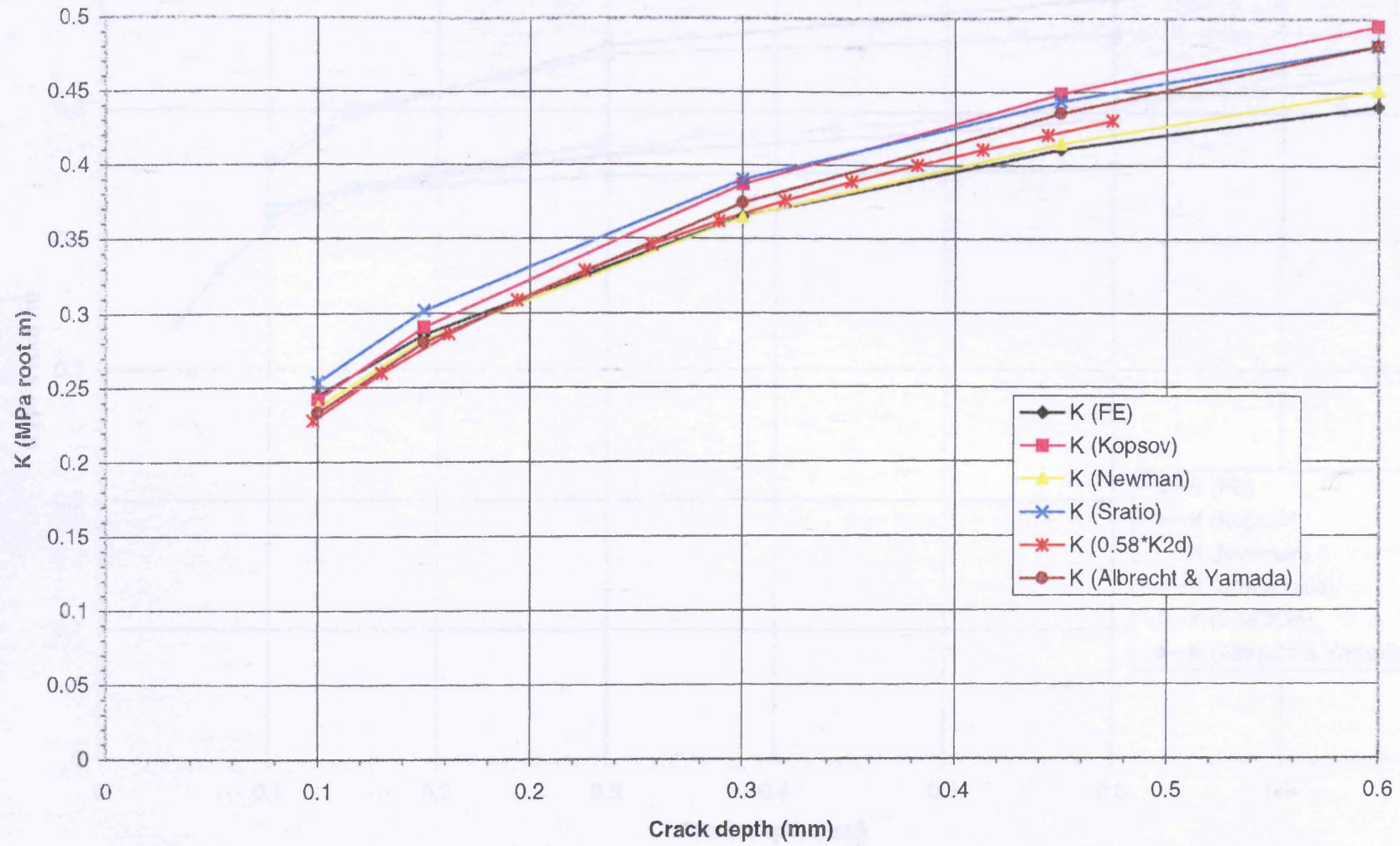


Figure 5.61 BRITE Notch 2 ($K_t=5.6$) : Comparison of K Solutions

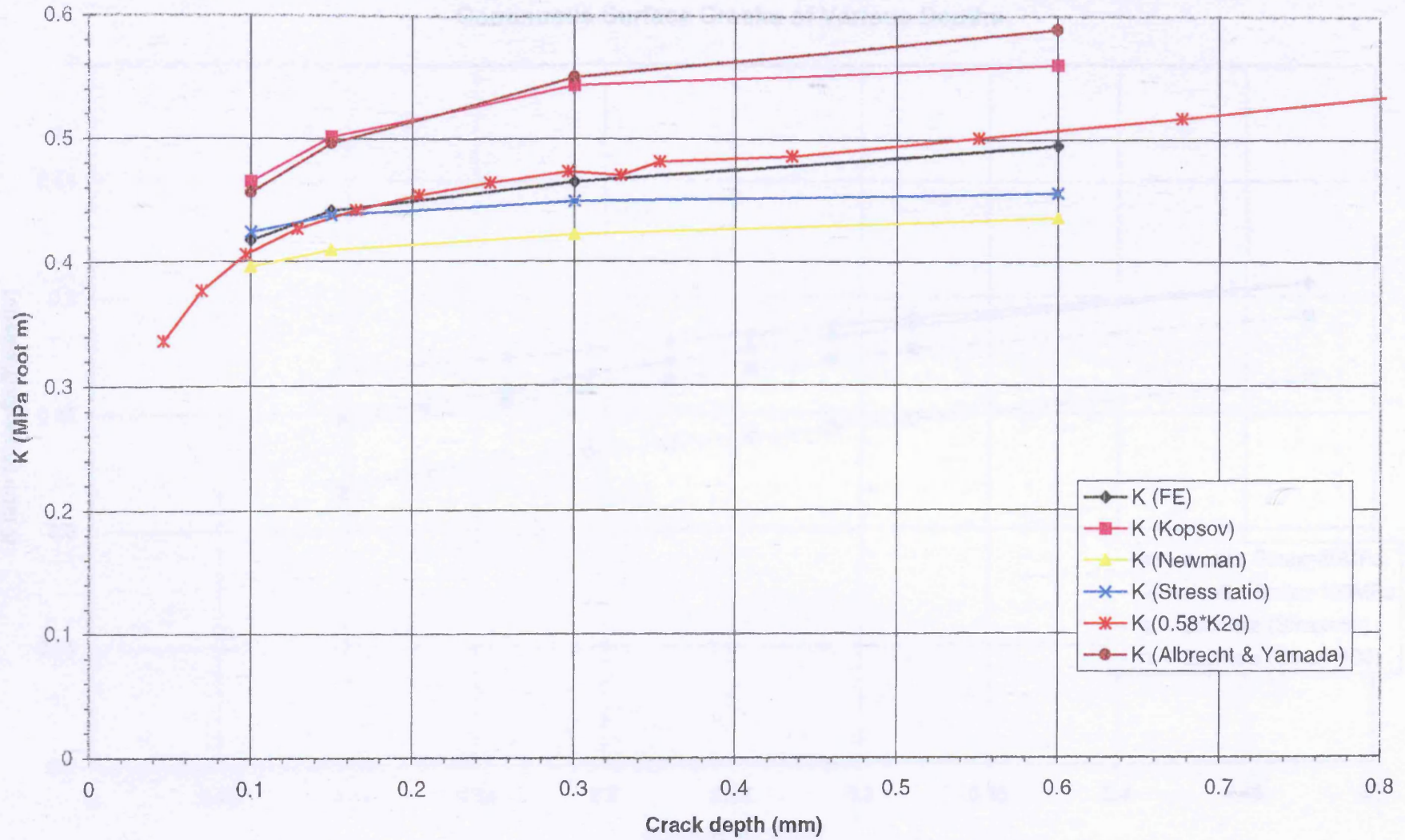


Figure 5.62 BRITE Notch 1 (Kt=2.2): Estimated Effect of Residual Stresses on K solutions for Continuous Surface Cracks of Various Depths

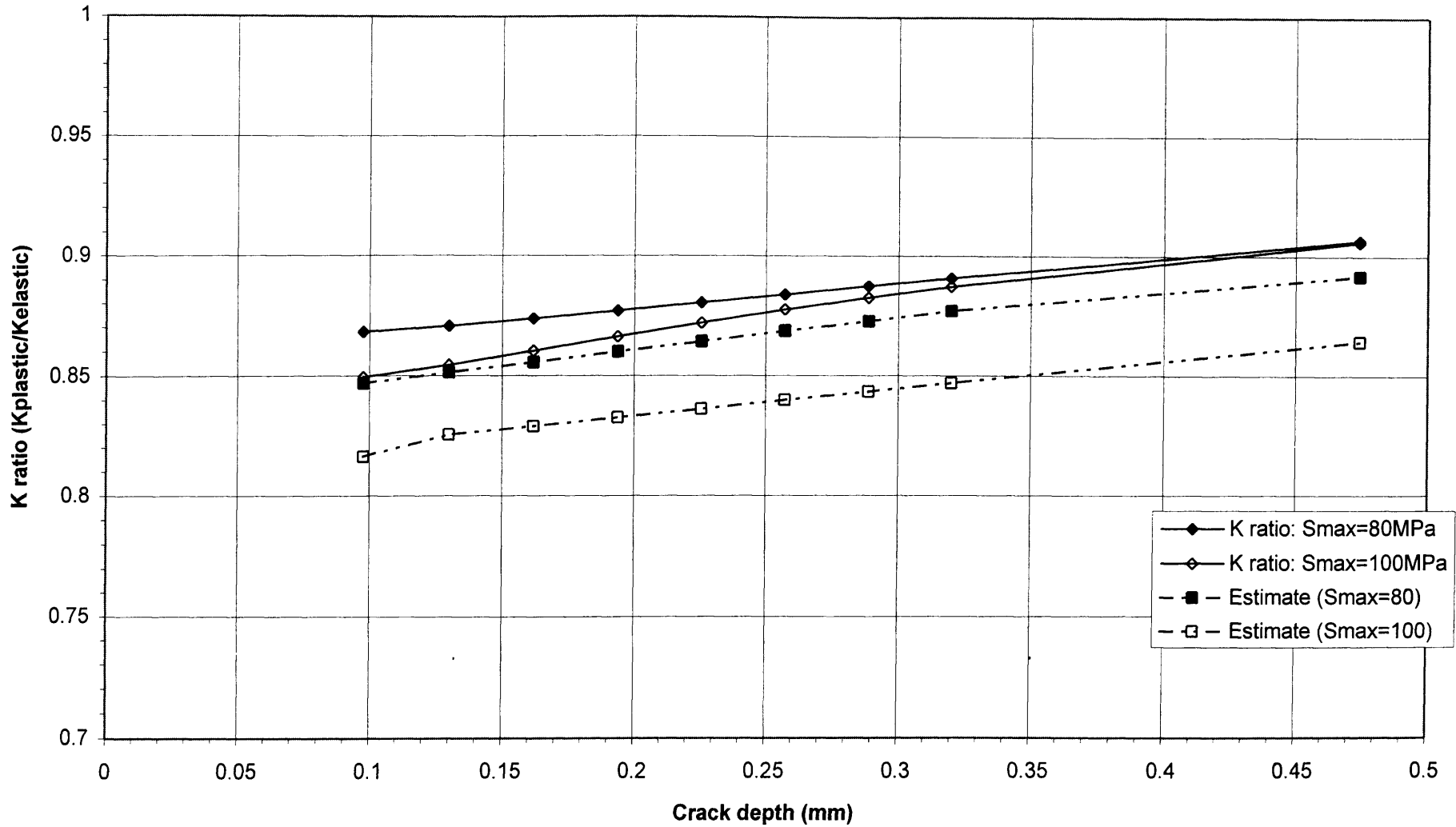


Figure 5.63 BRITE Notch 2 (Kt=5.6): Estimated Effect of Residual Stresses on K solutions for Continuous Surface Cracks of Various Depths

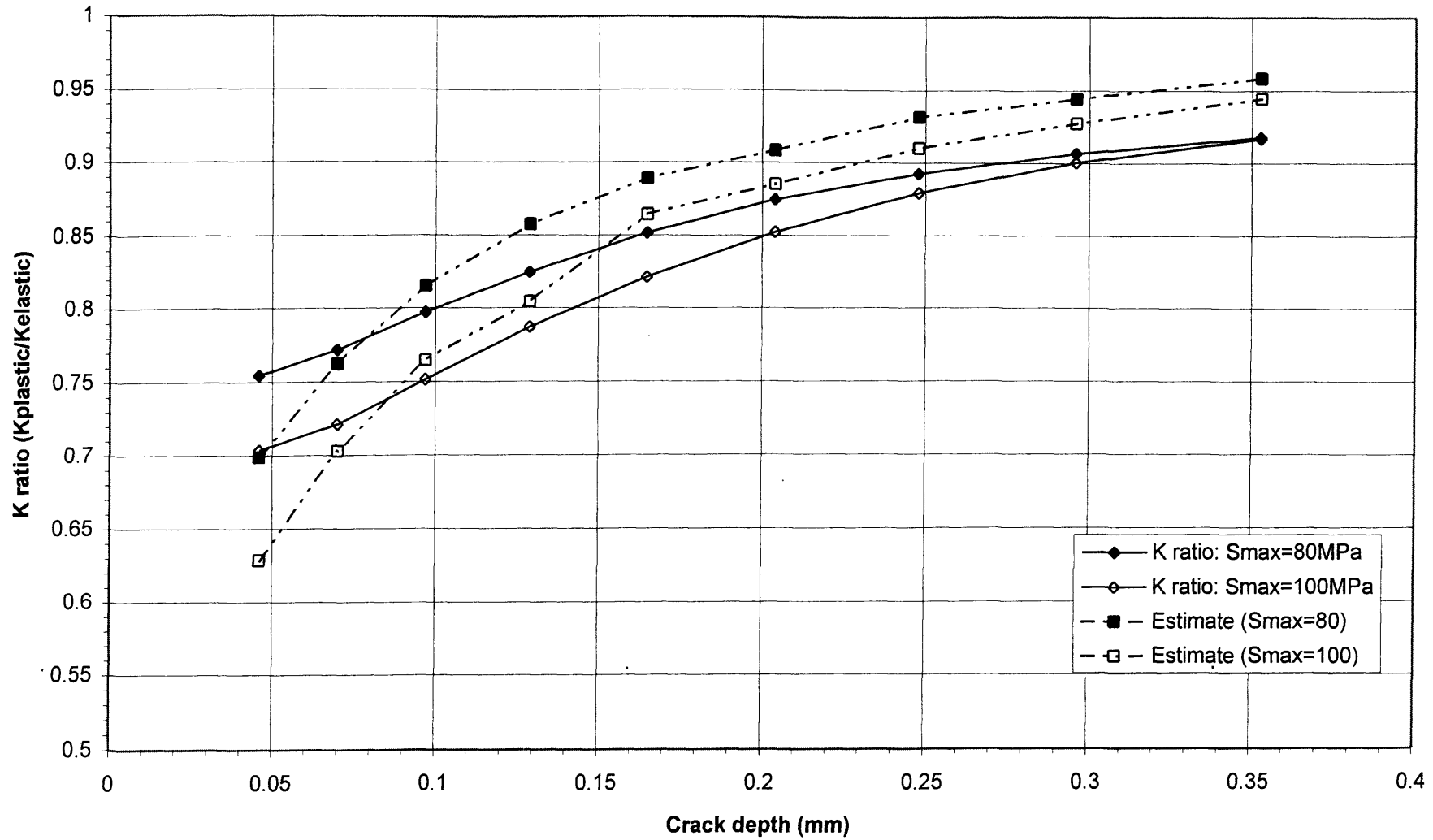


Figure 5.64 BRITE Notch 1 (Kt=2.2): Estimated Effect of Residual Stresses on K solutions for a 3-D Surface Crack (a = 0.3mm, a/c = 1.0) Over a Range of Applied Stress Levels

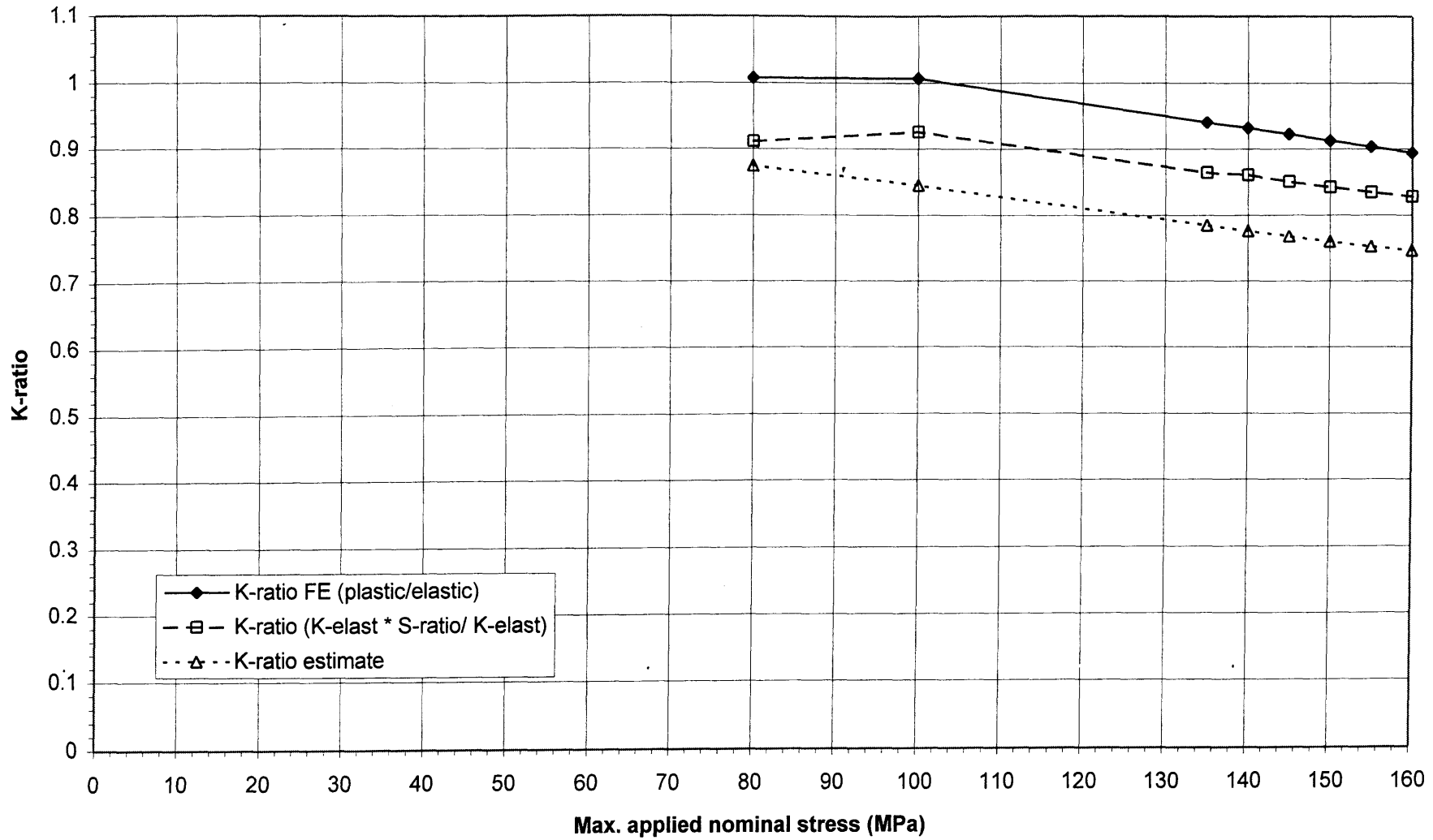


Figure 5.65 BRITE Notch 2 ($K_t=5.6$): Estimated Effect of Residual Stresses on K solutions for a 3-D Surface Crack ($a = 0.3\text{mm}$, $a/c = 1.0$) Over a Range of Applied Stress Levels

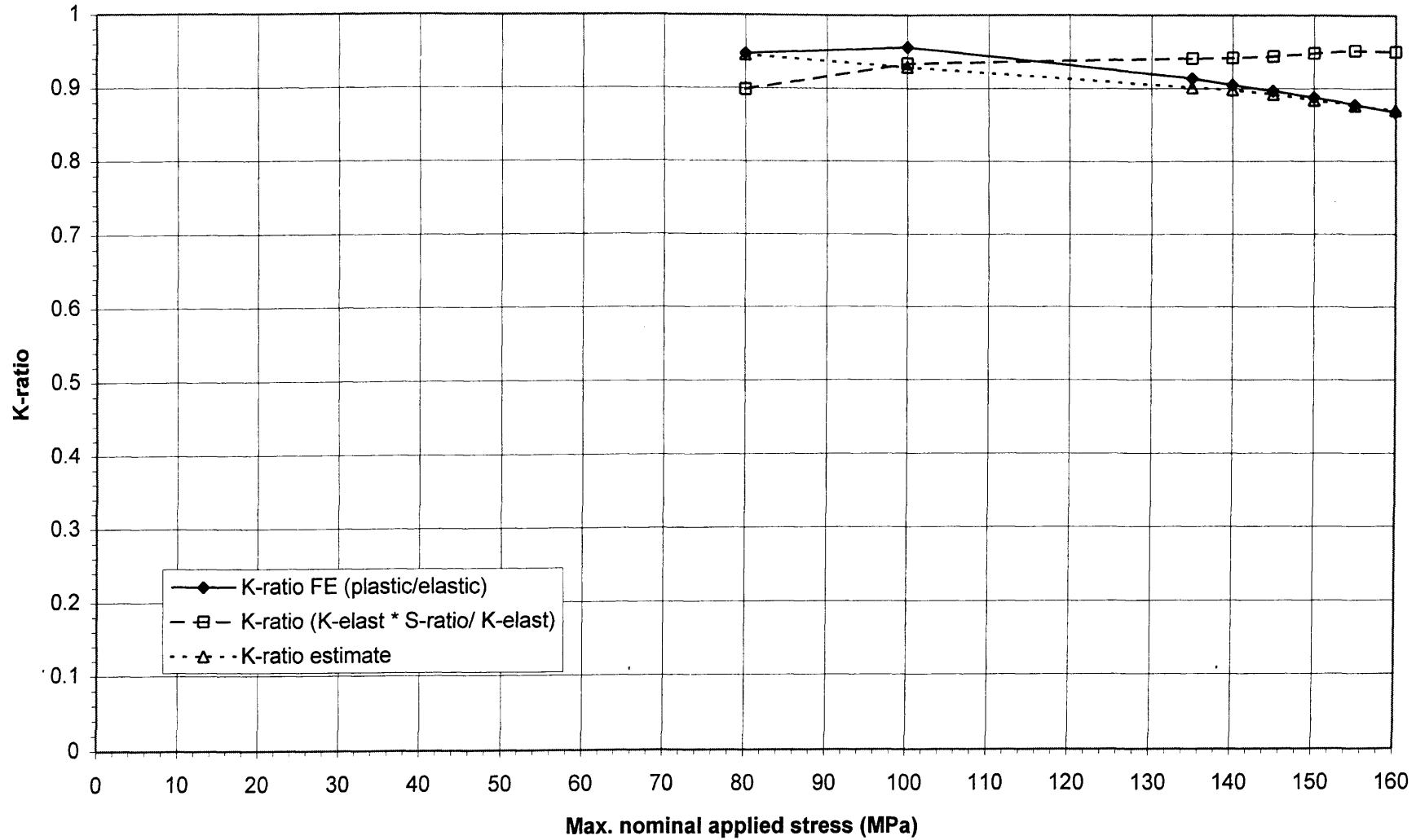


Figure 5.66 BRITE Notch 1 (Kt=2.2): Crack Mouth Displacement Ratios (Min.load/Max.load) for Various Depths of Continuous Surface Cracks - Comparison with Estimates Based on Local Stress Ratios

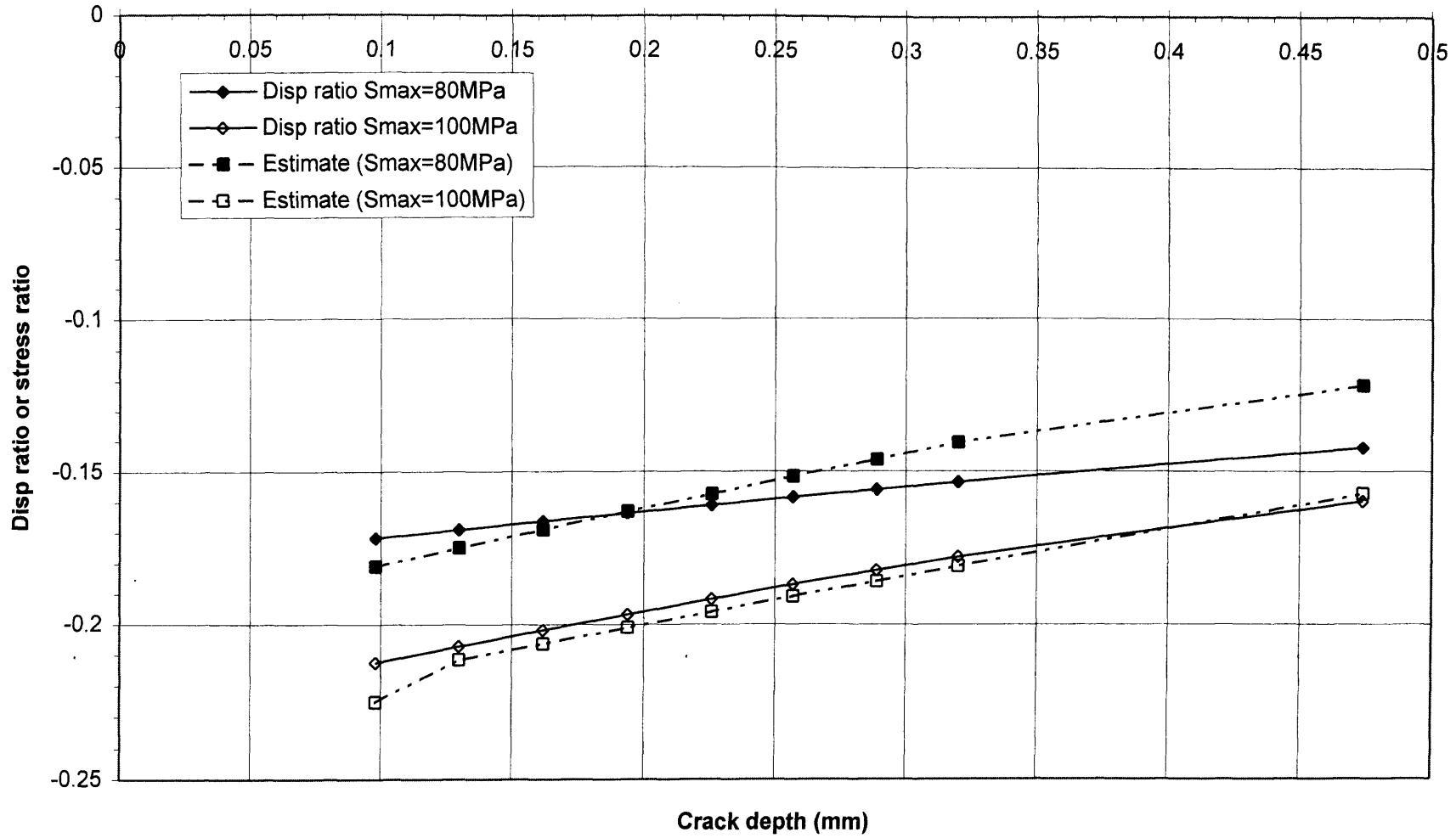


Figure 5.67 BRITE Notch 2 (Kt=5.6): Crack Mouth Displacement Ratios (Min.load/Max.load) for Various Depths of Continuous Surface Cracks - Comparison with Estimates Based on Local Stress Ratios

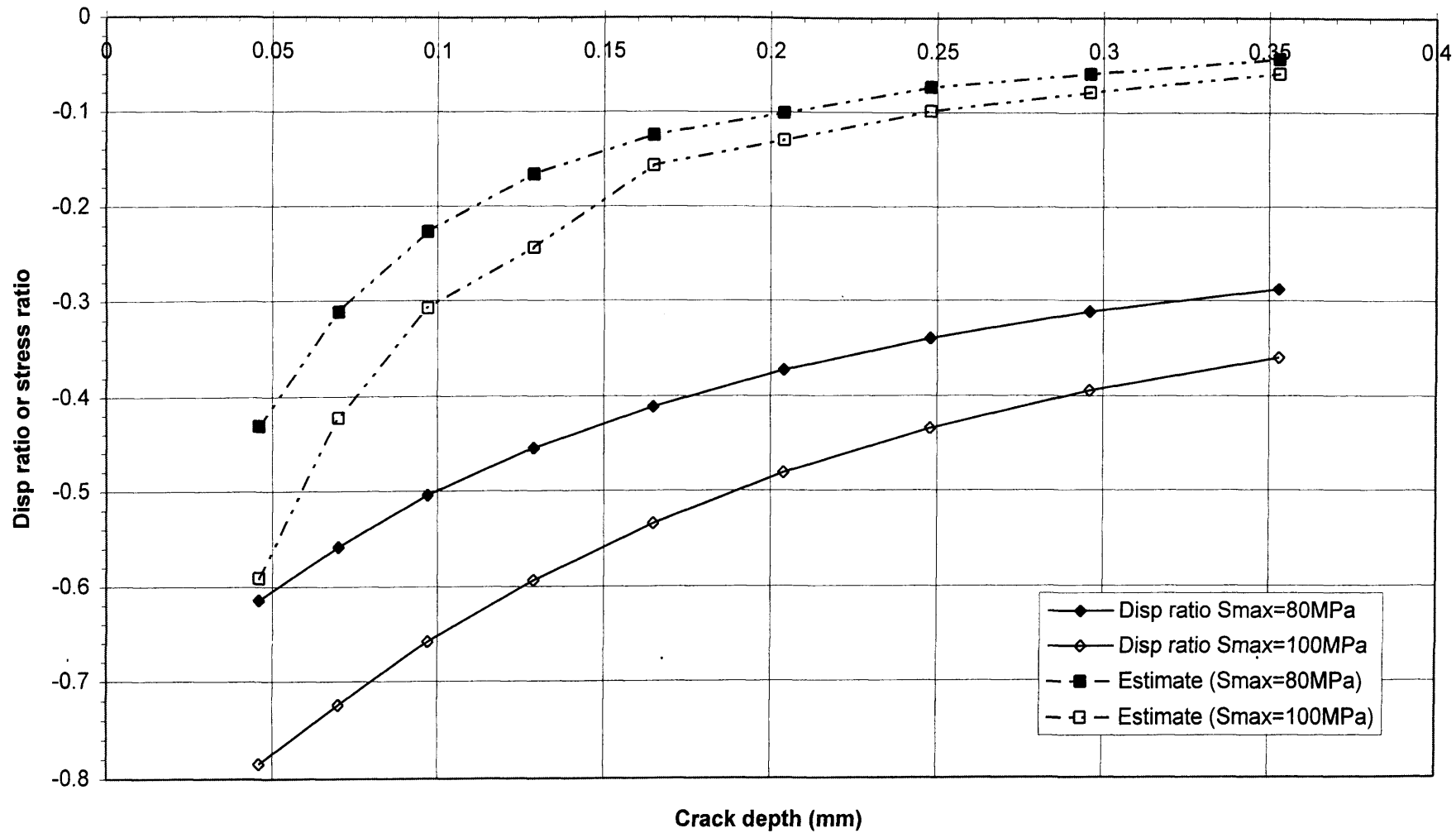


Figure 6.1 BRITE Notch 1 (Kt=2.2) Comparison of Predicted Fatigue Strengths with Experimental Results

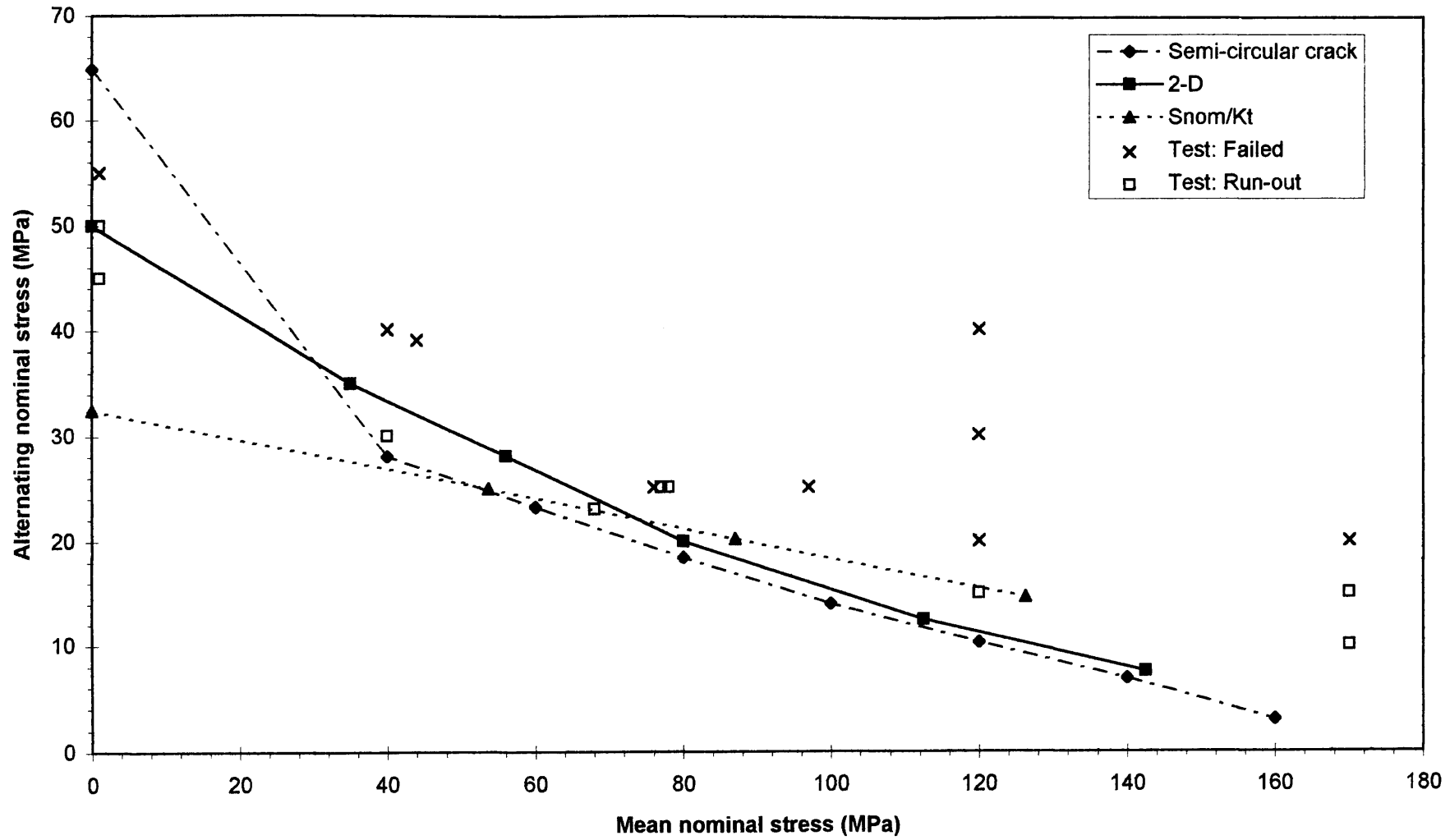


Figure 6.2 BRITE Notch 1 ($K_t=2.2$) Applied Delta K and Threshold Delta K Versus Crack Depth
 (Grade 17 Grey Cast Iron) Continuous Surface Cracks, $R = 0$

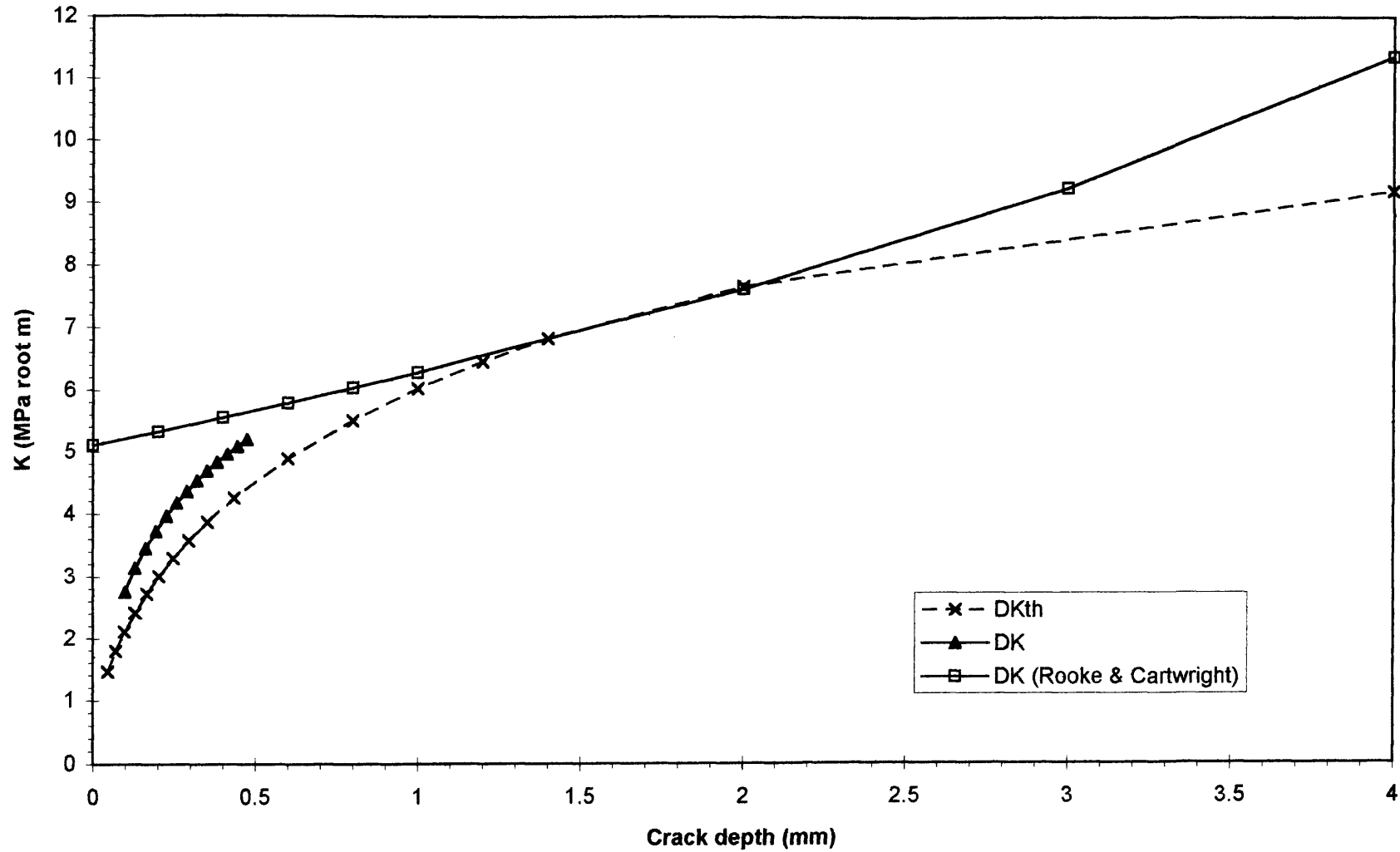


Figure 6.3 BRITE Notch 2 (Kt=5.6) Comparison of Predicted Fatigue Strengths with Experimental Results

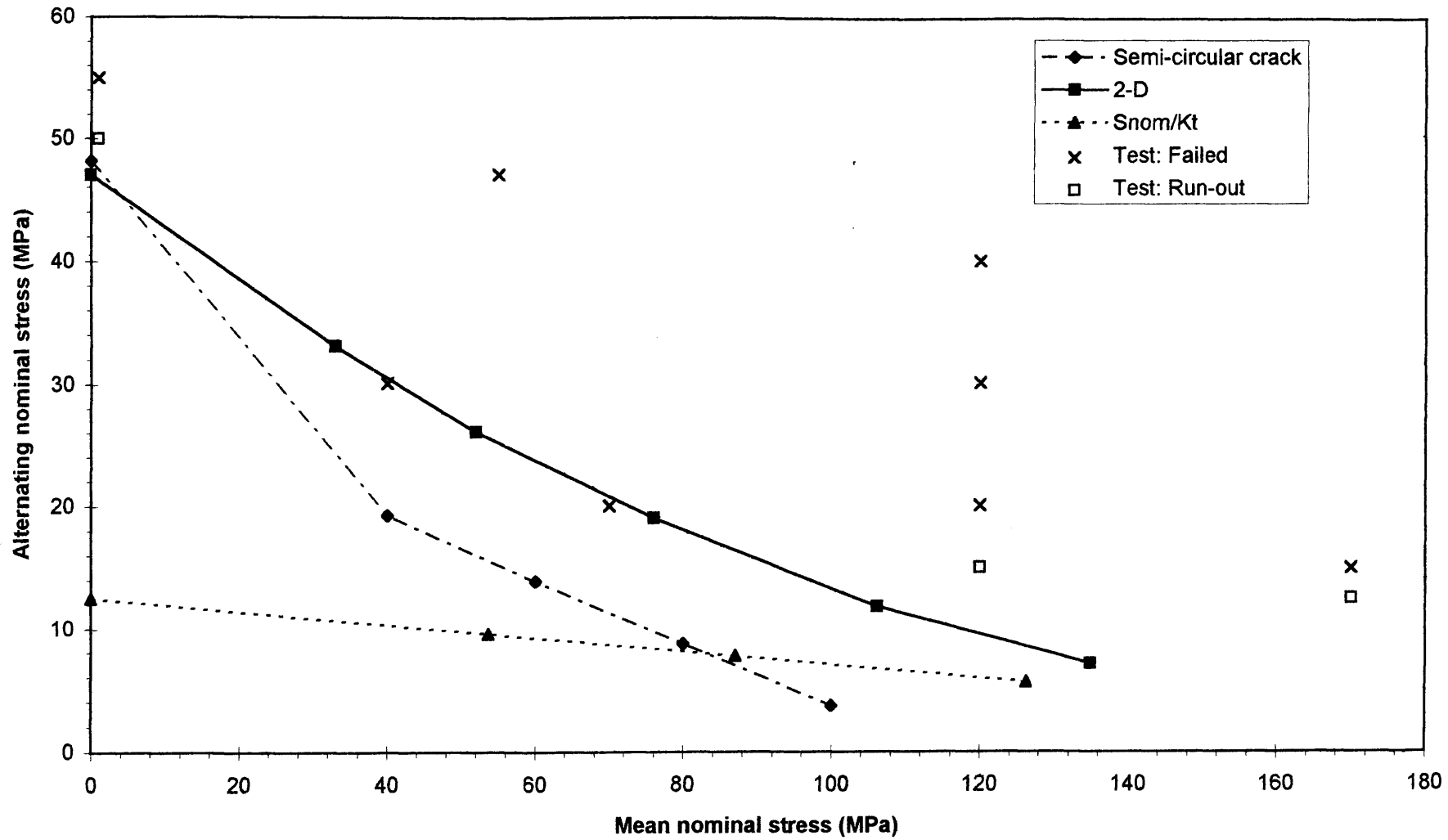


Figure 6.4 BRITE Notch 2 (Kt=5.6) Applied Delta K and Threshold Delta K Versus Crack Depth (Grade 17 Grey Cast Iron) Continuous Surface Cracks, R = 0

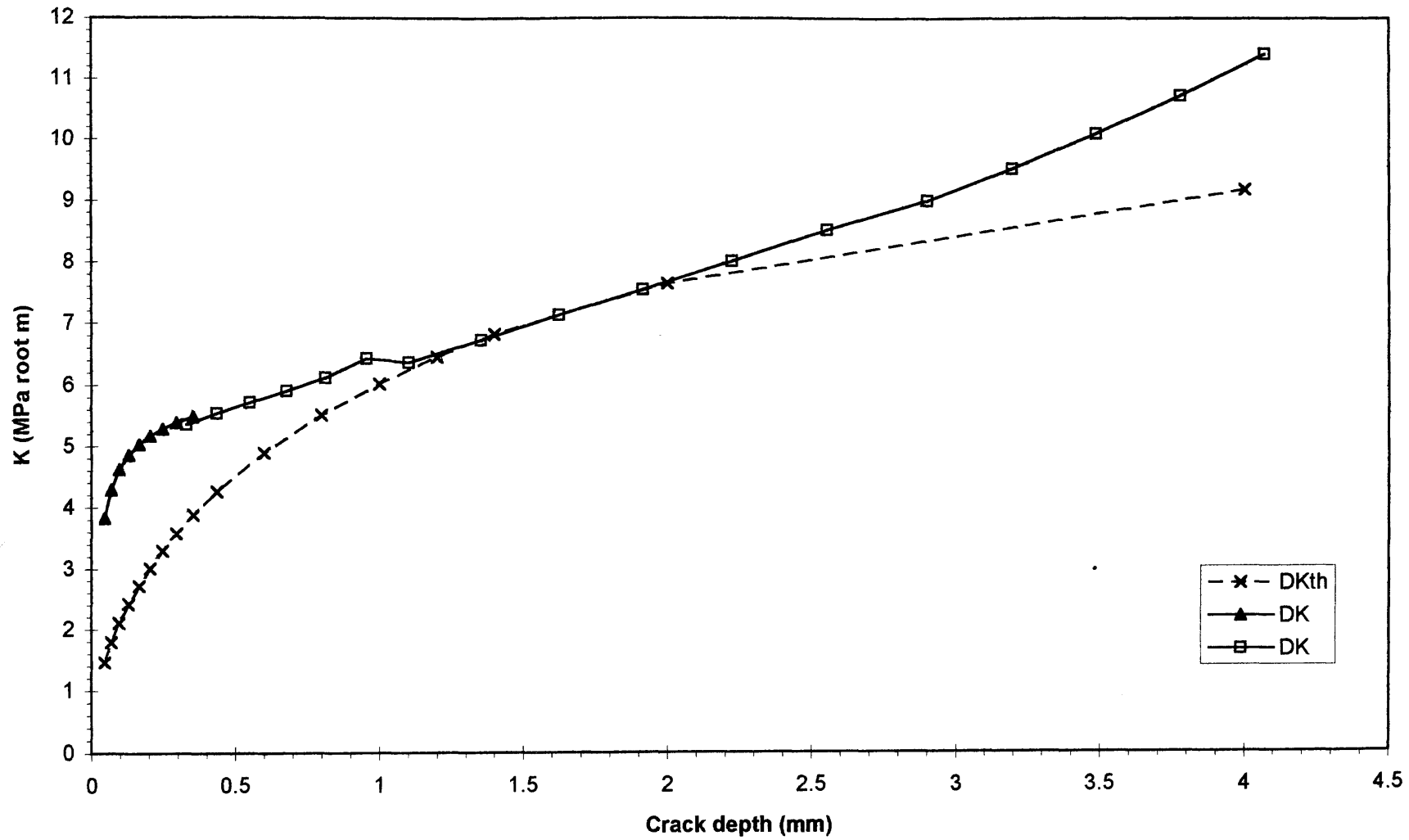


Figure 6.5 BRITE Component (Grade 17 Grey Cast Iron)
Comparison of Predicted Fatigue Strengths and Experimental Results

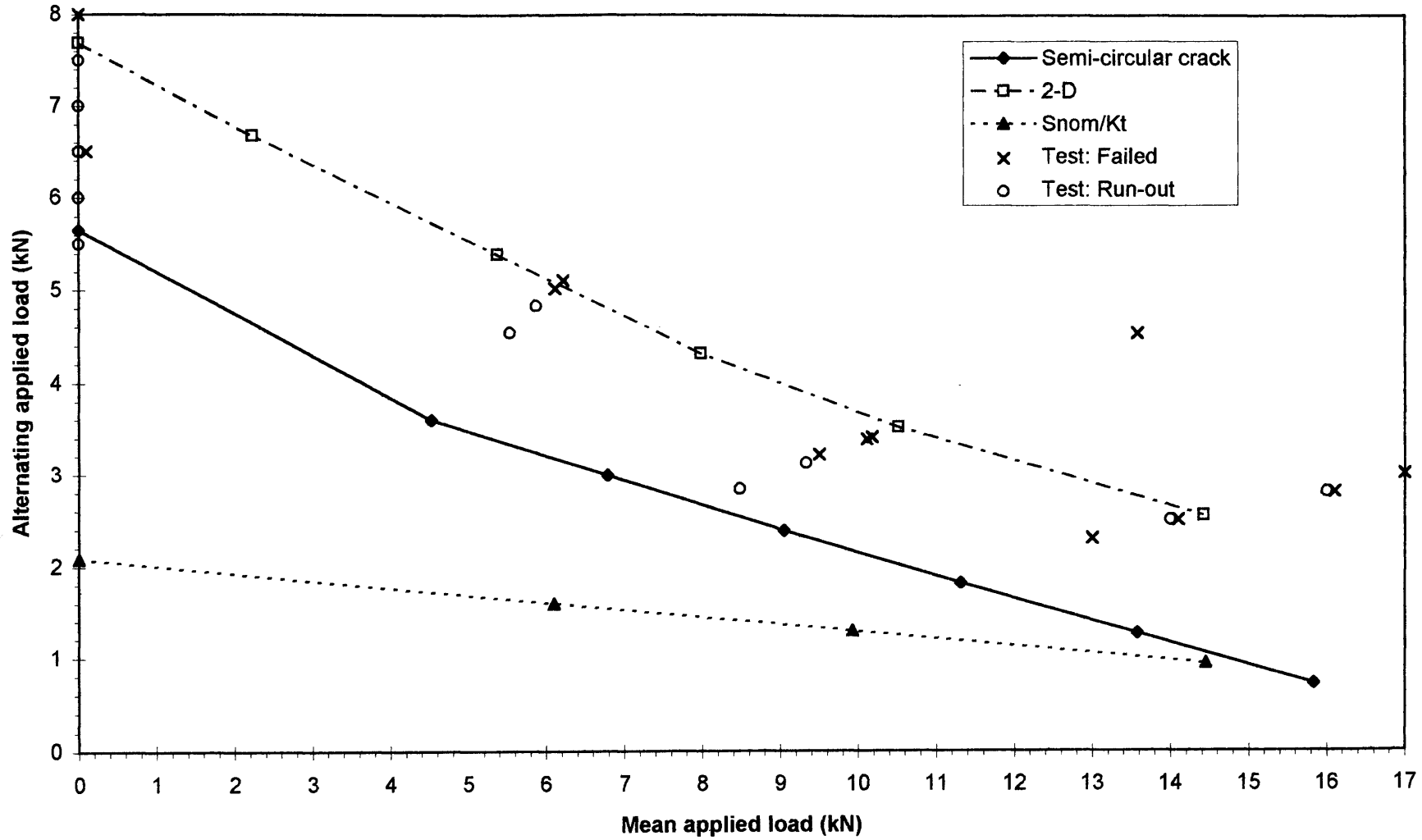


Figure 6.6 BRITE Component Applied Delta K and Threshold Delta K Versus Crack Depth (Grade 17 Grey Cast Iron) Continuous Surface Cracks

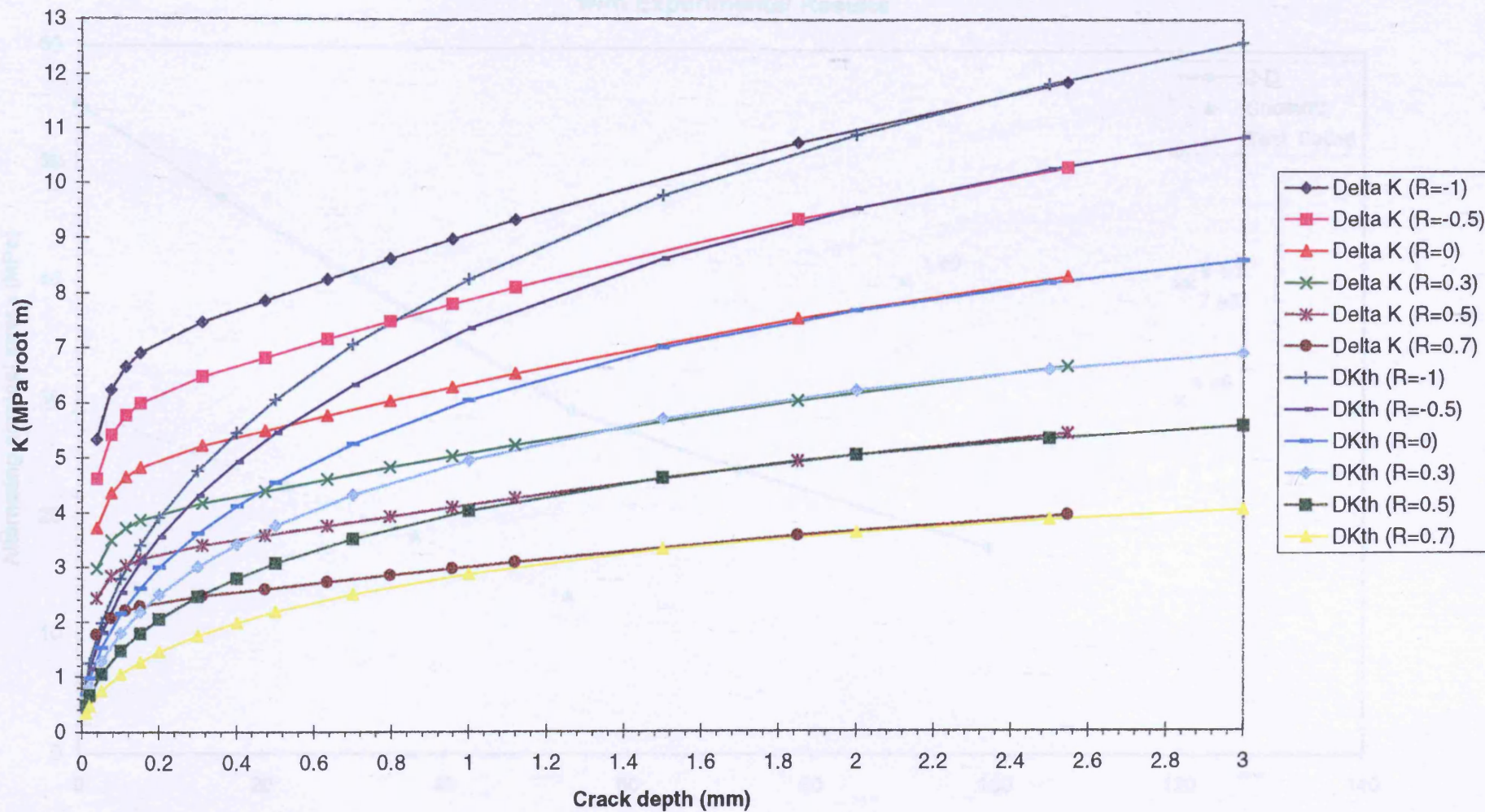


Figure 6.7 BRITE Three-point Bend (Kt=2.4): Comparison of Predicted Fatigue Strengths with Experimental Results

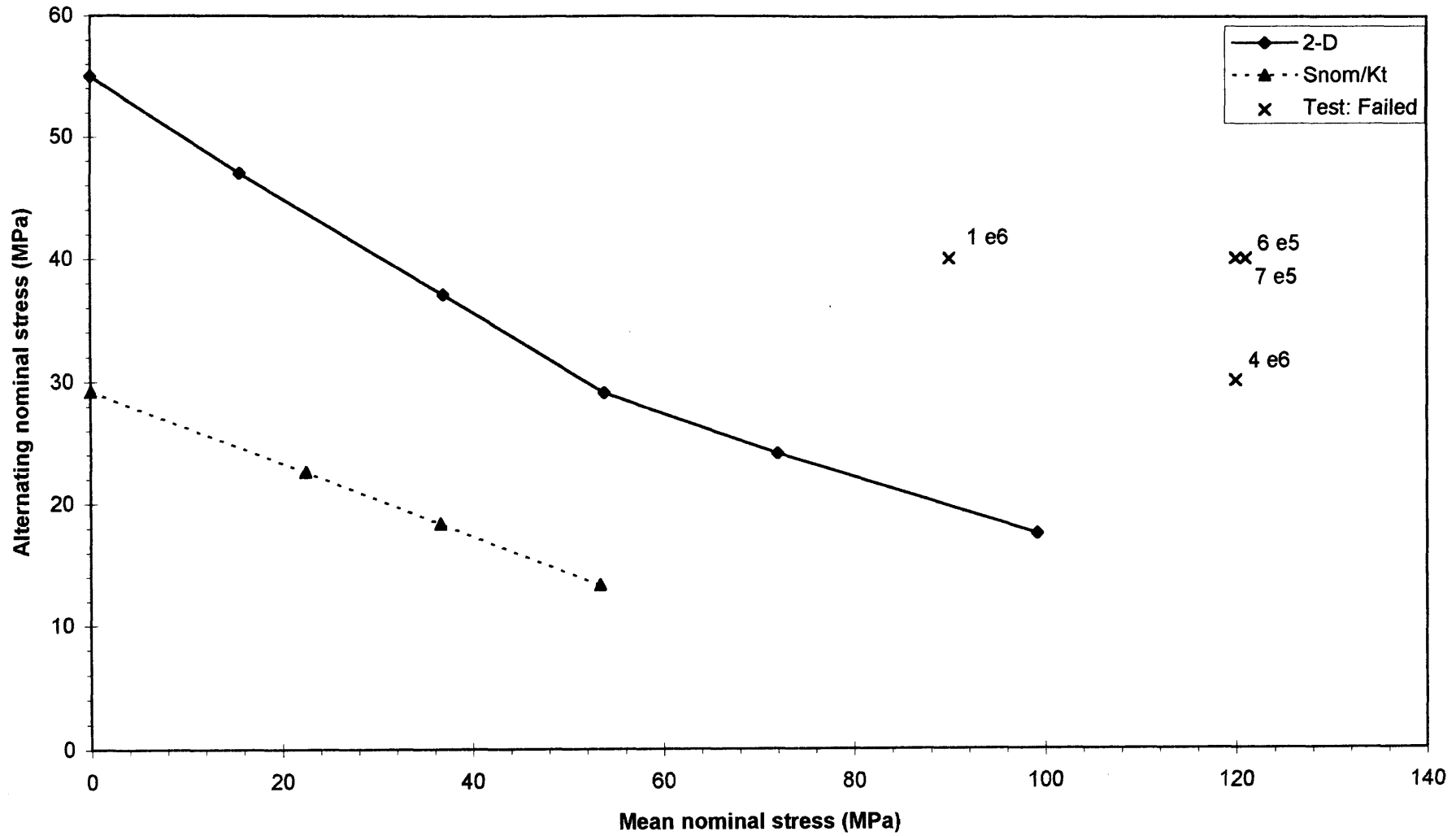


Figure 6.8 BRITE Three-point Bend (Kt=2.4): Applied ΔK and ΔK_{th} Versus Crack Depth (Grade 17 Grey Cast Iron) Continuous Surface Cracks

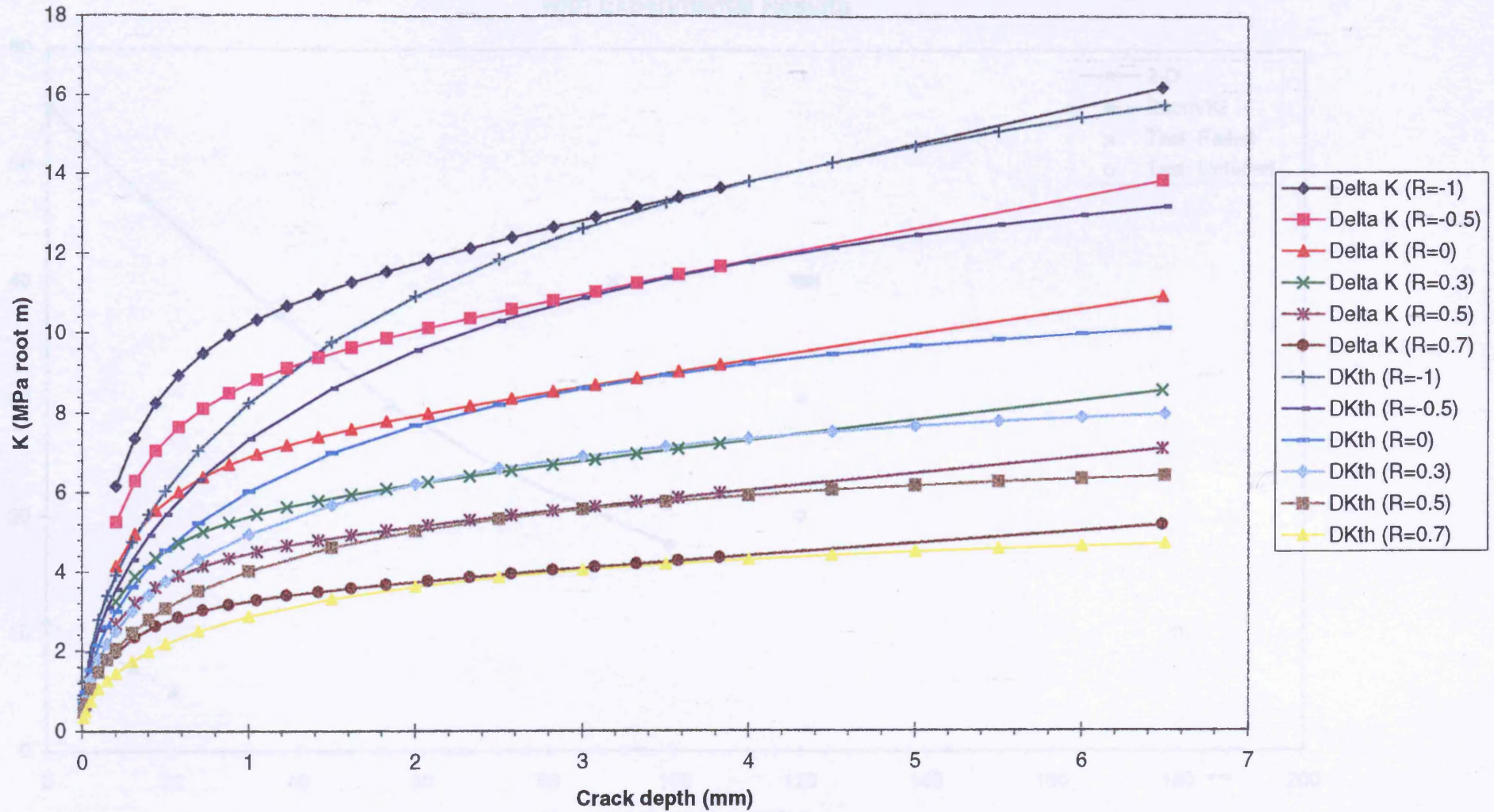


Figure 6.9 BRITE Three-point Bend (Kt=6.3): Comparison of Predicted Fatigue Strengths with Experimental Results

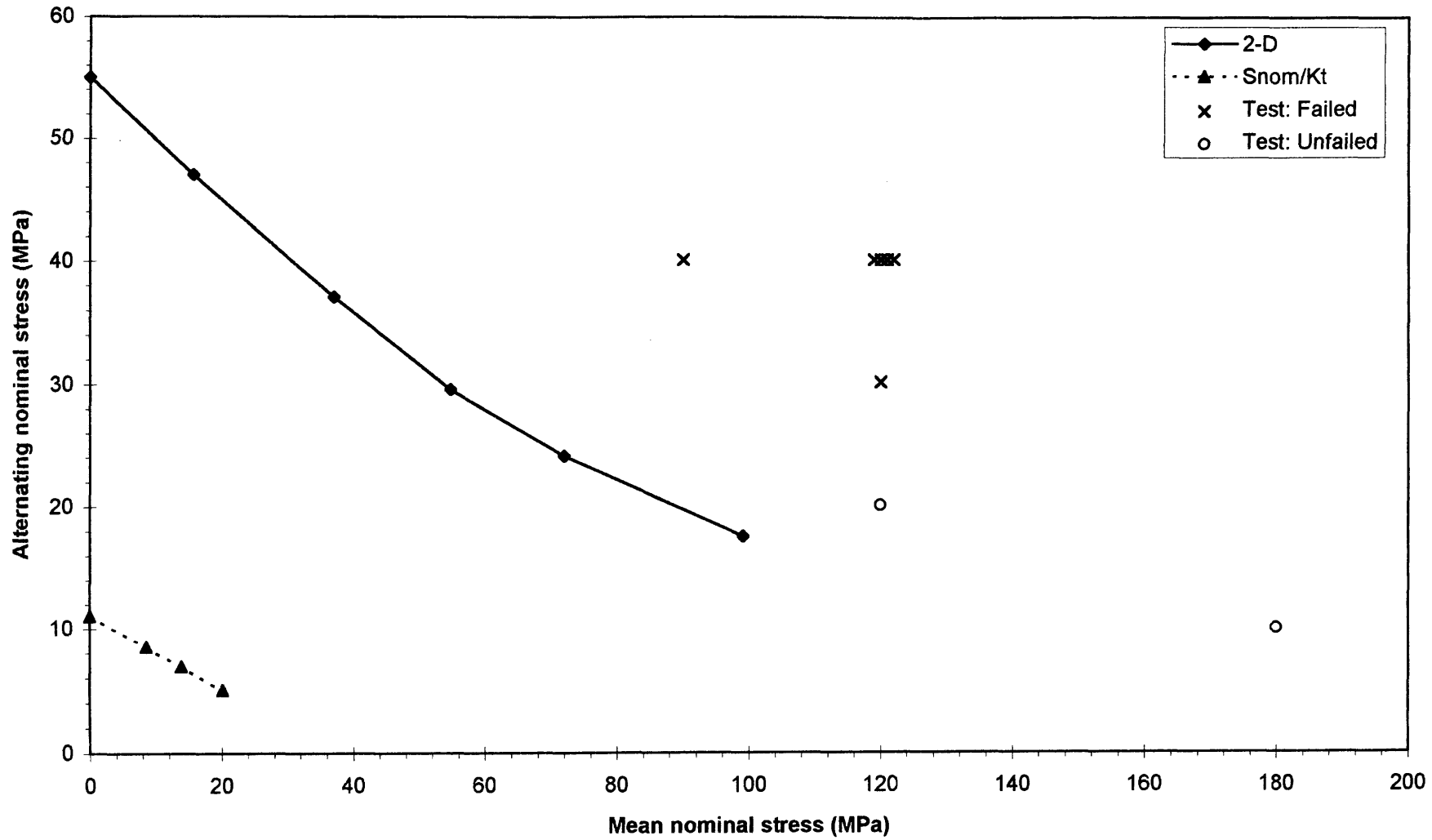


Figure 6.10 BRITE Three-point Bend (Kt=6.3): Applied ΔK and ΔK_{th} Versus Crack Depth (Grade 17 Grey Cast Iron) Continuous Surface Cracks

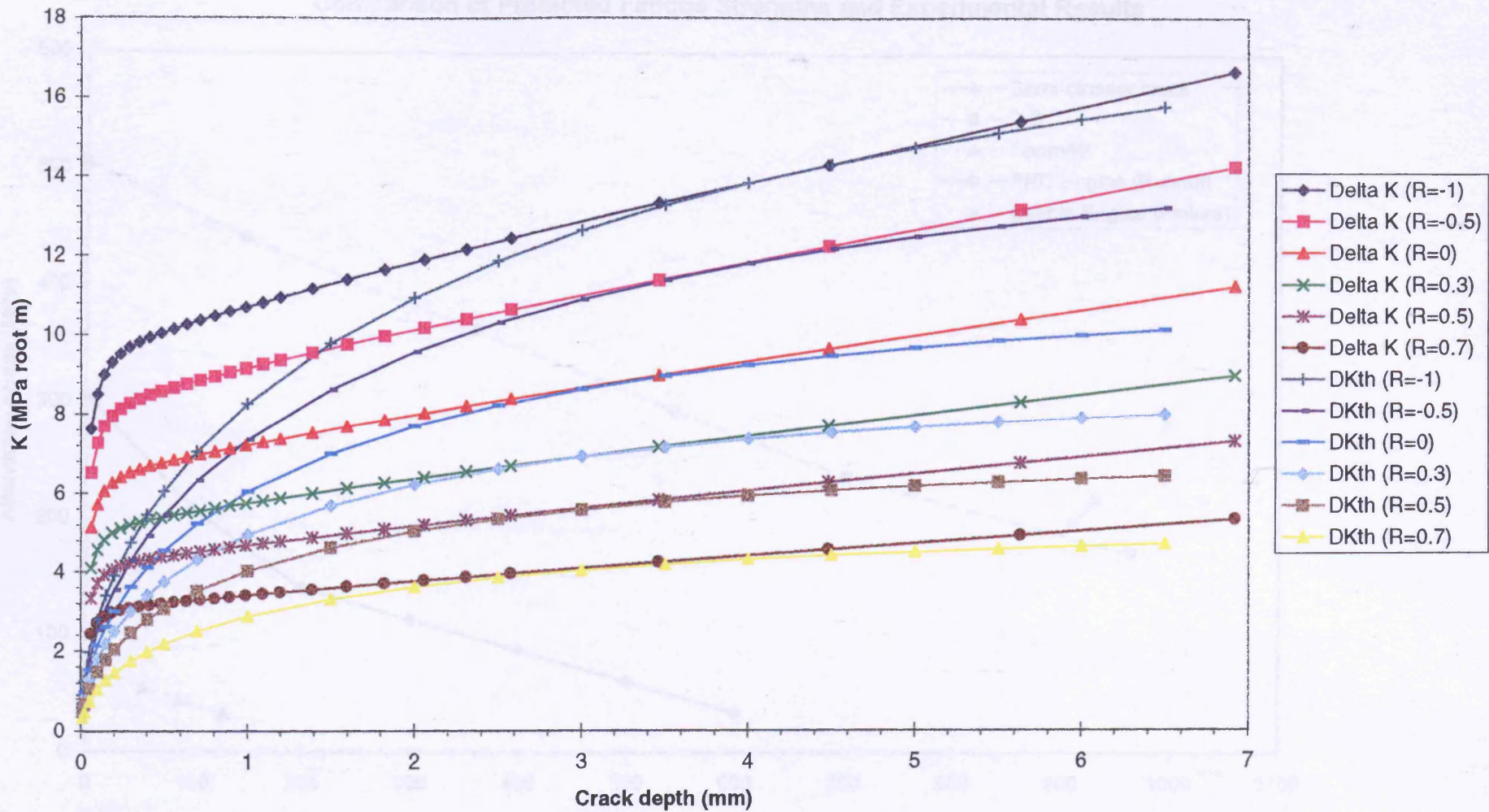


Figure 6.11 Engine Bedplates with Sharp (12 thou) Fillets (Grade 17 Grey Cast Iron)
Comparison of Predicted Fatigue Strengths and Experimental Results

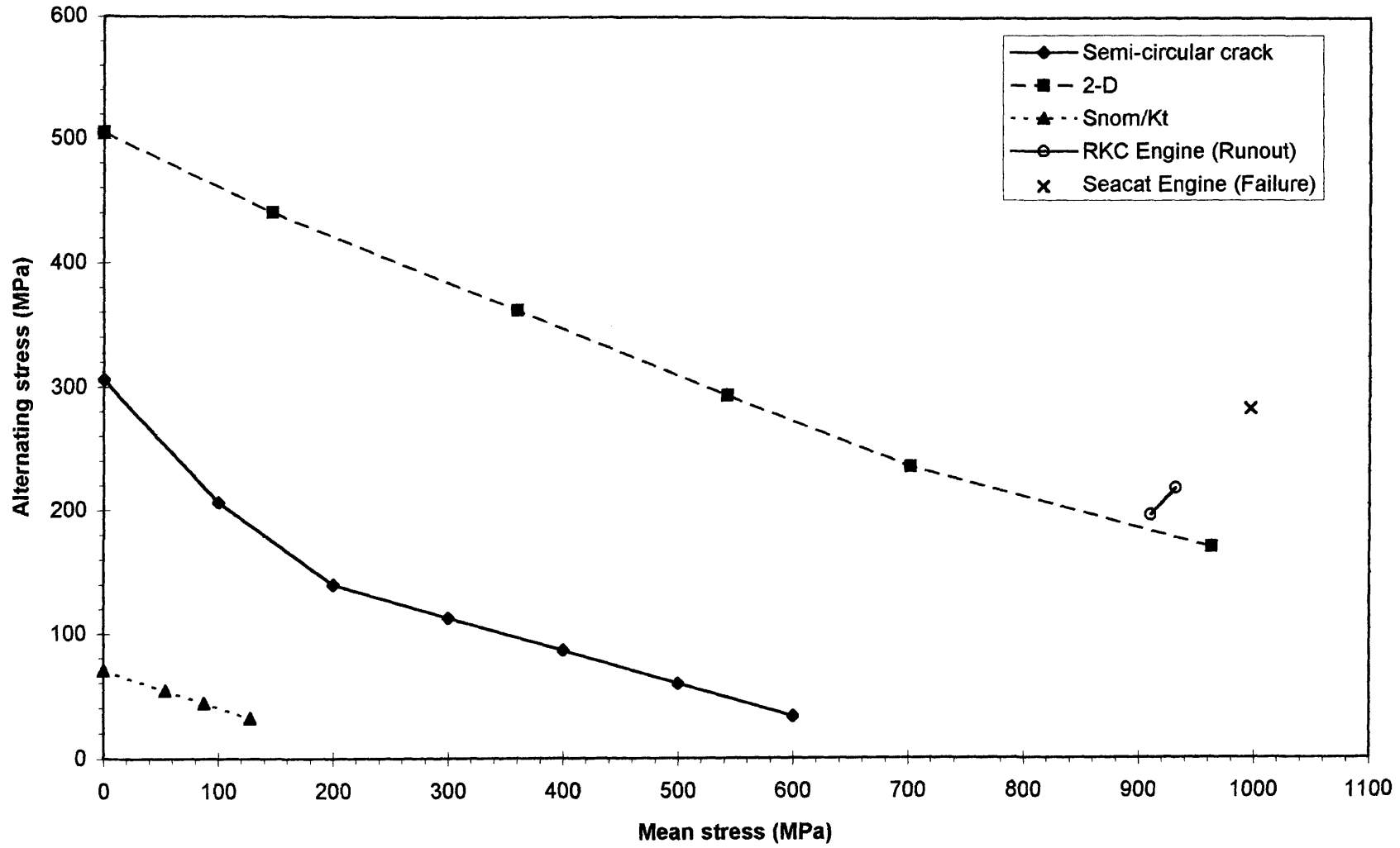


Figure 6.12 Engine Bedplate with 12 thou Fillet (Grade 17 Grey Cast Iron)
Applied Delta K and Threshold Delta K Versus Crack Depth for Continuous Surface Cracks

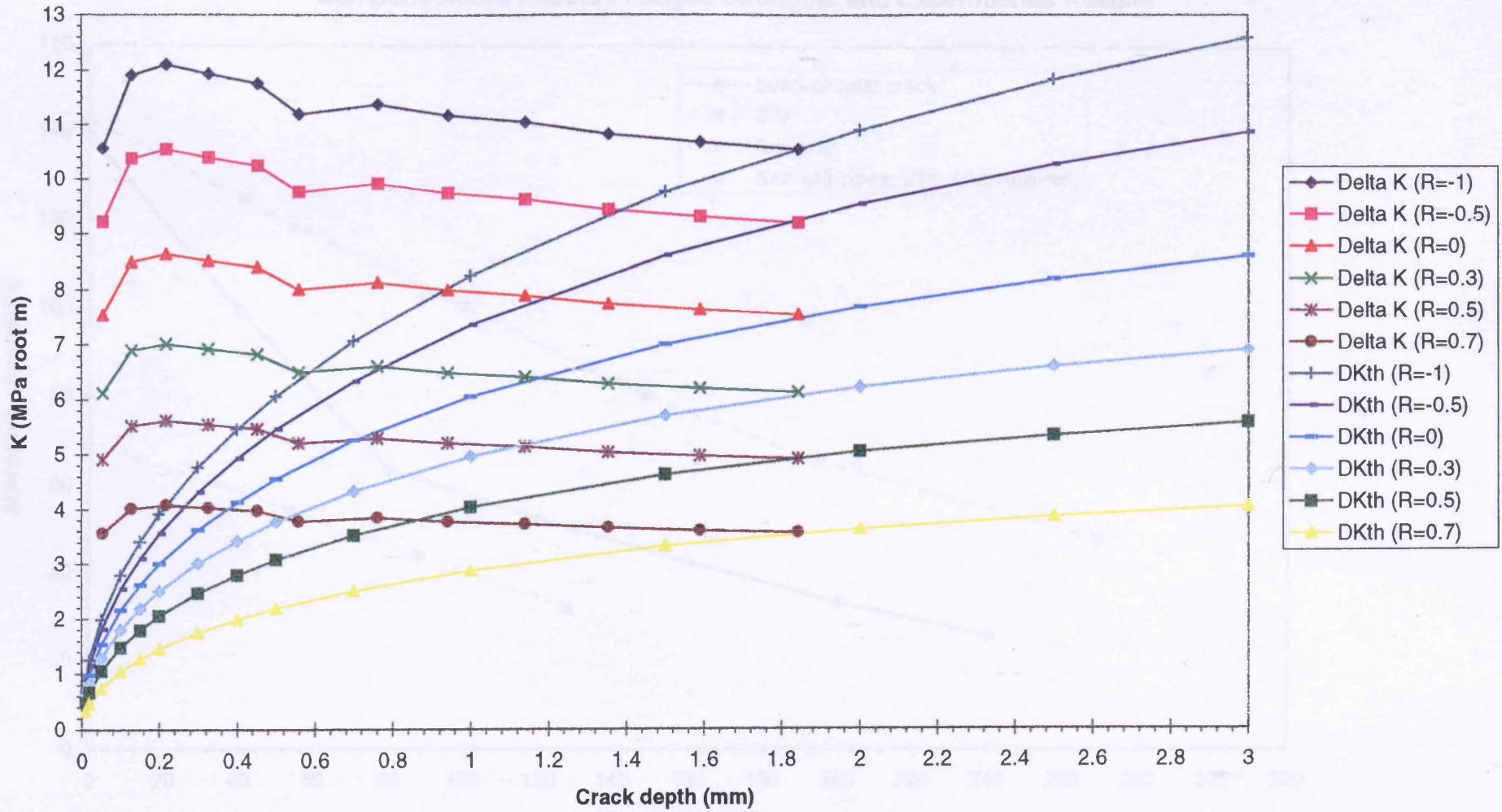


Figure 6.13 Seacat Engine Bedplates with 1/8th Fillet (Grade 17 Grey Cast Iron)
Comparison of Predicted Fatigue Strengths and Experimental Results

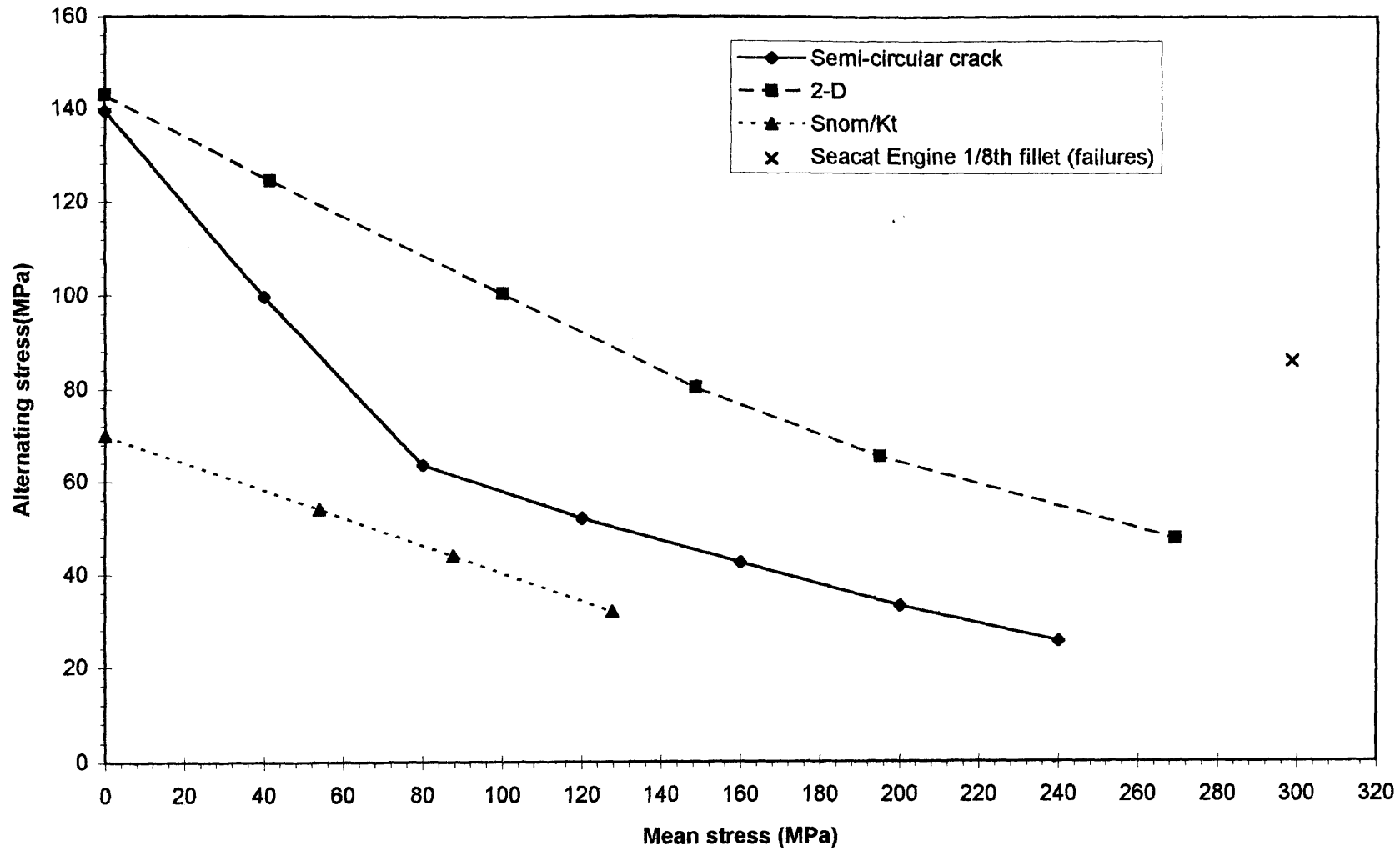


Figure 6.14 Seacat Engine Bedplate with 1/8th Fillet (Grade 17 Grey Cast Iron)
Applied Delta K and Threshold Delta K Versus Crack Depth for Continuous Surface Cracks

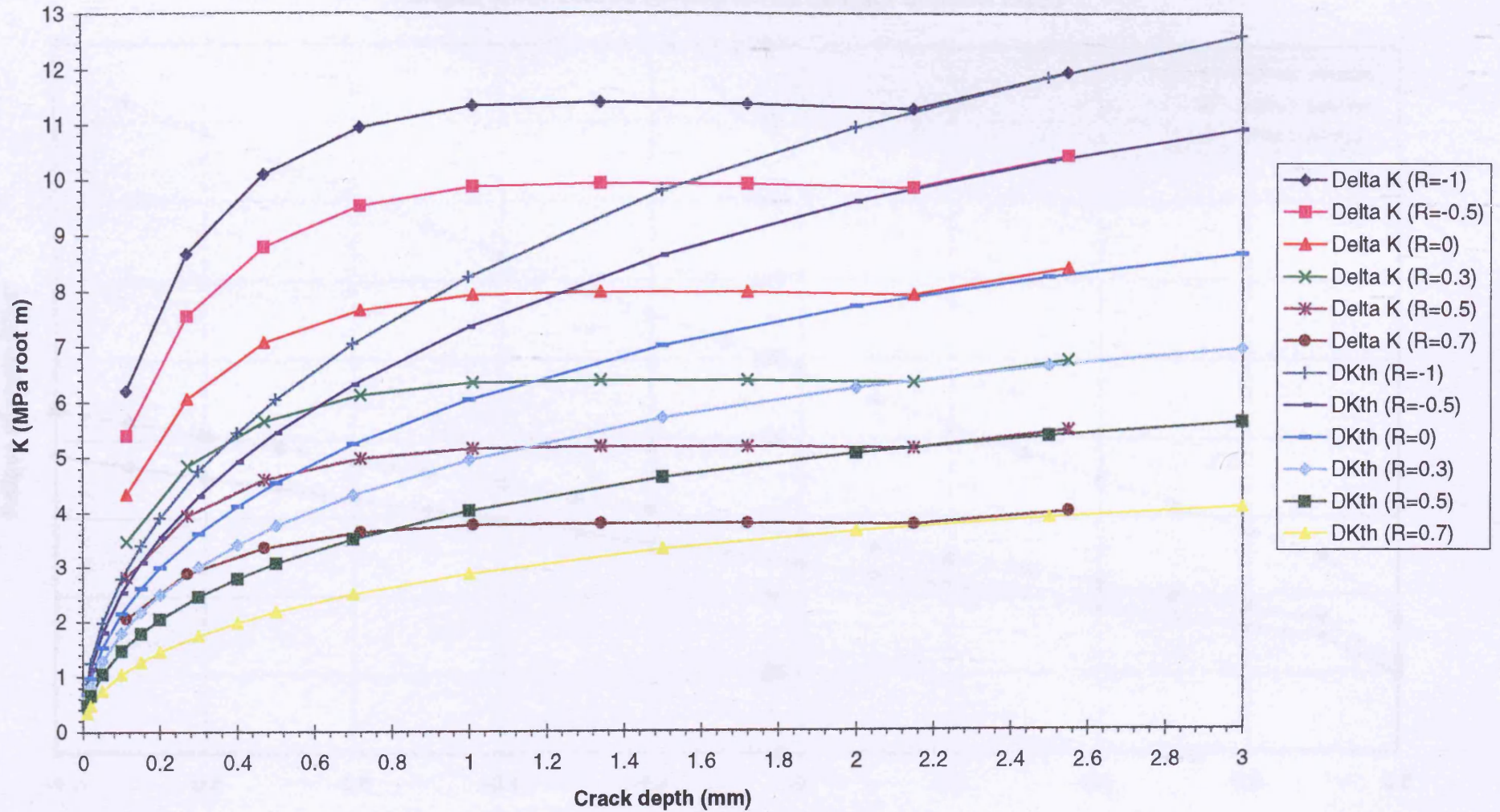


Figure 6.15 BCIRA Grade 250 Grey Cast Iron
Fatigue Limit versus R-ratio for three Cast Section Sizes

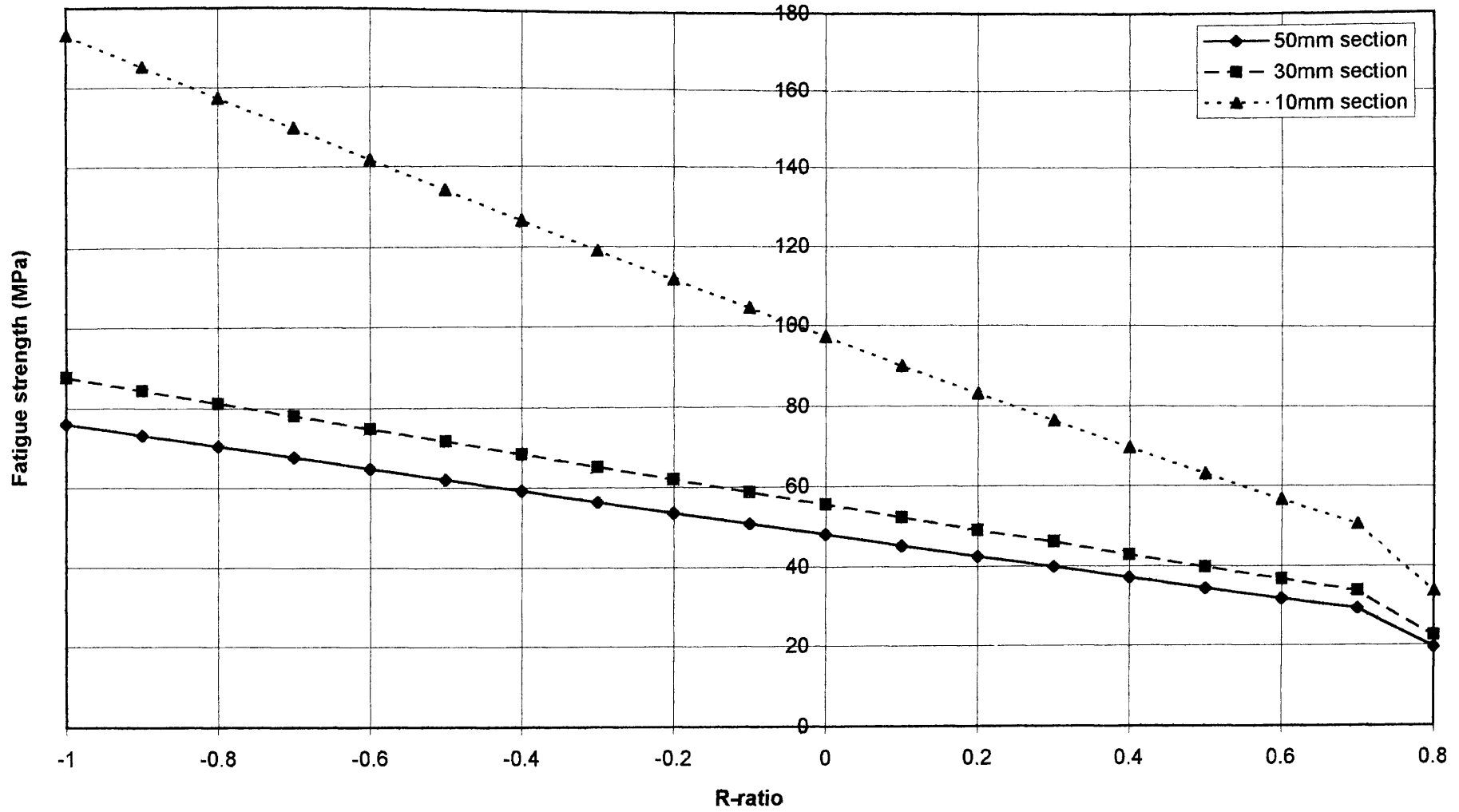


Figure 6.16 BCIRA Grade 250 Grey Cast Iron
Predicted Apparent Short Crack Growth Threshold - Continuous Surface Crack (R = 0.05)

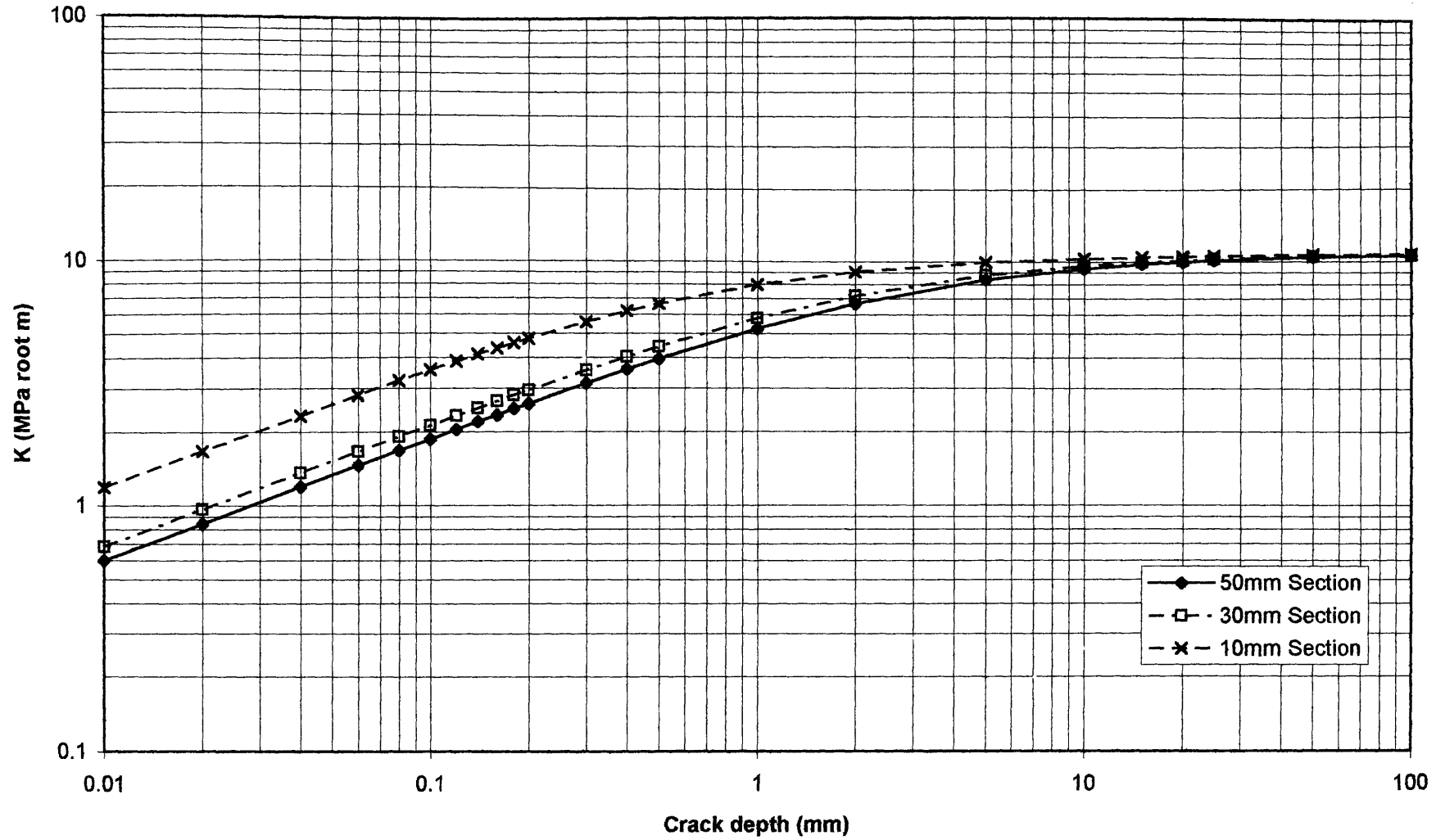


Figure 6.17 BCIRA n7a1 (10mm Cast Section Size, $K_t = 1.526$, Grade 250 Grey Iron)
 Comparison of Predicted Fatigue Strengths and Experimental Results

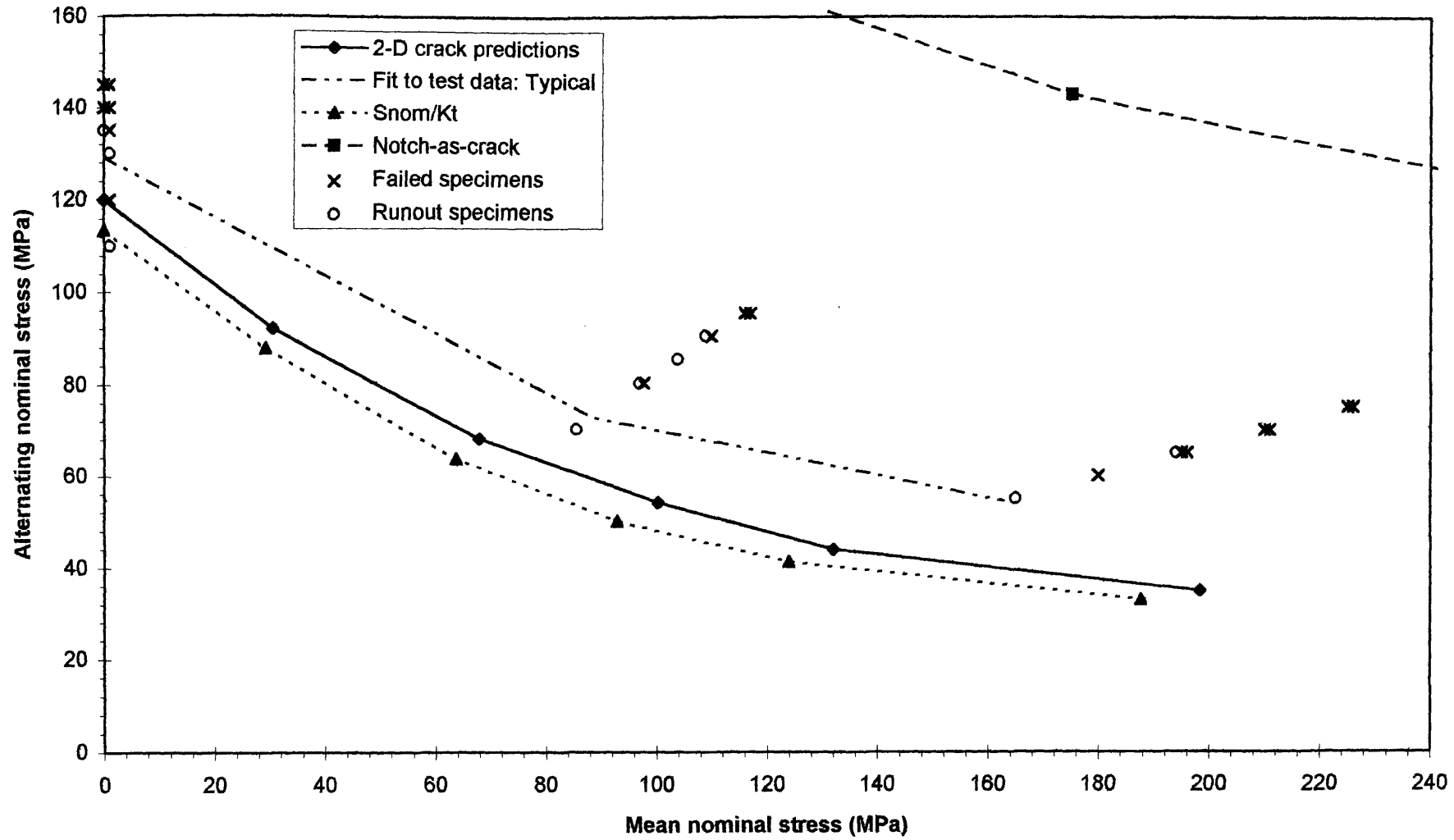


Figure 6.18 BCIRA n7a1 Applied Delta K and Threshold Delta K Versus Crack Depth (10mm Cast Section Size, $K_t = 1.526$, Grade 250 Grey Iron) Continuous Surface Cracks

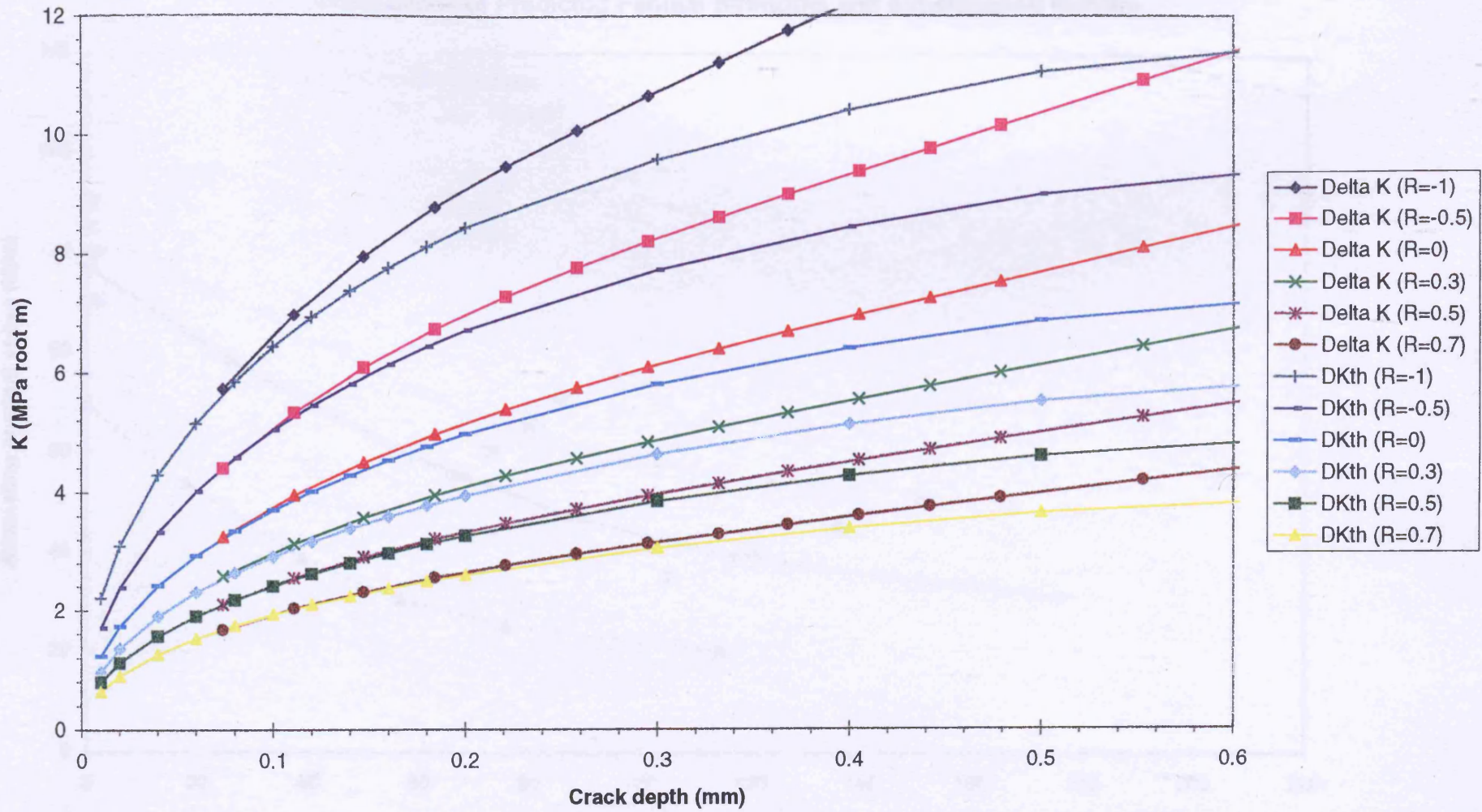


Figure 6.19 BCIRA n7a2 (10mm Cast Section Size, $K_t = 2.5$, Grade 250 Grey Iron)
 Comparison of Predicted Fatigue Strengths and Experimental Results

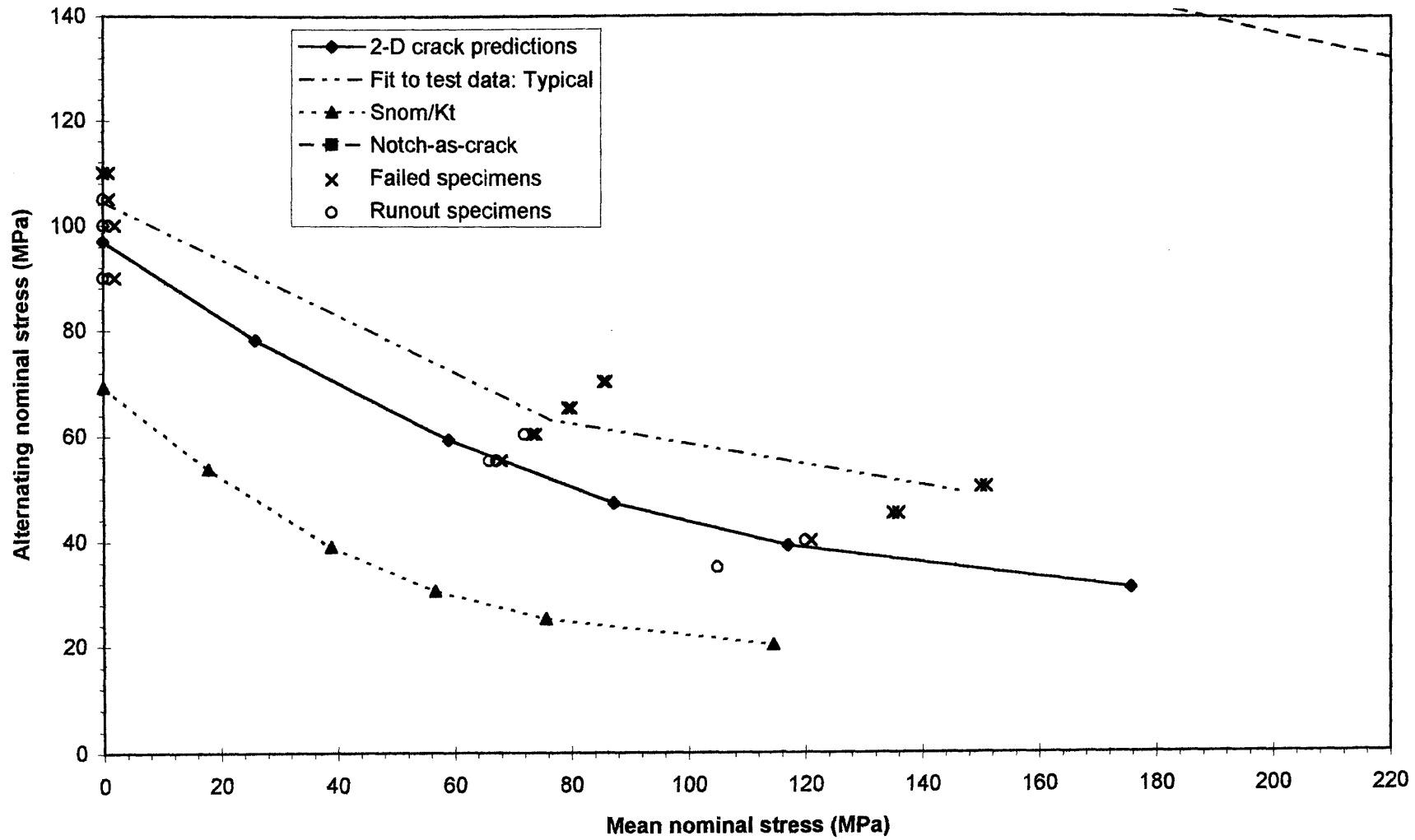
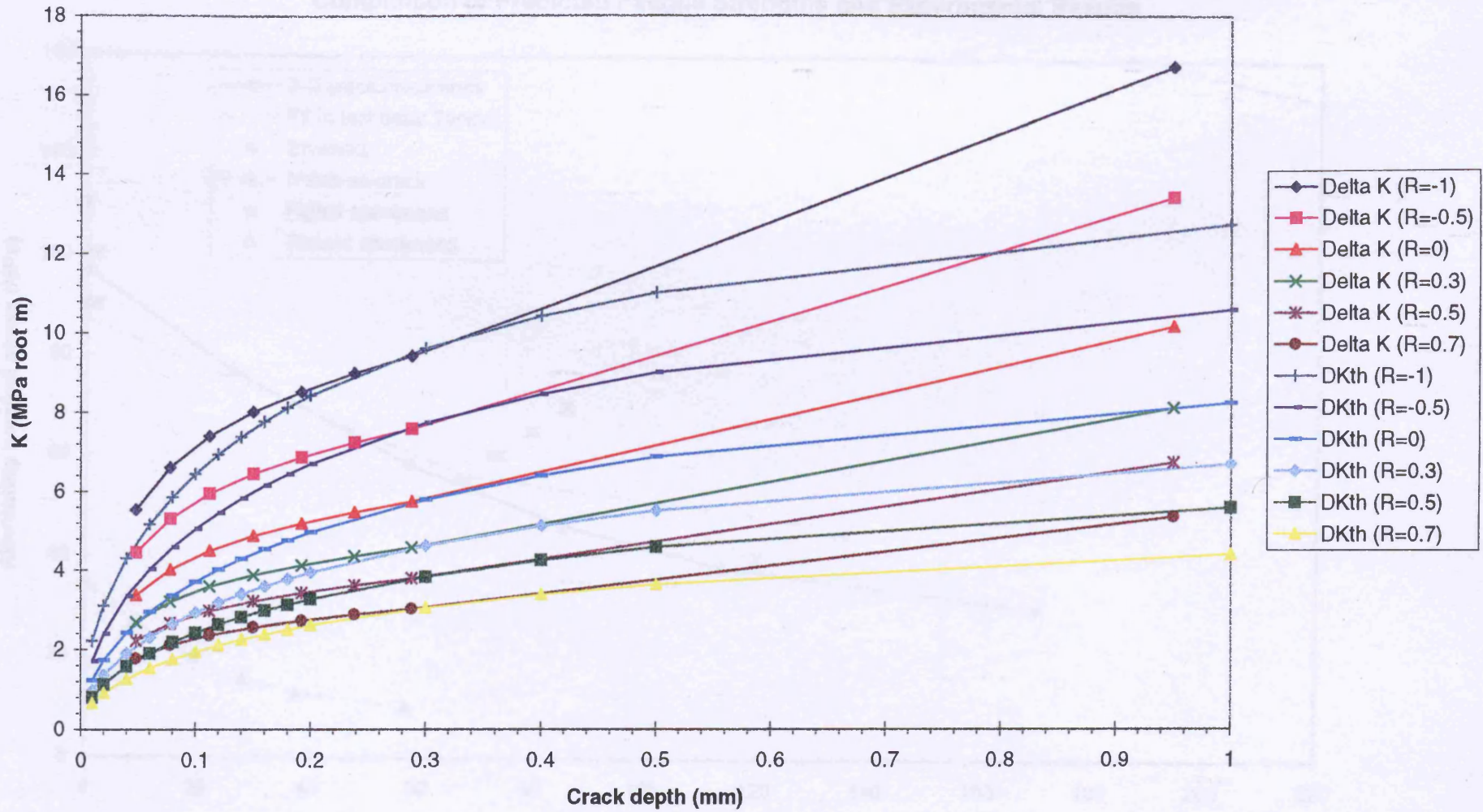


Figure 6.20 BCIRA n7a2 Applied Delta K and Threshold Delta K Versus Crack Depth (10mm Cast Section Size, $K_t = 2.2$, Grade 250 Grey Iron) Continuous Surface Cracks



**Figure 6.21 BCIRA n7a3 (10mm Cast Section Size, $K_t = 5.0$, Grade 250 Grey Iron)
Comparison of Predicted Fatigue Strengths and Experimental Results**

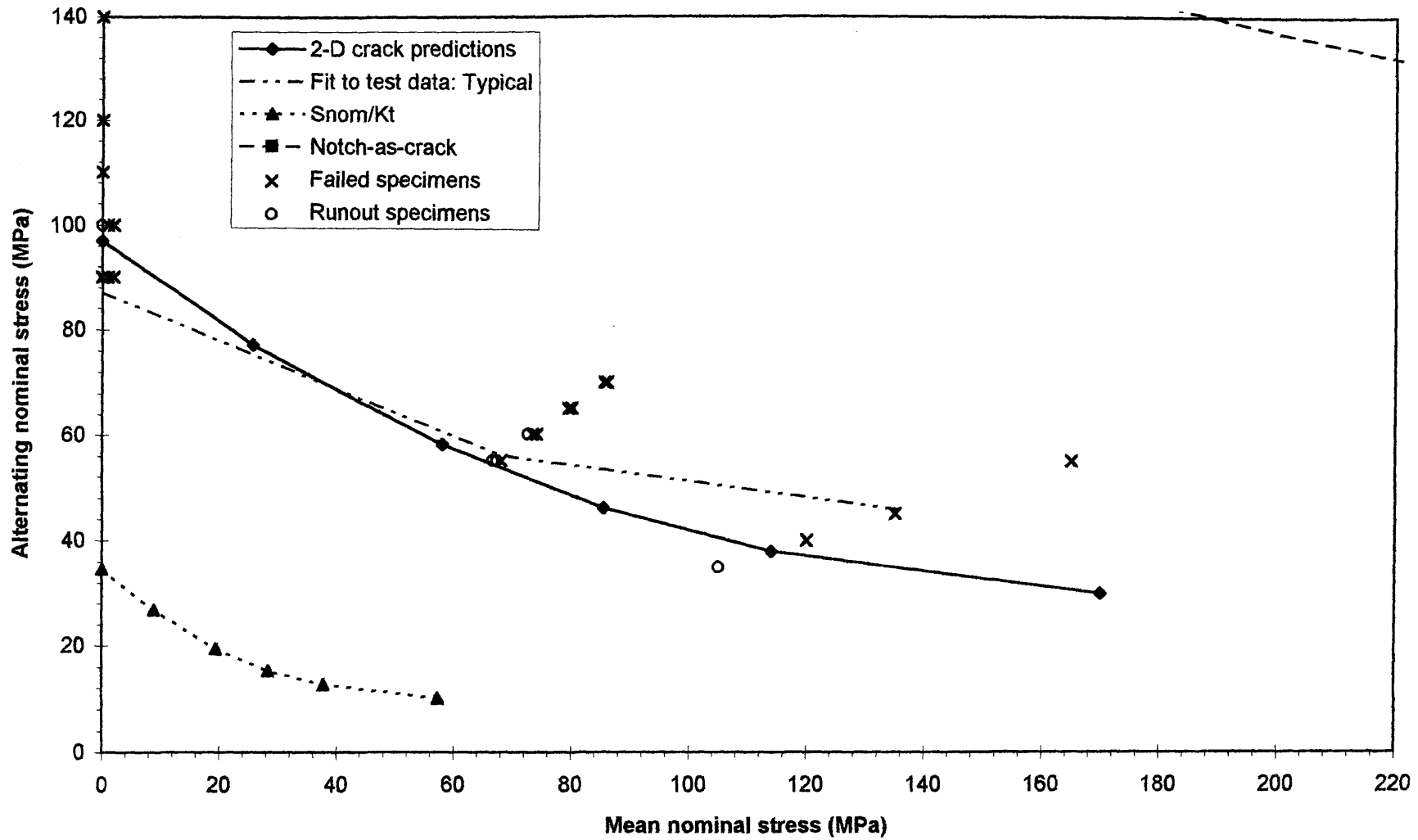


Figure 6.22 BCIRA n7a3 Applied Delta K and Threshold Delta K Versus Crack Depth (10mm Cast Section Size, $K_t = 5$, Grade 250 Grey Iron) Continuous Surface Cracks

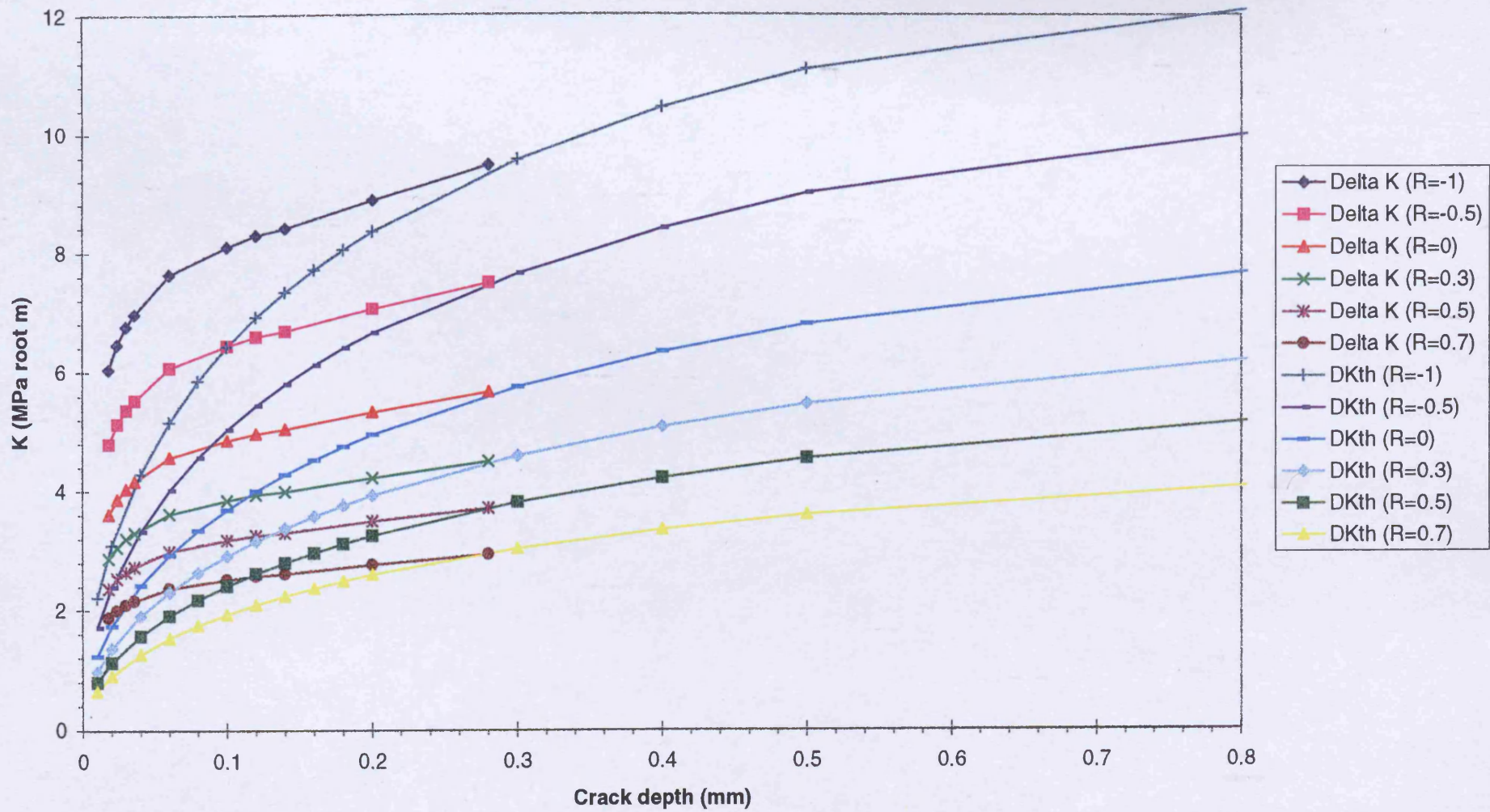


Figure 6.23 BCIRA n12a1 (30mm Cast Section Size, $K_t = 1.5$, Grade 250 Grey Iron)
Comparison of Predicted Fatigue Strengths and Experimental Results

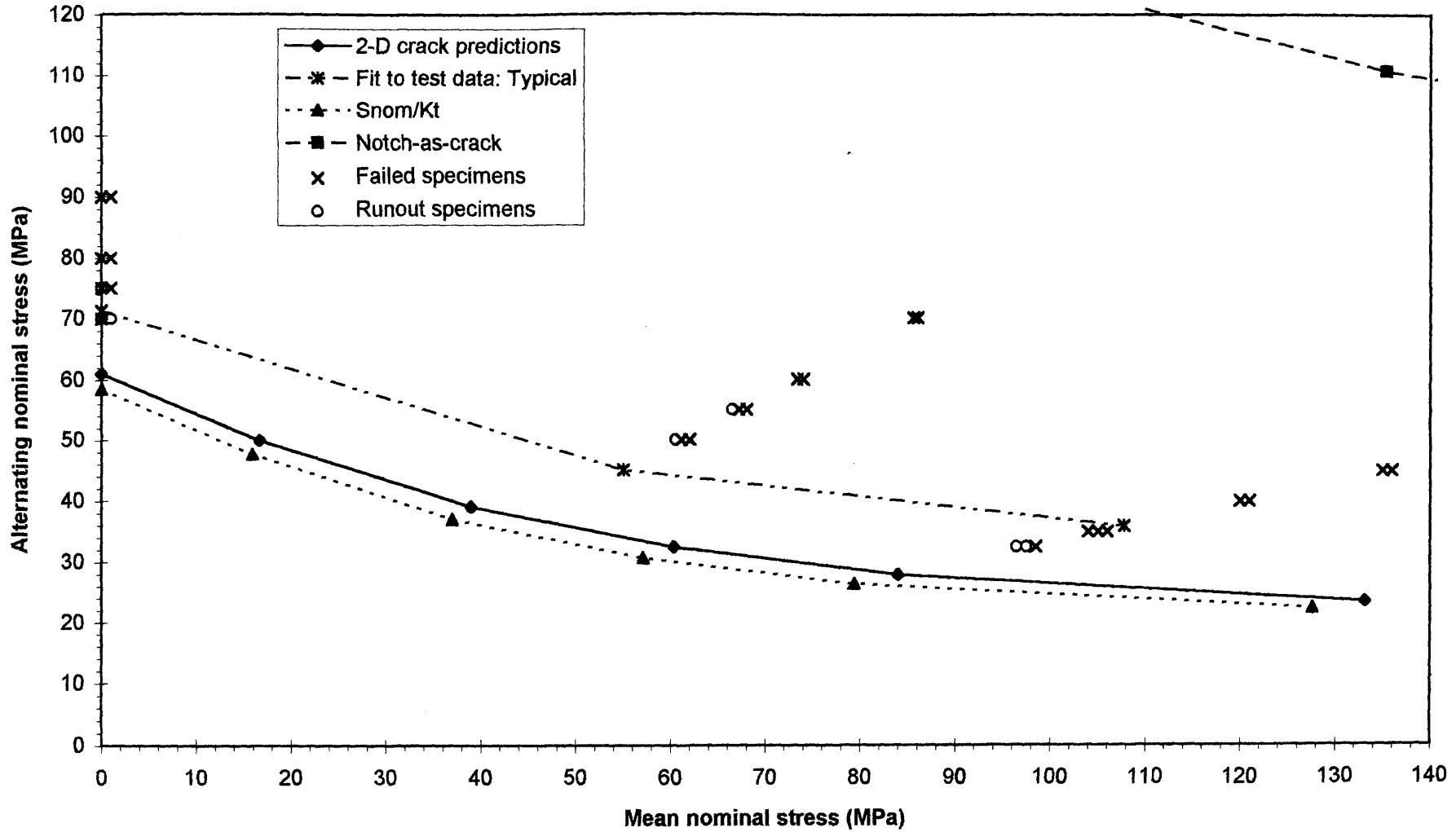


Figure 6.24 BCIRA n12a1 Applied Delta K and Threshold Delta K Versus Crack Depth (30mm Cast Section Size, $K_t = 1.5$, Grade 250 Grey Iron) Continuous Surface Cracks

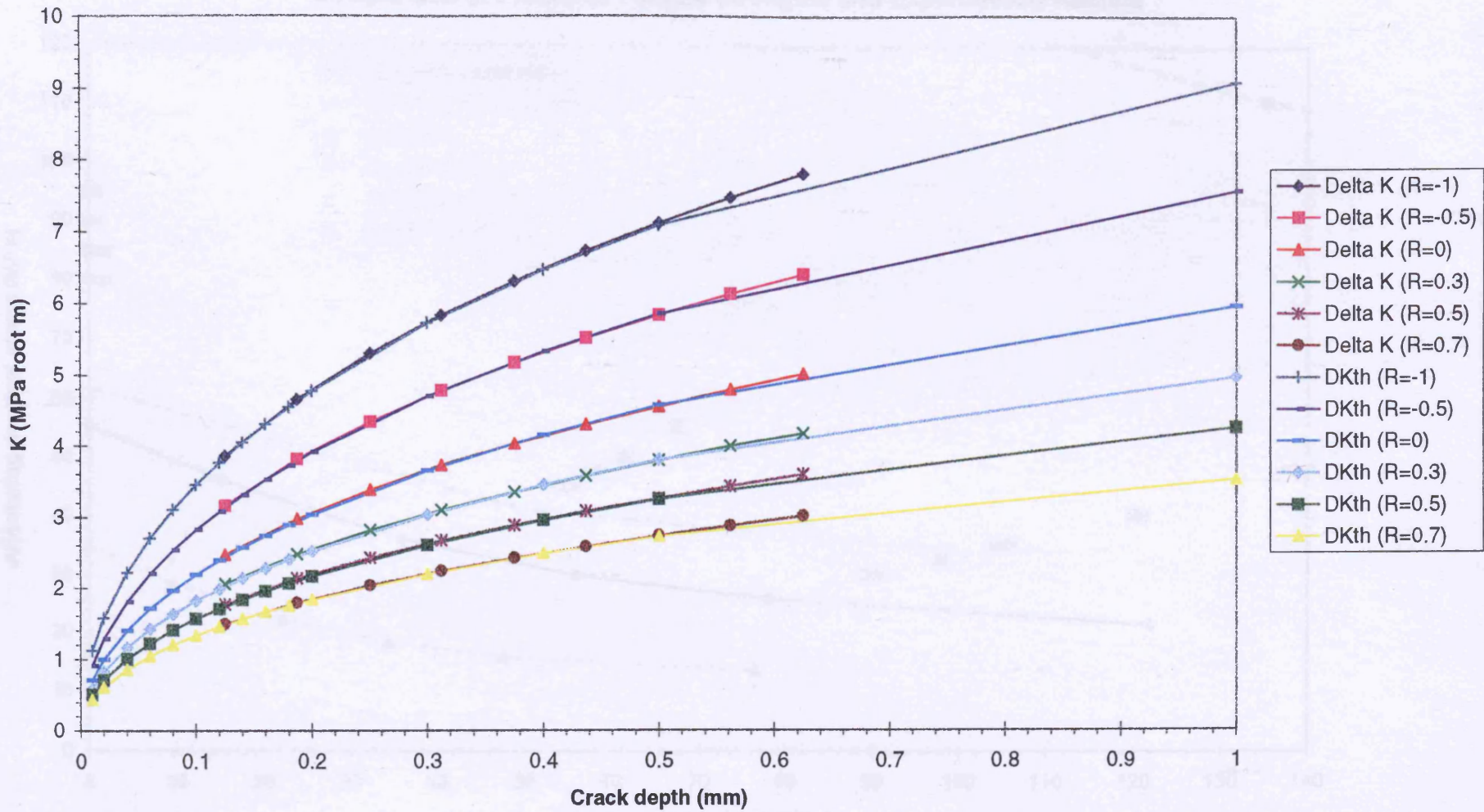


Figure 6.25 BCIRA n12a2 (30mm Cast Section Size, $K_t = 2.5$, Grade 250 Grey Iron)
 Comparison of Predicted Fatigue Strengths and Experimental Results

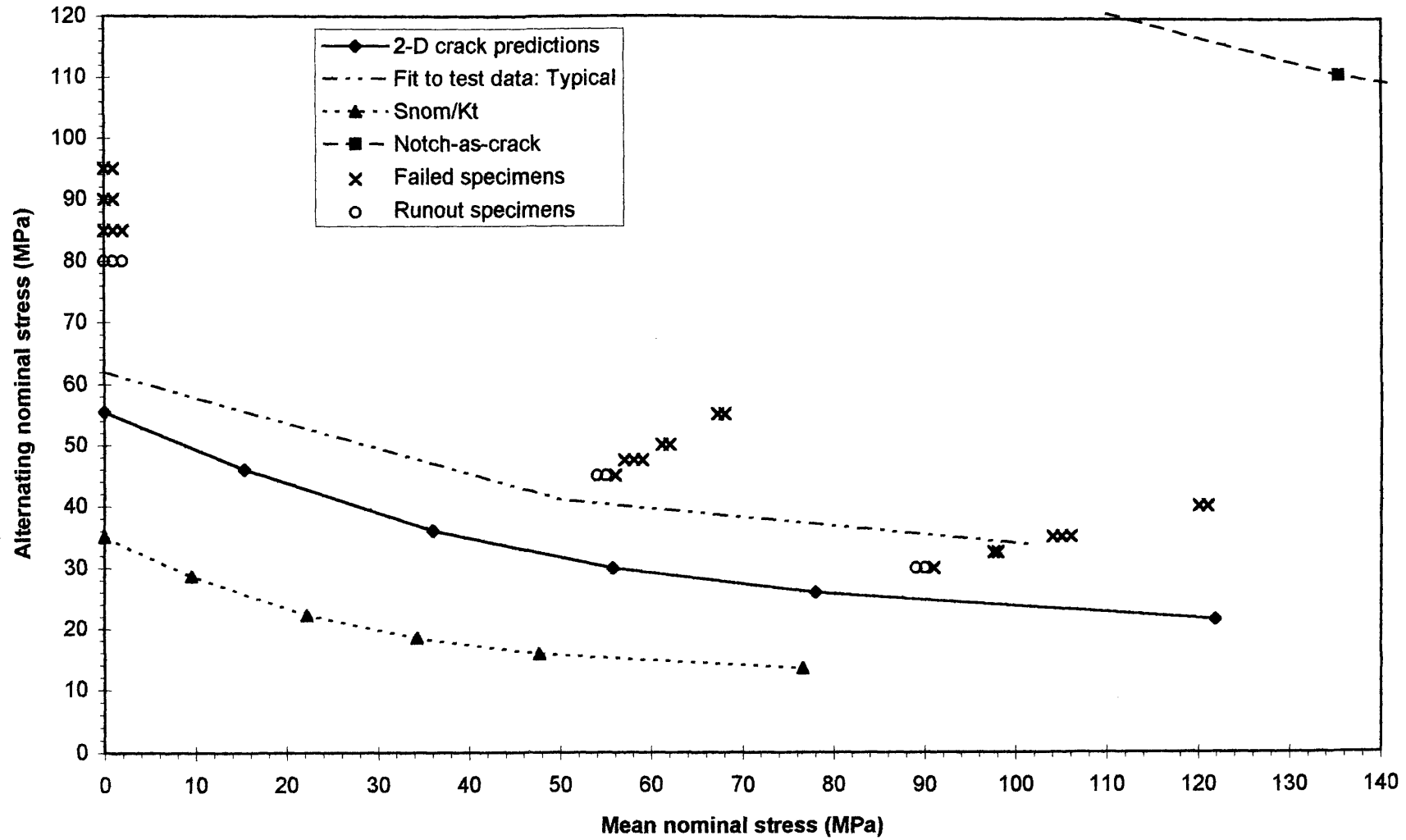


Figure 6.26 BCIRA n12a2 Applied Delta K and Threshold Delta K Versus Crack Depth (30mm Cast Section Size, $K_t = 2.5$, Grade 250 Grey Iron) Continuous Surface Cracks

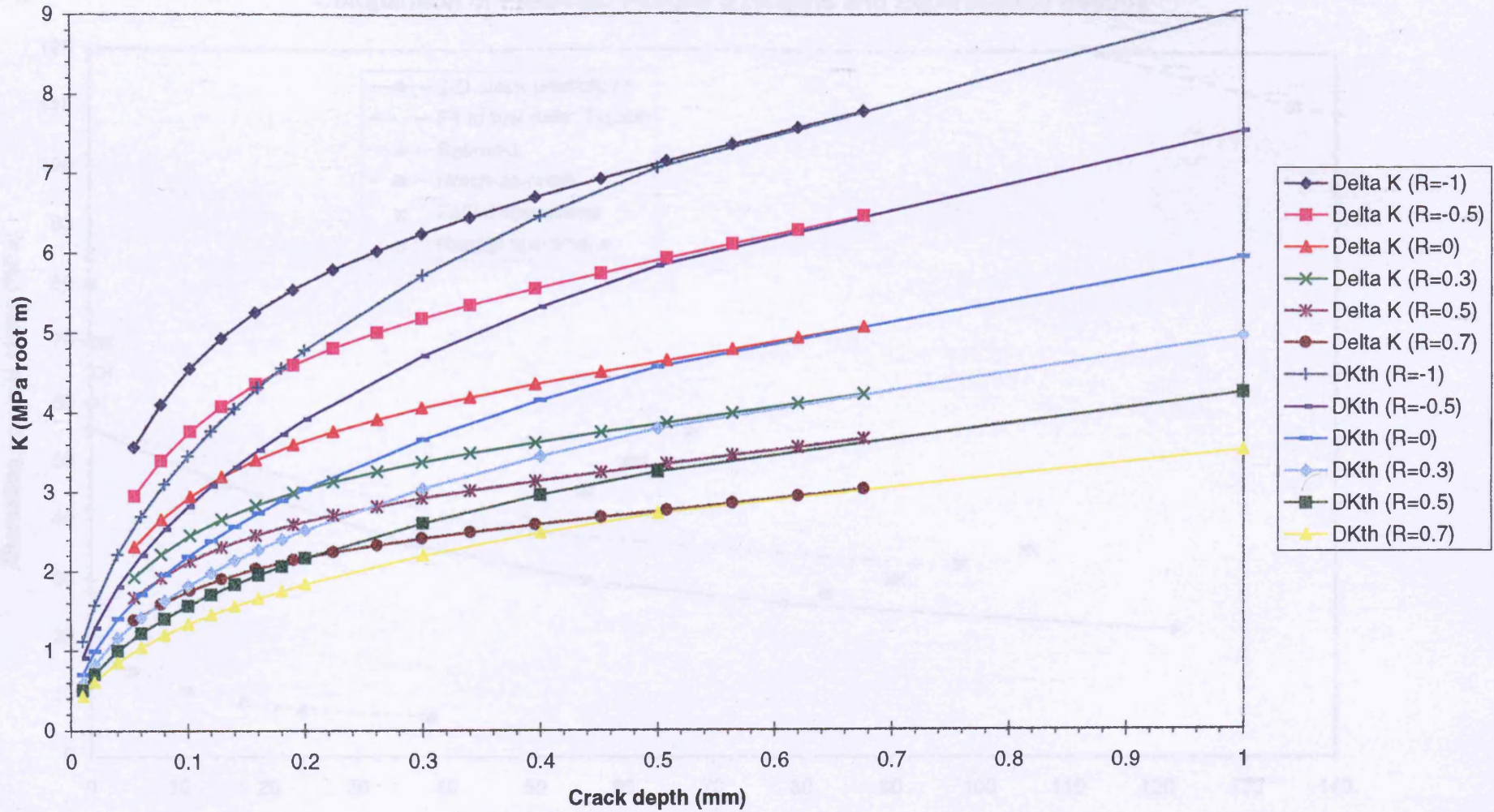


Figure 6.27 BCIRA n12a3 (30mm Cast Section Size, $K_t = 5.0$, Grade 250 Grey Iron)
 Comparison of Predicted Fatigue Strengths and Experimental Results

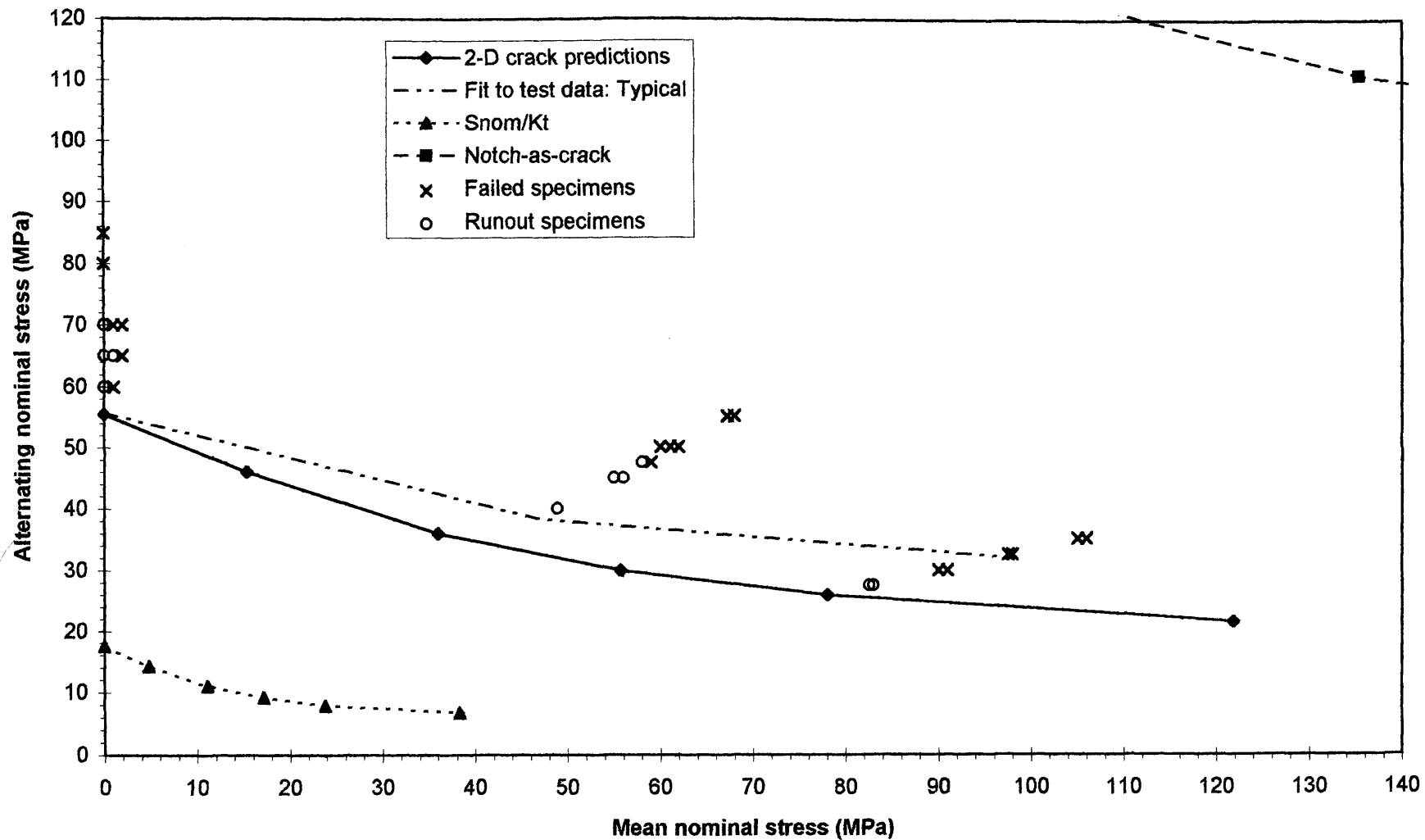
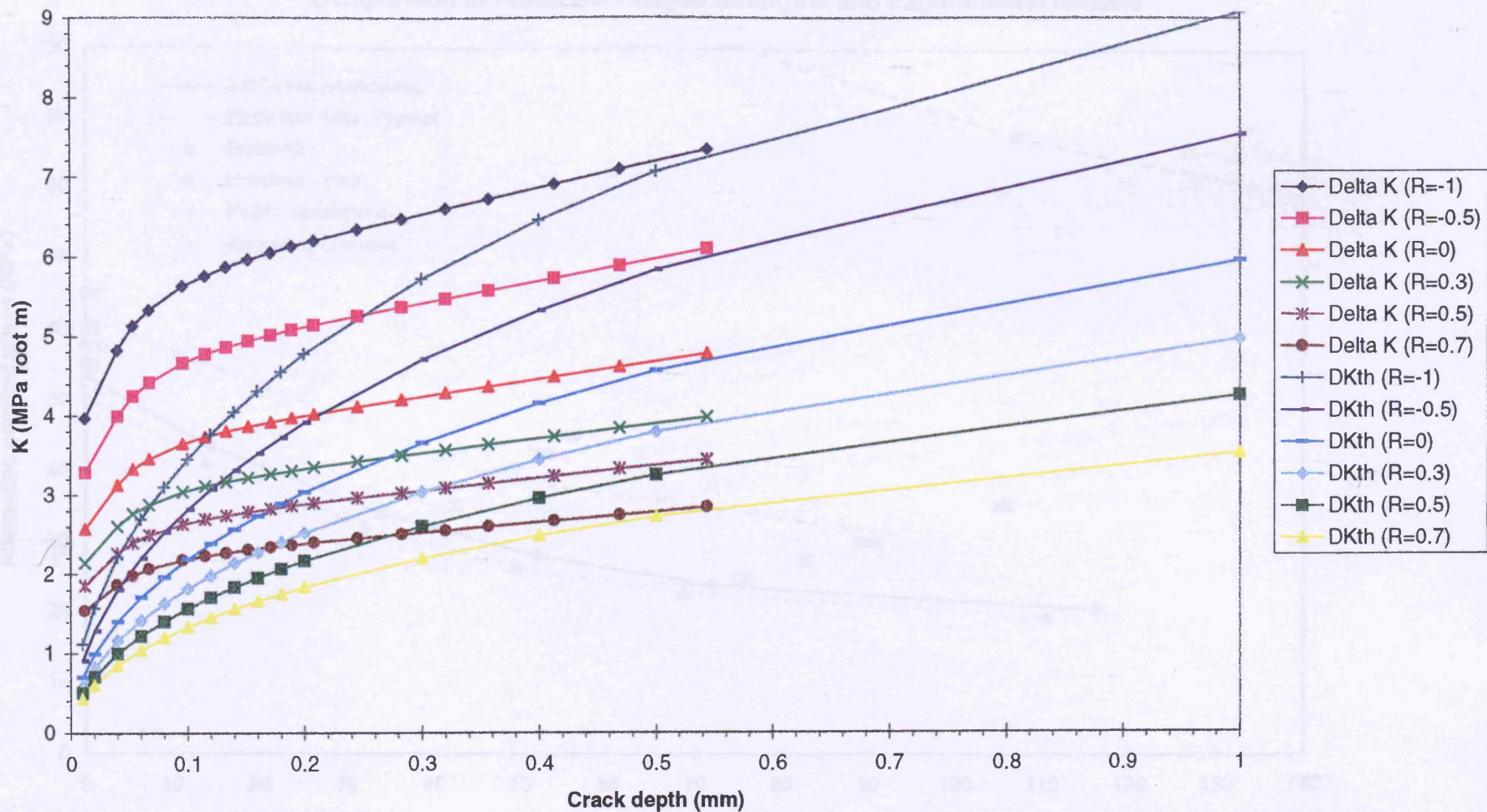


Figure 6.28 BCIRA n12a3 Applied Delta K and Threshold Delta K Versus Crack Depth (30mm Cast Section Size, $K_t = 5$, Grade 250 Grey Iron) Continuous Surface Cracks



**Figure 6.29 BCIRA n20a1 (50mm Cast Section Size, $K_t = 1.5$, Grade 250 Grey Iron)
Comparison of Predicted Fatigue Strengths and Experimental Results**

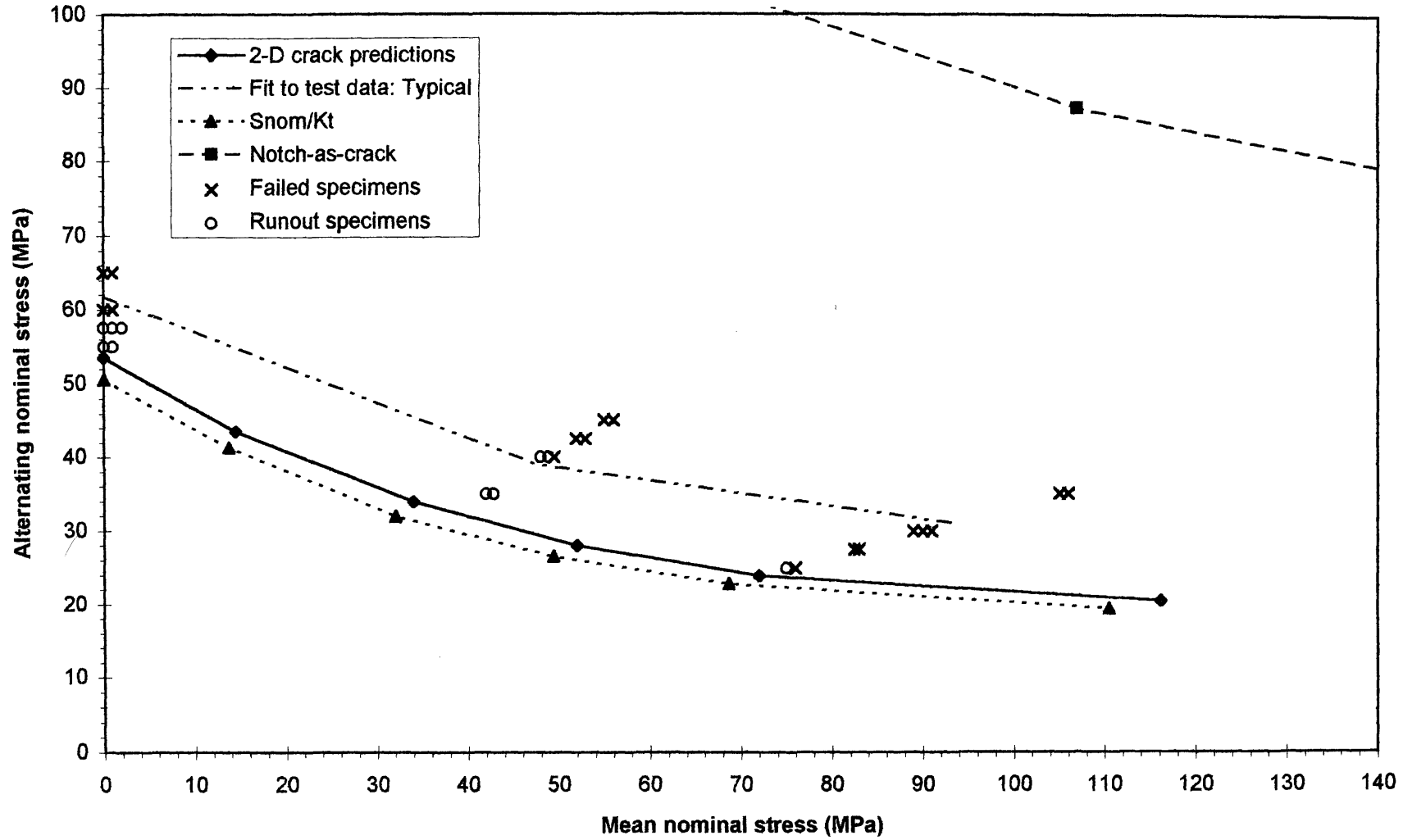


Figure 6.30 BCIRA n20a1 Applied Delta K and Threshold Delta K Versus Crack Depth (50mm Cast Section Size, $K_t = 1.5$, Grade 250 Grey Iron) Continuous Surface Cracks

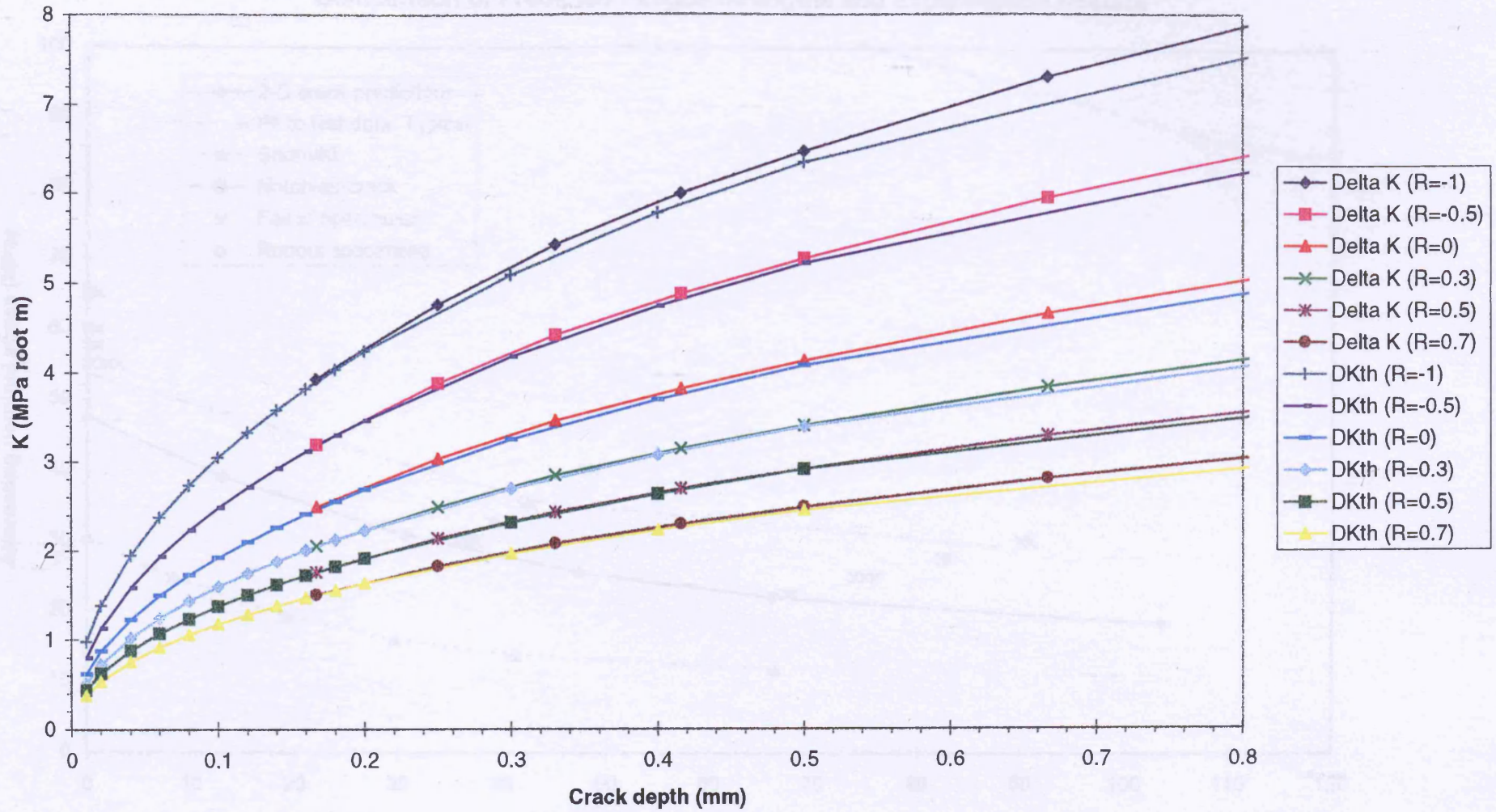


Figure 6.31 BCIRA n20a2 (50mm Cast Section Size, $K_t = 2.5$, Grade 250 Grey Iron)
Comparison of Predicted Fatigue Strengths and Experimental Results

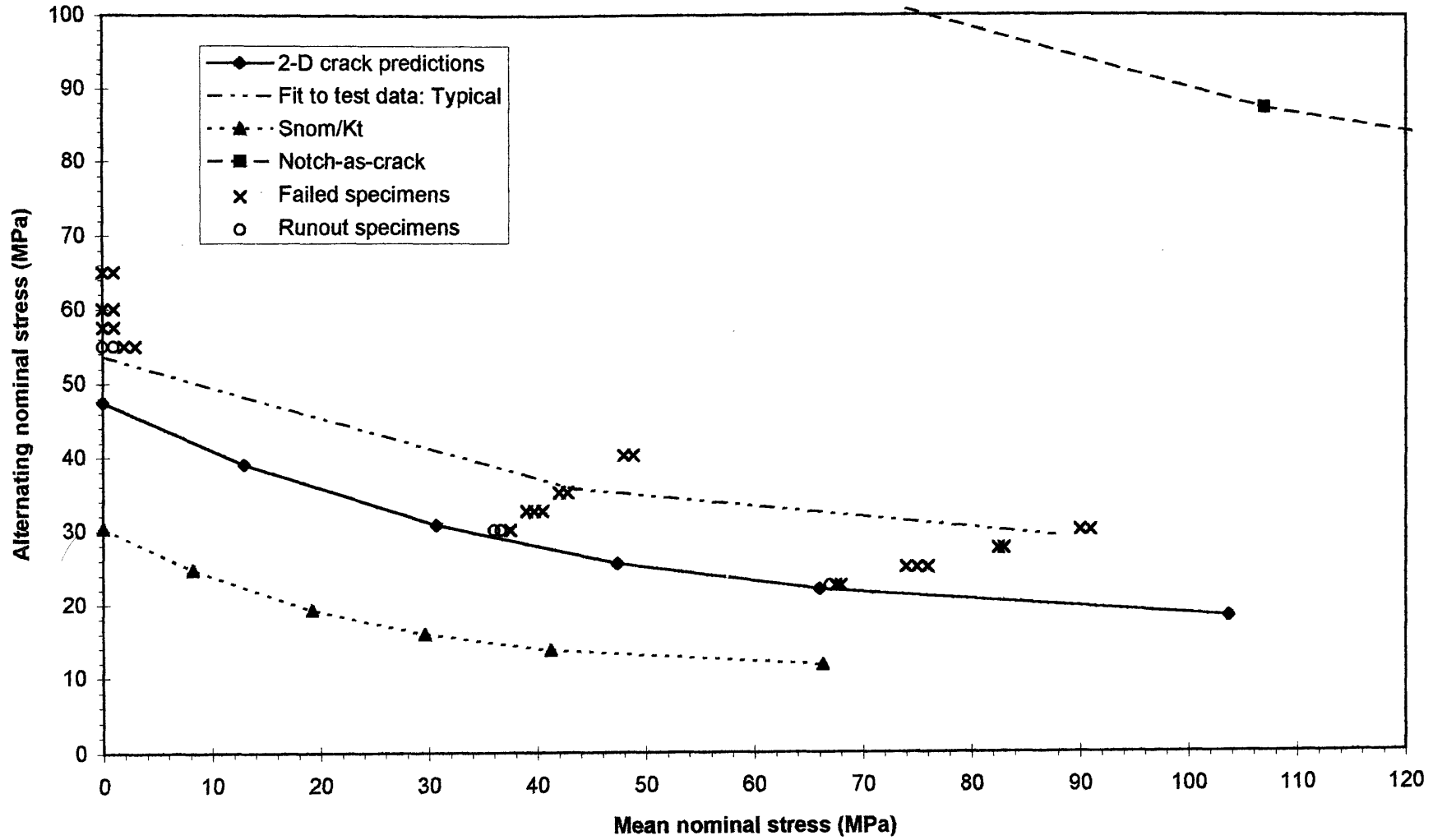


Figure 6.32 BCIRA n20a2 Applied Delta K and Threshold Delta K Versus Crack Depth (50mm Cast Section Size, $K_t = 2.5$, Grade 250 Grey Iron) Continuous Surface Cracks

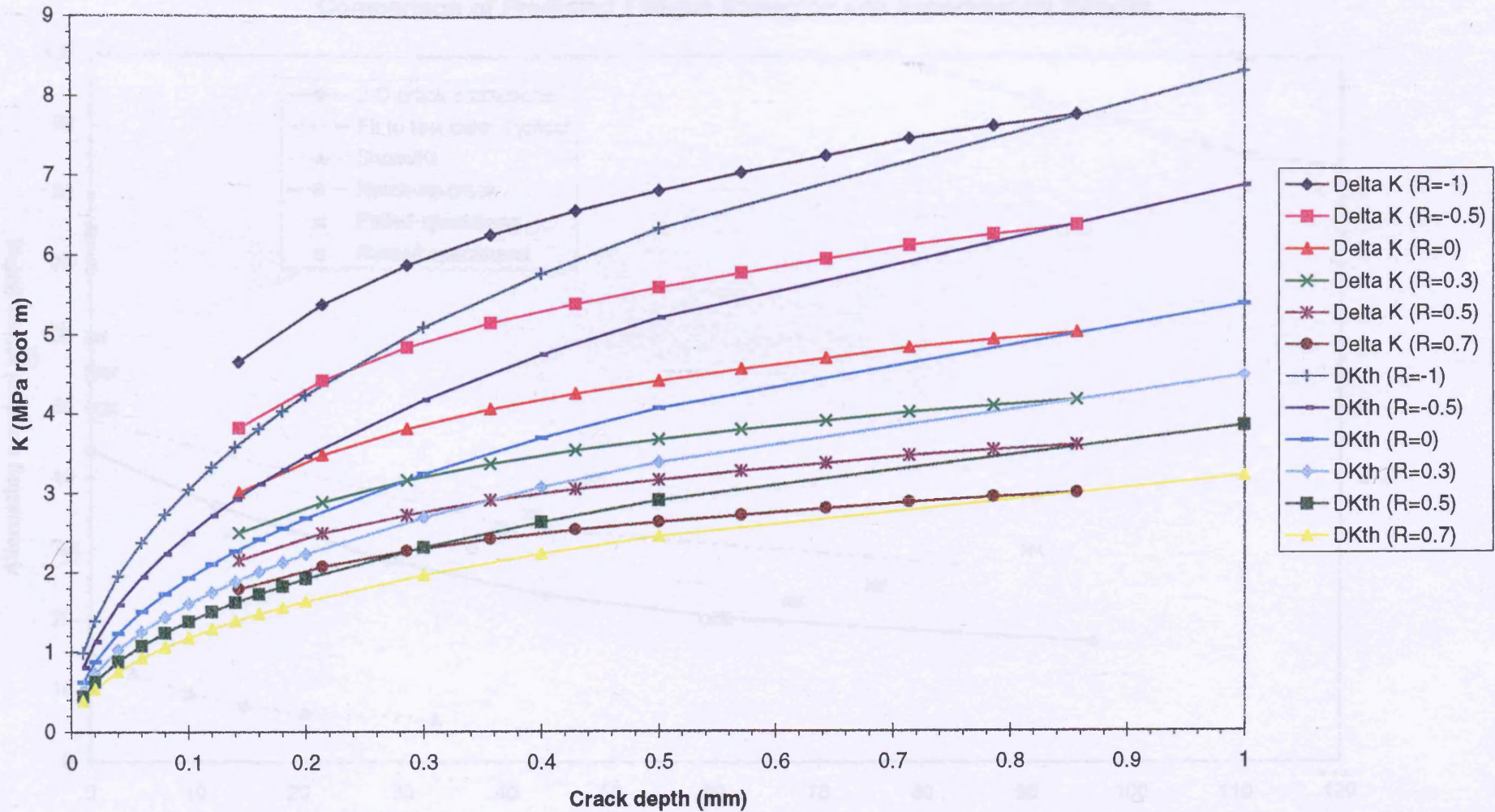


Figure 6.33 BCIRA n20a3 (50mm Cast Section Size, $K_t = 5.0$, Grade 250 Grey Iron)
 Comparison of Predicted Fatigue Strengths and Experimental Results

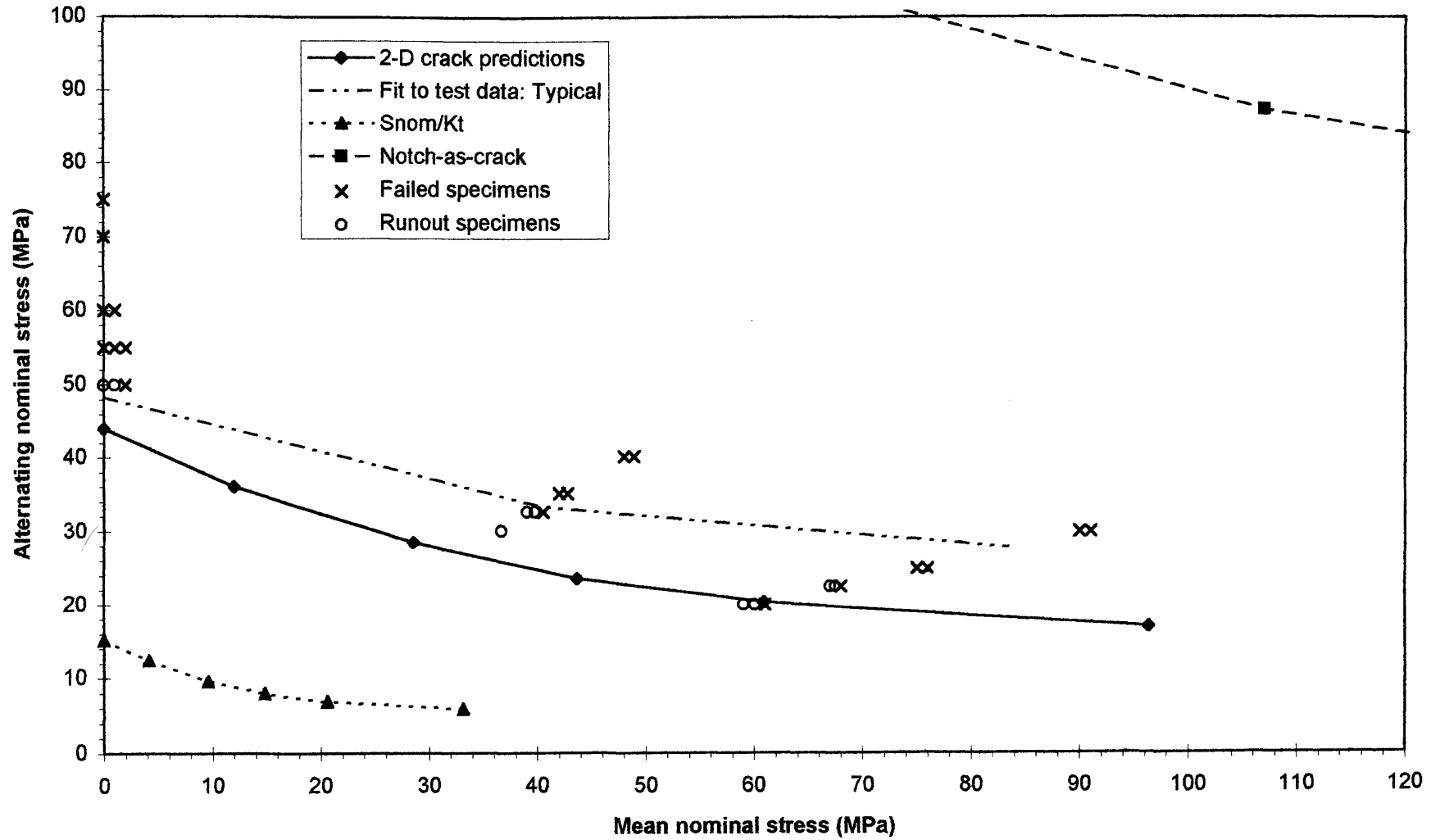


Figure 6.34 BCIRA n20a3 Applied Delta K and Threshold Delta K Versus Crack Depth (50mm Cast Section Size, $K_t = 5$, Grade 250 Grey Iron) Continuous Surface Cracks

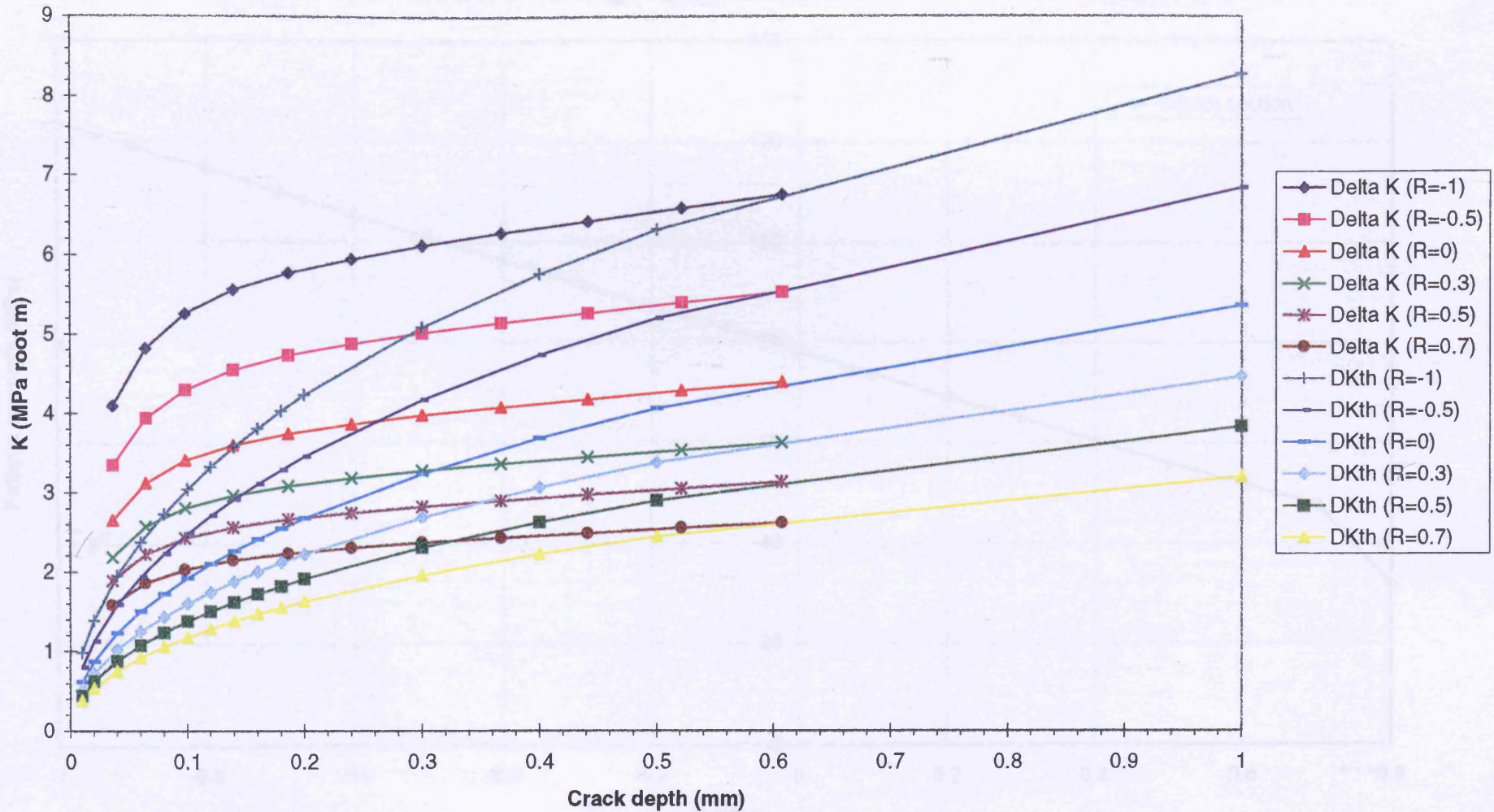


Figure 6.35 BCIRA Grade 350 Grey Cast Iron
Fatigue Limit Versus R-ratio

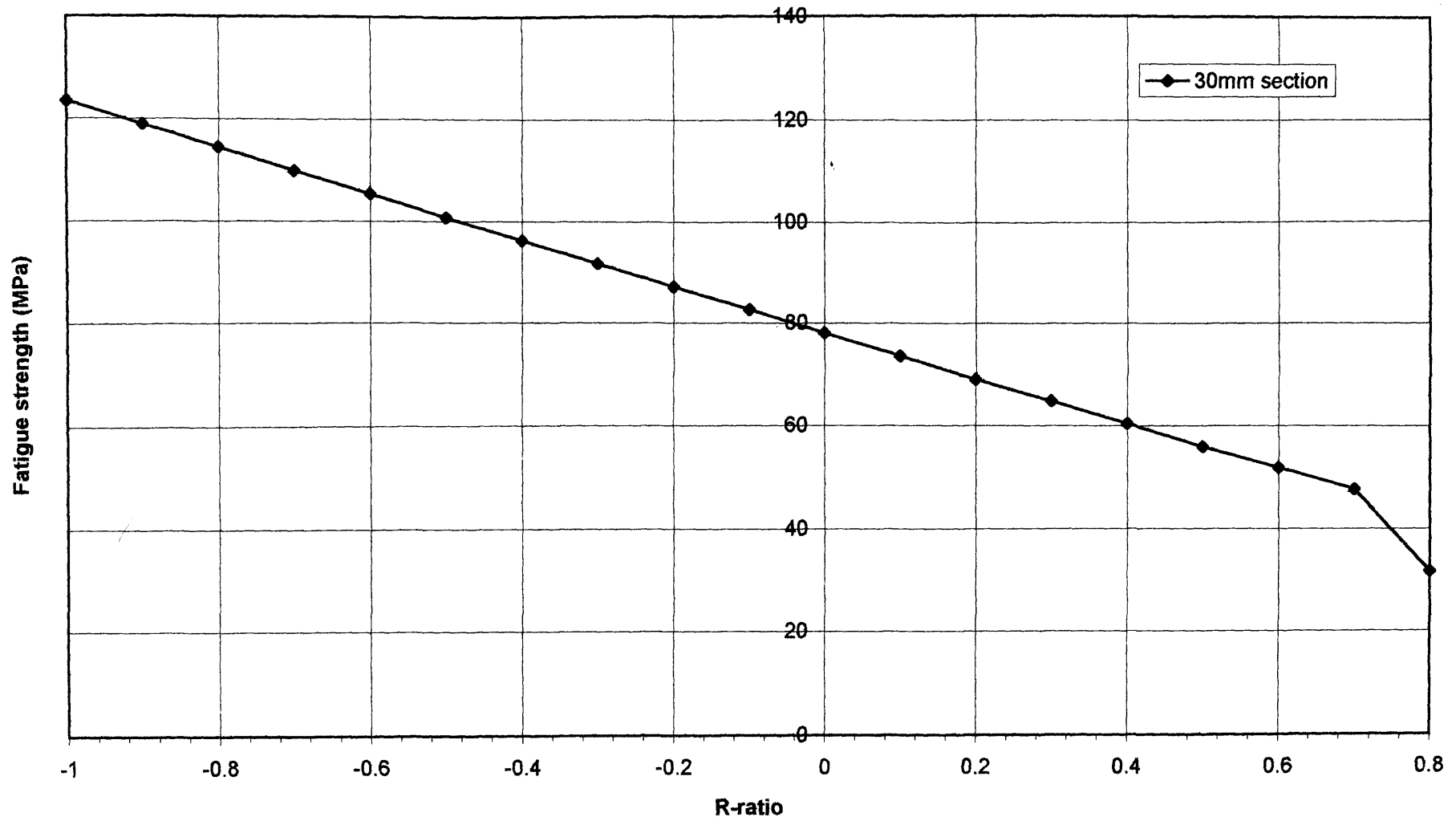


Figure 6.36 BCIRA Grade 350 Grey Cast Iron
Predicted Apparent Short Crack Threshold - Continuous Surface crack - R = 0.05 & 0.5

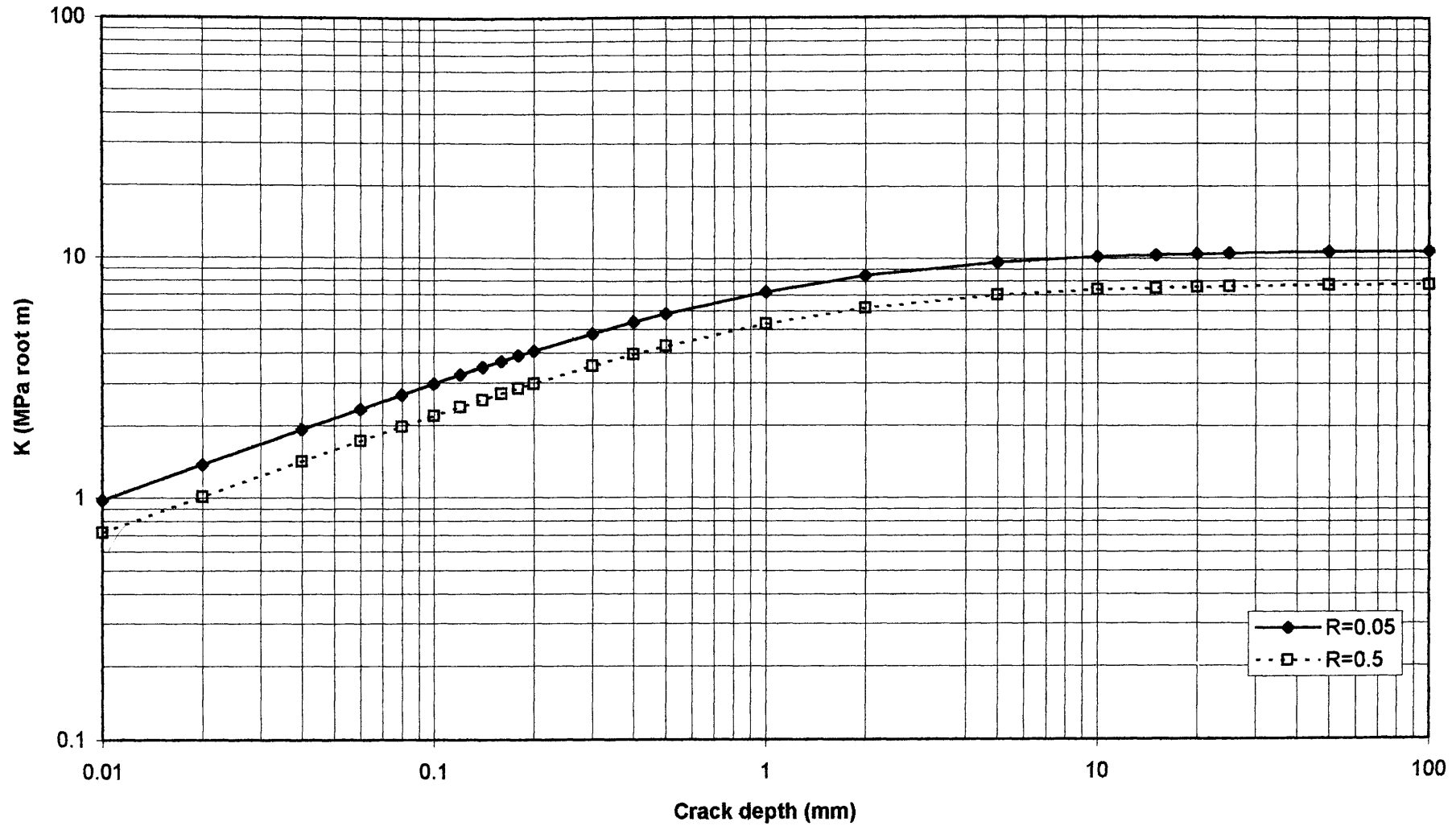


Figure 6.37 BCIRA n12b1 (30mm Cast Section Size, $K_t = 1.5$, Grade 350 Grey Iron)
 Comparison of Predicted Fatigue Strengths and Experimental Results

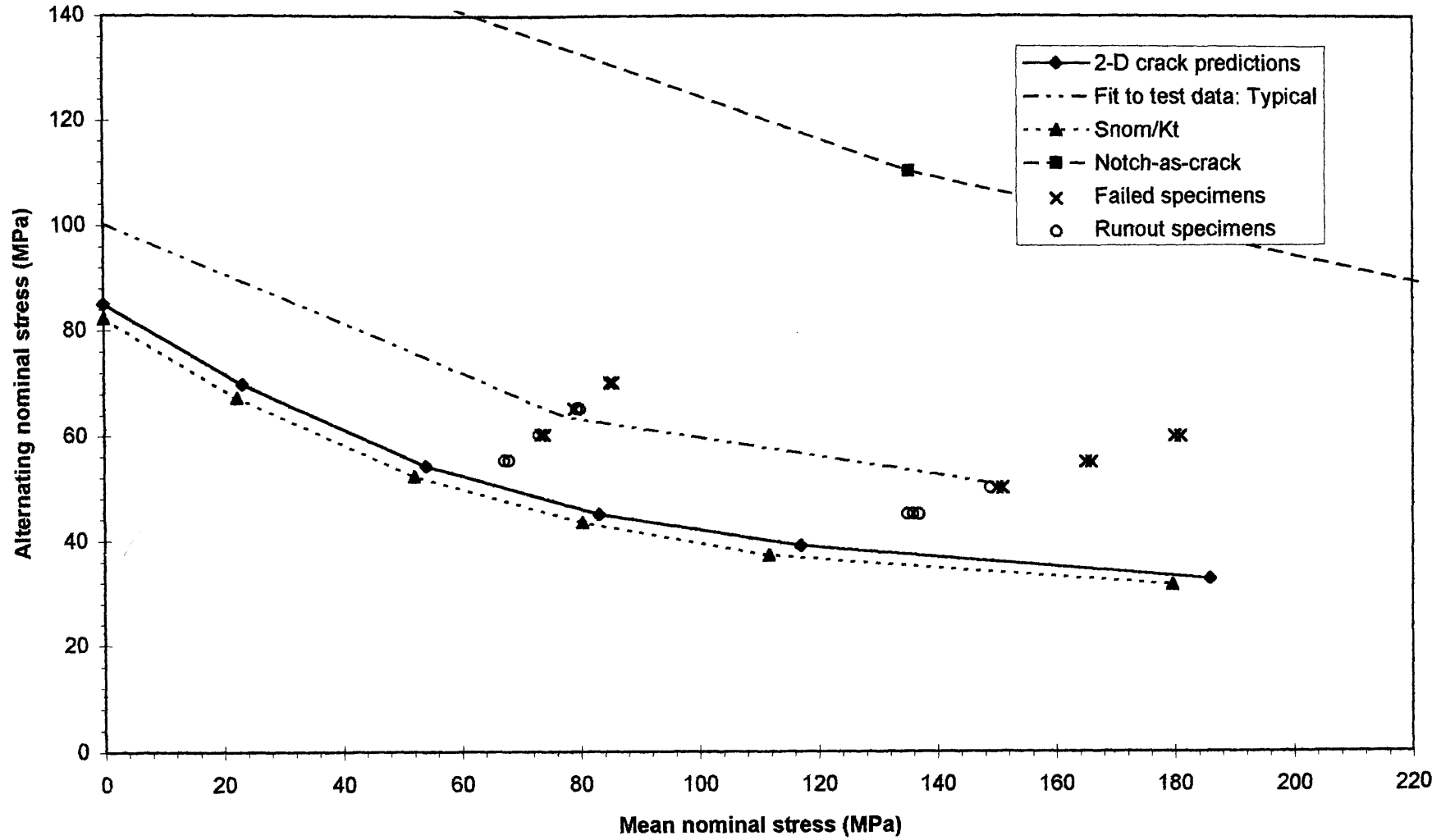


Figure 6.38 BCIRA n12b1 Applied Delta K and Threshold Delta K Versus Crack Depth (30mm Cast Section Size, $K_t = 1.5$, Grade 350 Grey Iron) Continuous Surface Cracks

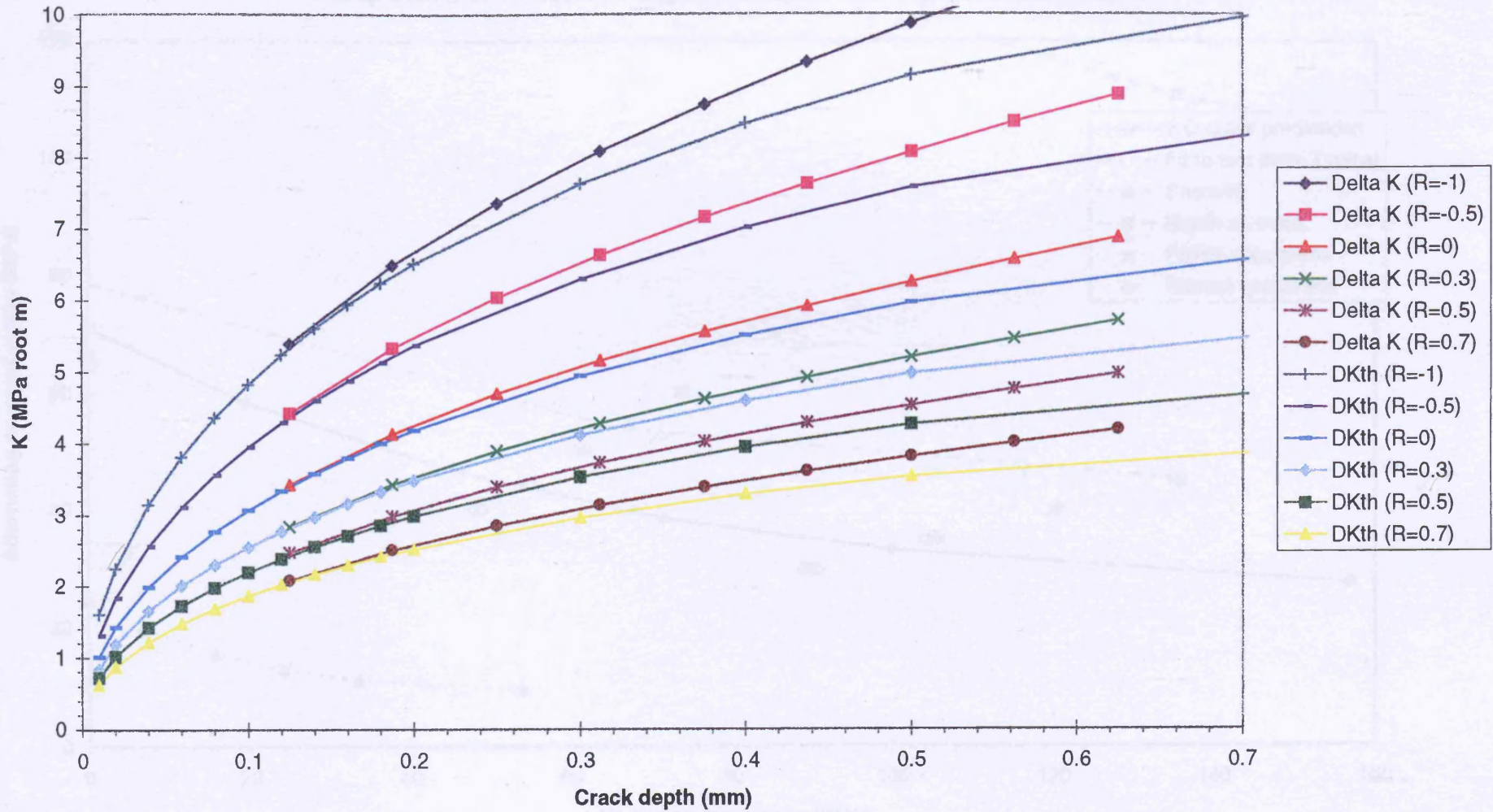


Figure 6.39 BCIRA n12b3 (30mm Cast Section Size, $K_t = 5$, Grade 350 Grey Iron)
 Comparison of Predicted Fatigue Strengths and Experimental Results

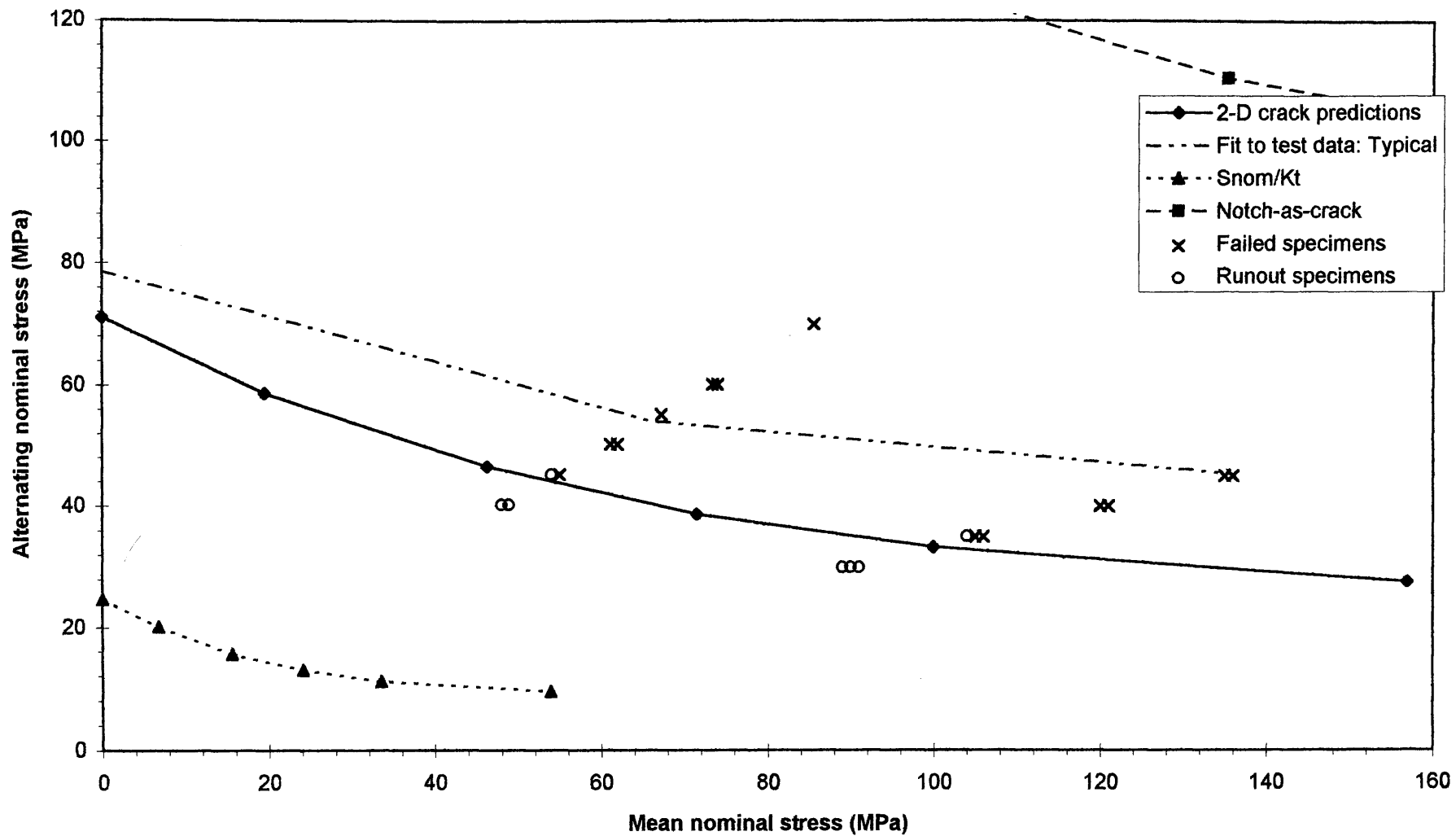


Figure 6.40 BCIRA n12b3 Applied Delta K and Threshold Delta K Versus Crack Depth (30mm Cast Section Size, $K_t = 5$, Grade 350 Grey Iron) Continuous Surface Cracks

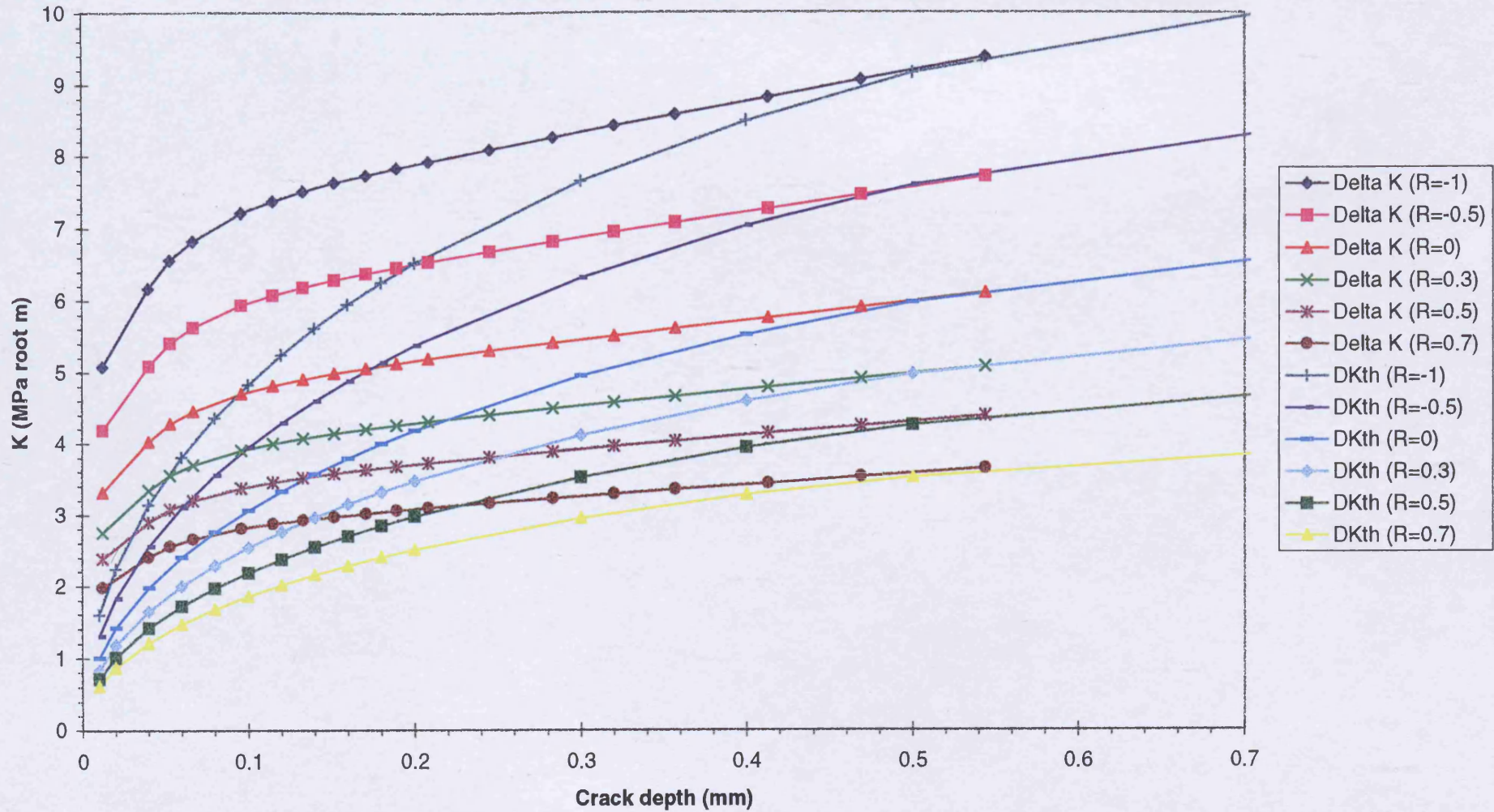


Figure 6.41 BCIRA Grade 400/18 SG Iron
Fatigue Limit Versus R-ratio for Three Cast Section Sizes

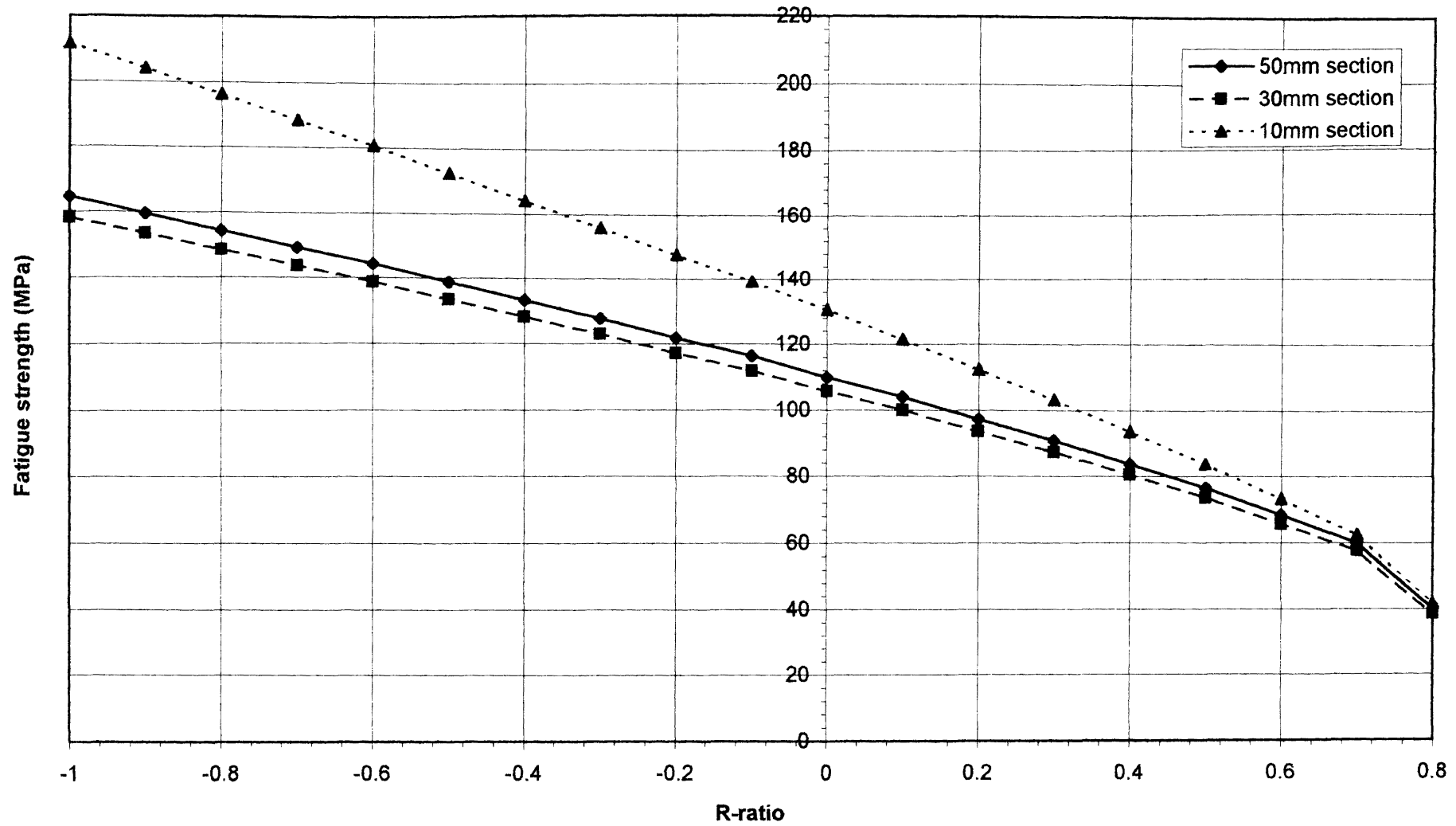
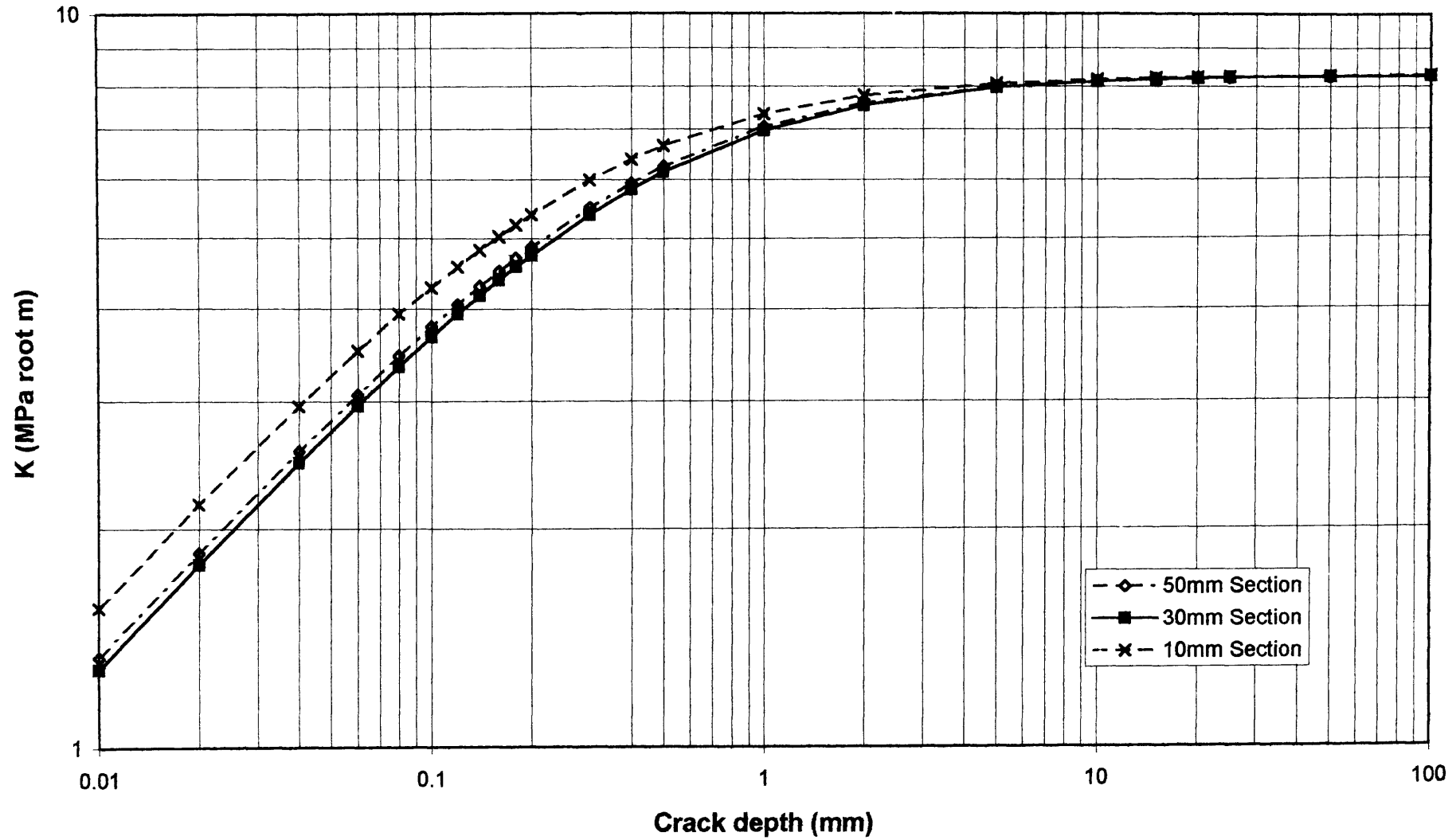


Figure 6.42 BCIRA Grade 400/18 SG Cast Iron
Predicted Apparent Short Crack Growth Threshold - Continuous Surface Crack (R = 0.05)



**Figure 6.43 BCIRA sg7a1 (10mm Cast Section Size, $K_t = 1.526$, Grade 400/18 SG Iron)
Comparison of Predicted Fatigue Strengths and Experimental Results**

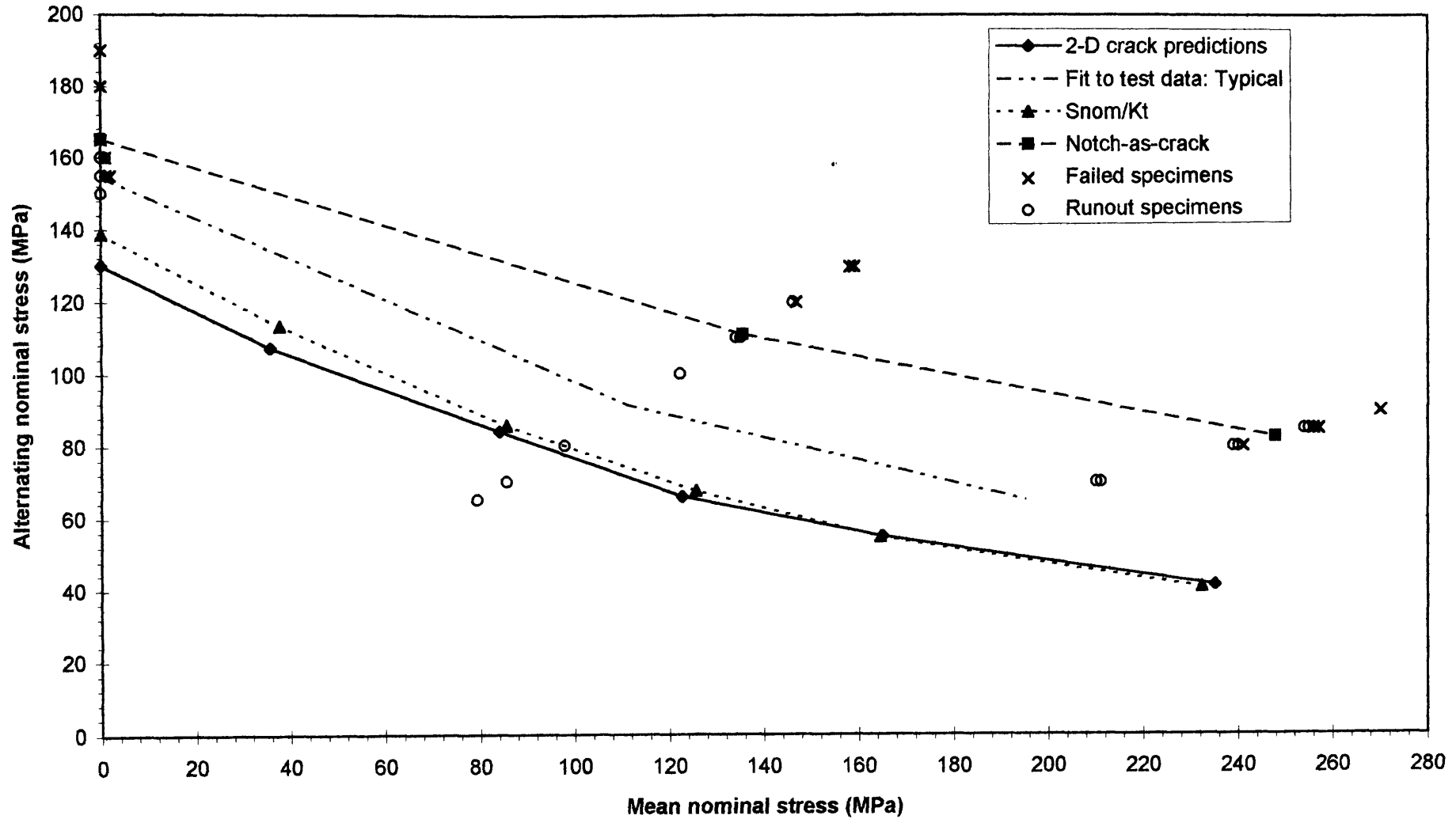
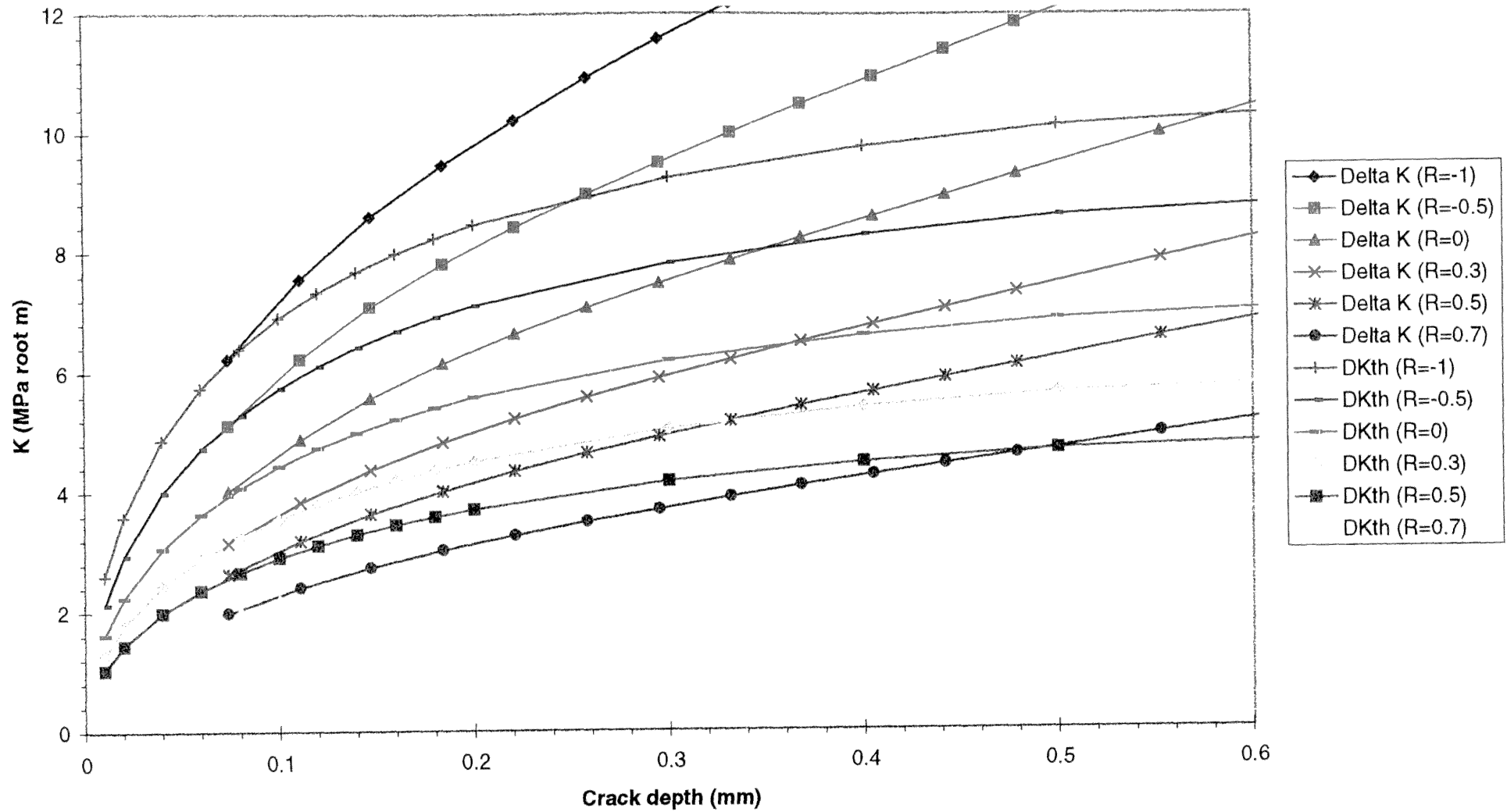


Figure 6.44 BCIRA sg7a1 Applied Delta K and Threshold Delta K Versus Crack Depth (10mm Cast Section Size, $K_t = 1.5$, Grade 400/18 SG Iron) Continuous Surface Cracks



**Figure 6.45 BCIRA sg7a2 (10mm Cast Section Size, $K_t = 2.5$, Grade 400/18 SG Iron)
Comparison of Predicted Fatigue Strengths and Experimental Results**

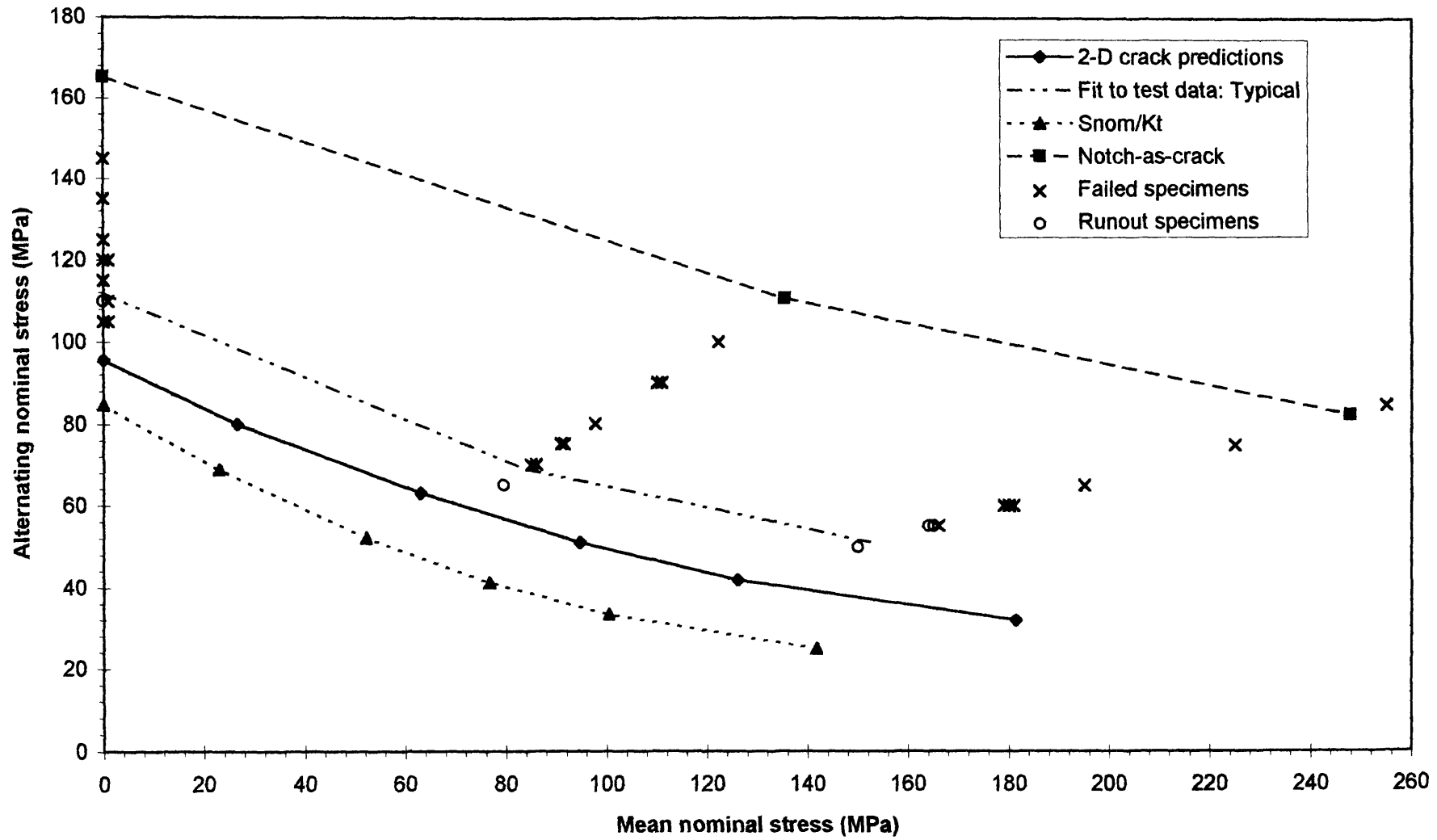


Figure 6.46 BCIRA sg7a2 Applied Delta K and Threshold Delta K Versus Crack Depth (10mm Cast Section Size, $K_t = 2.5$, Grade 400/18 SG Iron) Continuous Surface Cracks

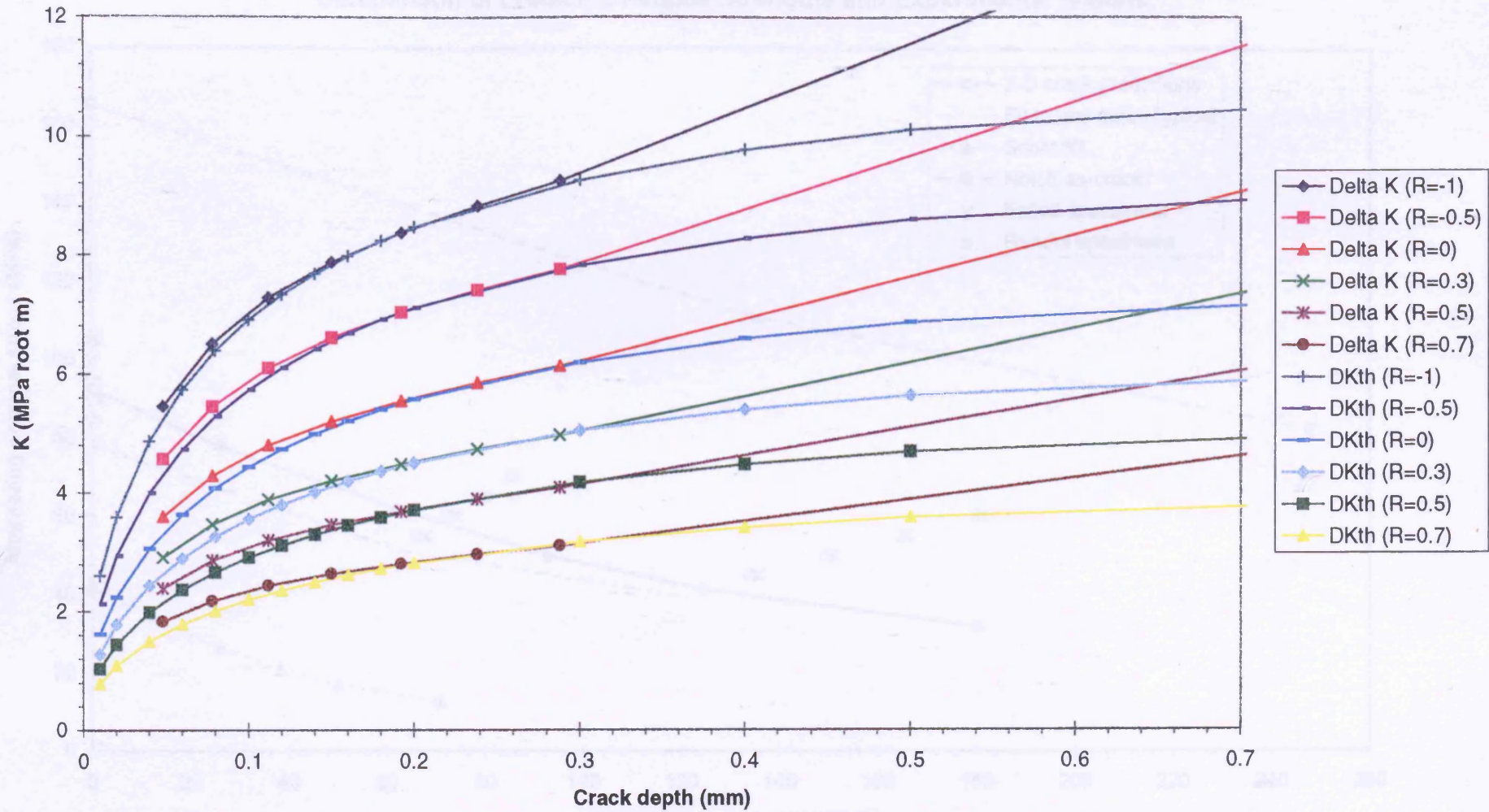


Figure 6.47 BCIRA sg7a3 (10mm Cast Section Size, $K_t = 5$, Grade 400/18 SG Iron)
Comparison of Predicted Fatigue Strengths and Experimental Results

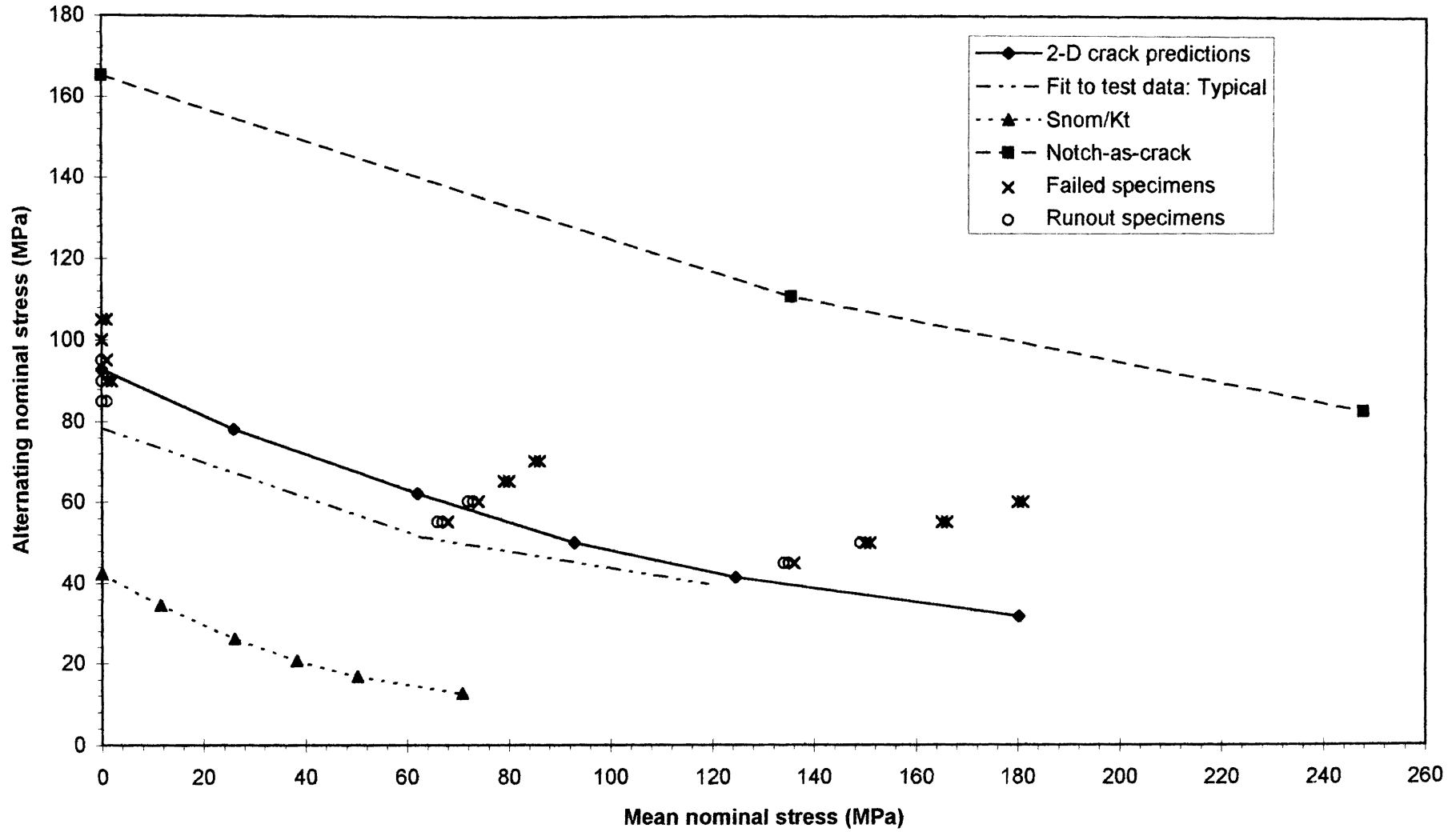


Figure 6.48 BCIRA sg7a3 Applied Delta K and Threshold Delta K Versus Crack Depth (10mm Cast Section Size, $K_t = 5$, Grade 400/18 SG Iron) Continuous Surface Cracks

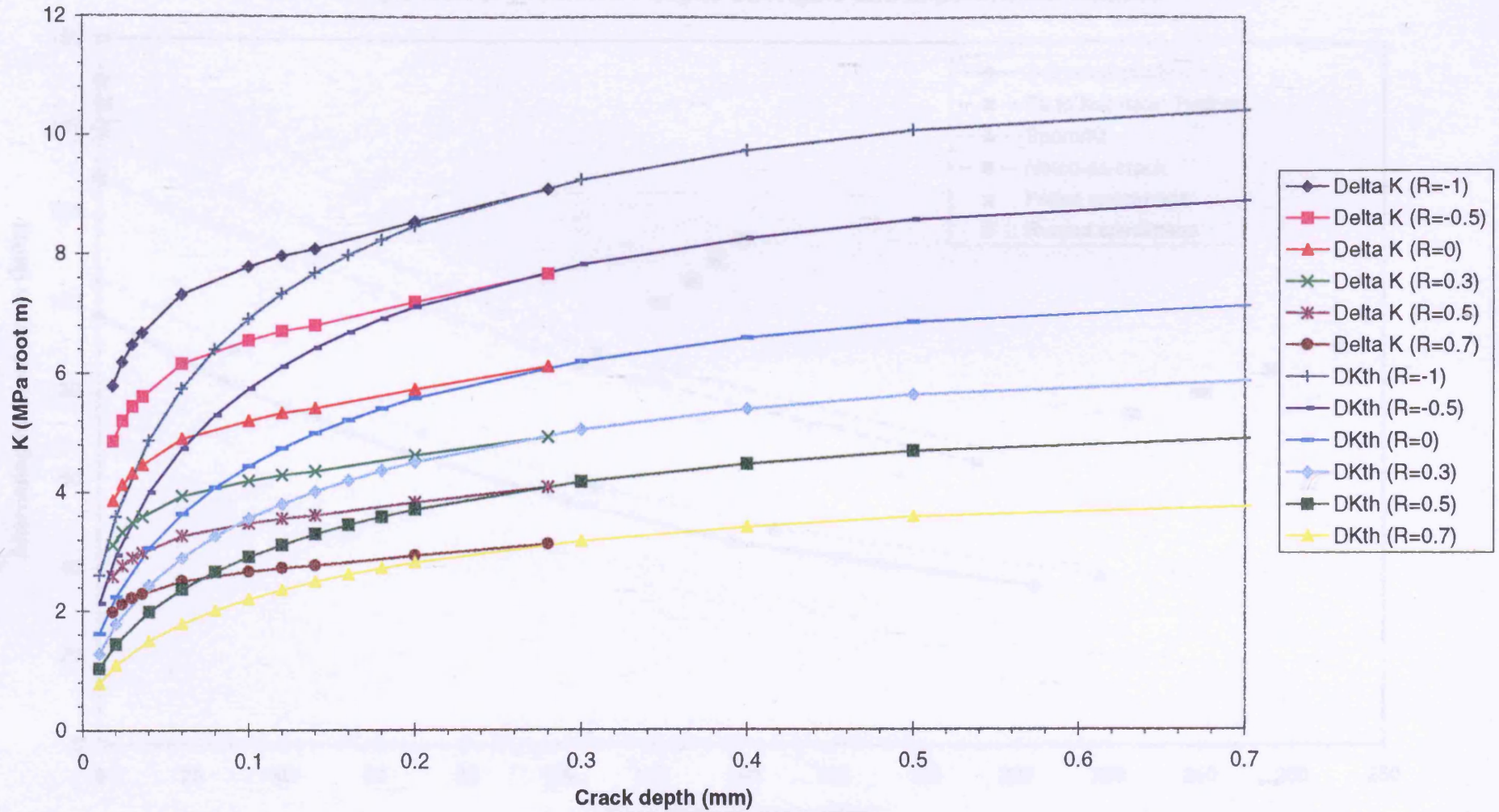


Figure 6.49 BCIRA sg12a1 (30mm Cast Section Size, $K_t = 1.5$, Grade 400/18 SG Iron)
Comparison of Predicted Fatigue Strengths and Experimental Results

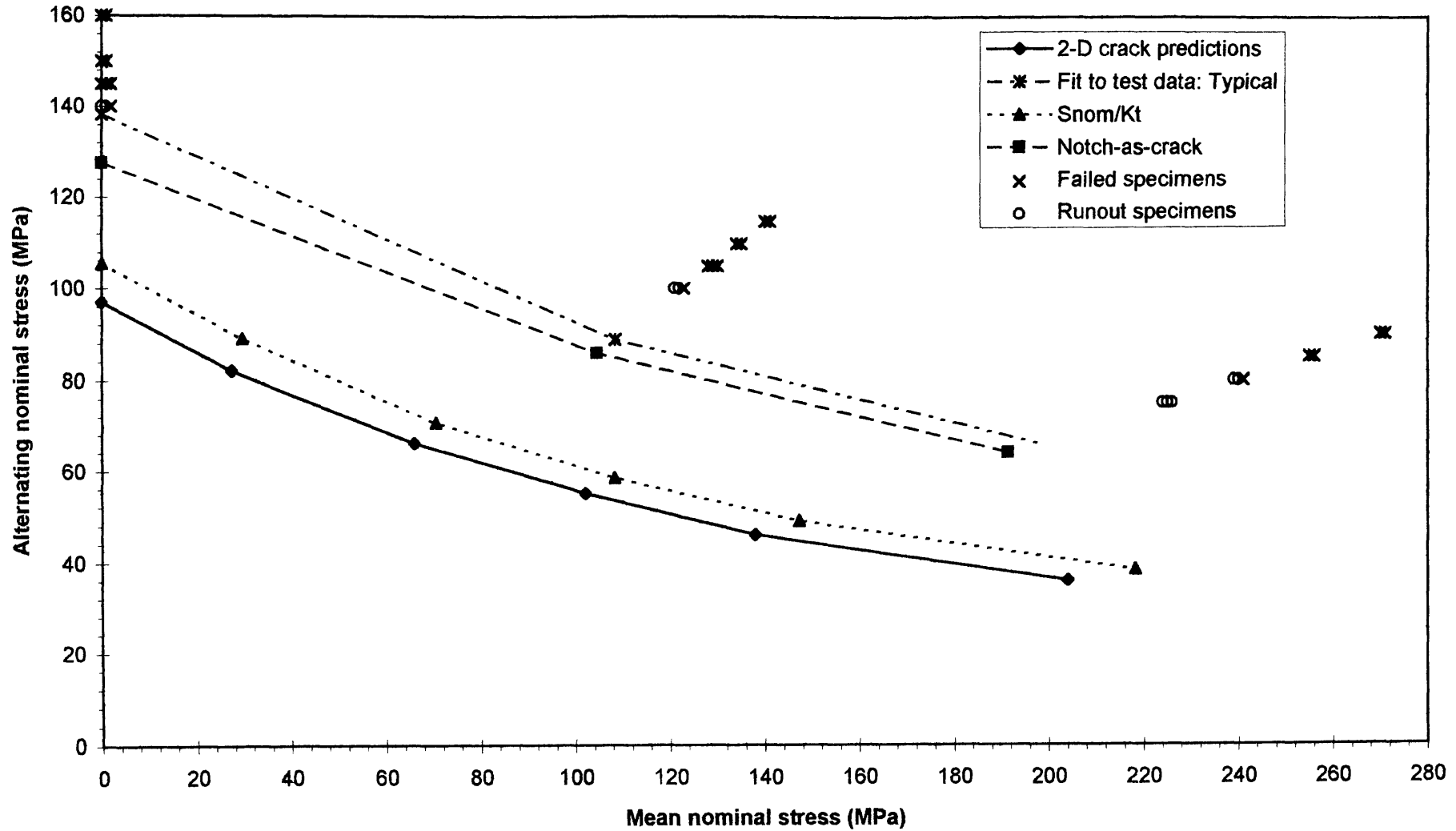


Figure 6.50 BCIRA sg12a1 Applied Delta K and Threshold Delta K Versus Crack Depth (30mm Cast Section Size, $K_t = 1.5$, Grade 400/18 SG Iron) Continuous Surface Cracks

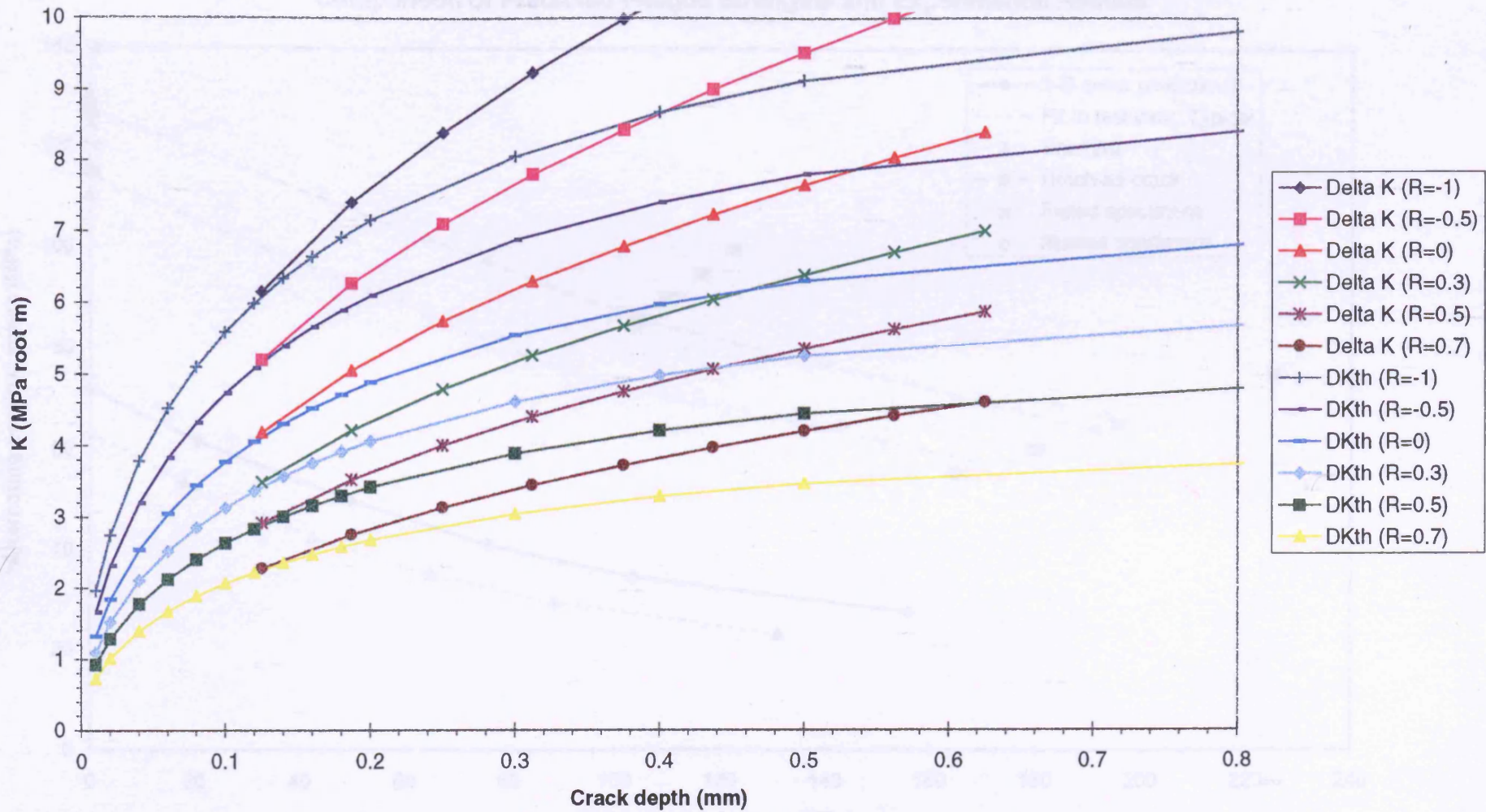


Figure 6.51 BCIRA sg12a2 (30mm Cast Section Size, $K_t = 2.5$, Grade 400/18 SG Iron)
 Comparison of Predicted Fatigue Strengths and Experimental Results

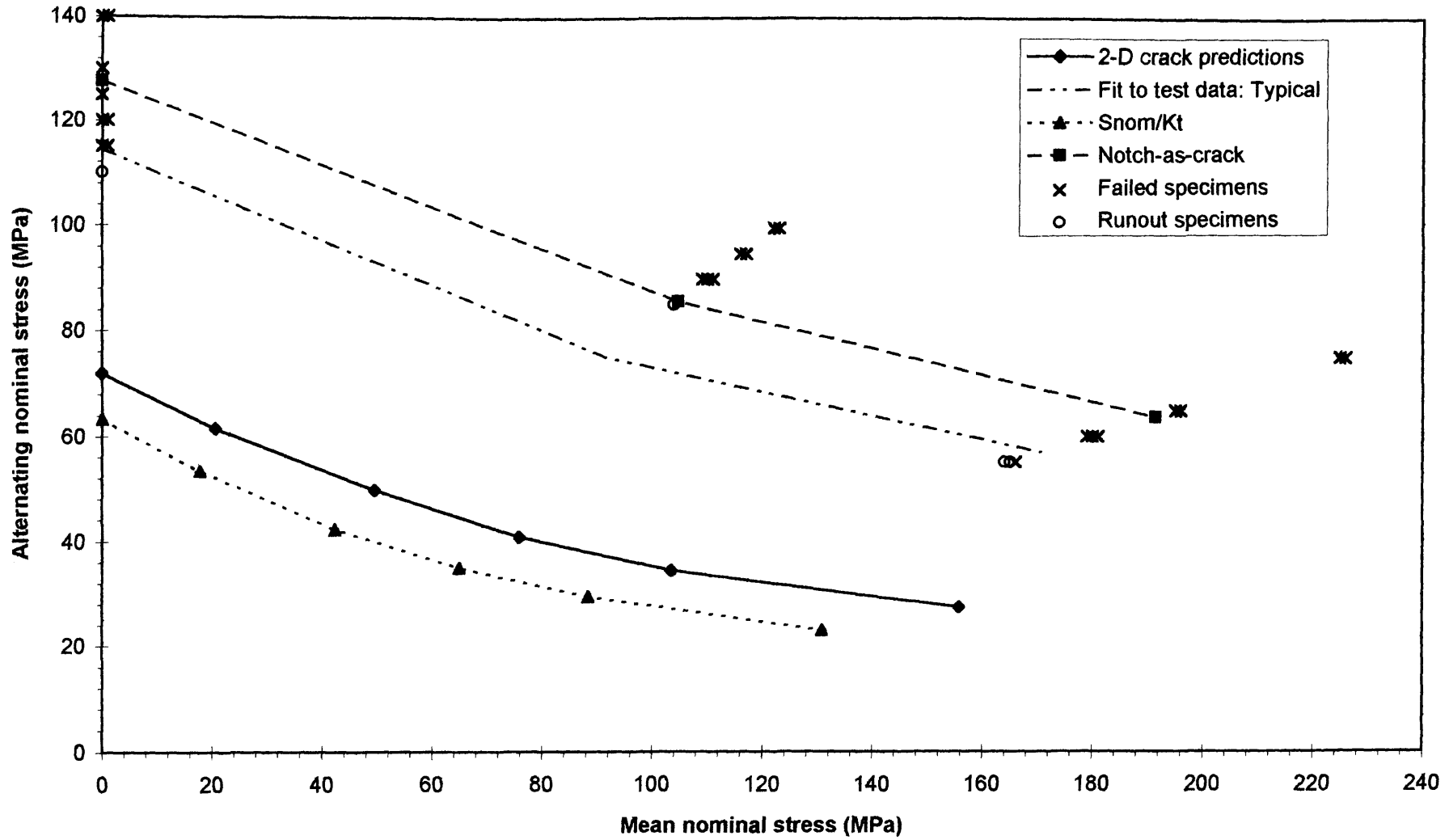


Figure 6.52 BCIRA sg12a2 Applied Delta K and Threshold Delta K Versus Crack Depth (30mm Cast Section Size, $K_t = 2.5$, Grade 400/18 SG Iron) Continuous Surface Cracks

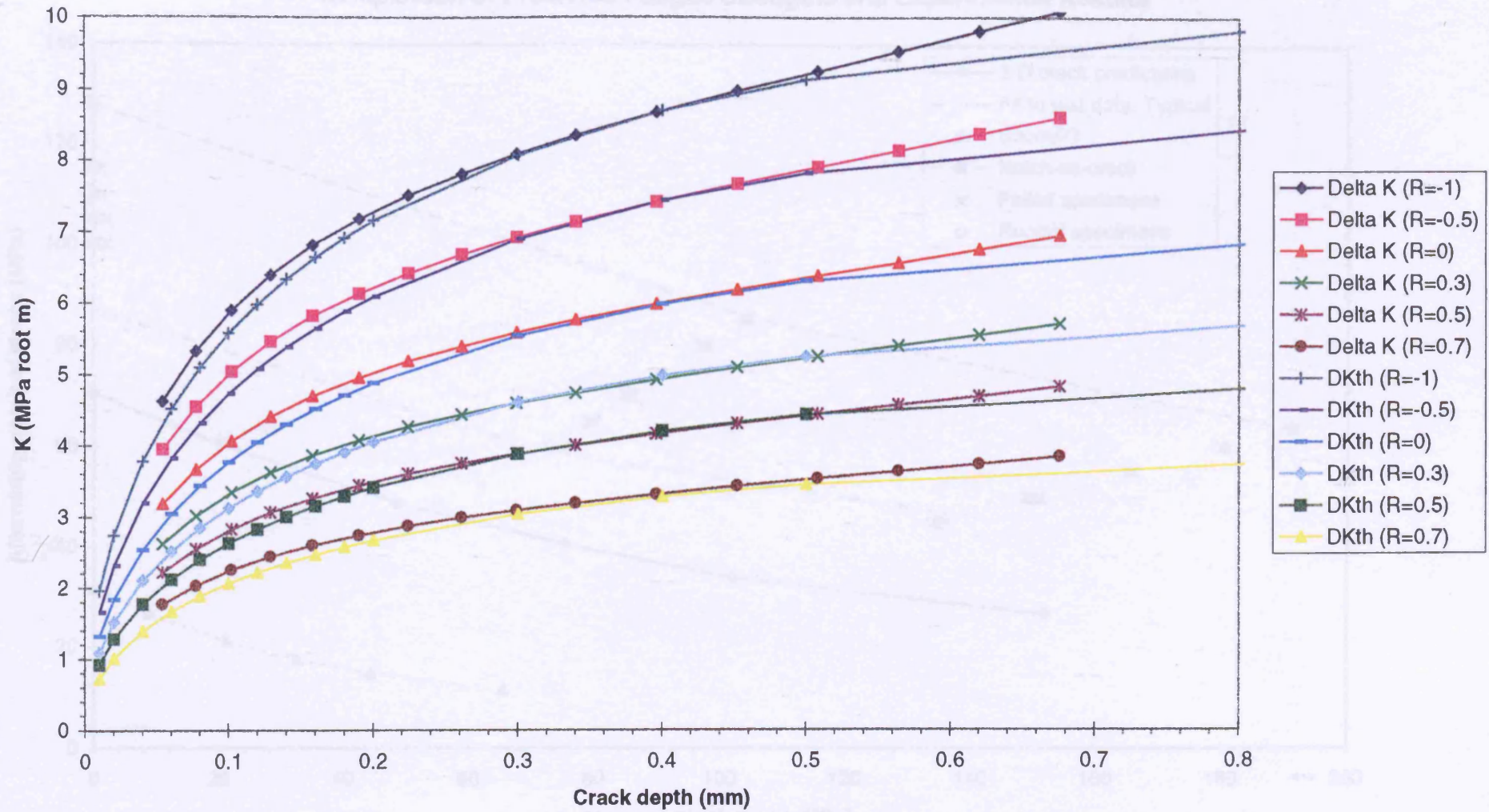


Figure 6.53 BCIRA sg12a3 (30mm Cast Section Size, $K_t = 5$, Grade 400/18 SG Iron)
Comparison of Predicted Fatigue Strengths and Experimental Results

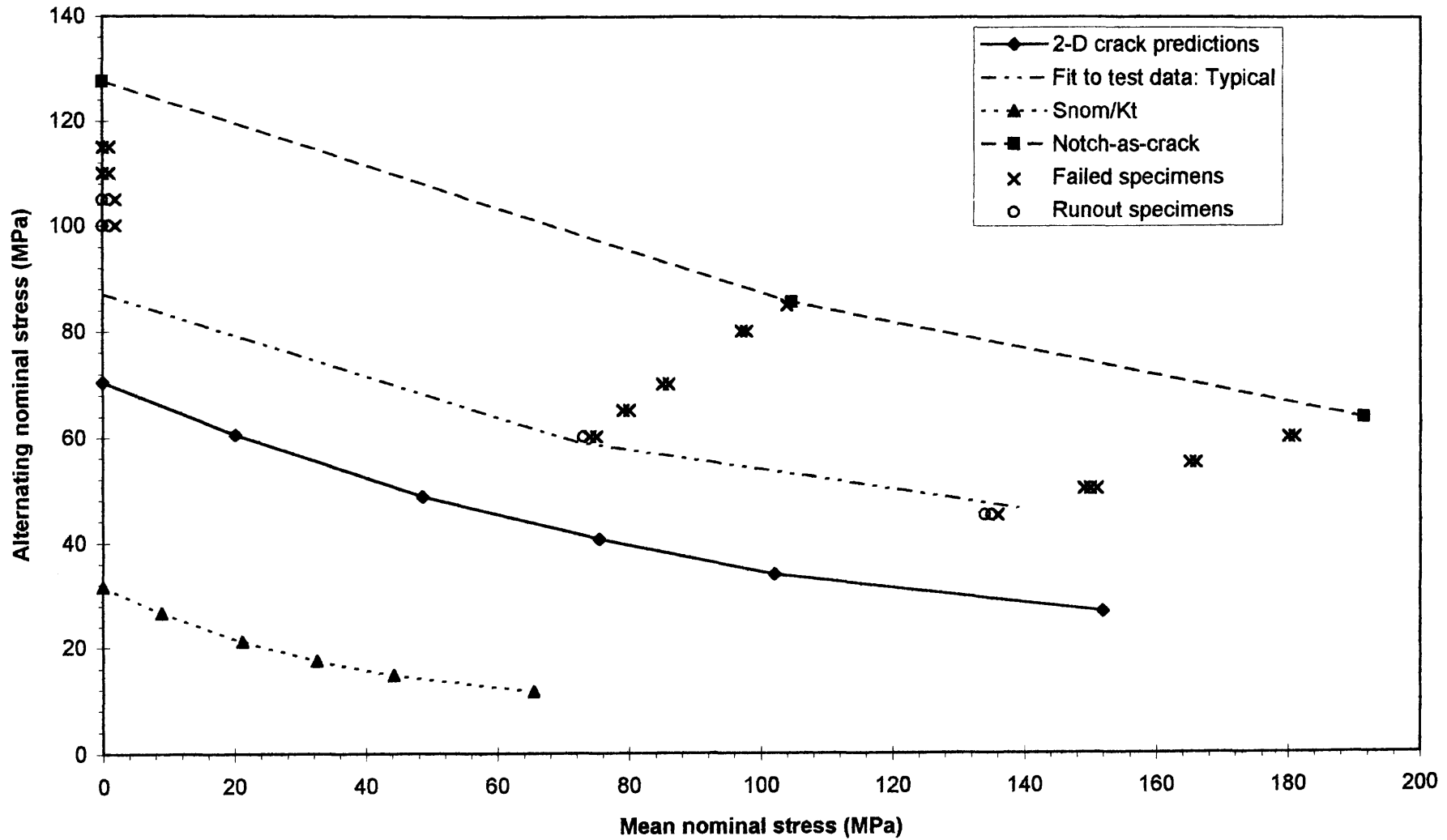


Figure 6.54 BCIRA sg12a3 Applied Delta K and Threshold Delta K Versus Crack Depth (30mm Cast Section Size, $K_t = 5$, Grade 400/18 SG Iron) Continuous Surface Cracks

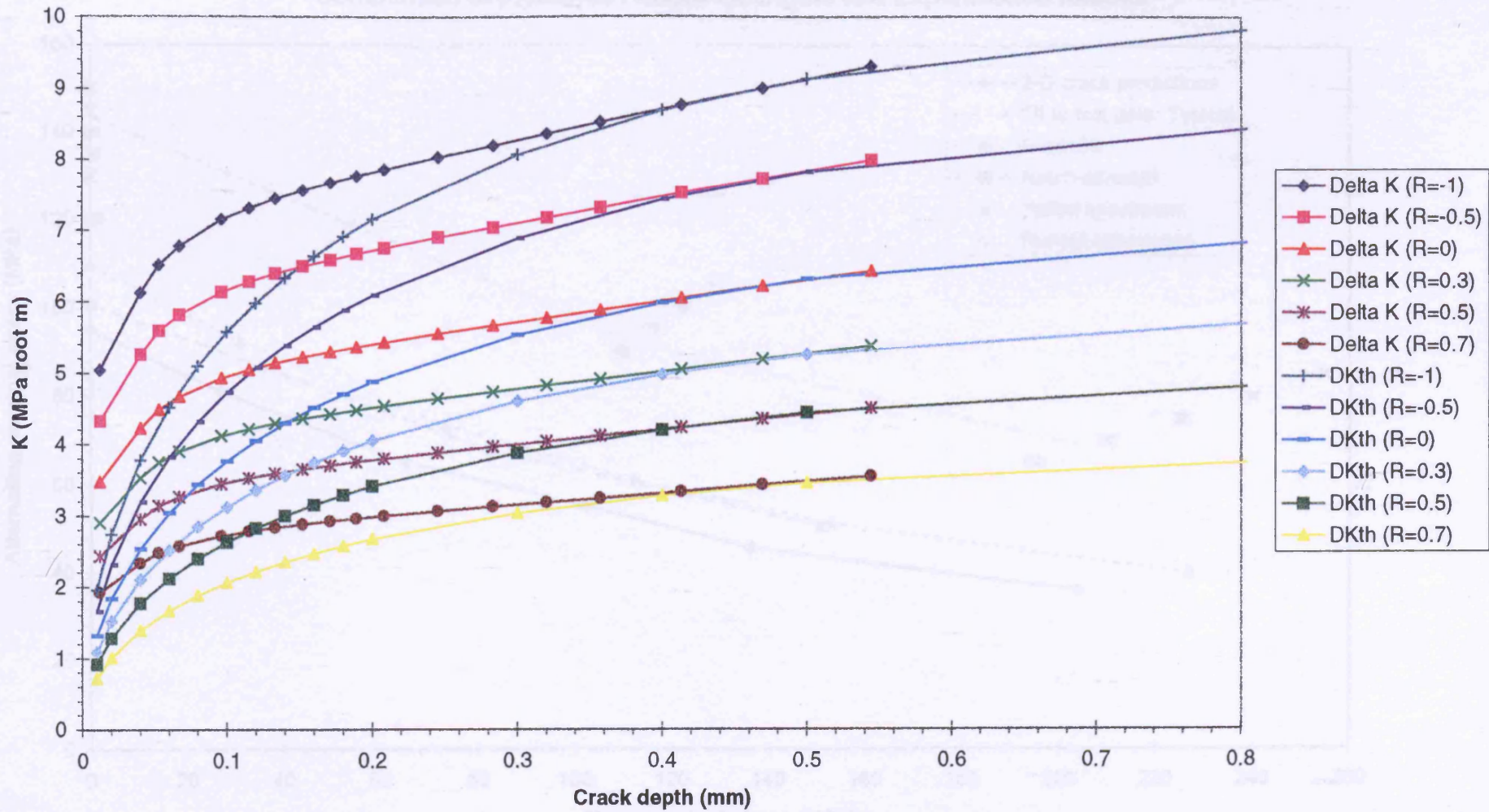


Figure 6.55 BCIRA sg20a1 (50mm Cast Section Size, $K_t = 1.5$, Grade 400/18 SG Iron)
Comparison of Predicted Fatigue Strengths and Experimental Results

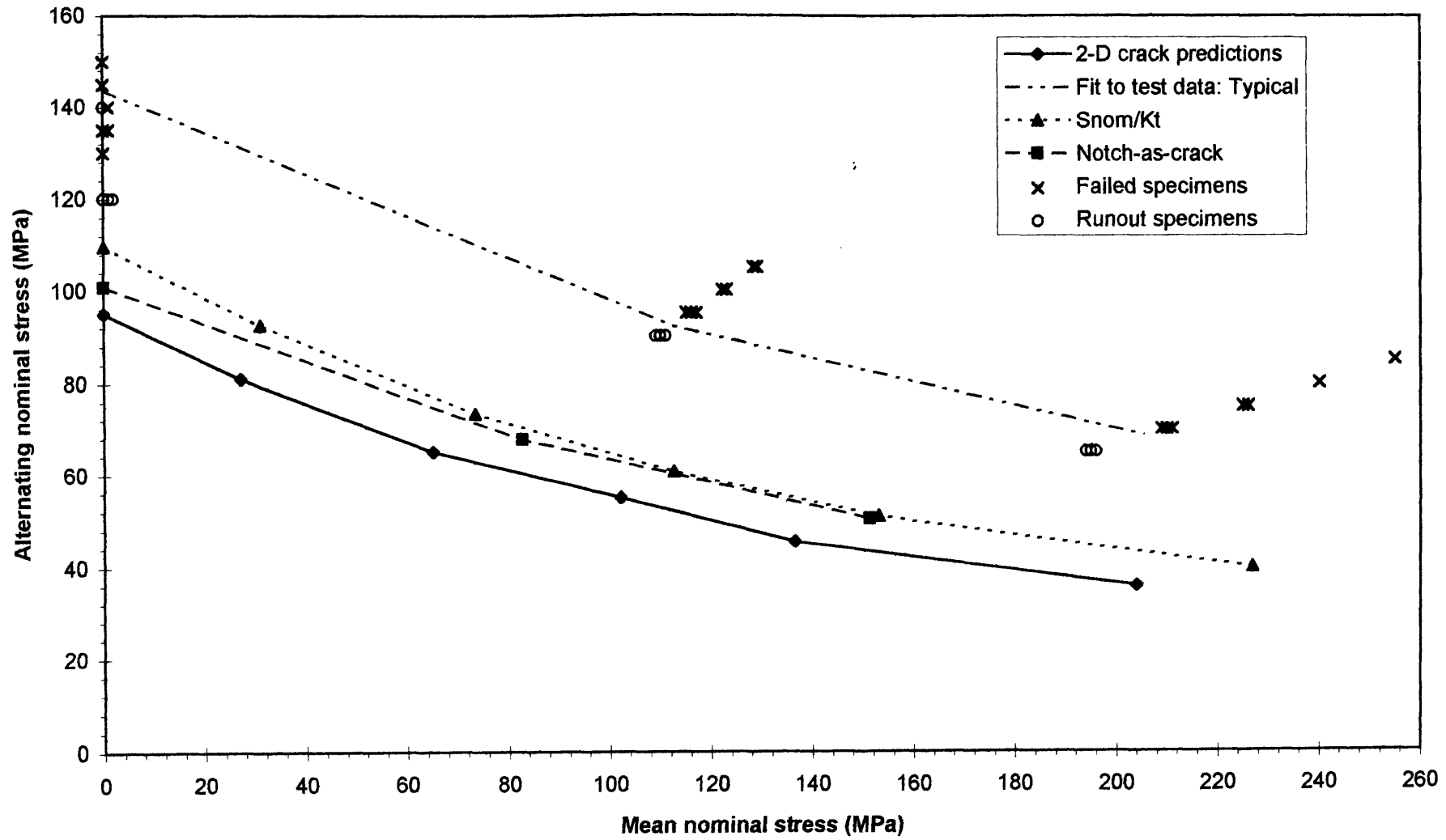
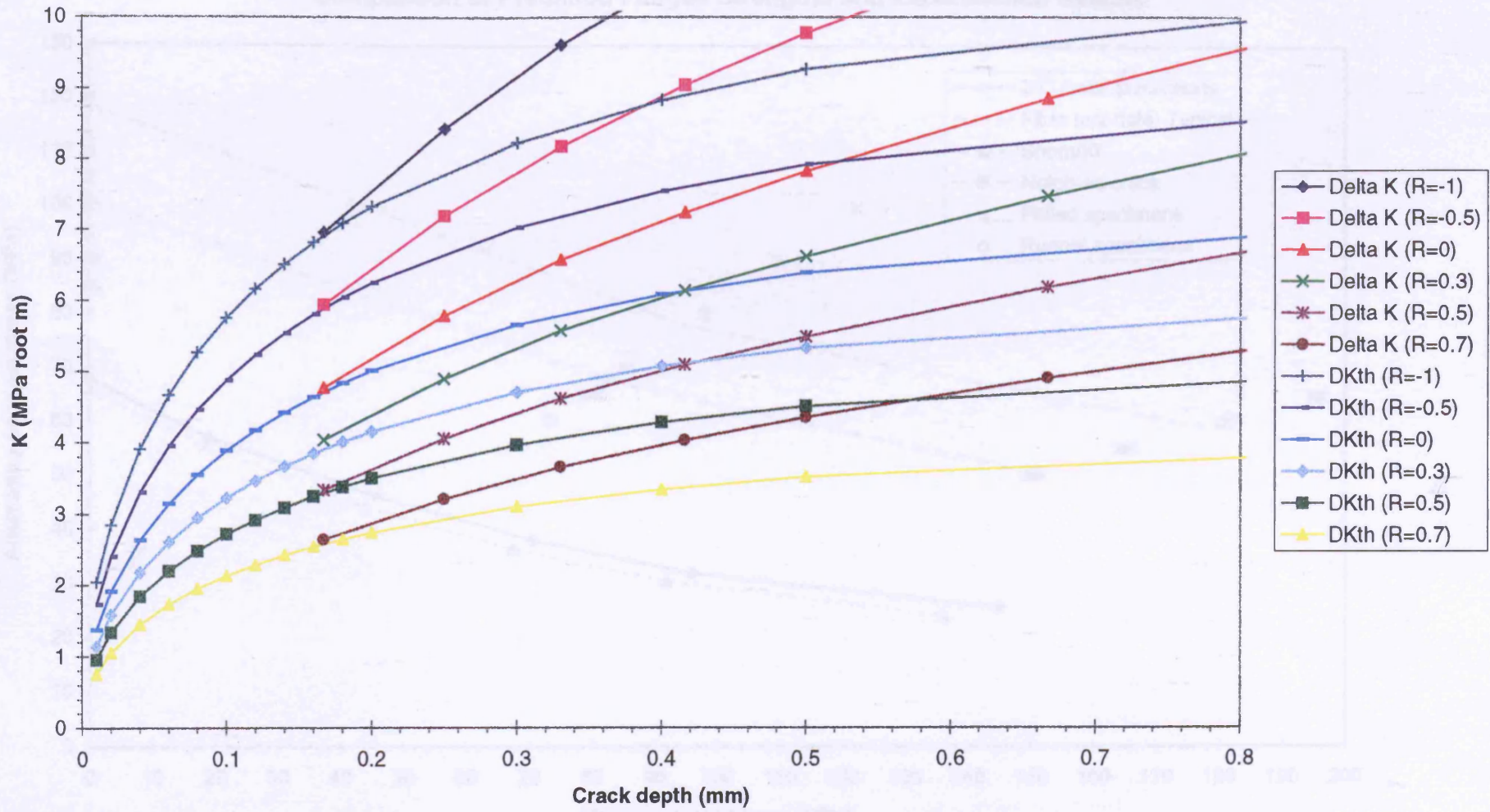


Figure 6.56 BCIRA sg20a1 Applied Delta K and Threshold Delta K Versus Crack Depth (50mm Cast Section Size, $K_t = 1.5$, Grade 400/18 SG Iron) Continuous Surface Cracks



**Figure 6.57 BCIRA sg20a2 (50mm Cast Section Size, Kt = 2.5, Grade 400/18 SG Iron)
Comparison of Predicted Fatigue Strengths and Experimental Results**

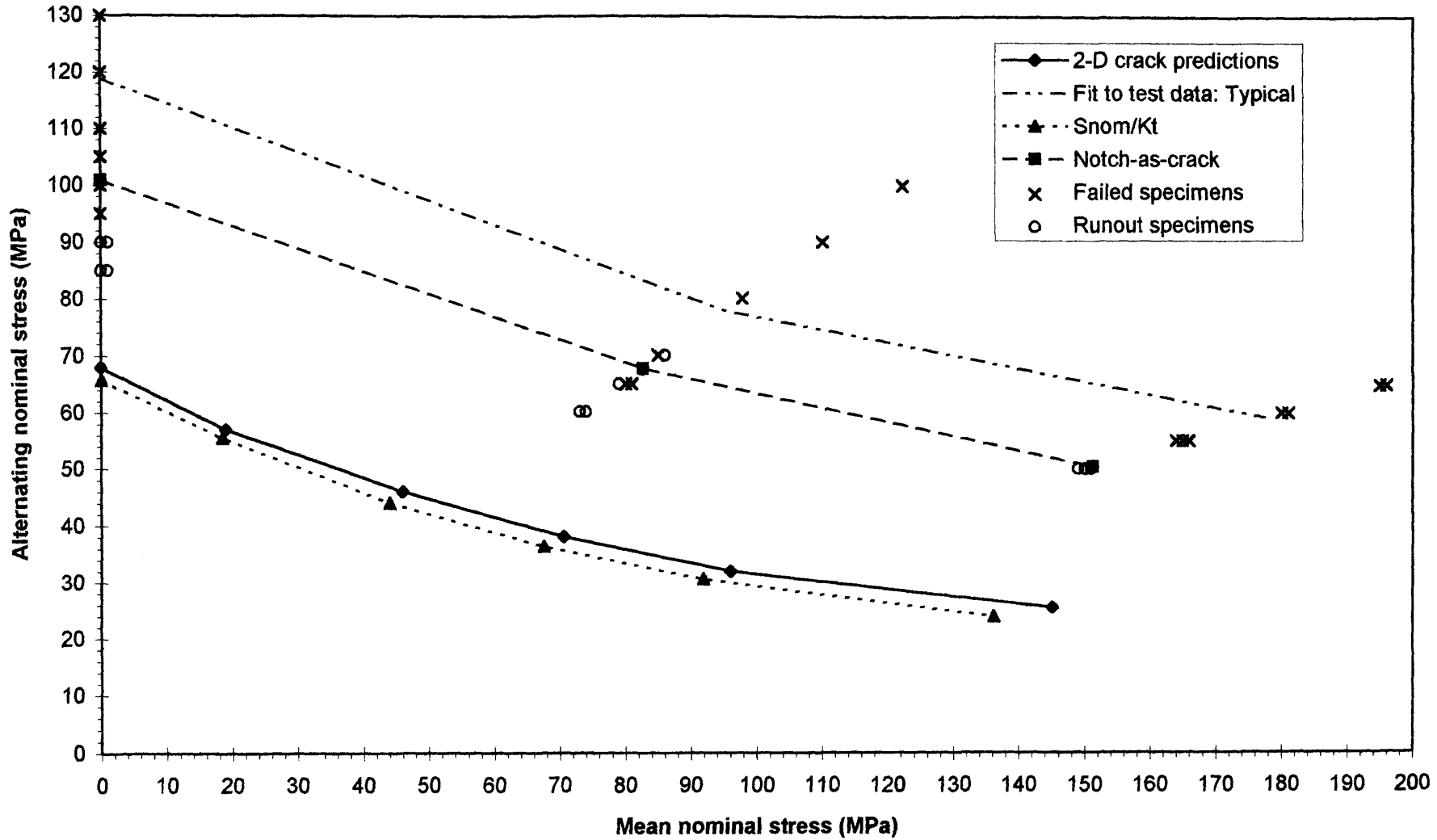


Figure 6.58 BCIRA sg20a2 Applied Delta K and Threshold Delta K Versus Crack Depth (50mm Cast Section Size, $K_t = 2.5$, Grade 400/18 SG Iron) Continuous Surface Cracks

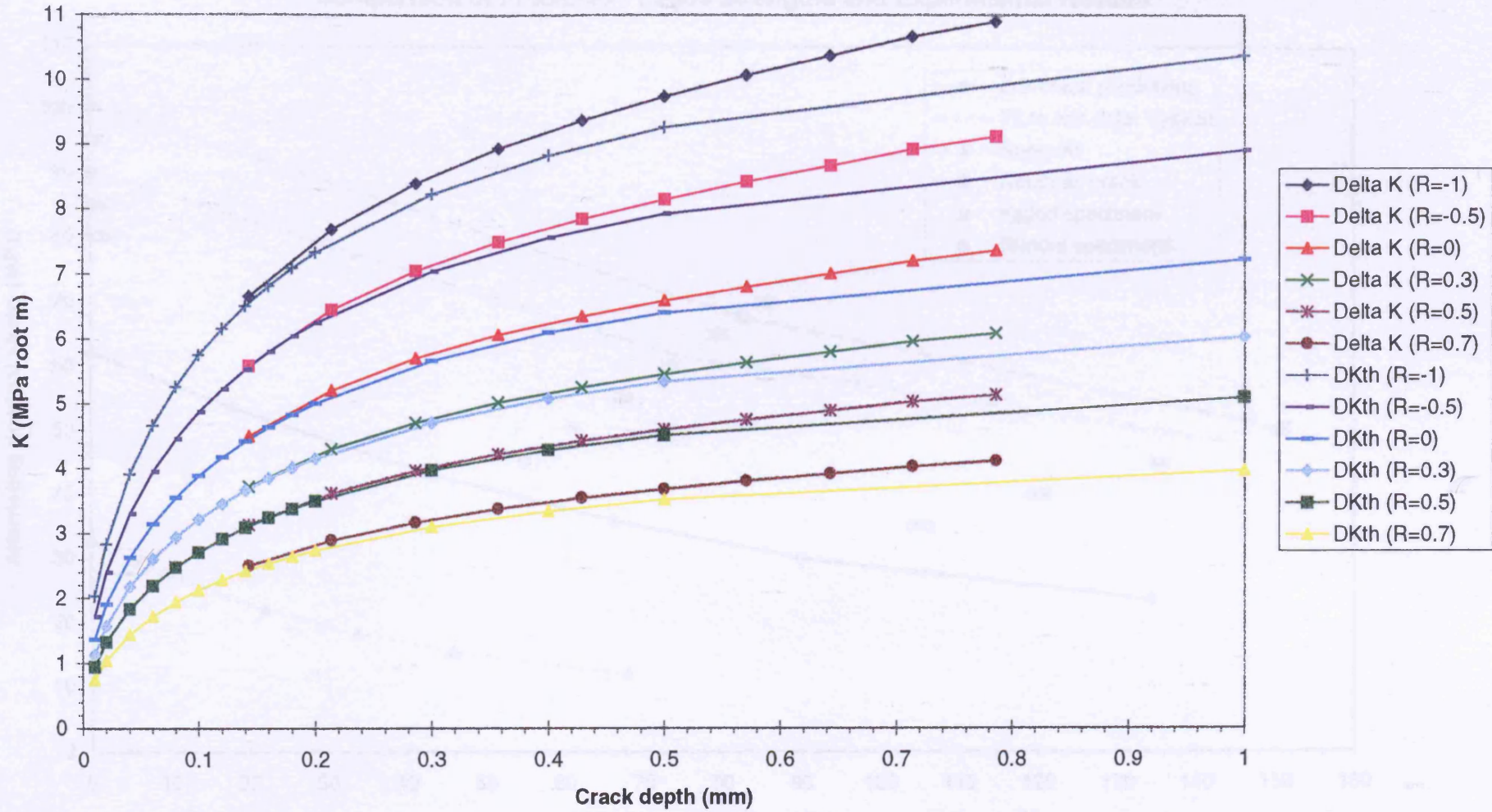


Figure 6.59 BCIRA sg20a3 (50mm Cast Section Size, $K_t = 5$, Grade 400/18 SG Iron)
Comparison of Predicted Fatigue Strengths and Experimental Results

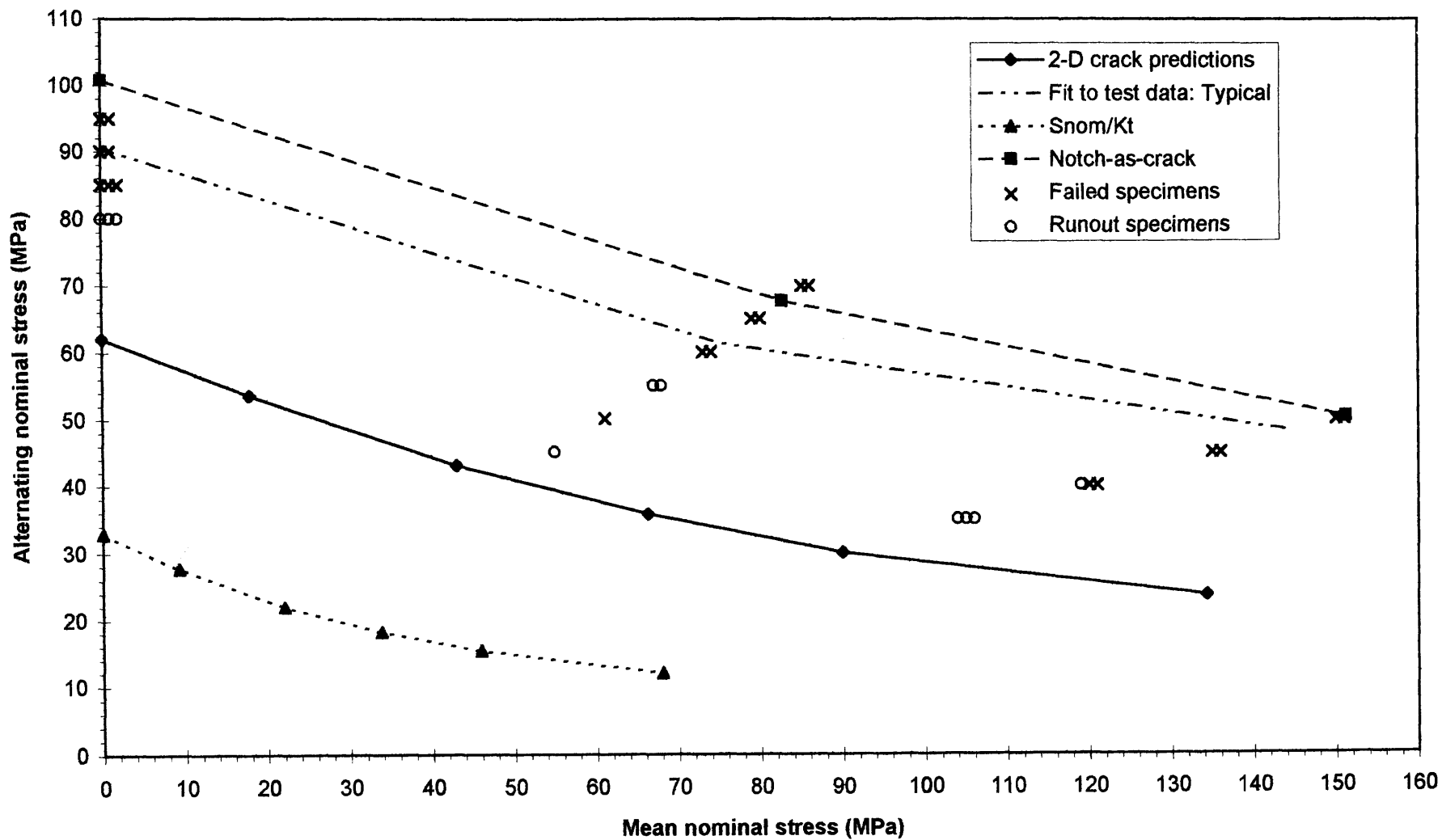


Figure 6.60 BCIRA sg20a3 Applied Delta K and Threshold Delta K Versus Crack Depth (50mm Cast Section Size, $K_t = 5$, Grade 400/18 SG Iron) Continuous Surface Cracks

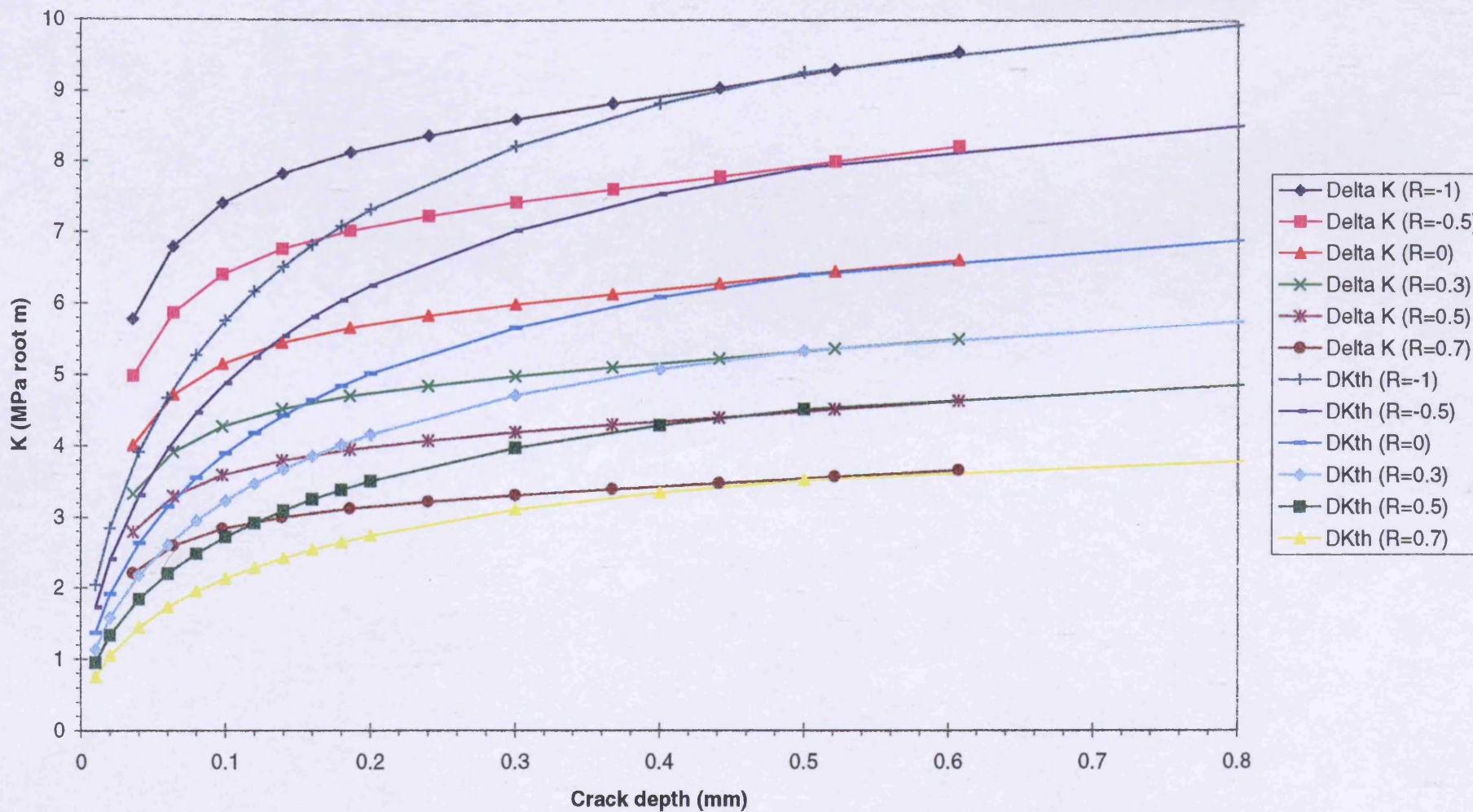


Figure 6.61 BCIRA Grade 500/7 SG Iron
Fatigue Limit Versus R-ratio

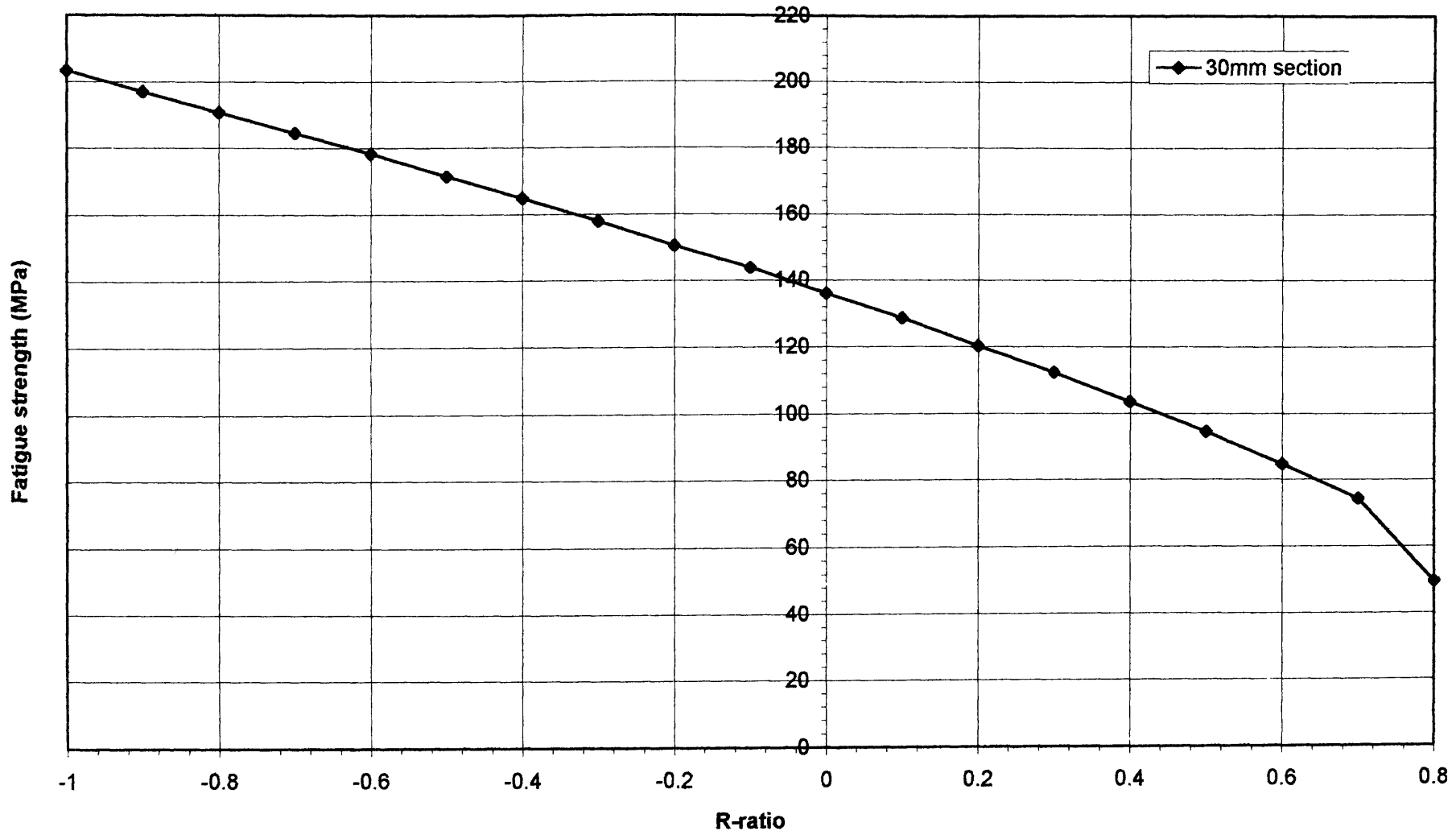


Figure 6.62 BCIRA Grade 500/7 SG Cast Iron
Predicted Apparent Short Crack Threshold - Continuous Surface Crack - R = 0.05 & 0.5

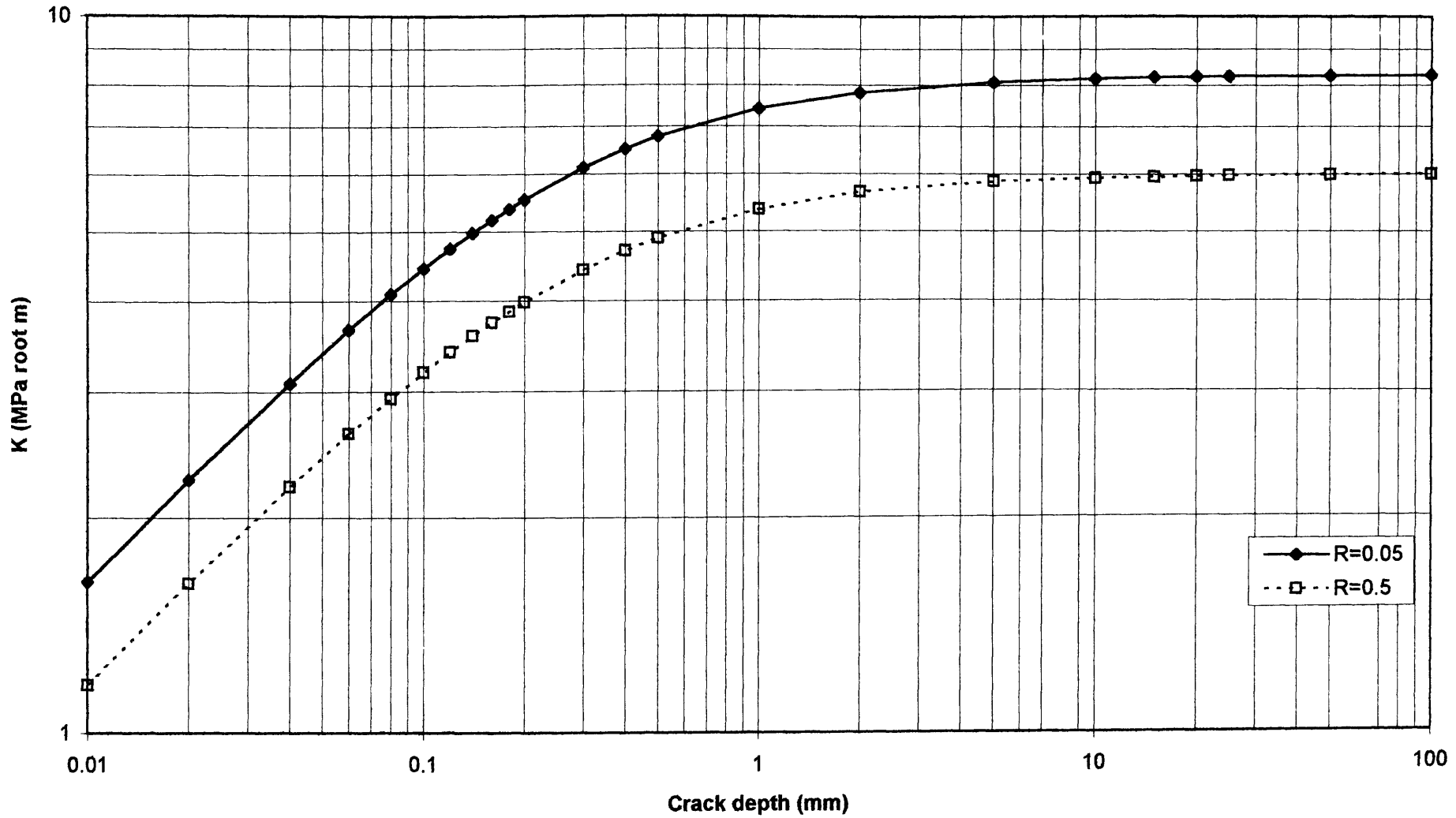


Figure 6.63 BCIRA sg12b1 (30mm Cast Section Size, $K_t = 1.5$, Grade 500/7 SG Iron)
Comparison of Predicted Fatigue Strengths and Experimental Results

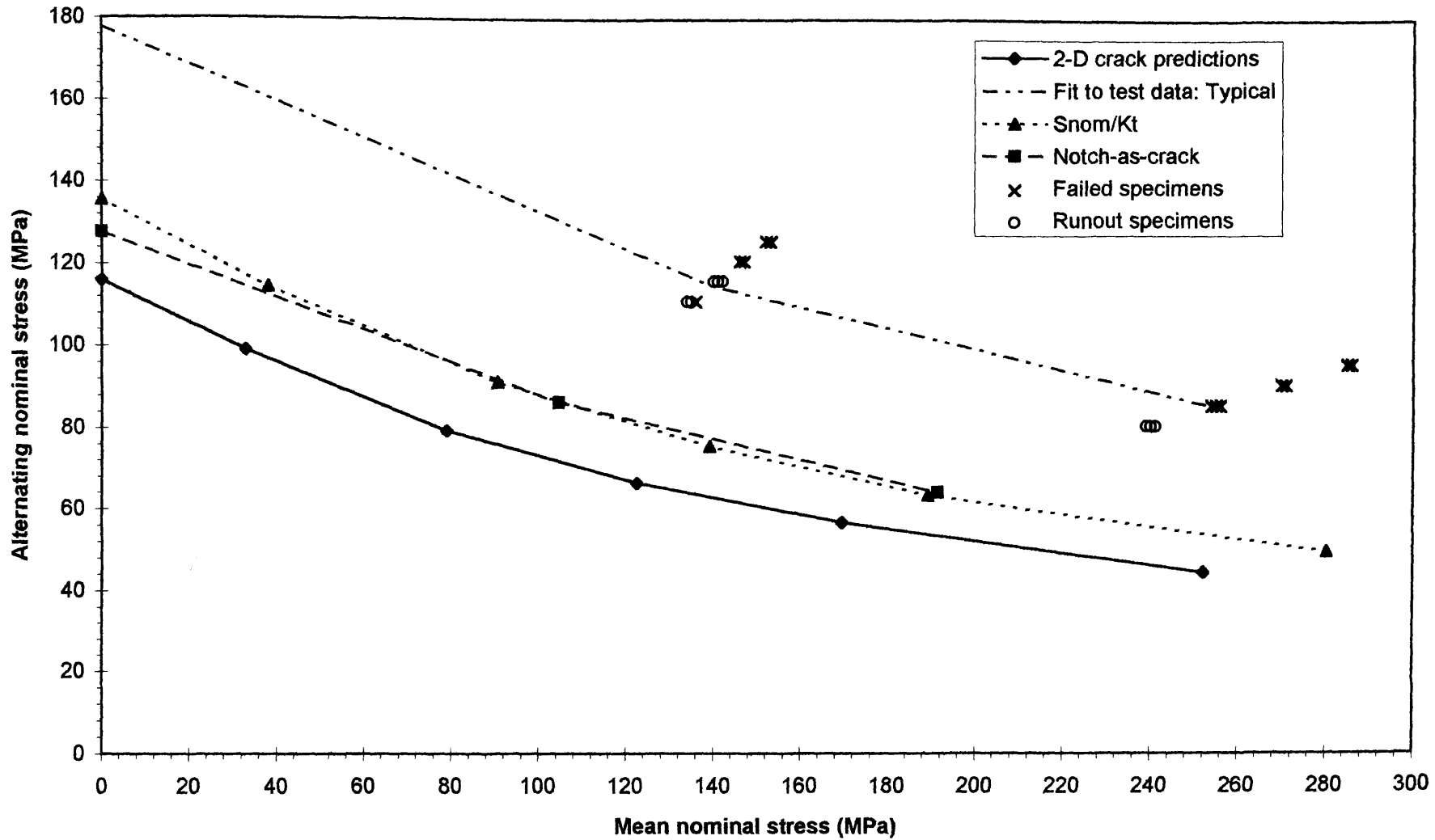


Figure 6.64 BCIRA sg12b1 Applied Delta K and Threshold Delta K Versus Crack Depth (30mm Cast Section Size, $K_t = 1.5$, Grade 500/7 SG Iron) Continuous Surface Cracks

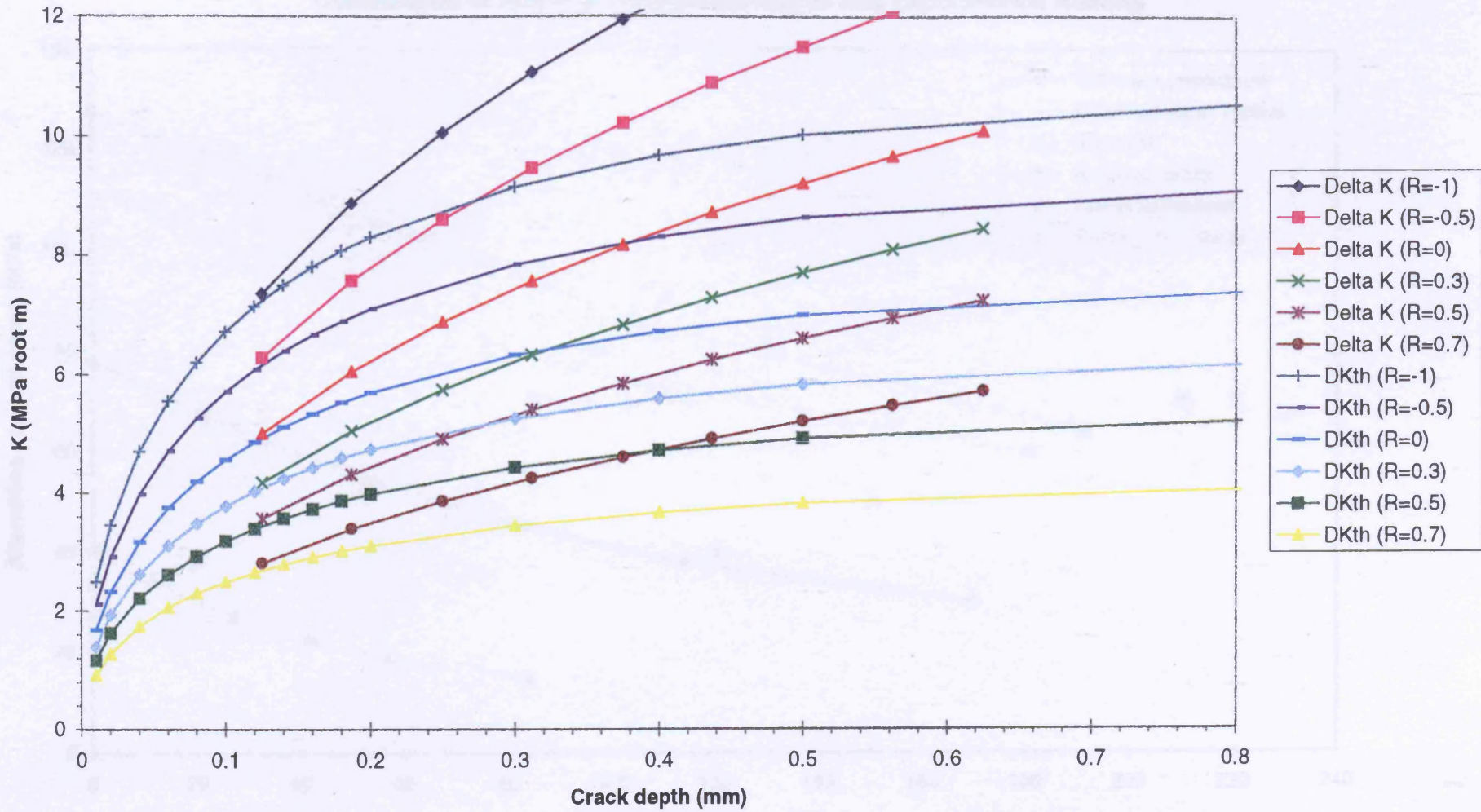


Figure 6.65 BCIRA sg12b3 (30mm Cast Section Size, $K_t = 5$, Grade 500/7 SG Iron)
Comparison of Predicted Fatigue Strengths and Experimental Results

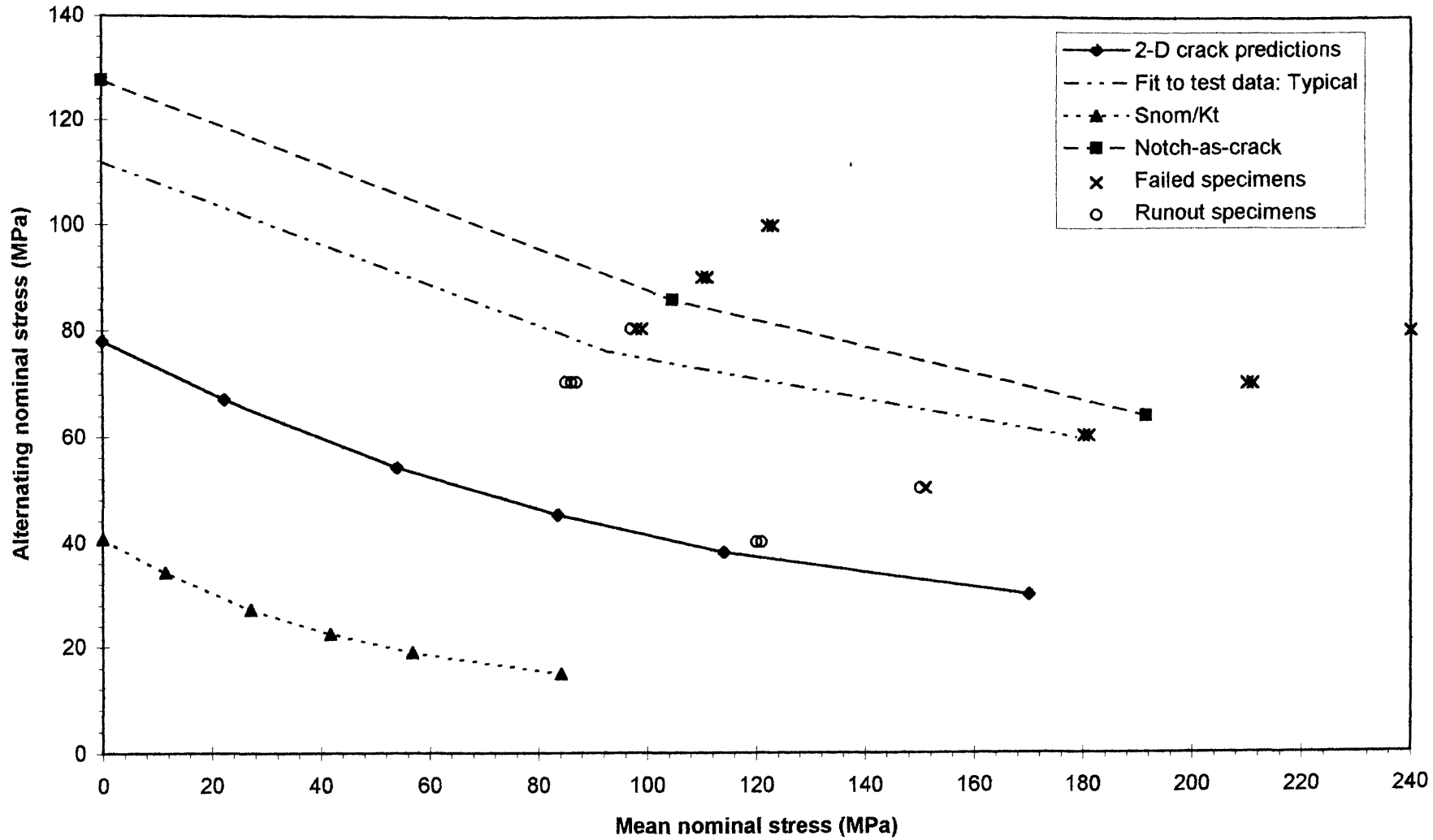
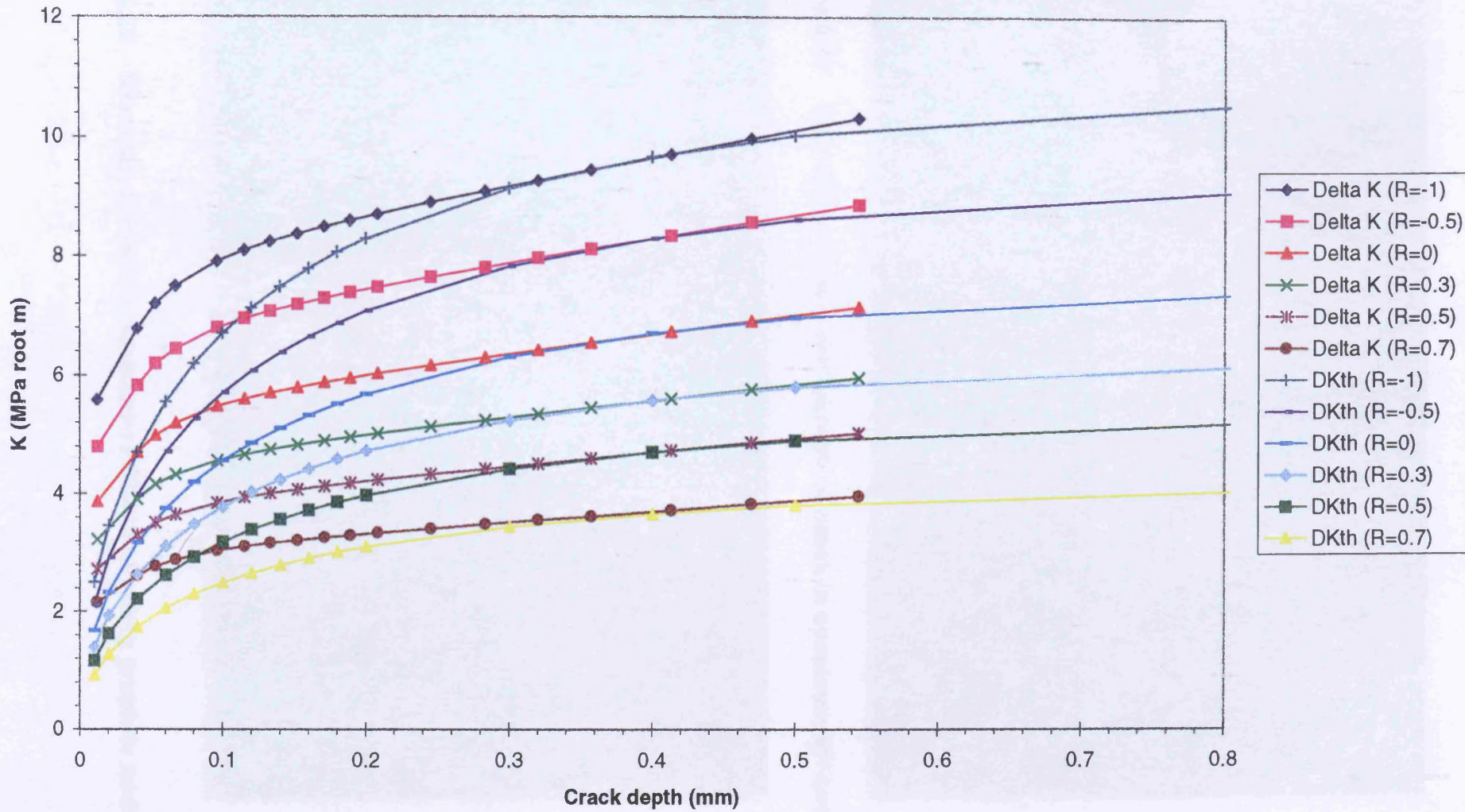


Figure 6.66 BCIRA sg12b3 Applied Delta K and Threshold Delta K Versus Crack Depth (30mm Cast Section Size, $K_t = 5$, Grade 500/7 SG Iron) Continuous Surface Cracks



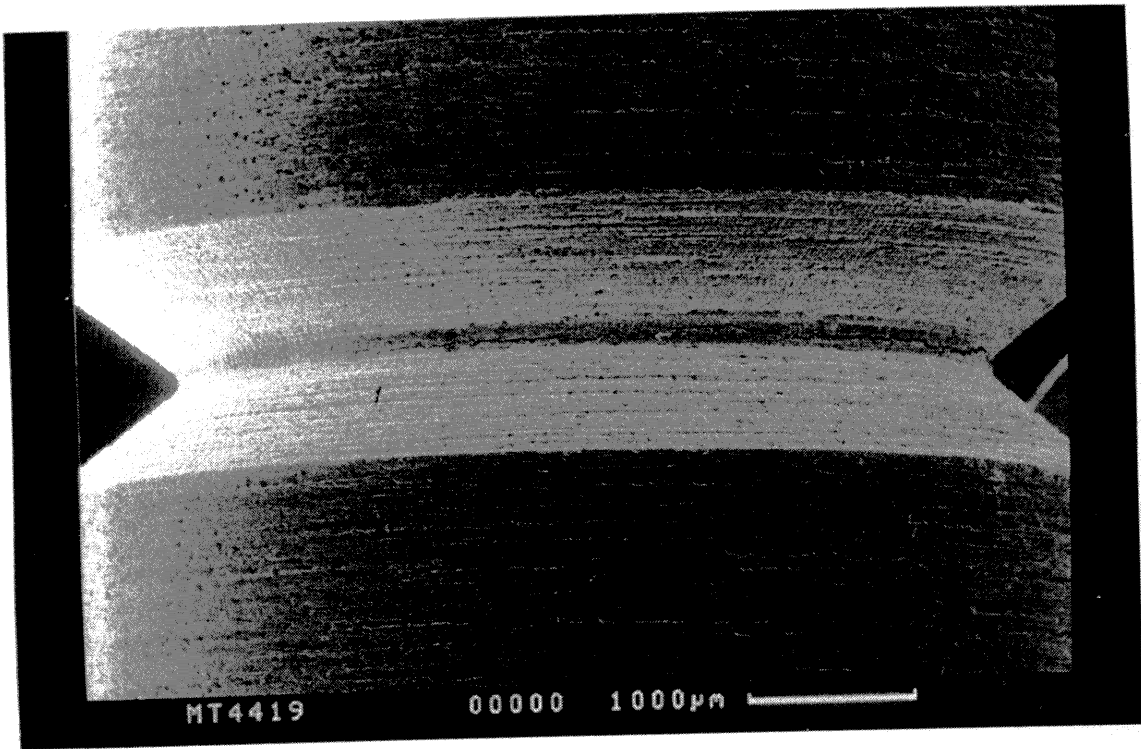


Figure 6.67 Scanning electron micrograph of crack in specimen MT4419

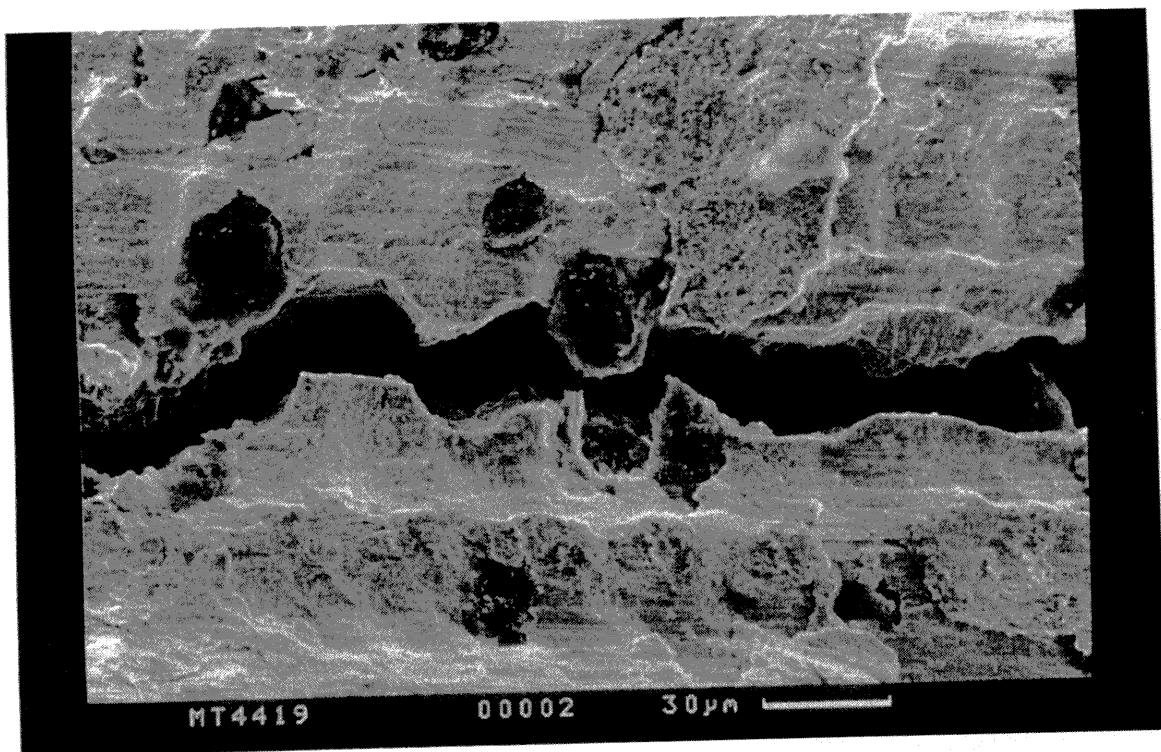


Figure 6.68 Close up of crack in specimen MT4419 showing graphite nodules

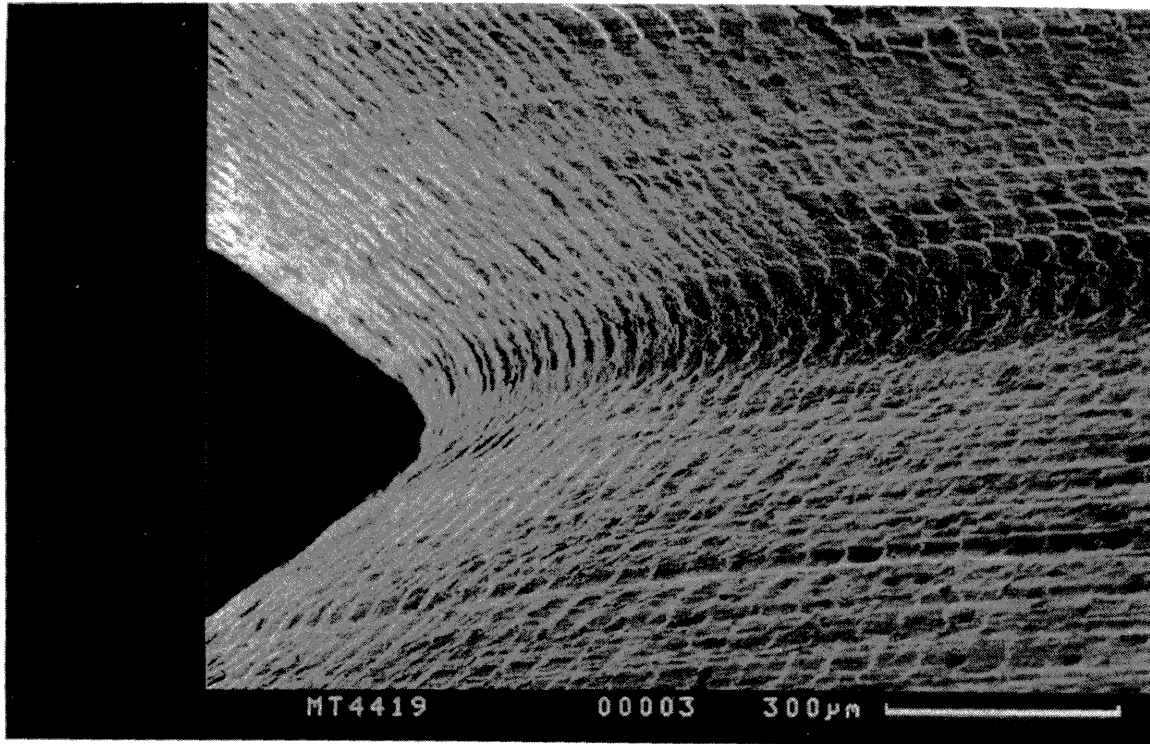


Figure 6.69 Scanning electron micrograph of specimen MT4419 showing machining marks

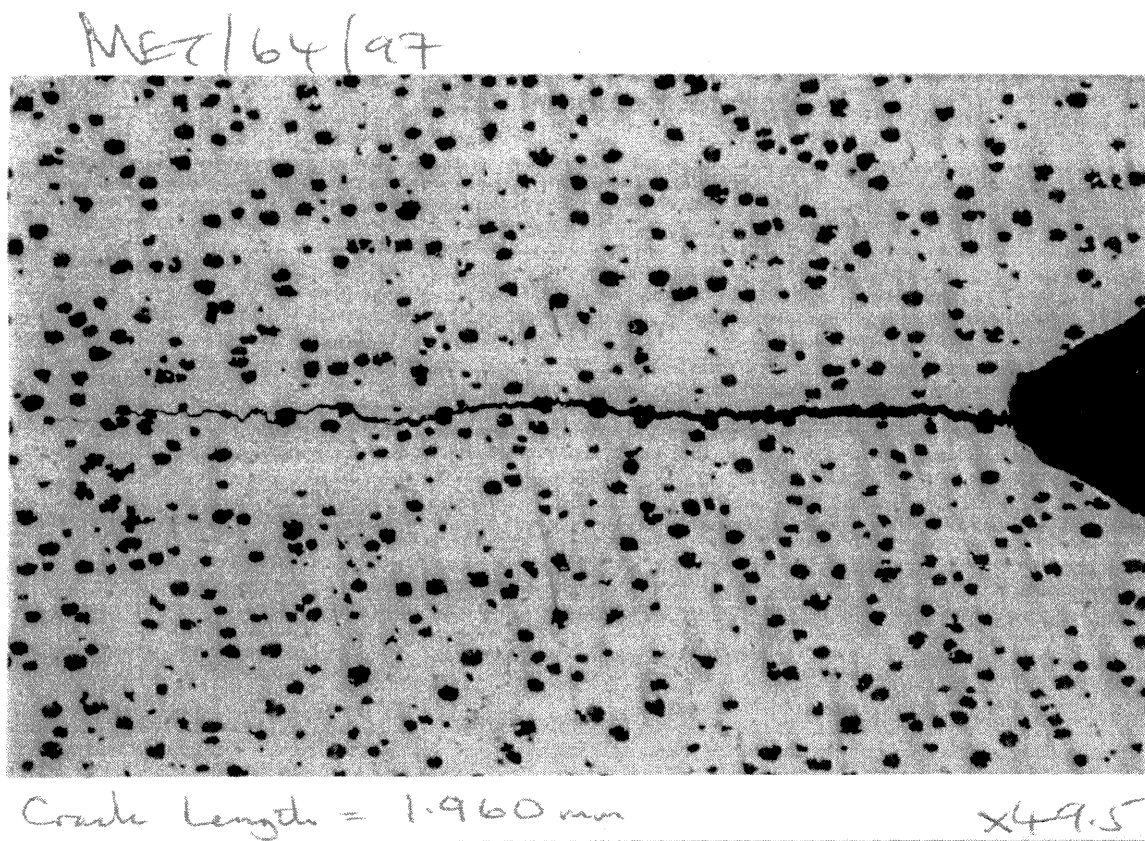


Figure 6.70 View of sectioned crack in specimen MT4419 (crack length = 1.96mm)

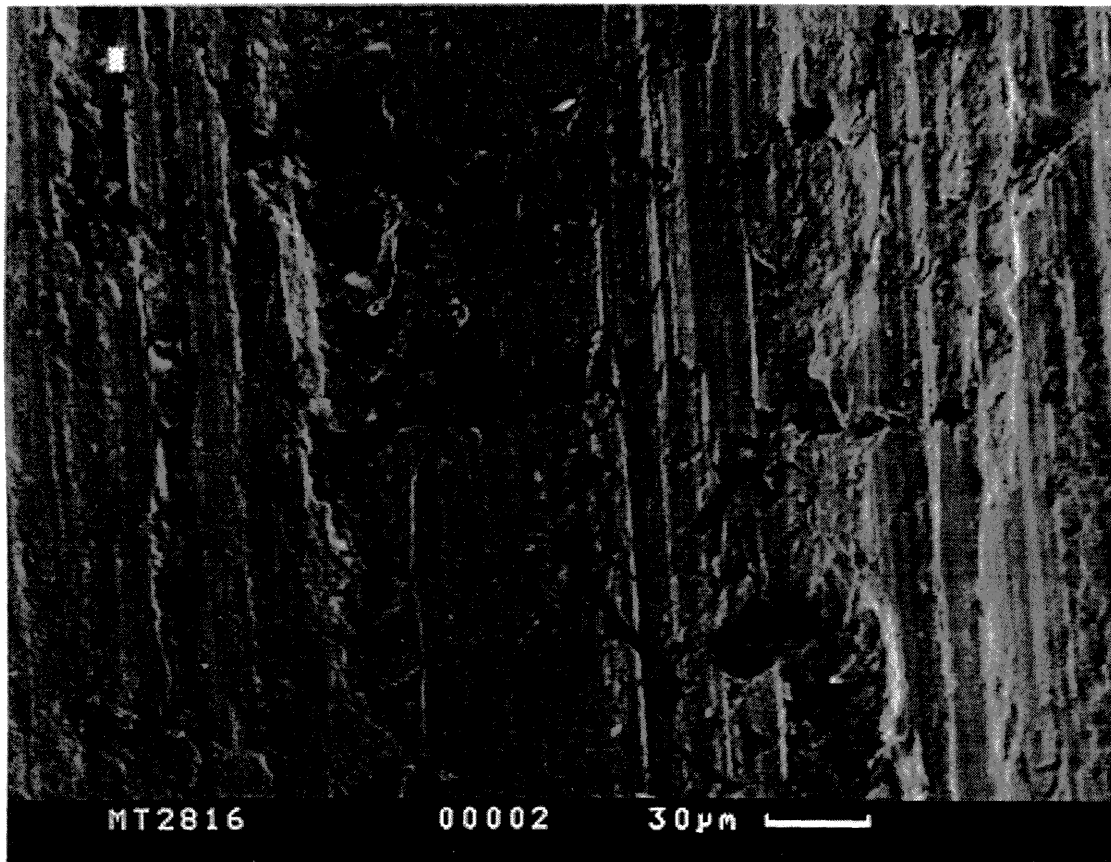


Figure 6.71 Scanning electron micrograph of grey iron specimen mt2816
- Detail in notch root region

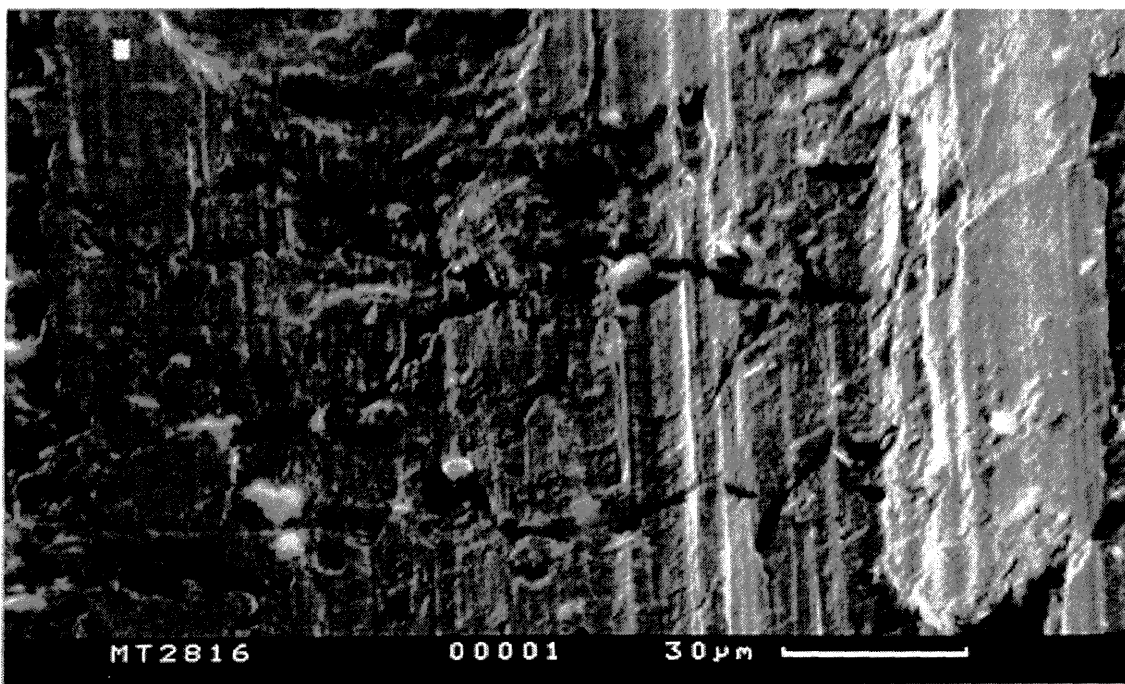


Figure 6.72 Scanning electron micrograph of grey iron specimen mt2816
- Detail in notch root region

Figure 6.73 Predicted variation of applied ΔK with crack depth for a load level just sufficient to match the predicted apparent short crack threshold
 - Notched specimen geometry is that from Frost (1955)

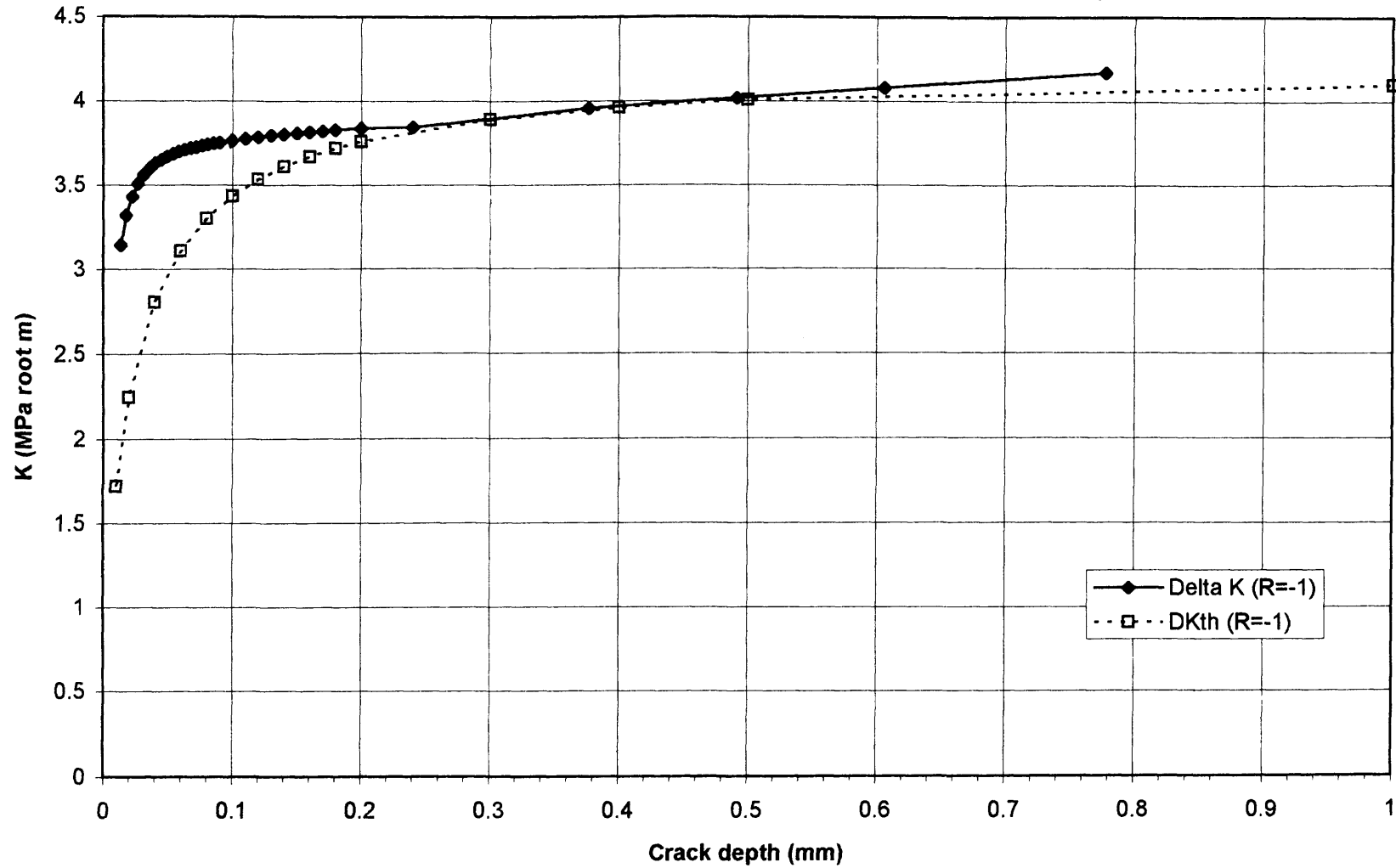


Figure 6.74 Comparison of fatigue strength predictions with experimental notched fatigue test results from Frost (1955)

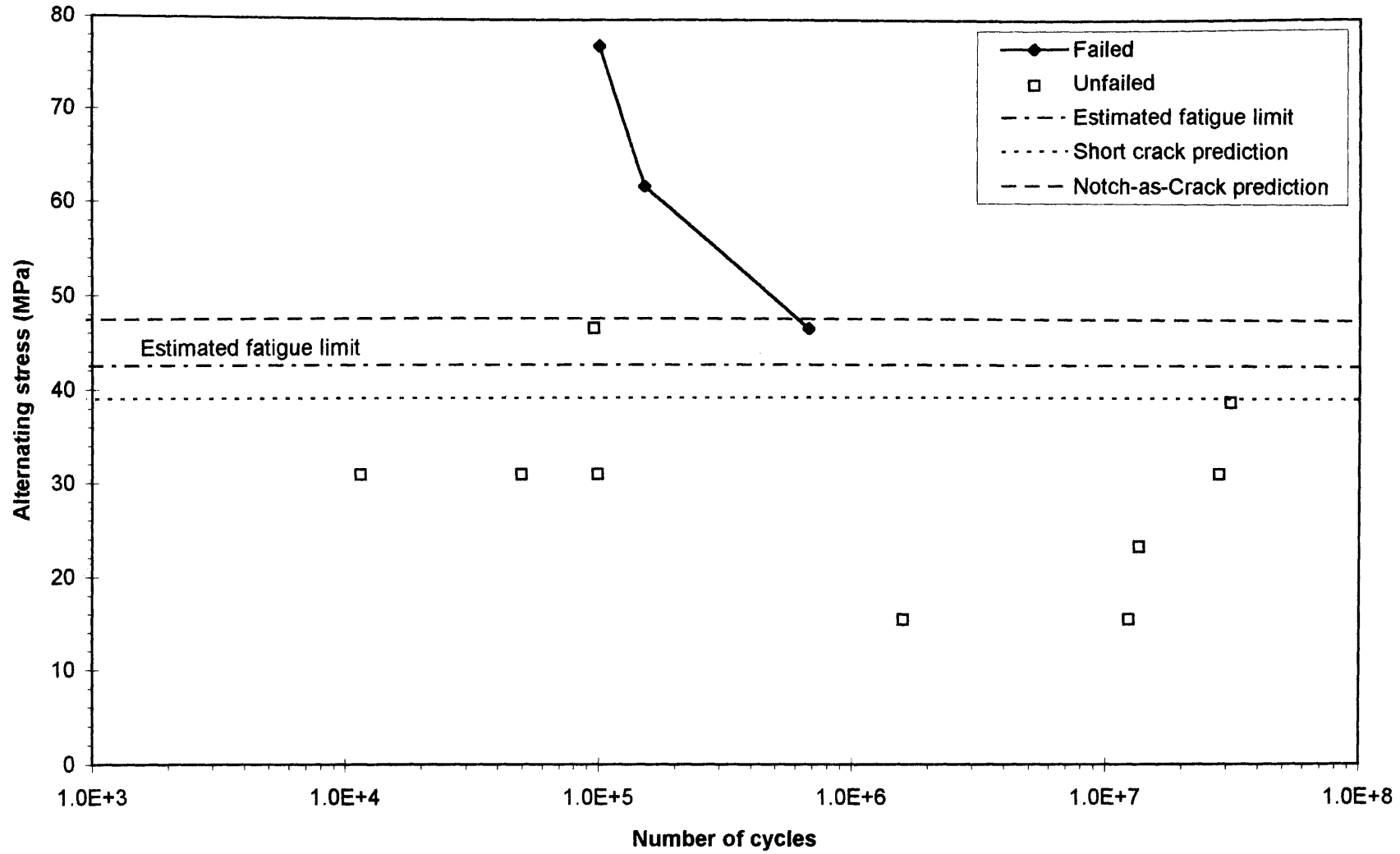


Figure 6.75 Comparison of measured non-propagating crack depths from Frost (1955) with predicted crack depths at the threshold condition

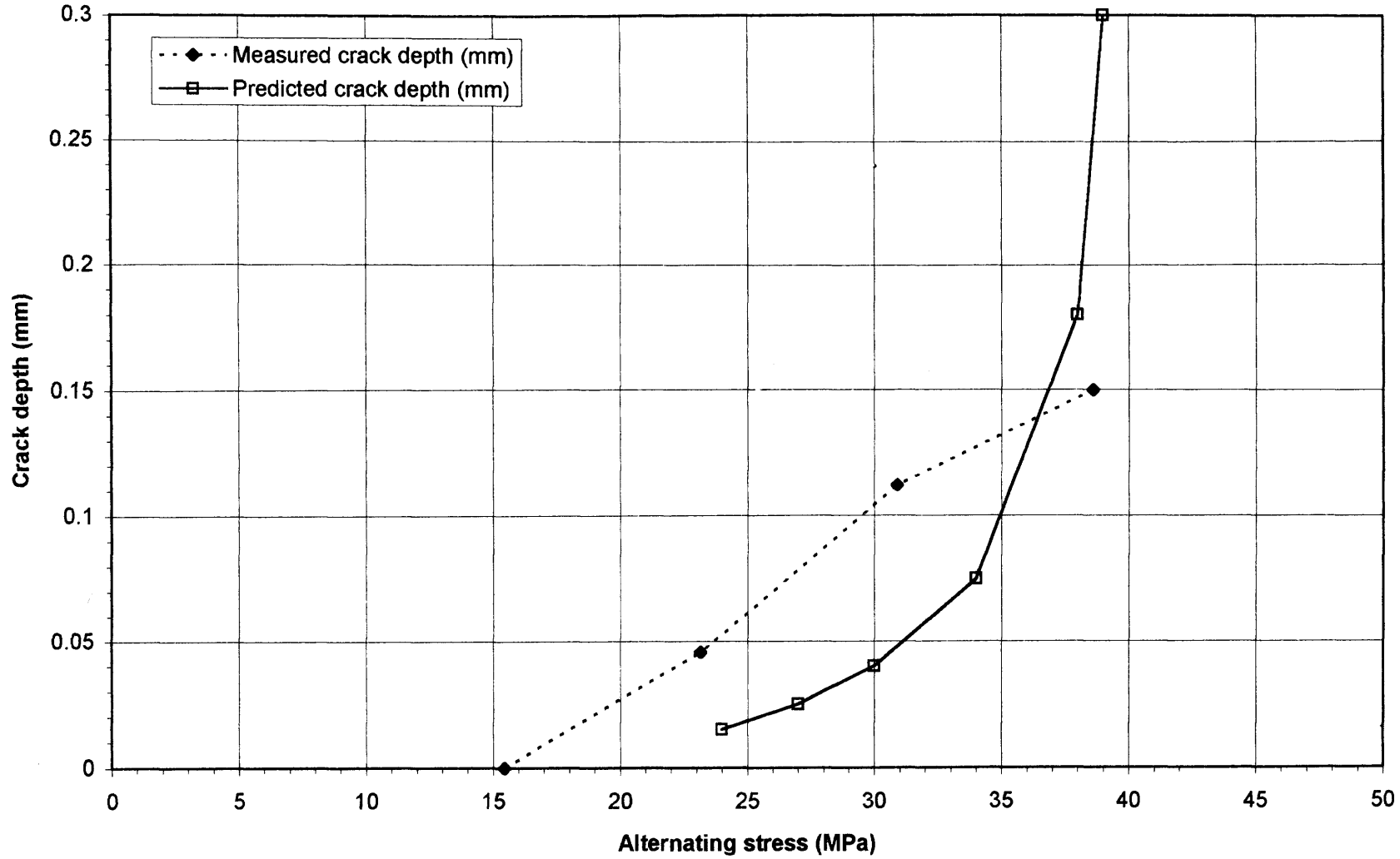


Figure 6.76 Comparison of fatigue strength predictions with experimental notched fatigue test results from Frost (1955) and predictions from Abdel-Raouf et al (1992) - Kitagawa Diagram

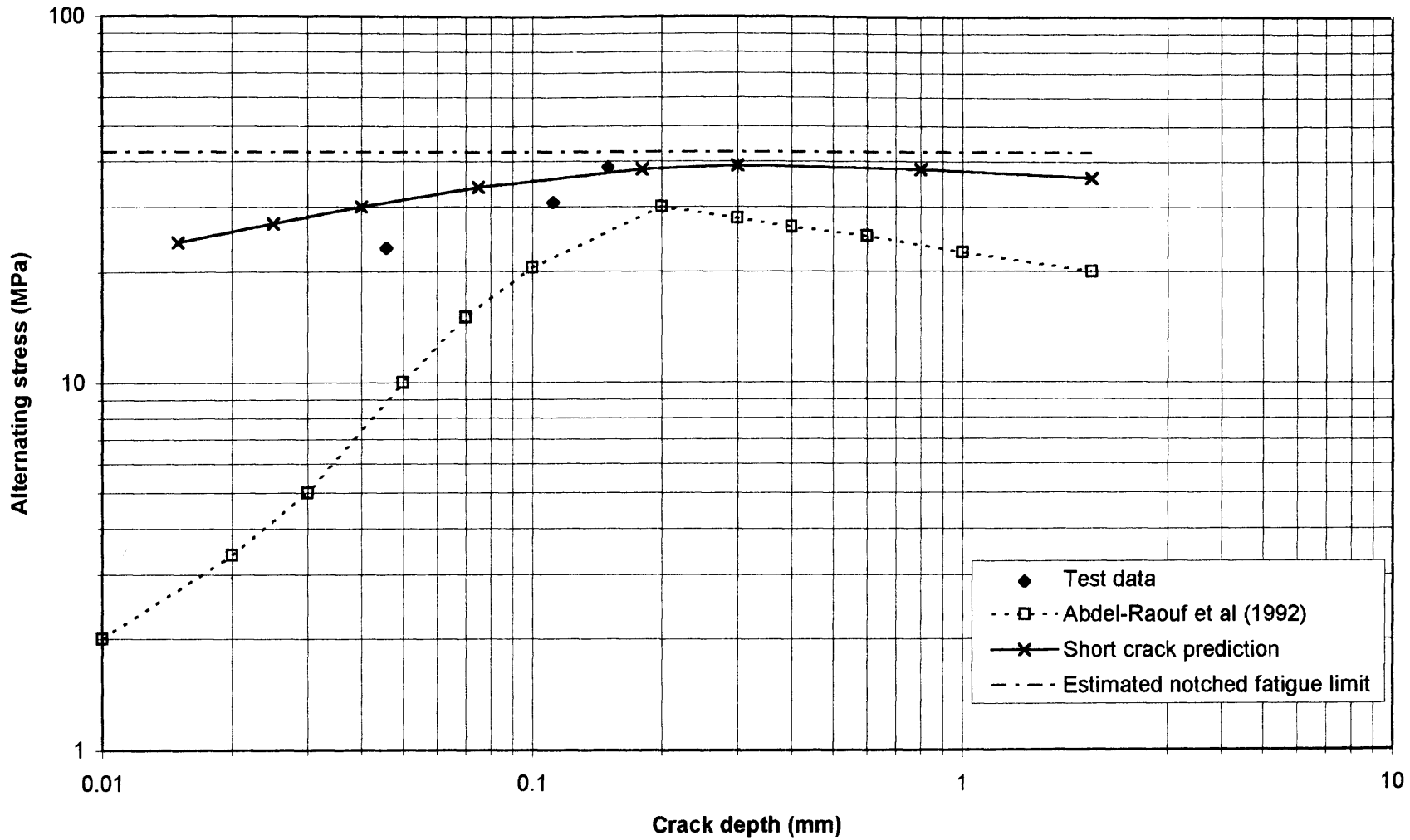


Figure 6.77 Kitagawa diagram for aluminium alloy BS L65 plain specimens (Frost, 1955a) using $\Delta K_{th} = 4.2 \text{ MPa root m}$ (Abdel-Raouf et al, 1992)

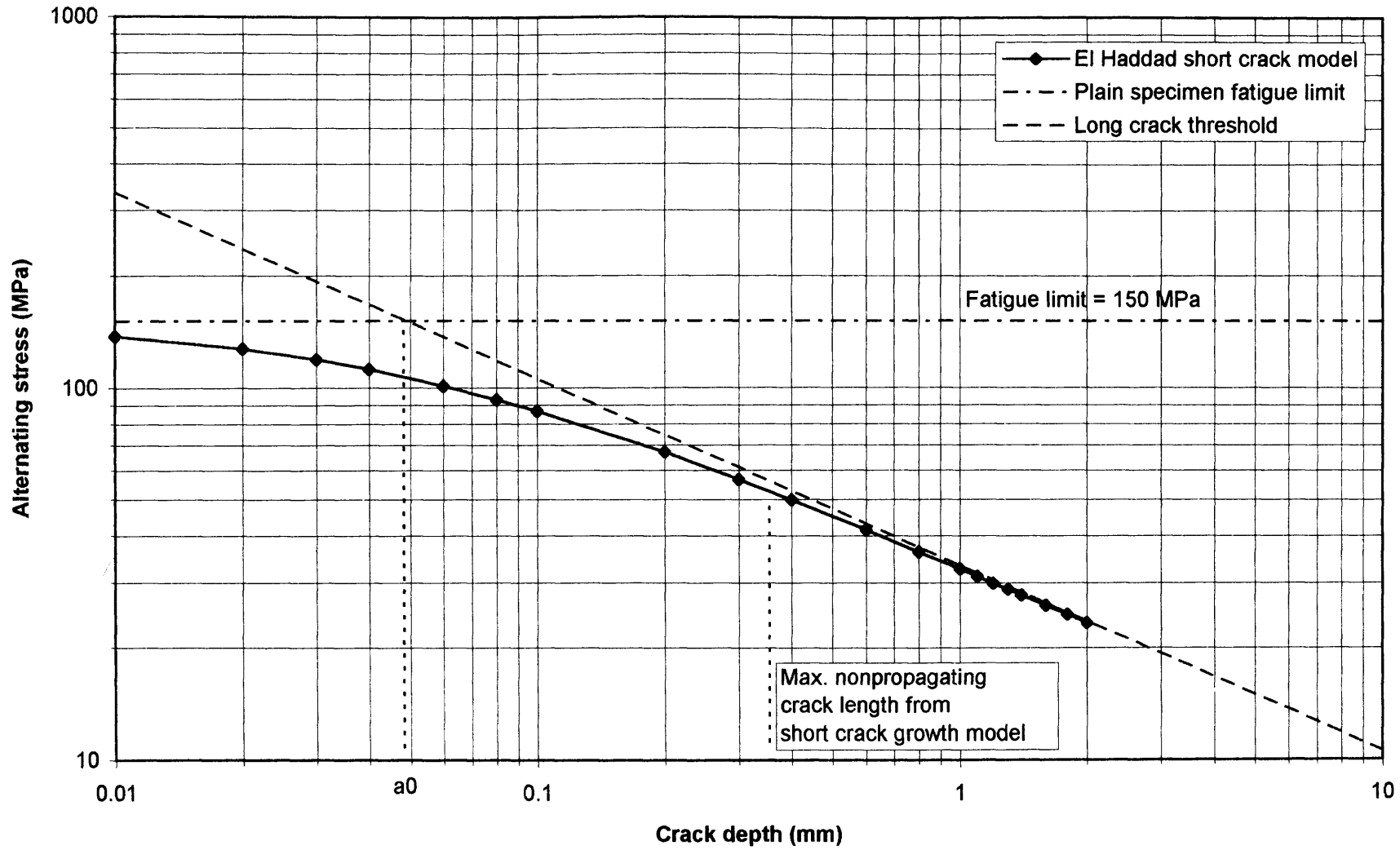


Figure 6.78 BCIRA Grade 250 Grey Cast Iron
Predicted Apparent Short Crack Growth Threshold (Smith's Model) - Continuous Surface Crack
(R=0.05)

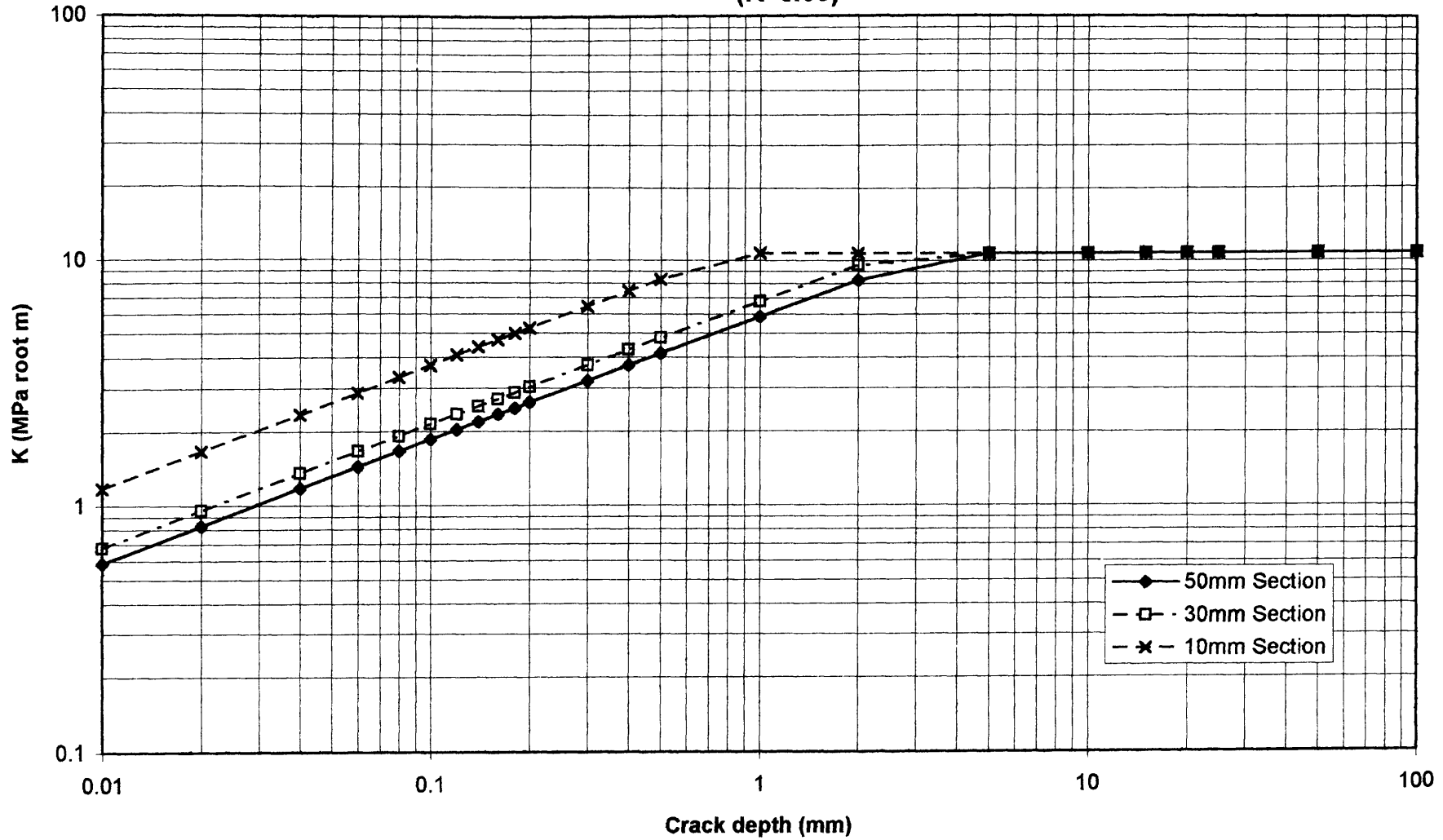


Figure 6.79 BCIRA n7a1 (10mm Cast Section Size, $K_t = 1.526$, Grade 250 Grey Iron)
Comparison of Predicted Fatigue Strengths using Smith's Threshold Model and Experimental Results

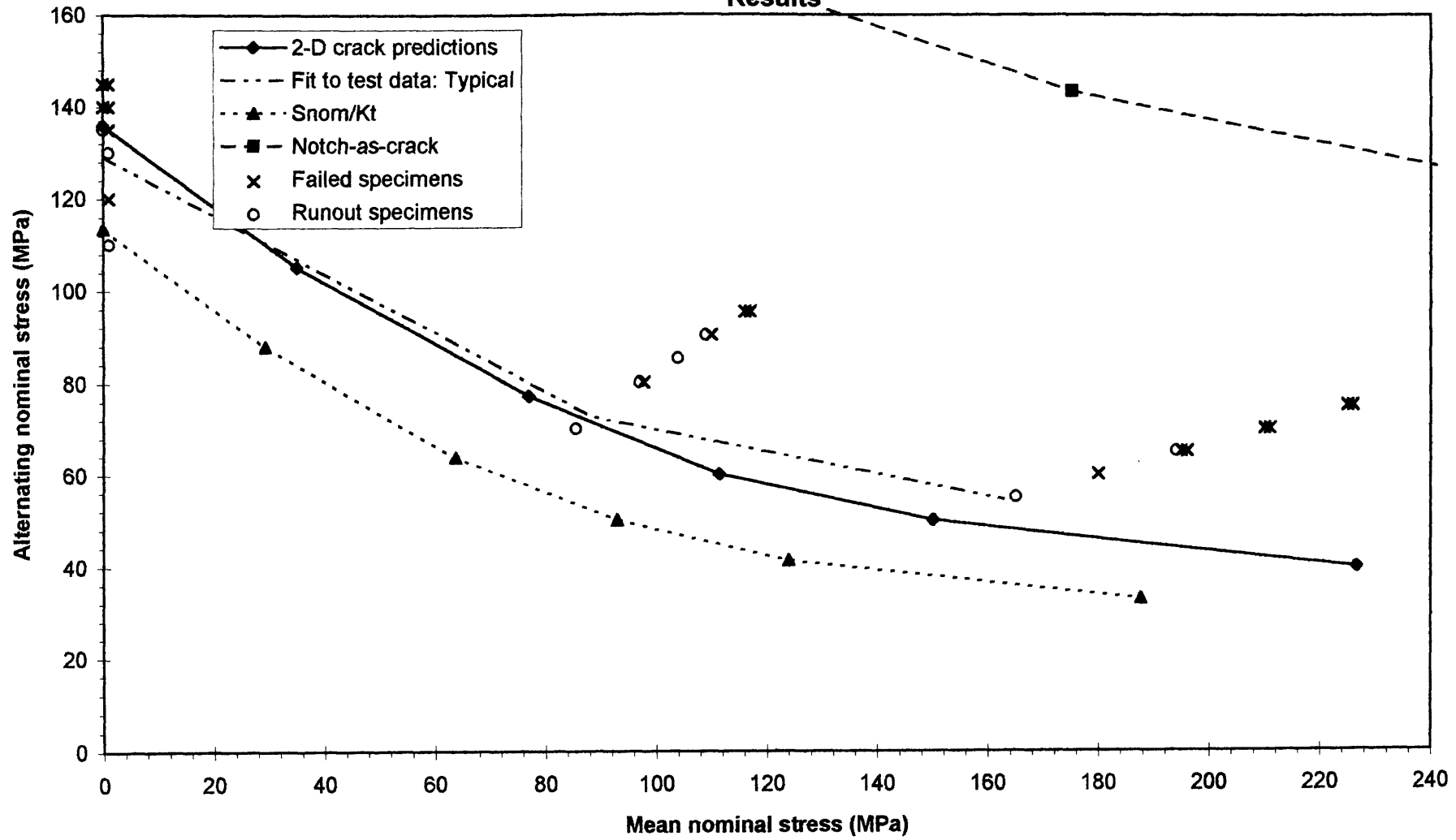


Figure 6.80 BCIRA n7a1 Applied Delta K and Threshold Delta K (Smith's Model) Versus Crack Depth

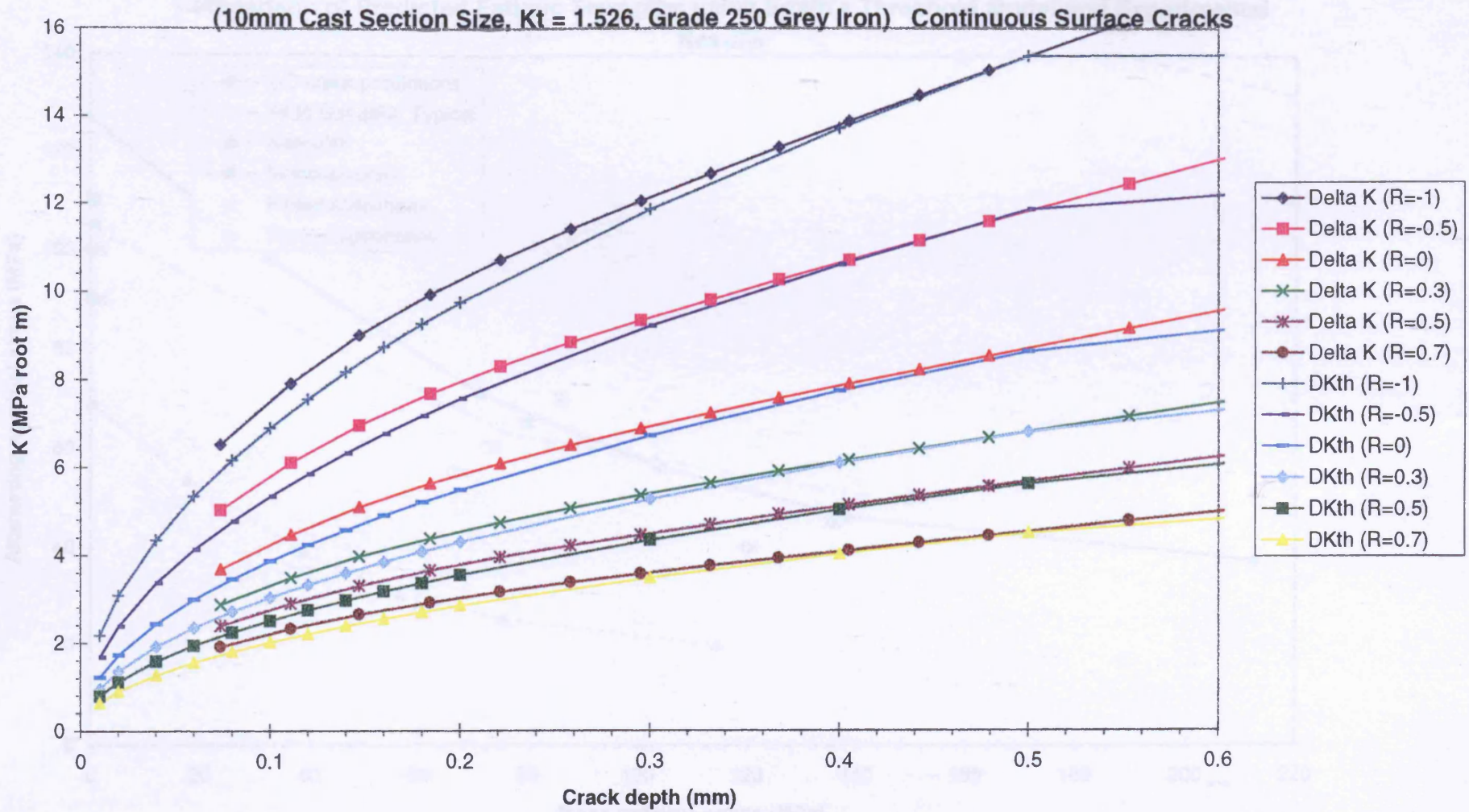


Figure 6.81 BCIRA n7a2 (10mm Cast Section Size, $K_t = 2.5$, Grade 250 Grey Iron)
Comparison of Predicted Fatigue Strengths using Smith's Threshold Model and Experimental Results

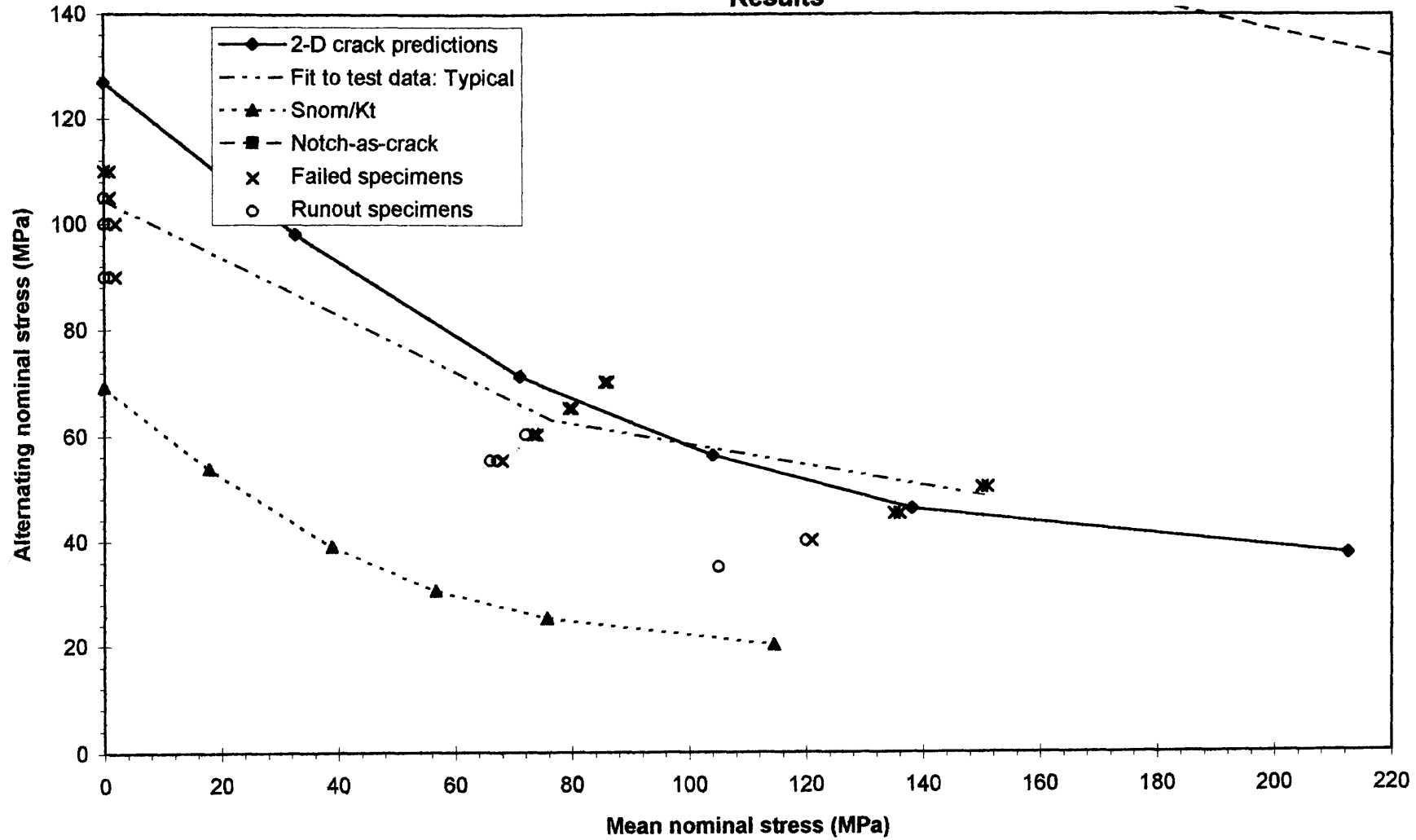
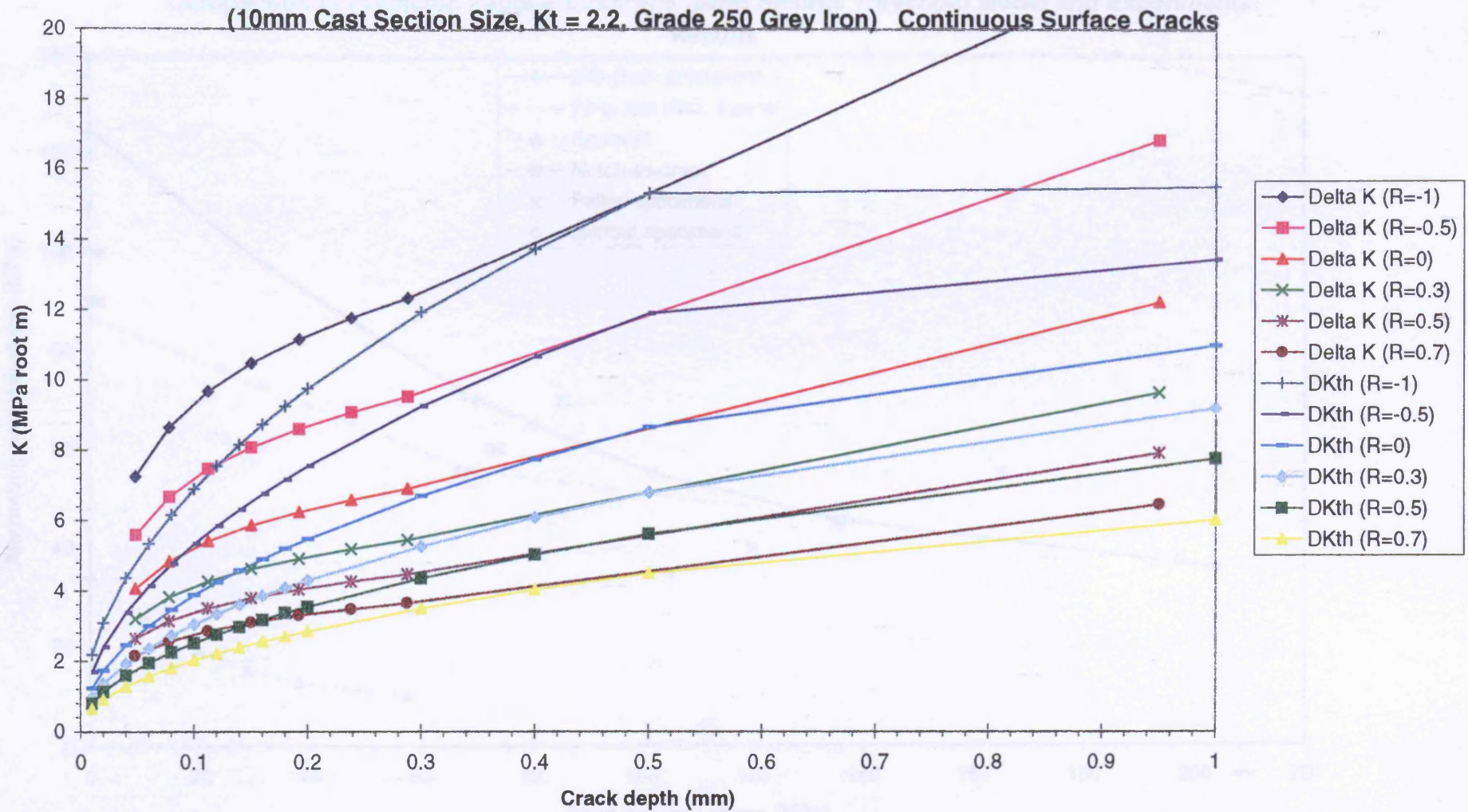


Figure 6.82 BCIRA n7a2 Applied Delta K and Threshold Delta K (Smith's Model) Versus Crack Depth



**Figure 6.83 BCIRA n7a3 (10mm Cast Section Size, $K_t = 5.0$, Grade 250 Grey Iron)
Comparison of Predicted Fatigue Strengths using Smith's Threshold Model and Experimental Results**

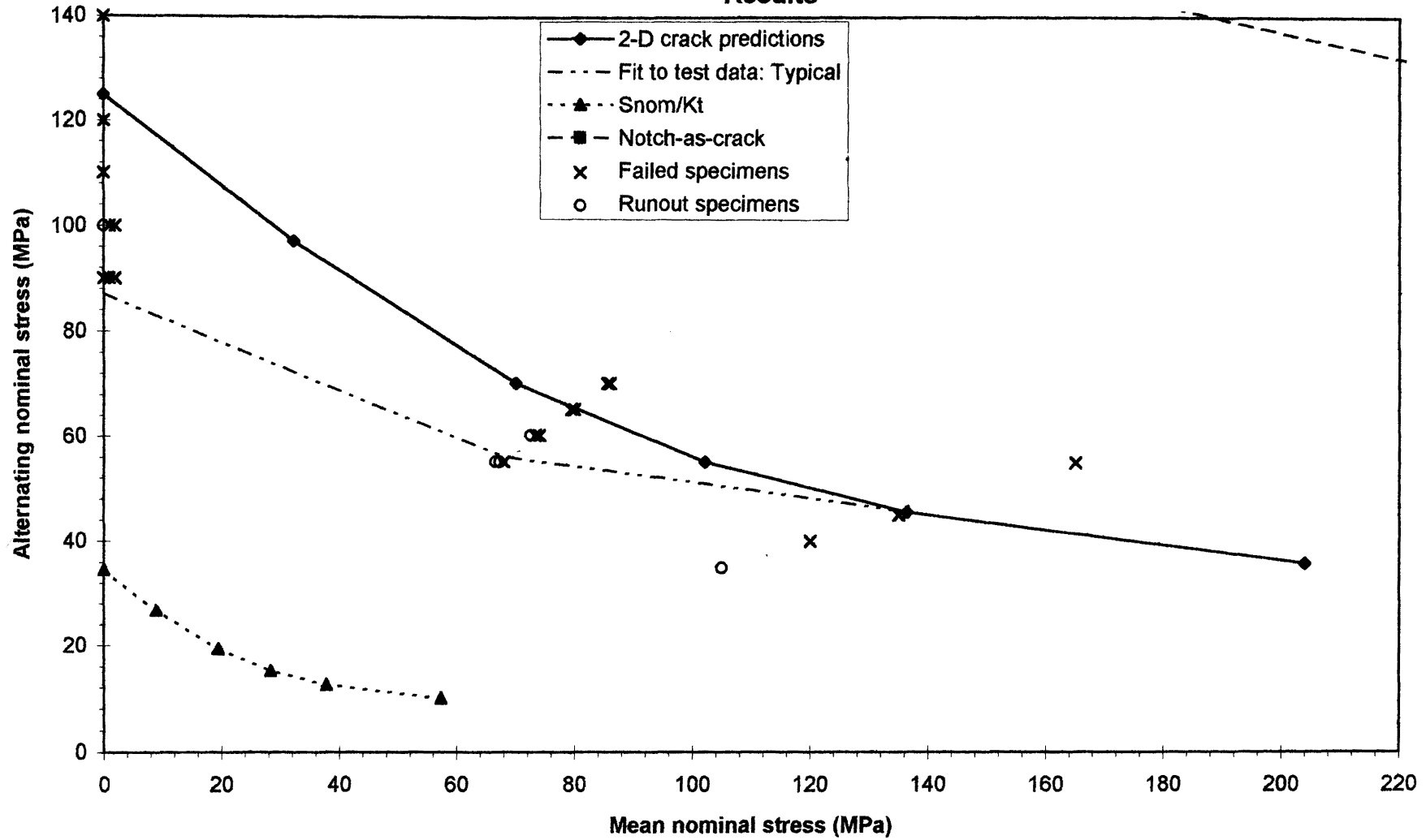


Figure 6.84 BCIRA n7a3 Applied Delta K and Threshold Delta K (Smith's Model) Versus Crack Depth
 (10mm Cast Section Size, $K_t = 5$, Grade 250 Grey Iron) Continuous Surface Cracks

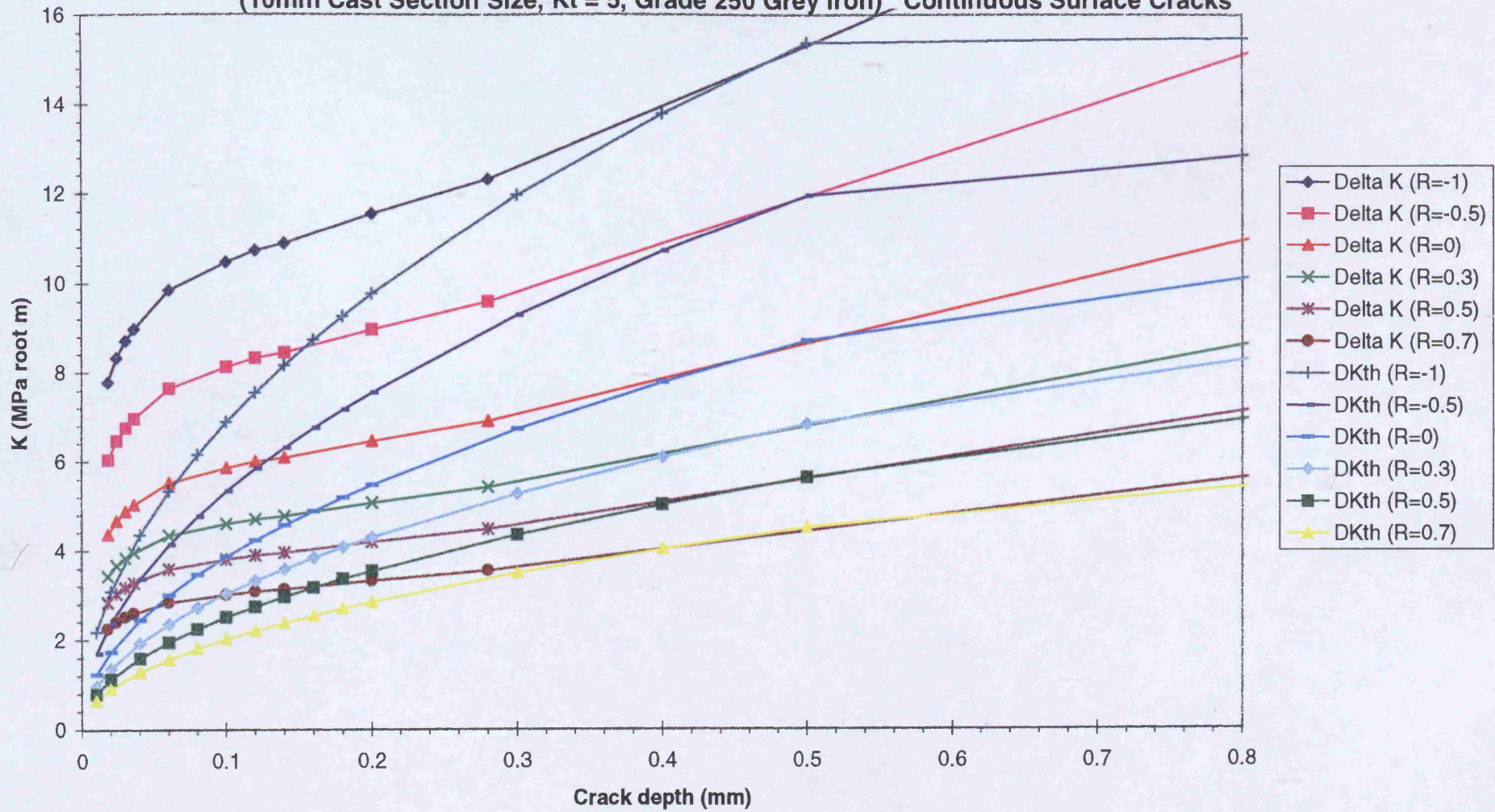


Figure 6.85 BCIRA n12a1 (30mm Cast Section Size, $K_t = 1.5$, Grade 250 Grey Iron)
Comparison of Predicted Fatigue Strengths using Smith's Threshold Model and Experimental Results

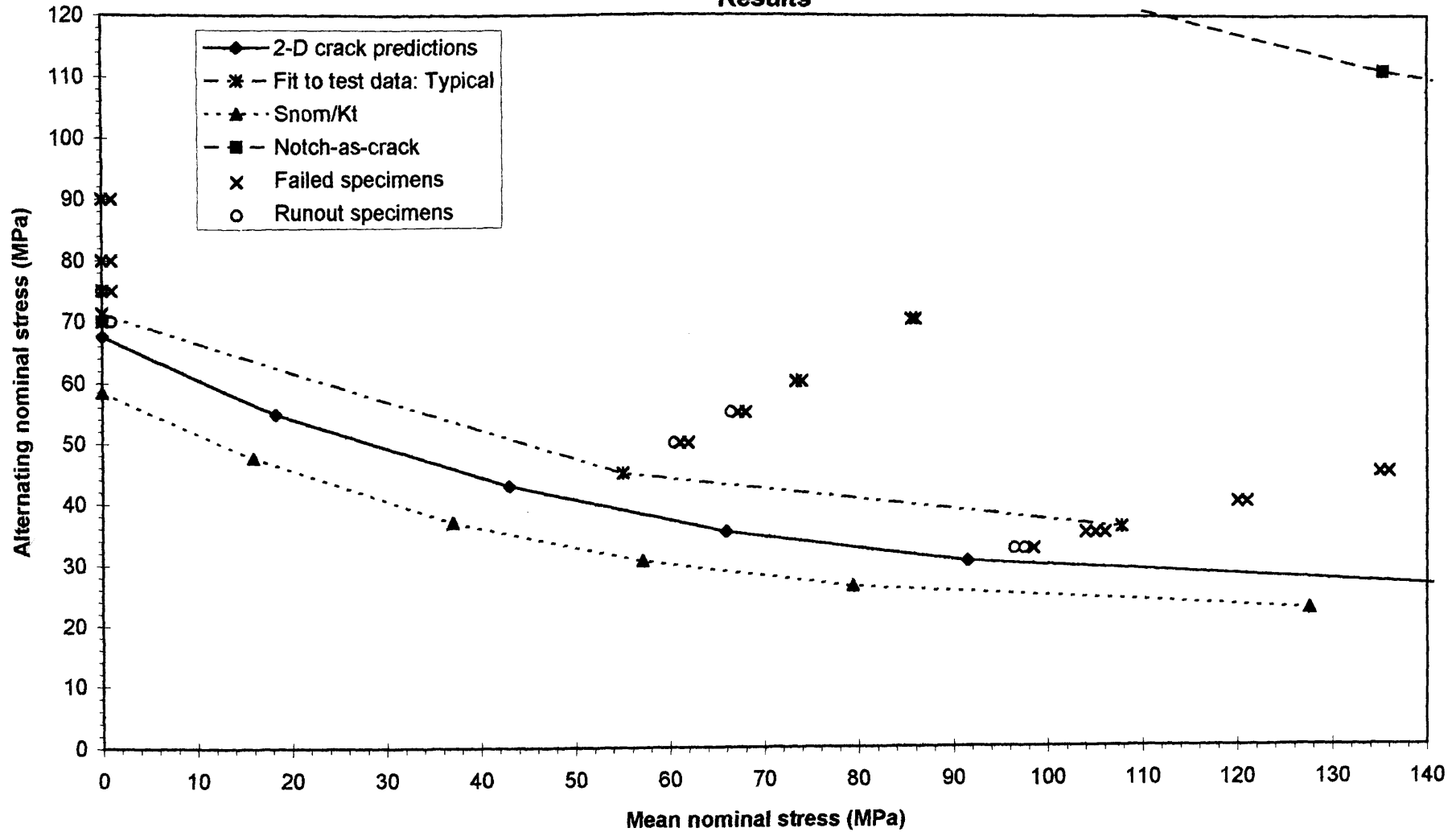
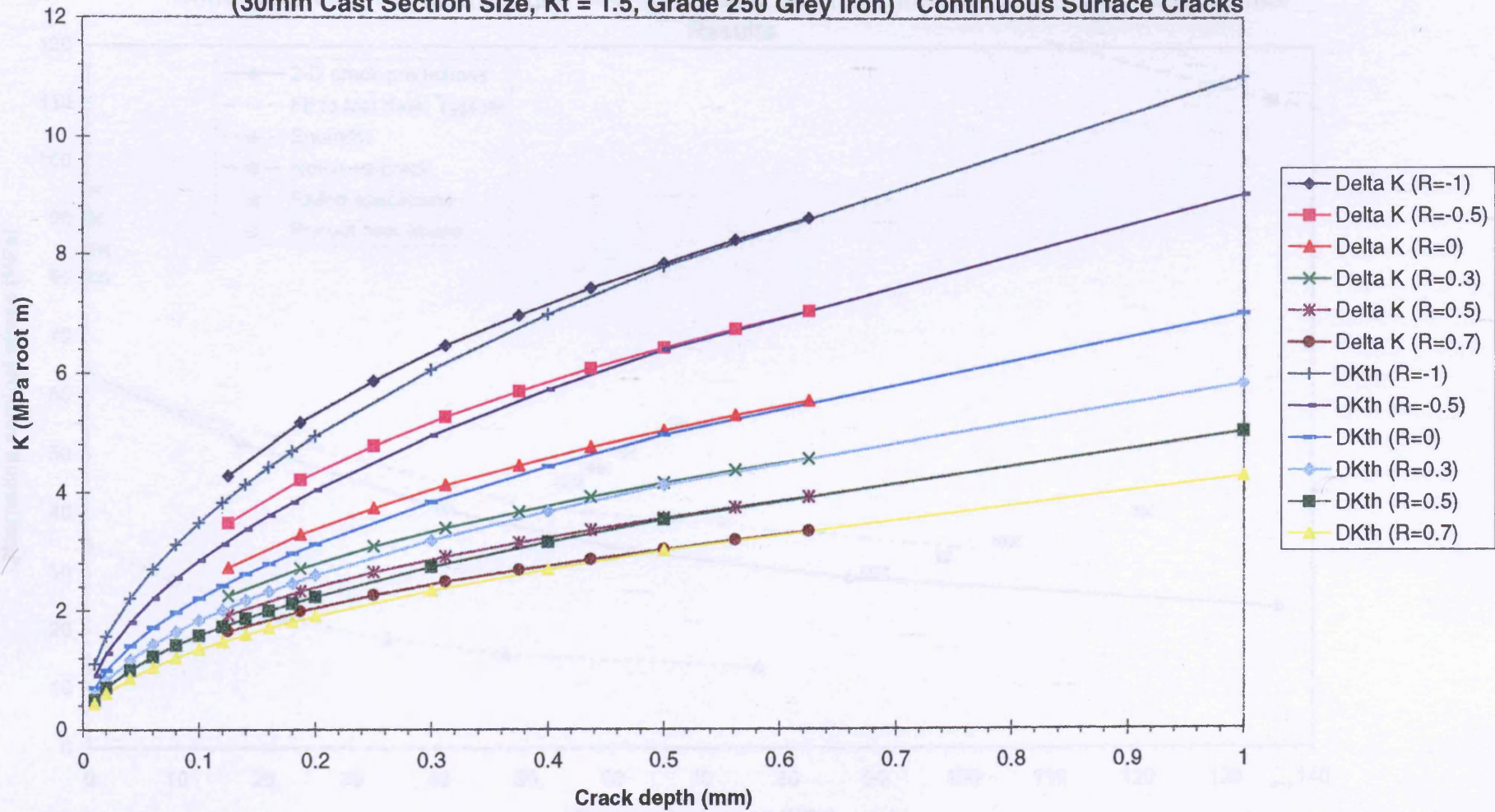


Figure 6.86 BCIRA n12a1 Applied Delta K and Threshold Delta K (Smith's Model) Versus Crack Depth
 (30mm Cast Section Size, $K_t = 1.5$, Grade 250 Grey Iron) Continuous Surface Cracks



**Figure 6.87 BCIRA n12a2 (30mm Cast Section Size, $K_t = 2.5$, Grade 250 Grey Iron)
Comparison of Predicted Fatigue Strengths using Smith's Threshold Model and Experimental Results**

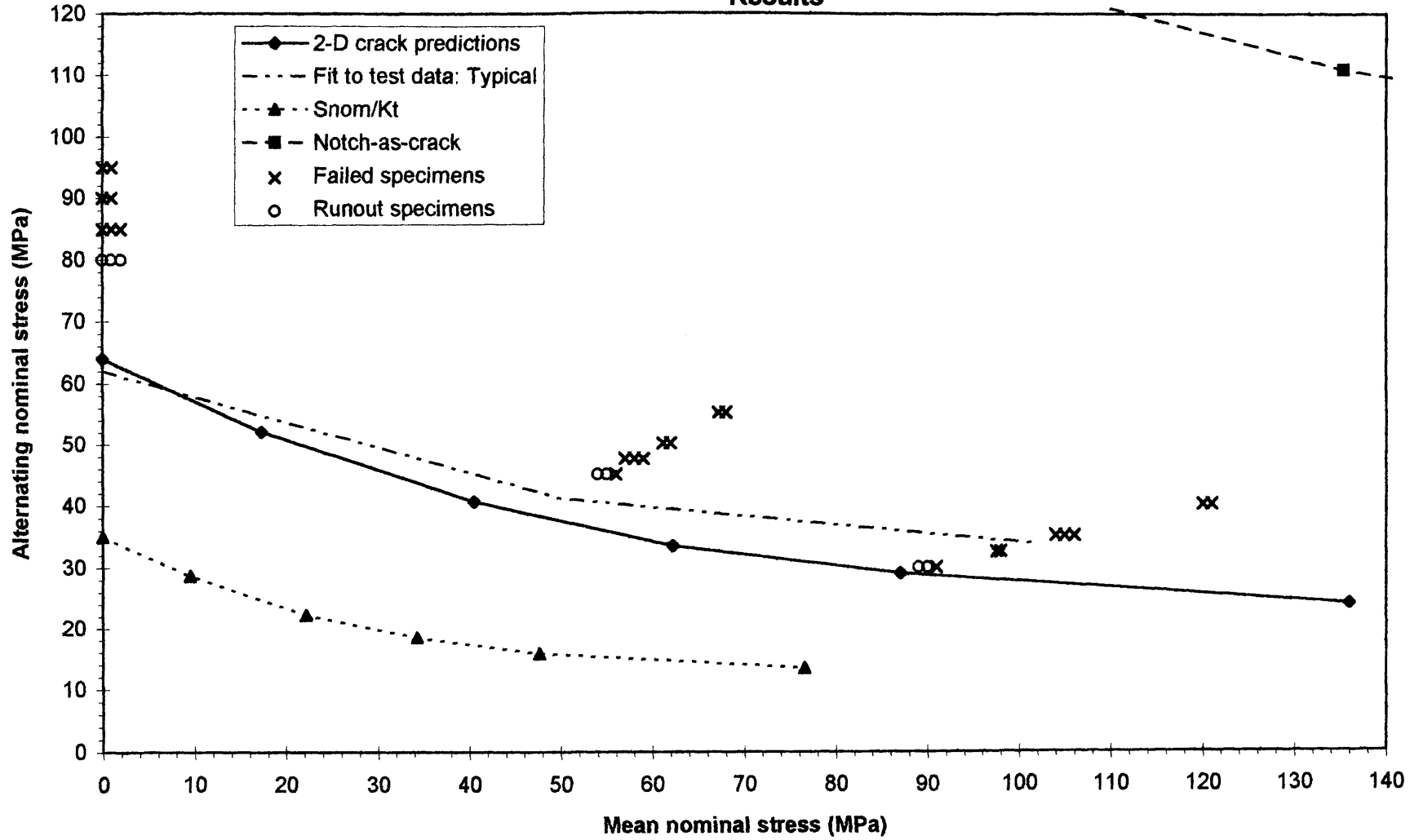


Figure 6.88 BCIRA n12a2 Applied Delta K and Threshold Delta K (Smith's Model) Versus Crack Depth
 (30mm Cast Section Size, $K_t = 2.5$, Grade 250 Grey Iron) Continuous Surface Cracks

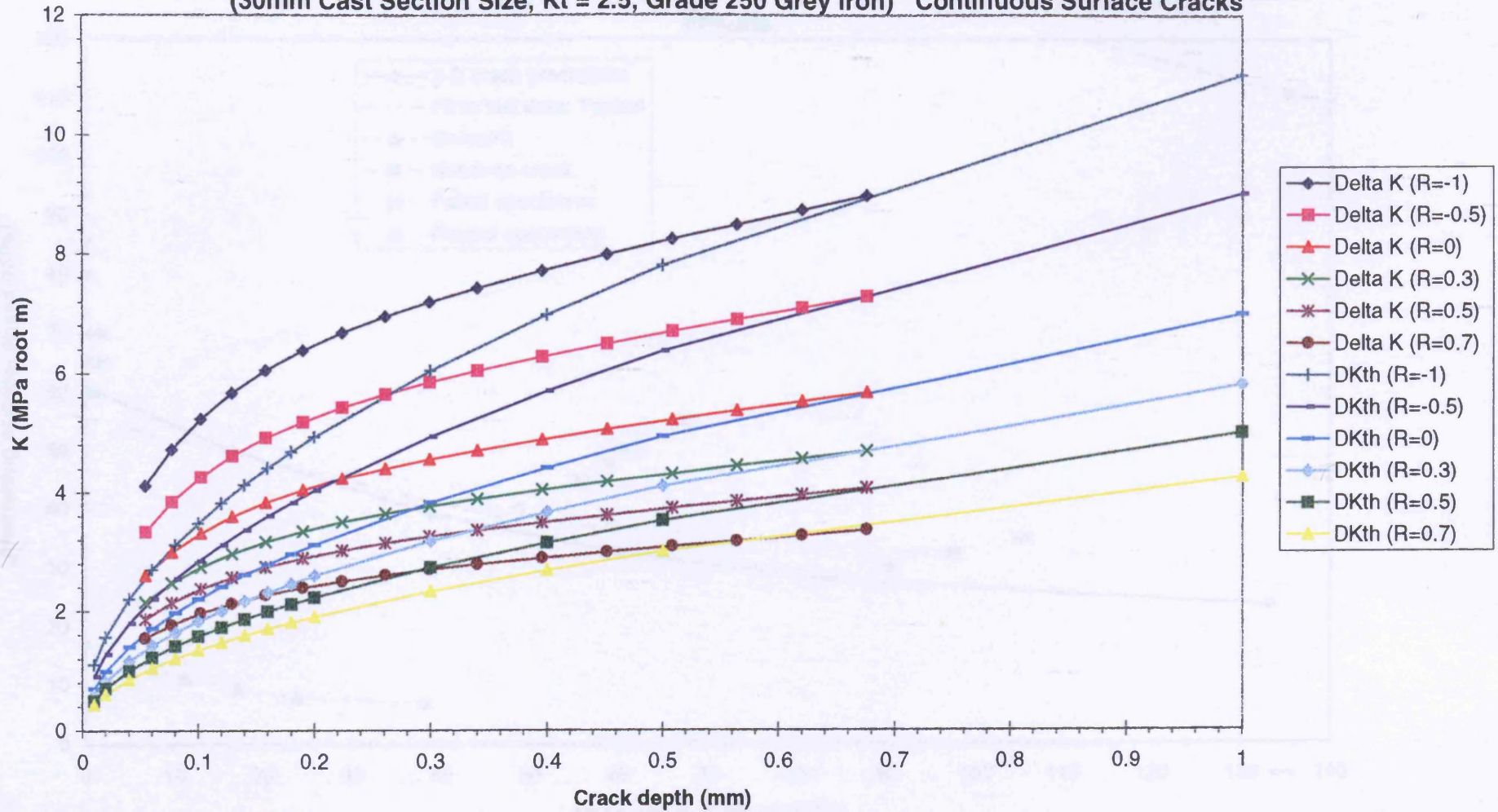


Figure 6.89 BCIRA n12a3 (30mm Cast Section Size, $K_t = 5.0$, Grade 250 Grey Iron)
Comparison of Predicted Fatigue Strengths using Smith's Threshold Model and Experimental Results

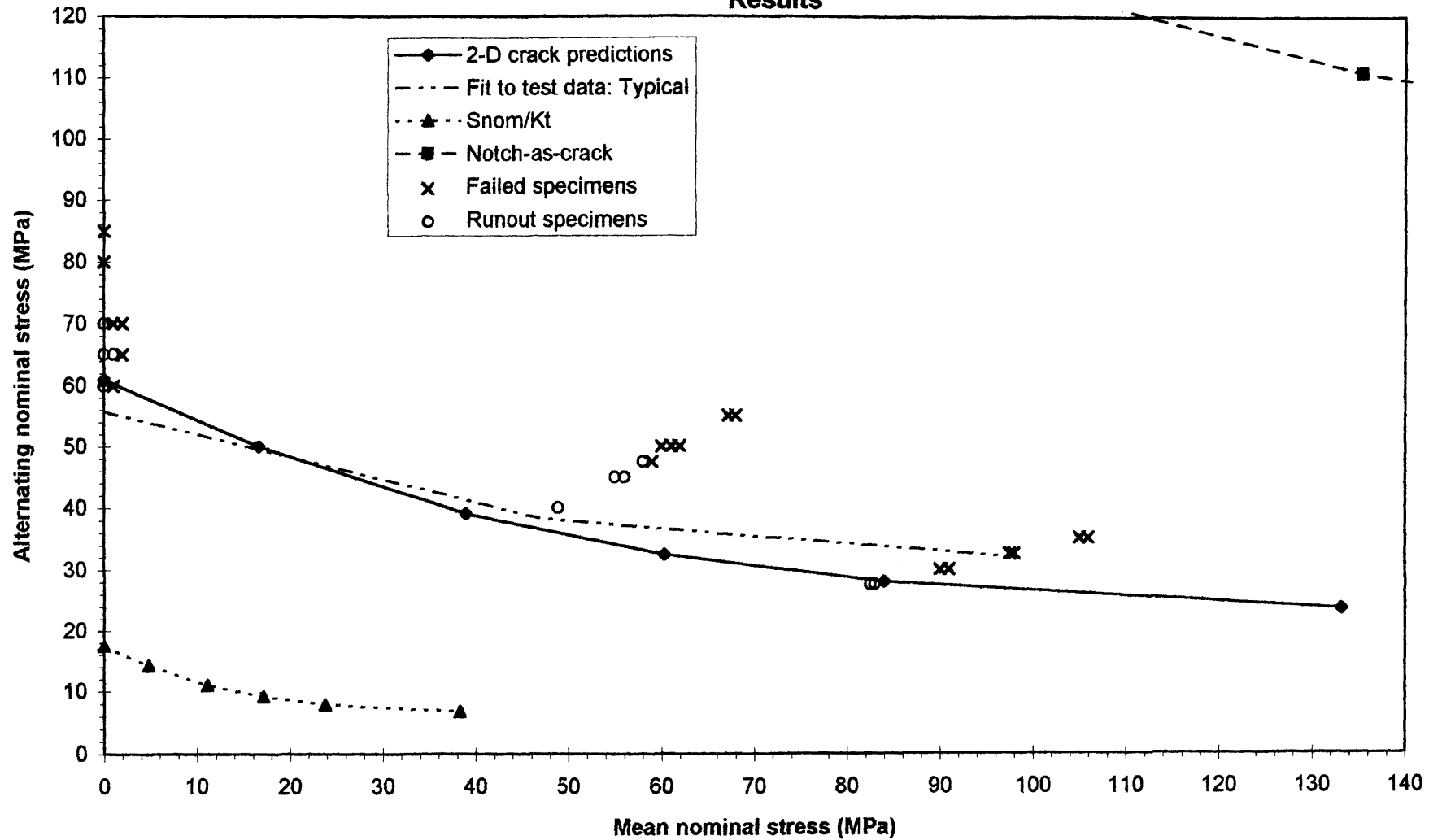


Figure 6.90 BCIRA n12a3 Applied Delta K and Threshold Delta K (Smith's Model) Versus Crack Depth

(30mm Cast Section Size, $K_t = 5$, Grade 250 Grey Iron) Continuous Surface Cracks

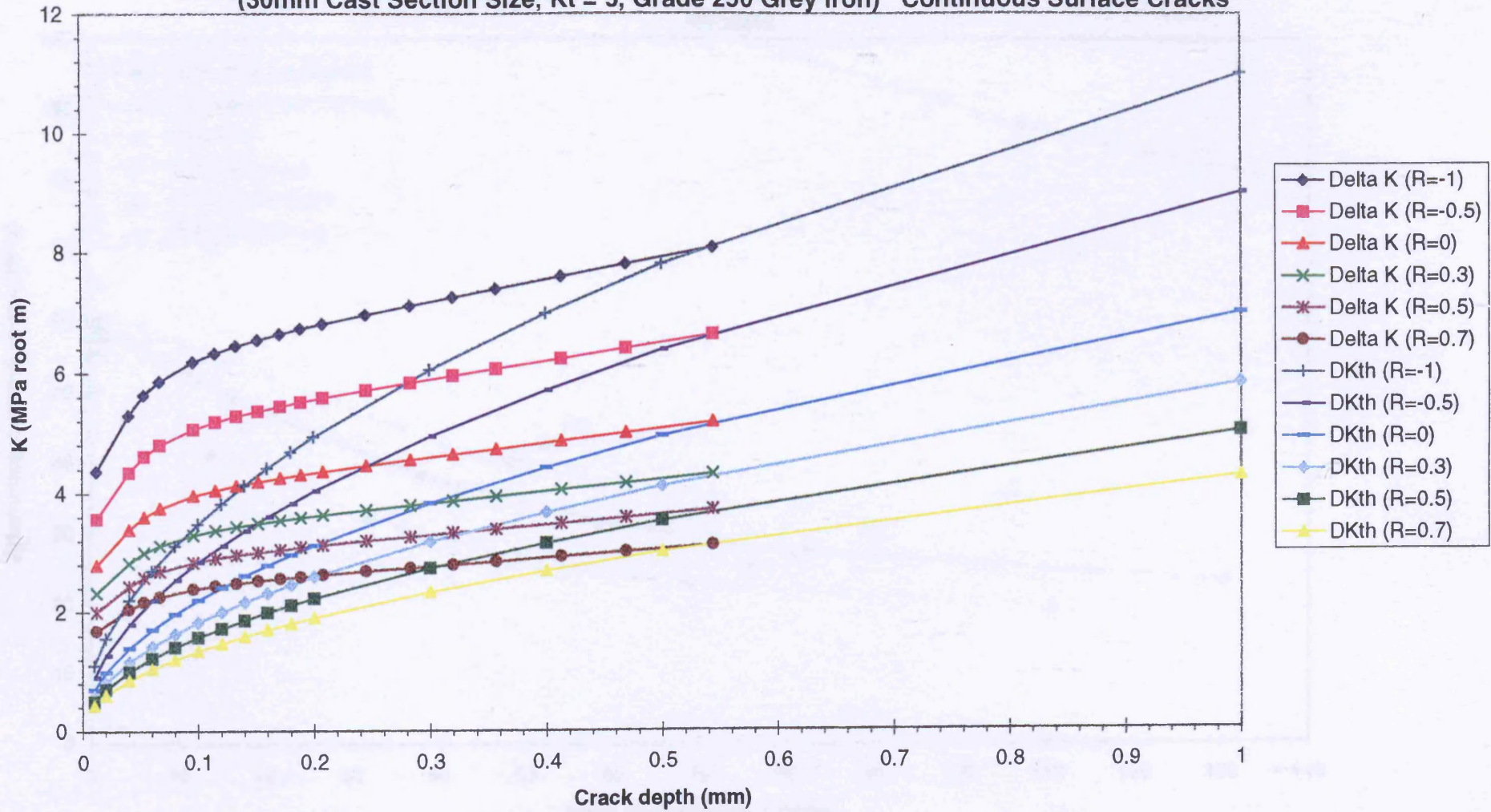


Figure 6.91 BCIRA n20a1 (50mm Cast Section Size, $K_t = 1.5$, Grade 250 Grey Iron)
Comparison of Predicted Fatigue Strengths using Smith's Threshold Model and Experimental Results

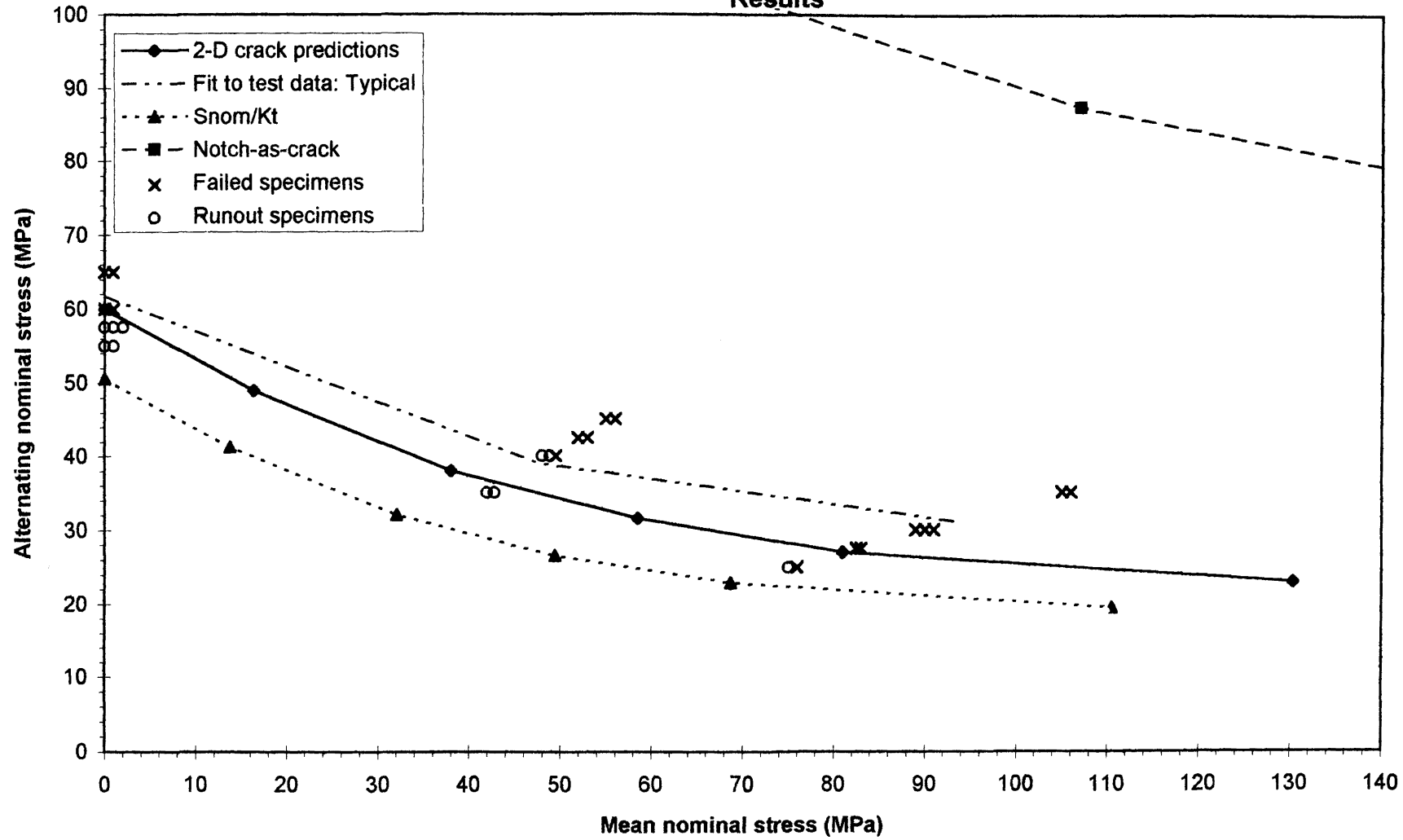


Figure 6.92 BCIRA n20a1 Applied Delta K and Threshold Delta K (Smith's Model) Versus Crack Depth

(50mm Cast Section Size, $K_t = 1.5$, Grade 250 Grey Iron) Continuous Surface Cracks

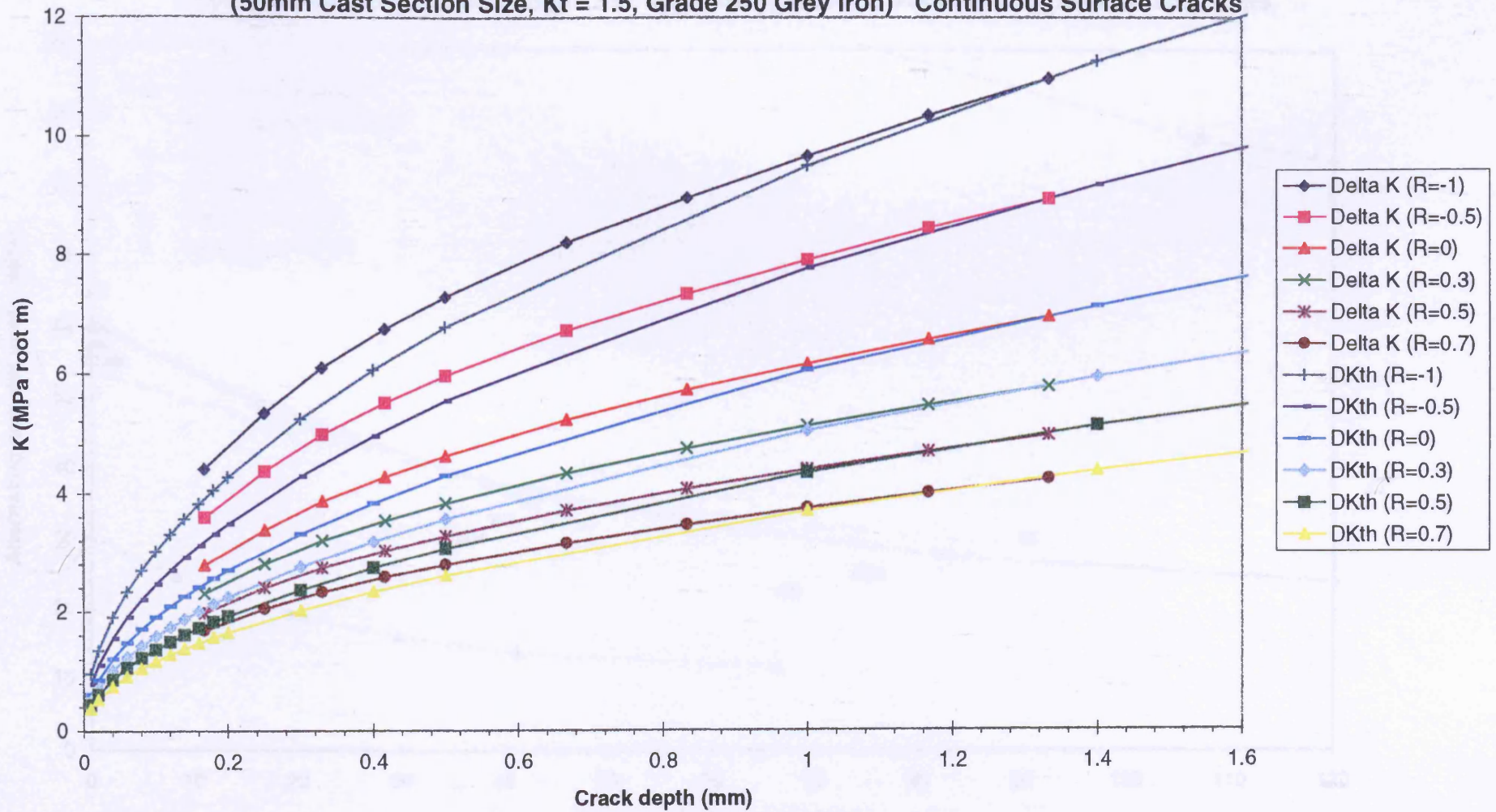


Figure 6.93 BCIRA n20a2 (50mm Cast Section Size, $K_t = 2.5$, Grade 250 Grey Iron)
Comparison of Predicted Fatigue Strengths using Smith's Model and Experimental Results

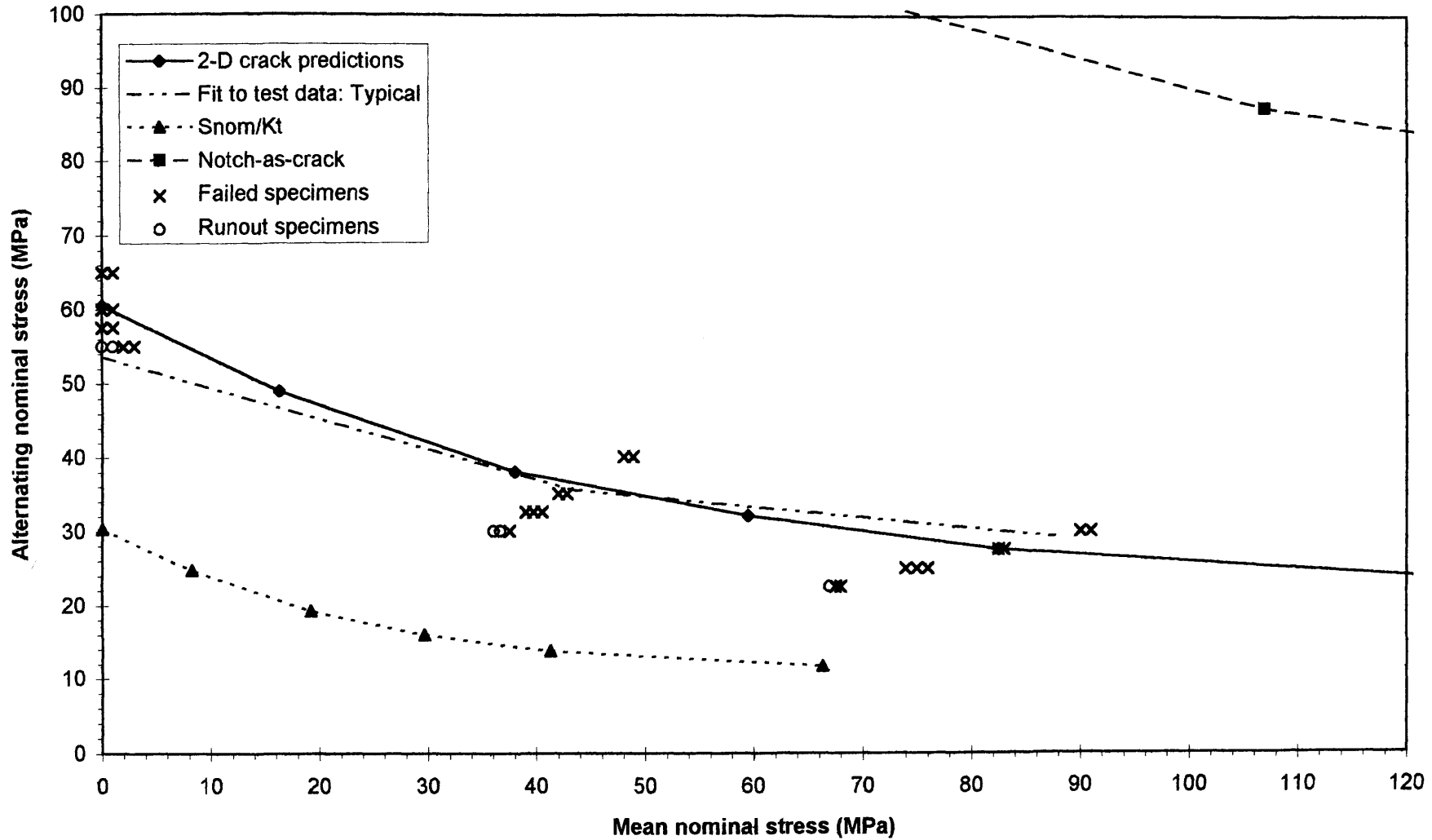


Figure 6.94 BCIRA n20a2 Applied Delta K and Threshold Delta K (Smith's Model) Versus Crack Depth

(50mm Cast Section Size, $K_t = 2.5$, Grade 250 Grey Iron) Continuous Surface Cracks

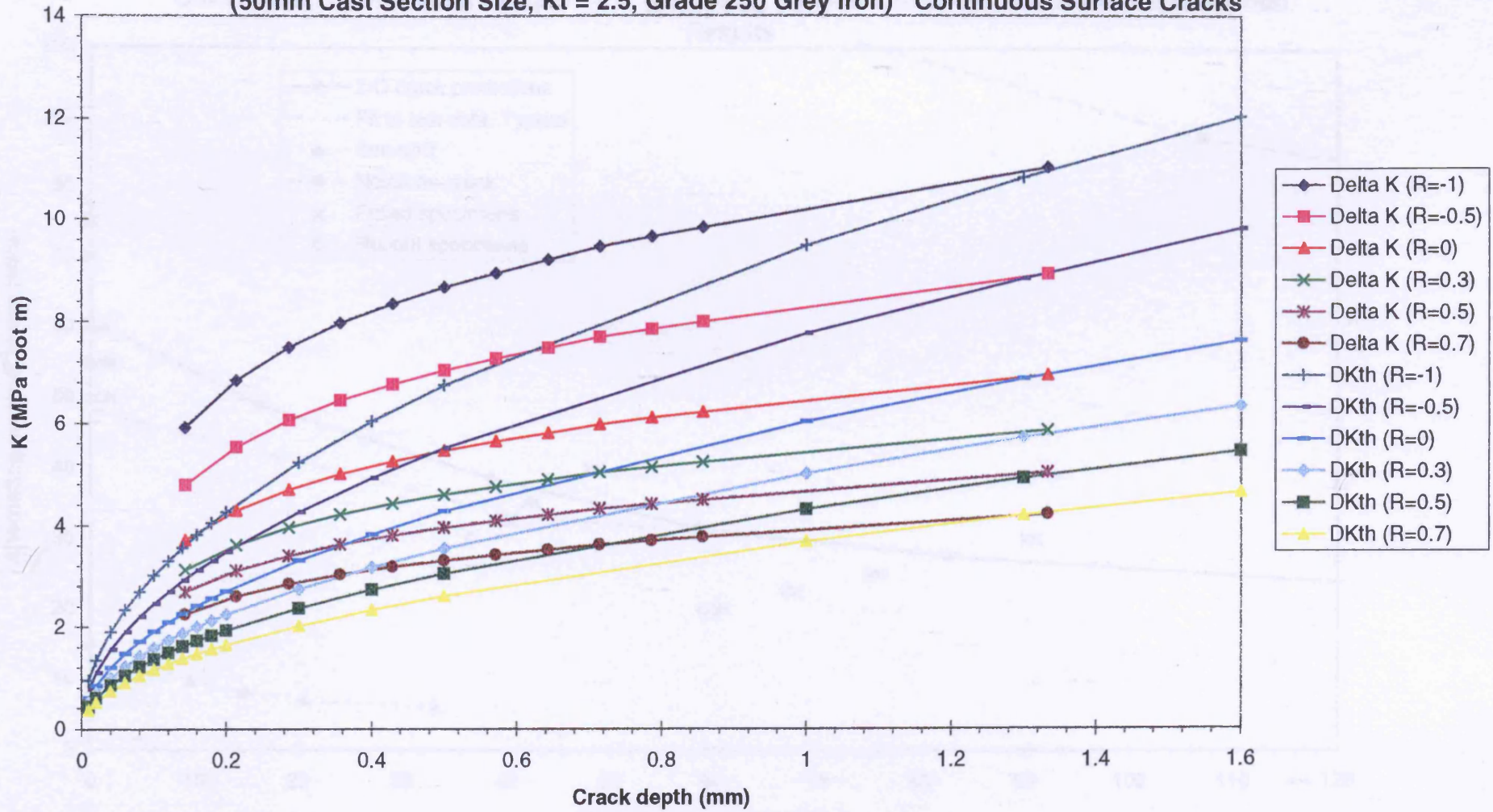


Figure 6.95 BCIRA n20a3 (50mm Cast Section Size, $K_t = 5.0$, Grade 250 Grey Iron)
Comparison of Predicted Fatigue Strengths using Smith's Threshold Model and Experimental Results

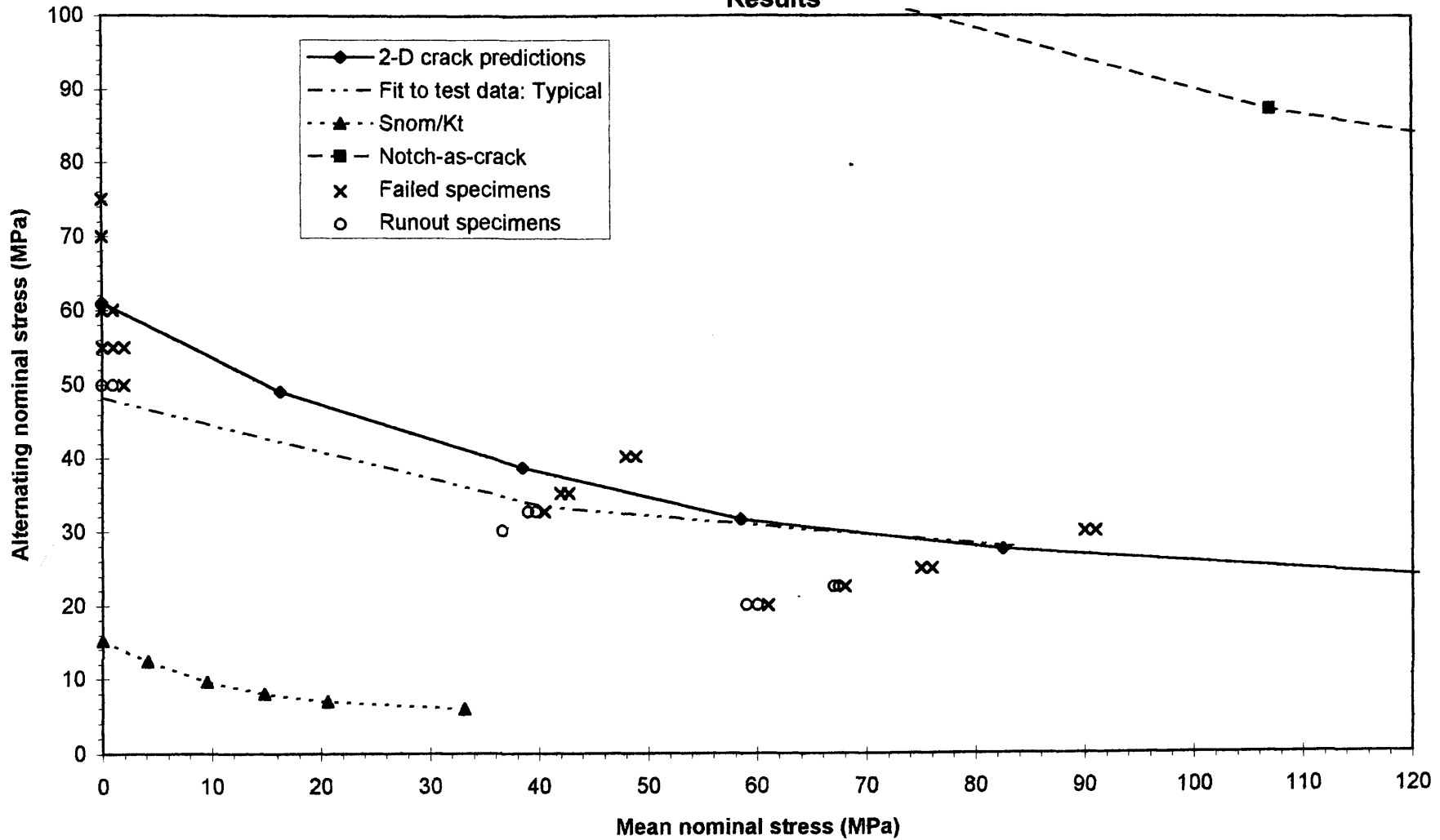


Figure 6.96 BCIRA n20a3 Applied Delta K and Threshold Delta K (Smith's Model) Versus Crack Depth

(50mm Cast Section Size, $K_t = 5$, Grade 250 Grey Iron) Continuous Surface Cracks

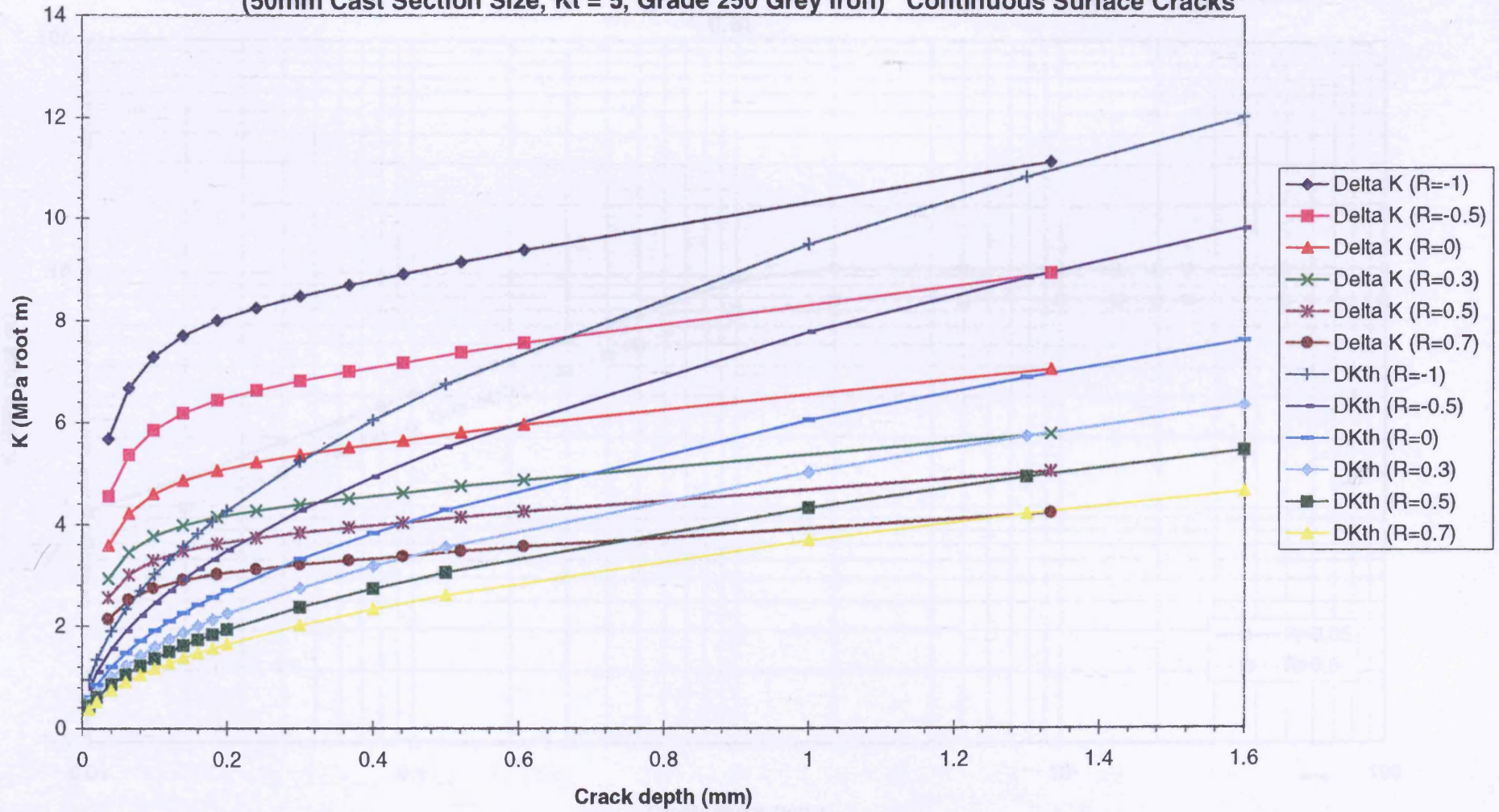


Figure 6.97 BCIRA Grade 350 Grey Cast Iron
Predicted Apparent Short Crack Threshold (Smith's Model) - Continuous Surface crack (R=0.05 & 0.5)

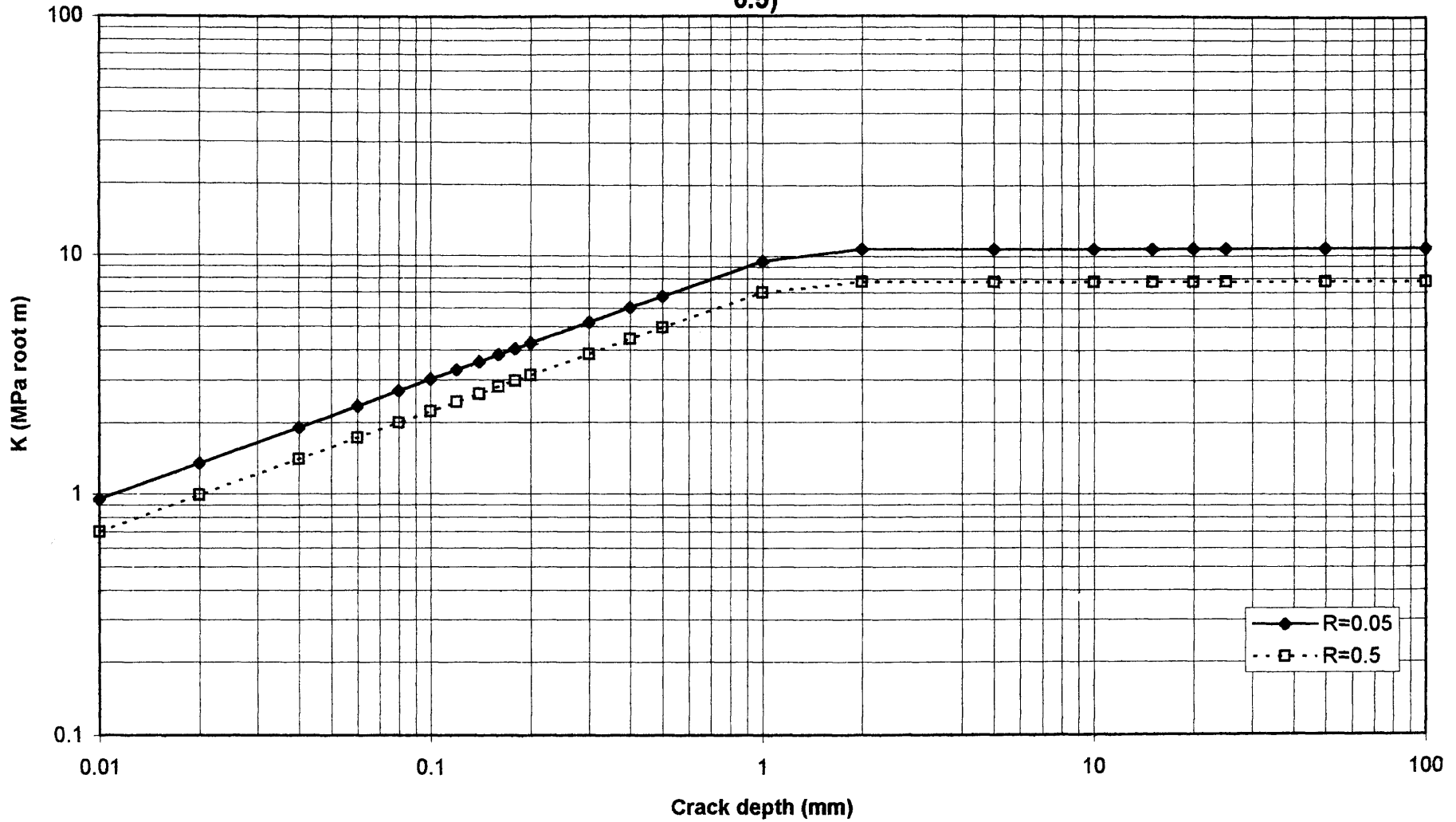


Figure 6.98 BCIRA n12b1 (30mm Cast Section Size, $K_t = 1.5$, Grade 350 Grey Iron)
Comparison of Predicted Fatigue Strengths using Smith's Threshold Model and Experimental Results

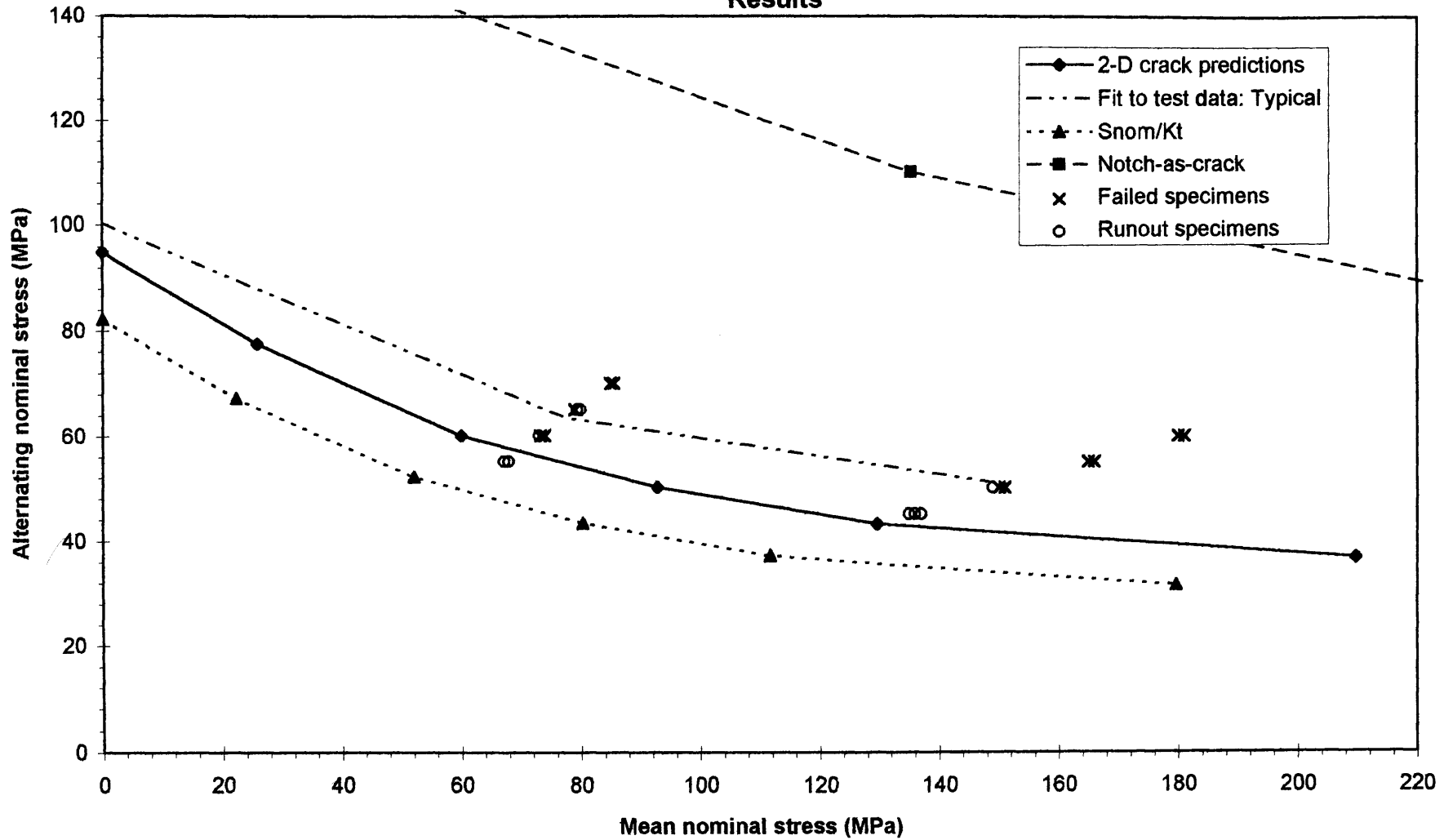


Figure 6.99 BCIRA n12b1 Applied Delta K and Threshold Delta K (Smith's Model) Versus Crack Depth
(30mm Cast Section Size, $K_t = 1.5$, Grade 350 Grey Iron) Continuous Surface Cracks

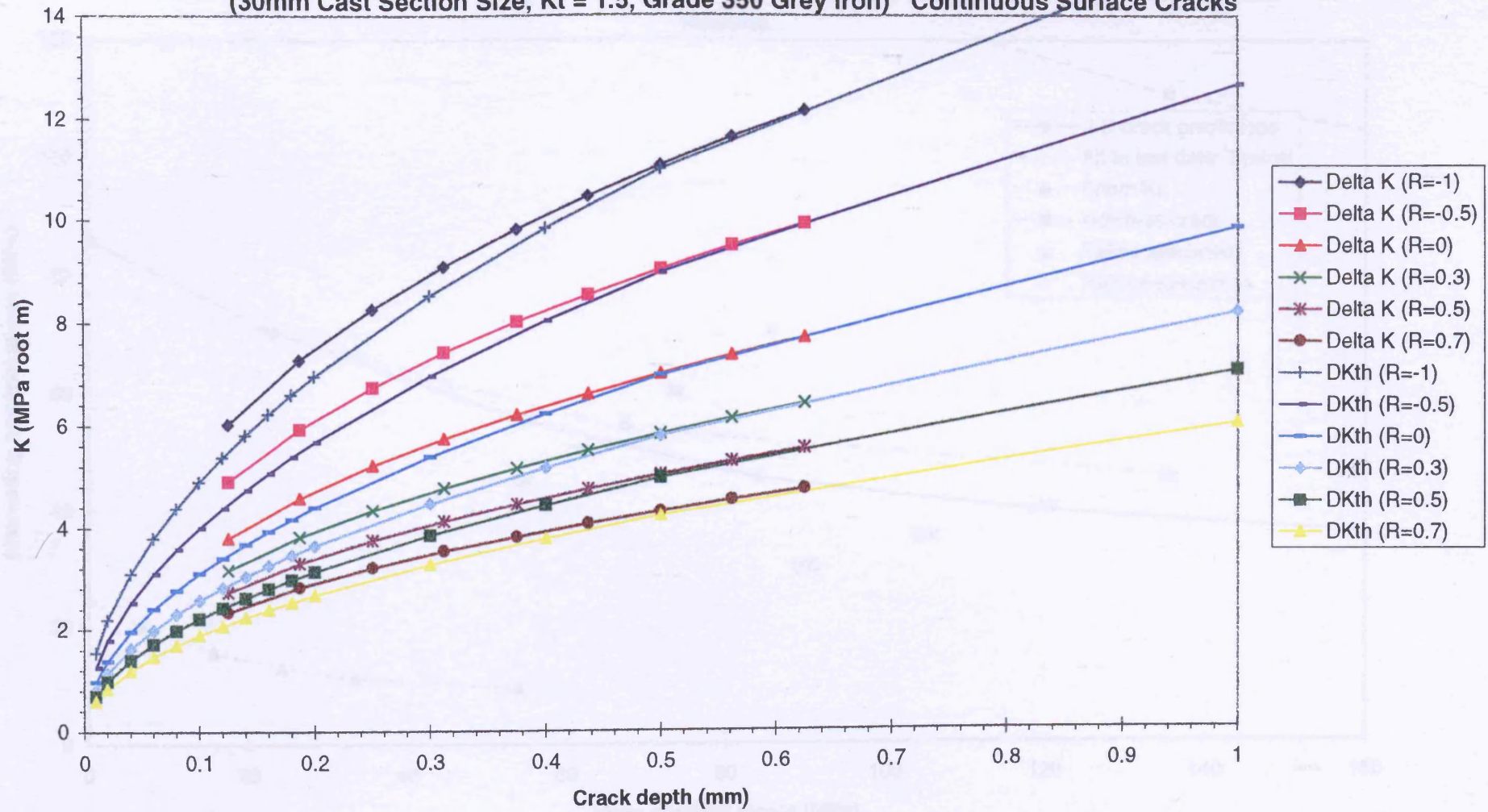


Figure 6.100 BCIRA n12b3 (30mm Cast Section Size, $K_t = 5$, Grade 350 Grey Iron)
Comparison of Predicted Fatigue Strengths using Smith's Threshold Model and Experimental Results

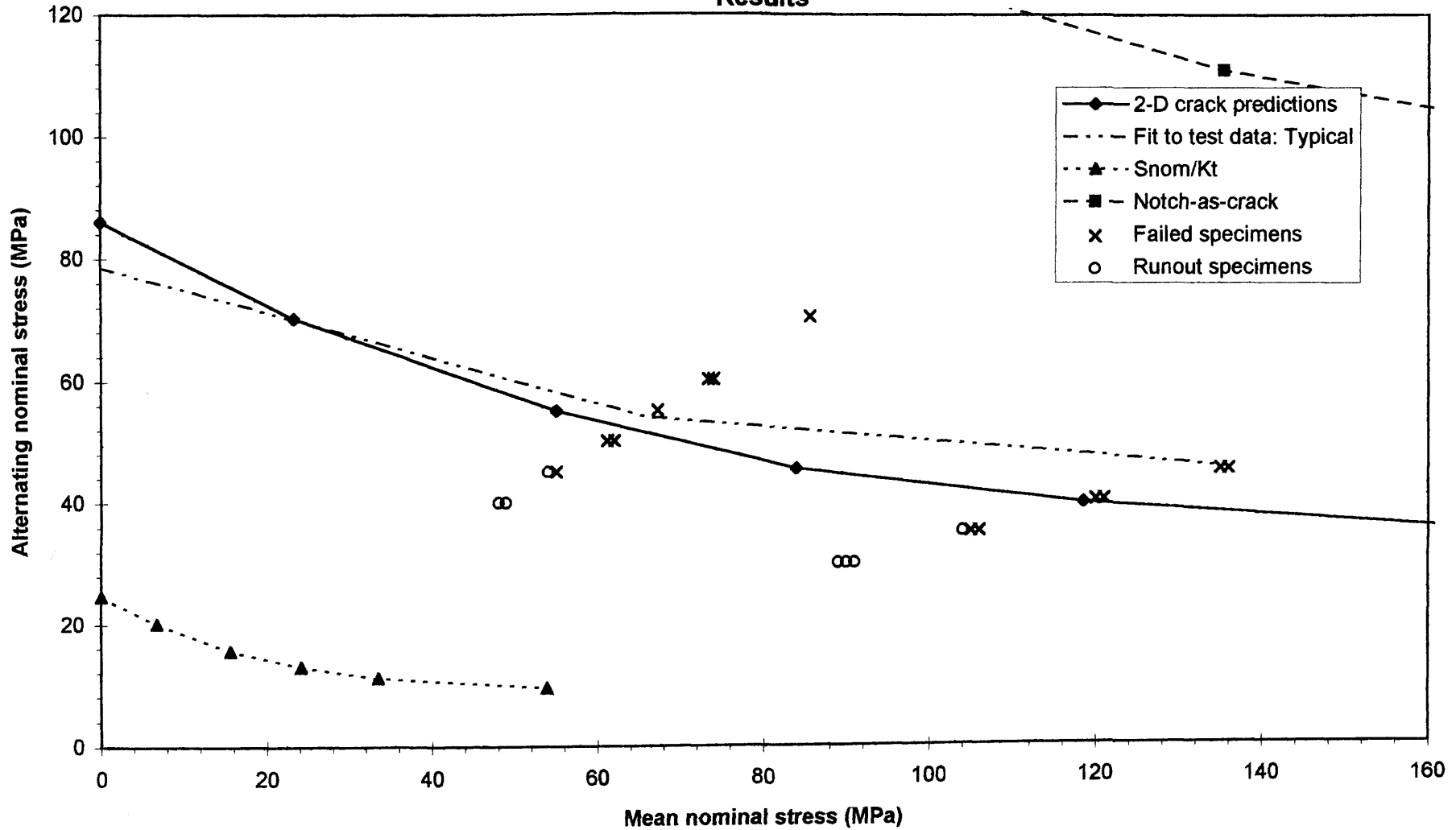


Figure 6.101 BCIRA n12b3 Applied Delta K and Threshold ΔK (Smith's Model) Versus Crack Depth (30mm Cast Section Size, $K_t = 5$, Grade 350 Grey Iron) Continuous Surface Cracks

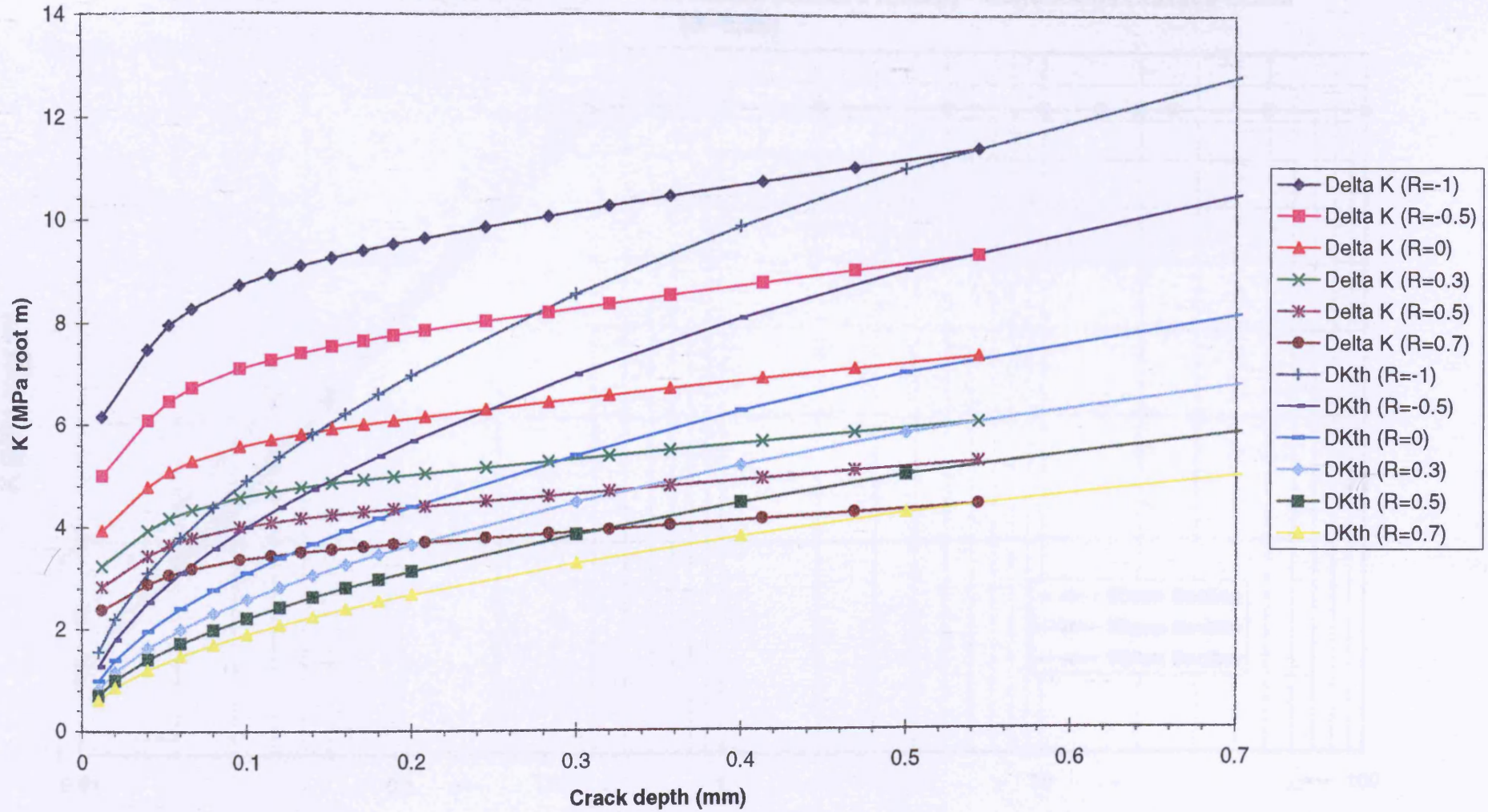


Figure 6.102 BCIRA Grade 400/18 SG Cast Iron
Predicted Apparent Short Crack Growth Threshold (Smith's Model) - Continuous Surface Crack
(R=0.05)

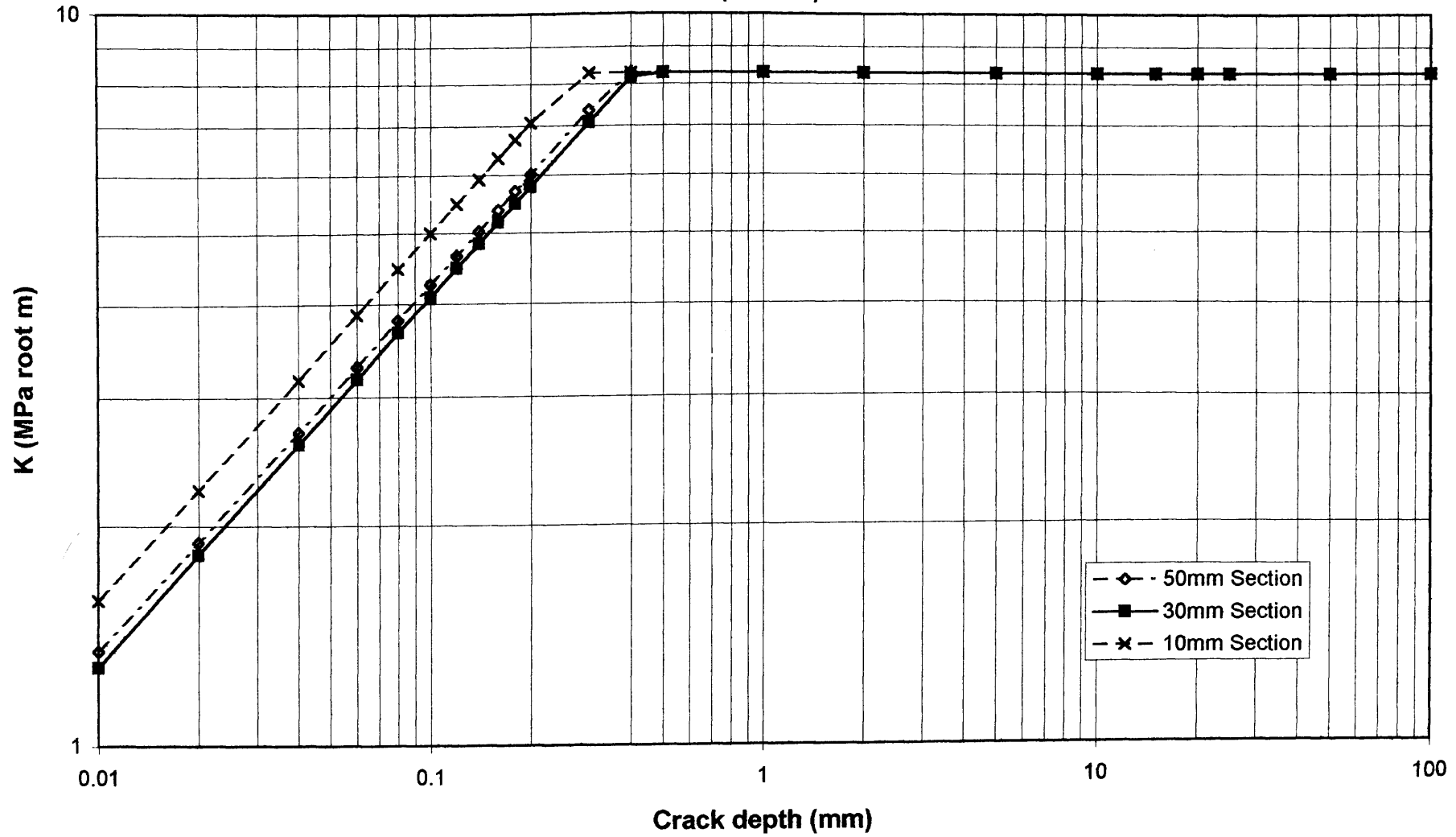


Figure 6.103 BCIRA sg7a1 (10mm Cast Section Size, $K_t = 1.526$, Grade 400/18 SG Iron)
Comparison of Predicted Fatigue Strengths (Smith's Model) and Experimental Results

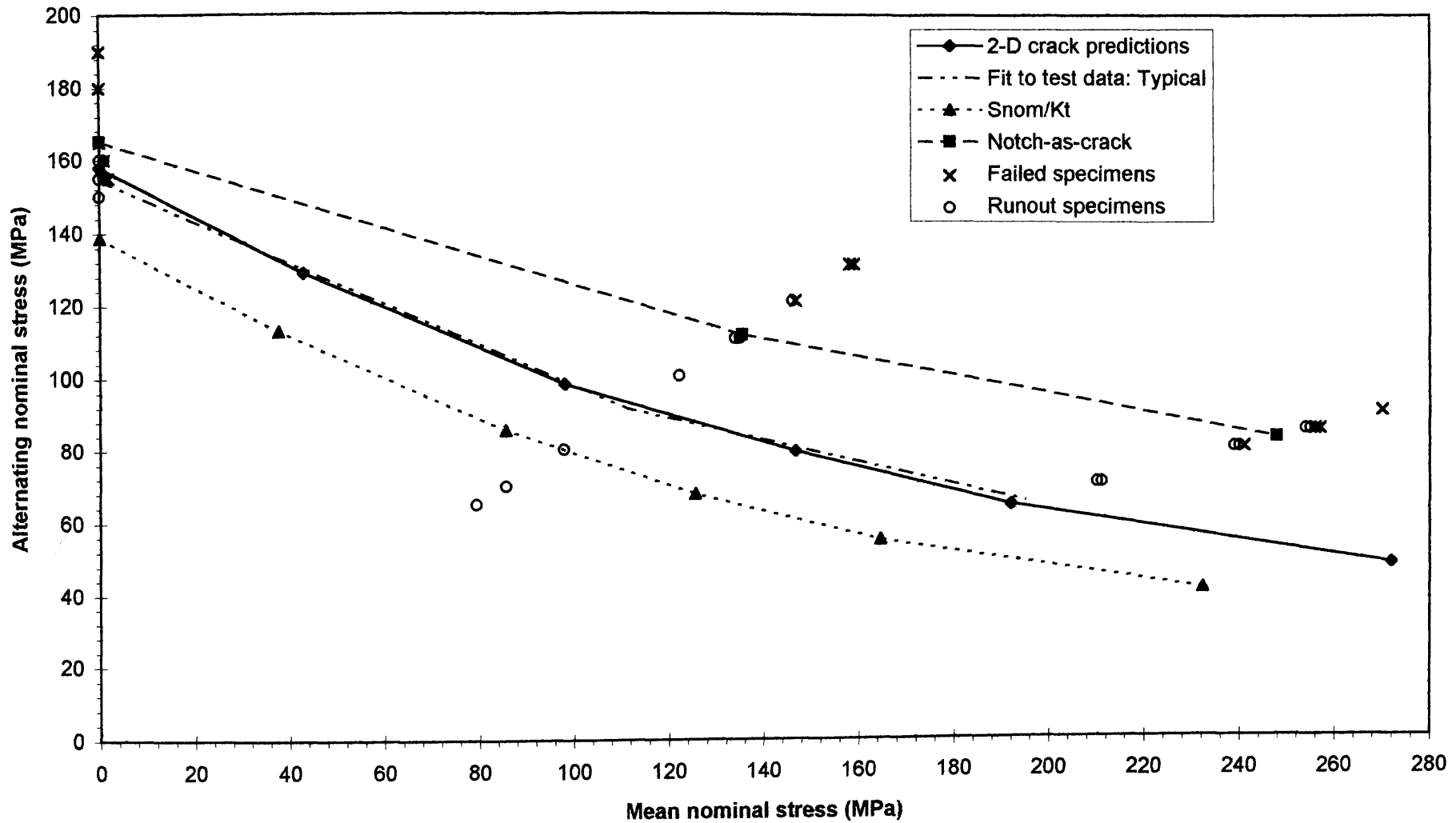


Figure 6.104 BCIRA sg7a1 Applied Delta K and Threshold ΔK (Smith's Model) Versus Crack Depth (10mm Cast Section Size, $K_t = 1.5$, Grade 400/18 SG Iron) Continuous Surface Cracks

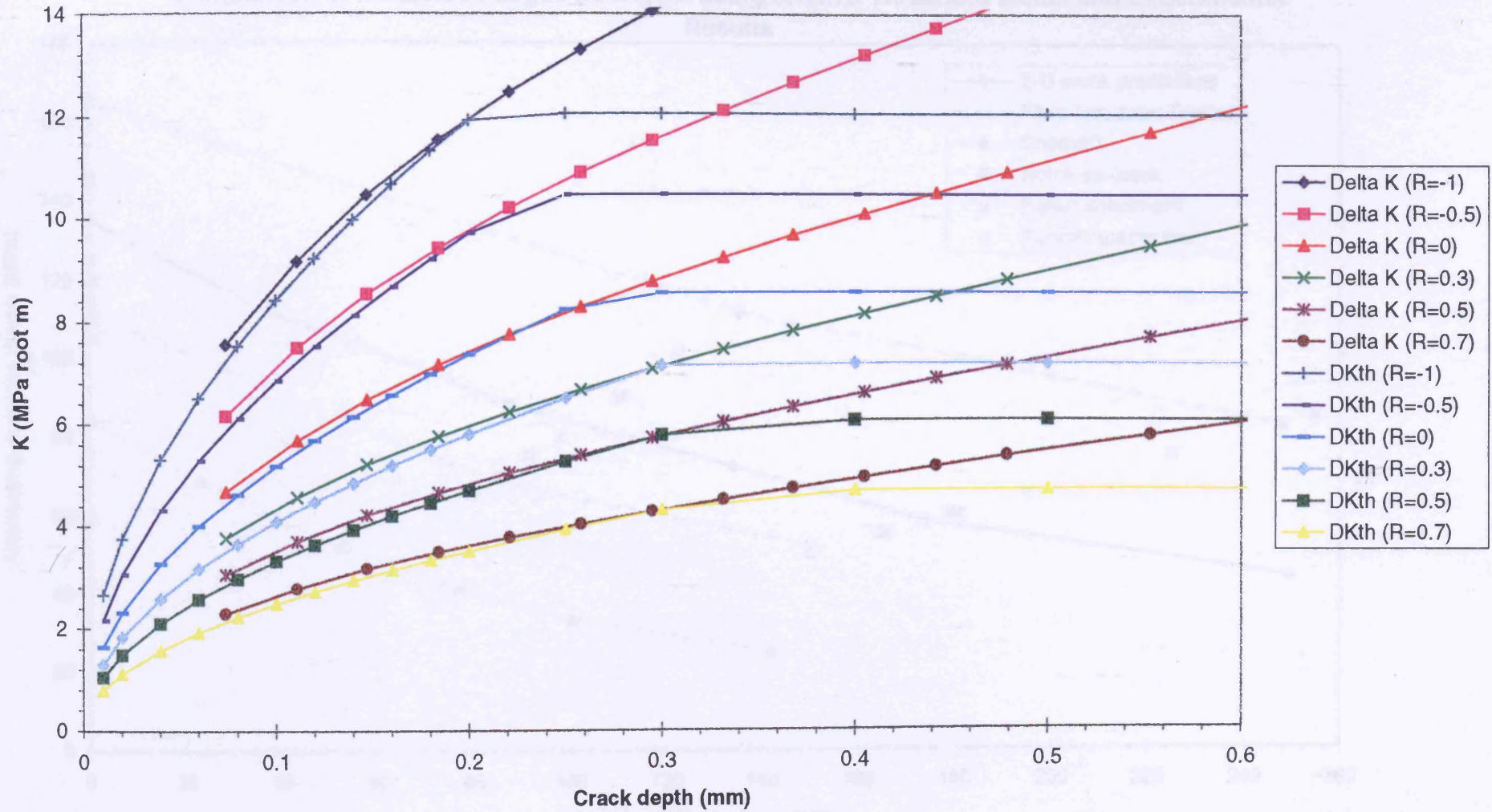


Figure 6.105 BCIRA sg7a2 (10mm Cast Section Size, $K_t = 2.5$, Grade 400/18 SG Iron)
Comparison of Predicted Fatigue Strengths using Smith's Threshold Model and Experimental Results

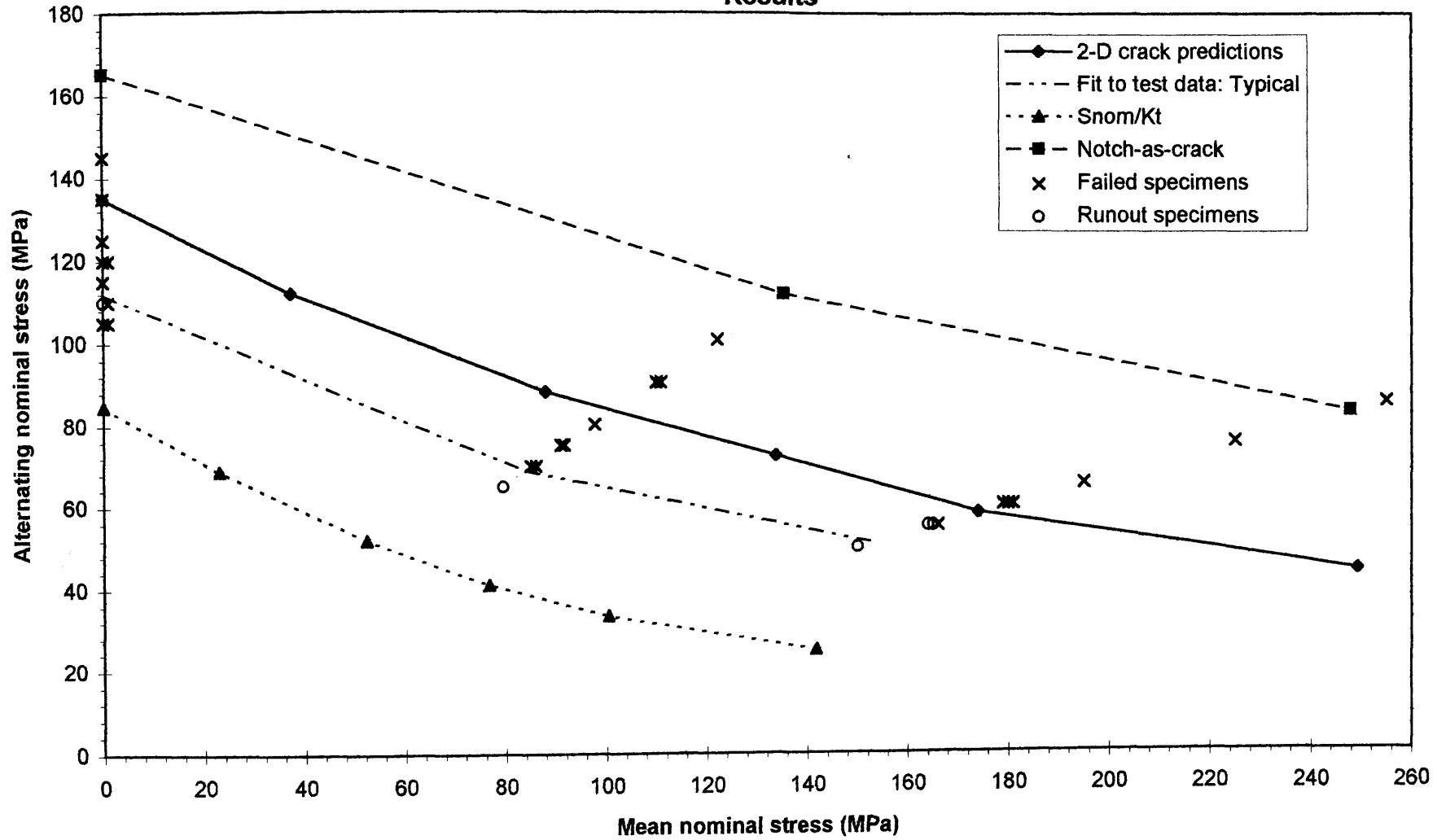


Figure 6.106 BCIRA sg7a2 Applied Delta K and Threshold ΔK (Smith's Model) Versus Crack Depth (10mm Cast Section Size, $K_t = 2.5$, Grade 400/18 SG Iron) Continuous Surface Cracks

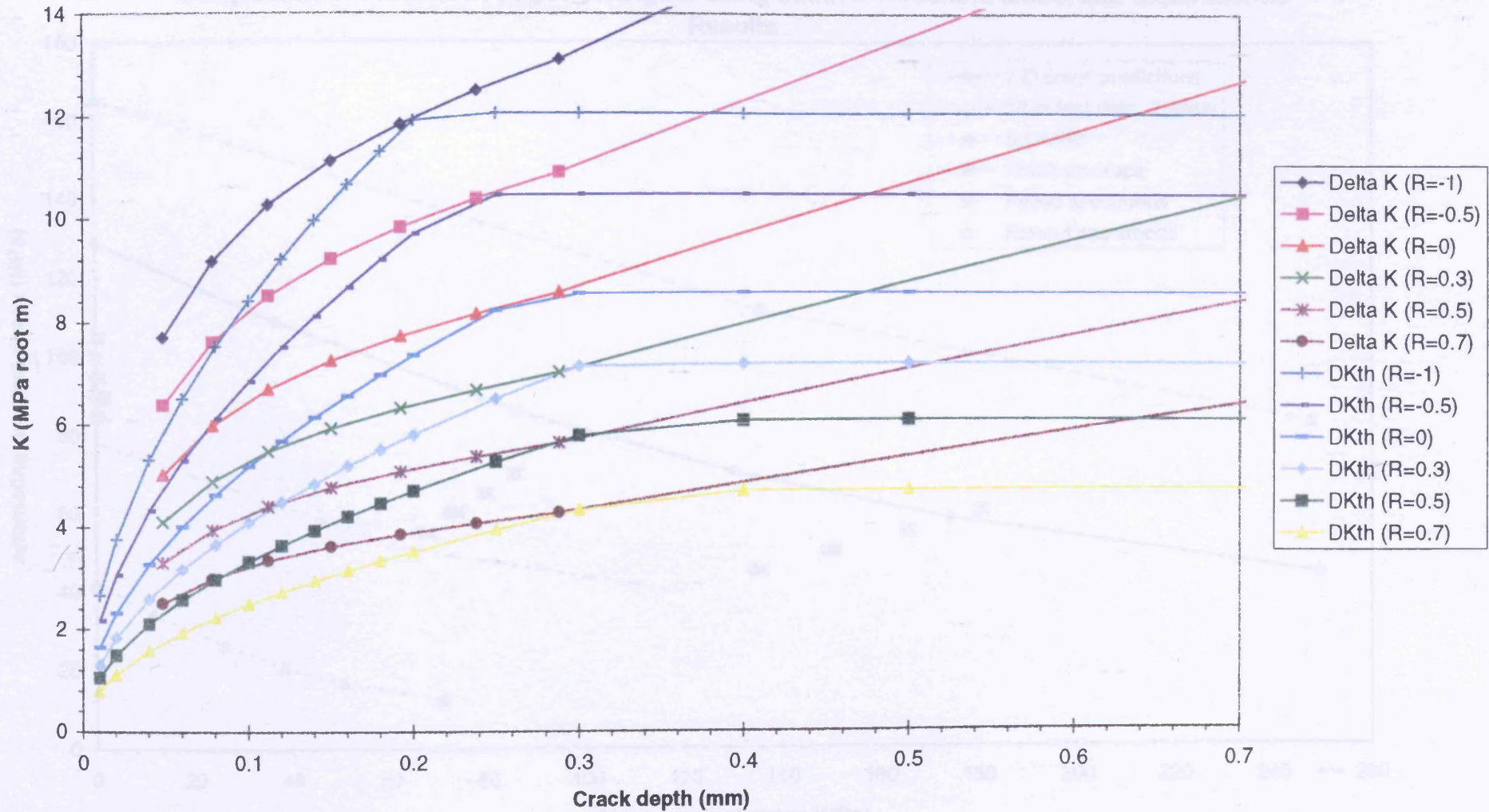


Figure 6.107 BCIRA sg7a3 (10mm Cast Section Size, Kt = 5, Grade 400/18 SG Iron)
Comparison of Predicted Fatigue Strengths using Smith's Threshold Model and Experimental Results

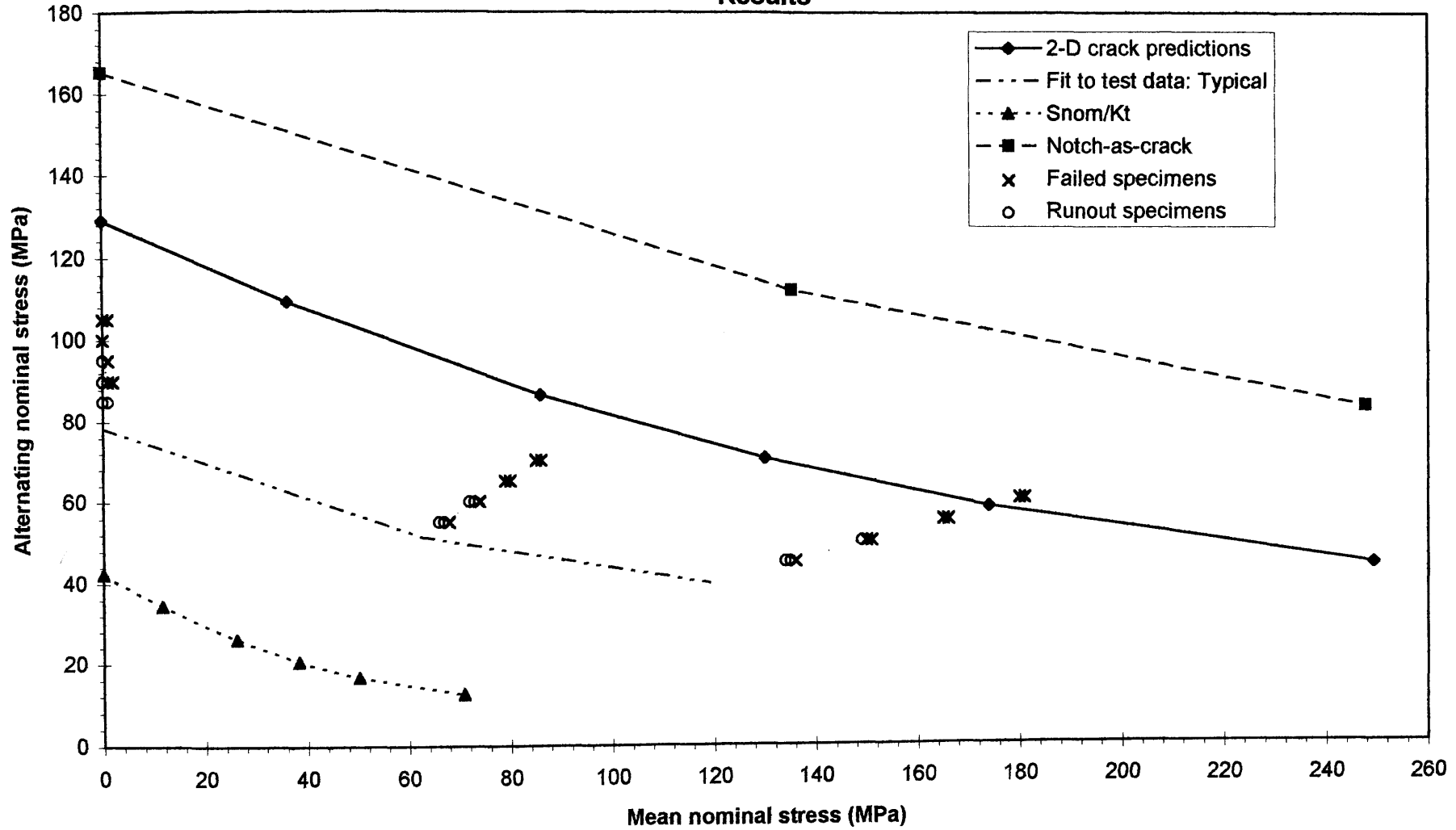


Figure 6.108 BCIRA sg7a3 Applied Delta K and Threshold ΔK (Smith's Model) Versus Crack Depth (10mm Cast Section Size, $K_t = 5$, Grade 400/18 SG Iron) Continuous Surface Cracks

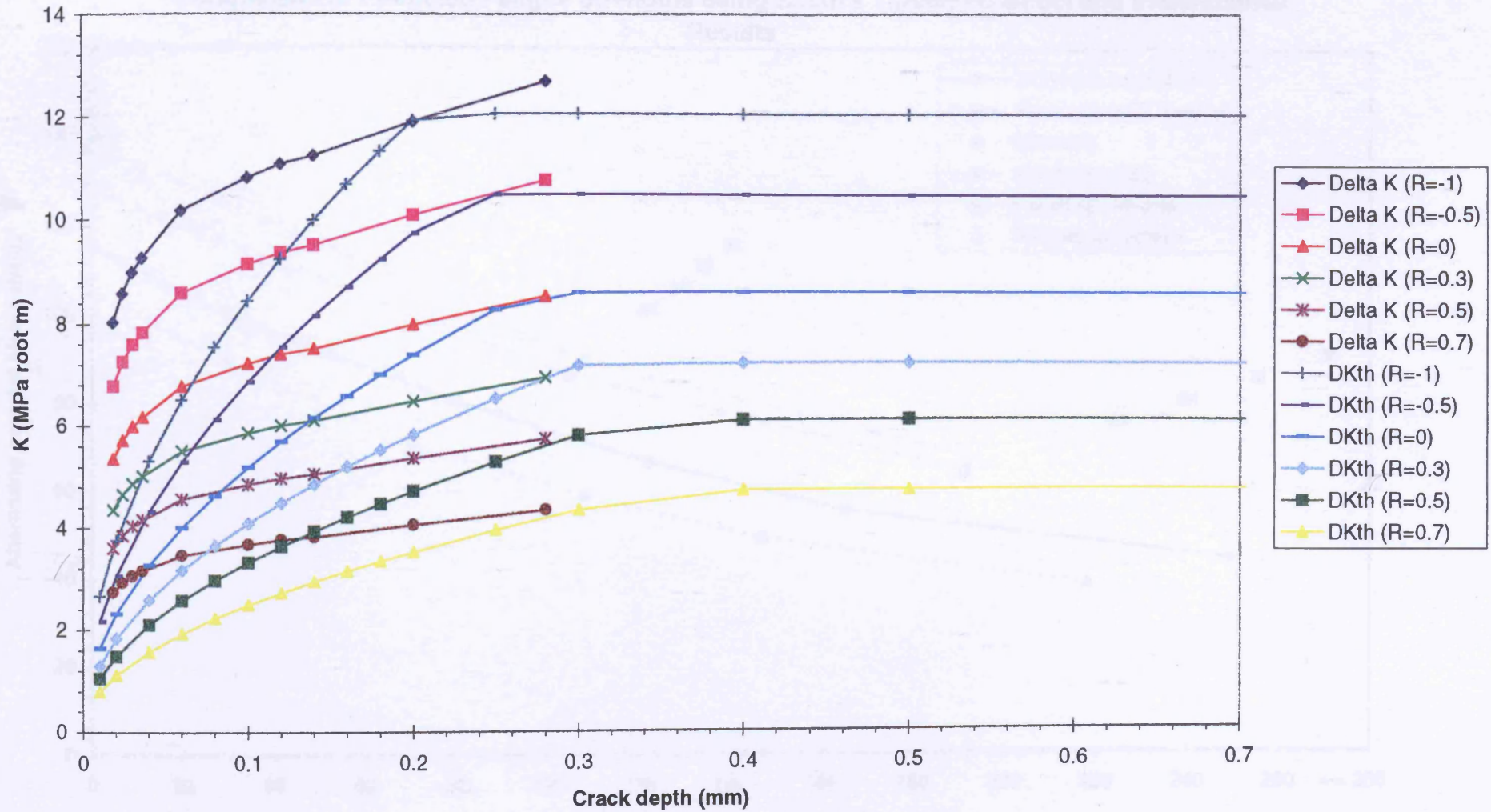


Figure 6.109 BCIRA sg12a1 (30mm Cast Section Size, $K_t = 1.5$, Grade 400/18 SG Iron)
Comparison of Predicted Fatigue Strengths using Smith's Threshold Model and Experimental Results

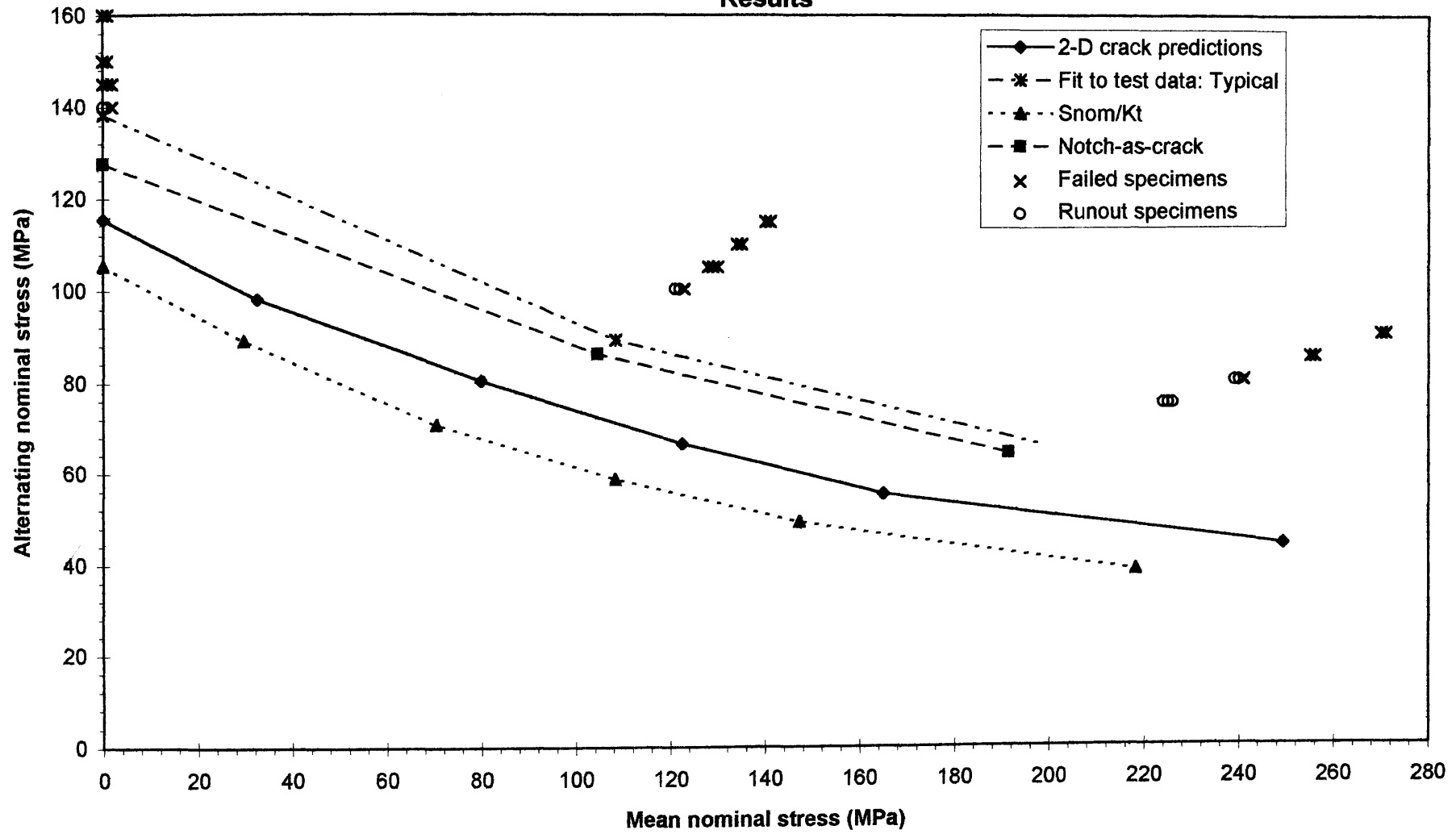


Figure 6.110 BCIRA sg12a1 Applied Delta K and Threshold ΔK (Smith's Model) Versus Crack Depth (30mm Cast Section Size, $K_t = 1.5$, Grade 400/18 SG Iron) Continuous Surface Cracks

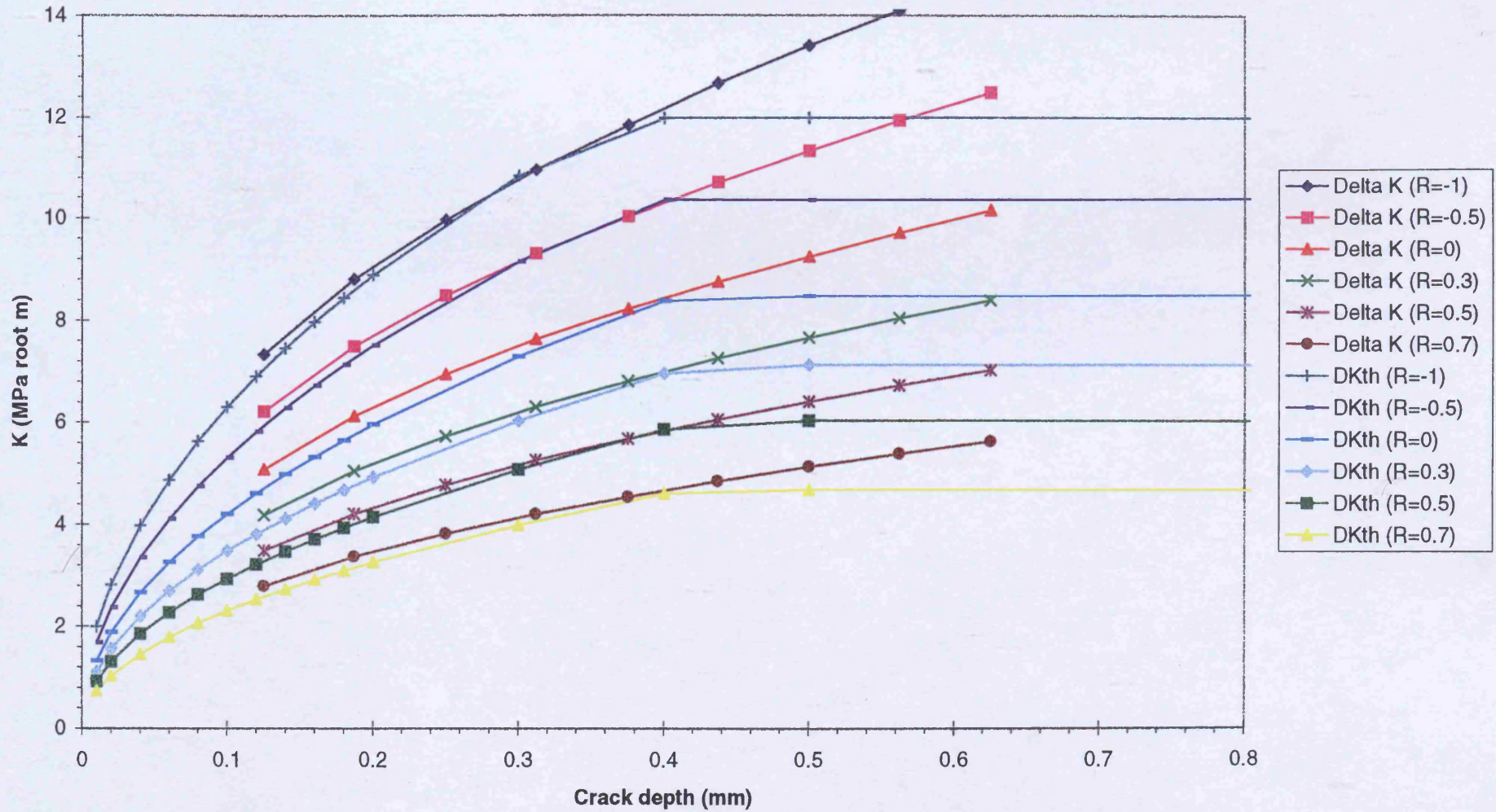


Figure 6.111 BCIRA sg12a2 (30mm Cast Section Size, $K_t = 2.5$, Grade 400/18 SG Iron)
Comparison of Predicted Fatigue Strengths using Smith's Threshold Model and Experimental Results

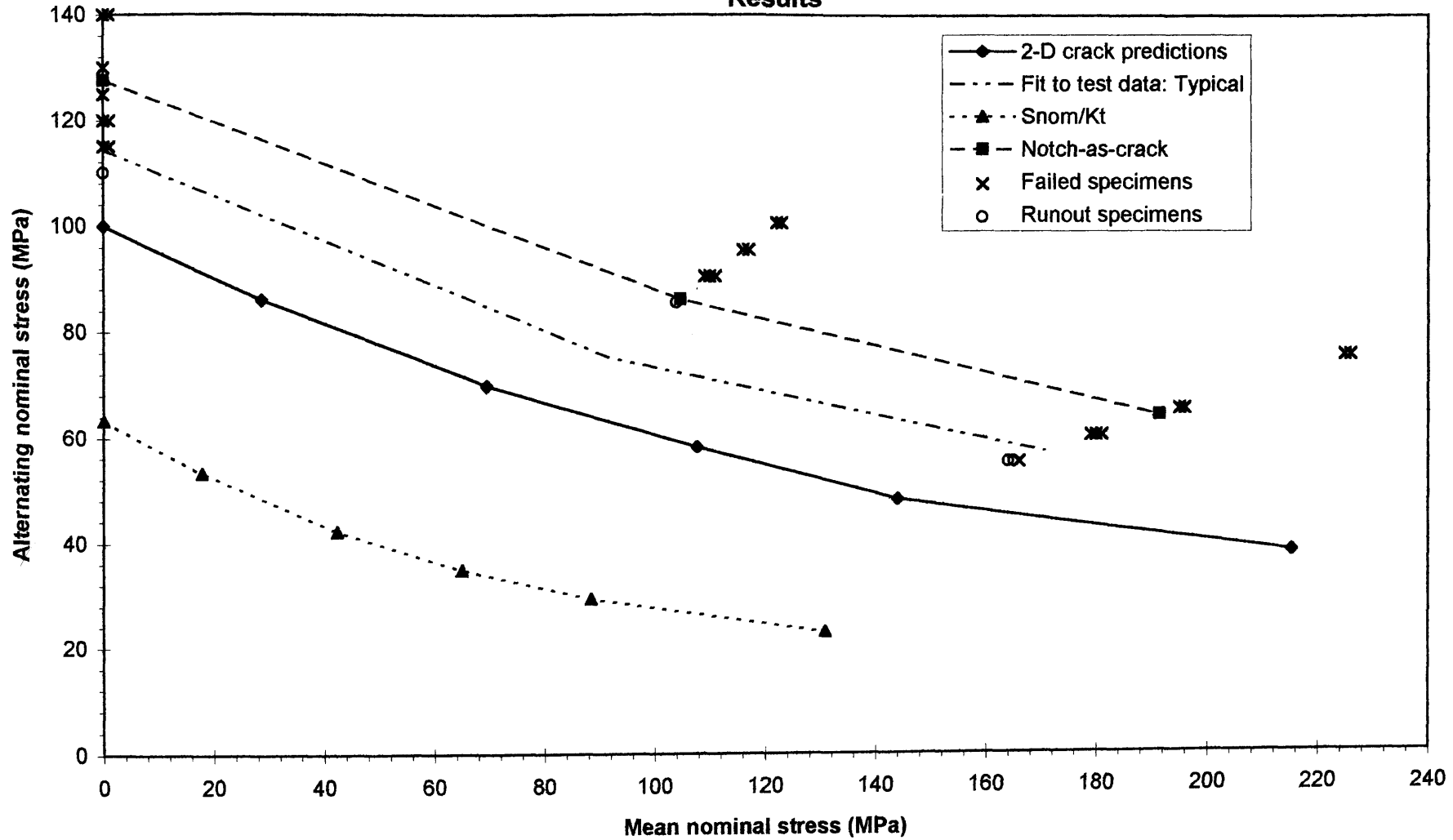


Figure 6.112 BCIRA sg12a2 Applied Delta K and Threshold ΔK (Smith's Model) Versus Crack Depth (30mm Cast Section Size, $K_t = 2.5$, Grade 400/18 SG Iron) Continuous Surface Cracks

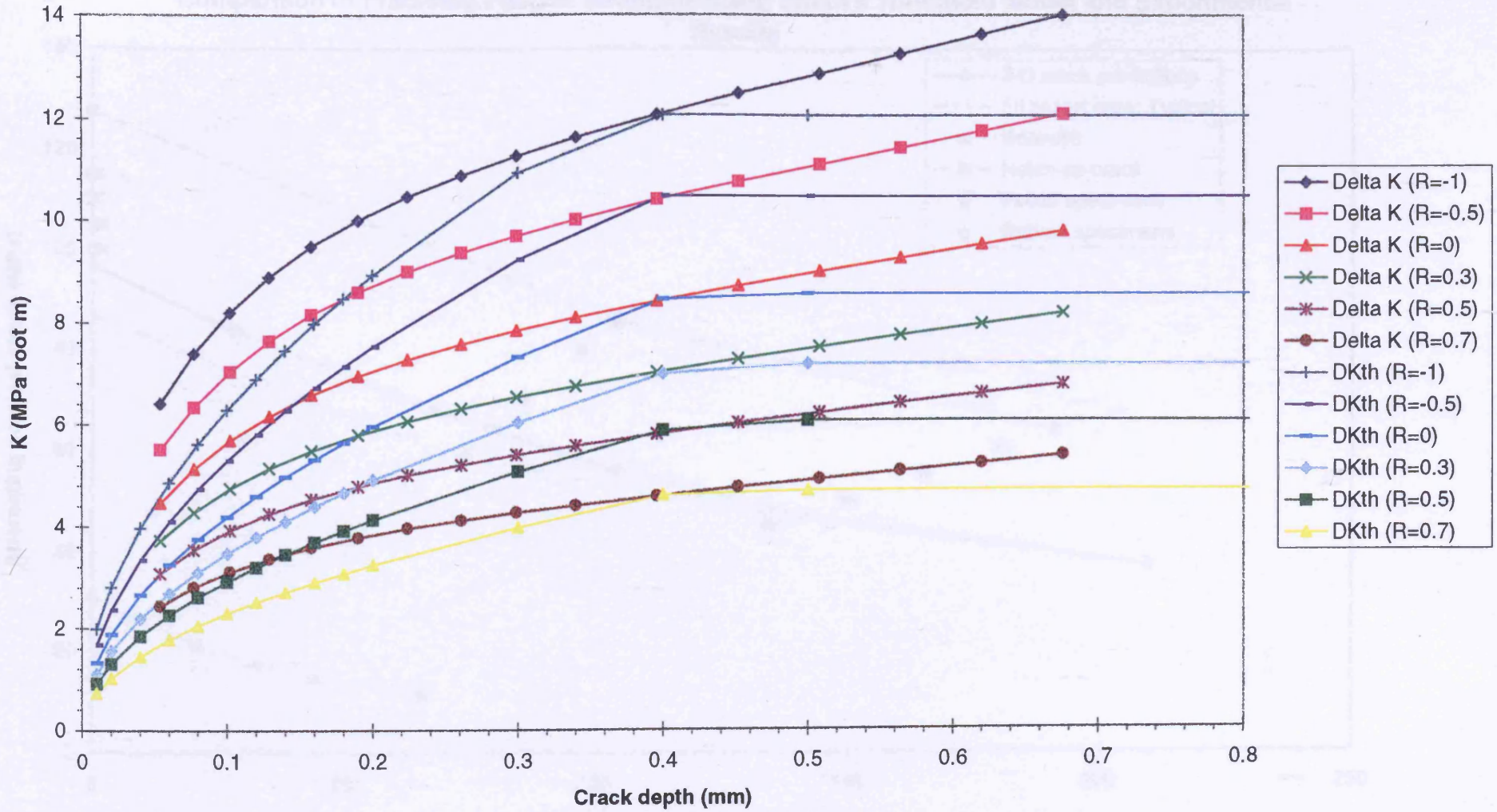


Figure 6.113 BCIRA sg12a3 (30mm Cast Section Size, $K_t = 5$, Grade 400/18 SG Iron)
Comparison of Predicted Fatigue Strengths using Smith's Threshold Model and Experimental Results

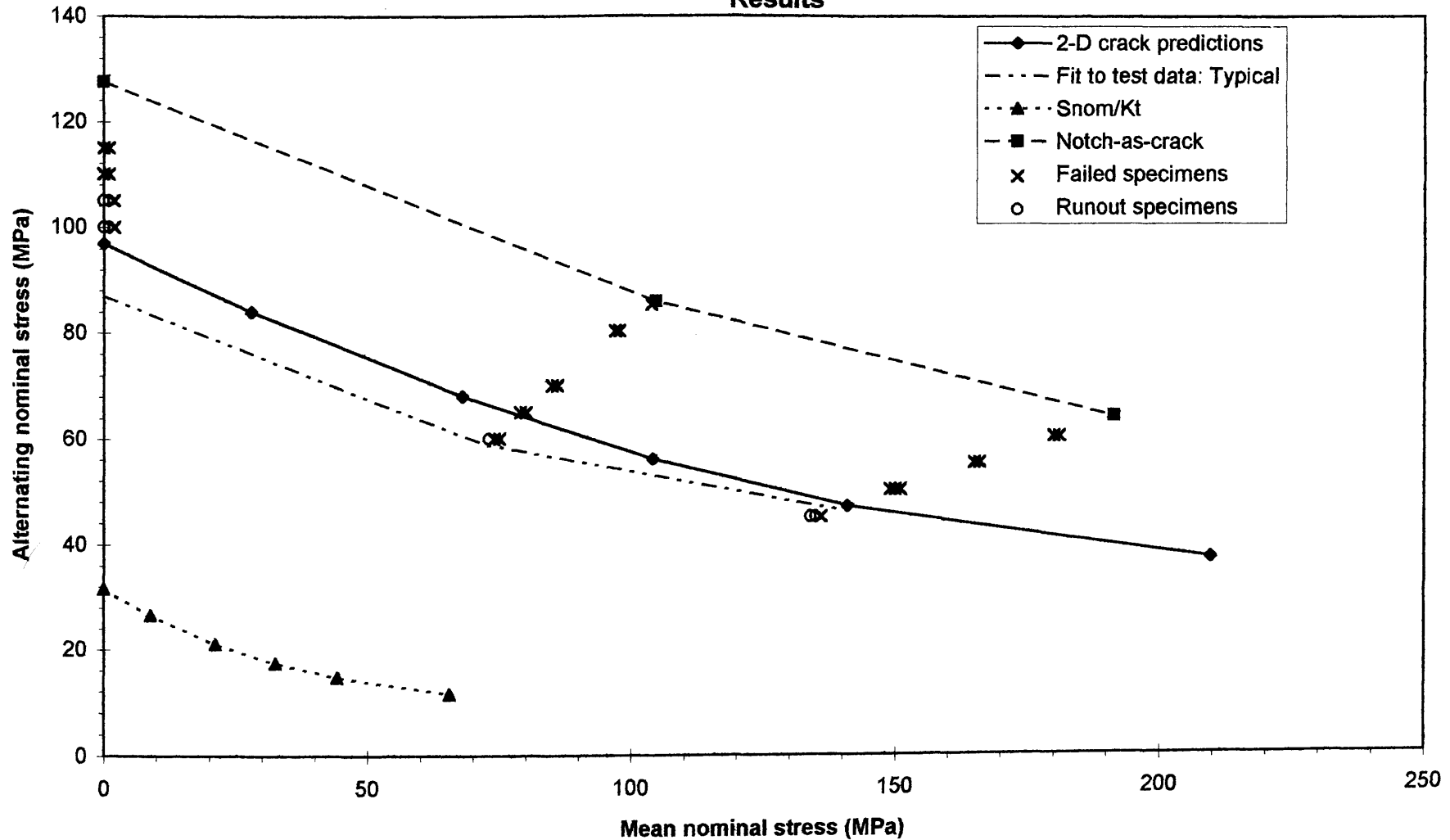


Figure 6.114 BCIRA sg12a3 Applied Delta K and Threshold ΔK (Smith's Model) Versus Crack Depth (30mm Cast Section Size, $K_t = 5$, Grade 400/18 SG Iron) Continuous Surface Cracks

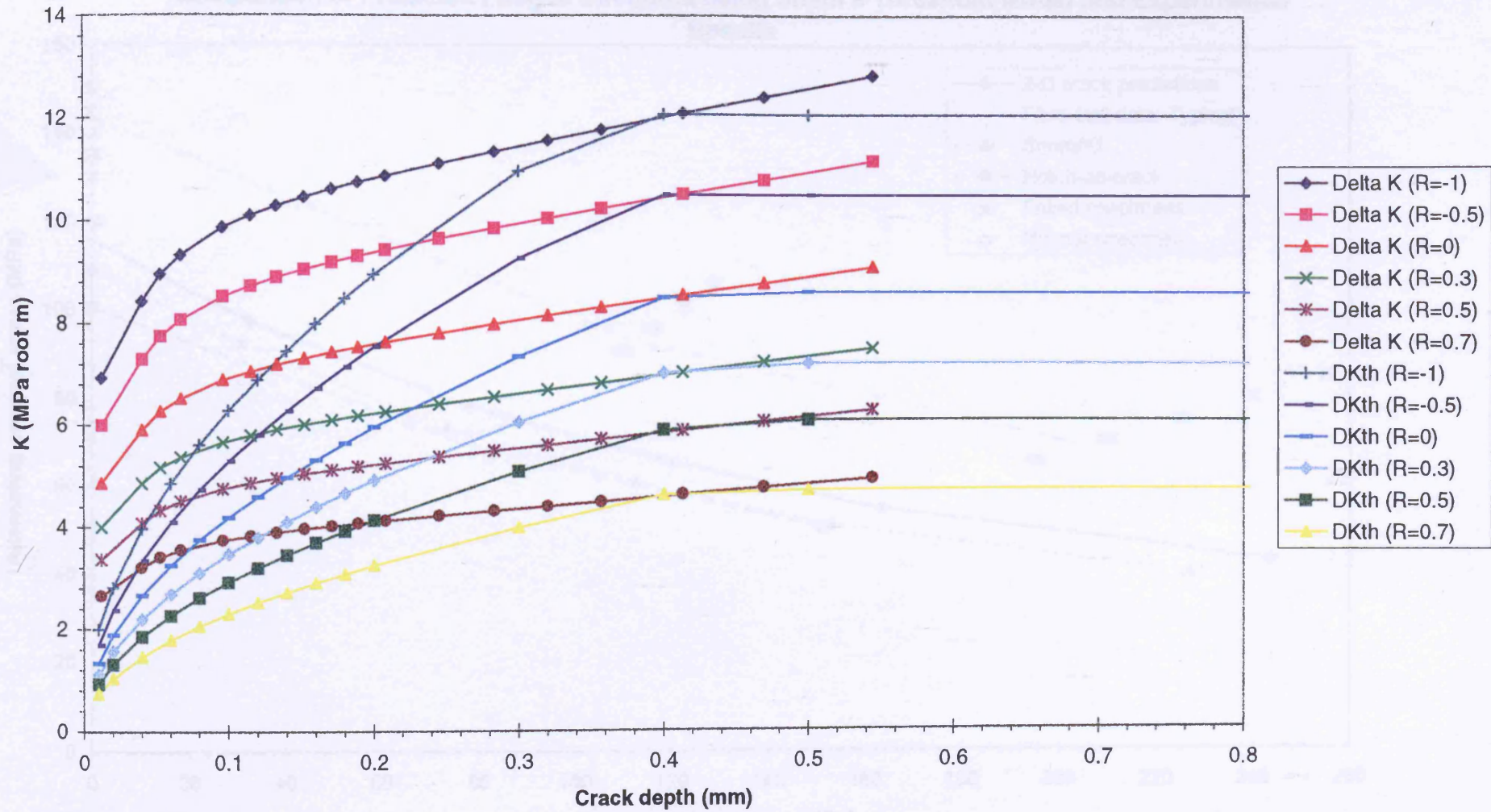


Figure 6.115 BCIRA sg20a1 (50mm Cast Section Size, $K_t = 1.5$, Grade 400/18 SG Iron)
Comparison of Predicted Fatigue Strengths using Smith's Threshold Model and Experimental Results

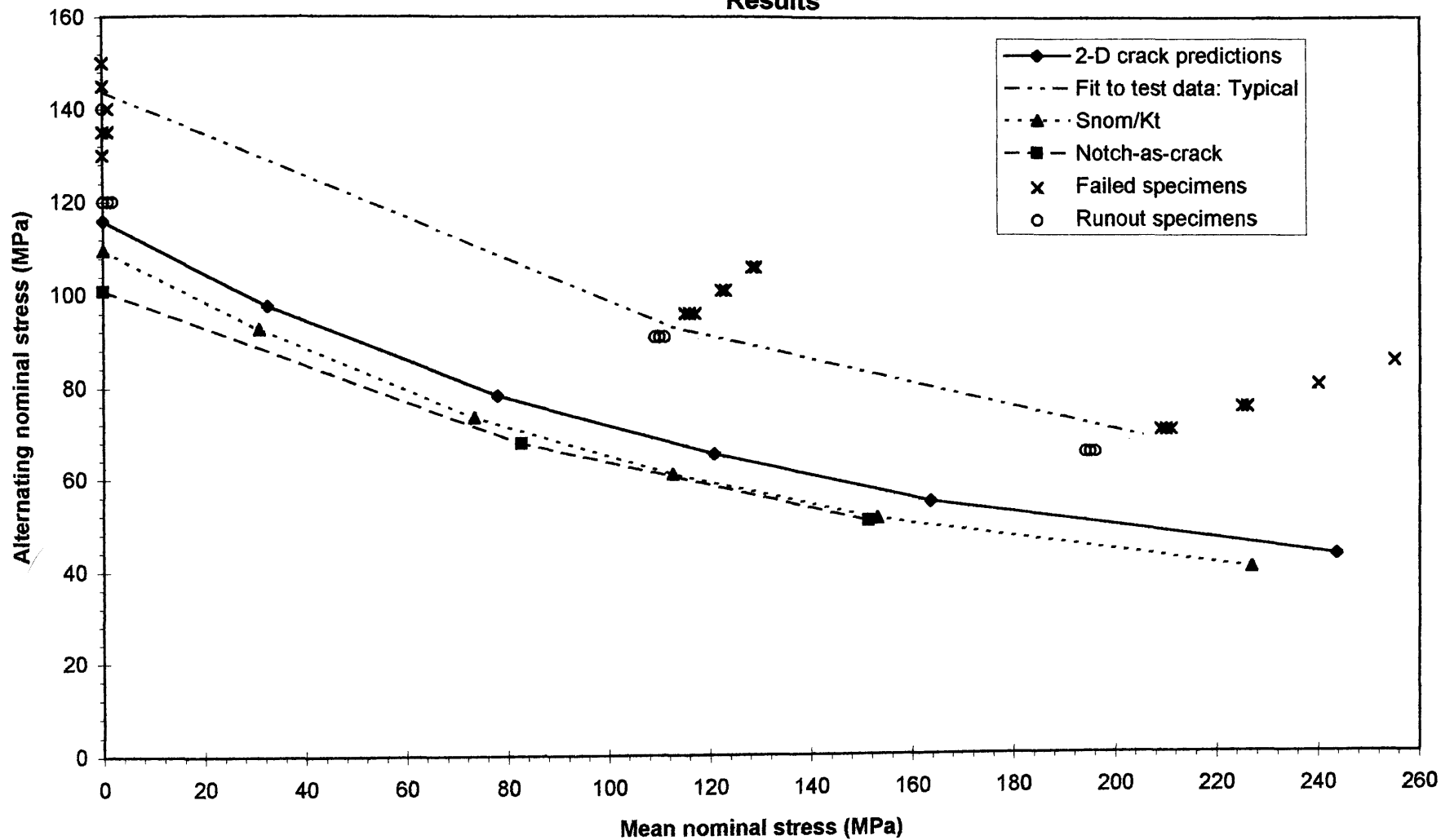


Figure 6.116 BCIRA sg20a1 Applied Delta K and Threshold ΔK (Smith's Model) Versus Crack Depth (50mm Cast Section Size, $K_t = 1.5$, Grade 400/18 SG Iron) Continuous Surface Cracks

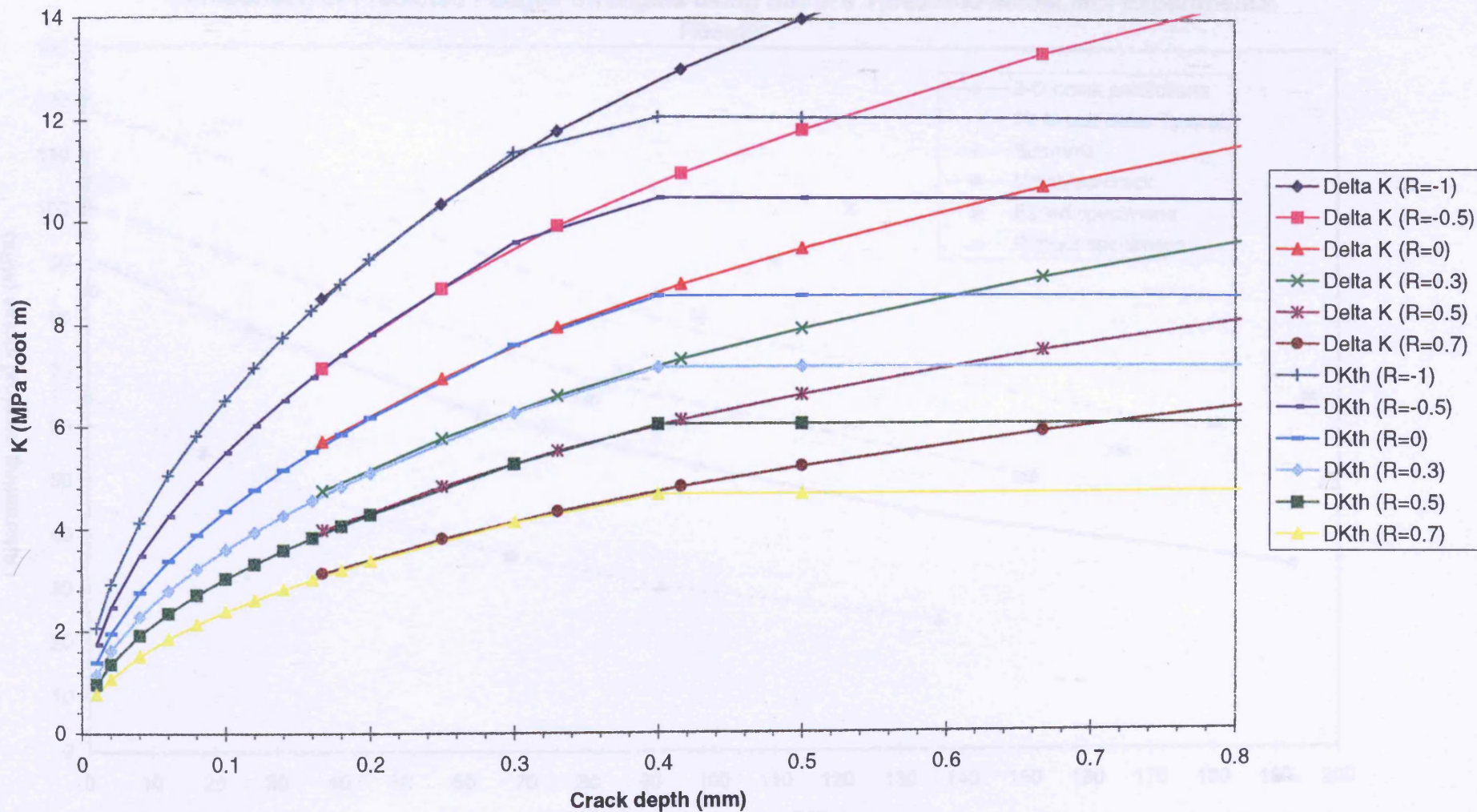


Figure 6.117 BCIRA sg20a2 (50mm Cast Section Size, $K_t = 2.5$, Grade 400/18 SG Iron)
Comparison of Predicted Fatigue Strengths using Smith's Threshold Model and Experimental Results

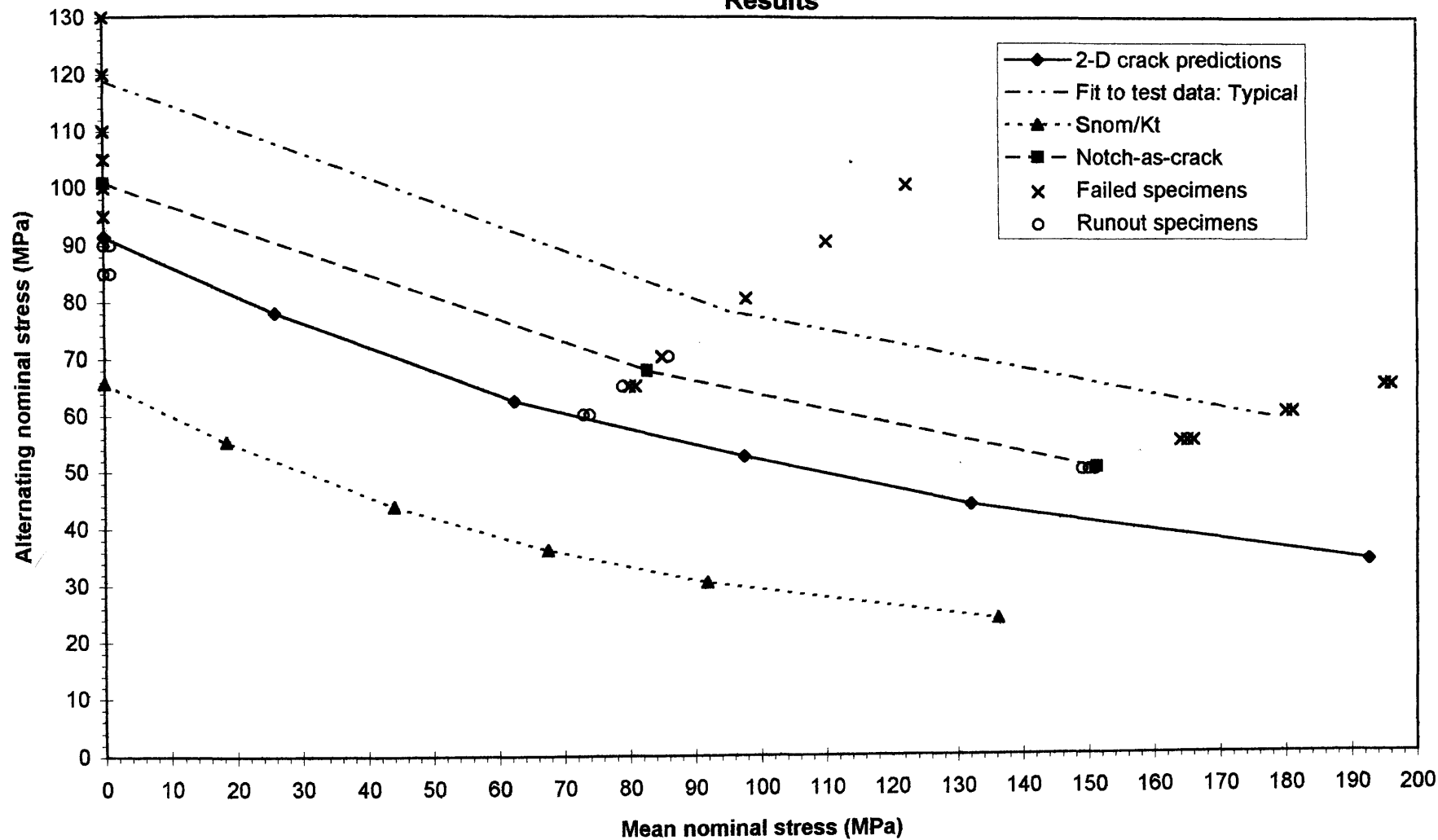


Figure 6.118 BCIRA sg20a2 Applied Delta K and Threshold ΔK (Smith's Model) Versus Crack Depth (50mm Cast Section Size, $K_t = 2.5$, Grade 400/18 SG Iron) Continuous Surface Cracks

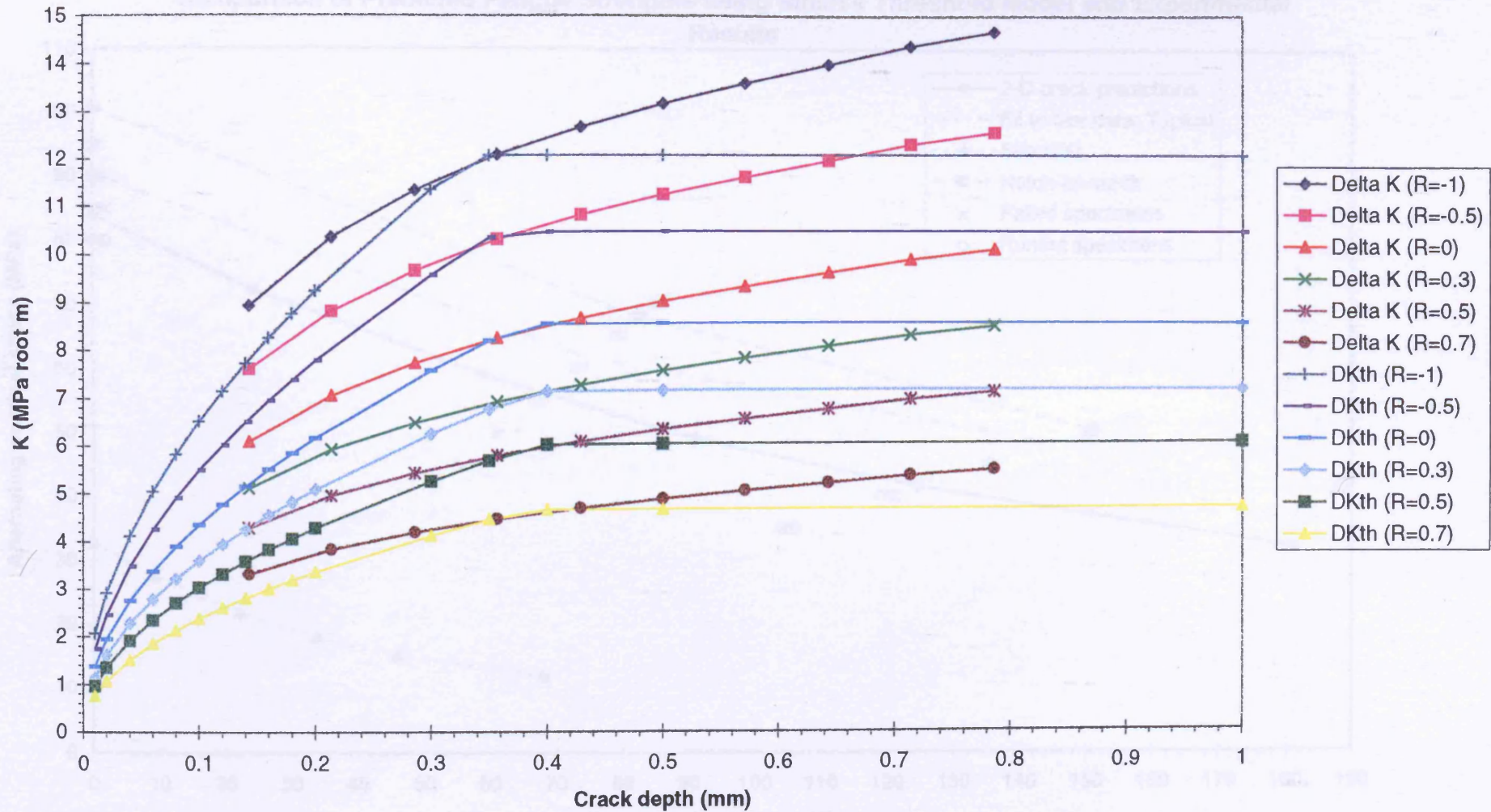


Figure 6.119 BCIRA sg20a3 (50mm Cast Section Size, Kt = 5, Grade 400/18 SG Iron)
Comparison of Predicted Fatigue Strengths using Smith's Threshold Model and Experimental Results

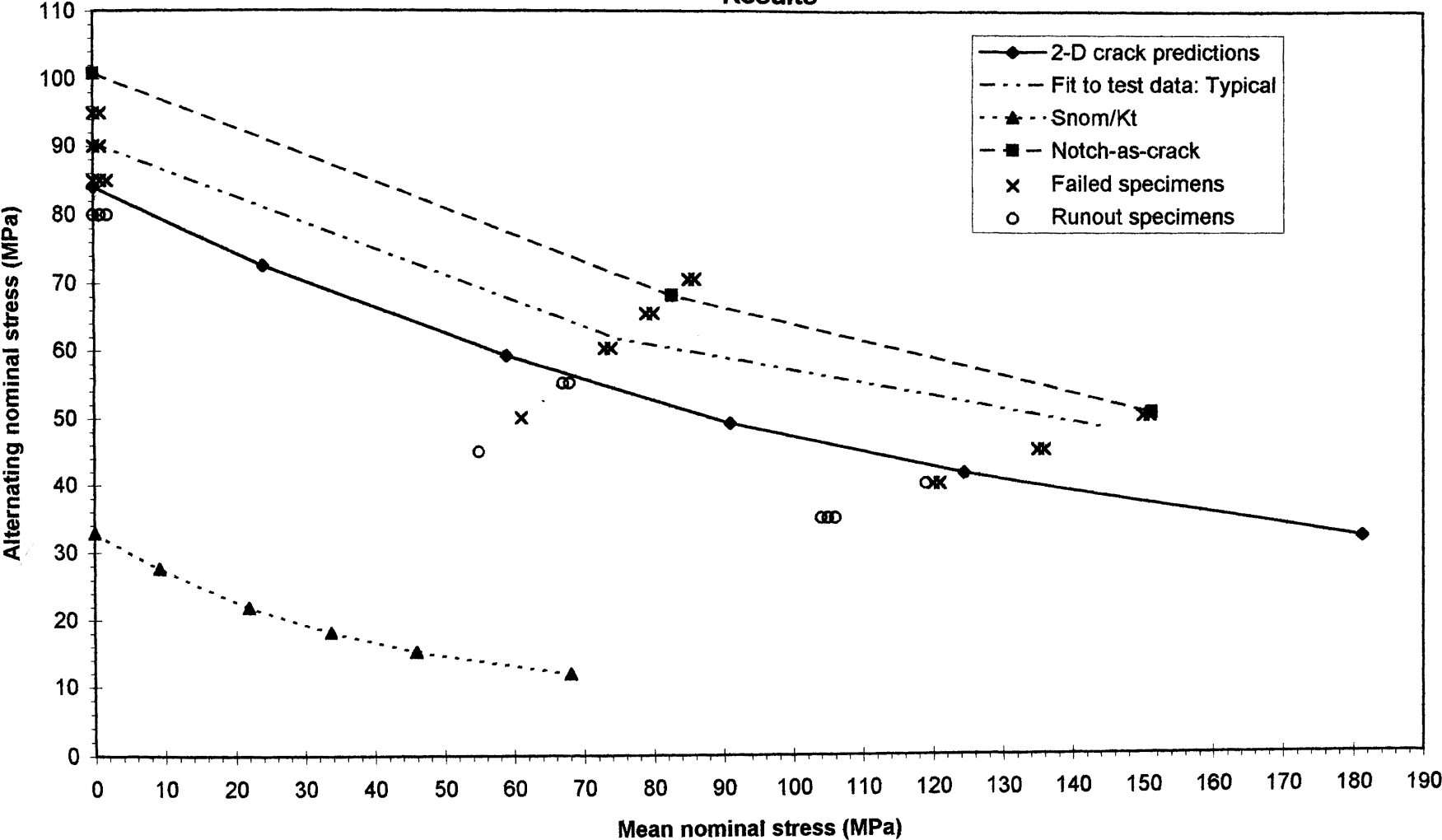


Figure 6.120 BCIRA sg20a3 Applied Delta K and Threshold ΔK (Smith's Model) Versus Crack Depth (50mm Cast Section Size, $K_t = 5$, Grade 400/18 SG Iron) Continuous Surface Cracks

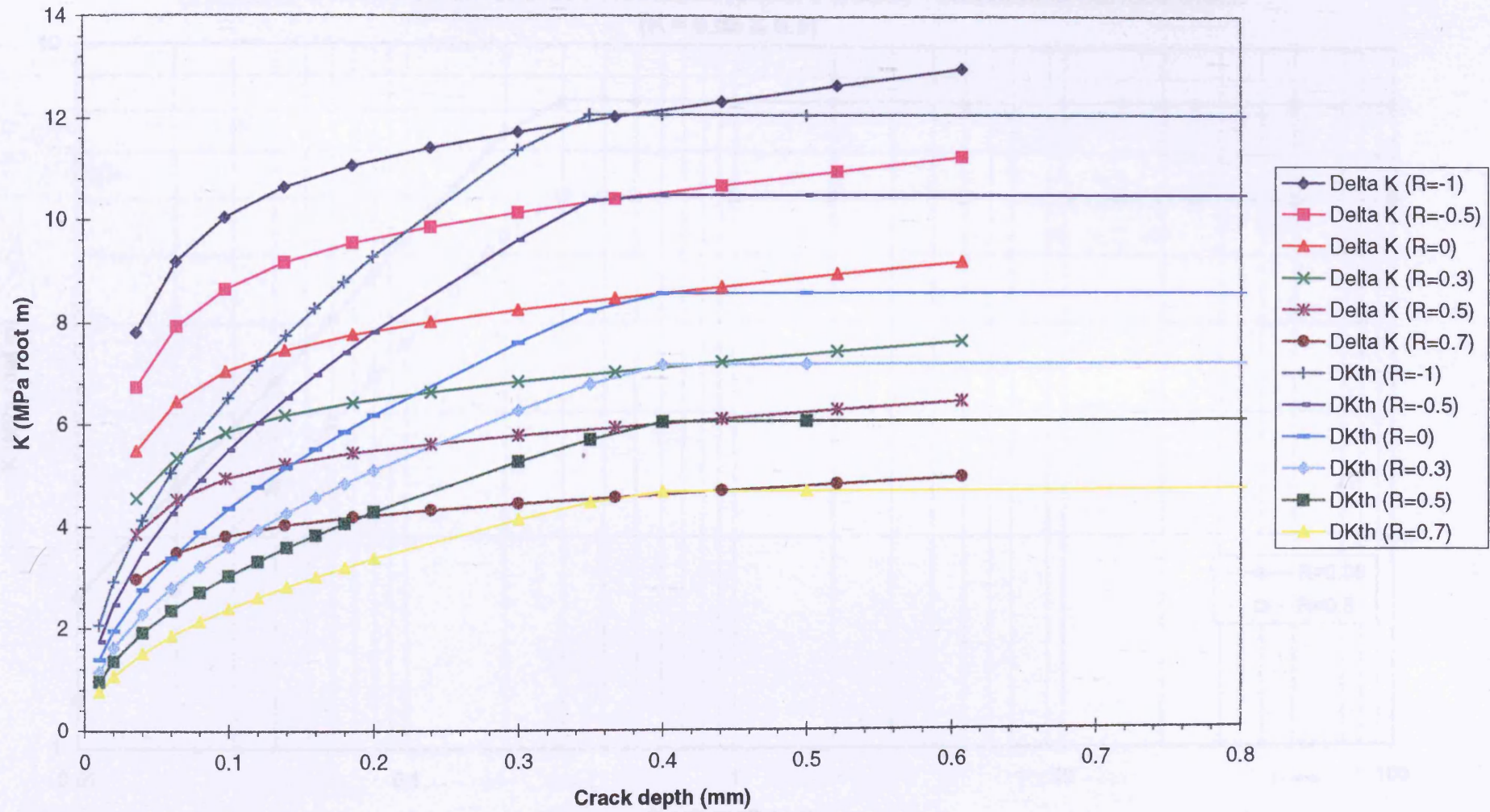


Figure 6.121 BCIRA Grade 500/7 SG Cast Iron
Predicted Apparent Short Crack Threshold (Smith's Model) - Continuous Surface Crack
(R = 0.05 & 0.5)

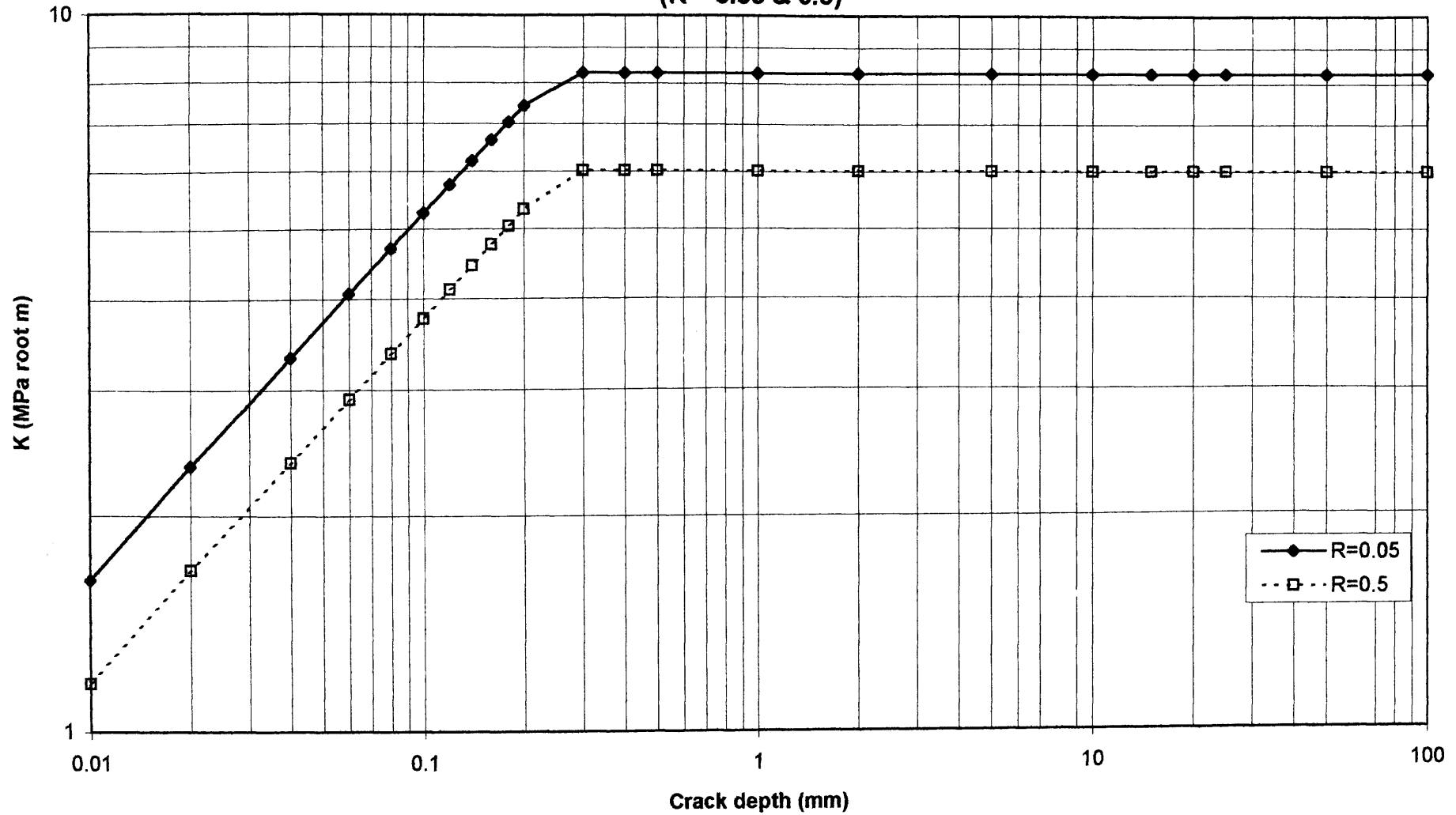


Figure 6.122 BCIRA sg12b1 (30mm Cast Section Size, $K_t = 1.5$, Grade 500/7 SG Iron)
Comparison of Predicted Fatigue Strengths using Smith's Threshold Model and Experimental Results

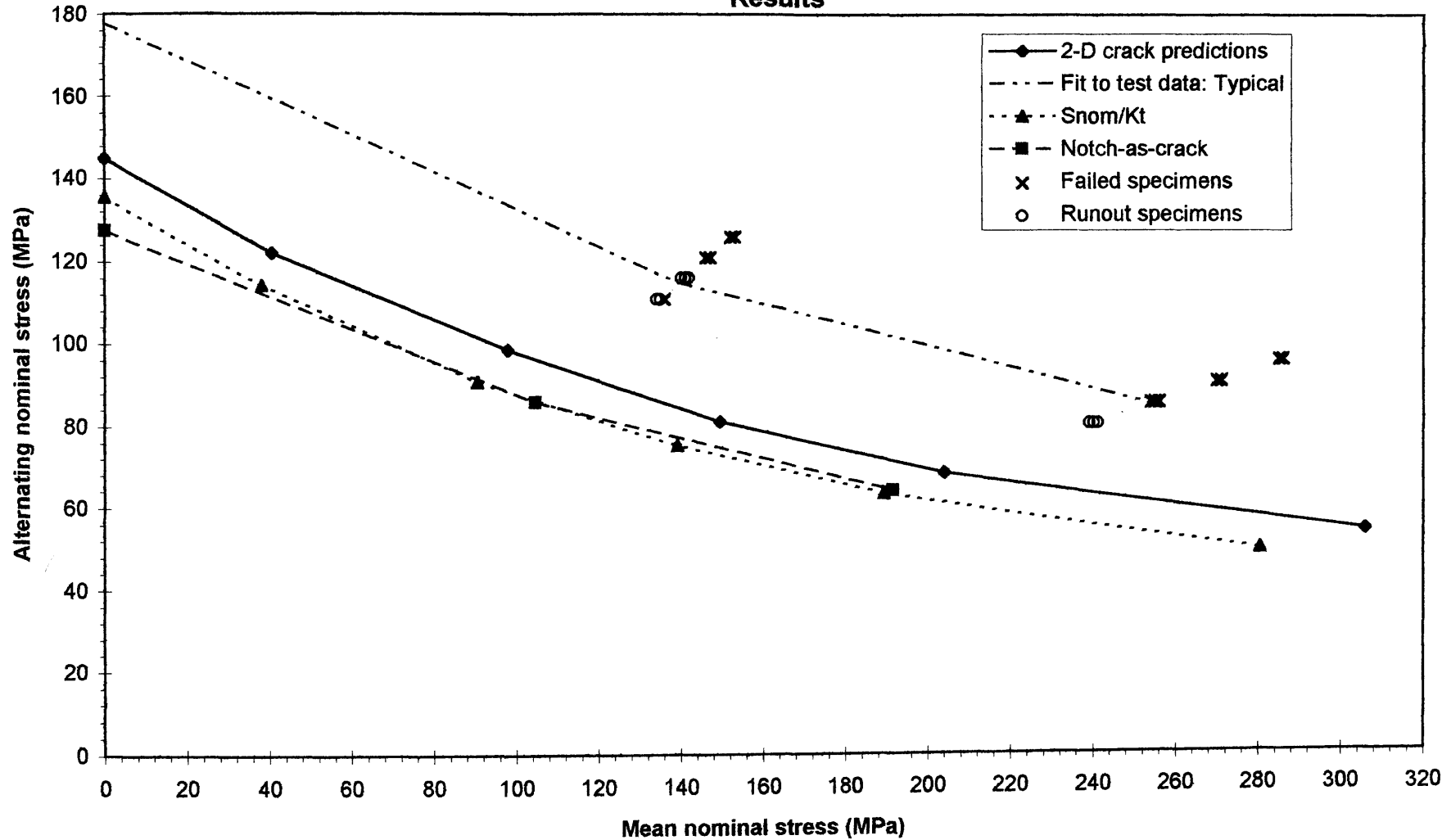


Figure 6.123 BCIRA sg12b1 Applied Delta K and Threshold ΔK (Smith's Model) Versus Crack Depth (30mm Cast Section Size, $K_t = 1.5$, Grade 500/7 SG Iron) Continuous Surface Cracks

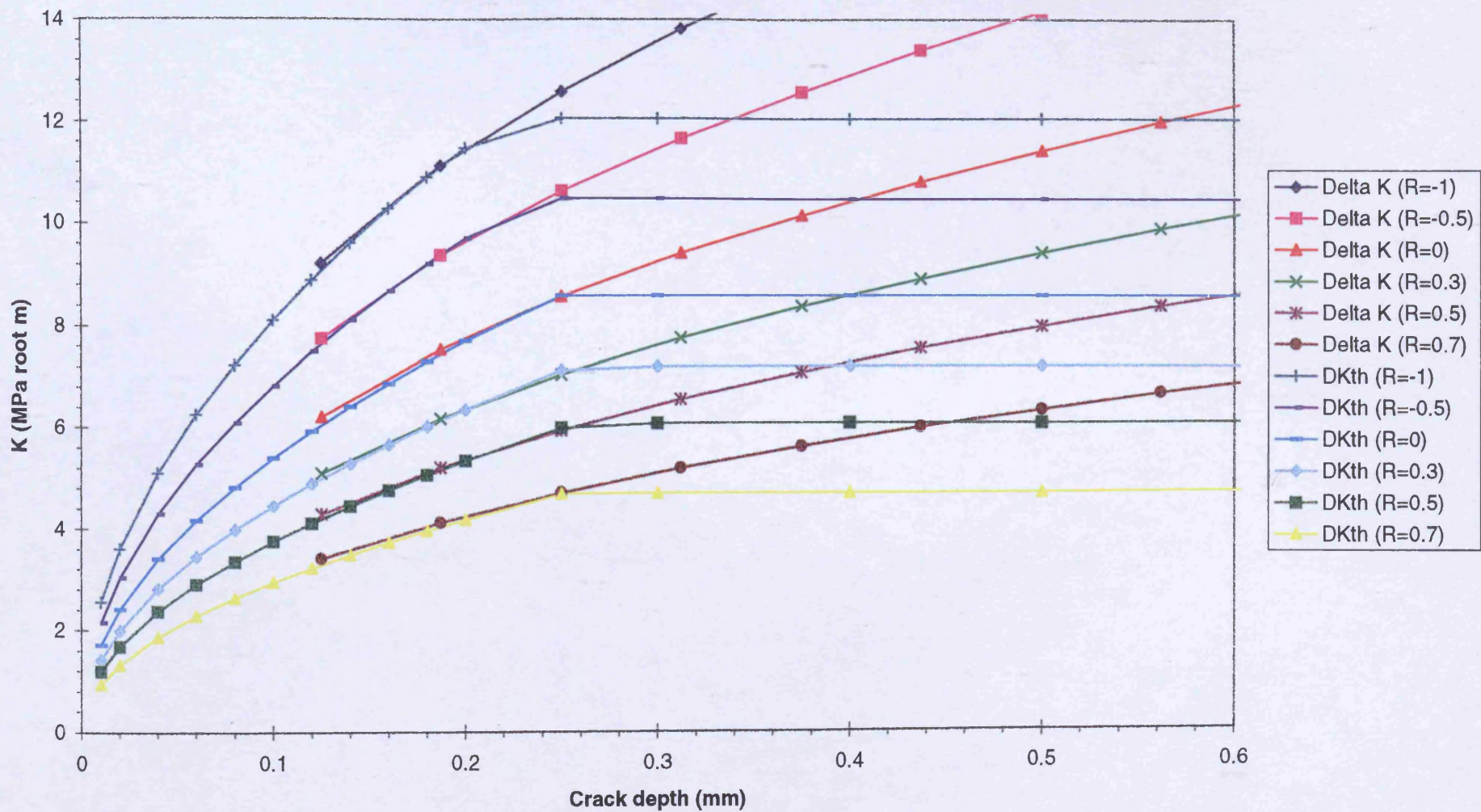


Figure 6.124 BCIRA sg12b3 (30mm Cast Section Size, $K_t = 5$, Grade 500/7 SG Iron)
Comparison of Predicted Fatigue Strengths using Smith's Threshold Model and Experimental Results

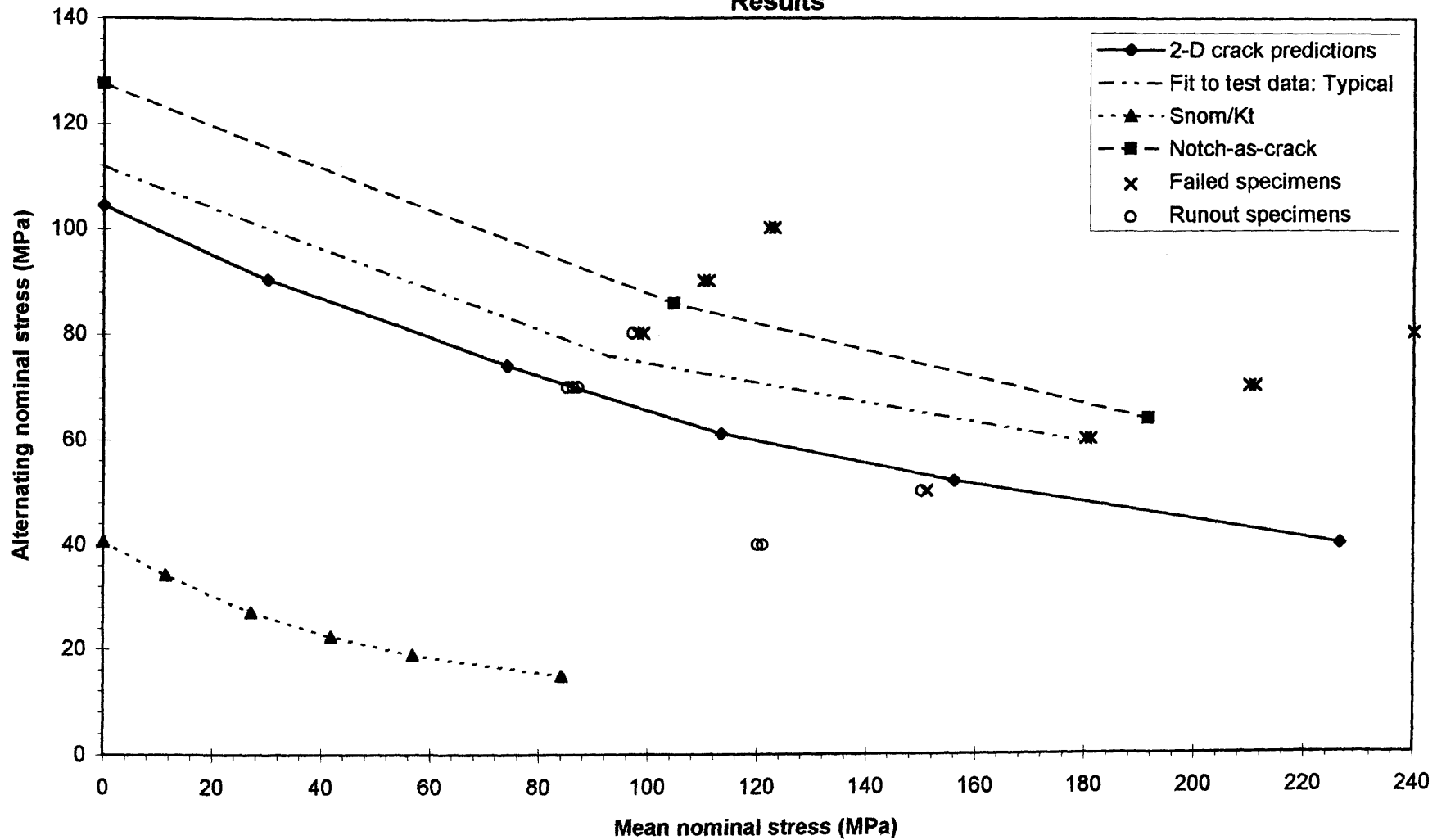


Figure 6.125 BCIRA sg12b3 Applied Delta K and Threshold ΔK (Smith's Model) Versus Crack Depth (30mm Cast Section Size, $K_t = 5$, Grade 500/7 SG Iron) Continuous Surface Cracks

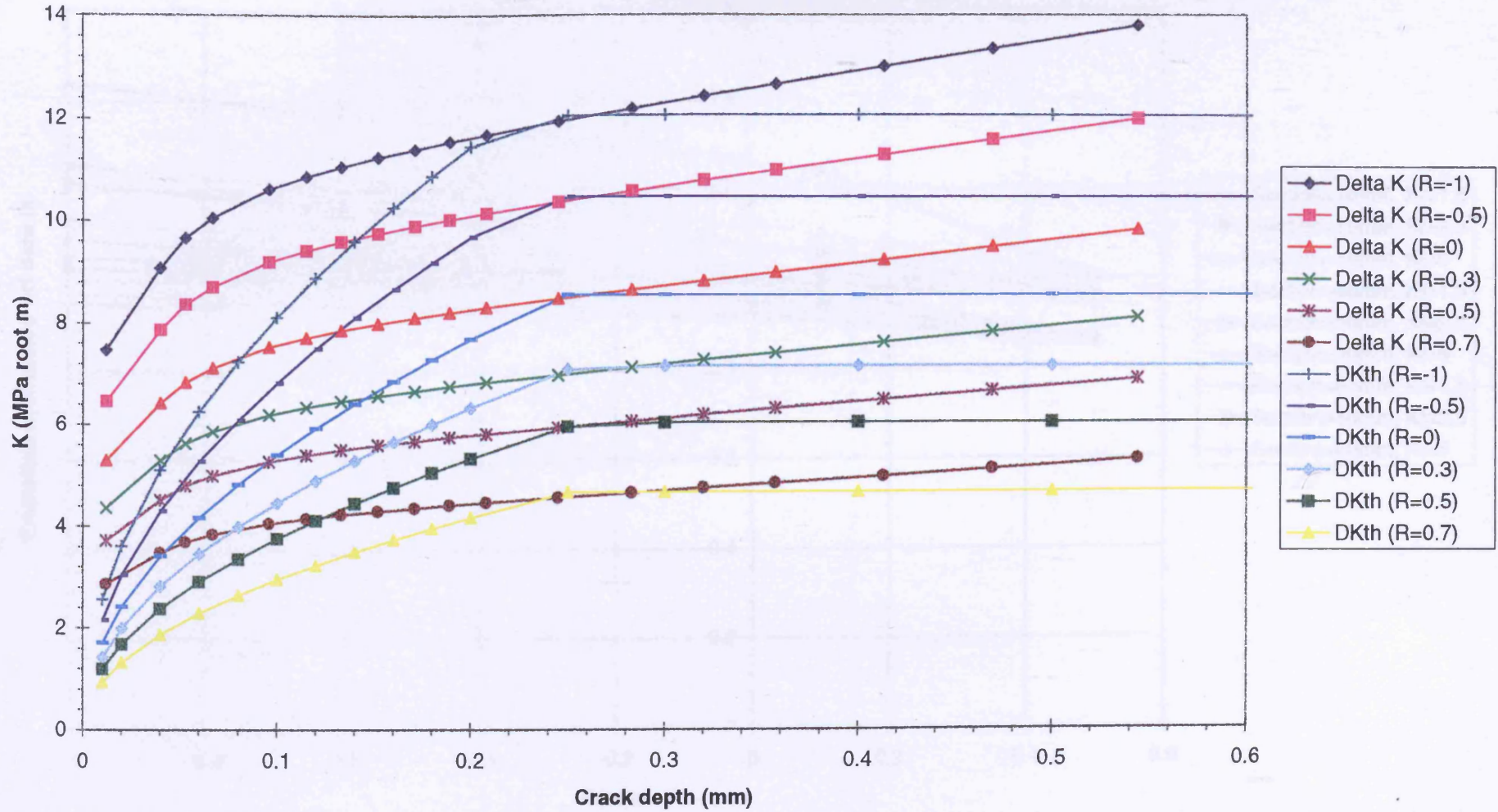


Figure 6.126 Grade 250 Grey Iron: Normalised Predictions of Fatigue Strength using Smith's Threshold Model for Various Kt Values and Section Sizes (Normalisation w.r.t. Curve Fit to Data)

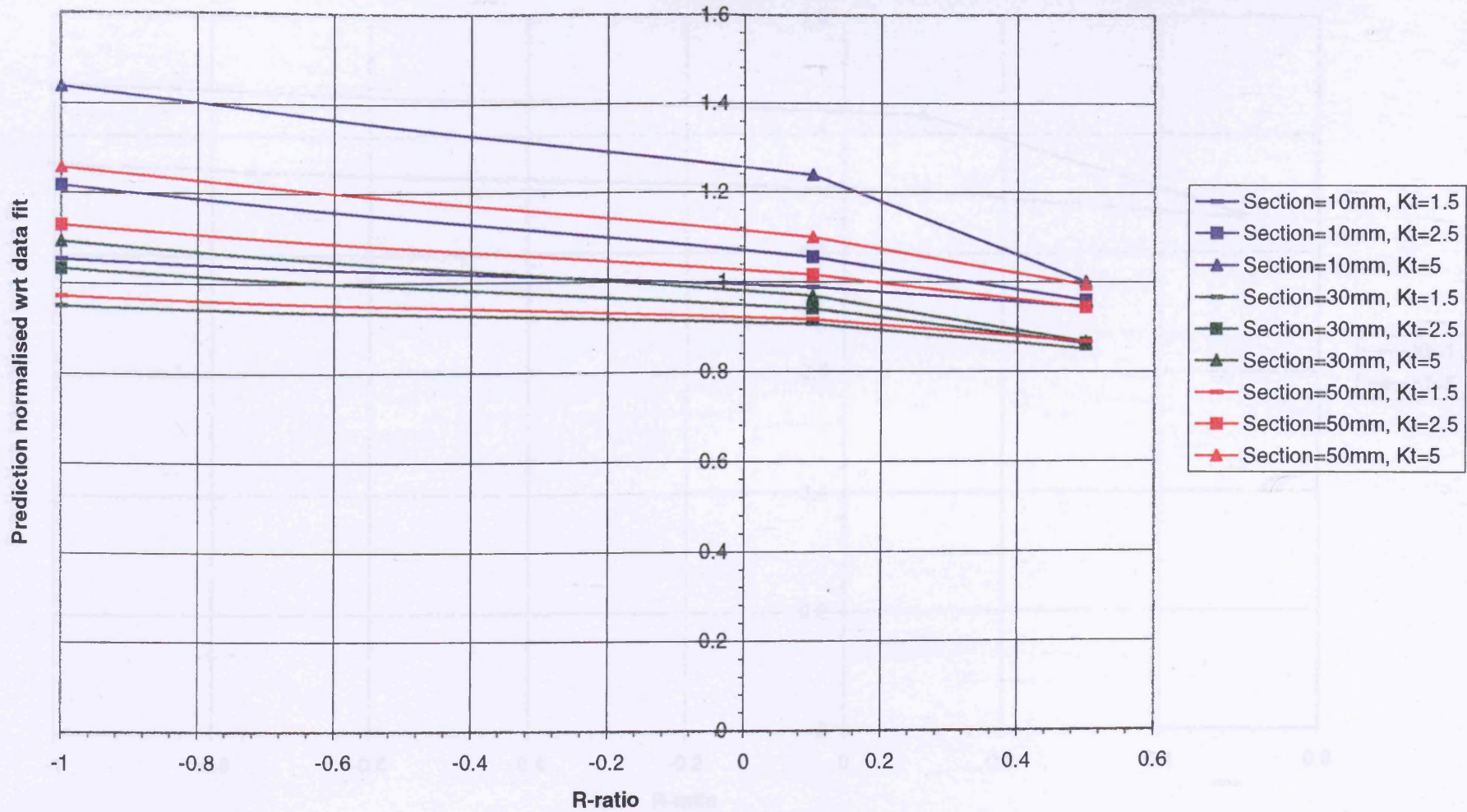


Figure 6.127 Grade 350 Grey Iron: Normalised Predictions of Fatigue Strength using Smith's Threshold Model for Various Kt Values (Normalisation wrt Curve Fit to Data) - 30mm Cast section

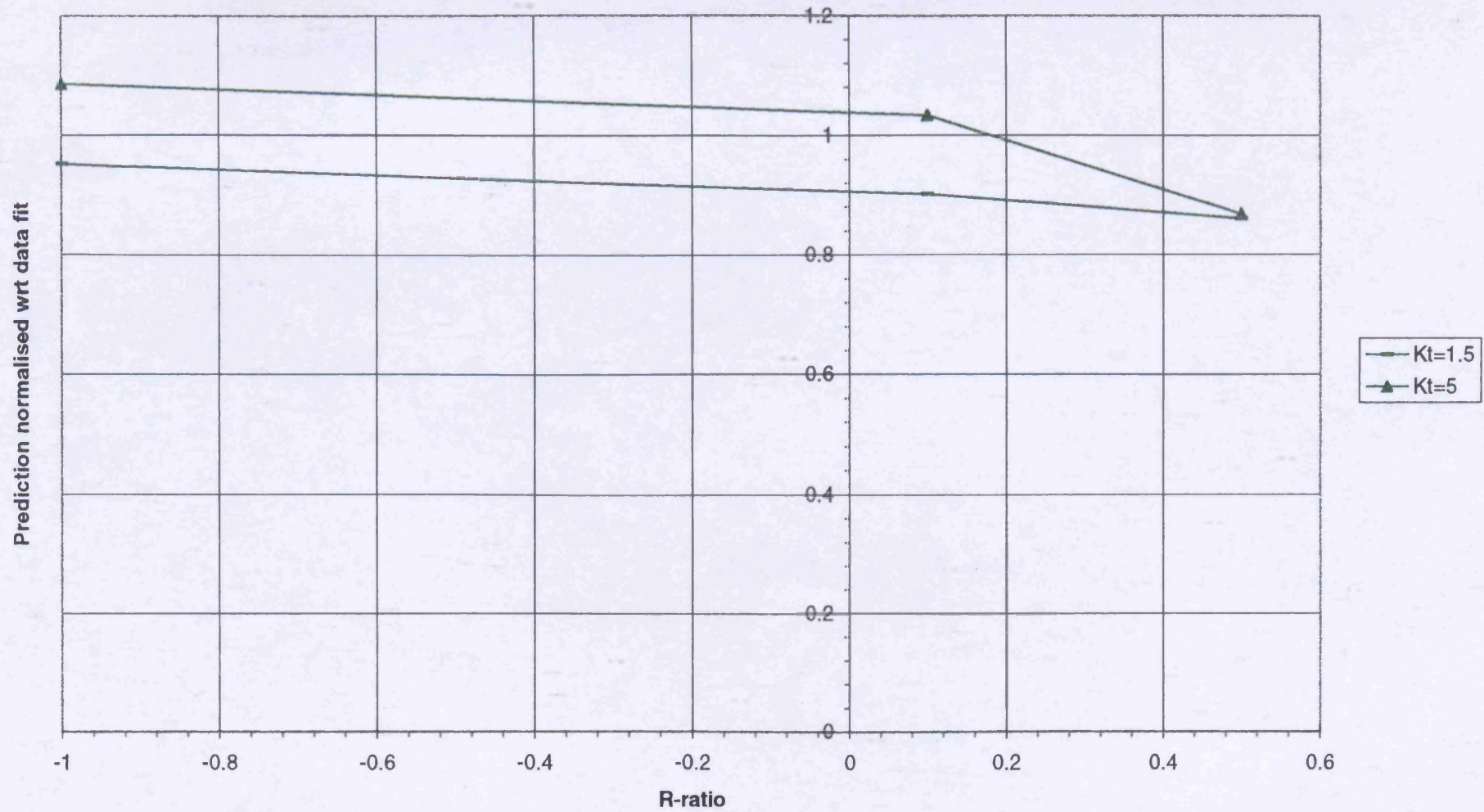


Figure 6.128 Grade 400/18 SG Iron: Normalised Predictions of Fatigue Strength using Smith's Threshold Model for Various Kt Values and Section Sizes (Normalisation w.r.t. Curve Fit to Data)

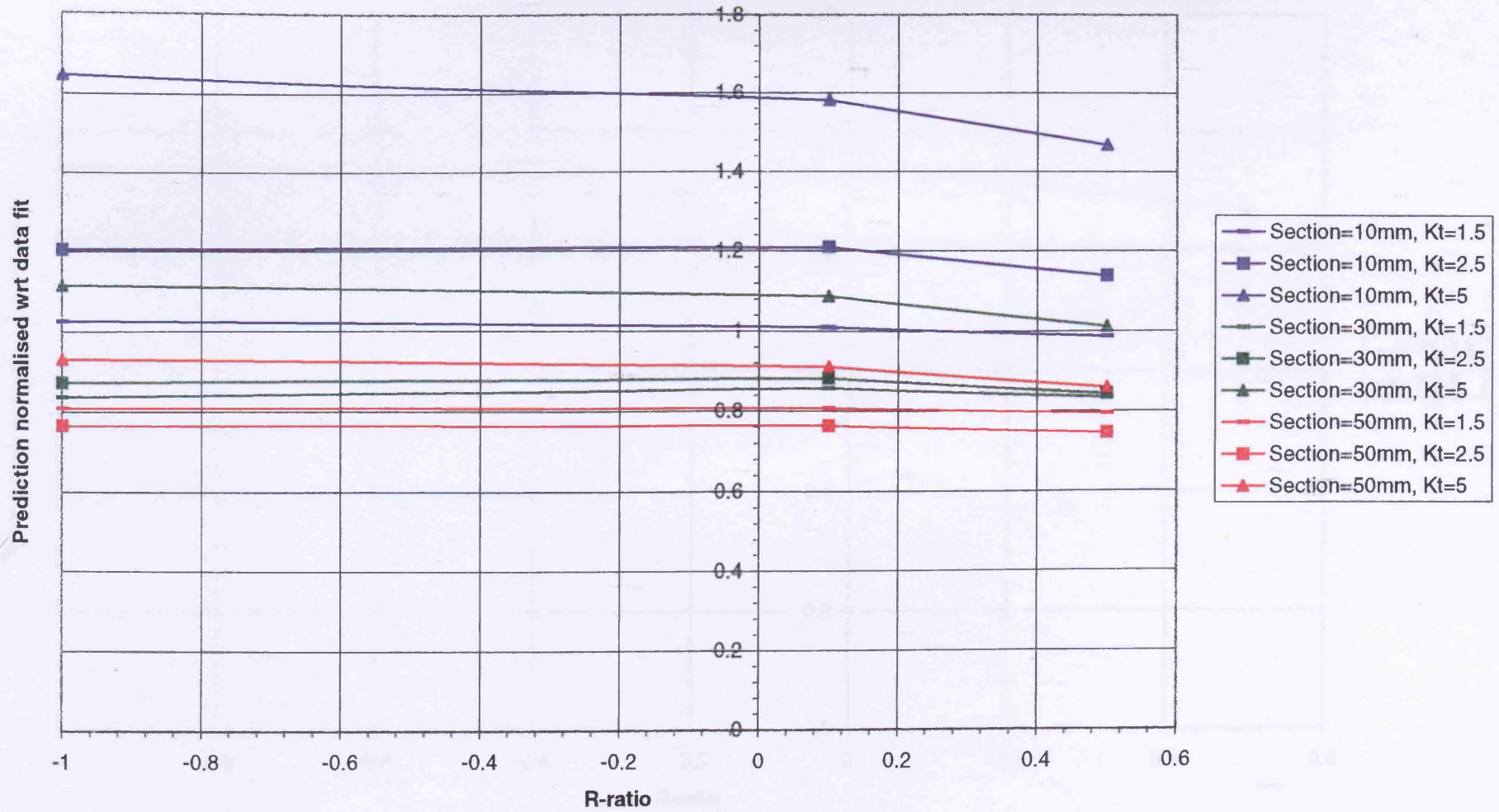


Figure 6.129 Grade 500/7 SG Iron: Normalised Predictions of Fatigue Strength using Smith's Threshold Model for Various Kt Values (Normalisation wrt Curve Fit to Data) - 30mm Cast section

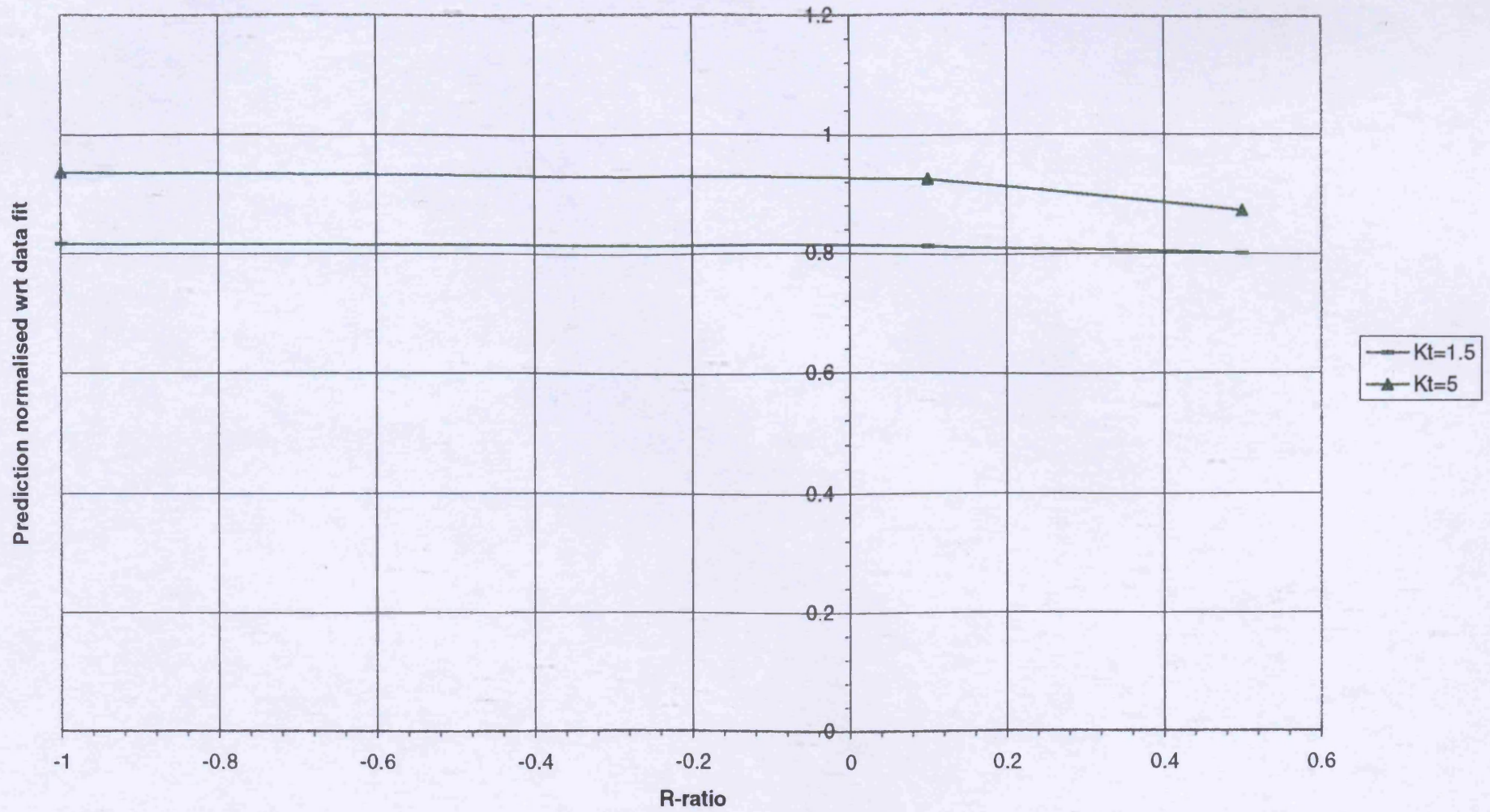
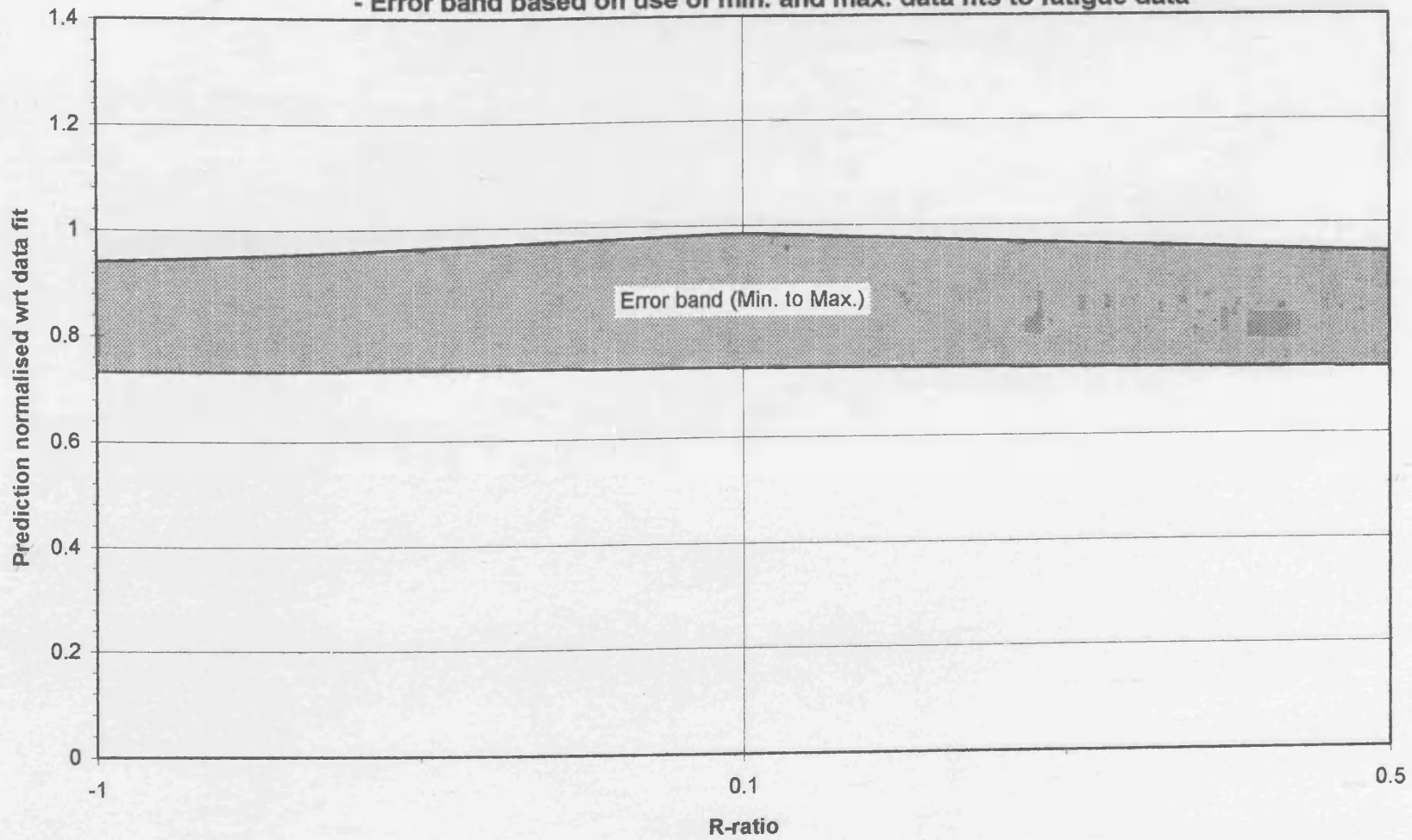


Chart 400 Error band (Kt=1.5)

Figure 6.130 Grade 400/18 SG Iron: Normalised Predictions of Fatigue Strength
(Kt=1.5, Section=30mm) using Smith's Threshold Model (Normalisation w.r.t. Curve Fit to Data)
- Error band based on use of min. and max. data fits to fatigue data



**Figure 6.131 Grade 400/18 SG Iron: Normalised Predictions of Fatigue Strength
(Kt=2.5, Section=30mm) using Smith's Threshold Model (Normalisation w.r.t. Curve Fit to Data)
- Error band based on use of min. and max. data fits to fatigue data**

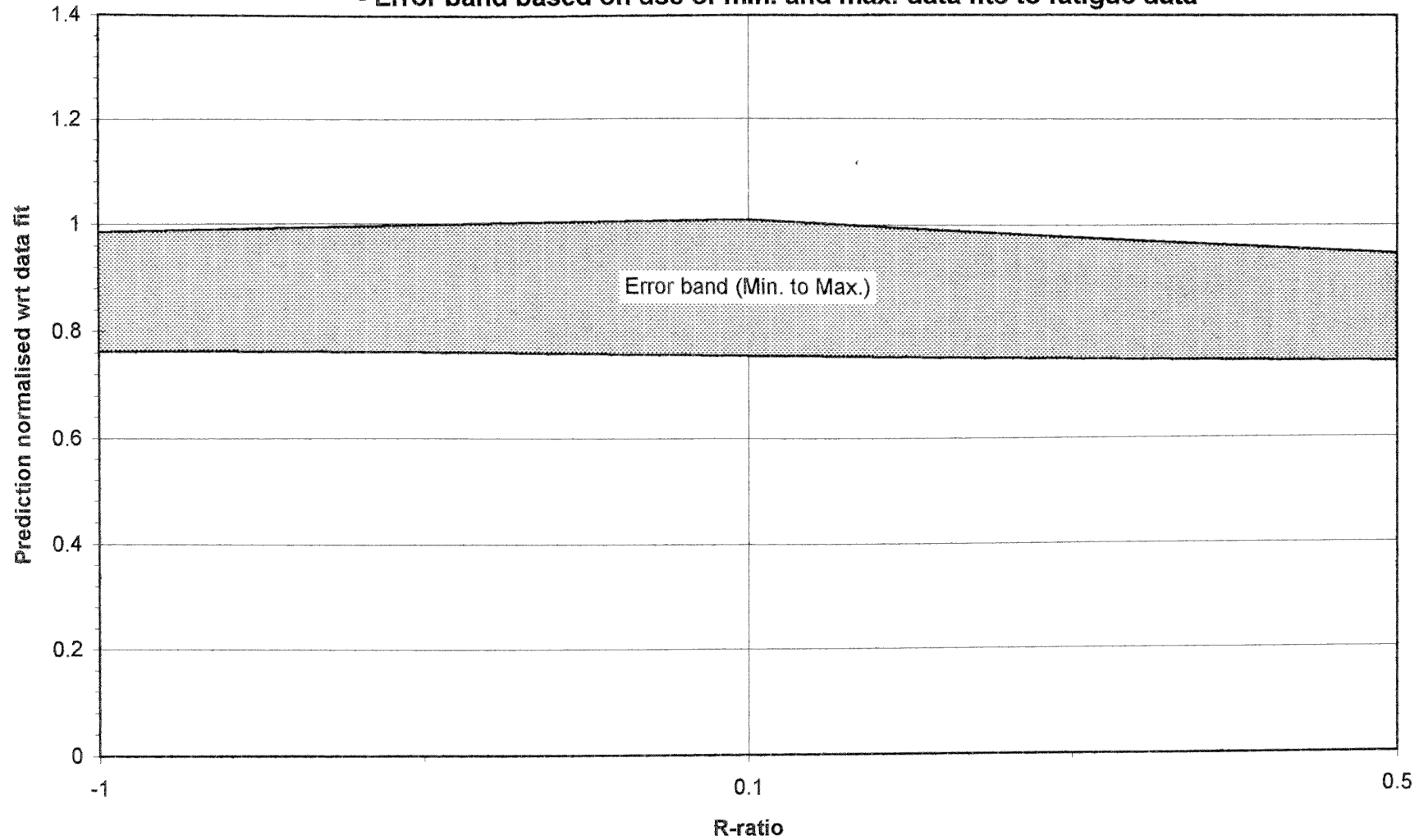


Figure 6.132 Grade 400/18 SG Iron: Normalised Predictions of Fatigue Strength
(Kt=5.0, Section=30mm) using Smith's Threshold Model (Normalisation w.r.t. Curve Fit to Data)
- Error band based on use of min. and max. data fits to fatigue data

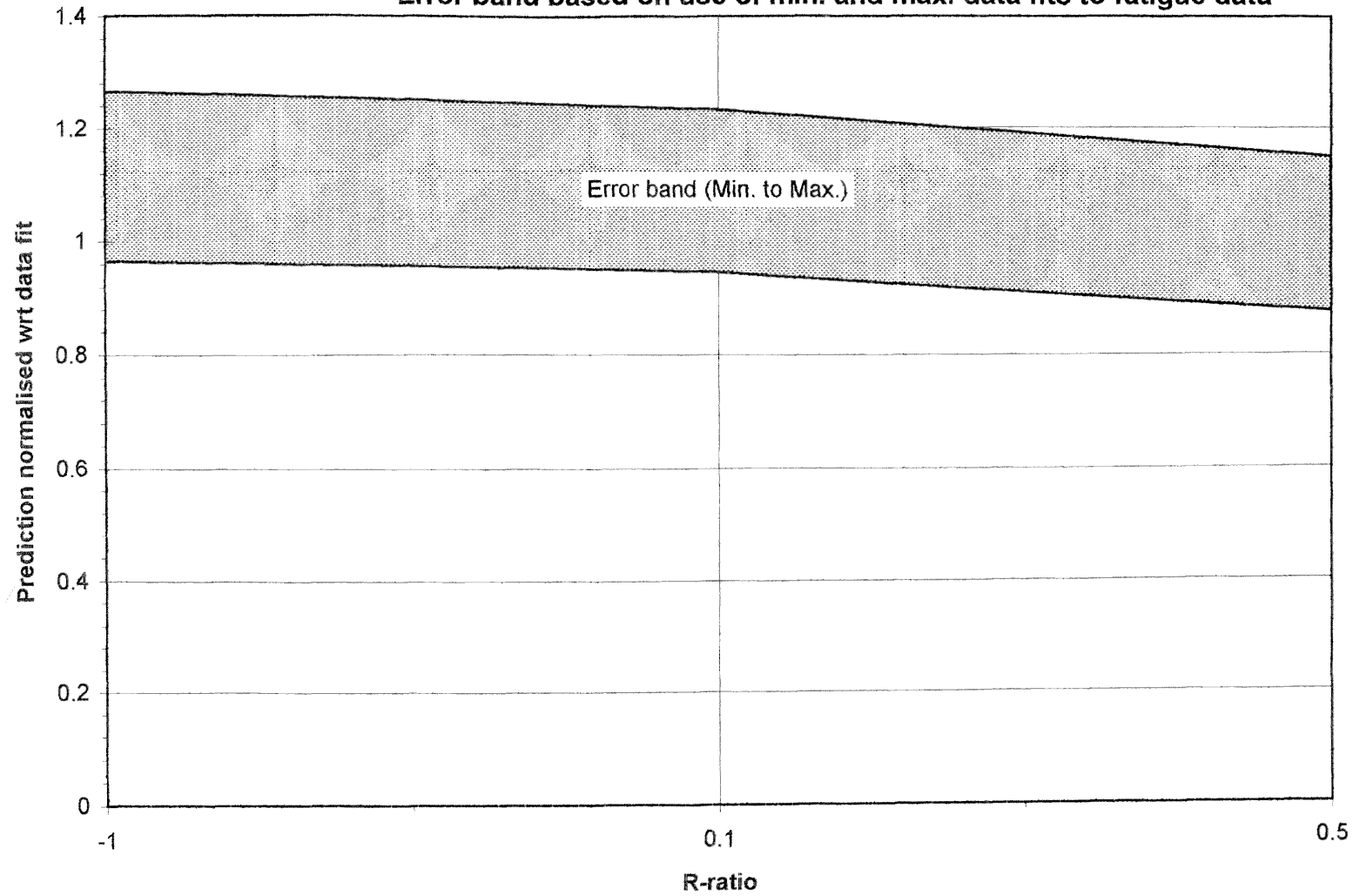


Figure 6.133 Grade 250 Grey Iron: Normalised Predictions of Fatigue Strength using Smith's Threshold Model for Various Kt Values and Section Sizes (Normalisation w.r.t. Local Fatigue Limit Estimates)

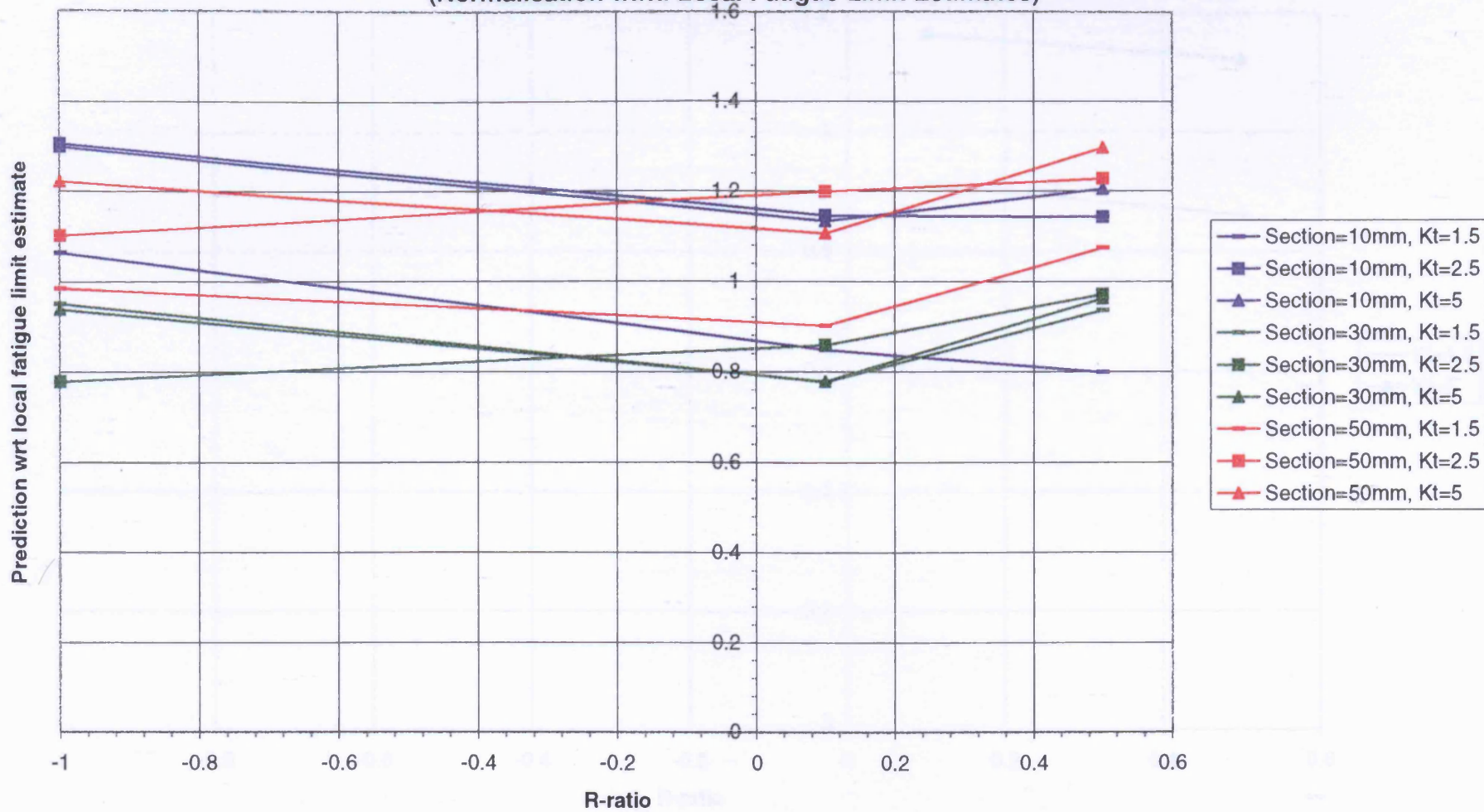


Figure 6.134 Grade 350 Grey Iron: Normalised Predictions of Fatigue Strength using Smith's Threshold Model for Various Kt Values and Section Sizes (Normalisation w.r.t. Local Fatigue Limit Estimates)

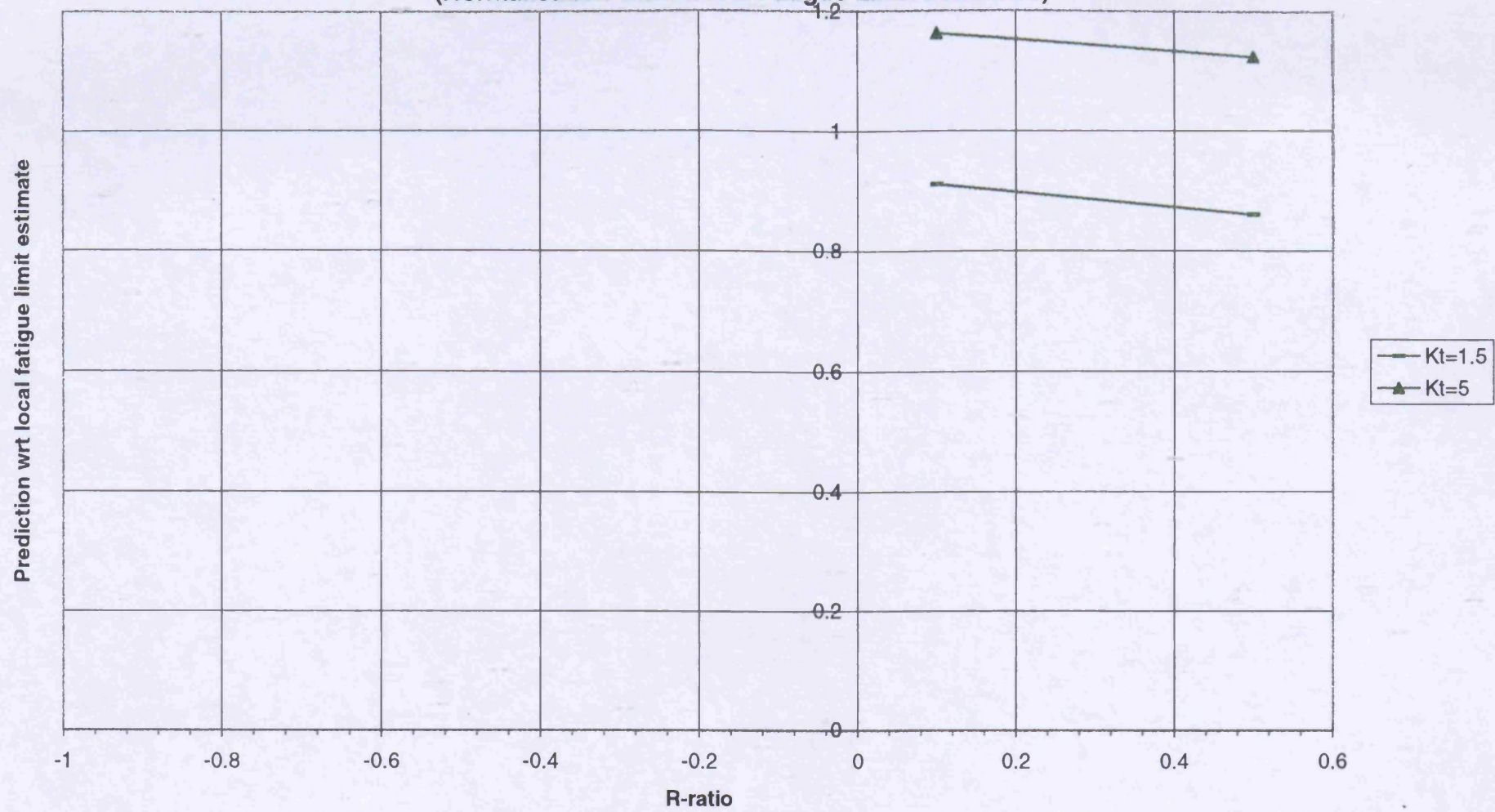


Figure 6.135 Grade 400/18 SG Iron: Normalised Predictions of Fatigue Strength using Smith's Threshold Model for Various Kt Values and Section Sizes
(Normalisation w.r.t. Local Fatigue Limit Estimates)

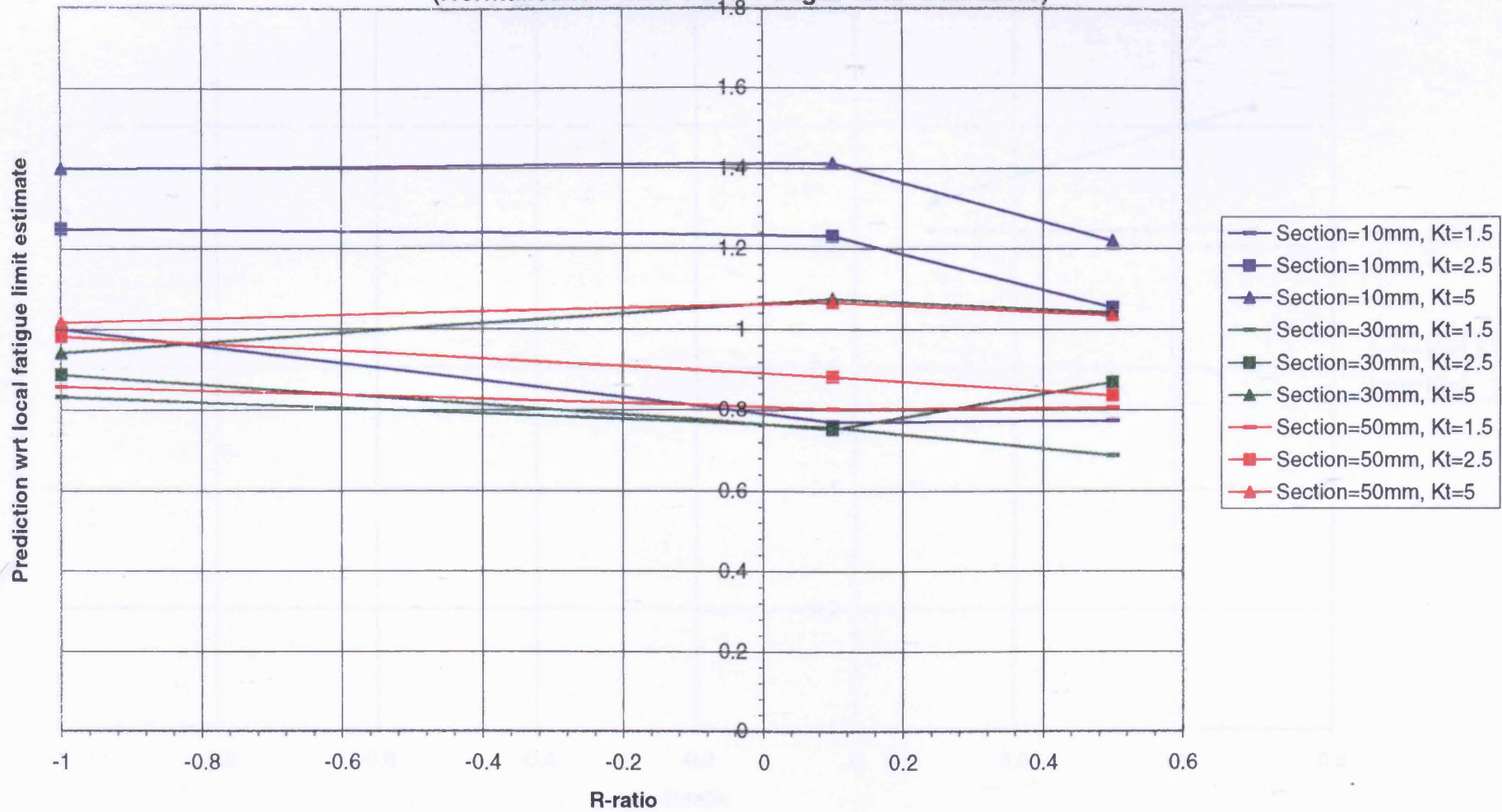


Figure 6.136 Grade 500/7 SG Iron: Normalised Predictions of Fatigue Strength using Smith's Threshold Model for Various Kt Values and Section Sizes (Normalisation w.r.t. Local Fatigue Limit Estimates)

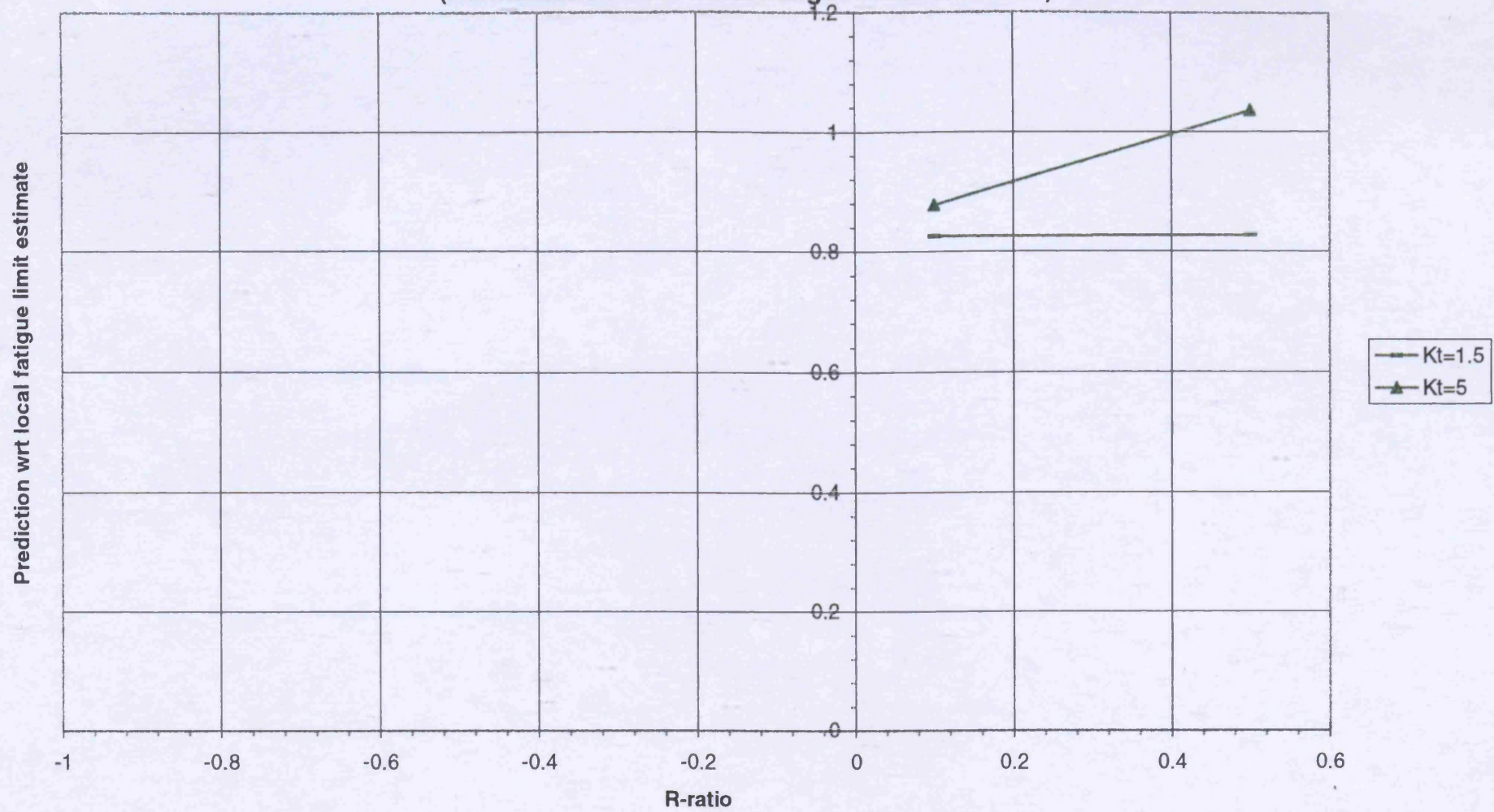


Figure 6.137 Grade 250 Grey Iron: Normalised Predictions of Fatigue Strength using El Haddad's Threshold Model for Various Kt Values and Section Sizes (Normalisation w.r.t. Curve Fit to Data)

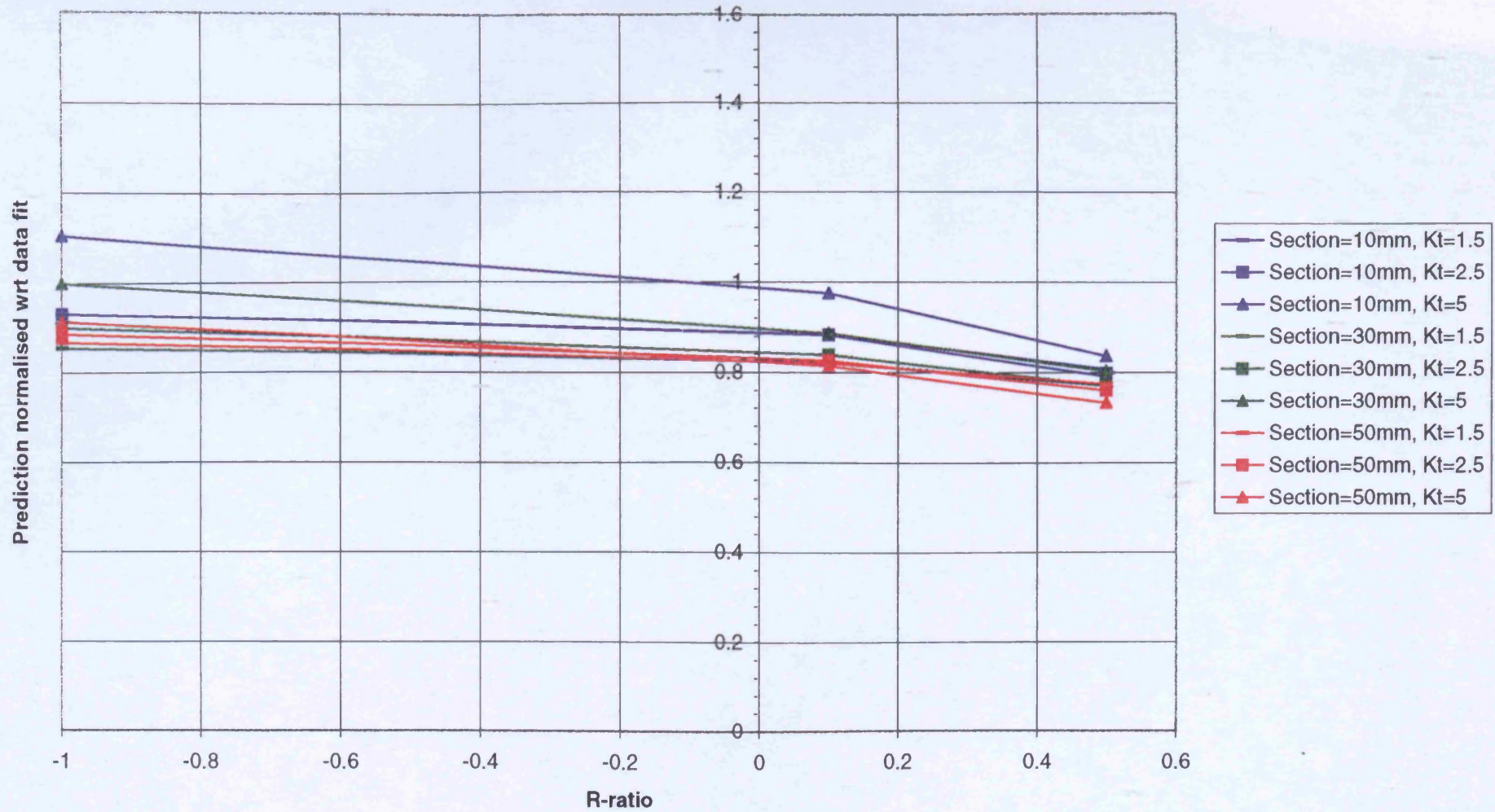


Figure 6.138 Grade 350 Grey Iron: Normalised Predictions of Fatigue Strength using El Haddad's Threshold Model for Various Kt Values (Normalisation wrt Curve Fit to Data) - 30mm Cast section

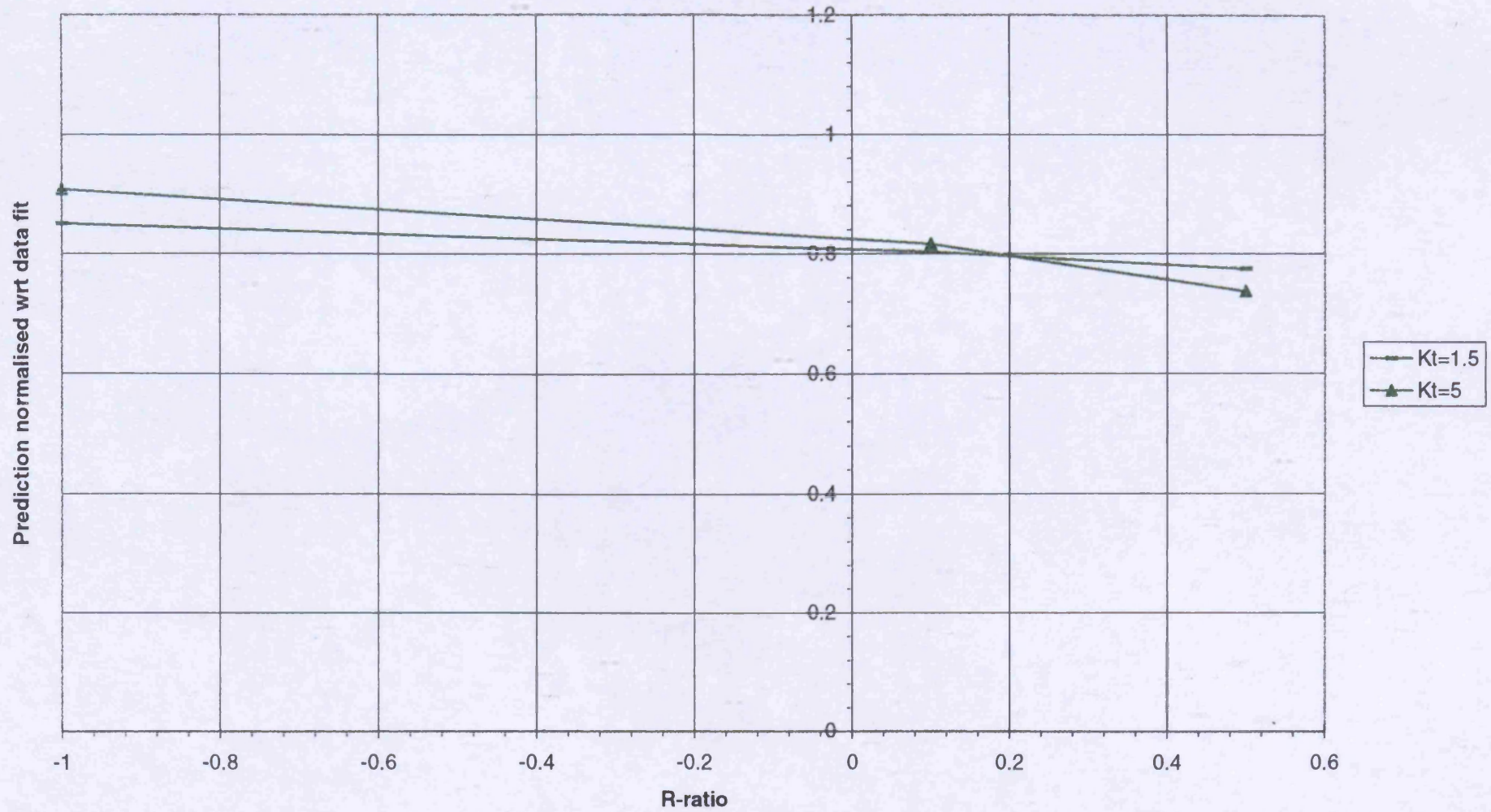


Figure 6.139 Grade 400/18 Grey Iron: Normalised Predictions of Fatigue Strength - El Haddad's Threshold Model for Various Kt Values (Normalisation wrt Curve Fit to Data) - 30mm Cast section

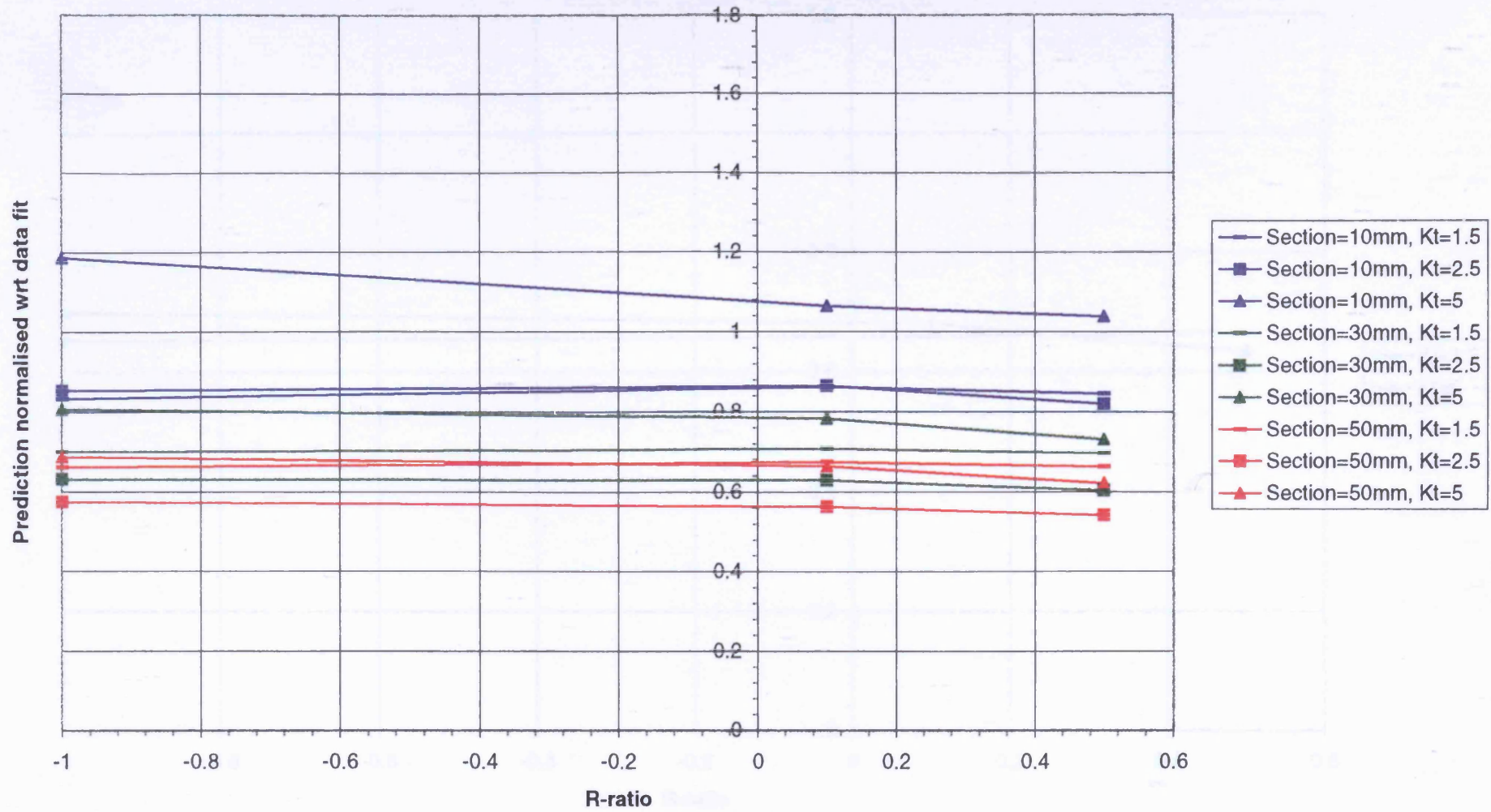


Figure 6.140 Grade 500/7 SG Iron: Normalised Predictions of Fatigue Strength - El Haddad's Threshold Model for Various Kt Values (Normalisation wrt Curve Fit to Data) - 30mm Cast section

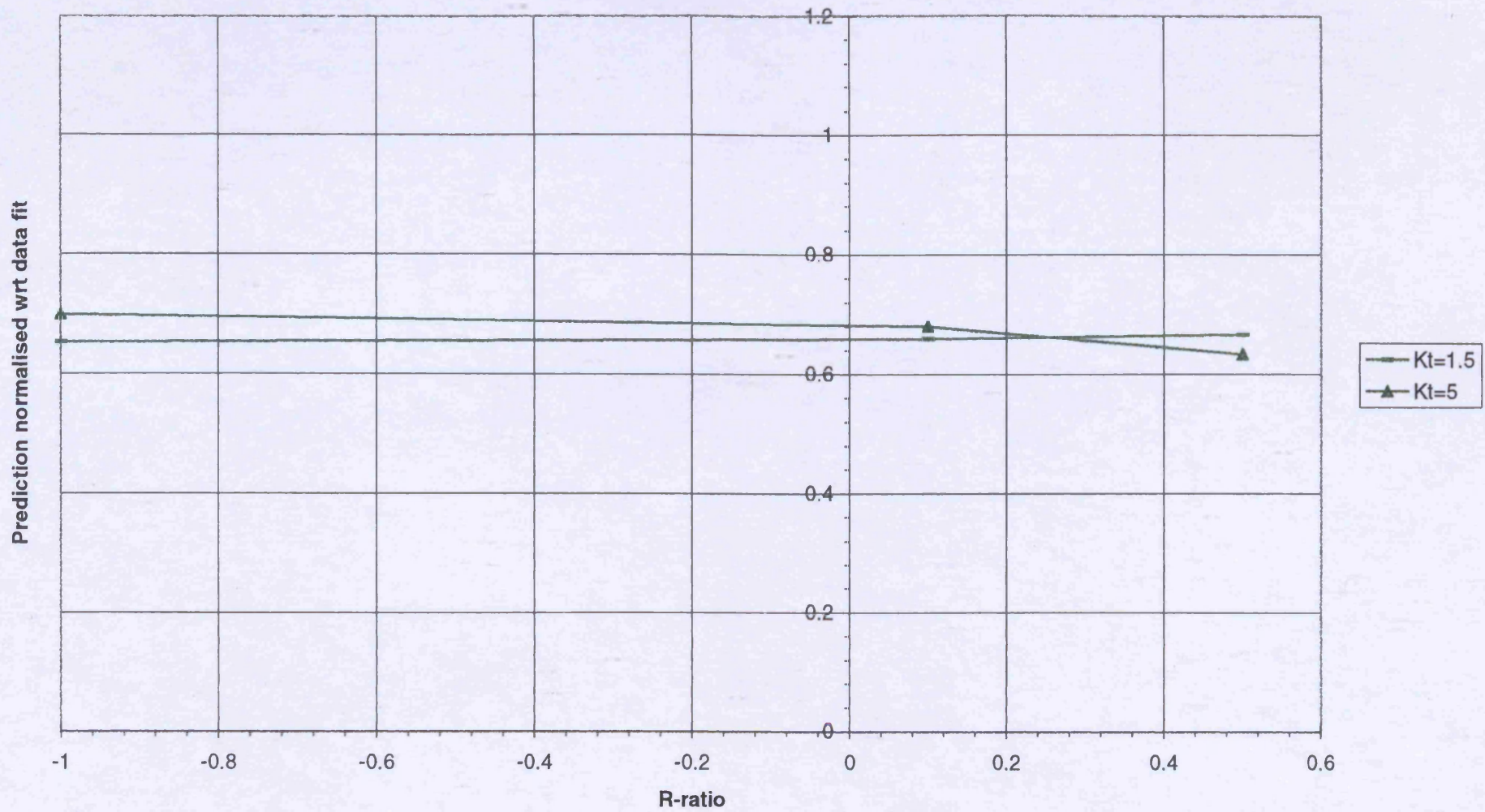


Figure 6.141 Grade 250 Grey Iron: Normalised Predictions of Fatigue Strength - El Haddad's Threshold Model for Various Kt Values and Section Sizes (Normalisation w.r.t. Local Fatigue Limit Estimates)

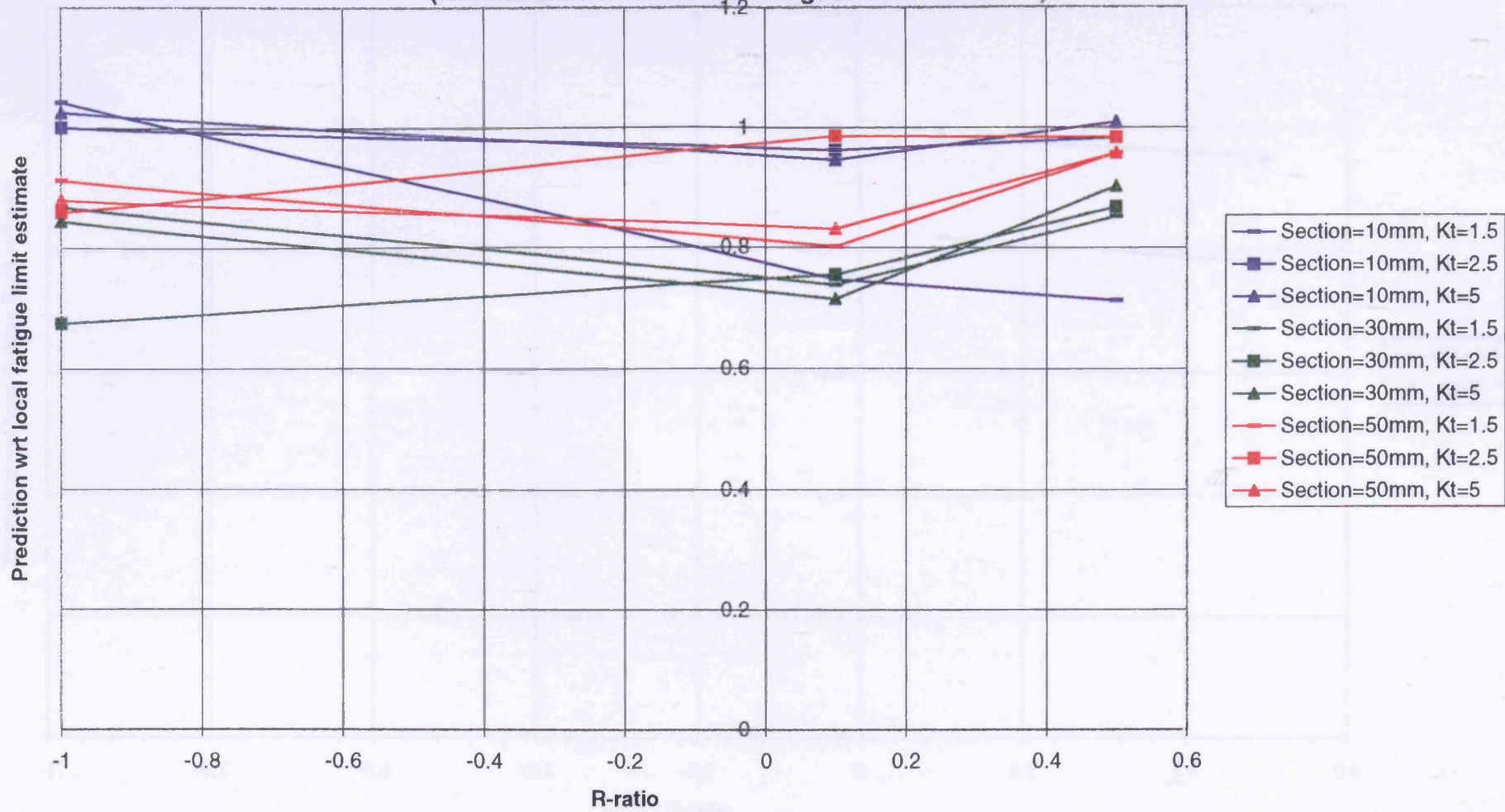
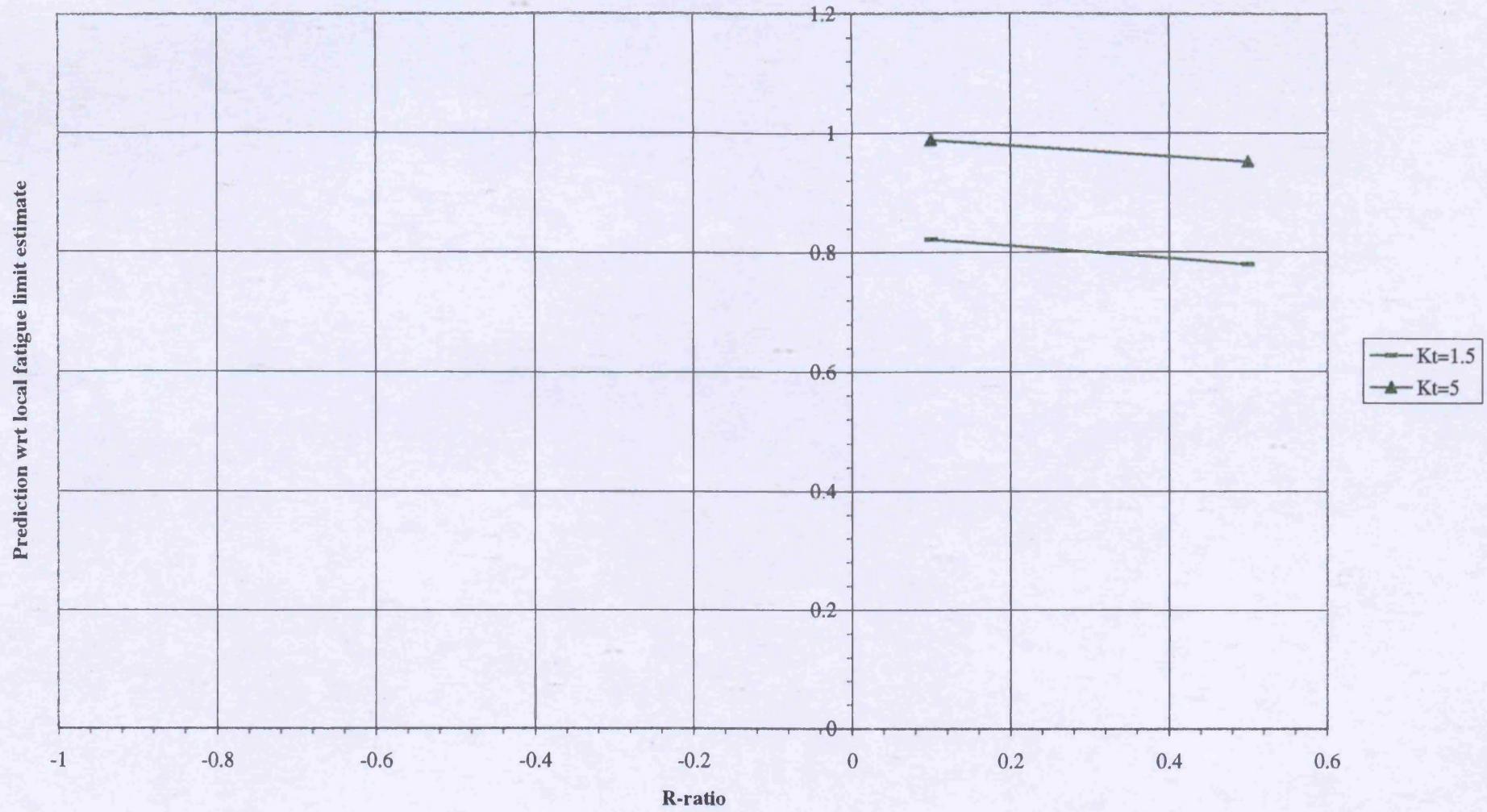


Figure 6.142 Grade 350 Grey Iron: Normalised Predictions of Fatigue Strength - El Haddad's Threshold Model for Various Kt Values - 30mm Section Size (Normalisation w.r.t. Local Fatigue Limit Estimates)



**Figure 6.143 Grade 400/18 SG Iron: Normalised Predictions of Fatigue Strength - El Haddad's Threshold
Model for Various Kt Values and Section Sizes
(Normalisation w.r.t. Local Fatigue Limit Estimates)**

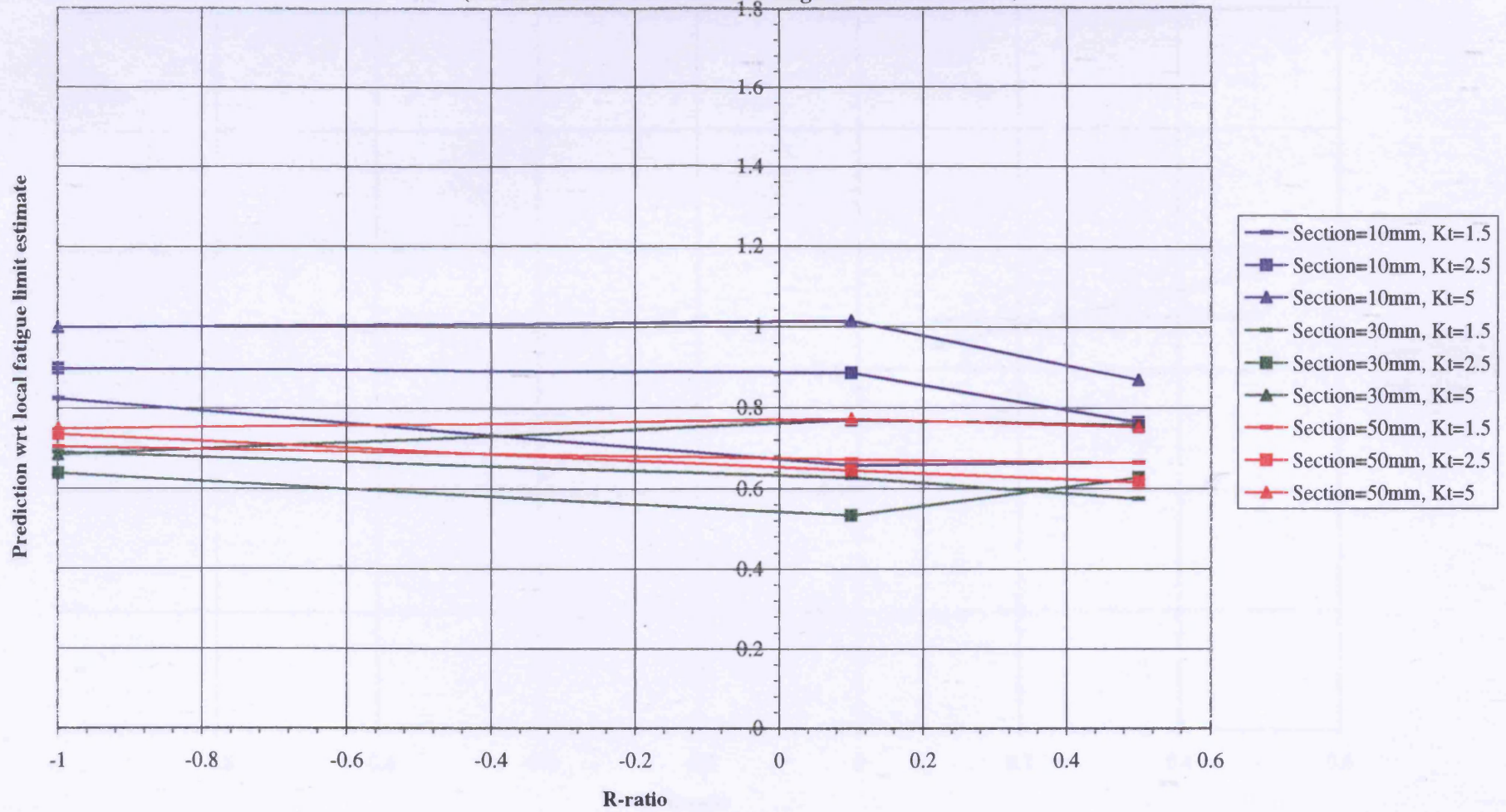


Figure 6.144 Grade 500/7 SG Iron: Normalised Predictions of Fatigue Strength - El Haddad's Threshold Model for Various Kt Values - 30mm Section Size (Normalisation w.r.t. Local Fatigue Limit Estimates)

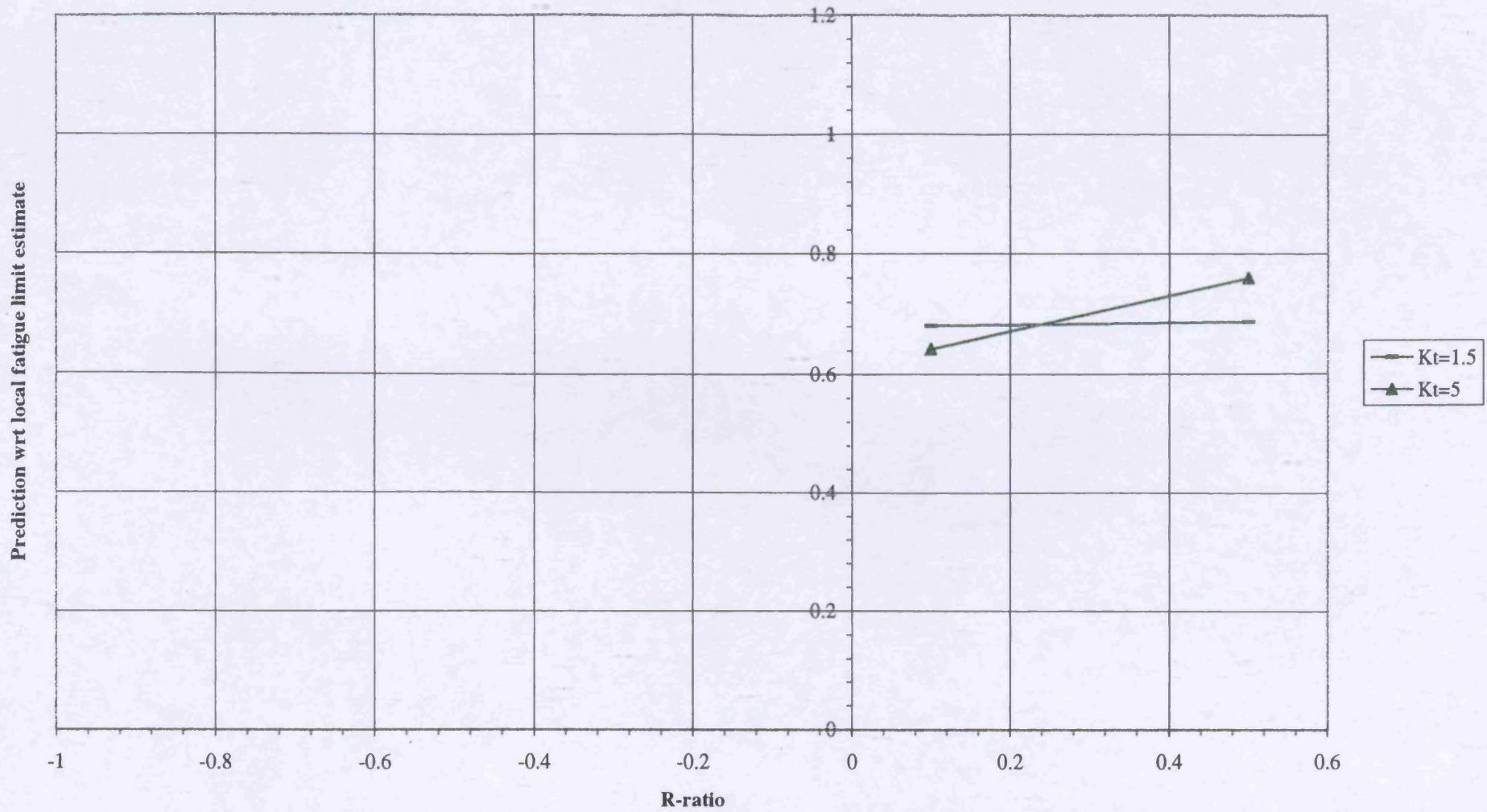


Figure 6.138 Grade 350 Grey Iron: Normalised Predictions of Fatigue Strength using El Haddad's Threshold Model for Various Kt Values (Normalisation wrt Curve Fit to Data) - 30mm Cast section

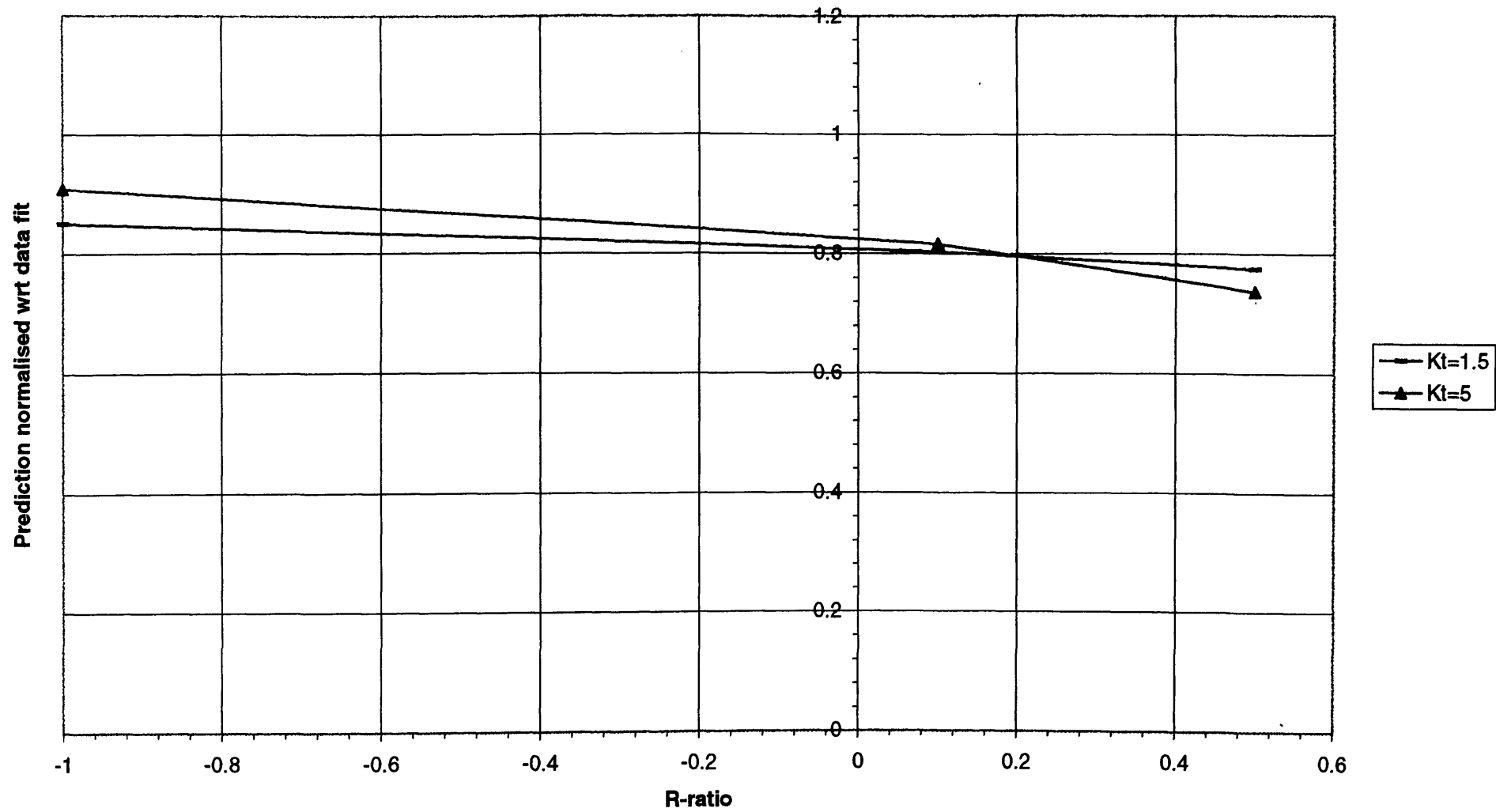


Figure 6.139 Grade 400/18 Grey Iron: Normalised Predictions of Fatigue Strength - El Haddad's Threshold Model for Various Kt Values (Normalisation wrt Curve Fit to Data) - 30mm Cast section

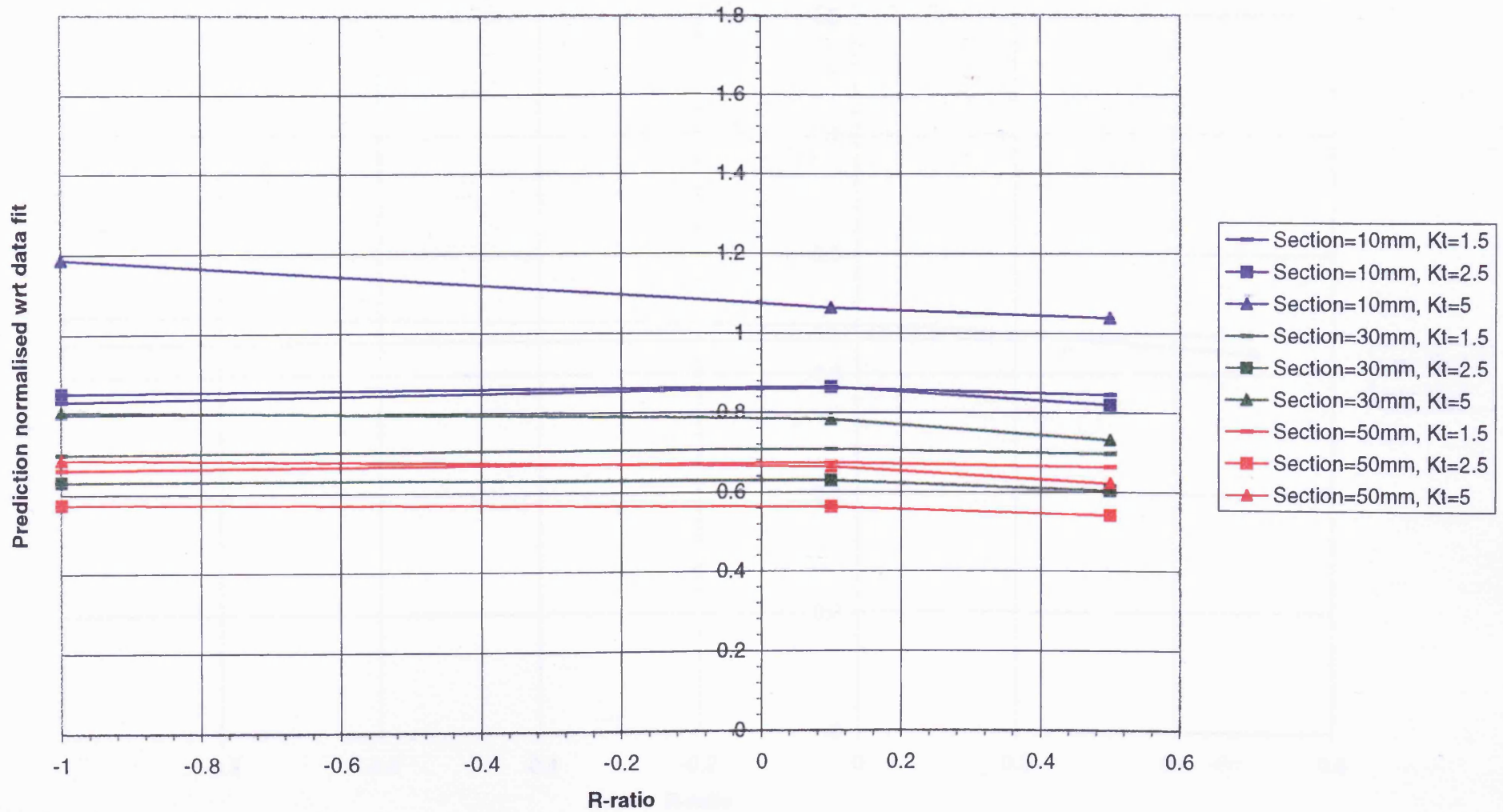


Figure 6.140 Grade 500/7 SG Iron: Normalised Predictions of Fatigue Strength - El Haddad's Threshold Model for Various Kt Values (Normalisation wrt Curve Fit to Data) - 30mm Cast section

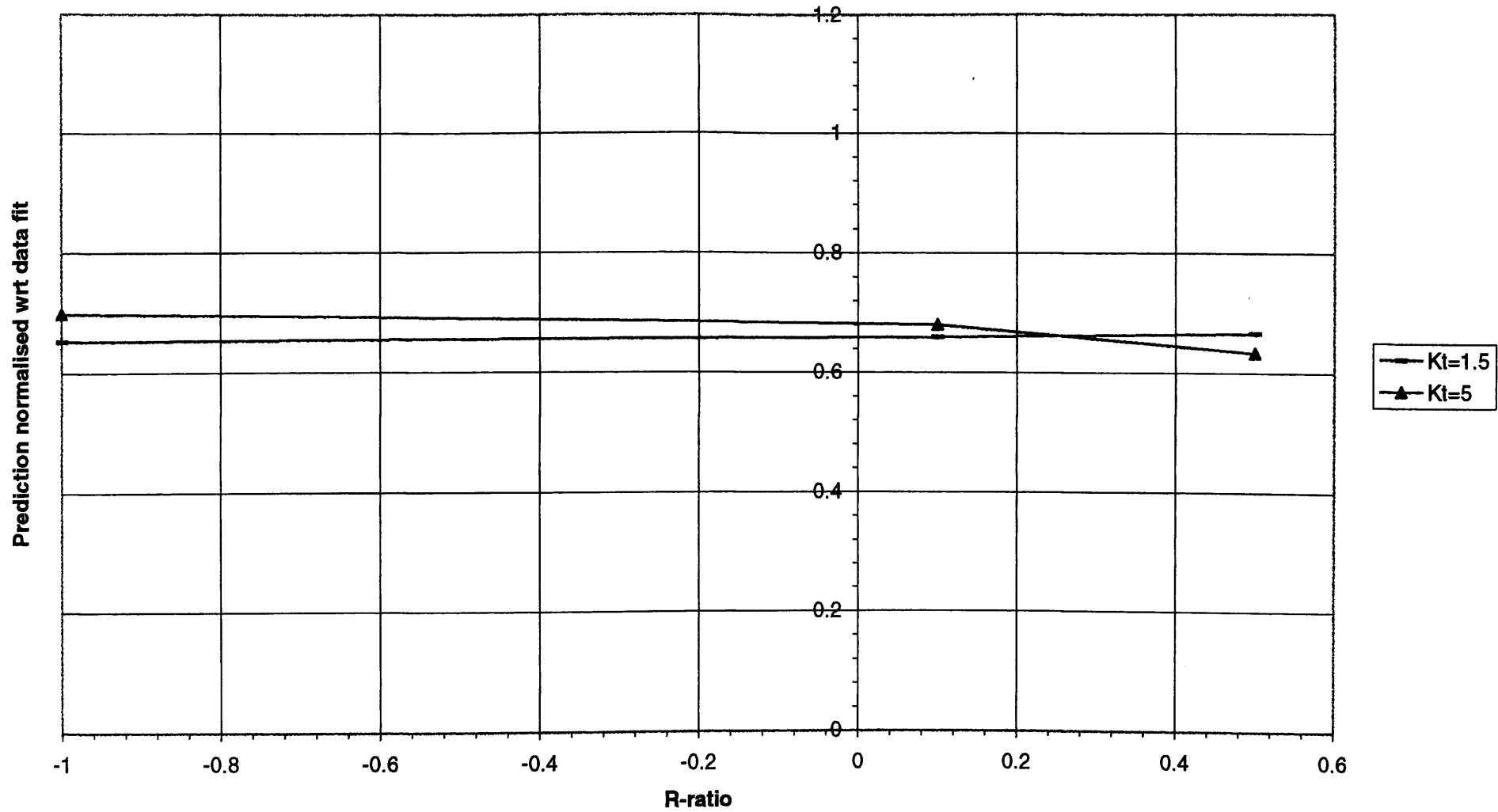


Figure 6.141 Grade 250 Grey Iron: Normalised Predictions of Fatigue Strength - El Haddad's Threshold Model for Various Kt Values and Section Sizes
(Normalisation w.r.t. Local Fatigue Limit Estimates)

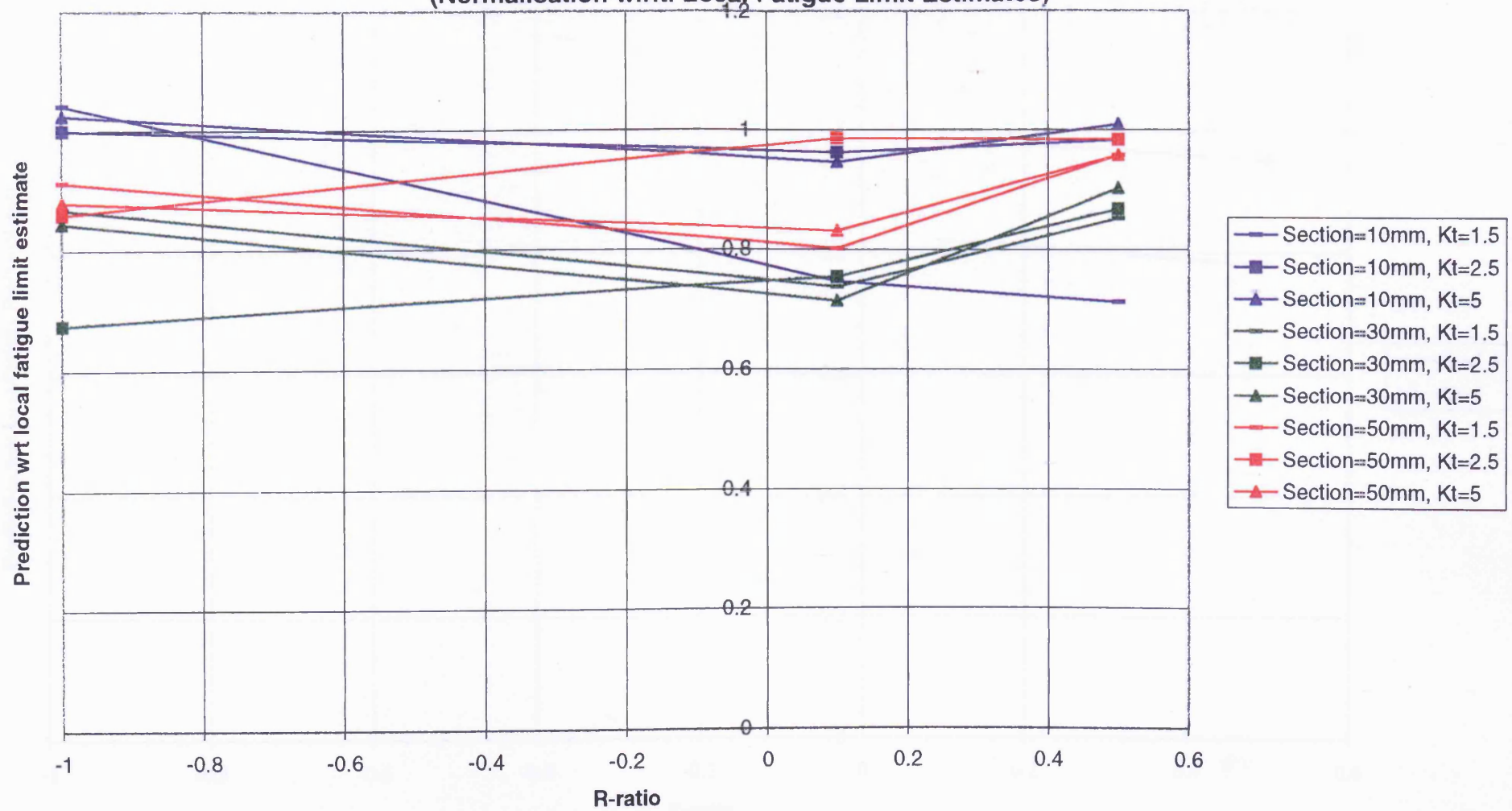


Figure 6.142 Grade 350 Grey Iron: Normalised Predictions of Fatigue Strength - El Haddad's Threshold Model for Various Kt Values - 30mm Section Size (Normalisation w.r.t. Local Fatigue Limit Estimates)

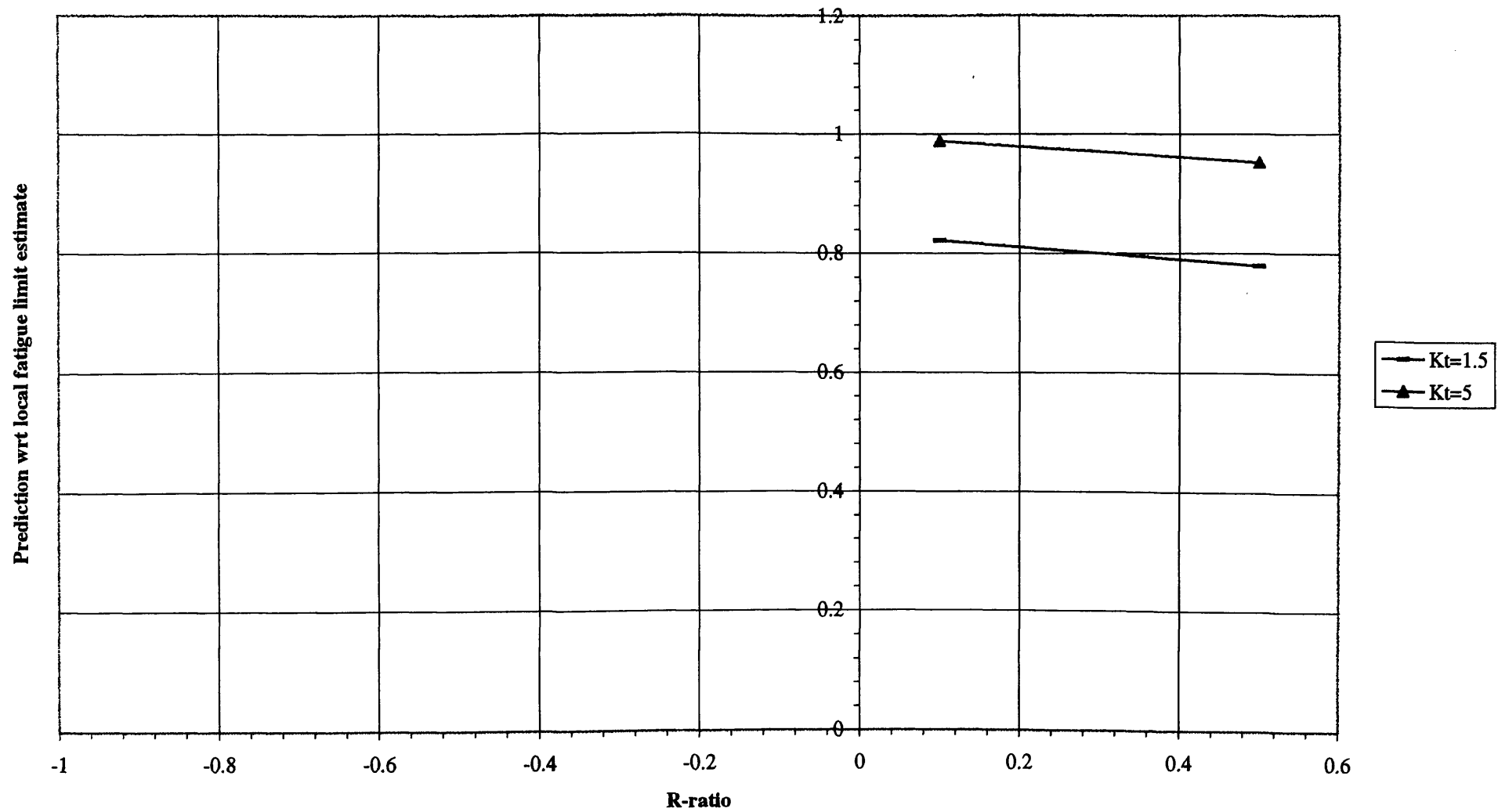


Figure 6.143 Grade 400/18 SG Iron: Normalised Predictions of Fatigue Strength - El Haddad's Threshold
 Model for Various Kt Values and Section Sizes
 (Normalisation w.r.t. Local Fatigue Limit Estimates)

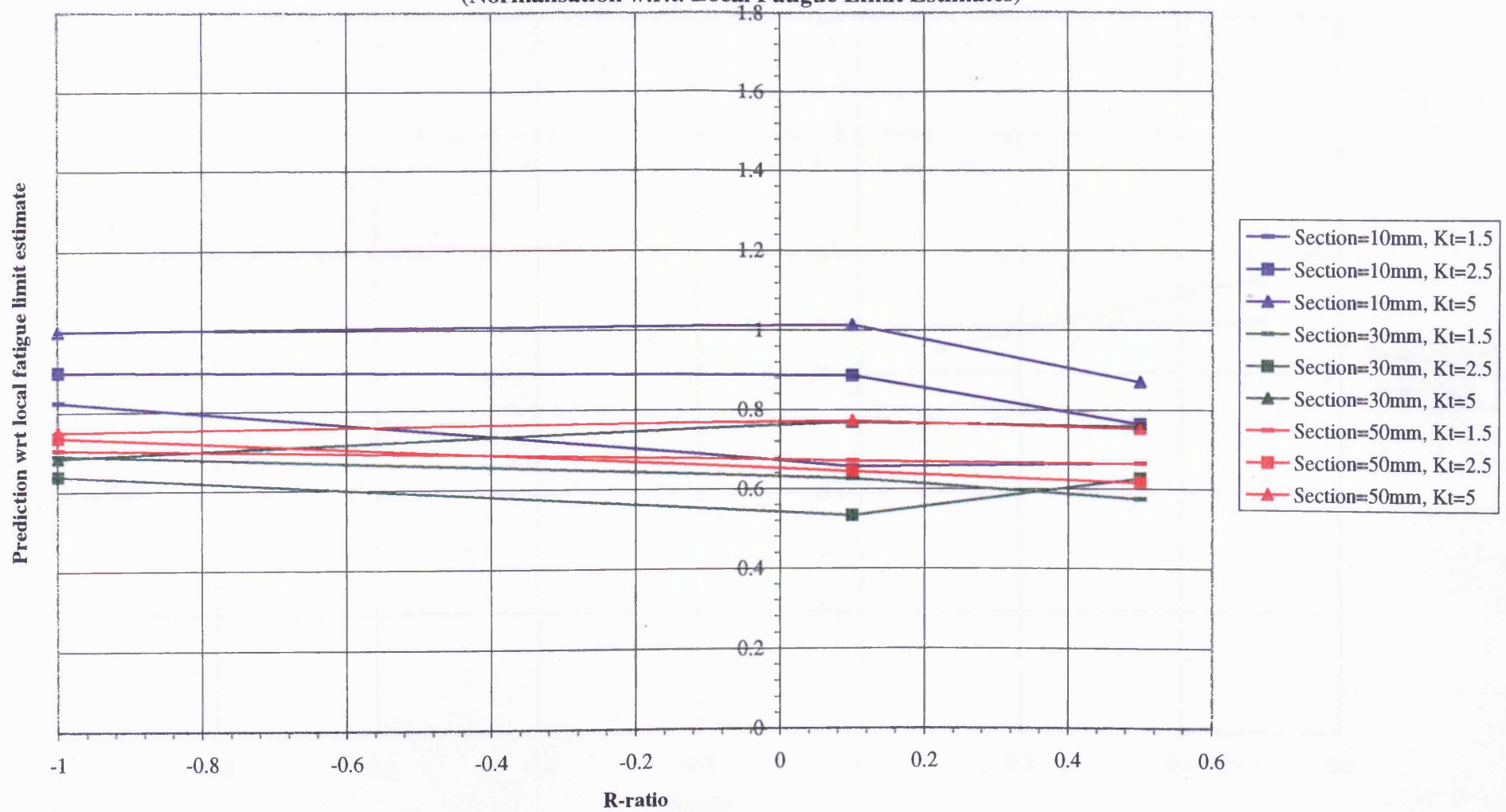


Figure 6.144 Grade 500/7 SG Iron: Normalised Predictions of Fatigue Strength - El Haddad's Threshold Model for Various Kt Values - 30mm Section Size (Normalisation w.r.t. Local Fatigue Limit Estimates)

